# Entscheidungen der Verfassungsgerichte der Länder

Xinggui Gu, Ben Zhong Tang (Eds.)
**Aggregation-Induced Emission**

## Also of Interest

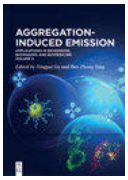


*Aggregation-Induced Emission*.
Applications in Biosensing,
Bioimaging and Biomedicine - Volume 2
Xinggui Gu, Ben Zhong Tang (Eds.), 2022
ISBN 978-3-11-067298-5, e-ISBN 978-3-11-067307-4


*Biosensors*.
*Fundamentals and Applications*
Chandra Mouli Pandey und Bansi Dhar Malhotra, 2019
ISBN 978-3-11-063780-9, e-ISBN 978-3-11-064108-0


*Metal Ions in Bio-Imaging Techniques*
Astrid Sigel, Eva Freisinger, Roland K.O. Sigel (Eds.), 2021
ISBN 978-3-11-068556-5, e-ISBN 978-3-11-068570-1

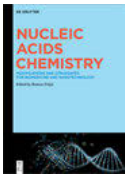


*Nucleic Acids Chemistry*.
*Modifications and Conjugates for Biomedicine*
*and Nanotechnology*
Ramon Eritja, 2021
ISBN 978-3-11-063579-9, e-ISBN 978-3-11-063953-7

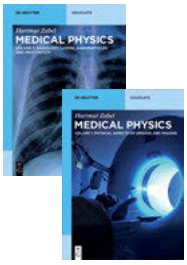


*Medical Physics*
Hartmut Zabel, 2017
*Volume 1: Physical Aspects of Organs and Imaging*
ISBN 978-3-11-037281-6, e-ISBN 978-3-11-037283-0
*Volume 2: Radiology, Lasers, Nanoparticles and Prosthetics*
ISBN 978-3-11-055310-9, e-ISBN 978-3-11-055311-6

# Aggregation-Induced Emission

Applications in Biosensing, Bioimaging and Biomedicine - Volume 1

Edited by
Xinggui Gu and Ben Zhong Tang

DE GRUYTER

**Editors**
**Prof. Xinggui Gu**
Beijing Advanced Innovation Center for Soft
Matter Science and Engineering,
Beijing University of Chemical Technology,
100029, Beijing,
People's Republic of China
guxinggui@mail.buct.edu.cn

**Prof. Ben Zhong Tang**
Shenzhen Institute of Aggregate Science and Technology,
School of Science and Engineering,
The Chinese University of Hong Kong (Shenzhen),
Shenzhen 518172,
People's Republic of China
tangbenz@cuhk.edu.cn

ISBN 978-3-11-067210-7
e-ISBN (PDF) 978-3-11-067222-0
e-ISBN (EPUB) 978-3-11-067234-3

**Library of Congress Control Number: 2021951722**

**Bibliographic information published by the Deutsche Nationalbibliothek**
The Deutsche Nationalbibliothek lists this publication in the Deutsche Nationalbibliografie; detailed bibliographic data are available on the Internet at http://dnb.dnb.de.


Typesetting: Integra Software Services Pvt. Ltd.
Printing and binding: CPI books GmbH, Leck

www.degruyter.com

# Contents

# Contributing authors

**Engui Zhao**
School of Science
Harbin Institute of Technology
Shenzhen, HIT Campus of University Town
Shenzhen 518055
People's Republic of China

**Hui Li**
Beijing Advanced Innovation Center for Soft Matter Science and Engineering
College of Materials Science and Engineering
Beijing University of Chemical Technology
Beijing 100029
People's Republic of China

**Xinggui Gu**
Beijing Advanced Innovation Center for Soft Matter Science and Engineering
College of Materials Science and Engineering
Beijing University of Chemical Technology
Beijing 100029
People's Republic of China
guxinggui@mail.buct.edu.cn

**Ben Zhong Tang**
Shenzhen Institute of Aggregate Science and Technology
School of Science and Engineering
The Chinese University of Hong Kong (Shenzhen)
Shenzhen 518172
People's Republic of China
tangbenz@cuhk.edu.cn

**Jing-Jing Hu**
State Key Laboratory of Biogeology and Environmental Geology
Faculty of Materials Science and Chemistry
China University of Geosciences
Wuhan 430074
People's Republic of China

**Hao Wang**
State Key Laboratory of Biogeology and Environmental Geology
Faculty of Materials Science and Chemistry
China University of Geosciences
Wuhan 430074
People's Republic of China

**Fan Xia**
State Key Laboratory of Biogeology and Environmental Geology
Faculty of Materials Science and Chemistry
China University of Geosciences
Wuhan 430074
People's Republic of China

**Xiaoding Lou**
State Key Laboratory of Biogeology and Environmental Geology
Faculty of Materials Science and Chemistry
China University of Geosciences
Wuhan 430074
People's Republic of China
louxiaoding@cug.edu.cn

**Jiao Liu**
National Center for Nanoscience and Technology (NCNST)
CAS Key Laboratory for Biomedical Effects of Nanomaterials
CAS Center for Excellence in Nanoscience
Beijing 100109
People's Republic of China
School of Pharmacy
Weifang Medical University
Weifang 261000
People's Republic of China

https://doi.org/10.1515/9783110672220-203

**Xiao Zhang**
National Center for Nanoscience and Technology (NCNST)
CAS Key Laboratory for Biomedical Effects of Nanomaterials
CAS Center for Excellence in Nanoscience
Beijing 100109
People's Republic of China
School of Pharmacy
Weifang Medical University
Weifang 261000
People's Republic of China

**Fang-ling Zhang**
National Center for Nanoscience and Technology (NCNST)
CAS Key Laboratory for Biomedical Effects of Nanomaterials
CAS Center for Excellence in Nanoscience
Beijing 100109
People's Republic of China

**Yi-ting Wang**
National Center for Nanoscience and Technology (NCNST)
CAS Key Laboratory for Biomedical Effects of Nanomaterials
CAS Center for Excellence in Nanoscience
Beijing 100109
People's Republic of China

**Yuan-yuan Gao**
School of Pharmacy
Weifang Medical University
Weifang 261000
People's Republic of China

**Tong-yi Sun**
School of Life Science and Technology
Weifang Medical University
Weifang 261000
People's Republic of China

**Li-Li Li**
National Center for Nanoscience and Technology (NCNST)
CAS Key Laboratory for Biomedical Effects of Nanomaterials
CAS Center for Excellence in Nanoscience
Beijing 100109
People's Republic of China
lill@nanoctr.cn

**Marie-Claire Giel**
Department of Chemistry and Physics
La Trobe Institute for Molecular Science
La Trobe University
Melbourne VIC 3086
Australia

**Yuning Hong**
Department of Chemistry and Physics
La Trobe Institute for Molecular Science
La Trobe University
Melbourne VIC 3086
Australia
Y.Hong@latrobe.edu.au

**Anh Tran Tam Pham**
Australia-China Joint Research Centre on Personal Health Technologies
Medical Device Research Institute
Flinders University
South Australia 5042
Australia

**Youhong Tang**
Australia-China Joint Research Centre on Personal Health Technologies
Medical Device Research Institute
Flinders University
South Australia 5042
Australia
youhong.tang@flinders.edu.au

**Na Zhao**
School of Chemistry & Chemical Engineering
Shaanxi Normal University
710119 Xi'an
People's Republic of China
nzhao@snnu.edu.cn

**Yahui Zhang**
Beijing Key Laboratory of Construction Tailorable Advanced Functional Materials and Green Applications
School of Materials Science & Engineering
Beijing Institute of Technology
Beijing 100081
People's Republic of China
Department of Chemistry
School of Science
Xihua University
Chengdu, 610039
People's Republic of China

**Zhengxu Cai**
Beijing Key Laboratory of Construction Tailorable Advanced Functional Materials and Green Applications
School of Materials Science & Engineering
Beijing Institute of Technology
Beijing 100081
People's Republic of China
caizx@bit.edu.cn

**Yuping Dong**
Beijing Key Laboratory of Construction Tailorable Advanced Functional Materials and Green Applications
School of Materials Science & Engineering
Beijing Institute of Technology
Beijing 100081
People's Republic of China
chdongyp@bit.edu.cn

**Minglun Liu**
State Key Laboratory of Coordination Chemistry
School of Chemistry and Chemical Engineering
Chemistry and Biomedicine Innovation Center (ChemBIC)
Nanjing University
Nanjing 210023
People's Republic of China

**Yuncong Chen**
State Key Laboratory of Coordination Chemistry
School of Chemistry and Chemical Engineering
Chemistry and Biomedicine Innovation Center (ChemBIC)
Nanjing University
Nanjing 210023
People's Republic of China
chenyc@nju.edu.cn

**Zijian Guo**
State Key Laboratory of Coordination Chemistry
School of Chemistry and Chemical Engineering
Chemistry and Biomedicine Innovation Center (ChemBIC)
Nanjing University
Nanjing 210023
People's Republic of China
zguo@nju.edu.cn

**Jiaxin Wang**
Key Laboratory of Functional Polymer Materials of Ministry of Education
State Key Laboratory of Medicinal Chemical Biology
Institute of Polymer Chemistry
College of Chemistry
Nankai University
Tianjin 300071
People's Republic of China

**Chunlei Zhu**
Key Laboratory of Functional Polymer Materials of Ministry of Education
State Key Laboratory of Medicinal Chemical Biology
Institute of Polymer Chemistry
College of Chemistry
Nankai University
Tianjin 300071
People's Republic of China
chunlei.zhu@nankai.edu.cn

**Miaomiao Kang**
Center for AIE Research
College of Materials Science and Engineering
Shenzhen University
Shenzhen, 518060
People's Republic of China

**Panpan Sun**
Center for AIE Research
College of Materials Science and Engineering
Shenzhen University
Shenzhen, 518060
People's Republic of China

**Dong Wang**
Center for AIE Research
College of Materials Science and Engineering
Shenzhen University
Shenzhen, 518060
People's Republic of China
wangd@szu.edu.cn

**Jiangman Sun**
Beijing Advanced Innovation Center for Soft Matter Science and Engineering
College of Materials Science and Engineering
Beijing University of Chemical Technology
Beijing 100029
People's Republic of China

Engui Zhao, Hui Li, Xinggui Gu, Ben Zhong Tang

# Chapter 1
# Introduction

As human living standard improves, healthcare and medicine have drawn increasing attention from both scientists and ordinary people, which promote the rapid development of advanced diagnostic and therapeutic techniques. Fluorescence, with the advantages of real-time imaging, high sensitivity, superb spatial and temporal resolution, and simple operation, has been employed for the development of novel diagnostic and therapeutic techniques [1, 2]. Most conventional fluorescent materials suffer from the aggregation-caused quenching (ACQ) effect, with bright emission in their dilute solutions, but weak or completely quenched fluorescence at high concentrations or in the aggregated state [3]. To avoid ACQ from taking effect, conventional fluorescent materials are mostly utilized at low concentrations, which introduce the problems of easy photobleaching, low imaging contrast, and unsatisfying therapeutic performance, and greatly hamper their widespread application in the biomedical field.

Materials with aggregation-induced emission (AIE) characteristics perfectly overcome these problems caused by the ACQ effect [3]. Since the concept of "aggregation-induced emission" was first coined by Tang in 2001 [4], investigations on AIE have been a hot topic in various research fields. Luminogens, with AIE attributes (AIEgens), exhibit no or weak emission in solutions, and intense fluorescence in the aggregated state. Thus, they break the fetters that traditional luminescent materials with ACQ properties encounter, solve the problems that bright emissions of luminogens in dilute solutions face such as weakened or quenched when the luminogens are concentrated or aggregated, and extend the real-world application of fluorescent materials in energy, health, and environment [5]. The past two decades have witnessed the blooming development of AIEgens in biological science and biomedical applications due to their unique merits of anti-quenching, high brightness, excellent

**Engui Zhao,** School of Science, Harbin Institute of Technology, Shenzhen, HIT Campus of University Town, Shenzhen, 518055, China
**Hui Li,** Beijing Advanced Innovation Center for Soft Matter Science and Engineering, College of Materials Science and Engineering, Beijing University of Chemical Technology, Beijing, 100029, China
**Xinggui Gu,** Beijing Advanced Innovation Center for Soft Matter Science and Engineering, College of Materials Science and Engineering, Beijing University of Chemical Technology, Beijing, 100029, China, e-mail: guxinggui@mail.buct.edu.cn
**Ben Zhong Tang,** Shenzhen Institute of Molecular Aggregate Science and Engineering, School of Science and Engineering, The Chinese University of Hong Kong (Shenzhen), Shenzhen, 518172, China, e-mail: tangbenz@cuhk.edu.cn

https://doi.org/10.1515/9783110672220-001

photostability, fluorescence turn-on fashion, and large Stokes shift [6–9]. These enthusiastic research efforts have resulted in many novel AIEgens with varied biomedical applications, which can be classified into three aspects of biosensor [10], bioimaging [11, 12] and biomedicine [13].

## 1.1 AIEgen-based biosensor

Many diseases are accompanied with abnormal activities and concentrations of biomarkers or biomolecules, such as nucleic acids [14], enzymes [15], metal ions [16] and bio-thiols [17]. Fluorescent biosensors are powerful analytical tools for these biological targets. Development of sensitive and selective fluorescent biosensors is of great importance, which may contribute to the early diagnosis and effective treatment of diseases. Thus, a large variety of luminogens, such as fluorescent proteins, organic dyes, and quantum dots [18–20], have been developed and utilized for sensing the quantity or activity of biological targets. In sensory applications, changes in fluorescence intensity, wavelength, or lifetime of the sensors, upon interacting with targets are the key outputs. Conventional luminogens with their rigid and coplanar molecular structures are emissive in solutions, which may result in high background fluorescence with low sensitivity, and add to the difficulty for sensor designs. In contrast, the novel AIEgens exhibit great practical benefits in sensory applications, which permit the use of dye solutions at any concentration for bioassays and enable the development of fluorescence "turn-on" biosensors by taking advantage of luminogen aggregation processes [21]. The fluorescence "turn-on" feature of AIE biosensors offers higher sensitivity and better accuracy over ACQ biosensors. Thus, a lot of outstanding AIE-active biosensors have been constructed for the detection of biomolecules and biomacromolecules, such as amino acid [22], glucose [23], ATP [24], nucleic acid [25], protease [26], and disease-related proteins [27], with the features of high sensitivity, fast response, high signal-to-noise ratio, and extremely low background fluorescence.

AIEgen-based fluorescent biosensors are commonly composed of AIE-active fluorophores and functional units. Tetraphenylethene (TPE) and tetraphenylsilole (TPS), and their modified derivatives account for a substantial portion of the fluorophores in AIE-active biosensors [28]. In sensors, the functional units play an important role in interacting with biological targets [29, 30]. Biomacromolecules, such as nucleic acids and proteins, possess excellent biocompatibility and outstanding specificity, and are frequently used as the functional units [31]. The combination of biomacromolecules and AIEgens not only endows the biosensors with high specificity but also improves the biological activity and water solubility of the probe for accurate and efficient biosensing. In the chapter, Modular Nucleic Acid-Functionalized AIEgen Probes for Biosensing Applications, we will introduce the design mechanism of modular nucleic acid-functionalized AIEgen probes (MNAPs) and their biosensing applications.

In the chapter, Peptide-AIEgen Conjugates for Biomedical Diagnosis and Bioimaging, we will discuss the design of AIEgens with various kinds of peptide modifications and their applications in biomedical diagnosis and bioimaging.

AIE-active sensors can also be constructed by taking advantages of their state transition process – when interacting with specific targets, the fluorescence of AIE-active sensors can be turned on upon switching AIEgens from the dispersive state to the aggregated state. Another widely used strategy for sensing with AIEgens is based on exploiting the reactions between the functional groups and the targets to realize the fluorescence turn-on process. In the chapter, The Application of Click Chemistry in the Design of Aggregation-Induced Emission Luminogens for Activity-Based Sensing, we will expound AIEgen-active sensors based on the mechanism of click chemistry.

Besides focusing on development of various AIEgen-based biosensors for recognizing and detecting different biomarkers, researchers also examined their feasibility in clinical practice by rigorous evaluations and experimentation. Some researchers have reported point-of-care in-vitro diagnostic (POC IVD) devices based on AIE biosensors, which greatly promote the development of AIE-based biosensors for clinical applications [32]. In the chapter, Point-of-Care in vitro Diagnostics Devices Based on Aggregation-Induced Emission Biosensors: Current Situation and Future Prospective, we will describe the current status in the development of POC IVD devices, based on luminescent materials, especially AIEgens.

## 1.2 AIEgen-based bioimaging

Cell is the constitutional and functional unit of organisms, which contains various subcellular structures and organelles, such as cell membrane, nucleus, mitochondrion, lipid droplet, lysosome, and endoplasmic reticulum [33]. These subcellular structures and organelles separate the cell into compartments, which form different biological environments, and carry out various processes for maintaining cellular homeostasis, including pH, viscosity, autophagy, mitophagy, and cellular apoptosis [11, 34]. In this sense, monitoring and understanding the morphologies, motions, and changes of microenvironment and physiological parameters in cells and subcellular organelles are of great importance for gaining insights into cell biology, pathological mechanism, and cellular responsive mechanism to therapy.

Fluorescence imaging is a ready-to-use method in biological labs with advantages of noninvasiveness, directness, and easy operation. By endowing targets with fluorescence, it increases the contrast of our targets and discriminates our targets from their background, enabling scientists to visualize biological processes. AIEgens with the properties of excellent photostability, large Stokes shift, high signal-to-noise ratio, superb resolution, and free of self-quenching effect, have thus been

extensively employed for bioimaging, such as cell tracking [35, 36], subcellular organelle imaging (mitochondrion, lipid droplets, lysosome, nuclear, etc.) [37], and microenvironment analysis (pH, viscosity, ROS and enzymes, etc.) [38–40]. In the chapters, AIEgens for Organelles Imaging and Biological Process Monitoring and AIE-active 1,3-Butadiene-Based Biosensors and Bioimagings, we will illustrate the applications of typical AIEgens in imaging organelles and monitoring their biological processes. In the chapter, AIEgens for Intracellular Microenvironment Analysis, we will show the applications of AIEgen-based sensors for intracellular microenvironment analysis.

Besides, AIEgens are superior in in-situ monitoring biological processes such as autophagy, mitophagy, mitochondrion-related dynamics, cell mitosis, long-term cellular tracing, and apoptosis, which provide comprehensive insights into the mechanism of life and pathogenesis of diseases, and precisely guide diagnosis and therapy [34]. In the chapter, Engineering the Bioprobes with AIE Properties to Study Tumor Hypoxia, we will present the design of hypoxia-responsive bioprobes based on AIEgens for studying tumor hypoxia.

Bacteria visualization constitutes an important part of biological imaging. Bacteria are diverse and ubiquitous in our daily life, especially in contaminated water and food [41], but bacterial infections can be fatal and can seriously threaten the health of people. Therefore, it is of vital importance to detect and identify bacteria in time, which may contribute to further diagnosis and treatment of bacteria [42]. In the chapter, AIE Probes for Bacterial Detection and Antibacterial Applications, we will summarize AIEgen-based probes for detecting, identifying, and killing of bacteria.

Over the past decades, fluorescence imaging with fluorescence microscopy, especially confocal laser scanning microscopy (CLSM), have made substantial progress [43]. However, due to optical diffraction, the lateral resolution of conventional fluorescence imaging is limited to around 200 nm [44]. For subcellular structures smaller than 200 nm, traditional fluorescence microscope only captures blurred images, which are incapable of precisely revealing their structures. In order to overcome the diffraction limit, super-resolution imaging techniques have been developed and considerable progress has been made, which enable the acquisition of accurate and detailed physiological information about the changes to cellular environment [45]. However, most of these super-resolution imaging techniques, including structured illumination microscopy (SIM) [46], stimulated emission depletion (STED) [47], and stochastic optical reconstruction microscopy (STORM) [48], raised higher demand on the fluorescent probes. By virtue of the excellent photostability, large Stokes shift, and superior biocompatibility of AIEgens, they have been extensively applied to super-resolution imaging techniques, especially STED and STORM [49–51]. In the chapter, AIE-Based Systems for Photoactivatable Imaging, Delivery, and Therapy, we will introduce some photoactivatable AIEgen-based materials and their progress in bioimaging. Besides, their applications in drug/gene delivery and therapy will also be covered.

For in-vivo fluorescence imaging, low penetration depth, and tissue autofluorescence are two major hurdles, which prevent its clinical application. To overcome these two hurdles, development of fluorescent materials with long wavelengths (especially those with far red/near infrared emission) and lifetimes are two practical ways; thus, research effort has been devoted to the investigations on phosphorescence imaging and photoacoustic imaging of blood vessel, tumor, and disease sites, as well as long-term tracking of cancer and stem cells in vivo [52, 53]. In the chapter, NIR Aggregate-Biohybrid Systems for Biomedical Applications, we will discuss the recent advancements of NIR aggregate-biohybrids for biomedical applications. In the chapter, Fluorescent and Afterglow Luminescent AIE Dots for Biomedical Applications, we will elaborate the advances of afterglow luminescent AIE dots for biomedical applications, including imaging, long-term tracking, image-guided surgery, and so on.

Besides, there have been lots of reports on advanced imaging techniques based on AIE-active bioprobes, including fluorescence-lifetime imaging (FLIM), with more reliable and stable signals than that of common fluorescence microscopy [54], multiphoton imaging with deeper tissue penetration, and less photo-damage to biological structure than that of single-photon imaging [55, 56], and multimodality imaging with two or more imaging modes and the superiority of high sensitivity, and deep penetration [57]. In the chapter, High-Order Nonlinear Optical in vivo Microscopy Based on AIEgens, we will overview the representative progress of AIEgens in high-order nonlinear fluorescence (HONF) microscopic imaging. In the chapter, Advanced Optical Imaging and Multimodality Imaging Based on AIEgens, we will focus on the applications of AIEgen-based probes in various advanced imaging techniques.

## 1.3 AIEgen-based biomedicine

Many diseases, such as cancer, infectious diseases, amyloid diseases, diabetes, and so on, have seriously affected people's health and happiness [58]. Varied therapeutic approaches, such as conventional chemotherapy, radiotherapy, and surgery, have been developed to treat these diseases. However, these therapeutic approaches are far from satisfying, with obvious weaknesses of drug resistance, high expense, complex procedures, and invisible treatment outcomes [59–61]. The drawbacks motivate the rapid development of efficient and novel therapeutic methods, such as photodynamic therapy (PDT) [62, 63], photothermal therapy (PTT) [64], and image-guided drug delivery or surgery [65, 66], for the treatment of these diseases. In the chapter, AIEgen-Based Delivery Systems: Application in the Treatment of Different Diseases, we will focus on elucidating the applications of AIEgen-based delivery systems for disease treatment.

Owing to the features of noninvasiveness, biocompatibility and high precision, PDT [67] is an emerging and effective technique for treatment of cancer and microbial infections. There are three essential factors involved in the process of PDT, including photosensitizer (PS), light, and oxygen. Under the irradiation of light at proper wavelength, PSs can transfer photon energy to molecular oxygen and then generate reactive oxygen species (ROS) [1], such as singlet oxygen ($^1O_2$), hydrogen peroxide ($H_2O_2$) and hydroxyl radical ($^{\cdot}OH$). ROS can damage biomolecules and kill cancer cells and bacteria to achieve antitumor treatment [68] or antibacterial therapy [69]. In PDT, PS is the most critical factor that determines the efficiency of ROS generation and the effect of PDT. In the chapter, AIEgen-Based Photosensitizers for Photodynamic Therapy, we will elucidate the mechanism of PDT and introduce some AIE-active photosensitizers employed for PDT.

Photothermal therapy (PTT) [70, 71] is another novel and promising tool for cancer treatment. Different from PDT, PTT converts photon energy to heat, causing tumor ablation with minimal side effect. In PTT, there is also accompanied photoacoustic effect due to the thermoelastic expansion caused by heat. Therefore, photoacoustic imaging (PAI), with deep tissue penetration, can greatly increase the accuracy of PTT by providing visualization [71]. To achieve even better therapeutic effect, many researchers combine PDT/PTT with fluorescence imaging, chemotherapy, or surgery to achieve image-guided therapies, which provide real-time guidance for precise diseases treatment [72, 73]. In the chapter, AIEgens for Photothermal Theranostics, we will introduce the applications of AIEgens in photothermal therapy.

In the past few years, AIEgens, integrated with the functionalities of long-wavelength (especially near-infrared I and II) excitation and emission, two-photon absorption, phosphorescence, high ROS generation efficiency, and high photothermal convention yield, have been developed [68, 72, 74]. Incorporating imaging and therapy into AIEgens boosts the development of multifunctional AIEgens for fluorescence image-guided chemotherapy, radiotherapy, PDT, surgery, photoacoustic image-guided PTT, and immunotherapy. Consequently, AIEgens not only provide an excellent platform for scientists to get a deep understanding of the nature of life, but also open up a toolbox for doctors to guide the theragnostic of diseases.

Furthermore, scientists also constructed many kinds of structures based on AIEgens for better biomedical performance, which include small AIE organic molecules [75], AIE polymers [76], AIE-based transition metal complexes [77], AIE-active supramolecular coordination complexes [78], and so on. These studies fully demonstrate the great progress and potential of AIEgens in biomedical applications. In the chapter, AIE Polymers for Fluorescence Imaging and Therapy, we will focus on introducing the outstanding development of AIE polymers in biological and biomedical fields. In the chapter, AIE-Based Transition Metal Complexes for Biological Applications, we will depict the diverse AIE-active transition metal complexes and their applications in biological fields. In the chapter, The Marriage of Aggregation-Induced Emission with Discrete Supramolecular Coordination Complexes: Brighter

AIEgens for Biomedical Applications, we will cover the construction of AIE-active discrete supramolecular coordination complexes (SCCs) and their promising applications in biomedical fields.

## References


[1] Zhou Z, Song J, Nie L, et al., Reactive oxygen species generating systems meeting challenges of photodynamic cancer therapy, Chem Soc Rev, 2016, 45, 6597–6626.

[2] Merian J, Gravier J, Navarro F, et al., Fluorescent nanoprobes dedicated to in vivo imaging: From preclinical validations to clinical translation, Molecules, 2012, 17, 5564–5591.

[3] Mei J, Leung NL, Kwok RT, et al., Aggregation-induced emission: Together we shine, United We Soar! Chem Rev, 2015, 115, 11718–11940.

[4] Luo J, Xie Z, Lam JW, et al., Aggregation-Induced Emission of 1-methyl-1,2,3,4,5-pentaphenylsilole, Chem Commun (Camb), 2001, 1740–1741.

[5] Hong Y, Lam JW, Tang BZ, Aggregation-Induced Emission, Chem Soc Rev, 2011, 40, 5361–5388.

[6] Guo M, Song H, Li K, et al., A new approach to developing diagnostics and therapeutics: Aggregation-induced emission-based fluorescence turn-on, Med Res Rev, 2020, 40, 27–53.

[7] He X, Xiong L-H, Huang Y, et al., AIE-based energy transfer systems for biosensing, imaging, and therapeutics, TrAC Trends Analyt Chem, 2020, 122.

[8] Liu H, Xiong LH, Kwok RTK, et al., AIE bioconjugates for biomedical applications, Adv Opt Mater, 2020, 8.

[9] Xu W, Wang D, Tang BZ, NIR-II AIEgens: A win-win integration towards bioapplications, Angew Chem Int Ed Engl, 2021, 60, 7476–7487.

[10] Mao L, Liu Y, Yang S, et al., Recent advances and progress of fluorescent bio-/chemosensors based on aggregation-induced emission molecules, Dyes Pigm, 2019, 162, 611–623.

[11] Wang YF, Zhang T, Liang XJ, Aggregation-induced emission: Lighting up cells, Revealing Life! Small, 2016, 12, 6451–6477.

[12] Dou Y, Zhu Q, Du K, Recent advances in two-photon aiegens and their application in biological systems, Chembiochem, 2021.

[13] Kang M, Zhang Z, Song N, et al., Aggregation-enhanced theranostics: AIE sparkles in biomedical field, Aggregate, 2020, 1, 80–106.

[14] Fleischhacker M, Schmidt B, Circulating nucleic acids (CNAs) and cancer–a survey, Biochim Biophys Acta, 2007, 1775, 181–232.

[15] Wijdeven RH, Neefjes J, Ovaa H, How chemistry supports cell biology: The chemical toolbox at your service, Trends Cell Biol, 2014, 24, 751–760.

[16] Carter KP, Young AM, Palmer AE, Fluorescent sensors for measuring metal ions in living systems, Chem Rev, 2014, 114, 4564–4601.

[17] Joè Rg B, Schulz J R L, Seyfried J, Dichgans J, Glutathione, oxidative stress and neurodegeneration, Eur J Biochem, 2000, 267, 4904–4911.

[18] Cormode DP, Jarzyna PA, Mulder WJ, et al., Modified natural nanoparticles as contrast agents for medical imaging, Adv Drug Deliv Rev, 2010, 62, 329–338.

[19] Shaner NC, Steinbach PA, Tsien RY, A guide to choosing fluorescent proteins, Nat Methods, 2005, 2, 905–909.

[20] Resch-Genger U, Grabolle M, Cavaliere-Jaricot S, et al., Quantum dots versus organic dyes as fluorescent labels, Nat Methods, 2008, 5, 763–775.

[21] Kwok RT, Leung CW, Lam JW, et al., Biosensing by luminogens with aggregation-induced emission characteristics, Chem Soc Rev, 2015, 44, 4228–4238.
[22] Zhang M, Saha ML, Wang M, et al., Multicomponent Platinum(II) Cages with Tunable Emission and Amino Acid Sensing, J Am Chem Soc, 2017, 139, 5067–5074.
[23] Liu Y, Deng C, Tang L, et al., Specific detection of D-glucose by a tetraphenylethene-based fluorescent sensor, J Am Chem Soc, 2011, 133, 660–663.
[24] Yang Y, Wang X, Cui Q, et al., Self-assembly of fluorescent organic nanoparticles for iron(III) sensing and cellular imaging, ACS Appl Mater Interfaces, 2016, 8, 7440–7448.
[25] Li Y, Kwok RTK, Tang BZ, et al., Specific nucleic acid detection based on fluorescent light-up probe from fluorogens with aggregation-induced emission characteristics, RSC Adv, 2013, 3.
[26] Xu JP, Fang Y, Song ZG, et al., BSA-tetraphenylethene derivative conjugates with aggregation-induced emission properties: Fluorescent probes for label-free and homogeneous detection of protease and alpha1-antitrypsin, Analyst, 2011, 136, 2315–2321.
[27] Xie S, Wong AYH, Chen S, et al., Fluorogenic detection and characterization of proteins by aggregation-induced emission methods, Chemistry, 2019, 25, 5824–5847.
[28] Ding D, Li K, Tang BZ, Bioprobes based on AIE fluorogens, Acc Chem Res, 2013, 46, 2441–2453.
[29] Qian X, Xu Z, Fluorescence imaging of metal ions implicated in diseases, Chem Soc Rev, 2015, 44, 4487–4493.
[30] Zhang L, Zhang ZY, Liang RP, et al., Boron-doped graphene quantum dots for selective glucose sensing based on the “abnormal” aggregation-induced photoluminescence enhancement, Anal Chem, 2014, 86, 4423–4430.
[31] Xia F, Wu J, Wu X, et al., Modular design of peptide- or DNA-modified AIEgen probes for biosensing applications, Acc Chem Res, 2019, 52, 3064–3074.
[32] Akraa S, Pham Tran Tam A, Shen H, et al, A smartphone-based point-of-care quantitative urinalysis device for chronic kidney disease patients, J Netw Comput Appl, 2018, 115, 59–69.
[33] Holthuis JC, Ungermann C, Cellular microcompartments constitute general suborganellar functional units in cells, Biol Chem, 2013, 394, 151–161.
[34] Gu X, Kwok RTK, Lam JWY, et al., AIEgens for biological process monitoring and disease theranostics, Biomaterials, 2017, 146, 115–135.
[35] Gui C, Zhao E, Kwok RTK, et al., AIE-active theranostic system: Selective staining and killing of cancer cells, Chem Sci, 2017, 8, 1822–1830.
[36] Hu R, Zhou F, Zhou T, et al., Specific discrimination of gram-positive bacteria and direct visualization of its infection towards mammalian cells by a DPAN-based AIEgen, Biomaterials, 2018, 187, 47–54.
[37] Song N, Xiao P, Ma K, et al., Recent advances of AIEgens for targeted imaging of subcellular organelles, Chem Res Chin Univ, 2021, 37, 52–65.
[38] Chen S, Hong Y, Zeng Y, et al., Mapping live cell viscosity with an aggregation-induced emission fluorogen by means of two-photon fluorescence lifetime imaging, Chemistry, 2015, 21, 4315–4320.
[39] Dai J, Duan C, Huang Y, et al., Aggregation-induced emission luminogens for RONS sensing, J Mater Chem B, 2020, 8, 3357–3370.
[40] Chen S, Hong Y, Liu Y, et al., Full-range intracellular pH sensing by an aggregation-induced emission-active two-channel ratiometric fluorogen, J Am Chem Soc, 2013, 135, 4926–4929.
[41] Hetrick EM, Schoenfisch MH, Reducing implant-related infections: Active release strategies, Chem Soc Rev, 2006, 35, 780–789.
[42] Roy E, Nagar A, Chaudhary S, et al., AIEgen-based fluorescent nanomaterials for bacterial detection and its inhibition, ChemistrySelect, 2020, 5, 722–735.

[43] Dunn KW, Kamocka MM, McDonald JH, A practical guide to evaluating colocalization in biological microscopy, Am J Physiol Cell Physiol, 2011, 300, C723–742.
[44] Schermelleh L, Ferrand A, Huser T, et al., Super-resolution microscopy demystified, Nat Cell Biol, 2019, 21, 72–84.
[45] Errico C, Pierre J, Pezet S, et al., Ultrafast ultrasound localization microscopy for deep super-resolution vascular imaging, Nature, 2015, 527, 499–502.
[46] Huang B, Babcock H, Zhuang X, Breaking the diffraction barrier: Super-resolution imaging of cells, Cell, 2010, 143, 1047–1058.
[47] Xu Y, Zhang H, Zhang N, et al., Deep-red fluorescent organic nanoparticles with high brightness and photostability for super-resolution in vitro and in vivo imaging using STED nanoscopy, ACS Appl Mater Interfaces, 2020, 12, 6814–6826.
[48] Rust MJ, Bates M, Zhuang X, Sub-diffraction-limit imaging by stochastic optical reconstruction microscopy (STORM), Nat Methods, 2006, 3, 793–795.
[49] Wang Y-L, Fan C, Xin B, et al., AIE-based super-resolution imaging probes for β-amyloid plaques in mouse brains, Mater Chem Front, 2018, 2, 1554–1562.
[50] Xu Y, Xu R, Wang Z, et al., Recent advances in luminescent materials for super-resolution imaging via stimulated emission depletion nanoscopy, Chem Soc Rev, 2021, 50, 667–690.
[51] Gu X, Zhao E, Zhao T, et al., A mitochondrion-specific photoactivatable fluorescence turn-on aie-based bioprobe for localization super-resolution microscope, Adv Mater, 2016, 28, 5064–5071.
[52] Li K, Liu B, Polymer-encapsulated organic nanoparticles for fluorescence and photoacoustic imaging, Chem Soc Rev, 2014, 43, 6570–6597.
[53] Lou X, Zhao Z, Tang BZ, Organic dots based on AIEgens for two-photon fluorescence bioimaging, Small, 2016, 12, 6430–6450.
[54] Wang Y, Yao H, Zhou J, et al., A water-soluble, AIE-active polyelectrolyte for conventional and fluorescence lifetime imaging of mouse neuroblastoma neuro-2A cells, J Polym Sci A Polym Chem, 2018, 56, 672–680.
[55] Wang Y, Chen M, Alifu N, et al., Aggregation-Induced emission luminogen with deep-red emission for through-skull three-photon fluorescence imaging of mouse, ACS Nano, 2017, 11, 10452–10461.
[56] Qin W, Zhang P, Li H, et al., Ultrabright red AIEgens for two-photon vascular imaging with high resolution and deep penetration, Chem Sci, 2018, 9, 2705–2710.
[57] He X, Zhao Z, Xiong LH, et al., Redox-active aiegen-derived plasmonic and fluorescent core@shell nanoparticles for multimodality bioimaging, J Am Chem Soc, 2018, 140, 6904–6911.
[58] Shubhakaran KP, Chin JH, The global burden of neurologic diseases, Neurology, 2015, 84, 758.
[59] Galmarini D, Galmarini CM, Galmarini FC, Cancer chemotherapy: A critical analysis of its 60 years of history, Crit Rev Oncol Hematol, 2012, 84, 181–199.
[60] Gao M, Tang BZ, AIE-based cancer theranostics, Coord Chem Rev, 2020, 402.
[61] Bianchini G, Balko JM, Mayer IA, et al., Triple-negative breast cancer: Challenges and opportunities of a heterogeneous disease, Nat Rev Clin Oncol, 2016, 13, 674–690.
[62] Fan H, Yan G, Zhao Z, et al., A smart photosensitizer-manganese dioxide nanosystem for enhanced photodynamic therapy by reducing glutathione levels in cancer cells, Angew Chem Int Ed Engl, 2016, 55, 5477–5482.
[63] Castano AP, Mroz P, Hamblin MR, Photodynamic therapy and anti-tumour immunity, Nat Rev Cancer, 2006, 6, 535–545.
[64] Wang J, Li J, Wang L, et al., AIEgen-based polymer nanocomposites for imaging-guided photothermal therapy, ACS Appl Polym Mater, 2020, 2, 4306–4318.

[65] Yi X, Hu JJ, Dai J, et al., Self-guiding polymeric prodrug micelles with two aggregation-induced emission photosensitizers for enhanced chemo-photodynamic therapy, ACS Nano, 2021, 15, 3026–3037.
[66] Gu X, Zhang X, Ma H, et al., Corannulene-incorporated AIE nanodots with highly suppressed nonradiative decay for boosted cancer phototheranostics in vivo, Adv Mater, 2018, 30, e1801065.
[67] Dougherty TJ, Gomer CJ, Henderson BW, et al., Photodynamic therapy, J Natl Cancer Inst, 1998, 90, 889–905.
[68] Hu F, Xu S, Liu B, Photosensitizers with aggregation-induced emission: Materials and biomedical applications, Adv Mater, 2018, 30, e1801350.
[69] Zhao E, Chen Y, Wang H, et al., Light-enhanced bacterial killing and wash-free imaging based on AIE fluorogen, ACS Appl Mater Interfaces, 2015, 7, 7180–7188.
[70] Jung HS, Verwilst P, Sharma A, et al., Organic molecule-based photothermal agents: An expanding photothermal therapy universe, Chem Soc Rev, 2018, 47, 2280–2297.
[71] Liu Y, Bhattarai P, Dai Z, et al., Photothermal therapy and photoacoustic imaging via nanotheranostics in fighting cancer, Chem Soc Rev, 2019, 48, 2053–2108.
[72] Wang Y, Zhang Y, Wang J, et al., Aggregation-induced emission (AIE) fluorophores as imaging tools to trace the biological fate of nano-based drug delivery systems, Adv Drug Deliv Rev, 2019, 143, 161–176.
[73] Ni X, Zhang X, Duan X, et al., Near-infrared afterglow luminescent aggregation-induced emission dots with ultrahigh tumor-to-liver signal ratio for promoted image-guided cancer surgery, Nano Lett, 2019, 19, 318–330.
[74] Zhang R, Duan Y, Liu B, Recent advances of AIE dots in NIR imaging and phototherapy, Nanoscale, 2019, 11, 19241–19250.
[75] Cai X, Liu B, Aggregation-induced emission: Recent advances in materials and biomedical applications, Angew Chem Int Ed Engl, 2020, 59, 9868–9886.
[76] Zhang X, Wang K, Liu M, et al., Polymeric AIE-based nanoprobes for biomedical applications: Recent advances and perspectives, Nanoscale, 2015, 7, 11486–11508.
[77] Sheet SK, Sen B, Patra SK, et al., Aggregation-induced emission-active ruthenium(II) complex of 4,7-Dichloro Phenanthroline for selective luminescent detection and ribosomal RNA imaging, ACS Appl Mater Interfaces, 2018, 10, 14356–14366.
[78] Jeyakkumar P, Liang Y, Guo M, et al., Emissive metallacycle-crosslinked supramolecular networks with tunable crosslinking densities for bacterial imaging and killing, Angew Chem Int Ed Engl, 2020, 59, 15199–15203.

Jing-Jing Hu, Hao Wang, Fan Xia, Xiaoding Lou

# Chapter 2
# Modular nucleic acid-functionalized AIEgen probes for biosensing applications

## 2.1 Introduction

Rapid development of biomedicine contributes to prevention, diagnosis, and treatment of diseases, and is used in the detection of biological targets and direct imaging cellular targets or processes. In biomedical study and clinical application, various imaging techniques that have the ability of making invisible bioprocesses into visible ones have been developed [1–5]. Among them, fluorescence-based methods can detect biomarkers with ease, visualize the living biomolecules in situ, and monitor dynamic processes in real time [6]. Therefore, numerous fluorescent imaging probes, including organic dyes, fluorescent proteins, quantum dots, and so on, have been designed and have exhibited advantages, such as superior spatial-temporal resolution, high sensitivity, fast responsiveness, as well as excellent biocompatibility [7–11]. However, photobleaching problem and high background signals restricted the development of traditional fluorescent probes. What is worse, they have to face the difficulty of aggregation-caused quenching (ACQ) effect, which would limit their effective working concentration and, thus, weaken performance in biosensing applications [12, 13].

Fortunately, in 2001, Tang et al. discovered that hexaphenylsiloles (HPS) molecule with phenyl rotors structure could emit intense fluorescence in its aggregate state, which was named aggregation-induced emission (AIE) characteristics [14]. When the AIE luminogens (AIEgens) are in dispersed state, phenyl rotors will rotate freely, and AIEgens will experience low-frequency motions to dissipate the excited-state energy nonradiatively, leading to weak or no emission. However, the intramolecular motions are restricted in aggregate state, resulting in strong emission. The aggregation of AIEgens also exhibits the superiority of large Stokes shift and great photobleaching resistance [15]. Hence, AIEgens are promising in biomedical fields. By the rational design of AIEgens-based probes, AIEgens are able to undergo the state transition with the influence of biomarkers. A common strategy is designing water-soluble AIEgen probes with relatively low fluorescence. After probes interacted with a specific target, the

**Jing-Jing Hu, Hao Wang, Fan Xia,** State Key Laboratory of Biogeology and Environmental Geology, Faculty of Materials Science and Chemistry, China University of Geosciences, Wuhan, 430074, China
**Xiaoding Lou,** State Key Laboratory of Biogeology and Environmental Geology, Faculty of Materials Science and Chemistry, China University of Geosciences, Wuhan, 430074, China, e-mail: louxiaoding@cug.edu.cn

https://doi.org/10.1515/9783110672220-002

binding caused restriction of intramolecular motion, or response-induced aggregates will produce the AIE emission, inducing the fluorescence turn-on effect for biosensing. In addition, this wash-free characteristic of hydrophilic AIEgens-based probes makes them more attractive in fluorescence imaging in cells and in vivo, with enhanced signal-to-noise ratios [16]. Nowadays, an increasing number of probes formed by linking biomolecules to AIEgens have been designed, of which tetraphenylethene (TPE) molecule, tetraphenylsilole (TPS) molecule, and their derivatives form a big part [17, 18]. It has been reported that functionalized AIEgens probes are able to detect diverse biological targets, including metal ions, amino acids, carbohydrates, biomacromolecules, etc. [19–25] and are useful in direct imaging different substances, like organelles, bacteria, cells, tissues, and small animals [26–30].

As the foundation of molecular biology, nucleic acids including deoxyribonucleic acid (DNA) and ribonucleic acid (RNA) carry genetic information. Specific sequences of nucleic acids endow them with particular genetic information and the ability to specifically and efficiently recognize targets [31]. Also, their abnormal concentration might be associated with the emergence of a disease [32]. Thus, with the advantages of specific recognition, rapid response, and good biocompatibility, modular nucleic acid-functionalized AIEgen probes (MNAPs) can be used to obtain complicated information in molecular level, evaluate the interaction between biomacromolecules, and investigate the pathogenesis. For MNAPs, the nucleic acid module library generally includes (i) an aptamer for specific recognition, (ii) a complementary strand for hybridizing the targeted oligonucleotide, (iii) G-rich sequence for forming G-quadruplex structure, or (iv) a sensitive strand for evaluating the activity of telomerase. These functional nucleic acid modules provide a variety of possibilities in applications of MNAPs. The methods of constructing the MNAPs between nucleic acid and AIEgen module mainly rely on electrostatic interaction and click chemistry to generate triazole bonds.

In this chapter, we summarize the representative MNAPs for biosensing applications. First, the MNAPs for detection of diverse bio-analytes are introduced. Then, the MNAPs for fluorescence imaging of cells and tissues are presented. We highlight the design concept, functional mechanism, and application of presentative examples, in each section. At the end, a few challenges and opportunities in this theme are also discussed. We hope this chapter would motivate groundbreaking ideas and encourage sustained progress in MNAPs.

## 2.2 MNAPs for detection

Using the advantages of functionalized nucleic acids and AIEgens modules, MNAPs are able to exhibit promising detection ability for biochemical molecules to indicate their activities or concentrations of the targets. The detection mechanism includes

the hybridized recognition, enzyme catalysis, etc. [33]. In this section, the representative design and applications of MNAPs are introduced and classified into three groups according to the targets: (i) small molecules, like metal ions and adenosine triphosphate (ATP); (ii) nucleic acids, like DNA and RNA; (iii) proteins, like enzymes and antigens [34].

### 2.2.1 Small molecules

The sensitive detection of small molecules is an important demand in clinical diagnosis, environmental monitoring, and food safety. Therefore, researchers have developed many methods to detect small molecules, such as fluorescence, spectrophotometry, mass spectrometry, enzyme method, and high-performance liquid chromatography. However, the experimental processes are complicated, expensive, and involve large-scale instruments and complex sample pretreatment, which are not conducive to real-time analysis and detection [35–37]. Compared to the traditional analytical methods, the detection strategy based on MNAPs has the advantages of good selectivity, high sensitivity, rapid response and low cost, ensuring their wide utilization. At present, the use of MNAPs to detect small molecules mainly depends on the change of nucleic acid configuration caused by small molecules, which leads to the change of AIE luminescence.

In 2010, Tang et al. described a label-free fluorescence detection sensor for $Hg^{2+}$ based on the complex of AIE probes and anti-$Hg^{2+}$ aptamer single-stranded DNA (ssDNA) formed by electrostatic interactions [38]. After the addition of $Hg^{2+}$, the aptamer ssDNA underwent conformational transformation due to the specific aptamer-$Hg^{2+}$ recognition and formed a compact hairpin structure, leading to the AIE molecules exhibiting a closer position. The enhancement of AIE fluorescence could be used in the selective identification and quantification of $Hg^{2+}$. The detection limit of the sensor was measured to be close to 0.224 mM when the signal-to-noise ratio was 3. In 2017, Xia and Lou et al. reported an AIEgen-modified nucleic acid probe (AFNAs) containing only fluorogen but no quenching molecule, which could detect $Hg^{2+}$ in real water samples (Figure 2.1A) [19]. High-sensitivity detection of the target was carried out by using a cyclic reaction based on the dual specific nuclease (DSN) enzyme. After the addition of $Hg^{2+}$, the DNA sequence labeled by AIEgens changed from ssDNA conformation to double-stranded DNA (dsDNA). In the meantime, the rigidity of the AFNAs increased, thereby inhibiting the rotation of AIEgens, resulting in an increase in the fluorescence signal. Then, DSN hydrolyzed dsDNA, leading to the release of $Hg^{2+}$, and thus, lighting up the fluorescence of AIEgens. The free $Hg^{2+}$ was then combined with another probe to initiate a new hydrolysis process. For detecting $Hg^{2+}$, this method highlights certain advantages. (i) Because of the high stability of thymine-$Hg^{2+}$-thymine (T-$Hg^{2+}$-T) pairing, it had strong specificity for $Hg^{2+}$. (ii) High sensitivity could be obtained by DSN-triggered isothermal

amplification in aqueous solution. (iii) One AIEgens marker in this AFNAs probe makes the synthesis cost lower and labor-saving.

Except detecting $Hg^{2+}$, Tan et al. [39] designed an AIE derivative-linked guanine (G)-rich oligonucleotide biosensor (TPE-oligonucleotide) for sensitive detection of $K^+$ (Figure 2.1B). Classic AIE molecule, TPE was used as reporting module, and G-quadruplex analogues acted as an effective sensing module that could form into a four-stranded oligonucleotide by univalent cation. Experimental results demonstrated that the sensitivity of the new probe was about 10 times higher than that of the common G-quadruplex-based $K^+$ fluorescent probe. There were several reasons behind the excellent sensitivity. The AIE characteristic of TPE was a prerequisite for the enhanced sensitivity. As displayed in Figure 2.1B, TPE-oligonucleotide probe was formed by covalently binding TPE derivatives to G-rich oligonucleotide by amide bond. The TPE-oligonucleotide probe would dissolve in water to form a random state. Then, the aggregation of TPE derivatives was conducive to face-to-face close packing and strong π-π packing interaction, so that the G-quadruplex structure was further stabilized. After adding $K^+$, TPE derivatives were aggregated through the formation of parallel G-tetraplex structure by ion selectivity, therefore impeding their intramolecular motion and resulting in enhanced emission. The sensitivity of the biosensor in buffer solution was as low as 5 μM. Based on these superiorities, TPE-oligonucleotide probe could be used to study and analyze $K^+$ function.

ATP is the most important energy source in organisms, which plays an important role in the cell metabolism, energy supplementation, and other life activities of animals and plants [40–42]. For ATP detection, Xu et al. reported an MNAP combining an AIE probe, water-soluble carbon nanotubes, and a DNA aptamer [43]. This system was a label-free and light-up sensor involving the specific binding principle between the aptamer and target, fluorescence quenching effect from carbon nanotubes, and AIE characteristics of the fluorescent probe. As shown in Figure 2.1C, specific binding to the target ATP resulted in the release of the aptamer from the carbon nanotubes. Therefore, the AIE probe attached to the aptamer surface, recovered fluorescence, and showed strong emission. The presence of water-soluble carbon nanotubes could produce low background fluorescence, which was conducive to the detection of ATP.

Ochratoxin A (OTA) is a toxic metabolite produced by penicillium and aspergillus, has nephrotoxicity and teratogenicity, and exhibits great harm to human body [44–46]. In 2018, Liu and coworkers reported a label-free fluorescent probe for the specific and ultra-sensitive detection of OTA, by utilizing the specific aptamer of OTA (OSA) as the recognizing module, AIE molecule DSAI (a 9,10-distyrylanthracene derivative) as a reporting module, and graphene oxide (GO) as the quenching agent [47]. Without OTA, the DSAI and OSA complex was adsorbed on the surface of GO. Because of the fluorescence resonance energy transfer (FRET), GO would quench the fluorescence of DSAI. With the addition of OTA, a more stable complex of OSA and OTA would form, thus releasing from the GO. Since the formation of DSAI/OSA-OTA complex, fluorescence of the complex gradually recovered and

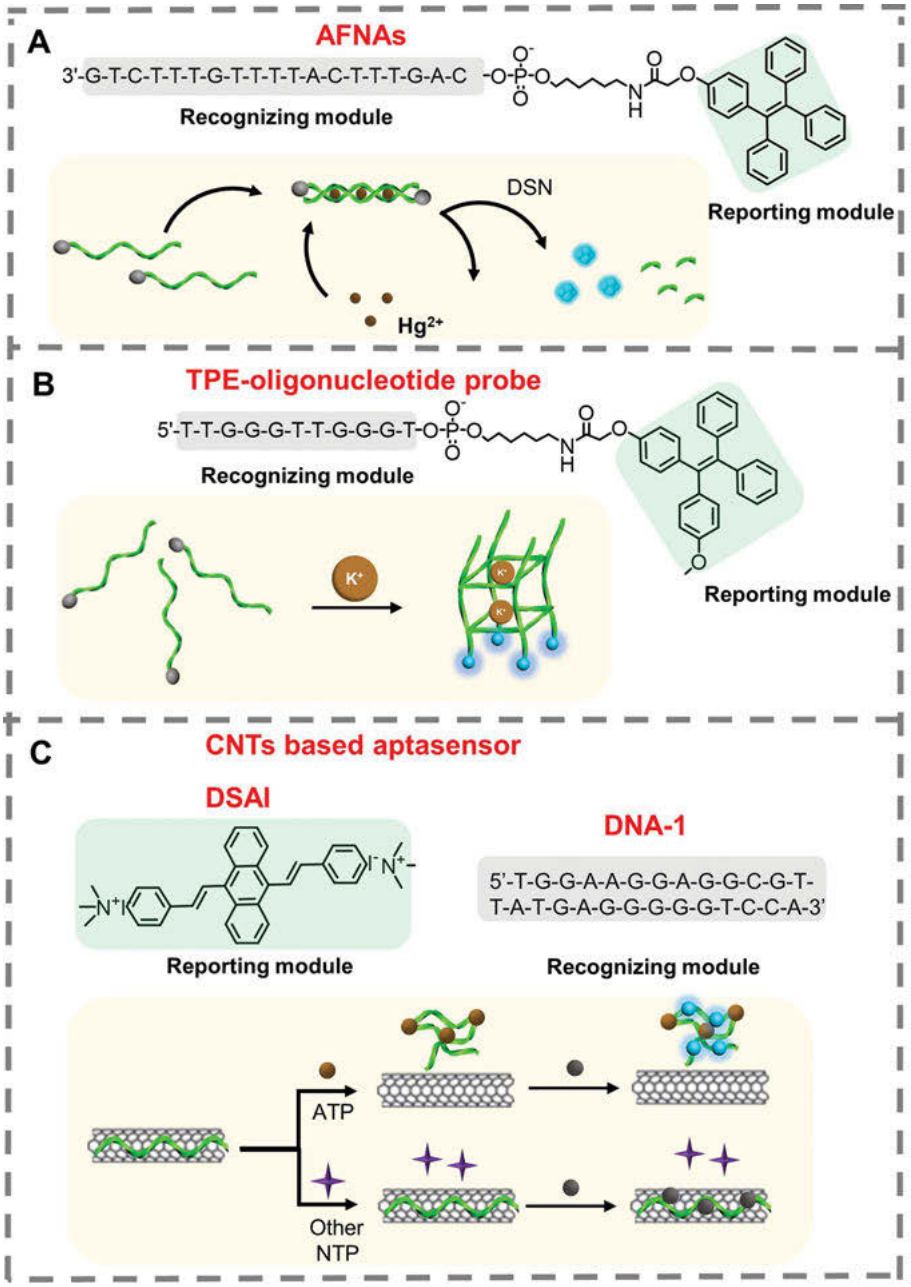


**Figure 2.1:** (A) Structure of AFNAs and schematic demonstration of the detection mechanism for $Hg^{2+}$ ions. (B) Structure of TPE-oligonucleotide probe and schematic demonstration of the detection mechanism for $K^{+}$ ions, based on the formation of G-quadruplex. (C) Structure of DSAI, sequence of DNA-1, and the biosensing principle for ATP.

enhanced. With the introduction of GO and DSAI, it was easy to switch the DSAI fluorescent signal from "off" to "on", after adding OTA. Therefore, through monitoring changes in fluorescence signal of DSAI, ultra-sensitive detection of OTA could be realized, and the detection limit was 0.324 nM.

### 2.2.2 Nucleic acids

Nucleic acids, which include DNA and RNA, form the basis of molecular biology. They play a vital role in biological processes, like growth, heredity, and variation. Once they are damaged, a variety of diseases may occur. Therefore, specific nucleic acid sensing is significant in the diagnosis and treatment of diseases.

In 2013, Liu et al. reported an MNAP for specific complementary DNA detection in solution by combining TPE and single-stranded oligonucleotides [48]. Subsequently, they developed another MNAP for specific DNA detection. They linked the bisazide-functionalized AIEgen to the single-stranded oligonucleotide to produce a two-armed probe [49]. The probe showed low emission fluorescence in aqueous medium and high emission fluorescence when hybridized with complementary chain. The probe had excellent performance for DNA detection with homogeneous sequence specificity, and could even identify the target sequence of single base mutation.

In 2014, Tian et al. designed an MNAP based on DSAI and GO for selective and sensitive detection of targeted DNA and thrombin (Figure 2.2A) [50]. Following this work, they further designed a label-free, ultra-sensitive, and "turn-on" MNAP based on the AIE and GO sensing platform to detect the target DNA sequence (Figure 2.2B) [51]. To explore the sensing mechanism and improve the sensing performance, several experiments were designed and conducted to comprehensively study the interaction of DNA with AIE probe and GO. Three AIE-active cationic DSA derivatives with different length alkyl chain substituents were used as fluorescent probes. Three kinds of GO with different oxidation levels were used for DNA structure identification and fluorescence quenching. Compared to the DSA derivatives substituted with long chain alkyl chains, those with short alkyl chains bound more strongly to dsDNA, which could avoid fluorescence quenching from GO, and thus, emitting high fluorescence signals. Moreover, GO with low oxidation degree could distinguish the structure of different DNA strands and quench the fluorescence more effectively, greatly sensing the platform background noise. By optimizing and tuning supramolecular interactions of DNA with AIE probe and GO, they could make the detection of target DNA sequences more sensitive and selective, with a detection limit as low as $0.17 \times 10^{-9}$ M.

In post-transcriptional regulation of gene expression and RNA silencing, microRNAs (miRNAs) play a significant part. As an oncogenic miRNA, miR-21 showed significantly abnormal expression in a range of tumor cells. Lou et al. reported an MNAP (TPE-DNA) to detect miR-21 in urine samples [52]. As shown in Figure 2.2C, TPE-DNA was designed and prepared via the click reaction between hydrophobic

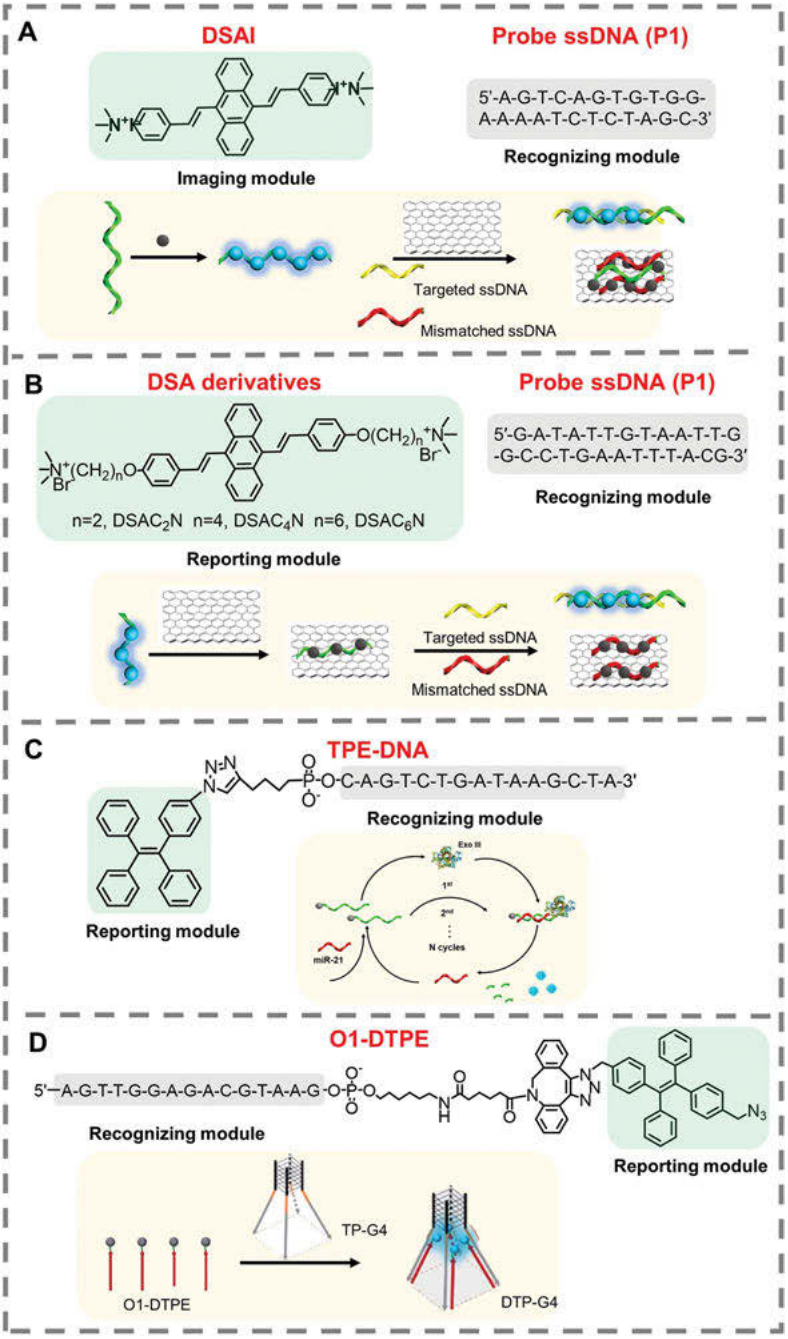


**Figure 2.2:** (A) Structure of DSAI, sequence of probe ssDNA, and schematic demonstration of the detection mechanism based on DSAI/GO probe for targeted ssDNA. (B) Structure of the DSA

TPE and hydrophilic DNA. When there was miR-21, random coil TPE-DNA could target miR-21 and form dsDNA through hybridization. The dsDNA was digested by the intervention exonuclease III (Exo III), which could lead to the release of miR-21, and the fluorescent signal reported TPE. Then, the released target would hybridize with another TPE-DNA probe to start a new cycle. Therefore, a single copy of miR-21 would generate a number of TPE molecules that would gather together to trigger the restriction of intramolecular motion (RIM) process, thereby blocking the radiation-free relaxation pathway of TPE and activating its fluorescence. In addition, by adjusting the reaction temperature, different miR-21 detection limits could be achieved. When incubated at 37 °C for 40 min, detection limit was 1 pM, while it was 10 aM at 4 °C for 7 d, mainly due to altered Exo III activity. The successful detection of miR-21 in the clinical urine samples of 21 bladder cancer patients indicated the possibility of TPE-DNA for early diagnosis of patients.

MicroRNA-141 (miR-141) is known to be involved in regulating proliferation, differentiation, and apoptosis of cells. In 2018, Xu, Lou, Zhang et al. synthesized an AIE-based superwettable chip to detect miR-141 by combining evaporative and concentrated superwettable chips with AIEgens [53]. The enrichment of AIEgens induced by evaporation enhances the output signal. Using the dual improvement effect of biosensor chip, the miR-141 detection had good repeatability, high specificity, and good selectivity. The sensor had a good signal-to-noise ratio, and the detection accuracy was 1 pM. As a simple biosensor platform, AIE-based microchips that were superwettable would promote the development of various open microchip platforms for the analysis and monitoring of biological environment samples.

MNAP could also be used to detect the G-quadruplex. Lei et al. reported a O1-DTPE probe via dibenzylcyclooctyne cycloaddition [54]. As shown in Figure 2.2D, when DNA existed as a single-stranded structure, there would be no fluorescence signal. After adding TP-G4, the AIEgen would cluster in the near center area of the parallel tetrapod DNA quadruple, and then emit strong fluorescence. The number of G-quartets and the length of the spacer between the core structure of the scaffold and the AIEgen could change the fluorescence intensity of AIEgens.

### 2.2.3 Proteins

As the essential component and main functional unit in life, labeling and detecting of proteins are significant in disease prevention and treatment. For instance,

**Figure 2.2** (continued)
derivatives and schematic demonstration of the detection mechanism for targeted ssDNA. (C) Structure of TPE-DNA and schematic demonstration for detection of miR-21. (D) Structure of O1-DTPE and schematic demonstration for detection of TP-G4.

telomerase, a ribonucleoprotein associated with the increase of tandem repeats at the 3′ end of telomere, had been reported to be active in cancer cells instead of healthy cells. Detecting telomerase activity is very important for cancer diagnosis and treatment. Xia et al. used MNAP composed of AIEgen TPE-Z and TS primer to detect telomerase activity in 2015 [55]. From Figure 2.3A, during telomere elongation, TPE-Z aggregated with DNA chain elongation through electrostatic adsorption. The telomerase in the detection system could extend the TS primers into long repeat sequences, thus enhancing fluorescence. This MNAP could specifically detect telomerase activity of various cell lines (like MCF-7, HeLa, or HLF). In addition, it had been successfully used to diagnose bladder cancer, ensuring its prospect for preclinical diagnosis. Subsequently, Lou et al. [56] constructed a modular Silole-R-QP probe (Figure 2.3B) for specific detection of telomerase activity by introducing a quencher group to significantly reduce the false background signal. In the blank solution, the quenching group basically eliminated the fluorescence of AIEgens and could greatly reduce the fluorescence background, thereby improving the signal-to-noise

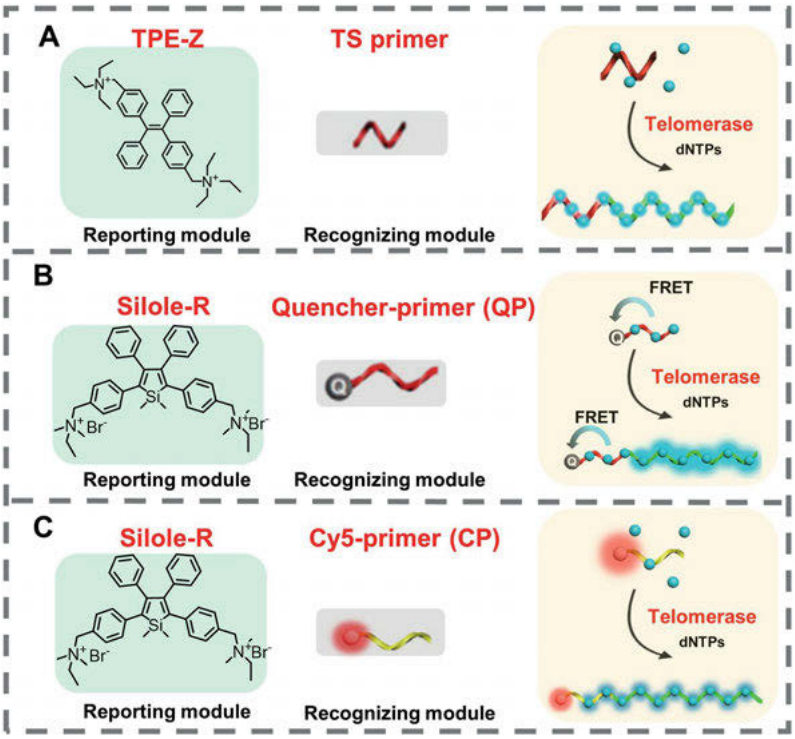


**Figure 2.3:** (A) The construction of TPE-Z-TS primer probe and schematic demonstration of the detection mechanism for telomerase. (B) Chemical structure of Silole-R, scheme of the quencher-primer, and scheme of the detection mechanism for telomerase. (C) Chemical structure of Silole-R, schematic demonstration of Cy5-primer, and scheme of telomerase detection.

ratio. In their follow-up work [57], as an internal reference, the stable red fluorophore Cy5 was modified at the 5′ end of the primer to improve the accuracy of Silole-R-TP probe (Figure 2.3C). In this method, telomerase was detected in 10 normal urine samples and 20 blood samples of bladder cancer, and the results were all 100% positive. The current research results would lead to new materials for the construction of biological probes and promote their application in clinical diagnosis.

DNA methylation refers to the covalent binding of a target cytosine (C) or adenine (A) base to a methyl group in a specific DNA sequence [58], which is important in the biological process of genome expression, transcription, and cell differentiation [59]. DNA methyltransferase (MTase) catalyzes the methylation process based on the methyl donor, S-adenosylmethionine (SAM). Monitoring DNA MTase activity is of significance in the clinical diagnosis of many diseases. Recently, the detection methods for DNA MTase contain electrochemistry [60], chemiluminescence [61], colorimetry [62], and fluorescence [63]. Among them, fluorescence method has merits of high sensitivity and simple operation. Yu and coworkers [64] utilized superquenching of AIE for detecting DNA MTase, in 2014. When ssDNA was present in the system, the positively charged TPE derivative would bind to the negatively charged ssDNA. Thus, the TPE derivative could aggregate and emit obvious fluorescence. However, when ssDNA was combined with a quenching part, the fluorescence of TPE derivative was effectively quenched. By applying AIE superquenching, even simple quenching molecules could quench the fluorescence of AIE. Based on this, a DNA MTase detection system included a quencher-labeled dsDNA with AIEgen aggregation was designed. With DNA MTase and endonuclease, the methylated DNA sequence was hydrolyzed to release the quenched part, resulting in significantly enhanced fluorescence. The false positive reactions could be reduced through the fluorescence light-up mode.

Besides enzymes, MNAP could also detect antigens. In 2017, a label-free fluorescent sensor based on AIE-$SiO_2$ nanoparticles (NPs) was reported to detect prostate-specific antigen (PSA), sensitively [65]. The positively charged amino-modified $SiO_2$ NPs was utilized as an effective nanotrapping agent to form $SiO_2$ NP-PA nanocomposites by electrostatic adsorption of single-chain PSA aptamer (PA) and the negatively charged TPE derivative 3 (TPE3). After PA bound to PSA to induce rigid aptamer conformation, PA was released from the surface of $SiO_2$ NPs. Thus, the remaining TPE3 would aggregate on the $SiO_2$ NPs surface and emit strong fluorescence. The detection limit of the MNAP for PSA could be as low as 0.5 ng/mL.

## 2.3 MNAPs for bioimaging

As opposed to detection that can only confirm the existence of targets and measure their concentration, bioimaging could obtain whole images of the bio-targets by collection of fluorescence signal. Owing to the high sensitivity and flexibility of fluorescence,

bioimaging could further provide the spatiotemporal information in situ and in real time, monitoring the bioanalysis at the molecular level and helping visualize the dynamic biological processes. The analysis objects of bioimaging could include the cell organelles, bacteria, cells, tissues, as well as small animals. For instance, cell fluorescence imaging is a powerful means to study the diverse structures and functions, particularly in the identification of different cell types. Unlike traditional organic fluorophore-based probes, AIEgens probes could realize the imaging with high signal-to-noise ratios and in a wash-free manner. In this section, the representative design of MNAPs for bioimaging is introduced.

## 2.3.1 Nucleic acids

With their ability to carry life genetic information and enable protein production, nucleic acids are crucial biomacromolecules in cells. Due to the diverse functions, DNA and RNA might be located at different places in the cells. Thus, imaging them would provide more sufficient information. To achieve the aims of in situ monitoring and tracing miR-21 in living cells, Lou et al. upgraded the mentioned TPE-DNA probe by changing the reporting module TPE to the TPEPy with a longer fluorescence emission wavelength, to obtain the TPEPy-LDNA (Figure 2.4A) [66]. TPEPy-LDNA could realize the detection in clinical urine samples and imaging of miR-21 in tumor cells with high expression of miR-21 (MCF-7 cells). Imaging results displayed that compared to the negligible fluorescence in HeLa cells and human lung fibroblasts (HLF) with relatively low expression of miR-21, remarkable yellow fluorescence of TPEPy aggregates could be observed in MCF-7 cells for more than one hour, proving the good specificity and photostability of TPEPy-LDNA probe. Furthermore, the detection limit of this probe to miR-21 was 1 pM in vitro.

In 2018, Xia and Lou et al. prepared an amphipathic DNA-binding AIE probe (TPE-R-DNA) that could image and analyze mRNA in tumors through Exo III-assisted target recovery strategy [67] (Figure 2.4B). TPE-R-DNA consisted of a hydrophobic signal reporting module, TPE-R-$N_3$, and a hydrophilic recognition module DNA strand. Without manganese superoxide dismutase (MnSOD) mRNA, nonfluorescence emission of TPE-R-DNA could be observed as a result of the good water solubility. However, after adding the MnSOD mRNA, TPE-R-DNA would be hydrolyzed by Exo III and then produce a number of hydrophobic fluorophores (TPE-R-AT). The aggregation of TPE-R-AT would induce strong red fluorescence. The detection limit of mRNA was 0.6 pM. Furthermore, TPE-R-DNA could be used to image MnSOD mRNA in tumor tissues. Results demonstrated that the expression of MnSOD mRNA in renal cancer adjacent tissue was higher than that in renal cancer.

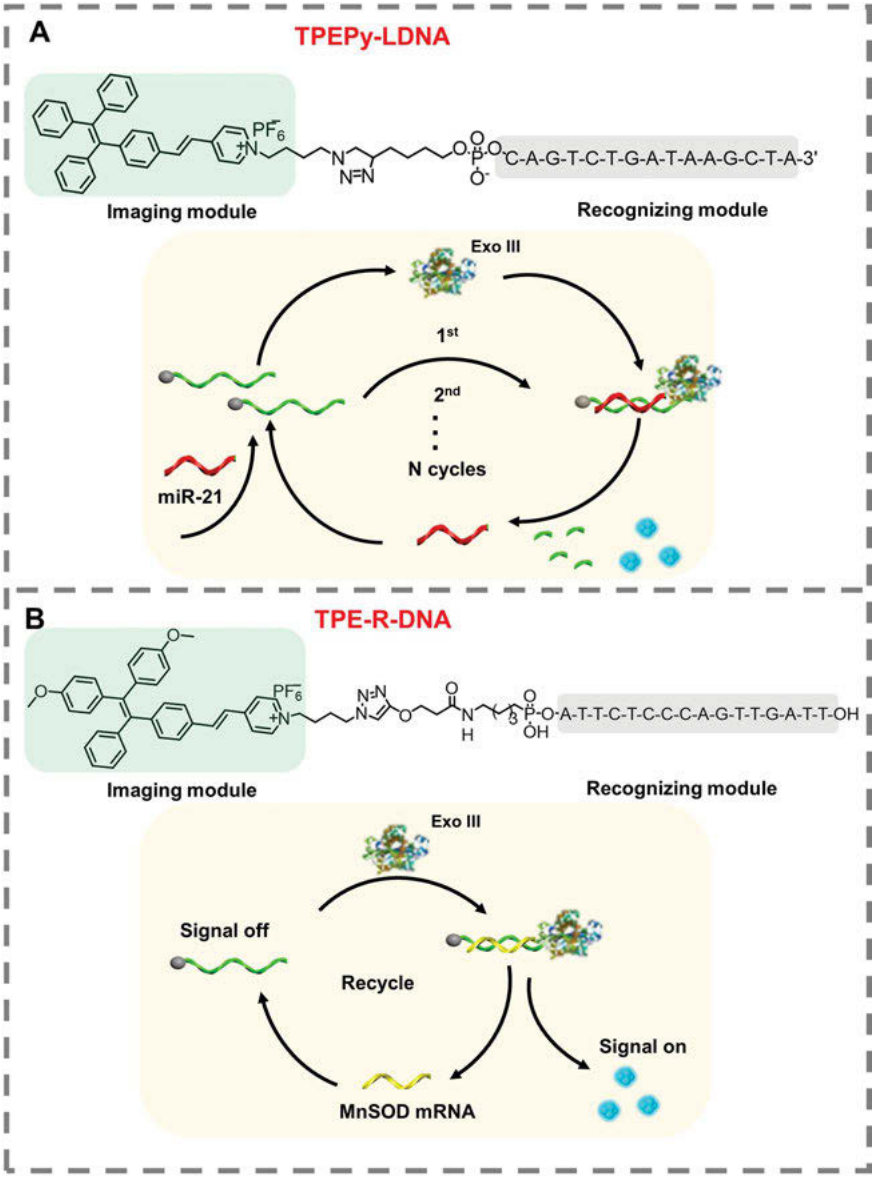


**Figure 2.4:** (A) Chemical Structure of TPEPy-LDNA and scheme of imaging miR-21, based on isothermal amplification strategy. (B) Chemical Structure of the TPE-R-DNA and scheme of detecting and imaging MnSOD mRNA.

### 2.3.2 Proteins

Both structural and functional proteins are essential for maintaining the normal physiological activities of cells. Due to the complexity of biological systems, it is important to specifically label targeted proteins with the interference of other intracellular proteins. Following the work in detecting the telomerase, Lou et al. have reported a series of work about in situ monitoring of intracellular telomerase activity for cancer diagnosis. In 2016, they reported a kind of MNAP with simple operation, rapid reaction, and superior photostability, which could be used for in situ "turn on" imaging of telomerase in living cells [68]. As shown in Figure 2.5A, in the presence of intracellular telomerase, TS primer labeled with quencher group (QP) could be extended in cells. In the meantime, the positively charged TPE-Py molecule could bind to the negatively charged primer and the extended repeat unit, leading to the generation of yellow fluorescence. Thus, yellow fluorescence signal could be used to indicate intracellular telomerase activity. Subsequently, Xia and Lou et al. designed an MNAP that utilized two AIEgens as fluorescent signals to enhance the monitoring effect of telomerase activity by avoiding autofluorescence interference (Figure 2.5B) [69]. In the presence of telomerase, Silole-R, TPE-H, QP and extension repeated units combined, inducing an increase in the fluorescent signal. This MNAP could detect the telomerase, which was extracted from several cell lines and urine samples, as also map telomerase activity in cells. The employment of two AIEgens ensured not only wider linear range, but also low background in cell imaging. Telomerase synthesizes telomere repeats at the telomere ends during the replication phase of the cell cycle; thus, the concentration of intracellular telomerase can be changed. Though a lot of previous work has been done in the biosensing of a reverse transcriptase catalytic component (TERT) mRNA and telomerase activity, the neglecting of heterogeneity in cell cycle may have an influence on the accuracy of detection. Very recently, Lou et al. designed the AIEgen-based biosensing system, which was constructed by PyTPA-DNA for detecting the intracellular concentration of TERT mRNA and Silole-R for detecting the activity of telomerase (Figure 2.5C) [70]. Results illustrated that in different cell cycles, the localization of TERT mRNA and telomerase activity were different. To be specific, in human cancer cells (HeLa), TERT mRNA and telomerase activity were boosted in S phase, while they reduced in G2/M phase. Therefore, this research not only realized the detecting and imaging of TERT mRNA and telomerase, but also illustrated the influence of cell cycle on them, which provided an advanced biosensor tool for accurately analyzing the cell cycle-dependent expression of TERT mRNA and activity of telomerase.

In 2020, Lou et al. developed an MNAP (TPE-Py-DNA) for detecting and imaging of DAM MTase, based on an Exo III-assisted target recovery strategy (Figure 2.5D) [71]. Here, the fluorescent imaging module TPE-Py was conjugated to the specific DNA

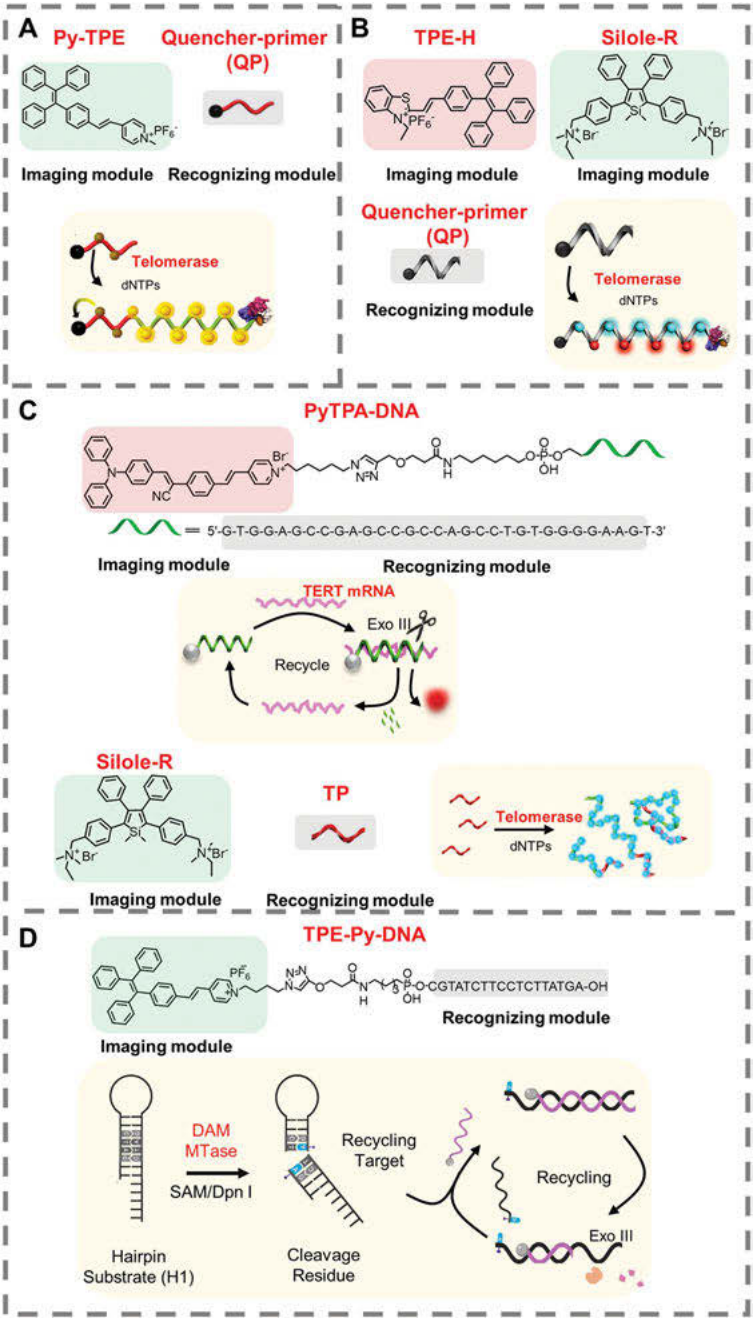


**Figure 2.5:** (A) Chemical structure of Py-TPE, schematic depiction of the quencher-primer (QP), and schematic demonstration of the detection mechanism for telomerase. (B) Chemical structures of

sequence that was used as a recognition module for targeted strand. With DAM MTase, the TPE-Py-DNA could be digested, and it generated aggregation of AIEgen with a significantly enhanced fluorescence signal. Results illustrated that the detection limit of TPE-Py-DNA for DAM MTase was $3.1 \times 10^{-5}$ U/mL. This ultrasensitive biosensing system could detect DAM MTase activity in real samples, evaluate DAM MTase inhibitors, as well as visualize the expression of DAM MTase in *E. coli* cells and *E. coli* cell-bearing tissue from confocal laser fluorescence microscopy (CLSM) images.

Interferon-gamma (IFN-γ) is a cytokine with antiviral and antiparasitic activity, which can also inhibit cellular proliferation [72, 73]. The common method for analyzing the IFN-γ expression is the ELISA test. However, the ELISA test is tedious, time-consuming, and not suitable for continuous monitoring. To image IFN-γ in living cells, Liu and his collaborators developed a fluorescent aptamer sensor, based on AIEgen (TPE-aptamer) with high biocompatibility, cell permeability, and noncytotoxicity [74]. TPE-aptamer was constructed by an oligonucleotide that could specifically recognize IFN-γ and a TPE derivate that functions as an imaging module. Since TPE-aptamer was water-dispersible, the probe exhibited no fluorescence without IFN-γ. After interacted with IFN-γ, it could show strong fluorescence that could be ascribed to the restriction of intramolecular rotations (RIR). TPE-aptamer could detect intracellular IFN-γ with a concentration of 10 pg/mL and be used for real-time biological imaging.

Nucleolin is a nucleolar phosphoprotein that is overexpressed on the surface of specific cancer cells, like the breast cancer cells (MCF-7). For instance, Xiang et al. have designed the AIEgen-encapsulated silica nanoparticles (AIE-FSNPs) to ensure brighter emission [75]. Then, specific DNA aptamer recognizing nucleolin was modified on the surface of AIE-FSNPs to construct the Apt-AIE-FSNPs. Compared to the weak fluorescence in MCF-10A cells (lacking nucleolin), an obvious fluorescence was found in MCF-7 cells, because the Apt-AIE-FSNPs could be internalized by the cells through the selective interaction between DNA aptamer and nucleolin on the cell membrane. Subsequently, a similar aptamer-anchored AIE dot was also developed for imaging the nucleolin in MCF-7 cells with high selectivity [76].

**Figure 2.5** (continued)
TPE-H (left) and Silole-R, schematic demonstration of the quencher-primer (QP), and schematic demonstration of the detection mechanism for telomerase. (C) Chemical structure of PyTPA-DNA, schematic demonstration of the detection mechanism for TERT mRNA, chemical structure of Silole-R, schematic demonstration of the TS primer, and schematic demonstration of the detection mechanism for telomerase activity. (D) Chemical structure of TPE-Py-DNA and scheme of detecting and imaging of DAM MTase.

## 2.4 Conclusion

Nowadays, nucleic acid-functionalized AIEgens have attracted increasing attention from researchers in many fields, such as biochemistry, molecular biology, biomedicines, etc. This chapter summarized the representative MNAPs with water solubility, biocompatibility, photostability, and specific recognition ability for biosensing applications. Firstly, the MNAPs for bio-analytes detection to achieve early-diagnosis and prognosis were introduced. Then, we highlighted the techniques and a few representative MNAPs for high-resolution fluorescence imaging of cell and tissue. Despite the inspiring study results, the development of MNAPs is still in its nascent stage, and there are many problems that should be overcame. i) The AIEgens adopted currently are mainly limited to TPE or TPS derivatives, whose wavelength is short. They are suitable for detection and imaging in vitro, while not in vivo owing to the inherent background of small animals. ii) Compared to other biomacromolecules-modified AIEgens probe, the quantity of MNAP is inadequate, because long-length DNA strands are not easily synthesized. iii) The functional linking method between nucleic acids and AIEgen module is limited and mainly relies on the electrostatic interaction and click chemistry. iv) To realize the satisfying biosensing outcome of MNAPs in cells or in vivo, equipping the MNAPs with more capabilities such as enhanced tumor accumulation or tumor cells internalization is necessary. v) The strategies such as signal amplification [77], edited dynamic ranges [78], as well as dual-signal-output nanochannels [79] could be used to achieve accurate quantification and high sensitivity of MNAPs. On the basis of rapid development, MNAPs are promising in solving the current biosensing problems. We hope that this chapter could propel the practical and clinical application of MNAPs in early-diagnosis, prognosis, and therapy of diseases.

## References

[1] Hong G, Antaris AL, Dai H, Near-infrared fluorophores for biomedical imaging, Nat Biomed Eng, 2017, 1, 1–22.
[2] Lenroot RK, Giedd JN, Brain development in children and adolescents: Insights from anatomical magnetic resonance imaging, Neurosci Biobehav Rev, 2006, 30, 718–729.
[3] Picano E, Sustainability of medical imaging, Bmj, 2004, 328, 578–580.
[4] Lindner JR, Microbubbles in medical imaging: Current applications and future directions, Nat Rev Drug Discov, 2004, 3, 527–533.
[5] Fujimoto JG, Pitris C, Boppart SA, Brezinski ME, Optical coherence tomography: An emerging technology for biomedical imaging and optical biopsy, Neoplasia, 2000, 2, 9–25.
[6] Wei W, He X, Ma N, DNA-templated assembly of a heterobivalent quantum dot nanoprobe for extra- and intracellular dual-targeting and imaging of live cancer cells, Angew Chem, 2014, 126, 5679–5683.
[7] Resch-Genger U, Grabolle M, Cavaliere-Jaricot S, Nitschke R, Nann T, Quantum dots versus organic dyes as fluorescent labels, Nat Methods, 2008, 5, 763.

[8] Giepmans BN, Adams SR, Ellisman MH, Tsien RY, The fluorescent toolbox for assessing protein location and function, Science, 2006, 312, 217–224.
[9] Shaner NC, Steinbach PA, Tsien RY, A guide to choosing fluorescent proteins, Nat Methods, 2005, 2, 905–909.
[10] Medintz IL, Uyeda HT, Goldman ER, Mattoussi H, Quantum dot bioconjugates for imaging, labelling and sensing, Nat Mater, 2005, 4, 435–446.
[11] Cormode DP, Jarzyna PA, Mulder WJ, Fayad ZA, Modified natural nanoparticles as contrast agents for medical imaging, Adv Drug Deliv Rev, 2010, 62, 329–338.
[12] Luo J, Xie Z, Lam JW, et al., Aggregation-induced emission of 1-methyl-1, 2, 3, 4, 5-pentaphenylsilole, Chem Commun, 2001, 1740–1741.
[13] Mei J, Leung NL, Kwok RT, Lam JW, Tang BZ, Aggregation-induced emission: Together we shine, united we soar, Chem Rev, 2015, 115, 11718–11940.
[14] Chen J, Law C, Lam J, Dong Y, et al., Synthesis, light emission, nanoaggregation, and restricted intramolecular rotation of 1,1-substituted 2,3,4,5-tetraphenylsiloles, Chem Mater, 2003, 15, 1535–1546.
[15] Zheng Z, Zhang T, Liu H, et al., Bright near-infrared aggregation-induced emission luminogens with strong two-photon absorption, excellent organelle specificity, and efficient photodynamic therapy potential, ACS Nano, 2018, 12, 8145–8159.
[16] Gui C, Zhao E, Kwok RT, et al., AIE-active theranostic system: Selective staining and killing of cancer cells, Chem Sci, 2017, 8, 1822–1830.
[17] Ding D, Li K, Liu B, Tang BZ, Bioprobes based on AIE fluorogens, Acc Chem Res, 2013, 46, 2441–2453.
[18] Sun Y, Li Y, Ma X, Duan L, A turn-on fluorescent probe for cyanide based on aggregation of terthienyl and its application for bioimaging, Sens Actuators B Chem, 2016, 224, 648–653.
[19] Ou X, Lou X, Xia F, A highly sensitive DNA-AIEgen-based “turn-on” fluorescence chemosensor for amplification analysis of $Hg^{2+}$ ions in real samples and living cells, Sci China Chem, 2017, 60, 663–669.
[20] Ou X, Hong F, Zhang Z, et al., A highly sensitive and facile graphene oxide-based nucleic acid probe: Label-free detection of telomerase activity in cancer patient’s urine using AIEgens, Biosens Bioelectron, 2017, 89, 417–421.
[21] Jia Y, Zuo X, Lou X, et al., Rational designed bipolar, conjugated polymer-DNA composite beacon for the sensitive detection of proteins and ions, Anal Chem, 2015, 87, 3890–3894.
[22] Zhang M, Saha ML, Wang M, et al., Multicomponent platinum (II) cages with tunable emission and amino acid sensing, J Am Chem Soc, 2017, 139, 5067–5074.
[23] Liu Y, Deng C, Tang L, et al., Specific detection of D-glucose by a tetraphenylethene-based fluorescent sensor, J Am Chem Soc, 2011, 133, 660–663.
[24] Li Y, Kwok RT, Tang BZ, Liu B, Specific nucleic acid detection based on fluorescent light-up probe from fluorogens with aggregation-induced emission characteristics, RSC Adv, 2013, 3, 10135–10138.
[25] La DD, Bhosale SV, Jones LA, Bhosale SV, Tetraphenylethylene-based AIE-active probes for sensing applications, ACS Appl Mater Interfaces, 2017, 10, 12189–12216.
[26] Gu X, Zhao E, Zhao T, et al., A mitochondrion-specific photoactivatable fluorescence turn-on AIE-based bioprobe for localization super-resolution microscope, Adv Mater, 2016, 28, 5064–5071.
[27] Wang YF, Zhang T, Liang XJ, Aggregation-induced emission: Lighting up cells, Revealing Life! Small, 2016, 12, 6451–6477.
[28] Zhao E, Chen Y, Wang H, et al., Light-enhanced bacterial killing and wash-free imaging based on AIE fluorogen, ACS Appl Mater Interfaces, 2015, 7, 7180–7188.

[29] Gao Y, Feng G, Jiang T, et al., Biocompatible nanoparticles based on Diketo-Pyrrolo-Pyrrole (DPP) with aggregation-induced Red/NIR emission for in vivo two-photon fluorescence imaging, Adv Funct Mater, 2015, 25, 2857–2866.
[30] Dang D, Liu H, Wang J, et al., Highly emissive AIEgens with multiple functions: Facile synthesis, chromism, specific lipid droplet imaging, apoptosis monitoring, and in vivo imaging, Chem Mater, 2018, 30, 7892–7901.
[31] Li S, Langenegger SM, Häner R, Control of aggregation-induced emission by DNA hybridization, Chem Commun, 2013, 49, 5835–5837.
[32] Fleischhacker M, Schmidt B, Circulating nucleic acids (CNAs) and cancer-A survey, Biochim Biophys Acta, 2007, Jan. 1775.
[33] Wu F, Wu X, Duan Z, et al., Biomacromolecule-functionalized AIEgens for advanced biomedical studies, Small, 2019, 15, e1804839.
[34] Biju V, Chemical modifications and bioconjugate reactions of nanomaterials for sensing, imaging, drug delivery and therapy, Chem Soc Rev, 2014, 43, 744–764.
[35] Santhiago M, Vieira IC, l-Cysteine determination in pharmaceutical formulations using a biosensor based on laccase from Aspergillus oryzae, Sens Actuators B Chem, 2007, 128, 279–285.
[36] Gill BD, Indyk HE, Development and application of a liquid chromatographic method for analysis of nucleotides and nucleosides in milk and infant formulas, Int Dairy, 2007, 17, 596–605.
[37] Asan A, Isildak I, Determination of major phenolic compounds in water by reversed-phase liquid chromatography after pre-column derivatization with benzoyl chloride, J Chromatogr A, 2003, 988, 145–149.
[38] Xu JP, Song ZG, Fang Y, et al., Label-free fluorescence detection of mercury(II) and glutathione based on Hg2+-DNA complexes stimulating aggregation-induced emission of a tetraphenylethene derivative, Analyst, 2010, 135, 3002–3007.
[39] Lu D, He L, Wang Y, et al., Tetraphenylethene derivative modified DNA oligonucleotide for in situ potassium ion detection and imaging in living cells, Talanta, 2017, 167, 550–556.
[40] Mandelbaum RT, Allan DL, Wackett LP, Isolation and characterization of a Pseudomonas sp. that mineralizes the s-triazine herbicide atrazine, Appl Environ Microbiol, 1995, 61, 1451–1457.
[41] Suri CR, Kaur J, Gandhi S, Shekhawat GS, Label-free ultra-sensitive detection of atrazine based on nanomechanics, Nanotechnology, 2008, 19, 235502.
[42] Pérez-Ruiz T, Martínez-Lozano C, Tomás V, Martín J, Determination of ATP via the photochemical generation of hydrogen peroxide using flow injection luminol chemiluminescence detection, Anal Bioanal Chem, 2003, 377, 189–194.
[43] Ma K, Wang H, Li H, et al., A label-free aptasensor for turn-on fluorescent detection of ATP based on AIE-active probe and water-soluble carbon nanotubes, Sens Actuators B Chem, 2016, 230, 556–558.
[44] Pfohl-Leszkowicz A, Manderville RA, Ochratoxin A, An overview on toxicity and carcinogenicity in animals and humans, Mol Nutr Food Res, 2007, 51, 61–99.
[45] Wang C, Qian J, Wang K, et al., Magnetic-fluorescent-targeting multifunctional aptasensor for highly sensitive and one-step rapid detection of ochratoxin A, Biosens Bioelectron, 2015, 68, 783–790.
[46] Wang C, Qian J, Wang K, et al., Colorimetric aptasensing of ochratoxin A using Au@ $Fe_3O_4$ nanoparticles as signal indicator and magnetic separator, Biosens Bioelectron, 2016, 77, 1183–1191.

[47] Ma L, Xu B, Liu L, Tian W, A label-free fluorescent aptasensor for turn-on monitoring ochratoxin a based on AIE-active probe and graphene oxide, Chem Res Chinese U, 2018, 34, 363–368.
[48] Li Y, Kwok RTK, Tang BZ, Liu B, Specific nucleic acid detection based on fluorescent light-up probe from fluorogens with aggregation-induced emission characteristics, RSC Adv, 2013, 3, 10135.
[49] Zhang R, Kwok RTK, Tang BZ, Liu B, Hybridization induced fluorescence turn-on of AIEgen-oligonucleotide conjugates for specific DNA detection, RSC Adv, 2015, 5, 28332–28337.
[50] Li X, Ma K, Zhu S, et al., Fluorescent aptasensor based on aggregation-induced emission probe and graphene oxide, Anal Chem, 2014, 86, 298–303.
[51] Wang H, Ma K, Xu B, Tian W, Tunable supramolecular interactions of aggregation-induced emission probe and graphene oxide with biomolecules: An approach toward ultrasensitive label-free and “turn-on” DNA sensing, Small, 2016, 12, 6613–6622.
[52] Min X, Zhuang Y, Zhang Z, et al., Lab in a tube: Sensitive detection of micrornas in urine samples from bladder cancer patients using a single-label DNA probe with AIEgens, ACS Appl Mater Interfaces, 2015, 7, 16813–16818.
[53] Chen Y, Min X, Zhang X, et al., AIE-based superwettable microchips for evaporation and aggregation induced fluorescence enhancement biosensing, Biosens Bioelectron, 2018, 111, 124–130.
[54] Zhu L, Zhou J, Xu G, et al., DNA quadruplexes as molecular scaffolds for controlled assembly of fluorogens with aggregation-induced emission, Chem Sci, 2018, 9, 2559–2566.
[55] Lou X, Zhuang Y, Zuo X, et al., Real-time, quantitative lighting-up detection of telomerase in urines of bladder cancer patients by AIEgens, Anal Chem, 2015, 87, 6822–6827.
[56] Zhuang Y, Zhang M, Chen B, et al., Quencher group induced high specificity detection of telomerase in clear and bloody urines by AIEgens, Anal Chem, 2015, 87, 9487–9493.
[57] Zhuang Y, Xu Q, Huang F, et al., Ratiometric fluorescent bioprobe for highly reproducible detection of telomerase in bloody urines of bladder cancer patients, ACS Sens, 2016, 1, 572–578.
[58] Cheng X, Roberts RJ, AdoMet-dependent methylation, DNA methyltransferases and base flipping, Nucleic Acids Res, 2001, 29, 3784–3795.
[59] Jaenisch R, Bird A, Epigenetic regulation of gene expression: How the genome integrates intrinsic and environmental signals, Nat Genet, 2003, 33, 245–254.
[60] Li W, Wu P, Zhang H, Cai C, Signal amplification of graphene oxide combining with restriction endonuclease for site-specific determination of DNA methylation and assay of methyltransferase activity, Anal Chem, 2012, 84, 7583–7590.
[61] Zeng YP, Hu J, Long Y, Zhang CY, Sensitive detection of DNA methyltransferase using hairpin probe-based primer generation rolling circle amplification-induced chemiluminescence, Anal Chem, 2013, 85, 6143–6150.
[62] Zheng XJ, Qiu JD, Zhang L, Wang ZX, Liang RP, Label-free colorimetric assay for DNA methylation based on unmodified Au nanorods as a signal sensing probe coupled with enzyme-linkage reactions, Chem Commun, 2013, 49, 3546–3548.
[63] Wang Y, Chen J, Chen Y, Li W, Yu C, Polymer-induced perylene probe excimer formation and selective sensing of DNA methyltransferase activity through the monomer–excimer transition, Anal Chem, 2014, 86, 4371–4378.
[64] Chen J, Wang Y, Li W, et al., Nucleic acid-induced tetraphenylethene probe noncovalent self-assembly and the superquenching of aggregation-induced emission, Anal Chem, 2014, 86, 9866–9872.

[65] Kong RM, Zhang X, Ding L, Yang D, Qu F, Label-free fluorescence turn-on aptasensor for prostate-specific antigen sensing based on aggregation-induced emission-silica nanospheres, Anal Bioanal Chem, 2017, 409, 5757–5765.
[66] Min X, Zhang M, Huang F, Lou X, Xia F, Live cell MicroRNA imaging using exonuclease III-aided recycling amplification based on aggregation-induced emission luminogens, ACS Appl Mater Interfaces, 2016, 8, 8998–9003.
[67] Wang X, Dai J, Min X, et al., DNA-conjugated amphiphilic aggregation-induced emission probe for cancer tissue imaging and prognosis analysis, Anal Chem, 2018, 90, 8162–8169.
[68] Zhuang Y, Huang F, Xu Q, et al., Facile, fast-responsive, and photostable imaging of telomerase activity in living cells with a fluorescence turn-on manner, Anal Chem, 2016, 88, 3289–3294.
[69] Zhuang Y, Shang C, Lou X, Xia F, Construction of AIEgens-based bioprobe with two fluorescent signals for enhanced monitor of extracellular and intracellular telomerase activity, Anal Chem, 2017, 89, 2073–2079.
[70] Wu X, Wu J, Dai J, et al., Role of cell cycle progression on analyzing telomerase in cancer cells based on aggregation-induced emission luminogens, Natl Sci Rev, 2021.
[71] Wu J, Hu Q, Chen Q, et al., Modular DNA-incorporated aggregation-induced emission probe for sensitive detection and imaging of DNA methyltransferase, ACS Appl Bio Mater, 2020, 3, 9002–9011.
[72] Song X, He J, Xu H, et al., The antiviral effects of acteoside and the underlying IFN-γ-inducing action, Food Funct, 2016, 7, 3017–3030.
[73] Marcano D, Acharya G, Pflugfelder SC, IFN-γ inhibits cell proliferation and outgrowth from cultured lacrimal gland tissues, Invest Ophthalmol Vis Sci, 2015, 56, 2491–2491.
[74] Ma K, Zhang F, Sayyadi N, et al., "Turn-on" fluorescent aptasensor based on AIEgen labeling for the localization of IFN-gamma in live cells, ACS Sens, 2018, 3, 320–326.
[75] Wang X, Song P, Peng L, Tong A, Xiang Y, Aggregation-induced emission luminogen-embedded silica nanoparticles containing DNA aptamers for targeted cell imaging, ACS Appl Mater Interfaces, 2016, 8, 609–616.
[76] Zhang P, Zhao Z, Li C, et al., Aptamer-decorated self-assembled aggregation-induced emission organic dots for cancer cell targeting and imaging, Anal Chem, 2018, 90, 1063–1067.
[77] Duan R, Lou X, Xia F, The development of nanostructure assisted isothermal amplification in biosensors, Chem Soc Rev, 2016, 45, 1738–1749.
[78] Vallée-Bélisle A, Ricci F, Plaxco KW, Engineering biosensors with extended, narrowed, or arbitrarily edited dynamic range, J Am Chem Soc, 2012, 134, 2876–2879.
[79] Long Z, Zhan S, Gao P, et al., Recent advances in solid nanopore/channel analysis, Anal Chem, 2018, 90, 577–588.

Jiao Liu, Xiao Zhang, Fang-ling Zhang, Yi-ting Wang,
Yuan-yuan Gao, Tong-yi Sun, Li-Li Li

# Chapter 3
# Peptide–AIEgen conjugates for biomedical diagnosis and bioimaging

## 3.1 Introduction

In recent years, increased number of fluorescent probes have been developed and used in the field of biology and medicine. They have been widely studied and utilized for their advantages of high sensitivity, quick response, and convenient operation [1]. However, traditional fluorescent groups still have some serious problems, such as photonic bleaching, fluorescence quenching due to aggregation in aqueous solution, spectral overlap with the auto-fluorescence of biological substrate itself, poor stability, and inapplicability to biological organisms, etc. In addition, traditional fluorescent probes have aggregation-induced quenching (ACQ) effect [2], affecting biological and medical applications of fluorescent molecules. Nevertheless, aggregation-induced luminescent molecules can solve the problem of traditional fluorescent probes. The concept of aggregation-induced emission (AIE) was proposed by Tang and his colleagues in 2001 [3]. It was used to describe the unique phenomenon that a series of fluorophores exhibit strong fluorescence in the highly aggregated state and weak emission or nonemission in the monolayer state. Luminescent agents with AIE properties were known as AIEgens. AIEgens show stronger fluorescence in the aggregated state and weaker fluorescence in good solvents [4, 5]; they are usually propeller shaped and act as a rotating unit [6]. AIEgens are nonfluorescent as monomers due to the rapid

**Acknowledgements:** This work was supported by National Key R&D Program of China (2018YFE0205400), General Project of National Natural Science Foundation of China (31671028, 51873045); Dr. L.-L. L. thanks the Youth Innovation Promotion, CAS (2017053).

**Jiao Liu, Xiao Zhang,** National Center for Nanoscience and Technology (NCNST), CAS Key Laboratory for Biomedical Effects of Nanomaterials, CAS Center for Excellence in Nanoscience, Beijing, 100109, China; School of Pharmacy, Weifang Medical University, Weifang, 261000, China
**Fang-ling Zhang, Yi-ting Wang,** National Center for Nanoscience and Technology (NCNST), CAS Key Laboratory for Biomedical Effects of Nanomaterials, CAS Center for Excellence in Nanoscience, Beijing, 100109, China
**Yuan-yuan Gao,** School of Pharmacy, Weifang Medical University, Weifang, 261000, China
**Tong-yi Sun,** School of Life Science and Technology, Weifang Medical University, Weifang, 261000, China
**Li-Li Li,** National Center for Nanoscience and Technology (NCNST), CAS Key Laboratory for Biomedical Effects of Nanomaterials, CAS Center for Excellence in Nanoscience, Beijing, 100109, China, e-mail: lill@nanoctr.cn

https://doi.org/10.1515/9783110672220-003

nonradiative decay of the excited state, caused by the molecular motion of the rotating unit, which reduces the excitation energy. However, in the aggregated state, due to impeded intramolecular rotation (RIM), minimized π-π stacking and limit of intramolecular motions [7], they block the energy dissipation of excited states and activate a barrier to nonradiation decay, and so AIEgens glow brightly. This fluorescent "turn-on" mechanism makes AIEgens ideal for the construction of fluorescent bioluminescent probes [8, 9]. Although AIEgens have solved the problems of traditional dyes to some extent and have made great progress, there is still much room for development of novel AIE fluorescent probes with all desirable biological imaging properties. For example, most of the existing AIE probes exhibit small Stokes shifts, lack specific organ-targeting capabilities, and poor water solubility, which restrict their application in tracking biological processes and pathologic pathways over long periods of time. And almost all of the previously reported chemical sensors based on AIE process probes have only been used in vitro because of their potential biotoxicity. Based on these limitations, AIEgens have been coupled with many active molecules (such as metals, DNA, proteins, sugars, etc.) [10–13]. Among them, the use of peptides or self-assembly peptides have the characteristics of small volume, easy to synthesize, functional capability, etc., which can improve the water-solubility of AIEgens and increase the application of AIEgens in disease diagnosis or treatment.

Peptide, a biological component, composed of dozens of amino acids, has attracted increased attention due to its simple structure, strong adjustability, diverse functions, low cost, and widespread application [14]. Self-assembly of peptides can be effectively realized through hydrogen bond and amino acid residue interaction, electrostatic interaction, hydrophobic interaction, and π-π stacking interaction [15–17]. Although it is not defined clearly at the genetic level, the nanoscale assembly of peptides can perform many key biological functions, and previous studies have highlighted the importance of peptide topological structure in maintaining the extracellular matrix and normal function of cells. As a kind of biological macromolecules, peptides are widely used in the detection of protein (enzyme) activity, molecular recognition, targeting tumor cells, building multi-functional polymers, and in other fields [18–20]. Therefore, peptides also have unique advantages in the construction of modular probes, as follows: (1) Peptides vary in structure and so play different roles in their function. (2) With the development of modern organic chemistry and molecular biology, we can design and synthesize peptide sequences. (3) Peptide is a kind of biocompatible molecule that can be used to construct multi-component nanostructures, together with other biological materials.

In summary, the modification of AIEgens with peptides or self-assembly peptides can not only overcome the physical and chemical drawbacks of AIEgens and reduce their toxicity, but can also enhance the fluorescence intensity and the anti-photonic bleaching ability of AIEgens [21]. Peptide–AIEgen conjugate can improve its biological activity through self-assembly or aggregation of peptides in vivo to make the conjugate stay in the body. Therefore, the peptide–AIEgen conjugate provides a new idea for

the application of AIEgens in vivo. In this paper, we first focus on the application of functional peptide in the biomedical field, followed by examples of functional peptide and AIEgens conjugates to improve the shortcomings of AIEgens and be used in the diagnosis and treatment of diseases. We focus on the study and utilization of the conjugates of environment-responsive peptides with AIEgens.

## 3.2 Peptide–AIEgens conjugation

### 3.2.1 Targeting peptides: modification

Targeting peptides are peptide fragments with specific amino acid sequences that can bind to specific receptors that are highly expressed in tumor tissues, and are easy to be synthesized and modified specifically [22]. By changing the charge distribution of the peptide molecular structure or connecting to specific target molecules, peptide can be targeted to specific sites such as tumor cell membrane and endoplasmic reticulum. Targeting peptides are widely used in tumor imaging and therapy because of their high specificity, strong function, and easy removal from nontargeted sites. The combination of targeted peptides and AIEgens can not only improve the imaging efficiency of targeted peptides but also improve the solubility of AIEgens, which has become a research hotspot in recent years (Table 3.1).

**Table 3.1:** Classifications and functions of targeting peptides.

| Name | AIEgens | Sequences | Target | Functions | Ref |
|---|---|---|---|---|---|
| Q1-PEP | Quino-1 | RACR | Endoplasmic reticulum | Targeted for vesicle transport monitoring and long-term biological imaging | [23] |
| TCNTP | PyTPE | RGD | $\alpha_v\beta_3$ | Nucleus-specific imaging, long-term low-toxicity follow-up of tumor cells | [24] |
| TPE-In-PSA@Au | TPE-In | CSKLQ-OH | Prostate specific antigen (PSA) | Imaging prostate cancer cells and diagnosing prostate cancer | [25] |
| TPECM-2GFLGD3-cRGD | TPECM | cRGD | Integrin | Light-up imaging and activatable photodynamic therapy | [26] |
| BTPEAQ-cRGD | BTPEAQ | cRGD | Integrin | Photoablation of tumor cells | [28] |

Targeting peptides binding AIEgens can target specific organelles for long-term biological imaging, such as small arginine-derived molecules that have been shown to interact specifically with proteins in the endoplasmic reticulum (ER). Shi et al. [23] reported a highly stable AIEgens fluorescent nanodots assembled from an amphiphilic quinolone derivative peptide conjugate, Quino-1-Fmoc-RACR (also known as Q1-PEP). The arginine-derived peptides contained in the nanodots has been shown to specifically interact with ER anchored proteins, thus providing the ability to target ER, enabling the monitoring of vesicular transport, and providing long-term biological imaging. Over a long time, specific enzymes and antigens are present in in tumor cells and other biomarkers and they can also be used as target peptides. For example, cNGR peptides targeted aminopeptidase N (CD13), the classical targeting sequence, arginine-glycine-asparagine (RGD), targeted integrin $\alpha_v\beta_3$, by combining a functional combination of peptides (TCNTs, which included two targeting peptides: cNGR and RGD), a cell-penetrating peptide (CPP), a nuclear localization signal (NLS), and a typical AIEgen tetraphenylacetylene derivative (PYTPE) as conjugate. Cheng et al. [24] designed a double-targeting conjugated peptides multifunctional fluorescent probe (CNGR-CPP-NLS-RGD-PYTPE, TCNTP) with AIE characteristics. The probe emitted strong yellow fluorescence after the functional combination peptide TCNT targeted the respective biomarkers. Through the AIE effect of PYTPE, highly efficient nuclear-specific imaging and long-term low-toxicity tracking of tumor cells could be achieved (Figure 3.1).

TPE and its derivatives are highly efficient and generable AIEgens. Ramya et al. [25] synthesized a TPE analogue (TPE-In), used gold nanoparticles as an enhanced Raman Scattering substrate, used TPE-In as roman reporter, and bounded with a specific peptide based on Cys-Ser-Lys-Leu-Gln-OH, which was famous for recognizing prostate-specific antigen (PSA), a specific tumor marker of prostate cancer. Such a conjugate could be specifically used to image prostate cancer cells and provide a new idea for the diagnosis and discovery of early prostate cancer. The RGD sequence consisted of arginine, glycine, and aspartic acid, and existed in various extracellular matrices. It could specifically bind to 11 integrins and effectively promote cell adhesion to biomaterial. The prodrugs could self-assemble into nanoparticles (CP-DOX NP) in aqueous media, and these nanoparticles could target cancer cells because of their surface functionalization with cRGD (TCP-DOX NP). Yuan et al. [26] engineered an AIE photosensitizer TPECM and integrated it with a cathepsin B reactive- Gly- Phe-Leu- Gly- (GFLG) peptide and a cRGD targeting ligand to develop TPECM-2GFLGD3-cRGD bioprobe for light-up imaging and activatable photodynamic therapy [27]. Similarly, Feng et al. [28] conjugated BTPEAQ, a polymeric-encapsulated AIE particle with cRGD peptide to obtain BTPEAQ-cRGD dots. cRGD also targeted cancer cells with overexpression of integrin, while maintaining the control cell intact. BTPEAQ-cRGD dots showed a good photoablation effect on MDA-MB-231 cells.

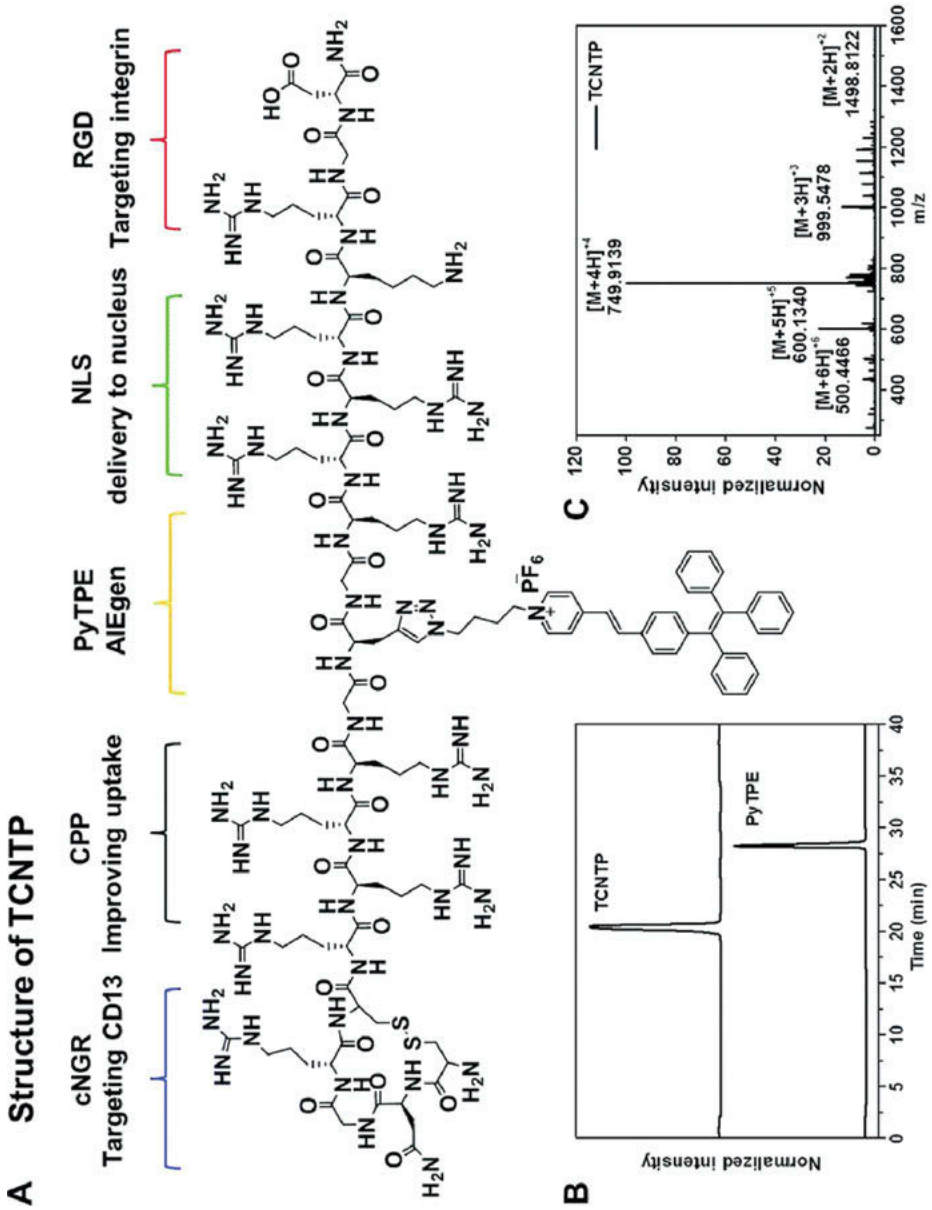


**Figure 3.1:** (A) Sequence and molecular structure of TCNTP; (B) High performance liquid chromatogram of TCNTP; C TCNTP mass spectrum results. Adapted with permission from ref [24]. Copyright © The Royal Society of Chemistry 2017.

### 3.2.2 Cell-penetrating peptide: conjugation

Cell, as the basic unit of life, can be used as both therapeutic drugs and targets of drugs. Cell-penetrating peptides (CPPs) are a class of short peptides that can penetrate cell membranes and can be modified to improve the efficiency of drug delivery. CPPs are getting a lot of attention, of late [29]. Basic CPPs can be divided into three types according to the differences in physical properties, such as hydrophobicity and polarity: cationic peptides, hydrophobic peptides, and amphipathic peptides. It is a feasible strategy to modify AIEgens with CPPs to obtain cell membrane penetrating probe. The advantages of AIE modified by cell-penetrating peptide is that it can pass through the cell, resulting in better cell uptake efficiency and cell image quality [30]. In this paper, the application of AIEgen-modified peptides in the diagnosis and treatment of diseases is summarized based on several typical sequences of cell-penetrating peptides (Table 3.2).

**Table 3.2:** Classifications and functions of cell penetrating peptides.

| Name | AIEgens | Functions | Ref. |
|---|---|---|---|
| AIE-PNPs | TPE-TCF | Cell fluorescence imaging was performed at a relatively low concentration of Aiegens | [31] |
| Tat-AIE dots | TPETPAFN | Tracking Cancer Cells | [32] |
| DPPCPP | DPP | As an effective fluorescent probe for single– and two-photon excitation fluorescence imaging | [33] |
| DOX-FCPPs-PyTPE, DFP | PyTPE | Control of drug delivery and accurate tracking of drug release in MMP-2 overexpressed cells | [35] |

The translation of HIV-1 trans activator, Tat, resulted in a protein containing 86 amino acids. In 1988, Green and Frankel et al. [30] confirmed experimentally, for the first time, that the trans-activating protein, Tat, of HIV-1 can actively transduce into the cell and participate in the biological process of the cell. Based on this principle, amino-functionalized AIE polymer NPs (AIE-PNPs) was effectively synthesized by Hu et al. [31] through the one-pot miniemulsion copolymerization of methyl methacrylate with functional comonomers containing amino groups. The surface of AIE-PNPs was further modified with the maleimide group and the HIV-1 Tat peptide, which significantly improved the cell uptake efficiency of AIE-PNPs and delivered better cell fluorescence imaging quality at a relatively low concentration of AIE-PNPs. Li et al. [32] also reported that the lipid polyethylene glycol (PEG) and lipid-PEG-$NH_2$ mixture was used as an encapsulation substrate to bio-combine AIEgen particles with the cell-penetrating peptide of HIV-1 Tat protein to obtain Tat-AIE dots with high cell-internalization efficiency. The CPPs probe obtained by combining cysteine-modified transmembrane peptides with AIE molecule has been widely used. Gao

et al. [33] used 1,2- distearoyl- sn- glycero- 3- phosphoethanol amine- N- [maleimide (polyethyleneglycol)-2000 (DSPE-PEG-Mal) as the encapsulation matrix. Furthermore, cysteine-modified CPPs and RKKKRRQRRRC peptide sequences were used for surface functionalization, and DPPCPP nanoparticles, with good water dispersion and biocompatibility, were obtained. The results indicated that DPPCPP nanoparticles can be highly ingested into the cell as a high efficiency fluorescent probe for single- and two-photon excitation fluorescence imaging. Arginine is also a typical membrane-penetrating amino acid. The Tat protein mentioned above is also an arginine-rich polypeptide structure. The arginine-rich peptides can not only enhance the water-solubility of AIEgens molecule and reduce the aggregation of AIE molecule, but also the positive charge of arginine can cause osmotic swelling and rupture of the cell membrane [34], and result in rapid delivery of a variety of substances into cells through the endosomal escape mechanism. Cheng et al. [35] reported a protease reaction prodrug (DOX-FCPPs-PyTPE, DFP), which consisted of three components: AIE active TPE derivative PyTPE, functionalized cell-penetrating peptide (FCPPS), which contained arginine-rich cell-penetrating peptide (CPP) and short protease reactive peptide (LGLAG), as well as therapeutic units (doxorubicin, DOX) that can enter the cell. It was selectively cleaved by the cancer-associated enzyme matrix metalloproteinase-2 (MMP-2) with AIE properties that controls drug delivery and accurately tracks drug release in living cells. It provided a new and promising method for controlled drug release and real-time tracking of drug release in MMP-2 overexpressed cells (Figure 3.2).

### 3.2.3 Stimuli responsive peptides-modification

In the complex biological environment, there are many biological stimuli and external stimuli. The introduction of stimulus-response characteristics of peptide enables their function to control the response to the required stimulus and becomes a potentially valuable tool for biological applications [36]. Peptides enable to respond to exogenous (temperature, magnetic field, light) [37] or endogenous (pH, enzyme, redox gradient) stimuli [38]. The advantages of the stimuli-responsive peptide–AIEgen conjugates are that they can perform specific structural changes in response to specific stimuli, to accurately perform imaging, diagnosing, and monitoring at specific sites. For example, Liu et al. [39] reported a reactive peptide–AIEgen conjugate that could induce furin activity. If the peptide sequence was designed as the substrate of furin, the cleavage product could be further self-assembled into fluorescent nanoparticles to detect the level of furin. They designed a probe Ac-Arg-Val-Arg-Arg-Cys(StBu)-Lys (TPE)-CBT, which contained an Ac-Arg-Val-Arg-Arg (RVRR) peptide sequence that was the zymolyte for furin cleavage, a CBT motif and a disulfided Cys motif for CBT–Cys condensation, and an AIEgen (TPE motif). The probe entered furin-overexpressing tumor cells. Its disulfide bond on the cysteine motifs was reduced by intracellular

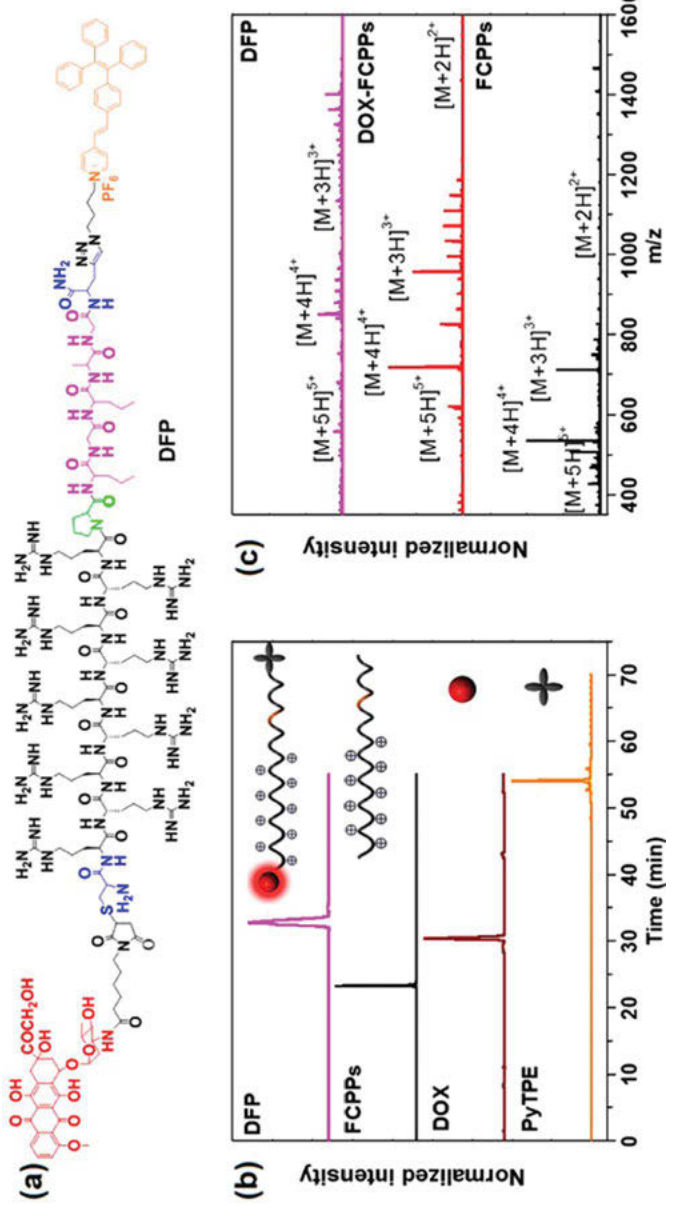


**Figure 3.2:** a) The molecular composition and structure of DFP; b) The results of high-performance liquid chromatogram; c) The results of mass spectrum. Adapted with permission from ref [35]. Copyright 2016, American Chemical Society.

glutathione (GSH) and its RVRR peptide substrate was cleaved by furin to yield the reactive intermediate. Then, the reactive intermediate lead to aggregation of the TPE fluorogen. This approach not only took advantages of the characteristic response of the peptide monomer to a specific stimulus, but also enabled the peptide monomer to be further assembled, and molecular simulation results showed that the assembly led to the orderly arrangement of AIEgens. This structure more effectively restricted the intramolecular rotation of the benzene ring, resulting in a strong emission [40]. The self-assembly properties of peptide make them more useful in coupling with AIEgens, as will be discussed below.

## 3.3 Triggered aggregations of peptide–AIEgens by environmental factors

### 3.3.1 Ionic strength-induced aggregation

Usually, AIEgens are combined with π-conjugated salt-responsive peptides in the structure to form a material with enhanced fluorescence emission. As the ionic strength increases, the fluorescence intensity of the molecule gradually increases [41]. This strategy can be applied to many traditional π-conjugated luminescent gelling agents, providing a general method for controlling the release of hydrogels. Zhang et al. [41] designed a salt-responsive peptide hydrogel TPE-Q19 with enhanced emission during gelation. This structure had two fragments with different functions. Tetraphenylethylene was used as a luminescent agent. TPE had almost no fluorescence in solution, but it could effectively emit fluorescence, when aggregated into nanoparticles in a poor solvent or made into a thin film in a solid state. (Figure 3.3).

If $Zn^{2+}$ can be directly detected in the living body, it is extremely important for human health. In the detection process of $Zn^{2+}$, most of the AIE chemical molecules are only used in vitro. Wang et al. [42] based on the Schiff reaction, used a fluorescent probe for detecting the biocompatibility of $Zn^{2+}$ combined with TPE, and the peptide was designed and synthesized. In the presence of $Zn^{2+}$, the TPE-peptide probe formed a self-assembled complex with the three histidine residues on the two peptide chains, and trigged the TPE group in the presence of $Zn^{2+}$, exhibited strong fluorescence. This strategy opened up a new way to study other metal ions or bioactive molecules that can bind to special peptides, and may be widely used in the field of biosensing.

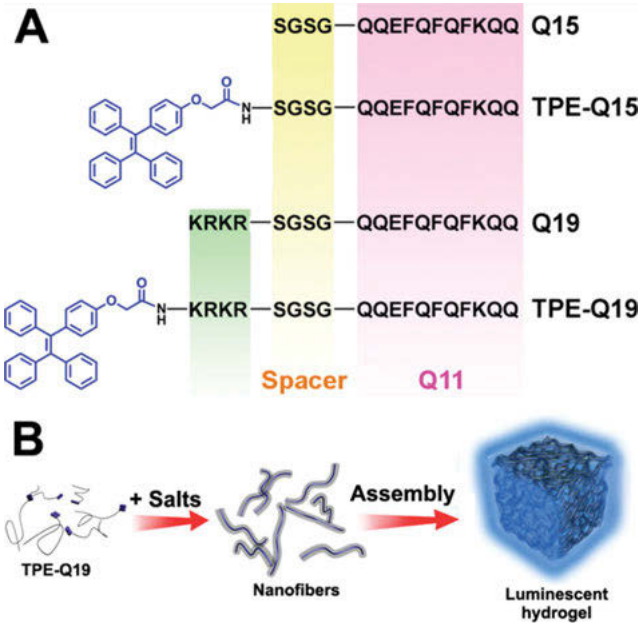


**Figure 3.3:** (A) Describes the chemical structure of the peptide used for molecular hydrogelation; (B) Schematic diagram of the preparation of luminescent hydrogel by TPE-Q19. Adapted with permission from ref [41]. Copyright 2014, American Chemical Society.

## 3.3.2 Redox-triggered aggregation

Inflammation plays a vital role in different stages of tumorigenesis, invasion, and metastasis. Reactive oxygen species (ROS) may cause mutations in neighboring cells. Hydrogen peroxide ($H_2O_2$) is one of the most important reactive oxygen species produced endogenously by cell respiration. In particular, abnormal levels of $H_2O_2$ are closely related to inflammation, neurodegenerative diseases, diabetes, and cancer [43]. Therefore, the use of peptide–AIEgen conjugate for $H_2O_2$ responsive aggregation has aroused increasing interest among researchers. Cheng et al. [44] designed a diagnostic probe with $H_2O_2$ response and AIE characteristics in which, TPE was partially modified with two tyrosines (Tyr). Due to the formation of $H_2O_2$-based dityrosine, Tyr-containing TPE (TT) would be connected to each other through dityrosine bonds to induce hydrophobic in aggregating and activating the AIE process, in response to $H_2O_2$. The emission-on result of TT conversion could be used for cell-selective imaging between inflammatory cells and normal cells. In addition, a large number of TT aggregate-induced mitochondrial damage and apoptosis (Figure 3.4).

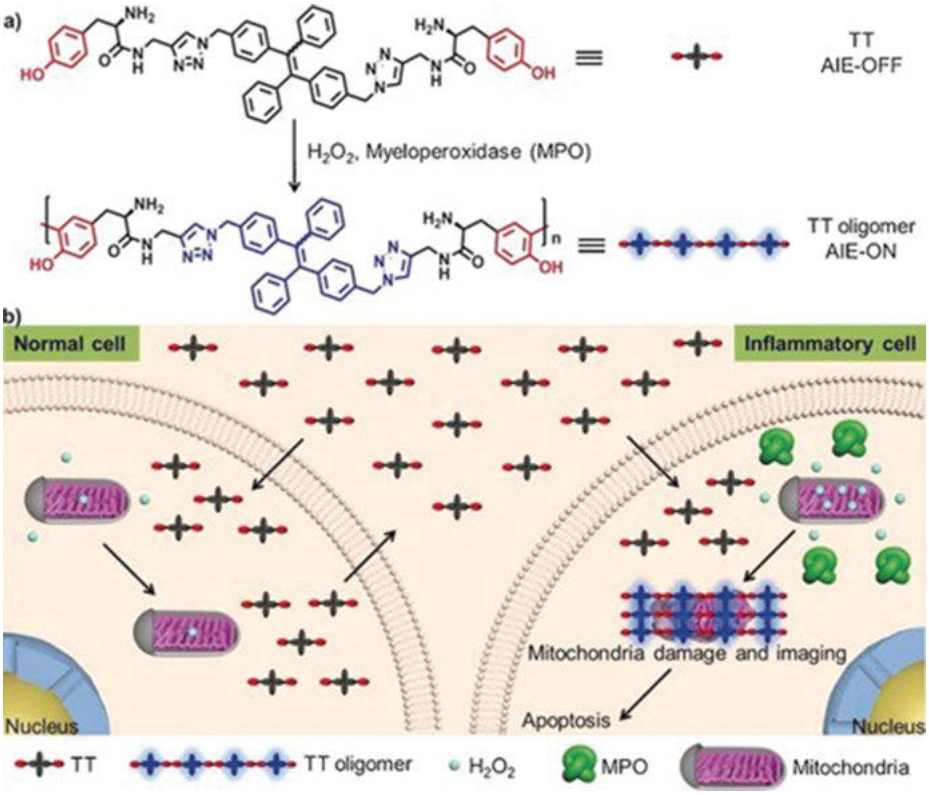


**Figure 3.4:** a) The reaction mechanism of TT is the formation of TT oligomers under the catalysis of $H_2O_2$ and peroxidase. b) TT acted on selective imaging and inhibition of cultured cells. Adapted with permission from ref [44]. Copyright © 2018 Wiley-VCH Verlag GmbH & Co. KGaA, Weinheim.

### 3.3.3 Enzyme-catalysis modulated aggregation

Enzymes are widely present in organisms and have high specificity and high catalytic efficiency for substrates. Enzyme deletion, activity reduction, or overexpression is closely related to the occurrence and development of diseases. Therefore, enzymes are often used as markers for disease detection and treatment. In order to detect enzyme activity and track drug release, AIE biological probes have been developed. Among them, the peptide-based AIE bio-probes have good biocompatibility and specificity, and are increasingly favored by researchers. Enzymatic hydrolysis of peptides can cause aggregation of AIEgens and drug release [45]. Specifically, the introduction of peptides can improve the hydrophilicity of AIEgens, which is conducive to the application of biological probes in the biomedical field. In addition, after the peptide is specifically cleaved by the enzyme, the fluorescence signal change caused

by the aggregation of the AIE bio-probes can be used to detect the activity of the enzyme, and the releasing drugs can be used to treat diseases [46]. This type of structure usually contains hydrophilic peptides and hydrophobic AIEgens. The covalent bonding of hydrophilic peptides and AIEgens make the biological probes in a dispersed state and nonfluorescence in the aqueous solution. When the hydrophilic peptide substrates are hydrolyzed by the enzyme, the remaining hydrophobic AIEgens rapidly precipitate and aggregate, resulting in bright fluorescence. Therefore, the change in the fluorescence signal may be closely related to the activity and location of the enzyme. This strategy can not only improve the biocompatibility and specificity of biological probes, but also improve the in-situ and real-time detection capabilities of biological probes. In order to develop a stable, convenient, and sensitive fluorescent probe for the detection of lipase, Tang et al. [47] combined the heterogeneous catalytic properties of lipase and synthesized a tetrastyrene (TPE) core and two glutamic acid units (Figure 3.5).

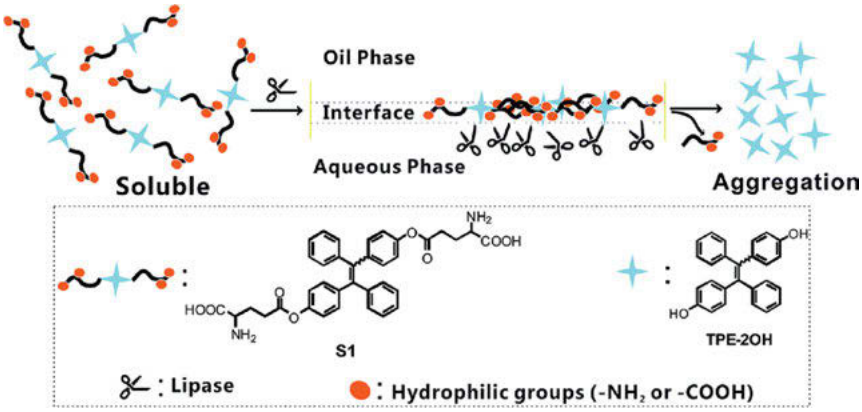


**Figure 3.5:** Described the chemical structure and sensing principle of probe S1 in lipase detection. Adapted with permission from ref [47]. Copyright © The Royal Society of Chemistry 2017.

When the molecules were hydrolyzed by lipase to remove the ester group, the TPE residue precipitated and emitted bright blue fluorescence. The experimental results showed that due to the presence of interface control and the specific shearing of glutamate by lipase, the detection had the characteristics of high sensitivity, low detection limit (0.13 U/l), and short response time (7 min), and it could be used to detect the level of lipase in real human serum samples. Furin is a member of the proprotein convertase family and is mainly located in the trans-Golgi apparatus. Its overexpression is highly correlated with tumor growth and metastasis. Therefore, it is very important to design a method to realize the in-situ detection and imaging of furin [48]. Based on this, Zhang et al. [49] developed a probe HPQF, which was composed of insoluble fluorescent molecules 2-(2′-hydroxyphenyl)-4(3H)-quinazolinone (HPQ) and

furin-cleavable composition of peptide RVRR. HPQF was water-soluble and nonfluorescent, but when it was hydrolyzed by furin, the released Cl-HPQ immediately precipitated and emitted bright fluorescence. Therefore, high-throughput fluorescence detection technology could monitor the activity and localization of furin protein in living cells, in real-time in situ.

## 3.4 Biomedical diagnosis and bioimaging by peptide – AIEgens

### 3.4.1 Bio-marker detection

The integrin $\alpha_v\beta_3$ is recognized as a mode protein target, because it plays an important role in adjusting the growth and transfer of tumor [50]. It expresses in tumor cells of different sources; the expression level is closely related to the invasion of the disease. As a recipient, who is exposed to matrix protein outside the cell of RGD sequence, integrin $\alpha_v\beta_3$ is a unique molecular target that cures fast growing tumors and can be used in early stage tests [51], considering the specificity and high affinity of integrin $\alpha_v\beta_3$ to annular RGD tripeptide (cRGD). In order to efficiently deliver fluorescent molecules into cells, Cheng et al. [52] designed a peptide–AIEgen conjugate named TNCP, including $T_D$NCP and $T_R$NCP, that mainly consisted of four parts: (1) A targeting peptide (DGR or RGD), which was a targeting ligand to integrin $\alpha_v\beta_3$ receptor; (2) A nuclear localization signal peptide (KRRRR), which played an important role in nuclear and cytoplasmic transport; (3) A cell-penetrating peptide (RRRR); (4) An AIE-based molecule azide-functionalized tetraphenylethene derivative (PyTPE) that had good fluorescence characteristics (Figure 3.6). With the help of cell-membrane targeting peptides, TNCP could be recognized and taken up by cell lines with high expression of integrin protein $\alpha_v\beta_3$; With the help of penetrating peptides, TNCP could easily enter the cell and quickly escape from the lysosome; with the help of nuclear localization sequence, TNCP could bind to the nuclear import protein and be transported to the nucleus, with the aid of AIEgens, TNCP could realize the regulation of fluorescent signals and long-term real-time tracking, that is, when TNCP was at a low concentration or did not bind to the target integrin protein $\alpha_v\beta_3$, there was almost no fluorescence and when TNCP was at a high concentration or when it was bounded to the target integrin protein $\alpha_v\beta_3$, a strong fluorescence signal could be generated. The results showed that $T_R$NCP had better nuclear selectivity, and $T_D$NCP had better gene drug loading capacity. Because of a similar principle, Liang et al. [5] designed a dual responsive and specific light-up probe to test and use in imaging of tumor biomarkers, LAPTMB4B. This probe was based on peptide (IHGHHIISVG) conjugated TPE. This peptide enabled specific binding on lysosomal protein transmembrane 4β (LAPT4B), which was overexpressed in tumor cells. The probe showed a specific

luminescent reaction to LAPTM4B; the limit of test was 1.0 mg/ml and it was used for expressing imaging of hepatocellular carcinoma cell in LAPTM4B. Transferrin receptor (TfR) plays an important role in iron cycle and cellular respiration. It is overexpressed on the surface of many cancer cells. Soluble transferrin receptor (sTfR) is a truncated extracellular form of transferrin receptor in serum and in iron deficiency anemia (IDA). In cancer patients with bone marrow failure, sTfR level in urine has been related to a specific kidney disease – Henoch – Schönlein purpura nephritis (HSPN). Zhang et al. [53] developed a kind of water-soluble peptide–AIEgen conjugate that had the characteristics of aggregation-induced emission. Using molecules to dissolve, tetraphenylethylene (TPE) could ignore emission and the probe, TPE-27, was used for sTfR light-up detection. The probe itself did not emit in an aqueous solution, but it turned on its fluorescence when interacting with sTfR and generated a detection limit of 0.27 g/ml, which was much lower than the sTfR level in IDA patients. In addition, the potential of the probe to diagnose HSPN through urinalysis had been proved through the proof-of-concept experiment.

### 3.4.2 Bacteria and cell tracking

Facing the challenge of bacterial infection, developing a timely, sensitive bacterial detection method is particularly important. Chen et al. [54] developed AIE active probe, AMP-2HBT, by using 2-(2-hydroxyphenyl) benzothiazole (HBT) to modify bacteriological peptide HHC36(KKWWKWWRR) (Figure 3.7).

This kind of AIE active probe showed excellent luminous fluorescence after binding to bacteria. It was able to timely monitor the combination process. In addition, similar time-dependent bactericidal kinetics were observed in active probe and HHC36 peptide, indicating that the bactericidal activity of peptides would not be damaged by modification with active probes. The bactericidal mechanism of HHC36 peptide was further studied by a super-resolution microscope – projection electron microscope and scanning electron microscope. The results showed that the probe was easy to accumulate and effectively destroy the membrane structure on the bacterial membrane, thus killing Gram-positive bacteria and Gram-negative bacteria. This kind of active probe provided a convenient tool for researching the bactericidal mechanism of AMPs.

### 3.4.3 In vivo bioimaging

Photodynamic therapy (PDT) is a strategy that has both diagnosis and treatment; which has the advantages of precise controllability and high accuracy. The active oxygen can damage DNA, active antioncogene, and block migration. It can also reduce damages to the surrounding healthy tissues to the maximum level; therefore,

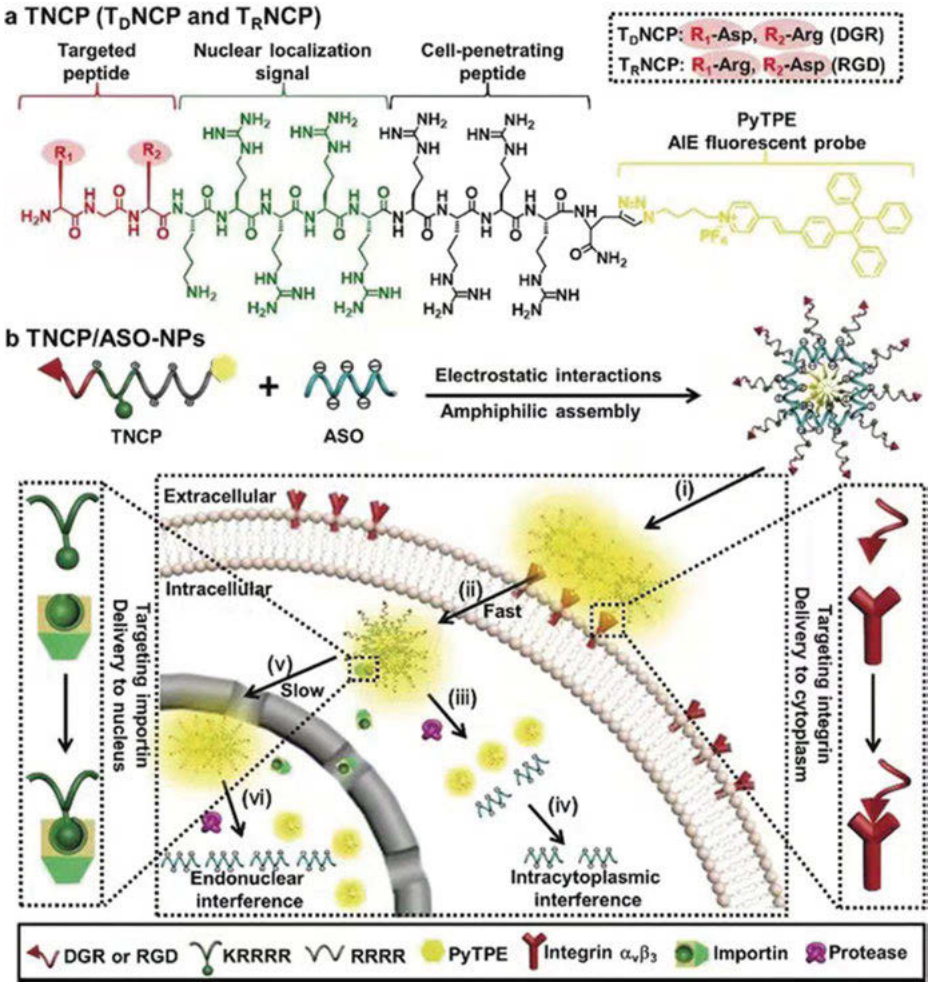


**Figure 3.6:** a) The chemical structure of TNCP; b) TNCP/antisense single-stranded DNA oligonucleotide – nanoparticles (TNCP/ASO-NPs) was used for efficient and controllable nuclear targeted transport and real-time tracking of gene drugs. Adapted with permission from ref [52]. Copyright © *2019 Wiley- VCH Verlag GmbH & Co. KGaA, Weinheim.*

near-infrared phosphor shows obvious advantages, minimizing biological background interference and improving detection sensitivity in biological tissues [55]. In addition, the low energy characteristic of near-infrared light is helpful for deep tissue imaging and tumor detection in vivo. Therefore, the development of near-infrared photosensitizer with a good reactive oxygen species generation ability is of great significance to achieve efficient image-guided photodynamic therapy. Dai et al. [56] designed an AIEgen containing an electron-accepting benzo[1,2-b:4,5-b'] dithiophene 1,1,5,5-tetraoxide core and electron-donating 4,4′-(2,2-diphenylethene-1,1-diyl) bis

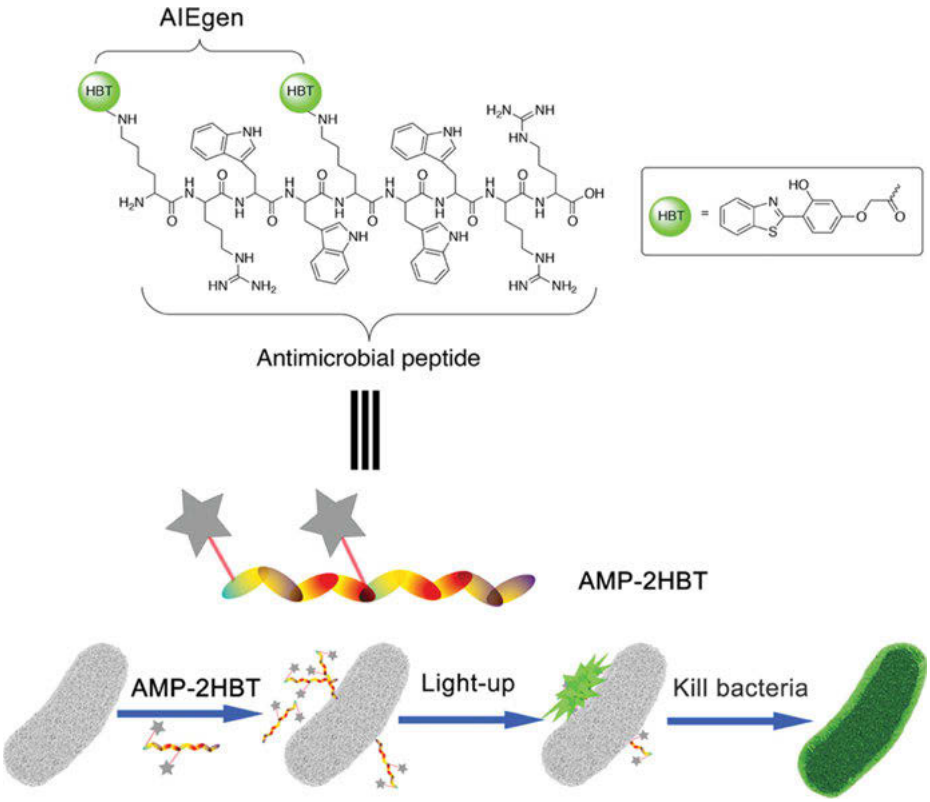


**Figure 3.7:** Described a schematic diagram of AMP-2HBT for bacterial imaging and sterilization. Adapted with permission from ref [54]. Copyright 2018, American Chemical Society.

(N,N-diphenylaniline) groups for image-guided targeting PDT application. The fluorescein TBB showed obvious AIE characteristics and strong infrared fluorescence, and it could effectively generate $O^{2\bullet-}$ and $_1O^2$ in sunlight. By wrapping TTB in a polymer matrix and then modifying it with RGD-4R, nanoparticles (RGD-4R-MPD/TTB) with near infrared emission (~730 nm), high light stability and low dark cytotoxicity (RGD-4R-MPD/TTB) were achieved. They showed excellent performance in the treatment of PC3, HeLa, and SKOV-3 cancer cells by targeting PDT in vitro. Pharmacokinetics, biodistribution and long-term tracking in vivo had shown that RGD-4R-MPD/TTB nanoparticles can be selectively accumulated in tumors for real-time and long-term image-guided photodynamic therapy. PDT, in a variety of xenotransplantation tumor models, mediated by RGD-4R-MPD/TTBNPs revealed that it can effectively inhibit the growth of cervical cancer, prostate cancer, and ovarian cancer in mice. These results suggested that the reagent of near infrared fluorescein TTB as photosensitizer was expected to be a candidate drug for image-guided photodynamic therapy in vivo (Figure 3.8).

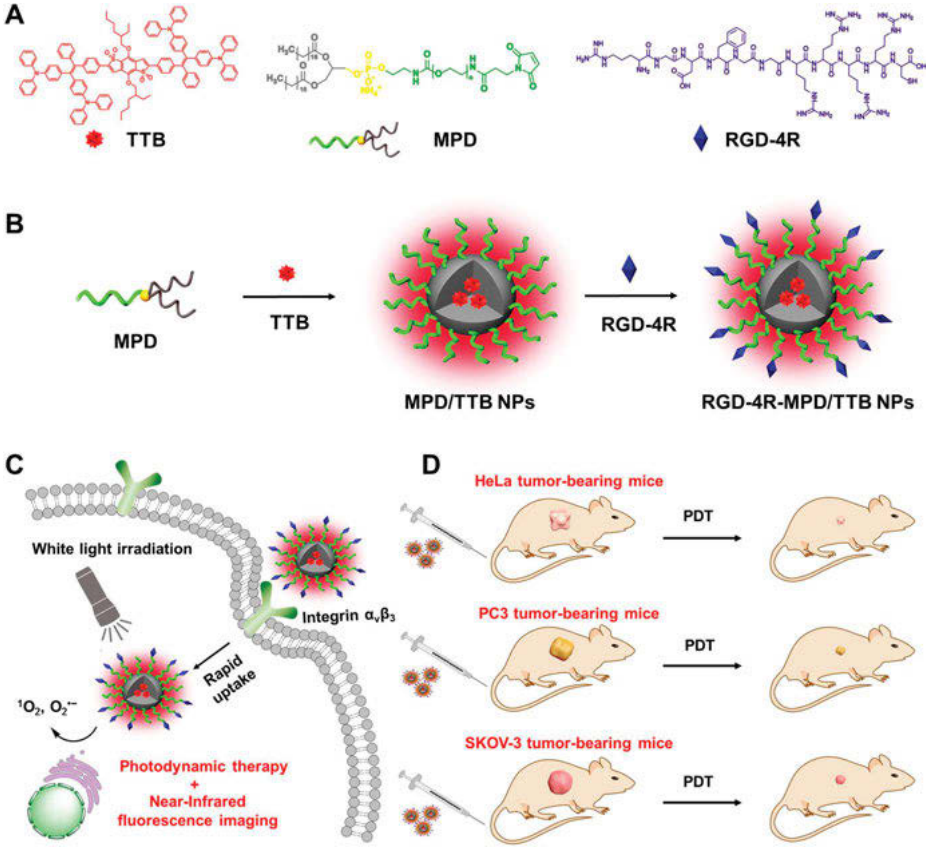


**Figure 3.8:** (A) The chemical structures of TTB, MPD and RGD-4R are described respectively. (B) Schematic diagram of the preparation of RGD-4R-MPD / TTB NP. (C) The process of cell absorption and photodynamic therapy of RGD-4R-MPD / TTB NPs is introduced. (D) HeLa, PC3 and SKOV-3 cells were used to establish xenograft tumor models of cervical cancer, prostate cancer and ovarian cancer. Adapted with permission from ref [56]. Copyright 2020, American Chemical Society.

## 3.4.4 In vitro cell imaging

Since most anti-cancer drugs induce cell death through apoptosis, the imaging of the cascade caspase activation is essential to screen the drugs and study their therapeutic effects. Yuan et al. [57] designed and synthesized a fluorescent probe that can simultaneously detect caspase-3 and caspase-8. The probe consisted of a water-soluble peptide that can be recognized by caspase-3 and caspase-8, and connected the AIE fluorophores that emit blue fluorescence and red fluorescence, respectively. The probe molecule did not emit light in the solution due to its good water solubility. Caspase-8 could cleave peptides and release water-insoluble blue fluorophores; caspase-

3 could cleave peptides and release water-insoluble red fluorophores; thus, realizing fluorescence detection for the activities of the two enzymes. The probe achieved good results in solution detection and intracellular imaging (Figure 3.9).

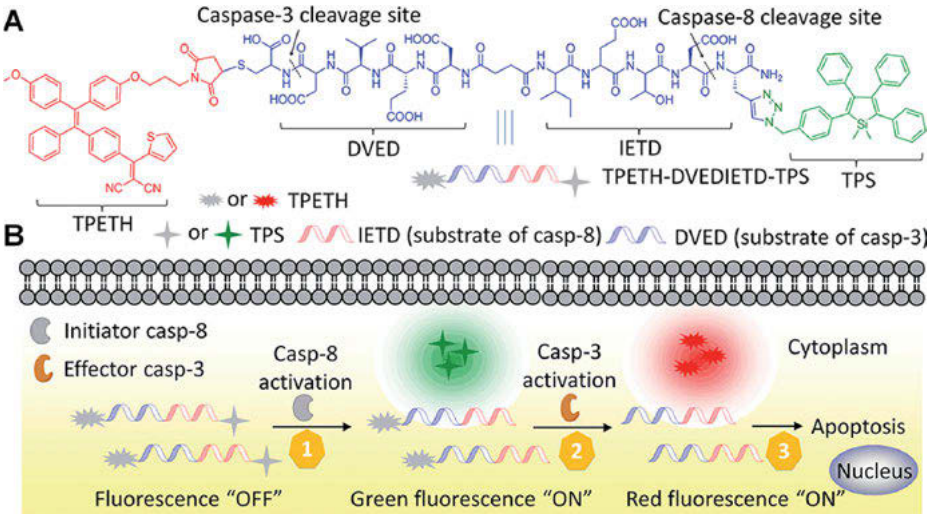


**Figure 3.9:** (A) Cleavage sites of caspase-3 and caspase-8; (B) A single fluorescent probe can target two caspase activities in living cells. Adapted with permission from ref [57] Copyright © The Royal Society of Chemistry 2017.

Qi et al. [58] designed an AIE gen-peptide-based fluorescent bioprobe (PyTPE-CRP). PyTPE-CRP mainly consisted of two parts: (1) an enzyme-cleavable peptide (NEAYVH-DAP); (2) an AIE molecule (PyTPE). PyTPE-CRP could be cleaved by casp-1 in macrophages that was infected by bacteria. The residues self-assembled in the cell, eventually leading to increased fluorescence in the cell. Therefore, it was possible to image macrophages that were infected by bacteria.

## 3.5 Conclusion and outlook

This chapter focused on the research progress of peptide–AIEgen aggregates. According to the different peptides, such as targeting peptides, cell-penetrating peptides, and stimuli responsive peptides, their combined effects with AIE were completely different. The combination of targeting peptides and AIEgens not only improved the imaging efficiency of targeting peptides but also improved the water solubility of AIEgens, which have become research hotspots in recent years. Targeting peptide-coupled AIEgens can target specific organelles for long-term biological imaging. AIEgens, modified with different types of cell penetrating peptides, for example, cationic peptides,

hydrophobic peptides and amphipathic peptides, can penetrate cells better to obtain good imaging characteristics. The advantages of the stimuli-responsive peptide–AIE conjugate are that it can perform specific structural changes in response to specific stimuli to accurately perform imaging, diagnosis, and monitoring at specific sites. In addition, the review introduces how environmental factors trigger the aggregation of peptide–AIEgens, such as ionic strength, $H_2O_2$-triggered aggregation, and enzyme-catalyzed aggregation. In specific applications, peptide–AIE aggregates also made up for the shortcomings of other traditional AIEgens in biomarker, bacteria and cell detection, and in vivo/vitro imaging.

Although these types of peptide–AIEgens show great scope and potential for diagnostic and imaging applications, there are still many challenges to overcome before their translational effectiveness can be realized. The first is how to design an intelligence-responsive peptide–AIEgens, since some biological problems can be more appropriately addressed using response-based radiologic diagnostic probes than traditional ones. The second is to search for an optimized reactivity-based multifunctional biological probe for specific therapeutic and diagnostic applications. These features include higher signal-to-noise ratios, alternative excitation schemes, and integration with other imaging methods. Finally, a comprehensive study of the long-term bio-behavior, toxicological effects, and overall biocompatibility of peptide–AIEgens is equally important if it is to facilitate the transformation or optimize its performance. Therefore, this requires the full cooperation and unrelenting efforts of experts from different disciplines to solve this problem and bring new hope for the clinical application of peptide.

**Conflicts of interest:** There are no conflicts to declare.

# References

[1] Gao M, Tang BZ, Fluorescent sensors based on aggregation-induced emission: recent advances and perspectives, ACS Sens, 2017, 2, 1382–1399.
[2] Feng G, Liu B, Aggregation-induced emission (AIE) dots: emerging theranostic nanolights, Acc Chem Res, 2018, 51, 1404–1414.
[3] Luo J, Xie Z, Lam JW, et al., Aggregation-induced emission of 1-methyl-1,2,3,4,5-pentaphenylsilole, Chem Commun, 2001, 1740–1741.
[4] Song Z, Hong Y, Kwok RTK, Lam JWY, Liu B, Tang BZ, A dual-mode fluorescence “turn-on” biosensor based on an aggregation-induced emission luminogen, J Mater Chem B, 2014, 2, 1717–1723.
[5] Liang J, Tang BZ, Liu B, Specific light-up bioprobes based on AIEgen conjugates, Chem Soc Rev, 2015, 44, 2798–2811.
[6] Cai X, Liu B, Aggregation-induced emission: recent advances in materials and biomedical applications, Angew Chem Int Ed Engl, 2020, 59, 9868–9886.

[7] Yuan Y, Feng G, Qin W, Tang BZ, Liu B, Targeted and image-guided photodynamic cancer therapy based on organic nanoparticles with aggregation-induced emission characteristics, Chem Commun, 2014, 50, 8757–8760.
[8] Geng J, Li K, Qin W, et al., Eccentric loading of fluorogen with aggregation-induced emission in plga matrix increases nanoparticle fluorescence quantum yield for targeted cellular imaging, Small, 2013, 9, 2012–2019.
[9] Ding D, Li K, Qin W, et al., Conjugated polymer amplified far-red/near-infrared fluorescence from nanoparticles with aggregation-induced emission characteristics for targeted in vivo imaging, Adv Healthc Mater, 2013, 2, 500–507.
[10] Zhang JF, Zhou Y, Yoon J, Kim JS, Recent progress in fluorescent and colorimetric chemosensors for detection of precious metal ions (silver, gold and platinum ions), Chem Soc Rev, 2011, 40, 3416–3429.
[11] Qian X, Xu Z, Fluorescence imaging of metal ions implicated in diseases, Chem Soc Rev, 2015, 44, 4487–4493.
[12] Liu Y, Tang Y, Barashkov NN, et al., Fluorescent chemosensor for detection and quantitation of carbon dioxide gas, J Am Chem Soc, 2010, 132, 13951–13953.
[13] Zhang L, Zhang ZY, Liang RP, Li YH, Qiu JD, Boron-doped graphene quantum dots for selective glucose sensing based on the “abnormal” aggregation-induced photoluminescence enhancement, Anal Chem, 2014, 86, 4423–4430.
[14] Braide-Moncoeur O, Tran NT, Long JR, Peptide-based synthetic pulmonary surfactant for the treatment of respiratory distress disorders, Curr Opin Chem Biol, 2016, 32, 22–28.
[15] Zou P, Chen WT, Sun T, Gao Y, Li LL, Wang H, Recent advances: peptides and self-assembled peptide-nanosystems for antimicrobial therapy and diagnosis, Biomater Sci, 2020, 8, 4975–4996.
[16] Yu Fan X-DL, Ping-Ping H, Xiao-Xue H, et al., A biomimetic peptide recognizes and traps bacteria in vivo as human defensin-6, Sci Adv, 2020, 6, eaaz4767.
[17] Macindoe I, Kwan AH, Ren Q, et al., Self-assembly of functional, amphipathic amyloid monolayers by the fungal hydrophobin eas, Proc Natl Acad Sci U S A, 2012, 109, E804–11.
[18] Pieszka M, Han S, Volkmann C, et al., Controlled supramolecular assembly inside living cells by sequential multistaged chemical reactions, J Am Chem Soc, 2020, 142, 15780–15789.
[19] Levin A, Hakala TA, Schnaider L, Bernardes GJL, Gazit E, Knowles TPJ, Biomimetic peptide self-assembly for functional materials, Nat, Rev Chem, 2020, 4, 615–634.
[20] Sis MJ, Webber MJ, Drug delivery with designed peptide assemblies, Trends Pharmacol Sci, 2019, 40, 747–762.
[21] Li K, Zhu Z, Cai P, et al., Organic dots with aggregation-induced emission (AIE dots) characteristics for dual-color cell tracing, Chem, Mater, 2013, 25, 4181–4187.
[22] Wang W, Hu Z, Targeting peptide-based probes for molecular imaging and diagnosis, Adv Mater, 2019, 31, e1804827.
[23] Shi L, Gao X, Yuan W, et al., Endoplasmic reticulum-targeted fluorescent nanodot with large stokes shift for vesicular transport monitoring and long-term bioimaging, Small, 2018, 14, e1800223.
[24] Cheng Y, Sun C, Ou X, Liu B, Lou X, Xia F, Dual-targeted peptide-conjugated multifunctional fluorescent probe with AIEgen for efficient nucleus-specific imaging and long-term tracing of cancer cells, Chem Sci, 2017, 8, 4571–4578.
[25] Ramya AN, Joseph MM, Nair JB, Karunakaran V, Narayanan N, Maiti KK, New insight of tetraphenylethylene-based raman signatures for targeted sers nanoprobe construction toward prostate cancer cell detection, ACS Appl Mater Interfaces, 2016, 8, 10220–10225.

[26] Yuan Y, Liu J, Liu B, Conjugated-polyelectrolyte-based polyprodrug: targeted and image-guided photodynamic and chemotherapy with on-demand drug release upon irradiation with a single light source, Angew Chem Int Ed Engl, 2014, 53, 7163–7168.
[27] Yuan Y, Zhang CJ, Gao M, Zhang R, Tang BZ, Liu B, Specific light-up bioprobe with aggregation-induced emission and activatable photoactivity for the targeted and image-guided photodynamic ablation of cancer cells, Angew Chem Int Ed Engl, 2015, 54, 1780–1786.
[28] Feng G, Wu W, Xu S, Liu B, Far red/near-infrared AIE dots for image-guided photodynamic cancer cell ablation, ACS Appl Mater Interfaces, 2016, 8, 21193–21200.
[29] Radis-Baptista G, Campelo IS, Morlighem JRL, Melo LM, Freitas V J F, Cell-penetrating peptides (cpps): From delivery of nucleic acids and antigens to transduction of engineered nucleases for application in transgenesis, J Biotechnol, 2017, 252, 15–26.
[30] Pabo AFC, Cellular uptake of the tat protein from human lmmunodeficiency virus, Cell, 1988.
[31] Hu Y, Liang X, Zhuang Z, et al., Cell-penetrating peptide modified AIE polymeric nanoparticles by miniemulsion polymerization and application for cell fluorescence imaging, Polym Chem, 2019, 10, 4220–4228.
[32] Li K, Qin W, Ding D, et al., Photostable fluorescent organic dots with aggregation-induced emission (AIE dots) for noninvasive long-term cell tracing, Sci Rep, 2013, 3, 1150.
[33] Gao Y, Feng G, Jiang T, et al., Biocompatible nanoparticles based on diketo-pyrrolo-pyrrole (DPP) with aggregation-induced Red/NIR emission for in vivo two-photon fluorescence imaging, Adv Funct Mater, 2015, 25, 2857–2866.
[34] Wojnilowicz M, Glab A, Bertucci A, Caruso F, Cavalieri F, Super-resolution imaging of proton sponge-triggered rupture of endosomes and cytosolic release of small interfering rna, ACS Nano, 2019, 13, 187–202.
[35] Cheng Y, Huang F, Min X, et al., Protease-responsive prodrug with aggregation-induced emission probe for controlled drug delivery and drug release tracking in living cells, Anal Chem, 2016, 88, 8913–8919.
[36] Ikeda M, Stimuli-responsive supramolecular systems guided by chemical reactions, Poly J, 2018, 51, 371–380.
[37] Zhang XH, Cheng DB, Ji L, et al., Photothermal-promoted morphology transformation in vivo monitored by photoacoustic imaging, Nano Lett, 2020, 20, 1286–1295.
[38] Mura S, Nicolas J, Couvreur P, Stimuli-responsive nanocarriers for drug delivery, Nat Mater, 2013, 12, 991–1003.
[39] Liu X, Liang G, Dual aggregation-induced emission for enhanced fluorescence sensing of furin activity in vitro and in living cells, Chem Commun (Camb), 2017, 53, 1037–1040.
[40] Wu T, Huang J, Yan Y, Self-assembly of aggregation-induced-emission molecules, Chem Asian J, 2019, 14, 730–750.
[41] Zhang C, Liu C, Xue X, et al., Salt-responsive self-assembly of luminescent hydrogel with intrinsic gelation-enhanced emission, ACS Appl Mater Interfaces, 2014, 6, 757–762.
[42] He X, Wang X, Zhang L, Fang G, Liu J, Wang S, Sensing and intracellular imaging of $Zn^{2+}$ based on affinity peptide using an aggregation induced emission fluorescence “switch-on” probe, Sens Actuators B: Chem, 2018, 271, 289–299.
[43] Shadel GS, Horvath TL, Mitochondrial ros signaling in organismal homeostasis, Cell, 2015, 163, 560–569.
[44] Cheng Y, Dai J, Sun C, et al., An intracellular $H_2O_2$ -responsive AIEgen for the peroxidase-mediated selective imaging and inhibition of inflammatory cells, Angew Chem Int Ed Engl, 2018, 57, 3123–3127.
[45] Yang J, Wei J, Luo F, et al., Enzyme-responsive peptide-based AIE bioprobes, Top Curr Chem, 2020, 378, 47.

[46] Qi GB, Gao YJ, Wang L, Wang H, Self-assembled peptide-based nanomaterials for biomedical imaging and therapy, Adv Mater, 2018, 30, e1703444.
[47] Shi J, Deng Q, Wan C, Zheng M, Huang F, Tang B, Fluorometric probing of the lipase level as acute pancreatitis biomarkers based on interfacially controlled aggregation-induced emission (AIE), Chem Sci, 2017, 8, 6188–6195.
[48] Thomas G, Furin at the cutting edge: From protein traffic to embryogenesis and disease, Nat Rev Mol Cell Biol, 2002, 3, 753–766.
[49] Li K, Hu XX, Liu HW, et al., In situ imaging of furin activity with a highly stable probe by releasing of precipitating fluorochrome, Anal Chem, 2018, 90, 11680–11687.
[50] Hodivala-Dilke KM, Reynolds AR, Reynolds LE, Integrins in angiogenesis: Multitalented molecules in a balancing act, Cell Tissue Res, 2003, 314, 131–144.
[51] Themelis G, Harlaar NJ, Kelder W, et al., Enhancing surgical vision by using real-time imaging of alphavbeta3-integrin targeted near-infrared fluorescent agent, Ann Surg Oncol, 2011, 18, 3506–3513.
[52] Cheng Y, Sun CL, Liu R, et al, A multifunctional peptide-conjugated AIEgen for efficient and sequential targeted gene delivery into the nucleus, Angew Chem Int Ed Engl, 2019, 58, 5049–5053.
[53] Zhang R, Sung SHP, Feng G, et al., Aggregation-induced emission probe for specific turn-on quantification of soluble transferrin receptor: An important disease marker for iron deficiency anemia and kidney diseases, Anal Chem, 2018, 90, 1154–1160.
[54] Chen J, Gao M, Wang L, et al., Aggregation-induced emission probe for study of the bactericidal mechanism of antimicrobial peptides, ACS Appl Mater Interfaces, 2018, 10, 11436–11442.
[55] Punjabi A, Wu X, Tokatli-Apollon A, et al., Amplifying the red-emission of upconverting nanoparticles for biocompatible clinically used prodrug-induced photodynamic therapy, ACS Nano, 2014, 8, 10621–10630.
[56] Dai J, Li Y, Long Z, et al., Efficient near-infrared photosensitizer with aggregation-induced emission for imaging-guided photodynamic therapy in multiple xenograft tumor models, ACS Nano, 2020, 14, 854–866.
[57] Yuan YY, Zhang CJ, Kwok RTK, et al., Light-up probe based on AIEgens: Dual signal turn-on for cascade caspase actvation monitoring, Chem Sci, 2017, 8, 2723–2728.
[58] Qi GB, Hu F, Kenry, et al., An AIEgen-peptide conjugate as a phototheranostic agent for phagosome-entrapped bacteria, Angew Chem Int Ed Engl, 2019, 58, 16229–16235.

Marie-Claire Giel, Yuning Hong

# Chapter 4
# The application of click chemistry in the design of aggregation-induced emission luminogens for activity-based sensing

## 4.1 Introduction

The development of sensitive and selective fluorescent sensors is of great importance for the visualization of numerous biological processes and the accurate diagnosis of diseases [1]. A wide variety of fluorescent probes have been developed and employed in sensing applications and have been shown to exhibit high sensitivity, fast responsiveness, and excellent biocompatibility [2, 3]. Activity-based sensing (ABS) has emerged as a powerful approach that exploits molecular reactivity rather than molecular recognition for analyte detection [4]. However, most of the fluorescent probes have been developed using a "lock and key" strategy; ABS offers several distinct advantages over the conventional lock-and-key molecular recognition approaches including high specificity and sensitivity, and accurate signal outputs.

Most conventional organic fluorophores such as fluorescein, rhodamine, cyanine, etc. suffer from aggregation-caused quenching (ACQ). This significantly limits the amount of labeling of the analyte with the fluorophores, as they must be diluted in solution or dispersed in matrix materials, which requires complicated preparation processes and results in severe photobleaching, low signal-to-noise ratio, and significantly compromised sensitivity [5]. The development of aggregation-induced emission luminogens (AIEgens) has provided an excellent class of fluorescent scaffolds for ABS. The concept of aggregation-induced emission (AIE) refers to a unique phenomenon where some fluorogens are nonemissive or weakly emissive in dilute solutions but become highly luminescent when the molecules are aggregated in concentrated solutions. The emergence of luminogens with AIE characteristics addresses the deficiencies of ACQ fluorophores [6]. AIEgens generally exhibit higher photostability, extremely high signal reliability, and high signal-to-noise ratio in comparison to traditional ACQ fluorophores. Furthermore, the "turn on" nature of AIEgens reduces the possibility of false positive or negative signals compared with the typical "turn off" counterparts. As a result of these advantages, AIEgens have been widely used in fluorescent sensing. The use of AIEgens in ABS has been proven to combine the advantages of ABS and

**Marie-Claire Giel,** Department of Chemistry and Physics, La Trobe Institute for Molecular Science, La Trobe University, Melbourne, VIC, 3086, Australia
**Yuning Hong,** Department of Chemistry and Physics, La Trobe Institute for Molecular Science, La Trobe University, Melbourne, VIC, 3086, Australia, e-mail: Y.Hong@latrobe.edu.au

https://doi.org/10.1515/9783110672220-004

AIEgens, leading to the successful development of a diverse array of sensors that have been constructed for the detection of many reactive chemical and biological species [7–9].

### 4.1.1 Design principles of activity-based AIE sensors

Compared to traditional "lock and key" strategies, an activity-based approach offers a reliable alternative for analyte detection due to the focus on molecular reactivity as opposed to molecular recognition, to achieve specificity. The AIEgen can only be activated by the desired analyte facilitating the targeted chemical transformation resulting in significant changes in fluorescence intensity, emission wavelengths, or fluorescence lifetime. The mechanism of AIE luminescence has been rationalized by the processes of restriction of intramolecular rotation (RIR) and/or restriction of intramolecular vibration (RIV). AIEgens properties can be modified with a specific reactive group for analyte recognition in order to obtain an activity-based AIE sensor. Several sensing principles have been applied in the AIEgen ABS approach including i) the modification of the AIEgen with a specific reactive moiety, which can be deactivated or cleaved by the target analyte to give a strong fluorescence as a result of dye aggregation caused by solubility changes (Figure 4.1A); ii) bioconjugation through a chemical reaction between the reactive groups of the AIEgen and a matrix to induce RIR/RIV of the AIEgen (Figure 4.1B); iii) through a chemical reaction between two orthogonal groups of the AIEgens that results in a fluorescence change of the AIEgens (Figure 4.1C).

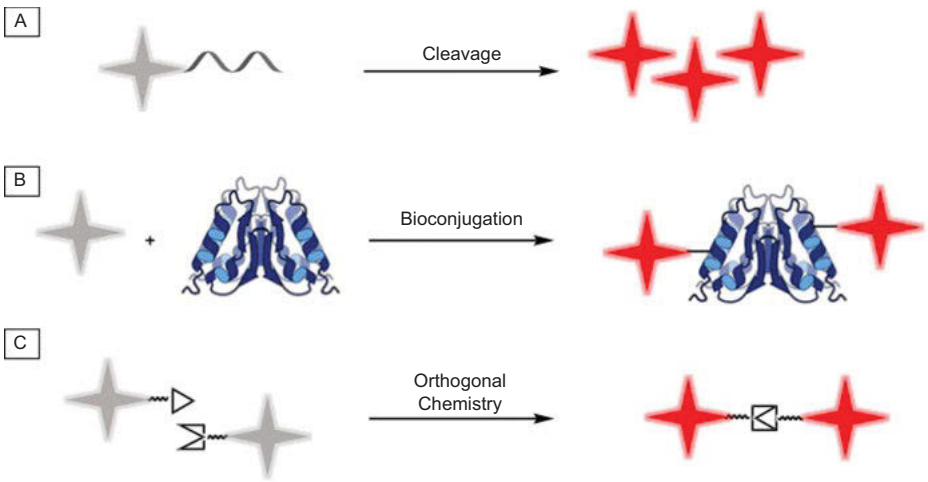


**Figure 4.1:** Illustration of the design principles of activity-based AIE sensors; (A) cleavage, (B) bioconjugation, and (C) orthogonal chemistry.

### 4.1.2 Click chemistry

Several classes of reactions have been employed in the AIEgen ABS approach, of which click chemistry has become prominent in the design of activity-based AIE sensors for a wide range of applications including the detection of metal ions and small molecules, tumor labeling, monitoring of DNA synthesis, and measurement of cellular unfolded protein load.

Click chemistry was conceived by Sharpless and coworkers in 2001 as a strategic method for the efficient combination of small modules together through heteroatom (C-X-C) bond formation to meet the demands of modern day chemistry [10]. Click chemistry focuses on reactions with a high thermodynamic driving force, usually greater than 20 $kcal^{-1}$. These reactions are often termed "spring-loaded," which generally proceed rapidly to completion and are highly selective for a single product. To formalize the concept of click chemistry, Sharpless and coworkers outlined a set of stringent criteria for reactions to be classified as "click reactions." A click reaction must be modular, wide in scope, high-yielding, simple to perform, and stereospecific; it must create only inoffensive by-products and require benign or easily removed solvent.

A selection of chemical transformations were initially identified as click reactions including cycloadditions of unsaturated species, nucleophilic substitution chemistry, ring-opening reactions, nonaldol carbonyl chemistry, and additions to carbon-carbon multiple bond (Michael reactions, thiol-ene click chemistry, etc.) (Figure 4.2) [11, 12]. The orthogonal and biocompatible nature of click reactions makes them ideally suited to be applied in the design of activity-based AIE sensors. In this chapter, we will summarize click chemistry methods applied in AIEgen ABS strategies, particularly focusing on cycloaddition and addition to carbon-carbon multiple bond reactions.

## 4.2 Cycloaddition reactions

### 4.2.1 $Cu^{I}$-Catalyzed Azide-Alkyne Cycloaddition (CuAAC)

Of all the reactions identified as click reactions, the $Cu^{I}$-catalyzed azide-alkyne cycloaddition (CuAAC) reaction to afford 1,4-disubstituted-1,2,3-triazoles has become the premier example of a click reaction and synonymous with click chemistry [13, 14]. Azides and alkynes can be easily introduced into a molecule and are tolerant to a wide variety of functional groups and reaction conditions, meaning they can be installed and remain unaffected through a number of subsequent transformations. The copper (I) catalyst results in excellent regioselectivity of the cycloaddition reaction and increases the reaction rate up to $10^7$ times, eliminating the need for high temperatures. The CuAAC reaction has been applied in AIEgen ABS strategies through bioconjugation reactions

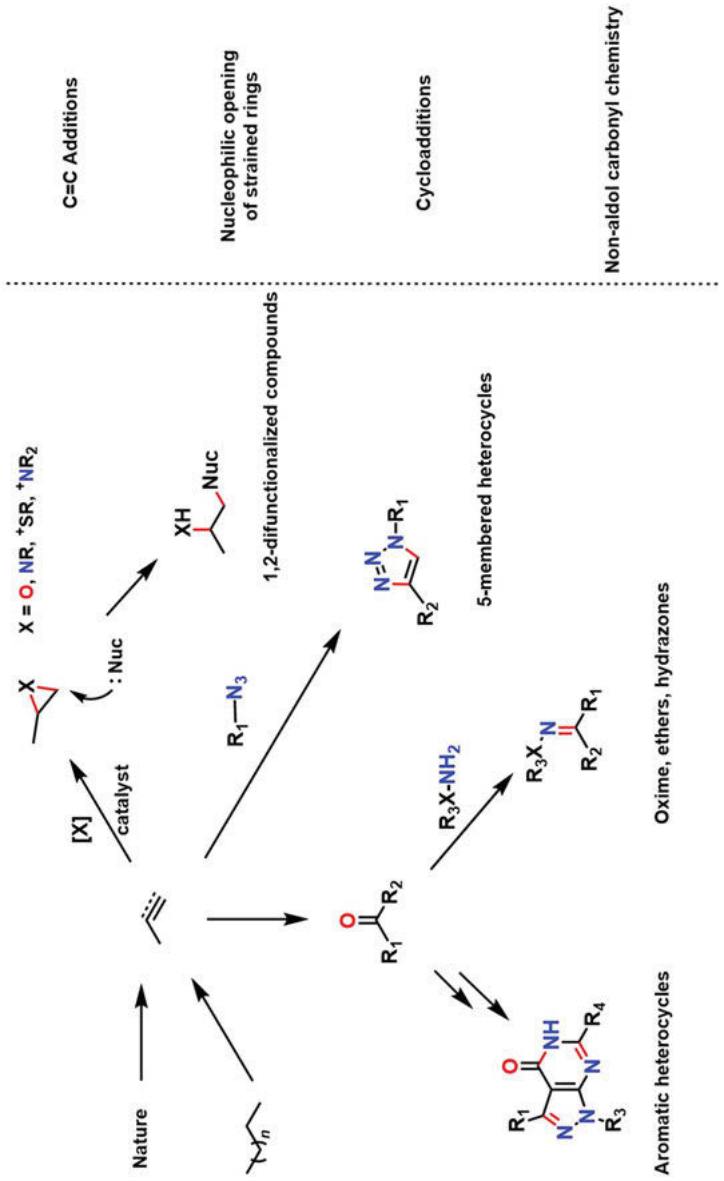


**Figure 4.2:** Reactions identified as meeting the click chemistry criteria.

between an alkyne- or azido-functionalized biomolecule and an AIEgen modified with the complementary reactive group (Figure 4.3).

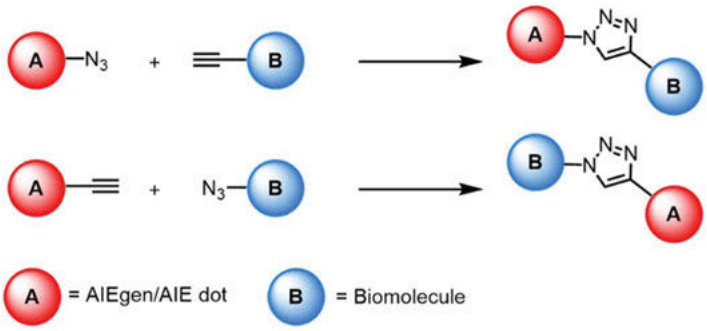


**Figure 4.3:** Schematic illustration of the use of the CuAAC reaction in AIEgen ABS.

In 2015, Tang and coworkers applied the CuAAC reaction in an ABS strategy for the detection of S-phase DNA synthesis and cell proliferation based on 5-ethynyl-2′-deoxyuridine (EdU) assay employing two azide-functionalized AIEgens (TPE-Py-$N_3$, **1** and Cy-Py-$N_3$, **2**) [15]. Given the biological importance of DNA synthesis, it is vital to develop techniques that aid in the understanding of the molecular mechanisms of DNA synthesis [16, 17]. Although radioactive probes have been successfully applied in the labeling of mitotically active cells, they suffer from several disadvantages. The radioactive reagents are hazardous, high cost, and require time-consuming procedures, limiting their use for high-throughput studies [18]. Fluorescence labeling offers many advantages in comparison to radioactive probes including rapid detection, high sensitivity, and less cytotoxicity. In this improved method, the thymidine analogue EdU bearing a terminal alkyne moiety was first incorporated into newly synthesized DNA, followed by incubation with the selected AIEgen, $CuSO_4$ and ascorbic acid to give a dye-labeled double-stranded DNA, enabling DNA synthesis and cell proliferation to be monitored in situ (Figure 4.4A). The capability of the two AIEgens (**1** and **2**) to detect DNA synthesis was first studied in proliferating human cervix carcinoma HeLa cells. The HeLa cells were incubated with EdU followed by staining with the AIEgens and the addition of $CuSO_4$ and ascorbic acid. The nuclei of the HeLa cells were found to emit intense light upon photoexcitation (Figure 4.4B). In contrast, the HeLa cells without EdU labelling displayed no detectable fluorescence, supporting the hypothesis that the origin of the nuclei fluorescence came from the DNA synthesis and EdU incorporation. The nuclei of the HeLa cells also became more emissive with a longer incubation time, implying that AIEgens **1** and **2** were able to monitor the procession of DNA synthesis in addition to cell proliferation. When compared on the Alexa-azide dye, a commercial DNA bioprobe, the AIEgens exhibited a much wider working concentration range (10 to 100 μM), higher brightness, and

stronger photostability, making AIEgens **1** and **2** promising candidates for intracellular DNA synthesis detection.

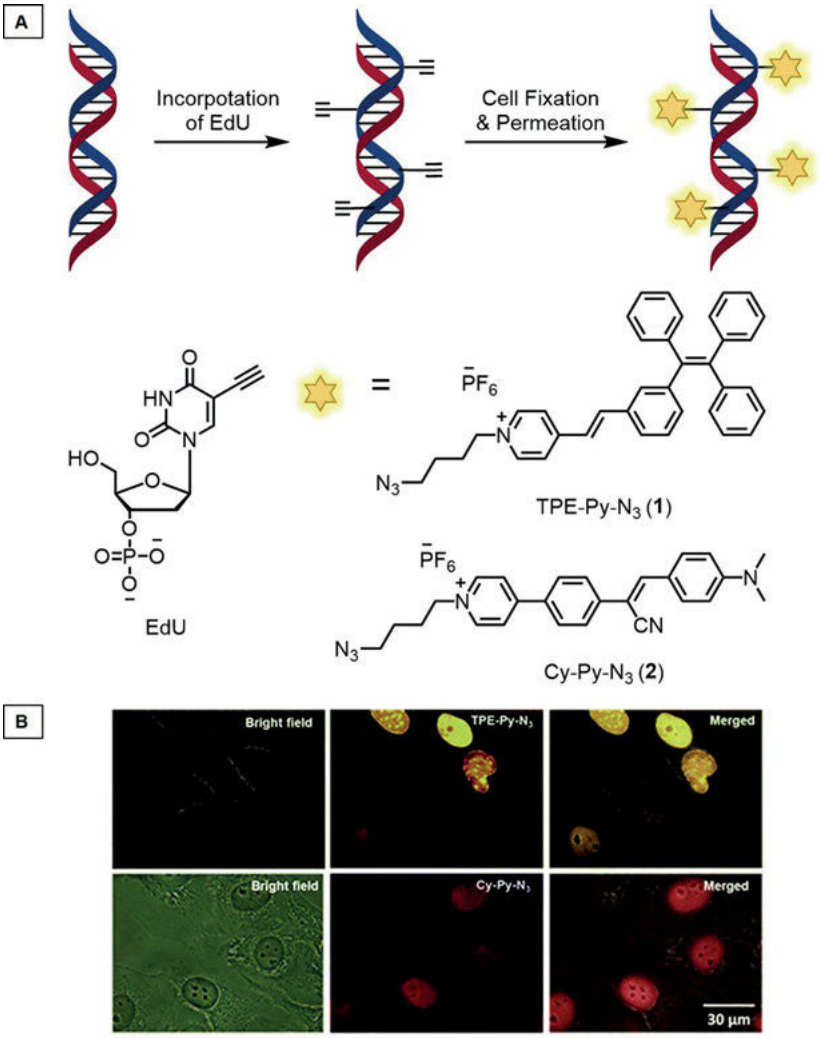


**Figure 4.4:** (A) DNA Synthesis Detection by AIEgens through EdU Assay; (B) Detection of S-Phase DNA Synthesis in HeLa cells by Fluorescence Microscopy; (B) Reproduced from ref. [15] with permission from Royal Society of Chemistry, copyright 2015.

Liu and coworkers designed a biorthogonal fluorescence "turn on" AIEgen for targeted cancer cell imaging and ablation using the CuAAC reaction [19]. Traditional labeling strategies that rely on biological interactions face problems of heterogeneity of cancer cells or saturation of receptors; therefore, conjugation with fluorescent

probes using biorthogonal reactions has become an attractive alternative [20]. Through metabolic approaches, unnatural targets with abiotic functional groups can be artificially introduced to specific cancer cells to achieve labeling through biorthogonal conjugation. To apply this strategy, an alkyne-functionalized TPE derivative, TPETSAI (**3**), was first synthesized. TPETSAI (**3**) was found to be almost nonfluorescent in aqueous media but displayed significant fluorescent enhancement upon restriction of molecular motion through the CuAAC reaction using 1,3,5-tris(azidomethyl)benzene as a model azide. To explore the potential of using TPETSAI (**3**) for biomolecular imaging in live cells, HeLa and breast cancer MDA-MB-231 cells were first incubated with preacetylated *N*-azidoacetylmannosamine ($Ac_4$ManNAz) (50 μM), which was incorporated to form azide-functionalized glycans on the cancer cell surface followed by the addition of TPETSAI (**3**) (10 μM), $CuSO_4$ (25 μM), tris(3-hydroxypropyltriazolylmethyl)amine (THPTA) (125 μM), and sodium ascorbate (2.5 mM) (Figure 4.5). A strong red fluorescence could then be observed in the membrane of HeLa cells that gradually increased as the CuAAC reaction progressed. Furthermore, the specially designed AIEgen **3** could to be applied as a therapeutic agent upon visible light (λ = 400–700 nm) irradiation to generate reactive oxygen species (ROS), resulting in cell necrosis. This approach of fluorescence labelling of target cancer cells is a particularly promising approach for phototherapy, as light can be applied precisely to the pathological region, while the normal cells are untouched.

In addition to the bioconjugation strategy, the CuAAC reaction has been employed in the development of activity-based AIE sensors for the detection of analytes required to induce the reaction between the azide and alkyne moieties. For example, the CuAAC reaction requires the copper catalyst, usually prepared with an appropriate chelating ligand, to be maintained in the $Cu^{I}$ oxidation state. The most convenient CuAAC procedure involves the use of an in situ reducing agent, often ascorbate ions. Banerjee, Chatterjee, and coworkers exploited the need for a reducing agent in the development of an AIE "turn on" fluorescent sensing method for the selective detection of ascorbate ions [21]. Ascorbic acid helps to endorse tissue growth and healthy cell development and protects tissues from oxidative damage [22]. Two TPE derivatives bearing azide and alkyne functionalities (**4** and **5**) were synthesized, which would be able to undergo the CuAAC reaction in the presence of $Cu^{II}$ and ascorbate ions. The $Cu^{II}$ ions were reduced to $Cu^{I}$ in the presence of the ascorbate ions and catalyzed the CuAAC reaction, initiating the formation of the polymer **6,** comprising several TPE moieties, which was insoluble in the solvent system ($H_2O$/THF = 93/7 *v/v*) and, as a result, the solution emitted blue fluorescent light (Figure 4.6A). The triazole polymer formation was established by IR spectroscopy of both TPE derivatives (**4** and **5**), and the CuAAC reaction product **6**. AIEgens **4** and **5** displayed strong alkyne (3,300 $cm^{-1}$) and azide (2,100 $cm^{-1}$), respectively, whereas the IR spectrum of the solid product showed a broad band for cyclic C =C, N =N absorption in the region 3,000–3,500 $cm^{-1}$, which is a characteristic peak of the 1,2,3-triazole moiety. In addition, the absorption band corresponding to the alkyne functionality disappeared, and the intensity of the

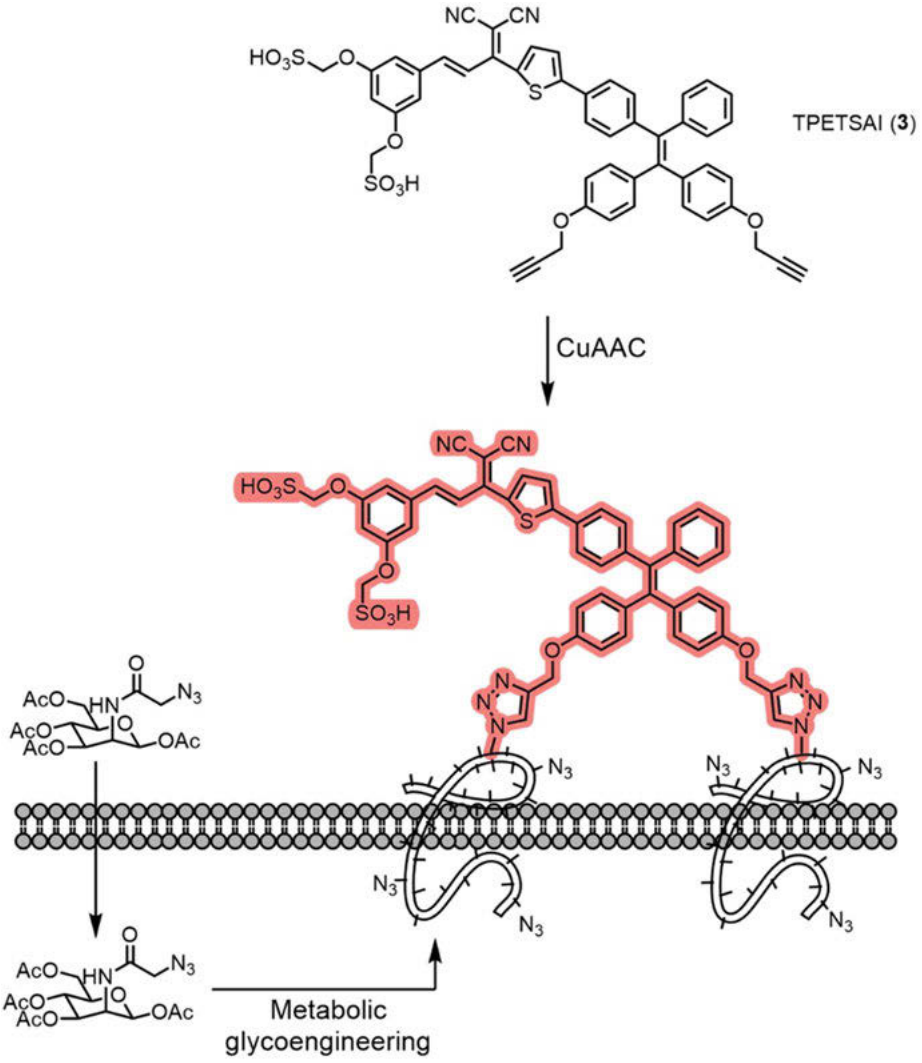


**Figure 4.5:** Turn on AIEgen TPETSAI (**3**) for cancer cell imaging and ablation using the CuAAC reaction.

azide was significantly reduced in the TPE polymer (**6**). The fluorescence sensing selectivity for ascorbate acid was examined in the presence of several other cations and anions, and the fluorescence response of the system was found to only increase in the presence of ascorbate and $Cu^{II}$, highlighting the selectivity towards ascorbate ions. The applicability of this sensing method for quantitative detection of ascorbate acid in commercially available Vitamin C tablets was also demonstrated, offering a rapid and economic method for the selective detection of ascorbic acid.

A similar approach was used by Costero and coworkers for the sensing of nitric oxide (NO) [23]. NO has a range of diverse physiological functions including acting as a messenger molecule in white blood cells, blood vessels, and the central nervous system [24]. Inhaled NO (iNO) improves oxygenation in respiratory failure and persistent pulmonary hypertension. The initial recommended concentration of iNO in these treatments is 20 ppm. Higher concentrations have not been shown to increase the effectiveness of the treatment and are associated with a higher incidence of methemoglobeinemia and nitrogen dioxide formation; therefore, the monitoring and control of iNO concentration is highly important [25]. A TPE derivative functionalized with an alkyne moiety (**7**) was synthesized and reacted with 1-azidohexane in the presence of a $Cu^{II}$ species, $Cu(OAc)_2$ and NO, which was able to generate the required $Cu^{I}$ from $Cu(OAc)_2$ allowing the click reaction to proceed (Figure 4.6B). The resultant triazole product has higher steric hindrance, promoting an increased fluorescent emission. A detection range and limit of detection (LoD) of NO was established through testing different concentrations of NO, ranging from 5 to 100 ppm. The selectivity of the system was confirmed when the gases $NO_2$, $CO_2$, CO, and $SO_2$ were individually bubbled through the same solution and no significant changes in the emission were seen, compared to the use of NO. The linearity range was determined to range from 20 to 80 ppm and have a LoD of 15 ppm. Although several sensors for NO have been reported, this sensing method offers several advantages, including the detection of gaseous nitric oxide and the use of lower pollutant compounds. In addition, the lowest concentration of iNO used in medical treatment is 20 ppm.

In 2011, Sanji, Tanaka, and coworkers used the CuAAC for the fluorescence turn-on detection of $Cu^{II}$, using an azide functionalized AIEgen (**9**) and a terminal diyne, diethylene glycol dipropiolate (**10**) [26]. Elevated levels of $Cu^{II}$ are associated with several neurodegenerative diseases, including Wilson's and Alzheimer's diseases [27]. Additionally, copper, usually found in the oxidized state, can be an environmental pollutant. Therefore, a sensitive and selective detection method for $Cu^{II}$ is critical. Upon the addition of $Cu^{II}$, AIEgen **9** and diethylene glycol dipropiolate (**10**), in the presence of sodium ascorbate, yielded covalently cross-linked networks **11,** which resulted in a dramatic enhancement in fluorescence due to restriction of intramolecular rotations (Figure 4.7). Upon addition of $Cu^{II}$ to a solution of the AIEgen **9** (20 μM), diyne **10** (40 μM), and sodium ascorbate (40 μM) in the detection solvent ($THF/H_2O$ = 11/1, *v*/*v*), the fluorescence emission increased gradually and reached a constant value within 48 h, although increasing the temperature to 50 °C decreased the detection time to 12 h. The emission intensity increased almost linearly with the concentration of $Cu^{II}$ in the range of 0–20 μM; however, further addition of $Cu^{II}$ caused a decrease in fluorescence. It was proposed that the fluorescence decrease was caused by the formation of highly cross-linked insoluble polymers. The detection limit was estimated to be approximately 1 μM. The assay was shown to be highly selective for $Cu^{II}$, as there was no increase in fluorescence when the assay was performed with various other metal ions ($Li^+$, $Na^+$, $K^+$, $Mg^{2+}$, $Ca^{2+}$, $Mn^{2+}$, $Fe^{2+}$, $Fe^{3+}$, $Co^{2+}$, $Ag^+$, and $Zn^{2+}$).

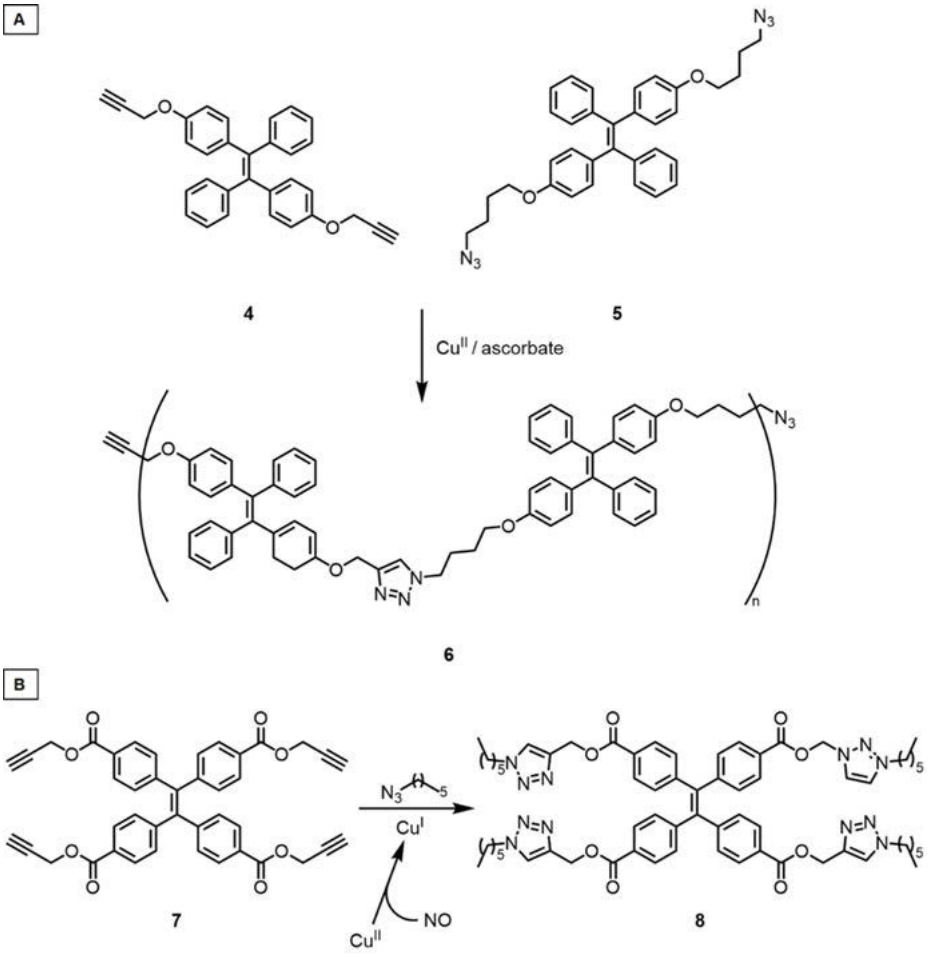


**Figure 4.6:** Sensing methods for detecting ascorbate ions (A) and NO (B) using the CuAAC reaction.

## 4.2.2 Strain-Promoted [3 +2] Azide-Alkyne Cycloaddition (SPAAC)

While the CuAAC reaction has emerged as a highly versatile strategy in the development of activity-based AIE sensors for a wide range of targets, the reaction is limited due to the toxicity of copper ions, and their difficult removal can limit the in vivo usage of the reaction. In 2004, Bertozzi and coworkers reported a copper-free strain-promoted [3 +2] azide-alkyne cycloaddition (SPAAC) for the selective modification of biomolecules and living cells without apparent physiological harm [28]. The research group employed cyclooctyne alkynes activated by ring strain, lowering the activation energy for the cycloaddition and enabling the reaction to be performed at lower temperatures, without the need for any catalysis. The SPAAC reaction has been used in

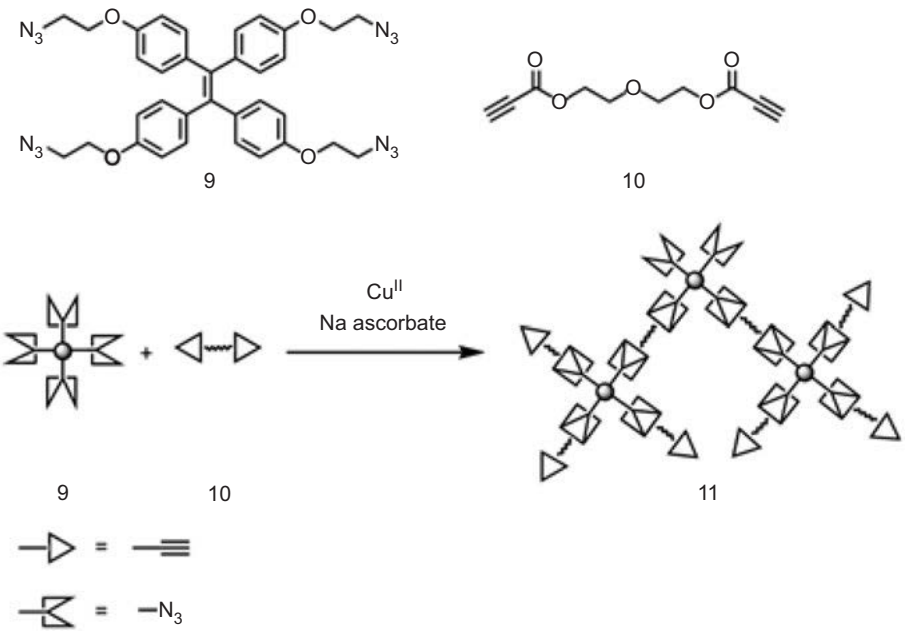


**Figure 4.7:** Sensing method for detecting $Cu^{II}$ using the CuAAC reaction.

ABS by modifying an AIEgen with a strained alkyne for bioconjugation with an azide-functionalized target biomolecule (Figure 4.8).

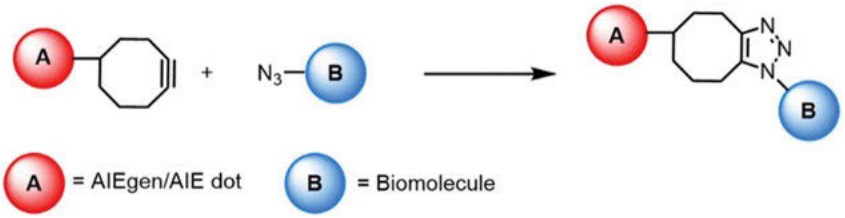


**Figure 4.8:** Schematic illustrating the use of the SPAAC reaction in an AIEgen ABS approach.

Liu and coworkers used the SPAAC reaction to further develop their aforementioned work on cancer cell imaging to in vivo labeling (See Section 4.2.1) [29]. The researchers designed a biorthogonal "turn on" AIEgen named BCN-TPET-TEG (**12**) composed of an AIE core (TPET), hydrophilic triethylene glycol (TEG), and the strain alkyne bicyclo[6.1.0]nonyne (BCN) (Figure 4.9A). In this design, it was envisioned that the hydrophilic nature of TEG endows BCN-TPET-TEG (**12**) with good water dispersibility, and therefore the AIEgen **12** would only emit low fluorescence until the BCN moieties undergo the SPAAC reaction with the azide groups on tumor cells previously pretreated

with azide modified acetyl sialic acid (AzACSA). Following the SPAAC reaction, the fluorescence of AIEgen **12** was expected to become significantly advanced due to RIM (Figure 4.9B). The "turn on" for BCN-TPET-TEG (**12**) was initially investigated through SPAAC polymerization with 1,3,5-tris(azidomethyl) benzene (TAB), which resulted in cross-linked aggregates and a 6-fold enhancement in fluorescence after 1 h in the detection solvent ($THF/H_2O$ = 1/10, *v*/*v*). The potential of BCN-TPET-TEG (**12**) was further evaluated by incubating the probe with ionic surfactants and solutions containing different biomolecules, including DNA, proteins, and cell lysates with no significant change in fluorescence, illustrating its potential for specific "turn on" imaging. The in vivo tumor imaging was studied in comparison to DBCO-Cy5, an "always on" commercial azide-reactive probe using a tumor-bearing mice model. BCN-TPET-TEG (**12**) administered mice showed rapid fluorescence only at tumor sites with no detectable signal from the rest of the mouse body, whereas DBCO-Cy5 requires approximately 24 h for background probe signal to disappear before the true tumor signal could be identified (Figure 4.9C). The photosensitizing ability of AIEgen **12** was also used to realize effective image-guided photodynamic therapy (PDT). At 6 h post injection of BCN-TPET-TEG (**12**), the tumor-bearing mice were irradiated with white light for 10 min for PDT evaluation. The tumor growth was found to be much slower in the BCN-TPET-TEG (**12**) click group in comparison to the control groups.

Zhang, Cai, Zhao, and coworkers used the SPAAC reaction in the development of fully humanized antibody conjugated AIE dots for in vivo cancer imaging [30]. Compared with traditional molecular dyes, AIE dots display extraordinarily high brightness, large Stokes shift, and excellent photostability. In addition, AIE dots are much more biocompatible than inorganic nanoprobes, providing great clinical translation opportunities [31]. The clickable AIE dots were synthesized by encapsulating an AIE-active polymer, PDFDP, in a strained alkyne, diarylcyclooctyne (DBCO), functionalized lipids. The AIE dots showed excellent optical and colloidal properties; the AIE dots displayed a wide absorption range (250–600 nm), a sharp emission peak at 660 nm, and a large Stokes shift. The strained alkyne-appendaged AIE dots were able to react with azide-functionalized anti-HER2 fully human antibody (RHA) with high specificity under mild reaction conditions, without the presence of copper ions to preserve the structure and function of the antibody (Figure 4.10A). The RHA-AIE dots were found to be stable for up to 8 months and possess high stability in different pH environments, biological buffer, culture media, and to oxidation and reduction agents. The RHA-AIE dots were first applied in HER2 positive SK-BR-3 cells and then HER2 negative MD-MB-231 cells for cancer cell imaging. SK-BR-3 cells treated with RHA-AIE dots were highly fluorescent in contrast to the MD-MB-231 cells, demonstrating an enhanced binding of RHA-AIE dots to the HER2 highly expressed breast cancer cells (Figure 4.10B). The RHA-AIE dots were then applied in a mouse model for in vivo experiments, which indicated that the RHA-AIE dots specifically accumulated in the SK-BR-3 tumor and emitted higher fluorescence signals, providing a clear in vivo cancer diagnosis.

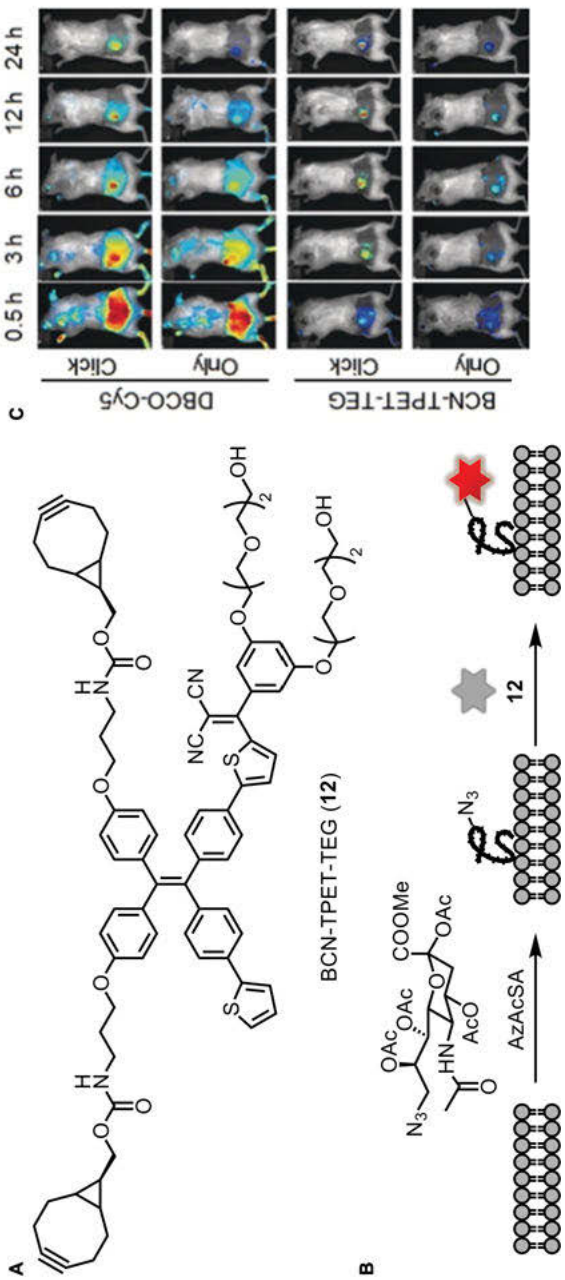


**Figure 4.9:** (A) The chemical structure of BCN-TPET-TEG (**12**); (B) Schematic illustration of azide expression on cancer cell membrane glycan and subsequent "turn-on" bio-orthogonal labeling using the SPAAC reaction; (C) Time-dependent fluorescence imaging of 4T1-bearing mice with/without AzAcSA (30 μL of 50 μM) pre-treatment after DBCO-Cy5/**12** administration (100 μL, 0.5 mg $mL^{-1}$); (C) Reproduced from ref. [29] with permission from John Wiley and Sons, copyright 2018.

In addition to functionalizing AIE dots with recognition moieties such as antibodies, in vivo tumor imaging can be achieved through reacting the AIE dots directly with metabolically labeled cancer cells. Tang and coworkers used the SPAAC reaction in this approach for in vivo cancer imaging [32]. In this system, a benzo[*d*] imidazole-cored AIEgen (2 TPE-2 T-BI, **13**) (Figure 4.10C) with long-wavelength emission was encapsulated within DBCO-functionalized lipid to form DBCO-AIE dots, which would be able to react with azides in the SPAAC reaction in a biological environment (Figure 4.10D). The maximum absorption and emission peaks of DBCO-AIE dots were 572 and 710 nm, respectively, offering the advantages of low excitation energy and autofluorescence in biological media. The DBCO-AIE dots also had a large Stokes shift of 138 nm to greatly minimize the self-absorption. The transmission electron microscopy (TEM) image and dynamic light scattering measurements indicated that the DBCO-AIE dots were spherically shaped, with an average size of approximately 85 nm, making them suitable for blood circulation in vivo. The DBCO-AIE dots were applied in a mouse model with the MCF-7 tumor pre-treated unnatural monosaccharides (Ac4ManNAz) to introduce azide bearing tumors. Following treatment with the DBCO-AIE dots, the fluorescence signal for Ac4ManNAz-treated mouse was almost exclusively located around the tumor. In comparison, the fluorescence signal in the mouse without Ac4ManNAz treatment was distributed across the whole body, indicating that the amount of accumulated DBCO-AIE dots in tumor tissue was highly increased in Ac4ManNAz treated mouse (Figure 4.10E). When compared to AIE dots with short-wavelength emission, the NIR emissive DBCO-AIE dots showed higher contrast and signal to noise ratio for in vivo imaging due to the lower autofluorescence from the body in the same emission wavelength window.

## 4.3 Michael addition reactions

The Michael addition reaction is a versatile synthetic methodology for the efficient coupling of electron-poor olefins with a vast array of nucleophiles [33]. The Michael addition reaction fulfils the key criteria that qualifies the reaction as a highly modular click reaction with the ability to product highly stereospecific and regiospecific products. The thermodynamically favored, facile methodology generates C-C, C-N, C-S and C-O bonds, requiring only mild reaction conditions and benefiting from a high functional group tolerance [34, 35]. In contrast to the CuAAC reaction, the Michael addition reaction proceeds under metal-free conditions and exploits the wealth of readily available substrates, including phenols, amines, and thiols eliminating the need for premodification with azide and alkyne functional groups, which is often challenging and can, possibly, alter the primary function of the biomolecule. Although the SPAAC reaction is catalyst free, it can still be limited by the need for expensive reagents, tedious optimizations, and complicated preparations. The application of Michael addition

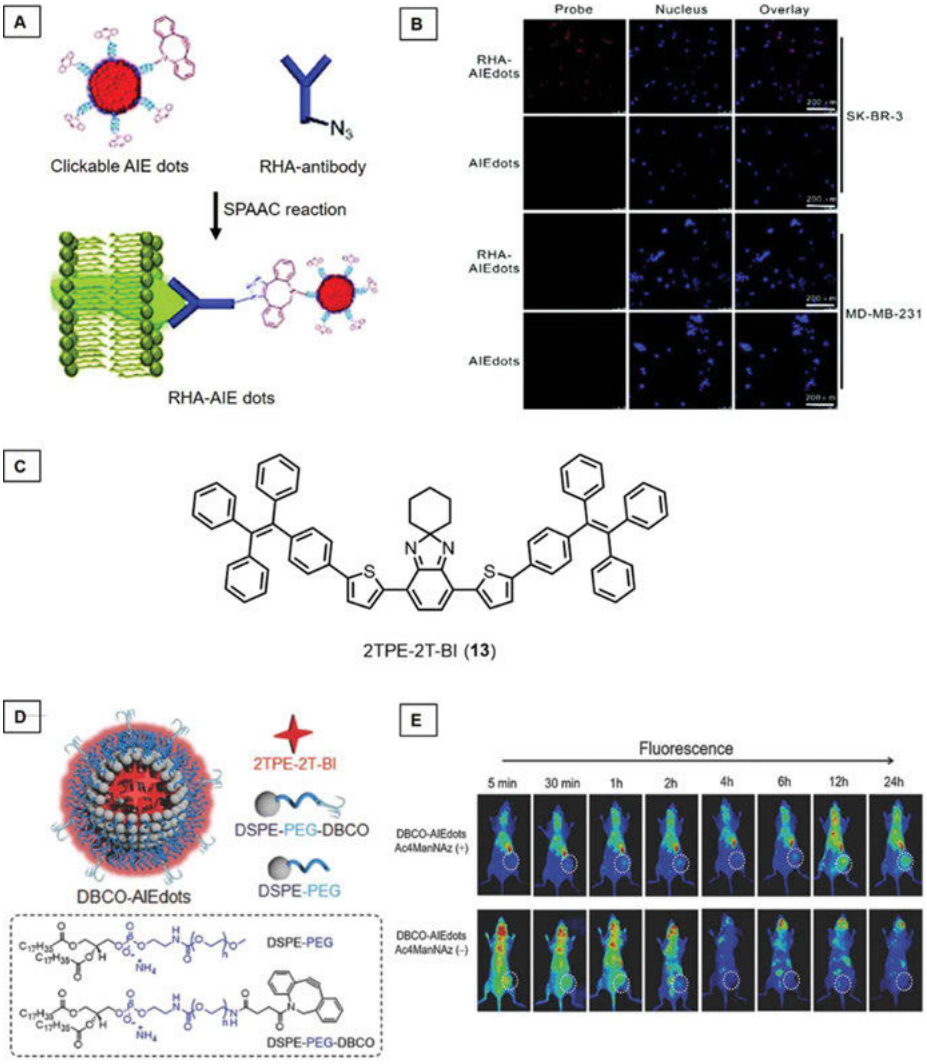


**Figure 4.10:** (A) Schematic illustration of the preparation of RHA-AIE dots; (B) Specific targeting and imaging of RHA-AIE dots in HER2 positive cells; (C) Chemical structure of 2 TPE-2T-BI (**13**); (D) Schematic illustration of DBCO-AIE dots composition; (E) Time-dependent fluorescence imaging of MCF-7 tumor veering mice with/without Ac4ManNAz pre-treatment after administration of DBCO-AIE dots; (A and B) Reproduced from ref. [30] with permission from Royal Society of Chemistry, copyright 2018; (D and E) Reproduced from ref. [32] with permission from John Wiley and Sons, copyright 2018.

reactions in ABS addresses the deficiencies of both the CuAAC and SPAAC reactions and has been widely used in the fluorescence labeling of biomolecules using AIEgens (Figure 4.11).

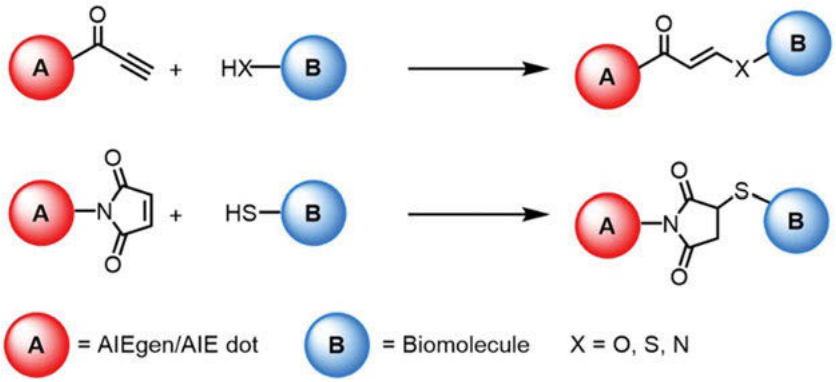


**Figure 4.11:** Schematic illustrating representing Michael addition reactions in an AIEgen ABS approach.

As a part of a proof-of-concept study, Tang and coworkers demonstrated that the abundant native groups, amine, thiol, and hydroxy can be directly reacted with activated alkynes, without any modification in the absence of metal catalysis (Figure 4.12) [36]. Two AIEgens bearing an electron-withdrawing carbonyl group activated alkyne, TPA-alkyne (**14**), and TPE-alkyne (**15**) were synthesized and examined for the fluorescence labeling of natural polysaccharides, amine terminated polyethylene glycol (PEG), bacteria, peptides, and proteins. Further application for rapid whole cell mapping and quick differentiation and labeling of gram-positive bacteria was also demonstrated. This strategy offers several attractive features including 100% atom efficiency, mild reaction conditions, and is catalyst-free, and therefore is a promising approach for the development of quick fluorescence labeling of many biotargets and biotarget-related processes in vitro and in vivo. However, site- and target-specific fluorescence labeling using this method lacks selectivity between amine, thiol, and hydroxy functionalities and, thus, has limitations in certain applications.

The Michael addition reaction has been widely applied in designing thiol-specific AIEgens for protein labeling. Cellular thiols are essential biomolecules that play a vital role in biological systems as key components of protein structures and metabolic intermediates. Abnormal concentrations of biothiols have been reported to be associated with many health problems including Alzheimer's disease, hepatic and renal failure, and impaired survival in HIV disease [37–39]. Tang and coworkers reported with the first example of thiol-specific AIEgen through functionalizing TPE with a maleimide (MI) group to give TPE-MI (**16**) (Figure 4.13A) [40]. TPE-MI was found to be nonfluorescent in both solution and the solid state as a result of the

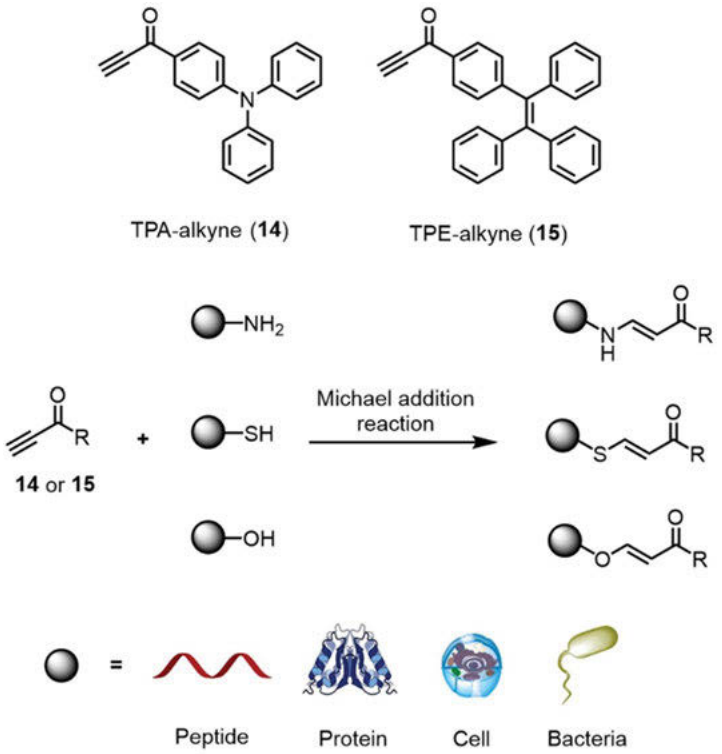


**Figure 4.12:** Schematic illustration of the metal-free click fluorescence labeling with native groups of biotargets.

exciton annihilation process associated with the n-π electronic conjugation of the carbonyl (C=O) and olefinic (C=C) group present in the MI moiety. The AIE activity was recovered by the Michael addition between the MI moiety and a free thiol group. As a result, the AIEgen **16** was applied in the selective detection of L-cysteine (Cys) on a TLC plate. When excited at 365 nm, the Cys spot emitted a bright blue light in the presence of the AIEgen **16,** while other non-thiol containing amino acid spots remained nonemissive. This technique was shown to be sensitive to Cys from 1 to 100 ng/mL. TPE-MI (**16**) was also applied in the selective detection of the small biothiol glutathione (GSH) using TLC plate. The sensing method was demonstrated to be a simple and convenient method for the detection of free thiols in solid state.

In 2017, Hong, Hatters and coworkers utilized TPE-MI (**16**) to measure cellular unfolded protein load through the Michael addition with free Cys thiols on proteins [41]. Disruption of the cellular protein homeostasis (proteostasis)) can promote protein unfolding, which, in turn, results in an accumulation of aggregated proteins, which is associated with many neurodegenerative diseases [42]. Cys residues are the least surface-exposed residue of all amino acids in proteins, and therefore an

abundance of accessible thiols is indicative of the levels of unfolded proteins. The suitability of TPE-MI (**16**) to be used to measure cellular unfolded protein load was first investigated using several model proteins, beginning with three proteins containing single free Cys residues buried in the core of the folded state (bovine β-lactoglobulin, yeast enolase and human peroxiredoxin-3). Each of the proteins displayed far greater reactivity to TPE-MI (**16**) when unfolded with guanidine hydrochloride than when in their native state, demonstrating selectively of TPE-MI towards unfolded proteins (**16**). The specificity for Cys was then demonstrated by reacting TPE-MI with ubiquitin, which lacks any Cys residues, which showed no reactivity. Furthermore, TPE-MI (**16**) was used to report the unfolding of proteins in living cells treated with stressors that induce protein unfolding, and to detect induced protein damage in anti-malaria drug-treated malaria parasites. This AIE-based strategy to measure unfolded load provides insight onto proteostasis capacity on cells, is easy to perform, efficient, and of low cost (Figure 4.13B). A follow-up study performed by Hong and coworkers reported a TPE-MI derivative named TPE-NMI (**17**), which offered improved water miscibility and red-shifted spectral profile, which is compatible with the commonly used 405 nm laser in most of the flow cytometers and confocal microscopes (Figure 4.13C) [43, 44]. Comparable with TPE-MI, TPE-NMI also displaced turn-on fluorescence upon reacting with unfolded protein in vitro and in live cells.

TPE-NMI was then further optimized to achieve a solvatochromic fluorogenic probe, NTPAN-MI (**18**), for assessing the polarity of the local environment surrounding unfolded proteins in cells (Figure 4.13C). To achieve environmental sensitivity, a phenyl ring of the TPE unit was replaced with an electron-withdrawing cyano group, creating a push-pull AIEgen. Push-pull dyes with both electron donor and acceptor experience excited-state charge transfer, which is stabilized by interactions with the dipoles of solvent, resulting in emission redshift in more polar solvents (Figure 4.13D). In contrast to TPE-MI (**16**) and TPE-NMI (**17**), AIEgen **18** offers the advantage for direct visualizing and quantifying unfolded proteins in both the cytoplasm and the nucleus. By using spectral phasor analysis, polarity surrounding the labeled unfolded proteins could be quantified in terms of dielectric constant ($\varepsilon$) in subcellular resolutions. The labeled unfolded proteins experienced $\varepsilon$ in a range of 22–32 in the hydrophobic environment of the endoplasmic reticulum, 32–36 at the interface of the endoplasmic reticulum and cytoplasm, and 36–45 inside the nucleus, where the environment is more hydrophilic. Under conditions that promote proteostasis imbalance such as tunicamycin, MG132 or puromycin treatment, **18** revealed a large shift of the nucleus environment to a highly hydrophilic environment ($\varepsilon$ = 45–54), suggesting the central role of nucleus in the stress response process. AIEgen **18** was further applied to reveal proteostasis collapse in cells upon influenza virus infection, demonstrating that such a process disrupts the protein quality control of the host cells. This approach offers future possibilities to investigate the role of subcellular polarity in protein quality control and stress response.

Differentiating between biological thiols such as Cys, homocysteine (Hcy), and GSH using activity-based sensors has proven challenging. In particular, Hcy is a

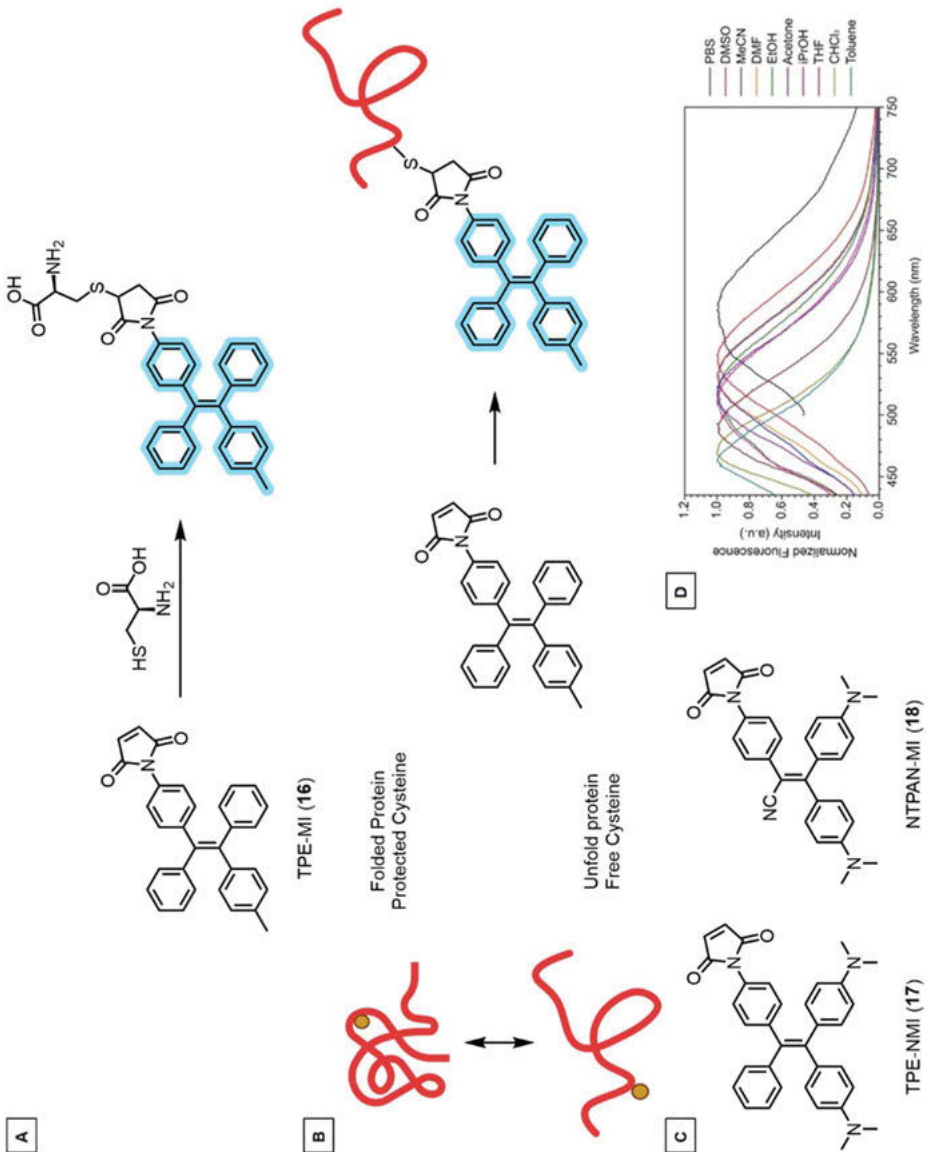


**Figure 4.13:** (A) Sensing of Cys using TPE-MI (**16**); (B) Schematic illustration of the strategy for determining unfolded protein load using TPE-MI (**16**); (C) Structures of TPE-NMI (**17**) and NTPAN-MI (**18**); (D) Normalized fluorescence spectra of thiol-conjugated NTPAN-MI (**18**) in solvents with different polarity; (D) Reproduced from ref. [44] with permission from John Wiley and Sons, copyright 2018.

homologue of Cys with only one additional methylene group, and therefore it can be difficult to distinguish between them. High blood levels of Hcy have been identified as risk factor in Alzheimer's disease, neural tube defects, inflammatory bowel disease, and osteoporosis, and, therefore, selective detection of Hcy is vital for early detection and treatment [45]. Tang and coworkers employed a red-emission AIE-active hemicyanine dye (TPE-Cy, **19**) for the selective detection of Hcy (Figure 4.16) [46]. Following the addition of Hcy, the red emission of TPE-Cy (**19**) in pH 8 buffer is suppressed and replaced with a strong blue emission. In the cases of Cys and GSH, only a very weak blue emission or no change in emission was observed, respectively. The selectivity of **19** for Hcy was attributed to extra methylene presence in Hcy, creating less steric hindrance, compared to Cys and GSH. In addition of the reactivity differences, Hcy is more hydrophobic than Cys, and, therefore, the Michael adduct of Hcy and **19** would have a higher tendency to aggregate in the aqueous buffer solution, resulting in an enhanced fluorescent emission. Zhao, Li, Tang and coworkers also developed a novel AIEgen (TPE-Py, **20**) for the selective detection of HCy [47]. AIEgen **20** contained α,β-unsaturated ketone units, which was able to undergo a Michael addition reaction with biothiols, resulting in the disruption of molecular conjugation and a fluorescence change. It was discovered that only Hcy triggered a significant ratiometric fluorescence change from yellow to blue, whereas quenching of fluorescence was observed in the presence of Cys or GSH. As with TPE-Cy (**19**), the selectivity for Hcy was attributed to the poorer solubility of the Hcy TPE-Py Michael addition product compared to the Cys and GSH adducts and, therefore, is more likely to form aggregates in the detection mixture.

A malonitrile-functionalized TPE derivative (TPE-DCV, **21**) was synthesized by Tang and coworkers, which was able to selectively detect GSH via a Michael addition reaction (Figure 4.15) [48]. The presence of GSH was found to trigger the fluorescence of TPE-DCV (**21**) (3 μM), whereas all the other amino acids (1 mM), including Cys and Hcy caused no fluorescence "turn on" effect of TPE-DCV (**21**) in the detection medium ($H_2O$/EtOH = 68:32 *v/v*). It was speculated that the selective response was to the varied solubility of the Michael adduct products. The increased hydrophilicity of the GSH adduct causes reduced solubility in the detection medium containing 32% ethanol and therefore forms aggregates, resulting in a fluorescence response. The selectivity of TPE-DCV (**21**) for GSH was applied in the real time monitoring of glutathione reductase (GR) activity, which cleaves glutathione disulfide (GSSG) to produce GSH to regulate the redox balance. As neither GSSG nor GR can "turn on" the fluorescence of TPE-DCV (**21**), the fluorescence of TPE-DCV (**21**) results solely on the GSH produced in the enzymatic reaction. A similar strategy has also been used in the malonitrile containing silole derivates, DMTPS-*p*-DCV (**22**) and DMTPS-*m*-DCV (**23**)n designed by Tang and coworkers for the detection of biothiols via a Michael addition reaction (Figure 4.15) [49]. DMTPS-*p*-DCV (**22**) was able to differentiate Cys and Hcy from GSH relying on the distinctive differences in kinetics, and DMTPS-*m*-DCV (**23**) had excellent sensitivity for Cysn with a detection limit lower than 0.5 μM.

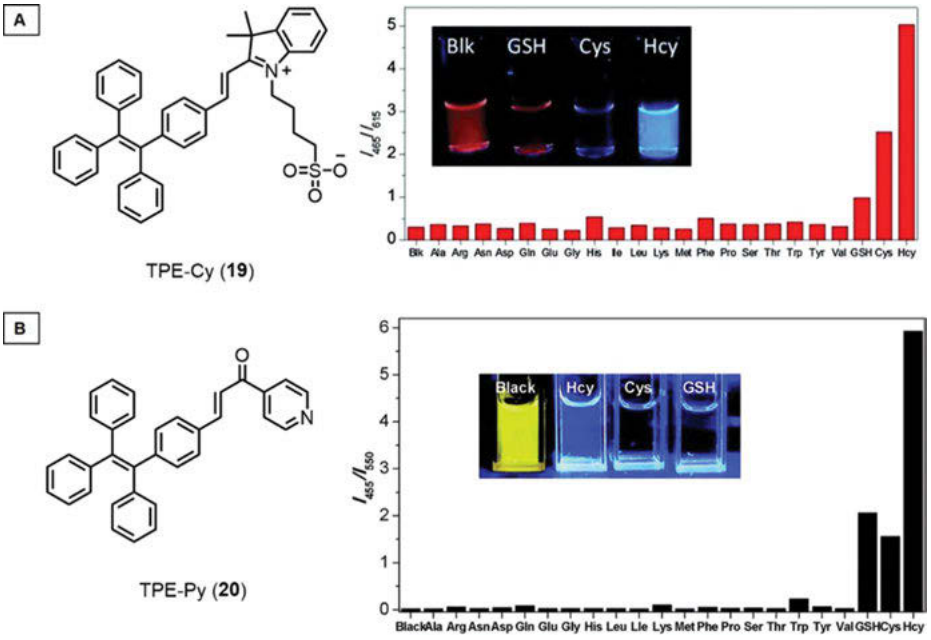


**Figure 4.14:** (A) Structure of TPE-Cy (**19**) and emission ratio change of probe **19** upon addition of 1 mM of different amino acids and GSH in pH buffer, inset: Photo of TPE-Cy in blank buffer or 10 μM GSH, Cys, and Hcy under UV lamp illumination; (B) Structure of TPE-Py (**20**) and emission ratio change of probe **20** upon addition of 60 mM of different amino acids and GSH in solution, inset: Photo of TPE-Py in blank solution or 60 mM Hcy, Cys and GSH under UV lamp illumination; (A) Reproduced from ref. [46] with permission from Royal Society of Chemistry, copyright 2014; (B) Reproduced from ref. [47] with permission from Royal Society of Chemistry, copyright 2015.

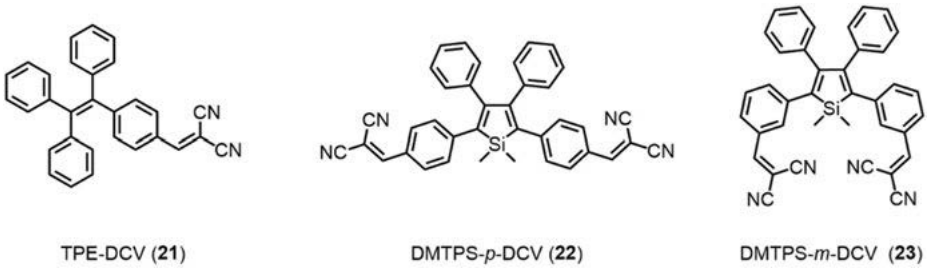


**Figure 4.15:** Structures of TPE-DCV (**21**), DMTPS-*p*-DCV (**22**), and DMTPS-*m*-DCV (**23**).

An excited-state intramolecular proton transfer (ESIPT)-based AIEgen was designed by Yoon and coworkers for the sensing of biothiols [50]. The AIEgen named AIE-S (**24**) was designed based on salicyaldazine, in which the hydroxyl group was protected by acryloyl group blocking the ESIPT, resulting in very weak fluorescent

emission. However, when AIE-S (**24**) (10 μM) was treated with Cys (50 μM) in PBS buffer (10 mM, pH 7.4) with 1% DMSO at 25 °C, a significant green fluorescence signal gradually increased at the maximum wavelength 505 nm over 30 min (Figure 4.16A). The thiol moiety of the cysteine first reacted with the acryloyl group via a Michael addition reaction, which was followed by a spontaneous intramolecular cyclization reaction to release the salicylazdazine AIEgen **25**. After the deprotection of the hydroxyl group, the ESIPT process was restored, and a strong fluorescence signal was induced. To investigate the ability of AIE-S (**24**) to detect other biothiols, the time-dependent fluorescence kinetic spectra of AIE-S (**24**) (10 μM) to Hcy, GSH, and $Na_2S$ (100 μM) were also tested in PBS buffer (10 mM, pH 7.4) with 1% DMSO at 25 °C, in comparison to Cys. After 40 min, strong fluorescent emissions were observed with both Cys and GSH but not with Hys or $Na_2S$. After 4 h, similar intensities were observed for Cys, GSH and Hys. However, as $Na_2S$ cannot induce the intramolecular cyclization reaction there was no significant change in fluorescence. The huge kinetic difference between Cys and Hcy was attributed to the kinetic rate of the intramolecular cyclization. The seven-membered ring formation in the case of Cys is kinetically favored in comparison to the eight-membered ring formed from the Hcy addition. Finally, AIE-S (**24**) was successfully used to image biothiols in living cells. When Cys and GSH were added to AIE-S pretreated HeLa cells, a strong green fluorescence was detected, following incubation for 40 min, but when Hcy was added, no fluorescence signal was observed in alignment with the previous kinetic experiment.

More recently, another ESIPT-based AIEgen, ABTT-MA (**26**) was reported by Zeng and coworkers for the selective detection of Cys [51]. The maleimide-appended ABTT-MA (**26**) fluorescence signal was quenched prior to incubation with biothiols in aqueous solution (containing 0.5% DMSO), due to the donor-excited photoinduced electron transfer (d-PET) from the fluorophore to maleimide moiety, while addition of Cys triggered a strong fluorescence response, which peaked at 502 nm, a 500-fold enhancement, compared to free ABTT-MA (**26**). Under the same conditions, however, the addition of Hcy resulted in a much weaker fluorescence enhancement, approximately a 61-fold increase, and GSH addition resulted in weak fluorescence peak at 475 nm. The high selectivity towards Cys was ascribed to the Michael addition of the thiol moiety to the alkene of the maleimide to afford the thiol-adduct, which subsequently undergoes an intramolecular *S*,*N*-rearrangement to give amino-adducts that exhibit strong fluorescence. The *S*,*N*-rearrangement from thio- to amino-adducts is thermodynamically favorable owing to the geometric arrangement between the amino group of Cys with thioether, involving a five-membered cyclic transition [52]. In the case of Hcy, however, the rearrangement reaction was slowed by the additional carbon-chain extension, resulting in a weaker fluorescence signal. While GSH possesses a free amino group, a similar rearrangement required 10-membered cyclic transition state, which is highly unfavorable. The selective detection of AIEgen **26** for Cys was also realized in a paper-based point-of-care test (POCT). The test papers were prepared from strips of polyamide

film, which were adsorbed with ABTT-MA in THF. Upon addition of Cys solution of varying concentrations (1–20 μM), the test papers emitted bright fluorescence under UV light, within 15 min. Finally, preliminary investigations demonstrated the capability of ABTT-MA for imaging exogenous and endogenous Cys in living cells.

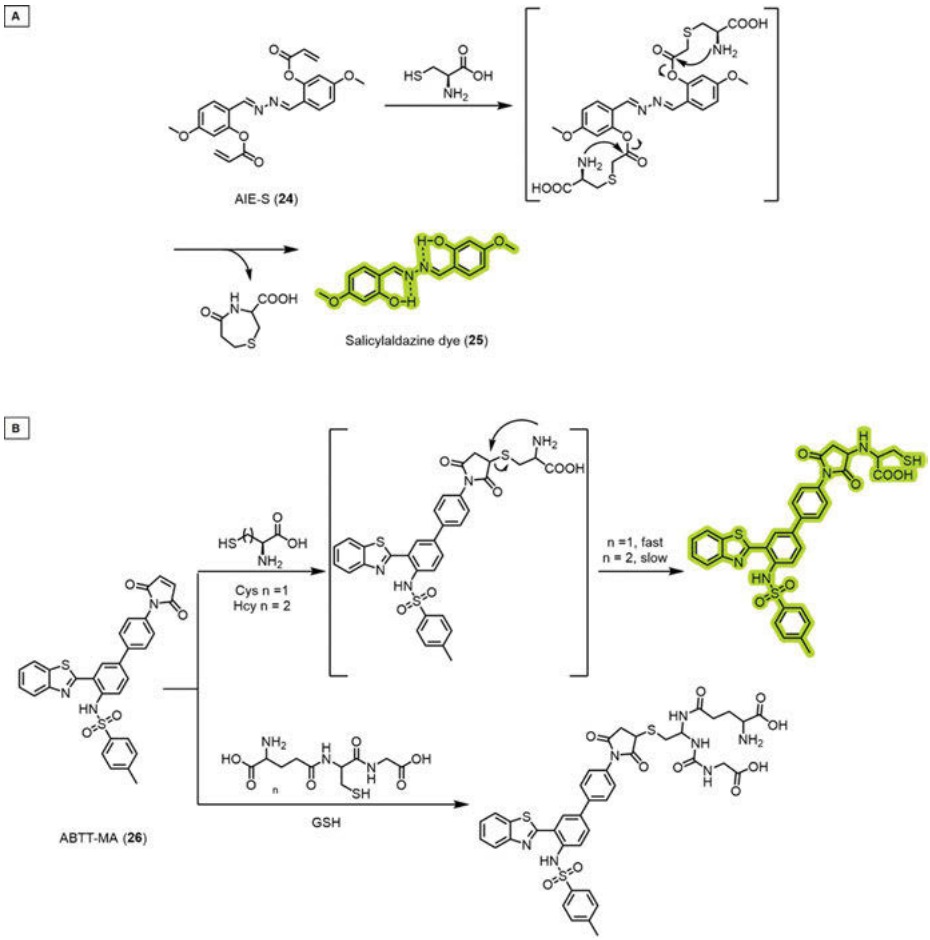


**Figure 4.16:** (A) Proposed sensing mechanisms of AIE-S (**24**) towards Cys; (B) Proposed sensing mechanisms of ABTT-MA (**26**) towards Cys, Hcy, and GSH.

## 4.4 Staudinger ligation

The Staudinger ligation developed by Bertozzi and coworkers is a modification of the classical Staudinger reaction reported in 1919, where a phosphane is reacted with an azide to form a phospha-aza ylide [53, 54]. In Staudinger ligation, a triaryl phosphine reagent bearing an ester ortho to the phosphine is employed as an electrophilic trap to react with the phospha-aza ylide to cleave the ester to form an amide bond and release the corresponding alcohol (Figure 4.17). The Staudinger ligation possesses the crucial characteristics for click chemistry including being high-yielding, biorthogonal, and being able to be performed under mild conditions, without any cytotoxic reagents or byproducts [55]. The Staudinger ligation has found numerous applications in various complex biological systems, including in the development of fluorescent probes for ABS [56].

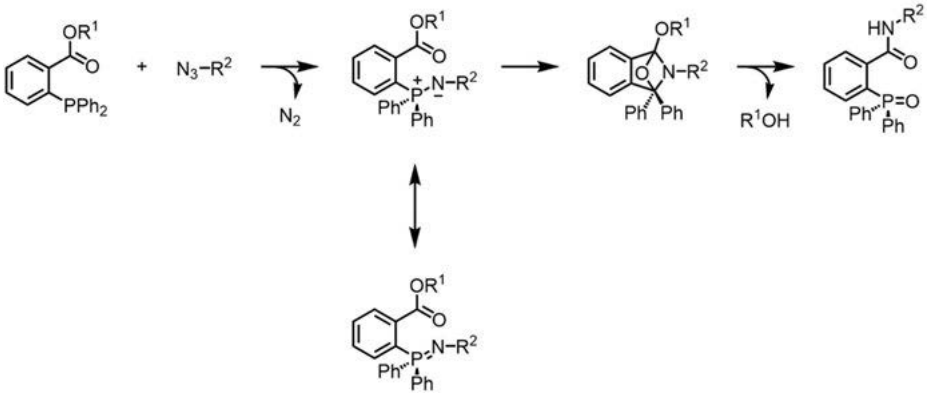


**Figure 4.17:** The Staudinger Ligation.

In 2021, Wang, Tang, and coworkers reported a ratiometric fluorescent probe (TCFPB-HNO, **27**) with AIE features for the detection and visualization of nitroxyl (HNO) using the Staudinger ligation [57]. HNO has been reported to possess unique and distinct biological and pharmacological properties [58]. For instance, HNO can interact with thiol-containing enzymes to regulate enzyme activity [59]. In addition, HNO has emerged as a novel therapy for congestive heart failure and a possible anticancer drug. However, due to HNO's high reactivity and short lifetime, fast, sensitive, and selective visualization of HNO in biological systems remaining challenging [60]. The probe TCFPB-HNO (**27**) was found to possess weak intramolecular charge transfer (ICT) effects due to the weak electron-donating ability of the ester group, which connected the luminescent moiety and the recognition moiety. The reaction between the AIEgen **27** (5 μM) and Angeli's salt (a donor of HNO, 50 μM) at 37 °C for 40 min generated the corresponding phospha-aza, which underwent a Staudinger ligation with

the ester moiety to give tricyanofuranyl iminosalicylaldehyde (TCFIS, **28**) with strong ICT effects (Figure 4.18A). While TCFPB-HNO (**27**) showed weak emission at 670 nm in phosphate buffered saline (PBS), after incubation with HNO, TCFPB-HNO exhibited typical ratiometric changes ($I_{618}/I_{670}$), with excellent sensitivity and photostability in PBS solution. The probe could also be used for HNO detection and selective imaging in vitro and in vivo with a high signal-to-noise ratio (Figure 4.18B). These results indicated that TCFPB-HNO could be successfully applied for ABS of HNO in living systems to provide an understanding of the physiological and pathological functions of HNO.

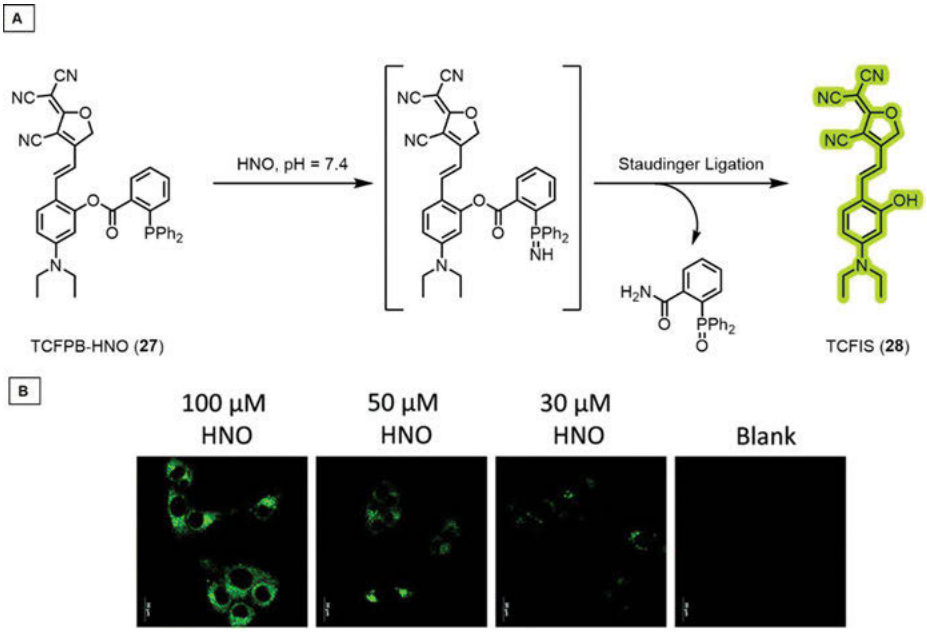


**Figure 4.18:** (A) Recognition mechanism of TCFPB-HNO (**27**) towards HNO; (B) Cell imaging of probe **27** (15 μM for 30 min at 37 °C) with different concentrations of HNO, $\lambda_{ex}$ = 543 nm; (B) Reproduced from ref. [56] with permission from Royal Society of Chemistry, copyright 2021.

## 4.5 Conclusion

This chapter has described the applications of click chemistry in the design of activity-based AIE sensors. The principles and advantages of AIE, ABS, and click chemistry have been introduced, and the compatibility and synergy between them have been highlighted through several examples. The structural design of AIEgens affords specific detection of analytes via click chemistry. These activity-based AIE sensors rely on both molecular reactivity and their AIE characteristics to selectively detect and image

an array of targets, including biothiols, toxic gases, and metal ions. These detections were achieved using a selection of click reactions with cycloadditions, with Michael addition reaction being the most prominently used. This chapter demonstrated the substantial progress in the development of activity-based AIE sensors, using click chemistry. However, many click reactions remain underexploited in the design of AIEgens for ABS and could be used to expand the diversity of AIEgens and analytes used in the ABS approach.

## References

[1] Yao J, Yang M, Duan Y, Chemistry, biology, and medicine of fluorescent nanomaterials and related systems: New insights into biosensing, bioimaging, genomics, diagnostics, and therapy, Chem Rev, 2014, 114, 6130–6178.
[2] Biju V, Chemical modifications and bioconjugate reactions of nanomaterials for sensing, imaging, drug delivery and therapy, Chem Soc Rev, 2014, 43, 744–764.
[3] Baker M, The whole picture, Nature, 2010, 463, 977–980.
[4] Bruemmer KJ, Crossley SWM, Chang CJ, Activity-based sensing: A synthetic methods approach for selective molecular imaging and beyond, Angew Chem Int Ed, 2020, 59, 13734–13762.
[5] Borisov SM, Wolfbeis OS, Optical biosensors, Chem Rev, 2008, 108, 423–461.
[6] Hong Y, Lam JWY, Tang BZ, Aggregation-induced emission, Chem Soc Rev, 2011, 40, 5361–5388.
[7] Kwok RTK, Leung CWT, Lam JWY, Tang BZ, Biosensing by luminogens with aggregation-induced emission characteristics, Chem Soc Rev, 2015, 44, 4228–4238.
[8] Chan J, Dodani SC, Chang CJ, Reaction-based small-molecule fluorescent probes for chemoselective bioimaging, Nat Chem, 2012, 4, 973–984.
[9] Wang D, Tang BZ, Aggregation-induced emission luminogens for activity-based sensing, Acc Chem Res, 2019, 52, 2559–2570.
[10] Kolb HC, Finn MG, Sharpless KB, Click chemistry: Diverse chemical function from a few good reactions, Angew Chem Int Ed, 2001, 40, 2004–2021.
[11] Nwe K, Brechbiel MW, Growing applications of “click chemistry” for bioconjugation in contemporary biomedical research, Cancer Biother Radiopharm, 2009, 24, 289–302.
[12] Moses JE, Moorhouse AD, The growing application of click chemistry, Chem Soc Rev, 2007, 36, 1249–1262.
[13] Rostovtsev VV, Green LG, Fokin VV, Sharpless KB, A stepwise huisgen cycloaddition process: Copper(I)-catalyzed regioselective “ligation” of azides and terminal alkynes, Angew Chem Int Ed, 2002, 41, 2596–2599.
[14] Liang L, Astruc D, The copper(I)-catalyzed alkyne-azide cycloaddition (CuAAC) “click” reaction and its applications. an overview, Coord Chem Rev, 2011, 255, 2933–2945.
[15] Zhao Y, Yu CYY, Kwok RTK, et al., Photostable AIE fluorogens for accurate and sensitive detection of S-phase DNA synthesis and cell proliferation, J Mater Chem B, 2015, 3, 4993–4996.
[16] Ferrell Jr. JE, Tsai T-C, Yang Q, Modeling the cell cycle: Why do certain circuits oscillate?, Cell, 2011, 144, 874–885.

[17] Enserink JM, Smolka MB, Zhou H, Kolodner RD, Checkpoint proteins control morphogenetic events during DNA replication stress in Saccharomyces cerevisiae, J Cell Biol, 2006, 175, 729–741.
[18] Maurer HR, Potential pitfalls of [3H]thymidine techniques to measure cell proliferation, Cell Prolif, 1981, 14, 111–120.
[19] Yuan Y, Xu S, Cheng X, Cai X, Liu B, Bioorthogonal turn-on probe based on aggregation-induced emission characteristics for cancer cell imaging and ablation, Angew Chem Int Ed, 2016, 55, 6457–6461.
[20] Langer R, Drug delivery and targeting, Nature, 1998, 392, 5–10.
[21] Khandare DG, Kumar V, Chattopadhyay A, Banerjee M, Chatterjee A, An aggregation-induced emission based "turn-on" fluorescent chemidisumeter for the selective detection of ascorbate ions, RSC Adv, 2013, 3, 16981–16985.
[22] Rose RC, Bode AM, Biology of free radical scavengers: An evaluation of ascorbate, FASEB J, 1993, 7, 1135–1142.
[23] Rodríguez-Nuévalos S, Parra M, Ceballos S, Gil S, Costero AM, A nitric oxide induced "click" reaction to trigger the aggregation induced emission (AIE) phenomena of a tetraphenyl ethylene derivative: A new fluorescent probe for NO, J Photochem Photobiol A Chem, 2020, 388, 112132.
[24] Moncada S, Palmer RMJ, Higgs EA, Nitric Oxide: Physiology, Pathophysiology, and Pharmacology, Pharmacol Rev, 1991, 43, 109–142.
[25] McGrowder D, Ragoobirsingh D, Brown P, Therapeutic uses of nitric oxide-donating drugs in the treatment of cardiovascular diseases, Int J Pharmacol, 2006, 2, 366–373.
[26] Sanji T, Nakamura M, Tanaka M, Fluorescence "turn-on" detection of Cu2+ ions with aggregation-induced emission-active tetraphenylethene based on click chemistry, Tetrahedron Lett, 2011, 52, 3283–3286.
[27] Gaggelli E, Kozlowski H, Valensin D, Valensin G, Copper homeostasis and neurodegenerative disorders (Alzheimer's, prion, and Parkinson's diseases and amyotrophic lateral sclerosis), Chem Rev, 2006, 106, 1995–2044.
[28] Agard NJ, Prescher JA, Bertozzi CR, A strain-promoted [3 + 2] azide-alkyne cycloaddition for covalent modification of biomolecules in living systems, J Am Chem Soc, 2004, 126, 15046–15047.
[29] Hu F, Mao D, Kenry, et al., A light-up probe with aggregation-induced emission for real-time bio-orthogonal tumor labeling and image-guided photodynamic therapy, Angew Chem Int Ed, 2018, 57, 10182–10186.
[30] Wu Y, Chen Z, Zhang P, et al., Recombinant-fully-human-antibody decorated highly-stable far-red AIEdots for in vivo HER-2 receptor-targeted imaging, Chem Commun, 2018, 54, 7314–7317.
[31] Li K, Liu B, Polymer-encapsulated organic nanoparticles for fluorescence and photoacoustic imaging, Chem Soc Rev, 2014, 43, 6570–6597.
[32] Ni JS, Zhang P, Jiang T, et al., Red/NIR-emissive benzo[d]imidazole-cored AIEgens: Facile molecular design for wavelength extending and in tumor metabolic imaging, Adv Mater, 2018, 30, 1805220.
[33] Mather BD, Viswanathan K, Miller KM, Long TE, Michael addition reactions in macromolecular design for emerging technologies, Prog Polym Sci, 2006, 31, 487–531.
[34] Nising CF, Bräse S, The oxa-Michael reaction: From recent developments to applications in natural product synthesis, Chem Soc Rev, 2008, 37, 1218–1228.
[35] Nair DP, Podgórski M, Chatani S, et al., The thiol-michael addition click reaction: A powerful and widely used tool in materials chemistry, Chem Mater, 2014, 26, 724–744.

[36] Hu X, Zhao X, He B, et al., A simple approach to bioconjugation at diverse levels: Metal-free click reactions of activated alkynes with native groups of biotargets without prefunctionalization, Research, 2018, 2018, 3152870.
[37] Herzenberg LA, De Rosa SC, Dubs JG, et al., Glutathione deficiency is associated with impaired survival in HIV disease, Proc Natl Acad Sci USA, 1997, 94, 1967–1972.
[38] Seshadri S, Beiser A, Selhub J, et al., Plasma homocysteine as a risk factor for dementia and Alzheimer's Disease, N Engl J Med, 2002, 346, 476–483.
[39] Townsend DM, Tew KD, Tapiero H, The importance of glutathione in human disease, Biomed Pharmacother, 2003, 57, 145–155.
[40] Liu Y, Yu Y, Lam JWY, et al., Simple biosensor with high selectivity and sensitivity: Thiol-specific biomolecular probing and intracellular imaging by AIE fluorogen on a TLC plate through a thiol-ene click mechanism, Chem Eur J, 2010, 16, 8433–8438.
[41] Chen MZ, Moily NS, Bridgford JL, et al., A thiol probe for measuring unfolded protein load and proteostasis in cells, Nat Commun, 2017, 8, 1–10.
[42] Wang M, Kaufman RJ, Protein misfolding in the endoplasmic reticulum as a conduit to human disease, Nature, 2016, 529, 326–335.
[43] Zhang S, Liu M, Tan LYF, et al., A maleimide-functionalized tetraphenylethene for measuring and imaging unfolded proteins in cells, Chem – An Asian J, 2019, 14, 904–909.
[44] Owying TC, Subedi P, Deng J, et al., A molecular chameleon for mapping subcellular polarity in an unfolded proteome environment, Angew Chem Int Ed, 2020, 59, 10129–10135.
[45] Carmel R, Jacobsen DW, Homocysteine in Health and Disease, Cambridge University Press, Cambridge, U.K, 2011.
[46] Chen S, Hong Y, Liu J, et al., Discrimination of homocysteine, cysteine and glutathione using an aggregation-induced-emission-active hemicyanine dye, J Mater Chem B, 2014, 2, 3919–3923.
[47] Zhao N, Gong Q, Zhang RX, et al., A fluorescent probe with aggregation-induced emission characteristics for distinguishing homocysteine over cysteine and glutathione, J Mater Chem C, 2015, 3, 8397–8402.
[48] Lou X, Hong Y, Chen S, et al., A selective glutathione probe based on AIE fluorogen and its application in enzymatic activity assay, Sci Rep, 2014, 4, 1–6.
[49] Mei J, Sun JZ, Qin A, Tang BZ, Comparative study of the dicyanovinyl-functionalized 1,1-dimethyl-2,3,4,5-tetraphenylsilole derivatives on their structures, properties, and applications in thiol detection, Dye Pigment, 2017, 141, 366–378.
[50] Cui L, Baek Y, Lee S, Kwon S, Kwon N, Yoon J, AIE and ESIPT based kinetic resolved fluorescent probe for biothiols, J Mater Chem C, 2016, 4, 2909–2914.
[51] Feng B, Liu Y, Huang S, et al., Highly selective discrimination of cysteine from glutathione and homo-cysteine with a novel AIE-ESIPT fluorescent probe, Sensor Actuat B-Chem, 2020, 325, 128786.
[52] Niu LY, Guan YS, Chen YZ, Wu LZ, Tung CH, Yang QZ, BODIPY-based ratiometric fluorescent sensor for highly selective detection of glutathione over cysteine and homocysteine, J Am Chem Soc, 2012, 134, 18928–18931.
[53] Staudinger H, Meyer J, Uber neue organische phosphorverbindungen III phosphinmethylenderivate und phosphinimine, Helv Chim Acta, 1919, 2, 635–646.
[54] Saxon E, Bertozzi CR, Cell surface engineering by a modified Staudinger reaction, Science, 2000, 287, 2007–2010.
[55] Bednarek C, Wehl I, Jung N, Schepers U, Bräse S, The staudinger ligation, Chem Rev, 2020, 120, 4301–4354.
[56] Köhn M, Breinbauer R, The staudinger ligation – a gift to chemical biology, Angew Chem Int Ed, 2004, 43, 3106–3116.

[57] Li C, Jiang G, Liu X, et al., An easily available ratiometric AIE probe for nitroxyl visualization: In vitro and in vivo, Mater Chem Front, 2021, 5, 1817–1823.
[58] Fukuto JM, Cisneros CJ, Kinkade RL, A comparison of the chemistry associated with the biological signaling and actions of nitroxyl (HNO) and nitric oxide (NO), J Inorg Biochem, 2013, 118, 201–208.
[59] DeMaster EG, Redfern B, Nagasawa HT, Mechanisms of inhibition of aldehyde dehydrogenase by nitroxyl, the active metabolite of the alcohol deterrent agent cyanamide, Biochem Pharmacol, 1998, 55, 2007–2015.
[60] Miranda KM, The chemistry of nitroxyl (HNO) and implications in biology, Coord Chem Rev, 2005, 249, 433–455.

Anh Tran Tam Pham, Youhong Tang

# Chapter 5
# Point-of-care in vitro diagnostics devices based on aggregation-induced emission biosensors: current situation and future prospective

## 5.1 In vitro diagnostic and point-of-care device development in health application

Over the last few decades, in vitro diagnostic (IVD) technologies have become powerful tools in diagnosing and monitoring diseases, providing prognosis, and predicting treatment response,, thanks to their convenient features, such as rapid results, increased patient comfort, simplicity, high portability, and cost-effectiveness [1, 2]. The testing targets of IVD methods are generally biological samples, comprising blood, sweat, saliva, skin tissues, and urine, which are diagnosed in a controlled environment, outside a living organism [1]. However, the traditional IVD tests are required to be performed in the laboratories with bulky and costly equipment, by professional staff. This requires the patients to visit the clinical facilities regularly, affecting their work routine, spending time for traveling and waiting for the test, as well as raising the cost to account for staff and facility's maintenance. Additionally, Mayeux (2004) reported that the possibility of infection, ethical responsibility, and longevity of samples are critical issues for the collection, transport, and storage of biological samples for the laboratory-conditioned measurements [3]. Recently, the rapid development of technological innovations in the electronics and bio-chemical fields has shifted the biomarker monitoring from traditional laboratory conditions to more user-friendly point-of-care (POC) devices [4]. The POC devices help users to carry out the measurements outside the laboratory, which not only reduces the demand of visiting the

**Acknowledgements:** We acknowledge the Australia-China Science and Research Fund, Joint Research Centre on Personal Health Technologies for financial support. We also thank Mr. Hao Fu, Ms. Xinyi Zhang, Mr. Clarence Chuah, Dr. Damian Tohl, and Dr. Angus Wallace for the initial discussions.

**Anh Tran Tam Pham,** Australia-China Joint Research Centre on Personal Health Technologies, Medical Device Research Institute, Flinders University, South Australia, 5042, Australia
**Youhong Tang,** Australia-China Joint Research Centre on Personal Health Technologies, Medical Device Research Institute, Flinders University, South Australia 5042, Australia,
e-mail: youhong.tang@flinders.edu.au

https://doi.org/10.1515/9783110672220-005

healthcare facilities regularly, but also minimizes the potential spread of infection amongst the crowd of diseased individuals [5]. The development of POC IVD devices will help improve the quality of people's healthcare activities.

## 5.2 POC IVD device based on optical methods for health application

According to the Australian Association of Clinical Biochemists, a POC device should satisfy certain requirements related to suitability for clinical purpose such as simple operation, connectivity between the user and the clinical teams, reliability, portability, rapid measurement, low cost, high feasibility, and an optimal approach for manufacturing [6]. Although numerous reports of the POC system developments in health application have been reported, there are a limited number of practical devices that can meet the above requirements. In fact, there are several factors affecting the feasibility of POC device development, including the biological samples' lifetime, the proper sample collection and preparation processes, the suitable electronics components for signal detection and analysis, and the signal's low detectable level of the analytes of interest [5]. The key factor that defines the feasibility of the POC IVD device development is the capability of the system in detecting and analyzing the signal related to the monitored biological analytes.

Thousands of POC devices have been reported and developed for health application in recent years, such as blood glucose meters, cholesterol tests, electrolyte analyzers, pregnancy tests, rapid test kits for infectious disease markers, and urinalysis test strips [7]. In most cases, the POC medical devices are designed following the biological analyte monitoring mechanism, as shown in Figure 5.1, in that, the target analytes react with the recognizing agents to produce an output signal, which can be an optical signal or an electrical signal. Then, a specific sensor collects that signal and sends it to a possessor component for analysis. From the analysis result, researchers obtain the signal's characteristics, comprising the brightness or intensity of the optical signal, or the voltage and current of the electrical signal. The output signal is claimed to have a certain relationship with the concentration of the target analytes in the testing samples. Hence, monitoring the level of the output signal helps researchers to monitor the concentration of the target of interest. Thus, establishing a portable disease monitoring device has the same meaning as developing a portable device that can monitor that output signal. From the explanation, the POC IVD device typically comprises of three major parts: (1) the consumables, (2) the hardware and (3) the software, as shown in Figure 5.2.

One of the most efficient methods to enhance the signal intensity in the measurement is optical evaluation. Amongst the POC devices, optical detection has become one of the most widely applied methods for identifying and monitoring biological

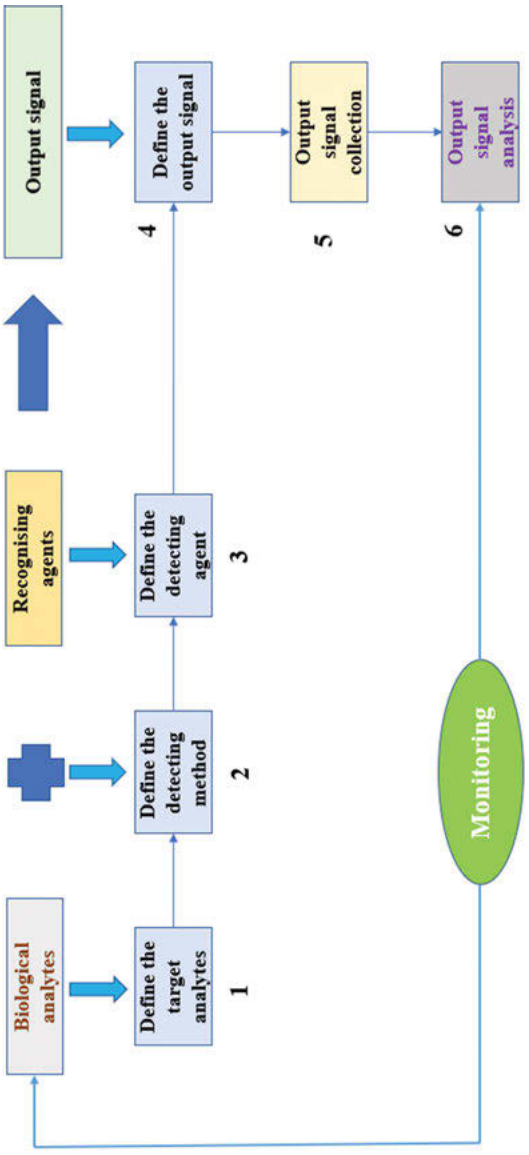


**Figure 5.1:** The flowchart for monitoring the biological analytes in body fluids in vitro. When the analyte (1) in body fluids reacts with the recognizing agents (3) following a specific method (2), the reaction produces an output signal that can be an optical signal or an electronical signal. By defining the type of the output signal (4), the suitable component to collect that signal (5) can be developed and the appropriate software to analyze its characteristics can be established (6). Finally, measuring the output signal helps researchers to monitor the level of the corresponding biomarkers in the biological sample in vitro.

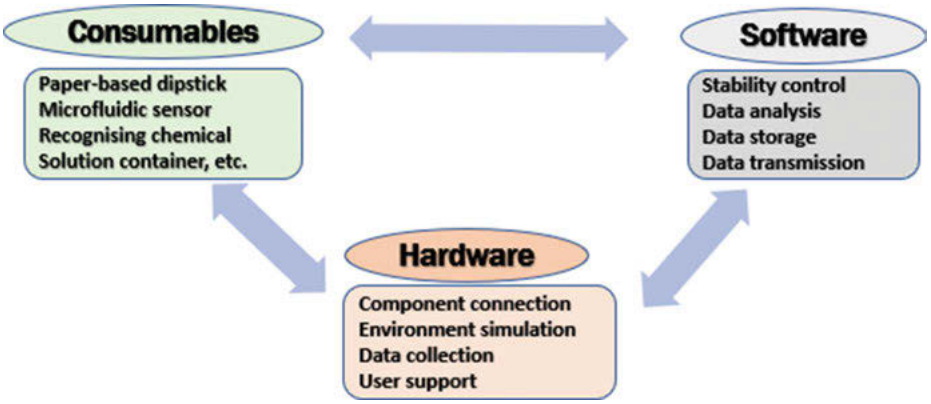


**Figure 5.2:** The general structure of a POC IVD device.

molecules in body fluids, in that, the highlighted optical measuring methods are (1) colorimetric: color changing of the final mixture, (2) chemiluminescent: a chemical reaction results in the mixture emitting photons; and (3) fluorescent/phosphorescent: activated molecules are excited by light of a specific wavelength to elevate from the normal energy levels to higher energy levels; when they return to their original energy levels, the excess energy is released in the form of photons, which creates the fluorescence [4–6, 8–17]. Their principles are based on the light response produced when the recognizing agents react with the specific analytes during the chemical or biochemical reactions. In comparison, although colorimetry measurement shows the highest portability, its sensitivity is inferior to those of the other two measurements. Thus, in this chapter, the POC IVD device development using fluorescence and chemiluminescence will be discussed. In most of the optical measurement designs, there are three parts, as shown in Figure 5.2, which cover the entire testing system, i.e., the chemical reaction environment, the luminescence observation area, and the data analyzing component. Device development is now presented in terms of three significant components: consumables, hardware, and software.

## 5.3 AIEgens and consumables development strategy in POC IVD devices

Firstly, the consumables include all components related to the chemical reaction between the analytes of interest and the recognizing reagents. They can be, but not limited to, the solution cuvettes, the detecting reagents, the sample containers, the paper-based test strip, the microfluidic sensor, or even the sterile wipes for the

chemical reaction-related components. In this component, the main target is the detecting agent, which is the first factor to define the feasibility of the portable device development and it relates to the signal intensity from the reaction between the agents and the target analytes. Innumerable reagents and methods have been researched in this field to enhance the optical response of the target analytes.

In the last two decades, aggregation-induced emission (AIE), the mechanism that can enhance the performance of biological analytes measurement in terms of high sensitivity, accuracy, large Stokes shift, excellent stability of fluorescence, and chemiluminescence evaluation, has been introduced and developed, as well as has drawn much attention from researchers in biomarker detection [18–21]. AIE bio-probes have been used in food safety, drug detection, treatment evaluation, therapy diagnosis, and disease monitoring, and have brought lots of benefits to healthcare research and applications, as shown in Table 5.1. However, although there are considerable number of reports of AIE biosensors for health application, further rigor in evaluation is required before they can be embedded with a POC IVD device. Hence, there are lots of opportunities for multidisciplinary researchers to develop AIE bio-probes embedded in POC IVD devices. From the above introduction, it can be seen that AIE bio-probes are majorly developed in the consumables section, which plays the role of creating a suitable case for chemical or biochemical reactions between the target analytes and the recognizing agents. The choice of consumable depends on the type of tests, which can either be a microfluidic paper-based test or a liquid-based test.

**Table 5.1:** Several reported AIEgens using fluorescence and chemiluminescence evaluations in health applications.

| Reference | AIE bio-probes | Medium | Analytes | Method | Achievements |
|---|---|---|---|---|---|
| [22] | BSPOTPE | Urine | Albumin | Fluorescence | LOD: 1 nM |
| [23] | TAE-Re(I) | Urine | Albumin | Fluorescence | LOD: 20 μM |
| [24] | TPE-4TA | Urine | Albumin | Fluorescence | LOD: 0.21 nM |
| [25] | Compound 1 | Saliva | Albumin | Fluorescence | Up to 80 mg/L |
| [26] | DIPIP-$Ag^+$ | Saliva | $SCN^-$ | Fluorescence | LOD: 7.8 nM |
| [27] | TPE-Tb | Aqueous sample | DPA | Fluorescence | LOD: 0.187 nM |
| [28] | APtN | Blood | $H_2O_2$ | Chemiluminescence | NA |
| [29] | SPN-NIR | Blood | $H_2O_2$ | Chemiluminescence | LOD: 8 nM |
| [30] | TCPO)-$H_2O_2$ | Water | $Hg^{2+}$ | Chemiluminescence | LOD: 3 ng/mL |

### 5.3.1 Paper-based assay protocols

The microfluidic paper-based strip was first invented by Martin and Synge in 1952, which was later developed and applied to chemical and biomedical analysis [4, 31]. Thanks to the paper strip's unique porous structure, created by pressing cellulosic or nitrocellulose fibers together in multiple layers, fluids can be transported from one point to the other end of the paper strip through capillary structures, without any requirement of external force. This transportation property can help the paper strip absorb and interact with the chosen fluids completely, which is a great advantage in chemical and biomedical analysis. Other enormous advantages are its simple usage, low-cost fabrication, high biocompatibility and biodegradation, and the nonrequirement of high-standard clinical facilities, proper infrastructure, and well-trained medical staff. This makes paper-based microfluidic platforms one of the best solutions for disease detection and monitoring in developing countries [31]. Nowadays, the technology for manufacturing paper-based microfluidic platforms has improved to be compatible with modern technologies for POC in vitro diagnostic applications, and most involve immunoassays, which utilize antibodies to track and detect the biomarkers of interest [32]. Although having been developed into different forms and applications, the paper-based microfluidic platform still follows the traditional principle of lateral flow, as shown in Figure 5.3 [31].

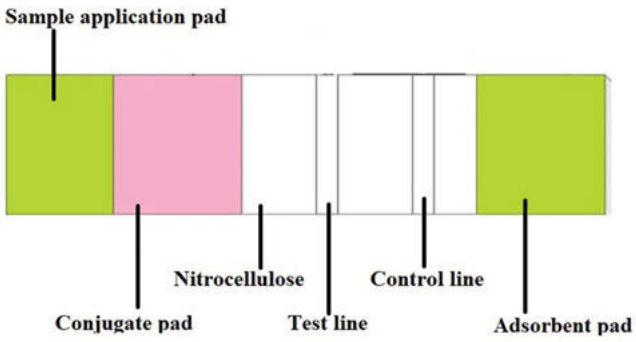


**Figure 5.3:** Traditional schematic diagram of the lateral flow assay [33].

There are two methods for observing the paper strip result, the sandwich and competitive strategies [32, 33]. Therefore, the principle of paper strip application in diagnosis involves chemical reactions between the biomarkers in the body fluid samples and the specific antibodies or antigens equipped in the cellulose or nitrocellulose membranes of the strip, leading to the fact that most of paper strip measurements follow optical detection methods [34]. In the following discussion, the application of paper-based assays with fluorescence and chemiluminescence in POC IVD device

development will be presented. Nowadays, paper strips are manufactured for commercial usage in clinical facilities with a standard design for common testing, such as monitoring the proteins or glucose in the urine, and pH and electrolytes in saliva and sweat samples. This results in a limitation on using commercial paper strips for detecting biological molecules in the research process, as different molecules require specific detection reagents, which may experience a decrease in their sensitivity, quality, and stability when assigned to the dry paper test strip. Therefore, researchers have developed microfluidic chips, which follow the capillary principle of the paper's porous structure and allow the chemical reaction in a solution state. This new development allows researchers to customize microfluidic paper-based chips to not only satisfy the requirement of their POC devices, but also ensure the performance of optical measurement.

For biomarker detection by the fluorescence method, an optical excitation source is needed. This stimulates the analyte/antigen or antibody complex to produce fluorescent light. Xie et al. [35] designed an AIE-based fluorescent test strip of OPD-TPE-Py-2CN to detect gaseous phosgene, an industrial chemical that can damage the pulmonary alveoli and lead to pulmonary edema, pulmonary emphysema, or death, as shown in Figure 5.4. When combined with phosgene, the AIE probe on the test strip can emit fluorescence and shift the color from blue to green when exposed to 365 nm UV light. This research approaches the limit of detection (LOD) of 1.87 ppm, much lower than the minimum allowed level for human health [35]. In 2020, [36] developed the filter paper loaded with AIEgen, i.e., $H^+$ $DQ_2$, to monitor the spoilage of seafood by detecting the biogenic amine vapors. The tested strip was excited by 365 nm UV light, and a 575 nm wavelength emission showed up in the presence of biogenic amine vapors in the salmon samples. This paper strip could detect 10 μM in 50 g of salmon sample. In 2021, Liu and co-workers reported a lateral flow immunoassay strip to detect Escherichia coli O157:H7 in food, which causes a dangerous foodborne pathogen [37]. The LOD of this test strip is $10^5$ CFU/mL.

In chemiluminescence detection, the paper-based microfluidic platform has also drawn significant attention from researchers in recent years. Not only do they achieve high sensitivity and selectivity as fluorescence methods, but chemiluminescence detection systems also do not require an excitation light source, which is indispensable in fluorescence methods. This reduces the size, power consumption, and the cost of the chemiluminescence devices [4, 38, 39]. Wang et al. [52] reported a lab-on-paper device, using sandwich chemiluminescence ELISA (CL-ELISA) and microfluidic paper-based analytical devices (μPADs) to detect α-fetoprotein (AFP), cancer antigen 125 (CA125), and carcinoembryonic antigen (CEA) in human serum. This measurement uses luminol-p-iodophenol-$H_2O_2$-HRP-CL as the substrate and shows a linear performance of 0.1–35.0 ng/mL for AFP, 0.5–80.0 U/mL for CA125, and 0.1–70.0 ng/mL for CA. The limits of detection were reported to be 0.06 ng/mL, 0.33 ng/mL, and 0.05 ng/mL for AFP, CA-125, and CEA, respectively [40]. Yang et al. [41] developed a gold nanocluster (AuNC) surface to enhance the chemiluminescence signal in

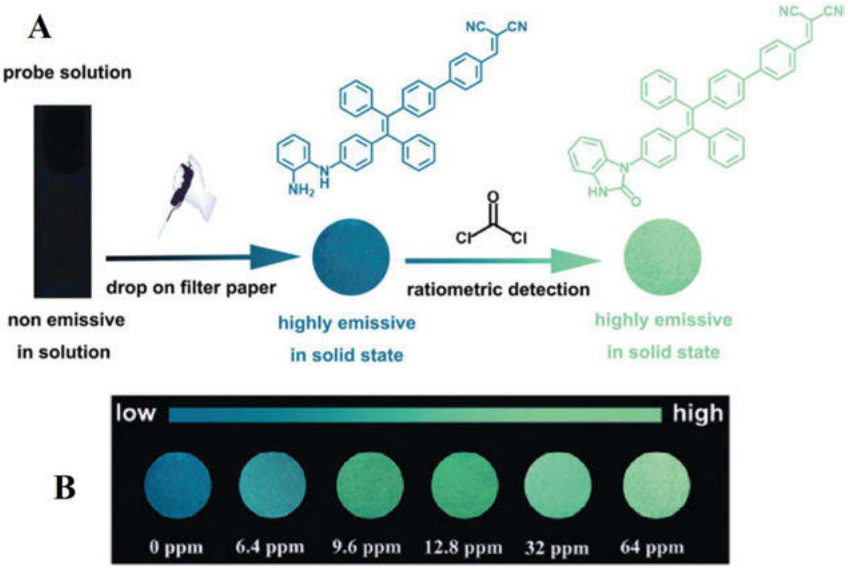


**Figure 5.4:** The custom microfluidic-based paper strip using AIE probe OPD-TPE-Py-2CN to detect gaseous phosgene; The pictures are taken when exposed to 365 nm UV. A) The schematic illustration of the custom test strip. The paper strip is embedded with the developed AIEgen OPD-TPE-Py-2CN. Without the presence of phosgene, the test strip stays nonfluorescent when excited by 365 nm UV. With the increase in phosgene's concentration, the fluorescence intensity rises dramatically. B) The variation in fluorescence intensity resulting from the OPD-TPE-Py-2CN loaded test strip when reacting with different phosgene concentrations [35].

staphylococcal enterotoxin B (SEB) detection to indicate foodborne disease. The luminescent signal is read by a cooled CCD sensor or a plate reader, and the sensitivity of this AuNCs sensor is reported to be 0.01 ng/mL [41].

From what has been mentioned above, the paper-based microfluidic platform has critically advanced in biomarker diagnostic research. The specifications of portability, low-cost fabrication, qualitative or semi-quantitative results, a simple test procedure, and long shelf-life characterize this dry-testing platform development along with the improvement of the POC IVD system, in recent years. However, there are some drawbacks in the paper-based platform, such as the uncontrolled sample volume consumption, sensitivity limit due to the restriction on testing volume, strict requirements in choosing the suitable antibodies and antigens to detect the biomarkers, the analyzing process's dependence on the nature of the sample, equipping the antibodies and antigens onto the paper surface, and the methods to ensure stability of the antibodies/antigens after being attached to the paper surface [4, 42]. These drawbacks mean that some biomarker detections are preferably processed in solution states of chemical and body fluid samples.

### 5.3.2 Liquid-based detections protocols

Although operating differently from the paper-based microfluidic platform, liquid-based biomarker detections also follow similar principles, in that, the obtained results come from reactions between the target biomarkers and the detecting agents. Some liquid-based biomarker detections are now presented for fluorescence and chemiluminescence methods for POC IVD systems. Akraa et al. [43] used a fluorescence-based AIE probe, BSPOTPE, to monitor HSA concentration in urine to indicate early signs of chronic kidney disease (CKD). A urine sample is mixed with BSPOTPE to produce the testing solution. If HSA is present in the urine sample, the solution can emit 480 nm fluorescence when excited by 340 nm UV, with the fluorescent intensity being proportional to the HSA concentration in the sample. Tu et al. [24] introduced the novel AIE probe, TPE-4TA, and used fluorescence evaluation to monitor albumin in the human urine sample. In the measurement, TPE-4TA is mixed with the urine sample and is examined when excited by 360 nm UV light. When there HAS is present, the solution will emit 480 nm fluorescence, with the fluorescent intensity being proportional to the HSA concentration in the sample. This AIEgen has LOD on HSA in urine of 0.21 nM, as shown in Figure 5.5 [24]. Recently, Su et al. presented the novel AIEgen, TPE-Tb, which can rapidly detect the pyridine-2,6-dicarboxylic acid (DPA), the anthrax spore biomarker, in aqueous solutions. This AIEgen can detect DPA level as low as 0.187 nM in aqueous samples [27]. Thus, the fluorescence-based AIEgens in solution state shows an excellent performance in detecting bio-analytes in body fluids.

For the chemiluminescence-based AIE bio-probe, in 2021 Hou and co-workers developed the first aggregation-induced chemiluminescence probe to measure the concentration of mercury $Hg^{2+}$ in a water source. The AIE probe works based on the chemiluminescence enhancement of bis(2,4,6- trichlorophenyl)oxalate (TCPO)-$H_2O_2$ system by aggregating the thiolate-protected gold complexes (Au(I)-thiolate complexes). This AIE probe shows a linear detecting range between 0.005 and 10 μgm/L and the LOD is 3 ng/mL [16].

In conclusion, the consumable is an essential and critical part for the POC IVD device development. It affects the mechanism of choosing the hardware and the software design. In particular, both technologies of the liquid-based test and the microfluidic paper-based assay have had a long development time and delivered numerous achievements in health applications. Considering the usage of these two techniques, the feasibility of practical POC IVD device development will increase in the future.

## 5.4 Hardware development strategy in POC IVD

The hardware part has two sub-components: the electronics and the solid support. The electronics component has several functions, including collecting the output

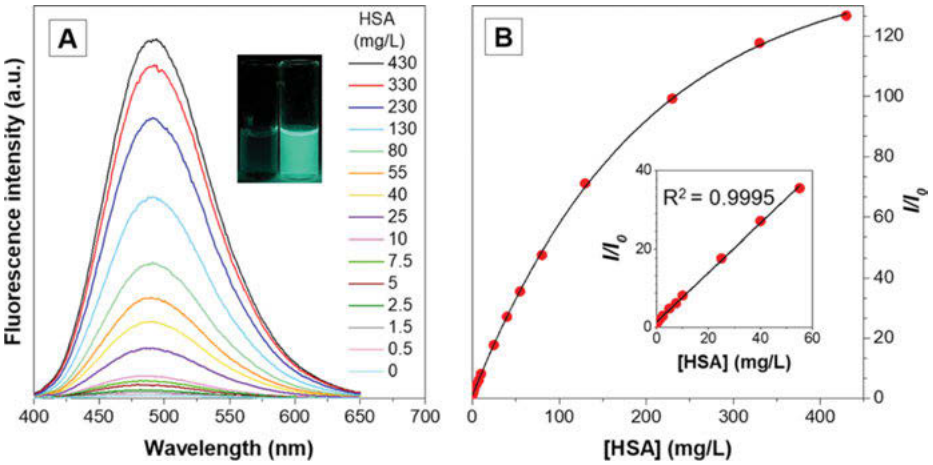


**Figure 5.5:** The fluorescent response of TPE-4TA to HSA in urine sample. A) The cuvette contains the mixture of urine sample and the AIEgen TPE-4TA. There is a critical difference in the mixture's luminescence under excitation conditions, in that, the solution without UV excitation, will stay nonemissive (left cuvette image) and turn fluorescent (right cuvette image) when exposed to 360 nm UV. The fluorescence intensity emitted from the mixture varies proportionally to the change in HSA concentration. B) The fluorescence intensity is proportional to HSA concentration in the range of 0–400 ng/mL [24].

signal, powering the device, as well as controlling the operation of the device. Whilst solid support is the key component that combines all different parts of the device together, protects the inner electronics and chemical reaction section, and specially, simulates the suitable testing environment for measurement. The general structure of the hardware consists of 3 key components: the solution and optical source container, the signal transferring room, and the signal collection section, arranged in the order, as shown in Figure 5.6.

From the sketched diagram above, the excitation light source generates light of a specific wavelength to excite the mixture of the recognizing reagent with the biological sample. If the target molecule is present in the sample, the mixture will emit a luminescent output signal. This output-light is transferred to the optical sensor through an isolated dark environment to prevent the noise of signal loss to the environment and the effect of external light from the outside area. Then, the optical sensor collects the output light for subsequent intensity analysis. When developing the hardware components for the optical POC devices, the objective is to achieve an efficient optical detection. From that purpose, some electronic components play essential roles in the hardware construction. Apart from having a high sensitivity and accuracy, these components are also required to have an effective cost and reasonable portability.

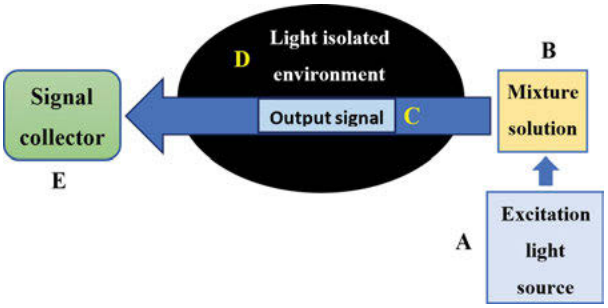


**Figure 5.6:** The hardware components of the optical POC IVD device. (A) and (B) The light source generates light of the specific wavelength to excite the mixture of recognizing reagent and biological sample in a controlled ratio. (C) If the target molecule is present in the sample, the mixture will emit fluorescence when exposed to the excitation light. (D) The light-isolated environment, i.e., a dark room-like section is a sealed room where the fluorescence transfers from the mixing solution to the imaging sensor. This minimizes the optical noise from the environment to the measurements. (E) The imaging component captures the fluorescent signal. This signal is analyzed for fluorescent intensity in the software component.

## 5.4.1 Excitation light source selection

The first component is the luminescence source, as it affects the entire system's operation. This component is also the typical difference between the fluorescence- and chemiluminescence-based devices. Fluorescence is a type of photoluminescence, the phenomenon where the molecules have the capability of glowing under certain conditions [39]. Fluorescence involves the electronic absorption of the molecules in a specific medium. In photoluminescence, molecules in a substance absorb photons of unique wavelengths and emit a longer wavelength photon in a critically short time [39, 44]. Hence, the fluorescence measuring devices require a light source with a suitable wavelength to stimulate the solution mixture. Whilst, the chemiluminescence measuring devices require no external excitation light source, the chemical or biochemical reactions produce the optical signal by themselves. This difference results in no requirement for light source design in the POC device that measures chemiluminescence. When developing the light source for the fluorescence device, there are three types of luminescence sources that could be considered: lamp, LED, and laser diode. The LED and laser diode have some similar characteristics and are more common for portable device development than the powered lamp. Depending on whether a scattered light or a strongly focused light beam is needed, LEDs or laser diodes, respectively, are employed. Table 5.2 shows the comparison of characteristics of the three types of light sources. Depending on the requirement of specific wavelength, stable intensity, or compact size, researchers will decide the proper component in order to satisfy not only the requirement of the IVD measurements, but the portable features of the POC devices.

**Table 5.2:** Comparison characteristics of LED, laser diode and lamp for luminescence source of portable device [45, 46].

| Light source | Size (mm) | Power required | Intensity | Light distribution | Popularity | Cost (AUD) | Electronic support |
|---|---|---|---|---|---|---|---|
| LED | ~ 5 | Low | Medium | Scattering | High | < 1 | Low, only power supply circuit required. |
| Laser diode | ~ 5 | Low | High | Focus beam | High | ~ 10 | Low, only power supply circuit required. |
| Lamp | ~ 10 | High | High | Scattering | Low | ~ 20 | High, require complex power supply circuit. |

## 5.4.2 Optical signal sensor selection

The choice of the optical signal sensor is also a significant factor defining the success of the POC device development. Recent years have witnessed a dramatic revolution of mobile technologies, with the introduction of smartphone as the essential personal equipment. Being equipped with a highly sensitive CMOS camera, many researchers have used the smartphone's camera in optical measuring devices, in that, the smartphone will be used to take the image of the optical signals. Aside the CMOS camera, CCD camera and photodiode are also potential options to measure the optical values from luminescence. A brief comparison among these optical sensors is presented in Table 5.3. Being similar to excitation light sources, the decision of the optical signal sensor depends on the requirement of the testing system in terms of signal sensitivity, power consumption, compact size, and affordability issues. Consequently, although some researchers use a CCD camera to have a better resolution in capturing optical images or apply a photodiode to evaluate the visual numeric data, the majority use smartphones integrated with a CMOS camera to support portable testing systems, helping to simplify the hardware design, as well as minimizing the device's cost.

## 5.4.3 Power supply system, calibration system and others

In addition, another factor contributing to a critical impact on the feasibility of the POC IVD device development is the power supply. Fluorescence detection requires a light source; so, the power supply should not be overlooked. Opinions vary about using an external power supply (adapter or battery assembly) or drawing energy from integrating the smartphone through an audio output jack or charging input plug. However, harvesting power from a smartphone to supply the luminescence source encounters obstacles: (1) it requires a complicated converter and an amplifier because the obtained

**Table 5.3:** Compare the pros and cons of CCD, CMOS cameras and photodiode.

| Camera | Data type | Resolution | Working Volt (V) | Popularity | Cost | Electronic support |
|---|---|---|---|---|---|---|
| CCD | Analog | High | 5–12 | Medium | High | High. Require electronic circuits to control the camera, regulate power supply, convert analogy-digital signal, etc. |
| CMOS | Digital | Medium | 3.3–5 | High | Medium | Low. Only power supply circuit required. |
| Photodiode | Analog | Low | ~ 1 | Low | Low | Medium. Require power supply circuit and the signal detecting circuit. |

current from the audio output jack or the charging input plug on the smartphone is significantly low and (2) the smartphone's USB charging port is specially manufactured with an integrated chip to protect the smartphone from overcharging damage; so, the power going through this port is limited. In fact, most developed portable devices use battery or outlet adapter to supply power for electronic components instead of drawing power from a smartphone's battery. Each solution has advantages and disadvantages, in that, the battery can efficiently satisfy the portable requirement, but its power reduces over time, which requires an indicator or a regulator component to manage the power supply from the battery. In contrast, the outer adapter has its own regulating component, which can guarantee stability of power supply to the device. However, the cons for using adapter are that it requires the power source and will affect the portability specification of the device. Depending on the requirements of the portable device, a suitable power supply can be considered. As well, most developed devices employ filters in the optical measurement process. In optical measurement, there are lots of confounding factors, such as effect of external light, light degradation of the luminescent source, reflecting or scattering of light inside the optical evaluating room, or noise from the chemical components themselves, which may add light of a different wavelength into the data collection. Using filters helps distinguish these noises from the preferred signal. This also reduces the complexity in designing the analyzing component, resulting in reduction of the device's size and cost.

Simultaneously, to ensure the precision of the testing system, quality control or calibration is an indispensable component for all developed portable devices. There are two opinions about the better method of operating calibration: (1) running periodic calibration and (2) running calibration in every sample test. For the latter method of embedding the calibration step into the device whenever users perform a single test, two results occur. i.e., one for the new test and one for the calibrated value. Both methods have advantages and disadvantages, and researchers select one according to the

requirement for the precision of the test or the design's simplicity. In this selection, consideration is given to the measurement results' liability, the device's portability, and cost. Although separated into three groups, each component has a reciprocal relationship with others. The harmonious association among these three components is a key determinant of success or failure in POC IVD development.

## 5.5 Software development strategy in POC IVD device

The software part analyzes the obtained signal to achieve the characteristics, which can be used to distinguish the various situations of measurement, such as the change in concentration of the analytes in the sample solution, the power shortage from the electronics components, or adding interference noise from the external environment.

### 5.5.1 Data analyzing

The analyzed target in fluorescence and chemiluminescence measurements are the change in output luminescence signal. There are two common methods for analyzing the output luminescent signal: (1) taking images of the luminescent signal, then analyzing the mean intensity values of the pixels in the images, or (2) using a photoelectric semiconductor device to convert the optical signal into electronic signal.

For the image processing method, Red – Green – Blue (RGB) analysis is the efficient technique that measures the RGB values of each pixel in the analyzed areas or the entire region of the image. With this method, researchers can observe the change in the luminescence intensity/color at the pixel level, which improves the sensitivity of the signal analysis. A camera is required to take the image of the output signal. In recent years, many researchers have used smartphones as a powerful assistant to take images of the output signal when designing portable medical analysis devices. With a high-resolution CMOS camera and a range of settings such as white balance, auto-focus, custom ISO value, as well as their efficient computing processor, high battery capacity and wired or wireless connections, such as Bluetooth, Wi-Fi, Internet, etc., smartphone-based medical devices have been upgraded to monitor human health conditions and to detect the micro signs of chemical or biological compounds [47]. For the optical-electronic converting method, an electronic component will convert the luminescent signal into a voltage value. According to the principle of photoelectric semiconductor device, the voltage value has a relationship with the luminescence arriving to the detector. By measuring voltage values, researchers can recalculate the intensity of the output signal. The common optical detector used in this method is the photodiode, which has several advantages in developing for the POC device, as shown in Table 5.3.

In both methods of signal analysis, with different options for the hardware component design, there are two typical strategies for making decision on software development, in that, the devices integrated with the processor, such as smartphones, will have the ability to run the analysis software themselves; whilst others are required to transfer the obtained signal to an external instrument for further analysis. If the output signal has a low detection range, or the noises require multiple steps to process, the optical detecting device will require the support from external devices for further processing. This external-device need is also a factor contributing to the feasibility of POC device development, where it increases the cost and the size of the developed device.

### 5.5.2 Others

When the processing signals are obtained from bio-molecule monitoring tests, researchers usually compare the obtained data with a standard to make calculations for the concentration value of the molecules in the samples. However, many chemicals, molecules, or specimens do not have standard data to refer to, leading to incorrect judgment of the results. There are several solutions for this issue, and the efficient one is using machine learning in data evaluation. Applying machine learning to data processing will help researchers to have a better overview of the bio-molecule measurements, as well as to establish a database as a premise for long-term research in the future.

## 5.6 Examples of AIEgen based POC IVD device systems to monitor biological analytes in body fluids

As mentioned in previous sections, although AIE bio-probes can enhance the optical response of the fluorescence and chemiluminescence measurements, there have been very few reports of POC IVD device development. However, those developments of the AIE biosensors offer numerous promising opportunities for researchers when developing the POC IVD devices. In this section, both portable AIE-relating and nonrelating devices in monitoring biological analytes in body fluids is presented to give the general view of the POC IVD device development presently.

### 5.6.1 POC IVD device systems with fluorescence methods

There are innumerable reports of AIEgen development without discussing the related devices. In 2017, Gabr and Pigge used an AIEgen to detect HSA in a urine sample [23]. The Re(I) tricarbonyl complex is prepared from bis (pyridyl)- and bis(quinolyl) tetraarylethylene (TAE) ligands, which are reported to enhance the fluorescent emission of the solution when combined with HSA. The final solution is excited by a 396 nm UV light and emits light blue fluorescence with a wavelength of 509 nm. This method is claimed to improve the LOD of HSA in urine sample to 20 μM. In the same year, [20] presented an assay using aggregation-induced emission (AIE)-active fluorophore (TPE-HPro) to detect L-Lactate oxidase (LOx) in an aqueous fluid. This assay is excited at 373 nm wavelength and yields a 570 nm green emission. The fluorescent signal stably lasts around 60 min, facilitating accurate measurement. The limitation of detection is reported to be as low as 5.5 μM. This research offers potential for applying AIE in tracking the L-Lactate presence in saliva and urine samples [20]. Also, in 2017, an AIE-based fluorescent test strip of OPD-TPE-Py-2CN was designed by Xie and co-workers to detect gaseous phosgene. Although having not displayed the design of the portable supporting device, researchers have introduced a nonlaboratory method for detecting gaseous phosgene [35]. In 2019, Yu and co-workers succeeded in preparing a portable test strip, embedded with the zinc-based metal-organic framework of pyromellitic acid (Zn-BTEC), which can detect chlortetracycline (CTC) at the low limit of 28 nM [48]. Meanwhile, [49] reviewed the components and clinical biomarkers in body fluids, such as blood, sweat, urine, and saliva, and the currently developed AIE bio-probes that can quantitatively detect disease-related biomarkers in these fluidic samples. The review also highlighted that several applications of AIE bio-probes, such as lateral-flow test strips and POC devices, are currently under development, and offer potential for improving the POC testing system by using the smartphone in data capture and data cloud storage.

Besides the studies on AIEgens without the related devices, there are also numerous reports of development of the POC devices working with AIE bio-probes to monitor biological molecules. There is a remarkable point, in that, not all, but most reported POC device development use smartphones as the supporting hardware component. In 2018, Akraa and co-workers reported the uTester, a smartphone-based prototype using a commercially available AIEgen, BSPOTPE, to detect HSA in urine sample. Preliminary evaluation of the device, combing with the AIEgen, has confirmed the effectiveness of the proposed solution and the viability of such a smartphone-based device for people who have already developed or are prone to CKD. The POC device is expected to support users to regularly perform urine test to self-monitor their own health conditions, without the demand for frequent visits to their clinical staff. Those results are as shown in Figure 5.7 [43]. In 2020, Huang and co-workers developed a coffee ring test kit using AIE bioprobe of TPE-TS@Eu/GMP ICPs to detect dipicolinic acid (DPA), a biomarker for Bacillus anthracis (B. anthracis) spores, which causes anthrax, after germination.

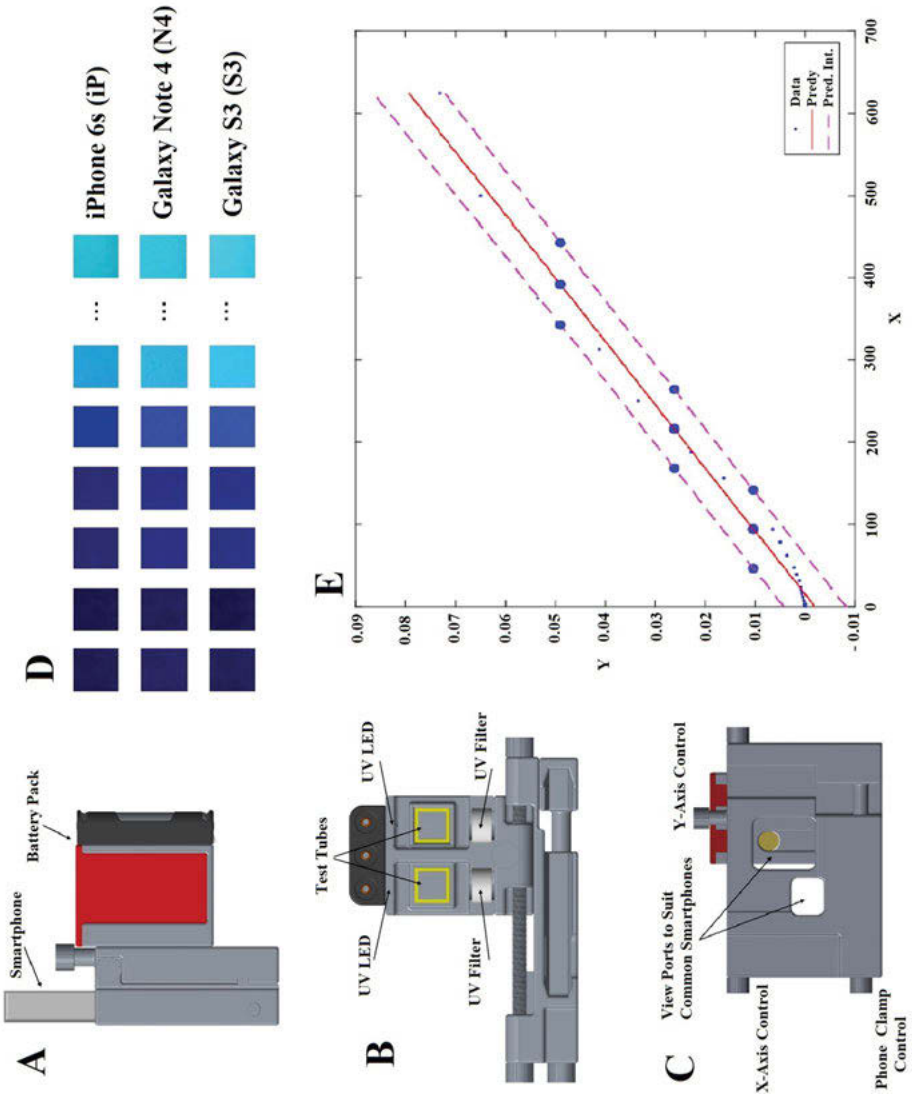


**Figure 5.7:** A) external and B) internal design of an imaging housing attached to a smartphone and C) adjustable viewports and clamp controls for the AIEgen-based 3D printing device. D) Images of different HSA concentration levels taken by 3 smartphones after the AIEgen, BSPOTPE, been added. E) Linear prediction model with internals with the x-axis of HSA concentration and the y-axis of light intensity of the AIEgen probe after combining with HSA [43].

A smartphone is used to take fluorescent images of the coffee ring when excited by a 405 nm UV lamp. Image processing focuses on analyzing the color pixel in blue channel (430–500 nm) and in the red channel (580–650 nm). On a smartphone, the software, Image J, analyzes the red and blue values and then generates the ratio between the red and blue values ($I_{Red}/I_{Blue}$). When the DPA level increases, the blue area on the coffee ring will extract, leading to a weakening of the blue signal. Meanwhile, the red area on the coffee ring expands and makes the red color brighter. Following this methodology, evaluating the red/blue ratio will give a quantitative result of the DPA level in the biological sample. The detection limit of this coffee ring sensor is claimed to be 27 nM [50]. In the same year, Ramasubramanian's group presented a novel AIE probe, the anthracene-conjugated imidazo[1,5-a]pyridine (TL19), and a three-dimension (3D) printed prototype that can track copper ($Cu^{2+}$) present in an aqueous medium. This prototype supports an android smartphone to take fluorescent images of the reaction between $Cu^{2+}$ and TL19. Then, the software, DAS-6, installed on the smartphone will analyze the RGB values to give a result of the $Cu^{2+}$ presence in the sample, with an LOD of 9 pM [51]. Chen et al. [52] initially developed a fluorescent paper analytical device (FPAD), using nanoparticles (PTDNPs-0.10) and two-dimension $MnO_2$ nanoflakes (2DMnNFs) to monitor the existence of organophosphorus pesticides (OPs). This device uses a smartphone to capture the variation of the fluorescent intensity, and a color recognizer will analyze the RGB values to give indication of the OP levels. This device can approach an LOD of 0.73 ng/mL [52].

POC IVD devices using a fluorescence method to detect biomarkers in body fluids are shown in Table 5.4. In summary, most developed devices using the fluorescence method in biomarker detection have a similar mechanism, in that, they use light of a specific wavelength to excite the mixed solution. To support the chemical reaction, prominent researchers prefer using a microfluidic paper-based assay to reduce the device's size and to broaden the observed section, where the fluorescent intensity or color change, which supports the image capturing process. The image processing mainly works on the analysis of the RGB values. A critical aspect of the portable device design is the solid support component that carries the entire system and secures the positions of every component, as well as provides a suitable environment for running measurements. Finally, alongside the development of digital and computing systems, the POC system is constantly being upgraded to integrate the analyzing software into portable devices, which reduces the testing time as well as improves the quality of the biomarker measurement.

## 5.6.2 POC IVD device systems with chemiluminescence methods

In chemiluminescence detection, testing devices do not require light source for excitation of the luminescent properties. This helps simplify the design and structure of such portable devices. Quimbar et al. [51] developed a smartphone-based dark

**Table 5.4:** Portable devices using the fluorescence method to detect biomarkers in body fluids.

| Ref | Target of interest | Consumable | Hardware | | | | Software | Result |
|---|---|---|---|---|---|---|---|---|
| | | | Supporting processor | $\lambda_{Exc}$ [nm] | $\lambda_{Ems}$ [nm] | Signal detector | | |
| [53] | NA. | Solution test | Smartphone (Nokia 1020). | 465 | Depending on the conjugated reagent. | Smartphone (CMOS camera). | Computer (Commercial app). | LOD: 80 fluorophores/ diffraction-limited spot. |
| [54] | Chloride in sweat | Solution test. | Smartphone [HTC One M9]. | 365 | 441 | Smartphone camera. | NA. | LOD: 0.8 nM of chloride in sweat. |
| [54] | Malaria, HIV and tuberculosis (TB) in whole blood. | Commercial paper test strips for each disease. | Smartphone (Samsung Galaxy SII) | 565 | Depending on the disease detections (NA) | Smartphone (CMOS camera) | Smartphone (Custom app) | Correctly qualitatively detect the infected patients. |
| [56] | Albumin in urine | Solution test. | Smartphone (Samsung Galaxy SII) | 532 | NA | Smartphone (CMOS camera). | Smartphone (Custom app) | LOD: 5–10 µg/mL |
| [57] | Chloride, sodium and zinc concentrations in sweat. | Custom test strip. | Smartphone (iPhone 6 Plus). | 451 | 511 nm for chloride. 515 nm for sodium. 519 nm for zinc. | Smartphone camera. | Smartphone (Custom app) | LOD: 28 mM for chloride; 36 mM for sodium; and 3.6 µM for zinc. |
| [43] | Albumin concentration in urine | Solution test. | Smartphone (iPhone 6s, Samsung Galaxy Note 4, and Galaxy S3]. | 340 | ~ 480 | Smartphone (CMOS camera). | Smartphone (Custom app) | Quantitatively detect albumin in urine |

(continued)

**Table 5.4** (continued)

| Ref | Target of interest | Consumable | Hardware | | | | Software | Result |
|---|---|---|---|---|---|---|---|---|
| | | | Supporting processor | $\lambda_{Exc}$ [nm] | $\lambda_{Ems}$ [nm] | Signal detector | | |
| [58] | E. coli K12 in urine. | Custom microfluidic chip. | Smartphone (iPhone 6S). | NA. | NA. | Smartphone (CMOS camera). | Smartphone (Custom app). | LOD: 240 CFU/mL for E. coli K12 in urine. |
| [59] | Human chorionic gonadotropin in urine. | Custom paper test strip. | Smartphone (iPhone 5S). | NA. | NA. | Smartphone (CMOS camera). | Smartphone (Custom app). | LOD: 45 pg/mL for hCG |
| [50] | Dipicolinic acid from Bacillus anthracis spores | Custom AIEgen-based paper coffee ring. | Smartphone | 405 | Blue (430–500 nm). Red (580–650 nm) | Smartphone (CMOS camera). | Smartphone (Image J). | LOD: 27 nM for DPA. |
| [60] | $Cu^{2+}$ in aqueous sample | Solution test | Raspberry Pi-ARM V11 | 365 | 510 | Raspberry Pi camera 5MP | Software DAS-6 from IBH to analyze RBG. | LOD: 9 pM of $Cu^{2+}$ ion. |

box, using a diagnostic platform, to monitor airway hydrogen peroxide ($H_2O_2$] using chemiluminescence. A 75 µL of exhaled breath condensate sample is added into 375 µL solution of 3.4 mM BPEA, 3.2 mM imidazole, and 1.9 mM CCPO in 9: 1 EtOAc: $CH_3CN$ to yield a 500 nm chemiluminescent emission. The luminescent picture is captured by the phone's built-in CMOS camera and a customized app on the phone runs intensity pixel analysis and then indicates the concentration of $H_2O_2$ in the sample. The dark box is $5 \times 7.5 \times 5.5$ inches and is attached to the smartphone case to secure the positioning of the camera and the 96-well plate located inside the box. The LOD of this platform is 264 nM of $H_2O_2$ in human-exhaled breath condensates [60]. Not all developed smartphone-based biomarker detecting devices can analyze the obtained signal themselves; some need an external device. Kim et al. [61] designed a 3D-printing holder to secure the positioning between a smartphone and a solution tube for chemiluminescent imaging in the quantitative measurement of the reporter bacteria OD600. The 490 nm luminescent images were captured by the smartphone's camera and then wirelessly transferred to the external PC for analysis by MATLAB. Kim and co-authors compared the performance of different brands, such as iPhone 5S, Samsung Galaxy S4, Samsung Galaxy Note 3, Oneplus One, and LG G2, finding that the measurement using Oneplus One showed the best the limit of detection of $7.9 \times 10^6$ CFU/mL. Table 5.5 shows some research using chemiluminescence detection with the developed portable biomarker detection devices [61].

## 5.7 Discussion and future prospective

The rapid development of mobile technology has promoted its application in human health monitoring in modern society. Although optical methods for biomarker detections have varied greatly over the last decade, applying the powerful processing of smartphones has brought numerous advantages in detecting disease markers in body fluids. Such detection gives early indications of critical diseases and informs the modification to suit different stages of treatment. Smartphone usage for this purpose satisfies the requirements of POC healthcare device design, such as simple usage, rapid result analysis, accessible communication between patients and healthcare staff, and high reliability. However, drawbacks still exist in designing the consumables and choosing the computing processor, which require further consideration. Firstly, the choice of a paper-based testing platform or fluidic-based testing platform depends on the compatible biomarker-detecting probes and the measurement conditions. The paper-based microfluid platform has undoubted advantages in biomarker diagnostics in terms of high portability, qualitative or semi-quantitative results, simple test procedure, and long shelf life in suitable storage conditions. Nevertheless, its limitations are also significant. The uncontrolled sample volume absorption and nonuniform chemical distribution on the paper surface results in low sensitivity. The strict requirements

**Table 5.5:** Portable devices using chemiluminescence method to detect biomarkers in body fluids.

| Ref | Target of interest | Consumable | Hardware | | | Data analyzer | Result |
|---|---|---|---|---|---|---|---|
| | | | Supporting processor | $\lambda_{Ems}$ [nm] | Signal detector | | |
| [61] | Reporter bacteria OD600 | Solution | Smartphone (OPO OnePlus One) | 490 | Smartphone (CMOS camera). | Computer (MATLAB) | LOD: $7.9 \times 10^6$ CFU/mL |
| [60] | Airway hydrogen peroxide in exhaled breath condensates. | Solution. | Smartphone (iPhone 6]. | 500 | Smartphone (CMOS camera). | Smartphone (Custom app) | LOD: 264 nM of $H_2O_2$ in human exhaled breath condensates. |
| [62] | Total bile acids and total cholesterol in serum. | Solution. | Smartphone (iPhone 5S). | NA. | Smartphone (CMOS camera). | Smartphone (Commercial app). | LOD: 0.5 µmol/L for total bile acids and 20 mg/dL for total cholesterol in serum. |
| [63] | Salivary cortisol. | Paper test strip. | Smartphone (NA smartphone's brand). | NA. | Smartphone (CMOS camera). | Smartphone (Custom app). | LOD: 0.3 ng/mL. |
| [64] | Prostate specific antigen in serum. | Custom microfluidic solution chip. | Smartphone (NA smartphone's brand). | NA. | Smartphone camera. | Smartphone (Custom app). | LOD: 0.1 ng/mL. |

for suitable capturing agents for biomarkers lead to a limitation in the detection of some disease types. The integration of biological molecule-detecting agents onto the paper surface presents some hurdles for paper-based testing platform fabrication. In contrast, the fluidic-based measurements may overcome the drawbacks of biomolecules detection in paper-based testing methods. However, liquid-based testing encounters trouble in dealing with the solution's stability, depending on the environment and time of storage. It is easily cross-contaminated and requires a training process for chemical preparation. Besides, the synthesis of the proper AIE bio-probes also encounters issues, in that, the techniques for synthesizing AIEgen require trained-skilled staff and a laboratory condition for operation. However, holding the outstanding features of being selective to specific analytes, high sensitivity, and low-resource cost for measurement, AIE biosensors promise potential for further development and embedding into POC IVD devices.

Secondly, although smartphones benefit the POC system design with a high-resolution camera, excellent mobility, powerful computing processor, and they are being improved along with the development of modern society, numerous drawbacks exist. The smartphone's built-in cameras used for capturing the optical signal yielded from chemical reactions have their setting functions, such as auto-focus, auto-white balance, auto-ISO, and auto-filter, which support the users' daily activities, but affect the optical result in chemical testing for biomarker detection. Some researchers prevented these manufacturer's functions from affecting results by turning off the auto-functions of the camera, or choosing the specific settings for running the test, or using a commercial or customized app to control the camera settings. This issue has led to not all brands of smartphones being used for biomarker detection systems. With android phones, users can interfere with the camera's customized system. Also, due to the wide range of optical bio-signals, some smartphones cannot be integrated with the analyzing software to process the obtained data. The evidence is that in many studies, smartphones only collect the optical signal and then transfer them to an external computing system for analysis. This results in the whole design becoming bulky and complicated to manufacture. The rapid role of technological development forces smartphones to be upgraded in terms of integrating more imaging functions, changing the imaging processor, expanding the phone's dimensions, raising their price, as well as replacing previous smartphone generations. These changes also contribute to the burden on the research and application of smartphones for mobile medical surveillance systems.

To deal with the obstacles mentioned above, some solutions have been applied for developing portable biomarker detectors. First, the cost-effective manufacturing technology of 3D printing shows the potential to reduce fabrication costs in prototyping the devices. Widespread use of 3D printing in the market has helped this fabricating method become more feasible for users and researchers. Besides, its high flexibility allows researchers to take the most benefit from the combination of other technologies, such as the smartphone, CCD camera, UV light source, or customized

microfluidic paper-based platform test strip. Secondly, for data analysis, currently, researchers have applied machine learning to data collection steps, as well as used digital cloud to store the obtained data. This not only helps with data processing of projects in operation, but also establishes a database as a premise for long-term research in the future. Thirdly, soft polymer, gels, and hydrogels dominate modern biomaterials and have gained attention from researchers for decades. These technologies can also be used as chemical carriers that can store the detecting reagents to increase their shelf life, or create a controlled environment for chemical reactions, as well as ensuring the stability of these chemicals. Although challenges still exist in designing POC medical devices and further research is needed, portable biomarker detectors have a promising future, in that, we can significantly improve our health monitoring standards.

## 5.8 Conclusion

In conclusion, the development of AIE bio-probes and POC IVD devices for detecting and monitoring biological analytes has been rapidly growing in recent years. Although still experiencing drawbacks, the contribution of mobile technologies in POC system design has a limitless potential for further development. Researchers can take advantage of the evolution of modern technology and novel bioprobes, such as AIEgens to improve the standards of POC IVD devices. Furthermore, designing portable biomarker detection devices, which minimizes the burden of needing high standard medical testing instruments for the same purpose in hospitals, helps open access to swift diagnosis for patients in rural areas or those with limited time and resources to visit clinical facilities for routine health checks.

**Conflicts of interest:** There are no conflicts to declare.

## References

[1] Li C zhong, Special topic: Point-of-Care Testing (POCT) and in vitro diagnostics (IVDs), J Anal Test, 2019, 3, 1–2, https://doi.org/10.1007/s41664-019-00095-y.

[2] Rohr UP, Binder C, Dieterle T, Giusti F, Messina CGM, Toerien E, Moch H, Hendrikschäfer H, The value of in vitro diagnostic testing in medical practice: A status report, PLoS One, 2016, 11, 1–16, https://doi.org/10.1371/journal.pone.0149856.

[3] Mayeux, R. Biomarkers: Potential Uses and Limitations. NeuroRx 2004, 1, 182-188, doi:10.1602/neurorx.1.2.182.

[4] Sanjay, S.T.; Fu, G.; Dou, M.; Xu, F.; Liu, R.; Qi, H.; Li, X. Biomarker detection for disease diagnosis using cost-effective microfluidic platforms. The Analyst 2015, 140, 7062–7081, doi:10.1039/c5an00780a.

[5] Senf B, Yeo WH, Kim JH, Recent Advances in Portable Biosensors for Biomarker Detection in Body Fluids, Biosensors, 2020, 10, https://doi.org/10.3390/BIOS10090127.
[6] Tirimacco, R.; St. John, A.; Astill, K.; Weinholt, L.; Merrilees, P. Point of Care Testing Implementation Guide. 2019.
[7] MHRA, Management and use of IVD point of care test devices, Med Healthc Prod Regul Agency, 2021, 1(2).
[8] Dincer C, Bruch R, Kling A, Dittrich S, Urban GA, Multiplexed point-of-care testing – XPOCT, Trends Biotechnol, 2017, 35, 728–742, https://doi.org/10.1016/j.tibtech.2017.03.013.
[9] Gao Z, Xu M, Lu M, Chen G, Tang D, Urchin-like (gold core)@(platinum shell) nanohybrids: A highly efficient peroxidase-mimetic system for in situ amplified colorimetric immunoassay, Biosens Bioelectron, 2015, 70, 194–201, https://doi.org/10.1016/j.bios.2015.03.039.
[10] John AS, P Price C, Existing and emerging technologies for point-of-care testing, Clin Biochem Rev, 2014, 35, 155–167.
[11] Li J, Li S, Yang F, Electrochemical Biosensors for Cancer Biomarker Detection, 2012, 2213–2229. https://doi.org/10.1002/elan.201200447.
[12] Liu Y, Deng C, Tang L, Qin A, Hu R, Sun JZ, Tang BZ, Specific detection of D-glucose by a tetraphenylethene-based fluorescent sensor, J Am Chem Soc, 2011, 133, 660–663, https://doi.org/10.1021/ja107086y.
[13] Mejía-Salazar JR, Cruz KR, Vásques EMM, De Oliveira ON, Microfluidic point-of-care devices: New trends and future prospects for ehealth diagnostics, Sensors (Switzerland), 2020, 20, 1–19, https://doi.org/10.3390/s20071951.
[14] Nimse SB, Sonawane MD, Song KS, Kim T, Biomarker detection technologies and future directions, Analyst, 2016, 141, 740–755, https://doi.org/10.1039/c5an01790d.
[15] Omidfar K, Ahmadi A, Syedmoradi L, Khoshfetrat SM, Larijani B, Point-of-care biosensors in medicine: A brief overview of our achievements in this field based on the conducted research in EMRI (endocrinology and metabolism research Institute of Tehran University of medical sciences) over the past fourteen years, Diabetes Metab Disord, 2020, https://doi.org/10.1007/s40200-020-00668-0.
[16] Tagit O, Hildebrandt N, Fluorescence Sensing of Circulating Diagnostic Biomarkers Using Molecular Probes and Nanoparticles, ACS Sens, 2017, 2, 31–45, https://doi.org/10.1021/acssensors.6b00625.
[17] Wang, H.; Da, L.; Yang, L.; Chu, S.; Yang, F.; Yu, S.; Jiang, C. Colorimetric fluorescent paper strip with smartphone platform for quantitative detection of cadmium ions in real samples. Journal of Hazardous Materials 2020, 392, 122506, doi:10.1016/j.jhazmat.2020.122506.
[18] Halder S, Samanta S, Das G, Exploring the potential of a urea derivative: An AIE-luminogen and its interaction with human serum albumin in aqueous medium, Analyst, 2019, 144, 2696–2703, https://doi.org/10.1039/c9an00102f.
[19] Luo J, Xie Z, Xie Z, Lam JWY, Cheng L, Chen H, Qiu C, Kwok HS, Zhan X, Liu Y, Zhu D, Tang BZ, Aggregation-induced emission of 1-methyl-1,2,3,4,5-pentaphenylsilole, Chem Commun, 2001, 18, 1740–1741, https://doi.org/10.1039/b105159h.
[20] Zhang Z, Kwok RTK, Yu Y, Tang BZ, Ng KM, Sensitive and specific detection of l -lactate using an AIE-active fluorophore, ACS Appl Mater Interfaces, 2017b, 9, 38153–38158, https://doi.org/10.1021/acsami.7b10178.
[21] Zhu C, Kwok RTK, Lam JWY, Tang BZ, Aggregation-induced emission: A trailblazing journey to the field of biomedicine, ACS Appl Bio Mater, 2018, 1, 1768–1786, https://doi.org/10.1021/acsabm.8b00600.
[22] Hong Y, Feng C, Yu Y, Liu J, Wing J, Lam Y, Luo KQ, Tang BZ, Quantitation, visualization, and monitoring of conformational transitions of human serum albumin by a tetraphenylethene derivative with aggregation-induced emission characteristics, 2010, 82, 7035–7043.

[23] Gabr MT, Pigge FC, Rhenium tricarbonyl complexes of AIE active tetraarylethylene ligands: Tuning luminescence properties and HSA-specific binding, Dalt Trans, 2017, 46, 15040–15047, https://doi.org/10.1039/c7dt03380j.
[24] Tu Y, Yu Y, Zhou Z, Xie S, Yao B, Guan S, Situ B, Liu Y, Kwok RTK, Lam JWY, Chen S, Huang X, Zeng Z, Tang BZ, Specific and Quantitative Detection of Albumin in Biological Fluids by Tetrazolate-Functionalized Water-Soluble AIEgens, 2019.https://doi.org/10.1021/acsami.9b10359.
[25] Dey N, Maji B, Bhattacharya S, Motion-induced changes in emission as an effective strategy for the ratiometric probing of human serum albumin and trypsin in biological fluids.pdf, Chem Asian, 2018, 664–671, https://doi.org/10.1002/asia.201701795.
[26] Bu F, Zhao B, Kan W, Wang L, Song B, Wang J, Zhang Z, Deng Q, Yin G, A phenanthro[9,10-d] imidazole-based AIE active fluorescence probe for sequential detection of Ag+-AgNPs and SCN– in water and saliva samples and its application in living cells pdf, Mol Biomol Spectrosc, 2019, 223, 1386–1425, https://doi.org/10.1016/j.saa.2019.117333.
[27] Su P, Liang L, Wang T, Zhou P, Cao J, Liu WS, Tang Y, AIE-based Tb3+ complex self-assembled nanoprobe for ratiometric fluorescence detection of anthrax spore biomarker in water solution and actual spore samples, Chem Eng J, 2021, 413, 127408, https://doi.org/10.1016/j.cej.2020.127408.
[28] Yang M, Huang J, Fan J, Du J, Pu K, Peng X, Chemiluminescence for bioimaging and therapeutics: Recent advances and challenges, Chem Soc Rev, 2020, 49, 6800–6815, https://doi.org/10.1039/d0cs00348d.
[29] Zhen X, Zhang C, Xie C, Miao Q, Lim KL, Pu K, Intraparticle energy level alignment of semiconducting polymer nanoparticles to amplify chemiluminescence for ultrasensitive in vivo imaging of reactive oxygen species, Nano, 2016, https://doi.org/10.1021/acsnano.6b02908.
[30] Hou Y, Chen Y, Guo X, Liu W, Zhang L, Lv C, Xu Y, Jin Y, Li B, Aggregation-induced chemiluminescence system for sensitive detection of mercury ions, 2021, 625–633.
[31] Shah P, Zhu X, Li CZ, Development of paper-based analytical kit for point-of-care testing, Expert Rev Mol Diagn, 2013, 13, 83–91, https://doi.org/10.1586/erm.12.130.
[32] Hristov DR, Rodriguez-Quijada C, Gomez-Marquez J, Hamad-Schifferli K, Designing paperbased immunoassays for biomedical applications, Sensors (Switzerland), 2019, 19, https://doi.org/10.3390/s19030554.
[33] Sajid M, Kawde AN, Daud M, Designs, formats and applications of lateral flow assay: A literature review, J Saudi Chem Soc, 2015, 19, 689–705, https://doi.org/10.1016/j.jscs.2014.09.001.
[34] Byrnes S, Thiessen G, Fu E, Progress in the development of paper-based diagnostics for lowresource point-of-care settings, Bioanalysis, 2013, 5, 2821–2836, https://doi.org/10.4155/bio.13.243.
[35] Xie H, Wu Y, Zeng F, Chen J, Wu S, An AIE-based fluorescent test strip for the portable detection of gaseous phosgene, Chem Commun, 2017, 53, 9813–9816, https://doi.org/10.1039/c7cc05313d.
[36] Jiang Y, Zhong Z, Ou W, Shi H, Alam P, Semi-quantitative evaluation of seafood spoilage using filter-paper strips loaded with an aggregation-induced emission luminogen, Food Chem, 2020, 327, 127056, https://doi.org/10.1016/j.foodchem.2020.127056.
[37] Liu C, Fang S, Tian Y, Wu Y, Wu M, Wang Z, Xu D, Hou D, Liu Q, An Aggregation-Induced Emission Material Labeling Antigen-Based Lateral Flow Immunoassay Strip for Rapid Detection of Escherichia coli O157: H7, 2021. https://doi.org/10.1177/2472630320981935.
[38] Obodovskiy I, Chapter 12 – Luminescence, in: Radiation, 2019, 207–220. https://doi.org/10.1016/b978-0-444-63979-0.00012-4.

[39] Pohl H, What is the difference between fluorescence, phosphorescence and luminescence? [WWW Document], 2019. URL https://www.enzolifesciences.com/science-center/technotes/2019/december/what-is-the-difference-between-fluorescence-phosphorescence-andluminescence?/ (accessed 8. 9.20).
[40] Wang S, Ge L, Song X, Yu J, Ge S, Huang J, Zeng F, Paper-based chemiluminescence ELISA: Lab-on-paper based on chitosan modified paper device and wax-screen-printing, Biosens Bioelectron, 2012, 31, 212–218, https://doi.org/10.1016/j.bios.2011.10.019.
[41] Yang M, Kostov Y, Bruck HA, Rasooly A, Gold nanoparticle-based enhanced chemiluminescence immunosensor for detection of Staphylococcal Enterotoxin B (SEB) in food, Int J Food Microbiol, 2009, 133, 265–271, https://doi.org/10.1016/j.ijfoodmicro.2009.05.029.
[42] Chen A, Wang R, Bever CRS, Xing S, Hammock BD, Pan T, Smartphone-interfaced lab-on-a chip devices for field-deployable enzyme-linked immunosorbent assay, Biomicrofluidics, 2014, 8, 1–11, https://doi.org/10.1063/1.4901348.
[43] Akraa S, Pham Tran T, Shen A, Tang H, Tang Y, Li BZ, Walker J, A smartphone-based point-of care quantitative urinalysis device for chronic kidney disease patients, J Netw Comput Appl, 2018, 115, 59–69, https://doi.org/10.1016/j.jnca.2018.04.012.
[44] Taraska JW, Zagotta WN, Fluorescence applications in molecular neurobiology, Neuron, 2010, 66, 170–189, https://doi.org/10.1016/j.neuron.2010.02.002.
[45] Toora BD, Rajagopal G, Measurement of creatinine by Jaffe's reaction–determination of concentration of sodium hydroxide required for maximum color development in standard, urine and protein free filtrate of serum, Indian J Exp Biol, 2002, 40, 352–354.
[46] Wang W, Optical Sources – Fiber Optic Sources, 2007, 1–123.
[47] Agu E, Pedersen P, Strong D, Tulu B, He Q, Wang L, Li Y, The smartphone as a medical device: Assessing enablers, benefits and challenges, 2013 IEEE Int Conf Sensing, Commun Networking, SECON, 2013, 2013, 76–80, https://doi.org/10.1109/SAHCN.2013.6644964.
[48] Yu L, Chen H, Yue J, Chen X, Sun M, Tan H, Asiri AM, Alamry KA, Wang X, Wang S, Metal – organic framework enhances aggregation-induced fluorescence of chlortetracycline and the application for detection, Anal Chem, 2019, 91, 5913–5921, https://doi.org/10.1021/acs.analchem.9b00319.
[49] Zhang X, Yao B, Hu Q, Hong Y, Wallace A, Reynolds K, Ramsey C, Maeder A, Reed R, Tang Y, Detection of biomarkers in body fluids using bioprobes based on aggregation-induced emission fluorogens, Mater Chem Front, 2020, 4, 2548–2570, https://doi.org/10.1039/D0QM00376J.
[50] Huang C, Ma R, Luo Y, Shi G, Deng J, Zhou T, Stimulus Response of TPE-TS@Eu/GMP ICPs: Toward Colorimetric Sensing of an Anthrax Biomarker with Double Ratiometric Fluorescence and Its Coffee Ring Test Kit for Point-of-Use Application, Anal Chem, 2020, 92, 12934–12942, https://doi.org/10.1021/acs.analchem.0c01570.
[51] Ramasubramanian K, Jaccob M, Velusamy M, Internet of Things-Enabled Aggregation-Induced Emission Probe for Cu2+ Ions: Comprehensive Investigations and Three-Dimensional Printed Portable Device Design, 2020. https://doi.org/10.1021/acsomega.0c05262.
[52] Chen J, Chen X, Zhao J, Liu S, Chi Z, Instrument-free and visual detection of organophosphorus pesticide using a smartphone by coupling aggregation-induced emission nanoparticle and two-dimension MnO2 nanoflake, Biosens Bioelectron, 2020, 170, 112668, https://doi.org/10.1016/j.bios.2020.112668.
[53] Wei Q, Acuna G, Kim S, Vietz C, Tseng D, Chae J, Shir D, Luo W, Tinnefeld P, Ozcan A, Plasmonics enhanced smartphone fluorescence microscopy, Sci Rep, 2017, 7, 1–10, https://doi.org/10.1038/s41598-017-02395-8.

[54] Zhang C, Kim JP, Creer M, Yang J, Liu Z, A smartphone-based chloridometer for point-of-care diagnostics of cystic fibrosis, Biosens Bioelectron, 2017a, 97, 164–168, https://doi.org/10.1016/j.bios.2017.05.048.
[55] Mudanyali O, Dimitrov S, Sikora U, Padmanabhan S, Navruz I, Ozcan A, Integrated rapid diagnostic-test reader platform on a cellphone, Lab Chip, 2012, 12, 2678–2686, https://doi.org/10.1039/c2lc40235a.
[56] Coskun AF, Nagia R, Sadeghia K, Phillips S, Ozcan A, Albumin testing in urine using a smartphone, Lab Chip, 2013, 13, 4231–4238, https://doi.org/10.1039/c3lc50785h.
[57] Sekine Y, Kim SB, Zhang Y, Bandodkar AJ, Xu S, Choi J, Irie M, Ray TR, Kohli P, Kozai N, Sugita T, Wu Y, Lee K, Lee KT, Ghaffari R, Rogers JA, A fluorometric skin-interfaced microfluidic device and smartphone imaging module for: In situ quantitative analysis of sweat chemistry, Lab Chip, 2018, 18, 2178–2186, https://doi.org/10.1039/c8lc00530c.
[58] Alves IP, Reis NM, Microfluidic smartphone quantitation of Escherichia coli in synthetic urine, Biosens Bioelectron, 2019, 145, 111624, https://doi.org/10.1016/j.bios.2019.111624.
[59] Paterson AS, Raja B, Mandadi V, Townsend B, Lee M, Buell A, Vu B, Brgoch J, Willson RC, A low-cost smartphone-based platform for highly sensitive point-of-care testing with persistent luminescent phosphors, Lab Chip, 2017, 17, 1051–1059, https://doi.org/10.1039/c6lc01167e.
[60] Quimbar ME, Krenek KM, Lippert AR, A chemiluminescent platform for smartphone monitoring of H2O2 in human exhaled breath condensates, Physiol Behav, 2017, 176, 139–148, https://doi.org/10.1016/j.ymeth.2016.05.017.A.
[61] Kim H, Jung Y, Doh IJ, Lozano-Mahecha RA, Applegate B, Bae E, Smartphone-based low light detection for bioluminescence application, Sci Rep, 2017, 7, 1–11, https://doi.org/10.1038/srep40203.
[62] Roda A, Michelini E, Cevenini L, Calabria D, Calabretta MM, Simoni P, Integrating biochemiluminescence detection on smartphones: Mobile chemistry platform for point-of need analysis, Anal Chem, 2014, 86, 7299–7304, https://doi.org/10.1021/ac502137s.
[63] Zangheri M, Cevenini L, Anfossi L, Baggiani C, Simoni P, Di Nardo F, Roda A, A simple and compact smartphone accessory for quantitative chemiluminescence-based lateral flow immunoassay for salivary cortisol detection, Biosens Bioelectron, 2015, 64, 63–68, https://doi.org/10.1016/j.bios.2014.08.048.
[64] Chen X, Liu B, Pang W, Duan X, Smartphone-enabled dynamic chemiluminescence biomarker quantitation using acoustic tweezers approach, Proc Annu Int Conf IEEE Eng Med Biol Soc EMBS 2020-July, 2020b, 5041–5044, https://doi.org/10.1109/EMBC44109.2020.9176259.

Na Zhao

# Chapter 6
# AIEgens for organelles imaging and biological process monitoring

## 6.1 Introduction

Cell is the basic building block of life, which contains diverse subcellular organelles, including plasma membrane, mitochondria, lysosomes, lipid droplets, endoplasmic reticulum, Golgi apparatus, nucleus, and so on. Each type of organelle has its own functions and plays a pivotal role in maintaining cellular homeostasis. For example, as the cellular powerhouse, mitochondrion offers energy for cell activity [1]. Lysosome is the workshop to degrade damaged, degenerated, and nonfunctional bio-macromolecules and organelles [2]. Lipid droplet is the dynamic center for neutral lipid storage [3]. In order to maintain the normal physiological functions, subcellular organelles also involve in many interconnected cellular processes, such as lysosome-mediated autophagy [4], mitochondrion-associated energy production [5], lipid droplet-regulated lipid metabolism [6], and so on. Dysfunctional subcellular organelles and abnormal organelle-associated biological processes could result in severe human diseases [7–9]. Consequently, visualization of the organelle morphology as well as the related biological processes is of great importance for both biomedical research and early diagnosis of diseases.

Taking advantage of fast response, noninvasive testing, and real-time tracking, the technique of fluorescence imaging provides a powerful tool to obtain the biochemical information at the cellular level [10–17]. The process of fluorescence imaging is dependent on the development of fluorescent probes, and most organic fluorescent probes flourished in recent years owing to the ease of derivation and excellent biocompatibility. However, the conventional organic fluorophores always encounter the aggregation-caused quenching (ACQ) effect [18], which results in drawbacks for cell imaging, such as low working concentration and poor signal-to-noise ratio. In 2001, Tang's group discovered the aggregation-induced emission (AIE) phenomenon [19]. Unlike the traditional fluorophores, the AIE luminogen (AIEgen) is weakly emissive in the dissolved state, but exhibits intense emission in the aggregated state, which is initiated from the mechanism

**Acknowledgements:** The work was financially supported by National Natural Science Foundation of China (21975149), Funded Projects for the Academic Leaders and Academic Backbones, Shaanxi Normal University (18QNGG007).

**Na Zhao,** School of Chemistry & Chemical Engineering, Shaanxi Normal University, Xi'an, 710119, China, e-mail: nzhao@snnu.edu.cn

https://doi.org/10.1515/9783110672220-006

of restriction of intramolecular motions [20–23]. It is noteworthy that AIEgens enjoy a high concentration and bright emission in the aggregated state or in an aqueous solution, which offers imaging merits, including high specificity, excellent signal-to-noise ratio, strong photostability, and long-term retention. Therefore, AIEgens have been widely applied for cell imaging and biology process monitoring [24–35].

In this chapter, we summarize the recent advances about AIE probes that can specifically stain the subcellular organelles, including plasma membrane, mitochondria, lysosomes, lipid droplets, endoplasmic reticulum, Golgi apparatus, and nucleus. Monitoring the organelle-related biological processes by employing AIE probes is also included in some sections. Finally, the perspectives for the future exploration of organelle-targeted AIE probes are discussed.

## 6.2 Plasma membrane

The cell plasma membrane is semi-permeable and is mainly composed of phospholipids and protein, which serve as a barrier to protect and keep the internal environment of cells. The plasma membrane also plays critical roles in several biological processes, including cell recognition and signal transduction [36, 37]. Most cell membrane-targeted probes are lipophilic, since they can insert into the phospholipid bilayer of the membrane [38, 39]. For instance, the commercial probes for cell membrane, 3,3′-dioctadecyloxacarbocyanine perchlorate (DiO) [40] and 1,1′-dioctadecyl-3,3,3′3′-tetramethylindocarbocyanine perchlorate (DiI) [41], both have long alkyl chains.

Inspired by the structure of DiO and DiI, some novel AIE probes for cell membrane have been developed. For example, Li and co-workers designed and synthesized a 1,8-naphthalimide derivative (FD-9), which contains one butyl and two hexyl chains (Figure 6.1a) [42]. FD-9 exhibited weak emission in methanol solution, but gave enhanced emission with increasing water contents, revealing its AIE feature. The 3-(4,5-dimethyl-2-thiazolyl)-2,5-diphenyl-2-H-tetrazolium bromide (MTT) assay indicated that the cell viability was more than 90% when the concentration of FD-9 varied from 10 to 50 μM, suggestive of its low cytotoxicity. After incubation with FD-9 in HepG-2 cells, a bright fluorescence emerged in the cell membrane region, whereas negligible fluorescence was observed in the cytoplasm or other organelles. Further, intracellular colocalization with DiI demonstrated that the fluorescent signals that originated from FD-9 were well colocalized with that of DiI, implying that FD-9 could exclusively stain the cell membrane. Compared to DiI, FD-9 displayed a much higher signal-to-noise ratio and photostability due to its special AIE effect. When the cells were stained with FD-9 for 4 days, strong and clear fluorescence from the cell membrane could still be observed, suggesting that FD-9 could act as an ideal agent for long-term tracking of cells (Figure 6.1b). The strong lipophilicity of FD-9 should be the main reason for its long-term targeting ability.

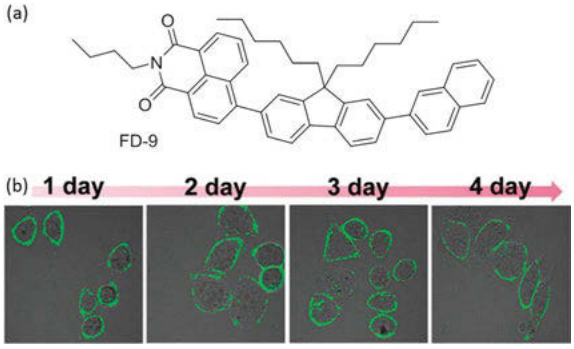


**Figure 6.1:** (a) Chemical structure of FD-9. (b) Tracking of living HepG-2 cells for 4 days by staining FD-9. Copyright 2013, Royal Society of Chemistry.

Liang's group reported an amphipathic molecule $TR_4$, which is composed of a TPE group, a palmitic acid, and a hydrophilic tetra-peptide sequence (Figure 6.2a) [43]. With the help of the hydrophilic peptide sequence, $TR_4$ dissolved in water and gave weak emission at low concentrations (<200 μM). At a high concentration (>200 μM), the fluorescence of $TR_4$ was turned on in water due to the formation of aggregates. After mixing $TR_4$ (50 μM) with liposomes, turn-on fluorescence was also observed, which was attributed to the restriction of free intramolecular rotation by the alkyl chains of the lipid bilayer. The positively charged arginine units of $TR_4$ can interact with the negatively charged cell membrane, and the long alkyl chain is able to embed in the membrane. Therefore, when the MCF-7 cells were incubated with $TR_4$, bright fluorescence from the cell membrane was observed, whereas no fluorescence appeared in the cytoplasm and nucleus. From the view of merged images between $TR_4$ and DiI, green fluorescence of $TR_4$ was colocalized with the red fluorescence of DiI (Figure 6.2b). Moreover, $TR_4$ exhibited higher photostability than DiI under laser irradiation, indicating that $TR_4$ is an alternative probe for selectively staining the cell membrane. Additionally, when excited by a 700 nm two-photon laser, the membrane of the HUVEC cells was also specifically visualized by $TR_4$.

The purine is a versatile fluorescent skeleton due to its large Stokes shift, excellent biocompatibility, and adjustable alkyl chain. Yu and co-workers developed a water-soluble AIE probe (Pent-TMP), based on the purine core (Figure 6.3a) [44]. For Pent-TMP, the ((trimethylammonium) propyl) pyridine group can label the plasma membranes through strong electrostatic interactions, and the hydrophobic pentyl group can embed into the membrane by hydrophobic interaction. As a result, fluorescence was remarkably triggered once the Pent-TMP was inserted into the plasma membrane. Owing to the unique AIE nature, Pent-TMP was able to image the cell membrane quickly and in a washing-free manner. Pent-TMP also exhibited good biocompatibility and long-time retention for cell membrane. The excellent membrane-staining ability made Pent-TMP distinctly visualize the membrane morphology

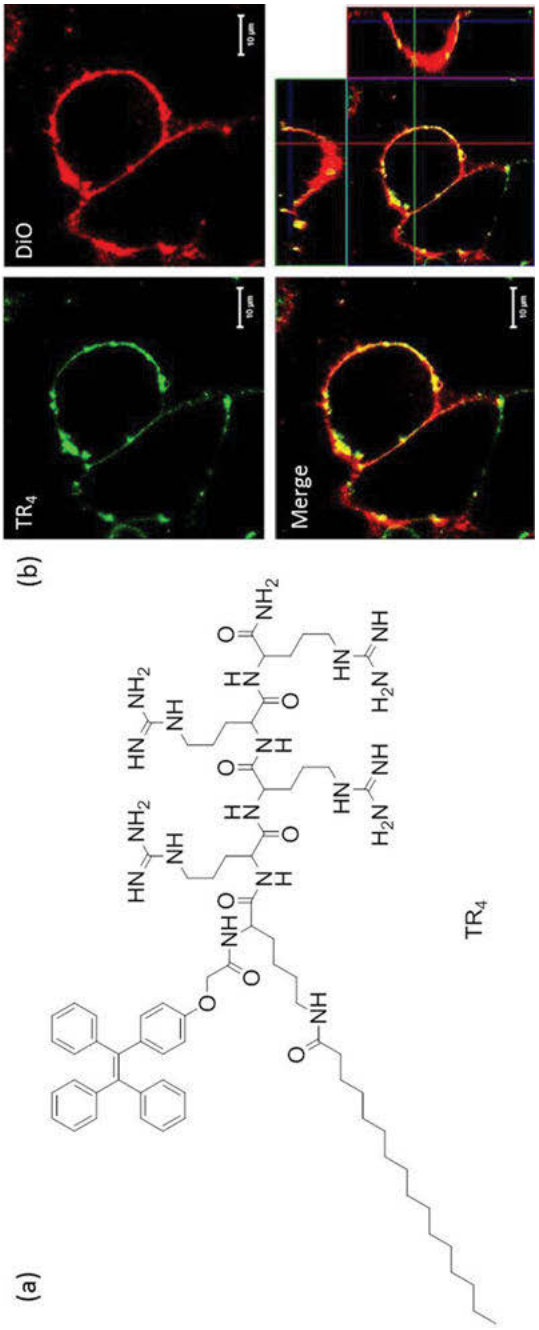


**Figure 6.2:** (a) Chemical structure of $TR_4$. (b) Confocal laser scanning microscope (CLSM) images of MCF-7 cells stained with $TR_4$, DiI and their merged image. Copyright 2014, American Chemical Society.

of neuronal cells, both in complex 2D and 3D models. Moreover, when the mouse brain tissue was stained with Pent-TMP, the hollow circle-shaped erythrocytes in the brain tissue were imaged very well (Figure 6.3b). It was the first fluorescent probe for single erythrocytes in the brain tissue. Furthermore, Pent-TMP could penetrate the hydrophilic surface of living zebrafish and selectively stain the plasma membranes of cells on the surface of zebrafish (Figure 6.3c).

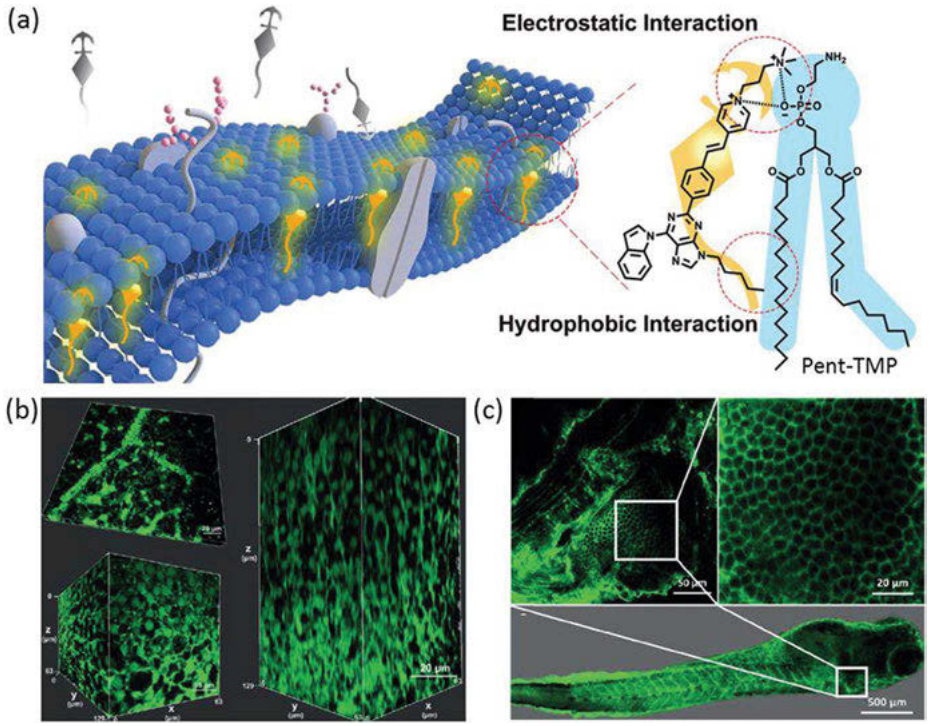


**Figure 6.3:** (a) The schematic diagram of Pent-TMP and plasma membrane. (b) The 3D image of erythrocytes stained with Pent-TMP and their distribution in the brain tissue. (c) Image of zebrafish gills stained with Pent-TMP and the enlarged picture of the surface of zebrafish gills. Copyright 2020, Wiley-VCH.

Using a similar strategy, Tong et al. developed an amphiphilic AIE probe TPNPDA-C12 with the long alkyl chain (Figure 6.4a) [45]. Dual-colored fluorescence was observed for TPNPDA-C12 at different states, which showed yellow emission for molecular aggregates and red emission, once the monomers were restricted. Interestingly, TPNPDA-C12 could simultaneously and selectively stain the cell membranes and mitochondria by distinct fluorescence channels (Figure 6.4b). When the HeLa cells were incubated with TPNPDA-C12, it inserted into the cell membrane through amphiphilic interaction, which restricted the monomers and resulted in red fluorescence. The colocalization

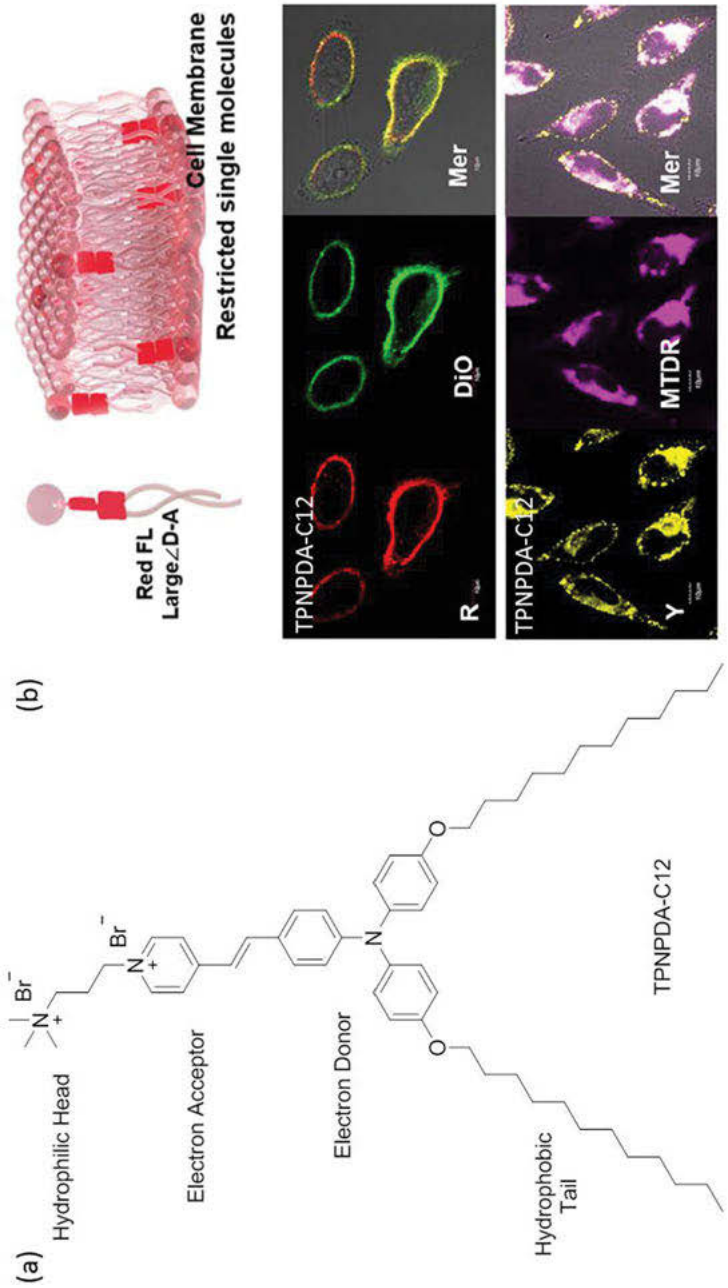


**Figure 6.4:** (a) Chemical structure of TPNPDA-C12. (b) The schematic diagram of TPNPDA-C12 with plasma membrane. (c) CLSM images of HeLa cells for colocalization of TPNPDA-C12 with DiO or MTDR. Copyright 2020, American Chemical Society.

experiments showed that the Pearson's correlation coefficient between TPNPDA-C12 and DiO was as high as 0.85. Meanwhile, TPNPDA-C12 also penetrated the cell membrane and accumulated in the mitochondria matrix, leading to molecular aggregates with yellow fluorescence. Additionally, TPNPDA-C12 could be used to dynamically visualize the cell membranes and mitochondria in the process of cell apoptosis and necrosis, triggered by reactive oxygen species (ROS) or cytotoxin.

Some AIE probes without alkyl chains were reported to stain the cell membranes. For instance, Tang and co-workers developed a cyanostilbene derivative (AS2CP-TPA), which was composed of a hydrophobic triphenylamino group and a hydrophilic pyridinium group (Figure 6.5a) [46]. Owing to the strong ICT effect, AS2CP-TPA emitted at around 700 nm in the aggregated state. When both the commercial probe CellMask Green Plasma Membrane and AS2CP-TPA were employed to co-stain the cells, it was clear that the fluorescence from AS2CP-TPA overlapped very well with the CellMask Green Plasma Membrane, suggesting that AS2CP-TPA could accumulate in the plasma membrane. Meanwhile, AS2CP-TPA exhibited better photostability than CellMask Green Plasma Membrane, which made it an ideal probe for monitoring the morphology change of membrane. As shown in Figure 6.5b, when the cells were pre-stained with AS2CP-TPA and then treated with $Hg^{2+}$ for 0 min and 40 min, an obvious bleb appeared, implying that the actin filament was disrupted by the $Hg^{2+}$. Conversely, a slight change of membrane morphology in the absence of $Hg^{2+}$ was obtained. AS2CP-TPA could also be applied to monitor the detachment process of adherent cells induced by trypsin.

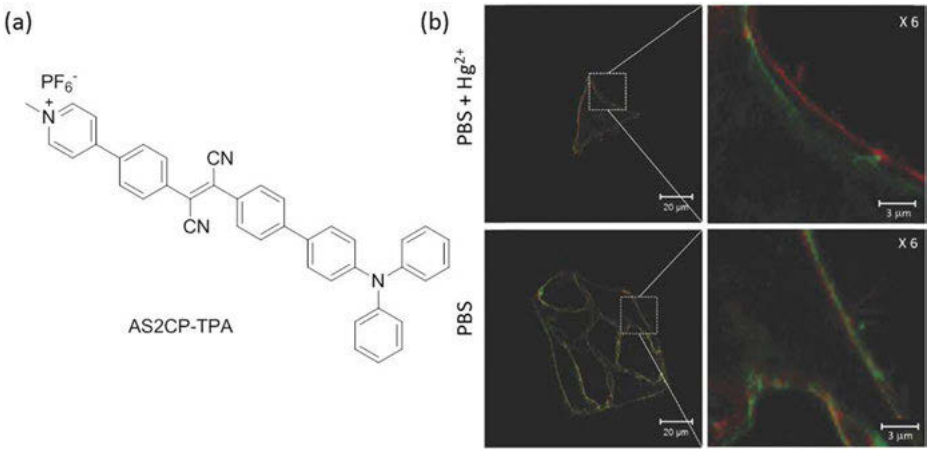


**Figure 6.5:** (a) Chemical structure of AS2CP-TPA. (b) CLSM images of AS2CP-TPA-stained HeLa cells before (red) and after (green) incubation with PBS containing $Hg^{2+}$ (100 μM) for 40 min or incubation with PBS alone for 40 min. Copyright 2018, Royal Society of Chemistry.

By connecting a coumarin with a TPE derivative through an a,β-unsaturated ketone group, another cell membrane-specific probe A, with AIE characteristic, was developed by Liu and co-workers (Figure 6.6a) [47]. It is noteworthy that the probe A exhibited dual emission wavelengths at 482 and 591 nm in an aqueous solution. Meanwhile, the probe A not only displayed low cytotoxicity and excellent photostability, but also gave high tolerance towards various anions, cations, and amino acids. Because of its strong lipophilicity, the probe A could target the cell membrane of different cell lines with high selectivity and the Pearson's correlation coefficient with commercial probe (Cellbrite NIR Membrane Dye) could reach 0.93 in MCF-7 cells. Benefitting from the special dual-emission of probe A, multiple-channel imaging of the cell membrane under different excitation wavelengths was achieved (Figure 6.6b).

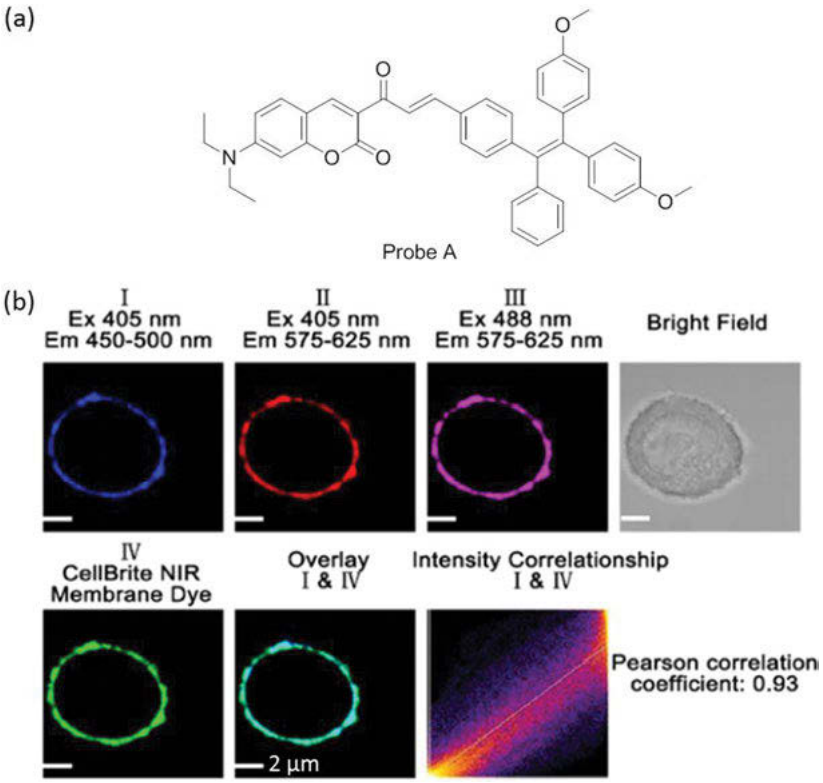


**Figure 6.6:** (a) Chemical structure of probe A. (b) CLSM images of MCF-7 cells incubated with probe A, CellBrite cytoplasmic NIR dye and their merged image. Copyright 2020, American Chemical Society.

## 6.3 Mitochondria

Mitochondrion, an important subcellular organelle, exists in most eukaryotic cells. As the energy generation center, mitochondria supply energy currency ATP for cells through oxidation of carbohydrates, fats, and amino acids. It participates in different biological possess, such as cell differentiation, signaling, and apoptosis. Mitochondria also regulate the cell growth and cycle. In order to synthesize ATP, mitochondria continuously oxidize substrates and maintain a proton gradient across the lipid bilayer with a large membrane potential [48]. This negative membrane potential provides an opportunity to develop appropriate probes for targeting mitochondria, and various cationic and lipophilic fluorophores such as cyanine dyes [49] and rhodamine [50] have been reported to image mitochondria. Based on a similar mechanism, a number of AIEgens have been developed to target mitochondria.

The triphenylphosphonium (TPP) group is a common targeting group for mitochondria. The first AIE probe for mitochondrial imaging is the TPE derivative tetraphenylethylene-triphenylphosphorus (TPE-TPP), which contains two TPP units (Figure 6.7a) [51]. TPE-TPP exhibited typical AIE characteristics and good biocompatibility. Upon incubation with TPE-TPP in HeLa cells, it could selectively light up the mitochondria, owing to its suitable lipophilic and cationic nature, which was confirmed by the colocalization experiment with the commercial probe, MitoTracker Red FM (MTR). Moreover, after treating the cells with carbonyl cyanide m-chlorophenylhydrazone (CCCP), an inducer that can decrease the mitochondrial membrane potential, MTR, showed no more specificity to mitochondria, but high sensitivity for mitochondria was still observed for TPE-TPP (Figure 6.7b). Thanks to its high tolerance toward microenvironment changes, TPE-TPP is a promising fluorescent probe for mitochondrial targeting and morphological change tracking (Figure 6.7c).

To extend the emission wavelength of AIEgens, a heteroatom-containing TPE-Py was developed by linking a pyridinium unit to a TPE unit, through a vinyl functional group (Figure 6.8a) [52]. By virtue of appropriate electron-withdrawing ability of the pyridinium unit, TPE-Py exhibited a typical intramolecular charge transfer (ICT) effect. TPE-Py was weakly emissive in THF, but became a strong yellow emitter, peaking at 600 nm in the aggregated state. When the cells were incubated with TPE-Py and MitoTracker Red CMXRos, the position and shape of mitochondria, imaged by TPE-Py, were the same as those by MitoTracker Red, indicating that TPE-Py could selectively stain the mitochondria in living cells (Figure 6.8b). Moreover, TPE-Py gave stronger photostability than MitoTracker Red, which enabled TPE-Py, as a potential candidate, to track the mitochondria morphology for a long time.

On the basis of TPE-Py, Zhao and co-workers synthesized a series of pyridinium-functionalized TPE salts (TPEPy-1 to TPEPy-4) with different alkyl chains ($n$-$C_3H_7$, $n$-$C_6H_{13}$, $n$-$C_9H_{19}$, and $n$-$C_{12}H_{25}$) and systematically investigated the influence of chain length on their optical performance as well as mitochondria-targeting ability [53]. These fluorophores displayed different emission colors in solid state due to their

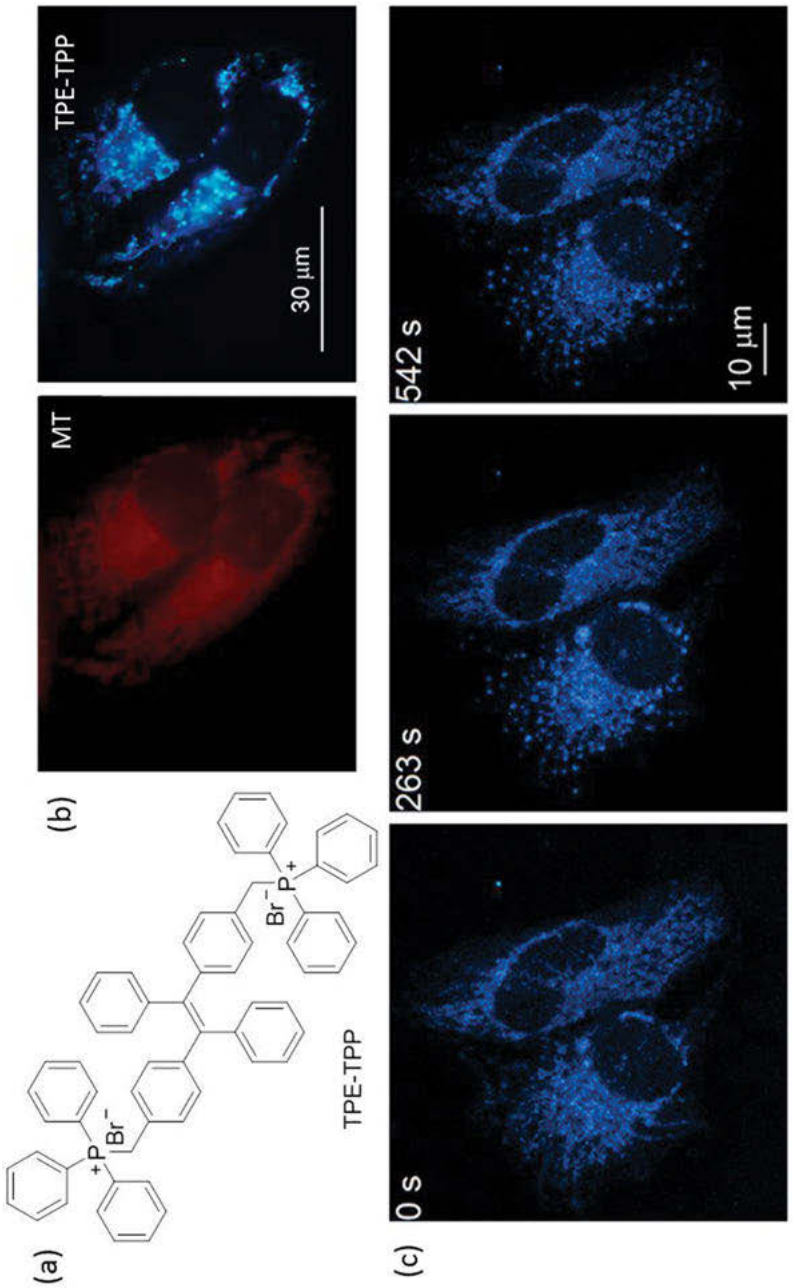


**Figure 6.7:** (a) Chemical structure of TPE-TPP. (b) CLSM images of CCCP pretreated HeLa cells stained with MTR and TPE-TPP. (c) CLSM images of CCCP pretreated HeLa cells stained with TPE-TPP with prolonging incubation time. Copyright 2013, American Chemical Society.

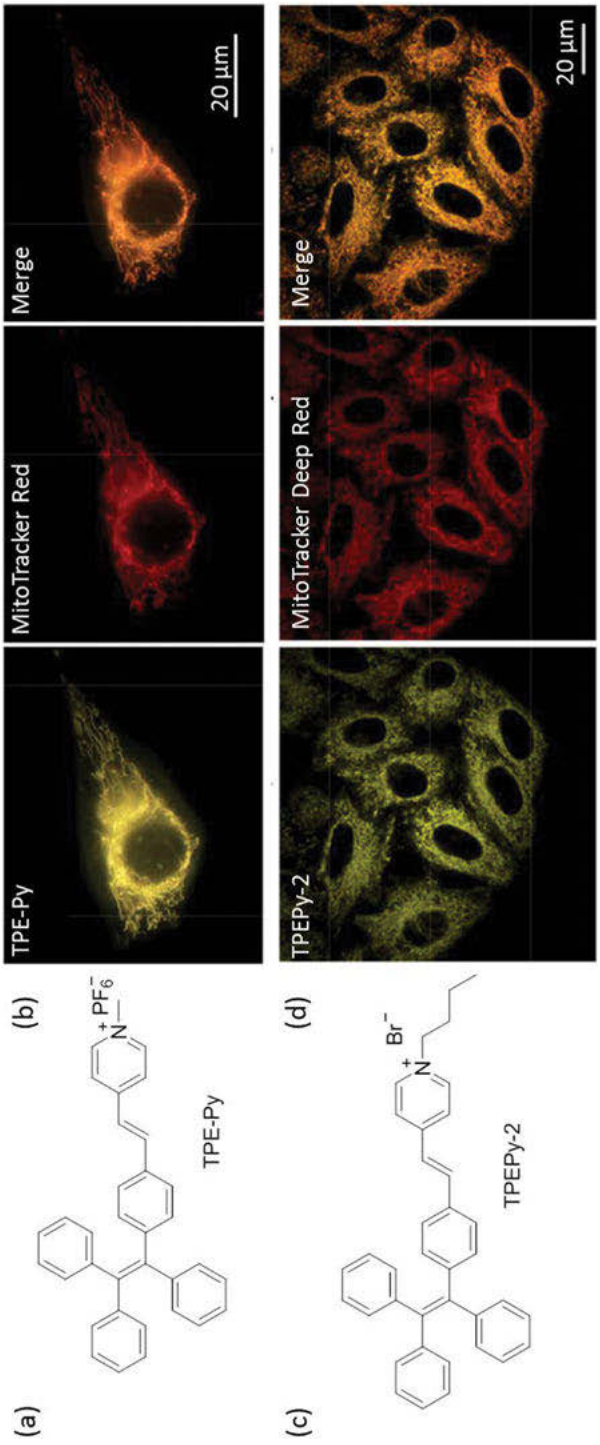


**Figure 6.8:** Chemical structures of (a) TPE-Py and (c) TPEPy-2. (b) CLSM images of HeLa cells co-stained with TPE-Py and MitoTracker Red. Copyright 2013, Royal Society of Chemistry. (d) CLSM images of HeLa cells co-stained with TPEPy-2 and MitoTracker Deep Red. Copyright 2018, American Chemical Society.

varied molecular packing modes. Interestingly, they showed obvious cellular uptake selectivity. Fluorophores, with a shorter chain length, (TPEPy-1 to TPEPy-3) could be effectively taken up by HeLa cells. But, TPEPy-4, with a longer chain length, could not enter the HeLa cells, which was mainly caused by its stronger hydrophobicity. The highest Pearson's correlation coefficient (0.84) between TPEPy-2 and commercial MitoTracker Deep Red after HeLa cells staining revealed the best imaging capability of TPEPy-2 for mitochondria (Figure 6.8c,d). The specific mitochondria-targeting of TPEPy-2 was also achieved in HEK-293T cells.

An analogue of TPE-$PyN_3$, which contains an azide group, was developed to image mitochondria and long-term observation cells (Figure 6.9a) [54]. HeLa cells were stained with TPE-$PyN_3$ and sub-cultured every day, and the cell images were then collected at each generation. As shown in Figure 6.9b, even after five generations, TPE-$PyN_3$ was still retained in the mitochondria and gave intense emission. But, 5-chloromethylfluorescein diacetate (CMFDA), a commercial probe for long-term tracking of cells, could only retain in cells for a few hours at physiological conditions. The unique AIE feature of TPE-$PyN_3$ should be responsible for its excellent long-time retention in cells. Additionally, TPE-$PyN_3$ was able to penetrate the cell membrane and reveal the shape, boundary, and location in zebrafish embryos (Figure 6.9c).

Another TPE-Py derivative of TPE-Py-NCS, containing an amine-reactive isothiocyanate (NCS) unit, was designed and synthesized by Tang and co-workers (Figure 6.9d) [55]. TPE-Py-NCS can conjugate to the mitochondrial proteins, which makes it suitable to track the mitochondria in real-time and over long-term. The HeLa cells were pre-incubated with both TPE-Py-NCS and LysoTracker Red DND-99 (LTR); rapamycin was then added to induce mitophagy, and the mitophagy process was monitored using the above two probes. As displayed in Figure 6.9e, there was no noticeable change initially (0–72 min). At 73.5 min, however, a new red spot emerged that overlapped with the yellow fluorescent signals from mitochondria, suggesting the acidic autophagosome was formed. The red spot was retained for a few minutes and disappeared at 79.5 min, implying that the mitophagy process was completed. On the contrary, the commercial MTR and LysoTracker green (LTG) were not conducive to monitor the late mitophagy process because of their serious photobleaching.

A series of full-color AIEgens (DPI-B, DPI-A, DPI-BP, and DPI-In), based on the imidazole molecular rotors, were reported for specific imaging of mitochondria (Figure 6.10a) [56]. When the different electron acceptors, including cyano, pyridinium, and indolium were introduced, the emission color of AIEgens could be adjusted from blue to deep red. All these imidazole-based AIEgens showed low cytotoxicity at low concentrations. After incubation with four AIEgens in HeLa cells, all of them could accumulate in the mitochondria (Figure 6.10b). Meanwhile, the DPI-BP exhibited the best mitochondria targeting, while the overlapping coefficient with MTR was 0.92, which should be attributed to the pyridinium moiety in DPI-BP.

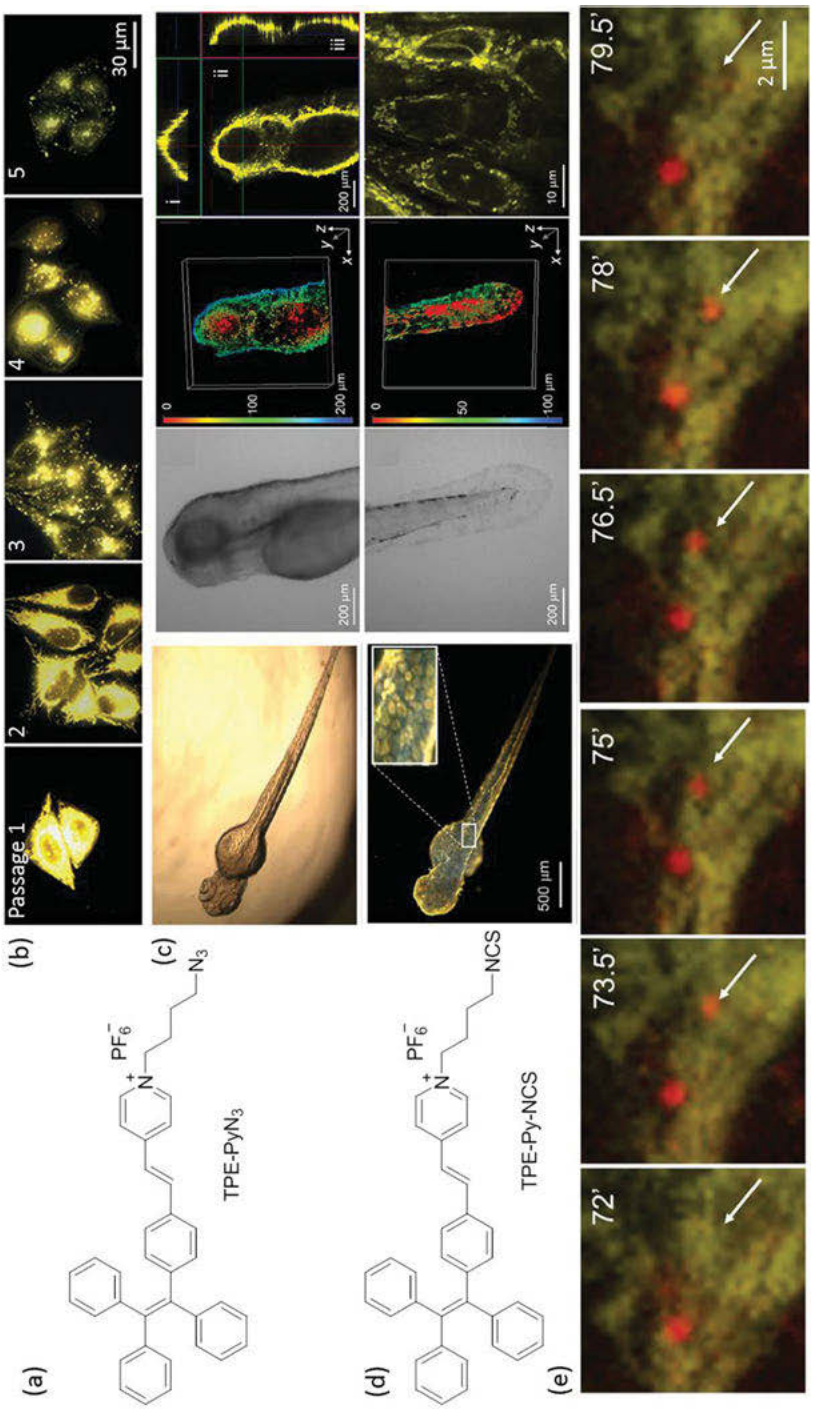


**Figure 6.9:** Chemical structures of (a) TPE-PyN$_3$ and (d) TPE-Py-NCS. (b) Images of TPE-PyN$_3$-stained HeLa cells at different passages. Copyright 2016, Wiley-VCH. (c) Images of TPE-PyN$_3$-stained living zebrafish. Copyright 2016, Wiley-VCH. (e) Images of TPE-Py-NCS (yellow) and LysoTracker Red DND-99 (red) co-stained HeLa cells after incubating with rapamycin at different times. Copyright 2016, Royal Society of Chemistry.

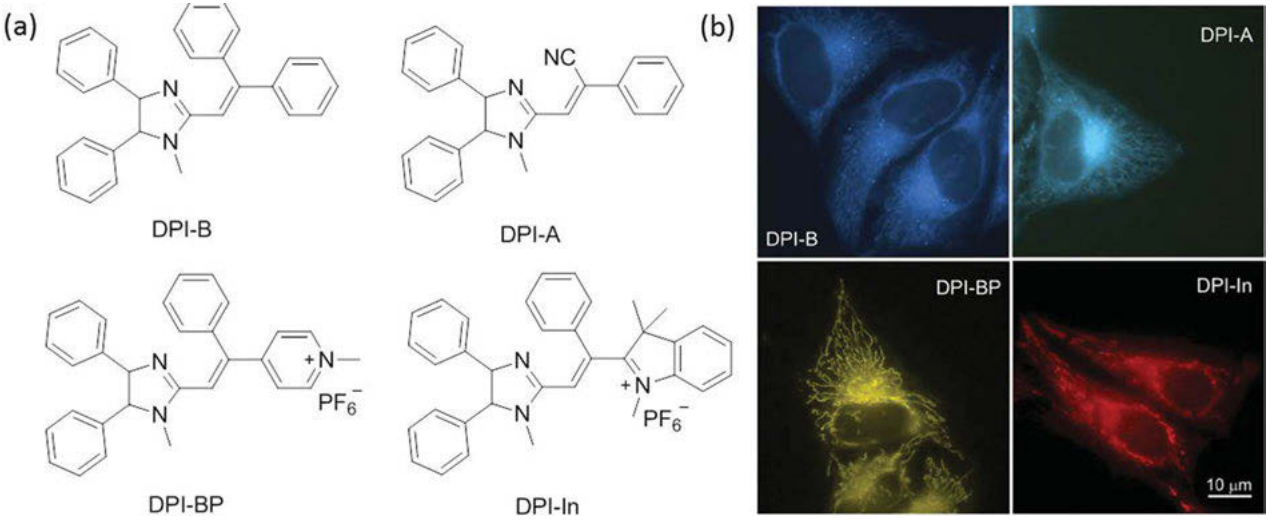


**Figure 6.10:** (a) Chemical structures of DPI-B, DPI-A, DPI-BP, and DPI-In. (b) Fluorescent images of HeLa cells stained with DPI-B, DPI-A, DPI-BP, and DPI-In. Copyright 2016, Wiley-VCH.

Mitochondrial membrane potential (MMP) is an important parameter reflecting the mitochondrial functional status, and is therefore related to the cell health, injury, and biofunctions [57]. By introducing the strong electron-withdrawing group of indolium, a TPE-based red emitter of TPE-Ph-In was developed for detecting the change of MMP (Figure 6.11a) [58]. It is noteworthy that the extra benzene ring of TPE-Ph-In endowed it with strong AIE activity and good biocompatibility. Cell imaging experiments implied that TPE-Ph-In not only accumulated in mitochondria but was also sensitive to the change of MMP (Figure 6.11b). HeLa cells were pre-stained by TPE-Ph-In and then treated with oligomycin. As shown in Figure 6.11c, the fluorescent intensity of TPE-Ph-In in cells increased about 1.5-fold and maintained for a few minutes. Subsequently, adding CCCP in the cell culture medium resulted in the obvious decrease of fluorescent intensity, indicating the sensitive response of TPE-Ph-In toward the MMP change in situ. Inspired by its excellent sensitivity for MMP, the TPE-Ph-In was further employed to evaluate sperm vitality. As illustrated in Figure 6.11d, the bright red fluorescent signals came from the energetic sperms when the sperms were stained with the TPE-Ph-In, while the faint red signals were observed for the unvital sperms.

Another MMP-sensitive AIEgen was developed, based on the TPE group (Figure 6.12a) [59]. Unlike the above-mentioned TPE-TPP, probe 2 contains one TPP group, and this TPP group is conjugated to TPE unit through the double bond, resulting in a longer emission wavelength. On the other hand, one TPP group can eliminate the strong intermolecular electrostatic repulsive interactions, which enables probe 2 to be sensitive to the change of MMP. In the presence of various biothiols or ROS, no observable emission change was achieved for probe 2, suggesting its excellent stability. The specificity of probe 2 for mitochondria was obtained in the co-staining experiment with MTR (Pearson's correlation coefficient = 0.97). When the HeLa cells were pre-stained with probe 2 or Rhodamine 123 (a commercial fluorescent probe to evaluate the MMP) and then treated with CCCP, a dramatic decrease of fluorescent intensity was observed for probe 2. In sharp contrast, Rhodamine 123 exhibited a slight fluorescence change (Figure 6.12b). The results demonstrated that probe 2 exhibited a higher sensitive response to MMP. The $H_2O_2$-induced apoptosis of the mitochondria membrane was successfully assessed by employing probe 2.

It has been reported that cancer cells show higher MMP than that of normal cells [60]. This intrinsic difference between cancer cells and normal cells offers an opportunity to develop an appropriate AIE probe to differentiate the cancer cells. For instance, a series of cationic AIEgens were constructed through a simple one-pot multicomponent reaction between alkyne, aldehyde, and amine (Figure 6.13a, c) [61, 62]. The cationic feature of these AIEgens makes them with high specificity for mitochondria. Importantly, since their cellular uptake is highly dependent on the MMP, they can be utilized to differentiate cancer cells over normal cells. As shown in Figure 6.13b, when the different cell lines were stained by TPE-IQ-2O (200 nM) for 20 min, all the cancer cells, including MDA-MB-231, MCF-7, PC-9, A549, HCC-827, and HepG2, showed strong

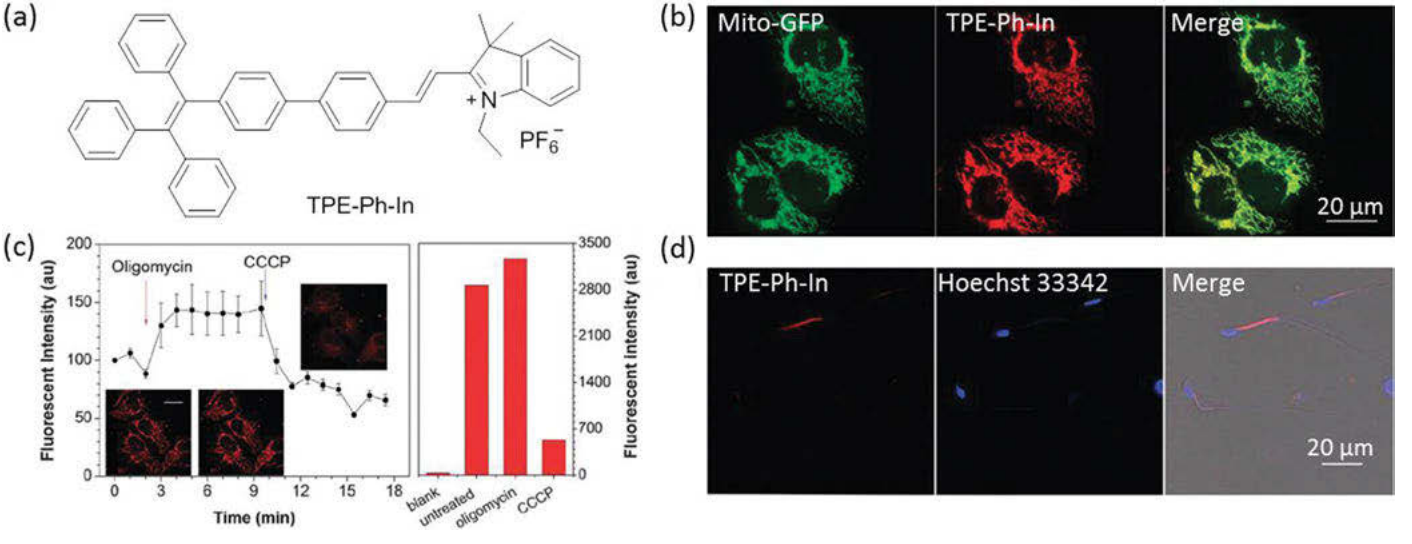


**Figure 6.11:** (a) Chemical structure of TPE-Ph-In. (b) Co-staining experiments of TPE-Ph-In with Mito-GFP. (c) Changes of emission intensity of HeLa cells stained with TPE-Ph-In upon treatment with oligomycin and CCCP. (d) CLSM of mouse sperm cells stained with TPE-Ph-In, Hoechst 33,342 and merged image. Copyright 2015, Royal Society of Chemistry.

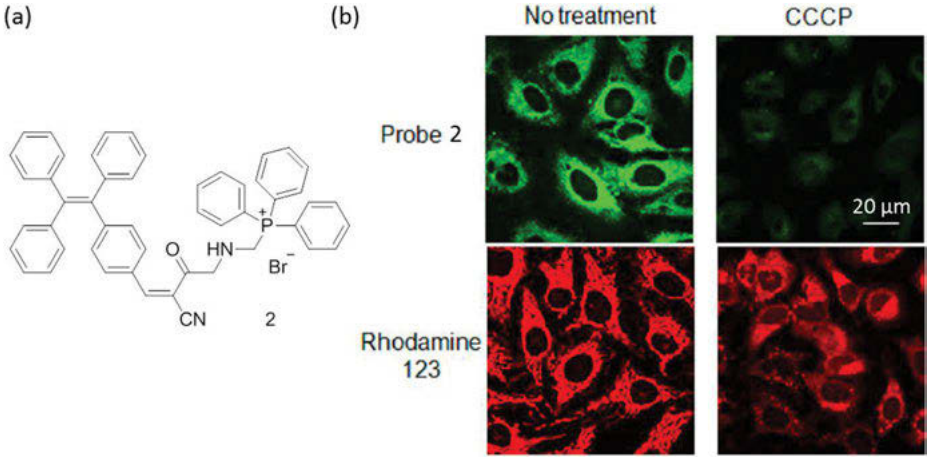


**Figure 6.12:** (a) Chemical structure of probe 2. (b) CLSM images of HeLa cells incubated with or without CCCP and then incubated with probe 2 or Rhodamine 123. Copyright 2018, American Chemical Society.

greenish-yellow fluorescence. In contrast, normal cells (LX-2, HEK-293, and MDCK-II) exhibited very faint fluorescence. It is visualized that the fluorescent intensity from stained cancer cells was much stronger than that from normal cells. When HeLa cells and Cos-7 cells in the same dish were simultaneously stained by other three analogues of IQ-Naph, IQ-DPA, and IQ-TPA at the appropriate concentration, the obvious fluorescent signals came from the HeLa cells, rather than Cos-7 cells (Figure 6.13d). The results indicated these AIEgens could distinguish cancer cells over normal cells even when both cell types are co-cultured together.

Mitophagy assists cells to remove dysfunctional mitochondria and recycles their constituent in a lysosome-dependent manner [63]. By integrating an electron-donating alkoxyl group and different electron-accepting moieties (vinyl pyridinium or vinyl pyridine) into the TPE unit, two AIEgens of AIE-Red and AIE-Green, with similar absorption but different emission wavelengths, were developed to visualize the mitophagy process (Figure 6.14a) [64]. Cationic AIE-Red and morpholine-functionalized AIE-Green enabled them to target the mitochondria and lysosome, respectively, with distinguishable emission, upon single wavelength excitation. After 60 scans, the signal loss of AIE-Red and AIE-Green was less than 8%; however, the signal loss was more than 82% for the commercial MitoTracker Green FM and LysoTracker Red DND-99, indicating both AIEgens exhibited great photostability. Benefitting from the dual organelles specificity, AIE-Red and AIE-Green were further selected to real-time monitor the mitophagy process. The HeLa cells were pre-stained with AIE-Red and AIE-Green, and then treated with rapamycin. As the incubation time prolonged, the overlap between red signals and green signals gradually increased, demonstrating the occurrence of the mitophagy process (Figure 6.14b).

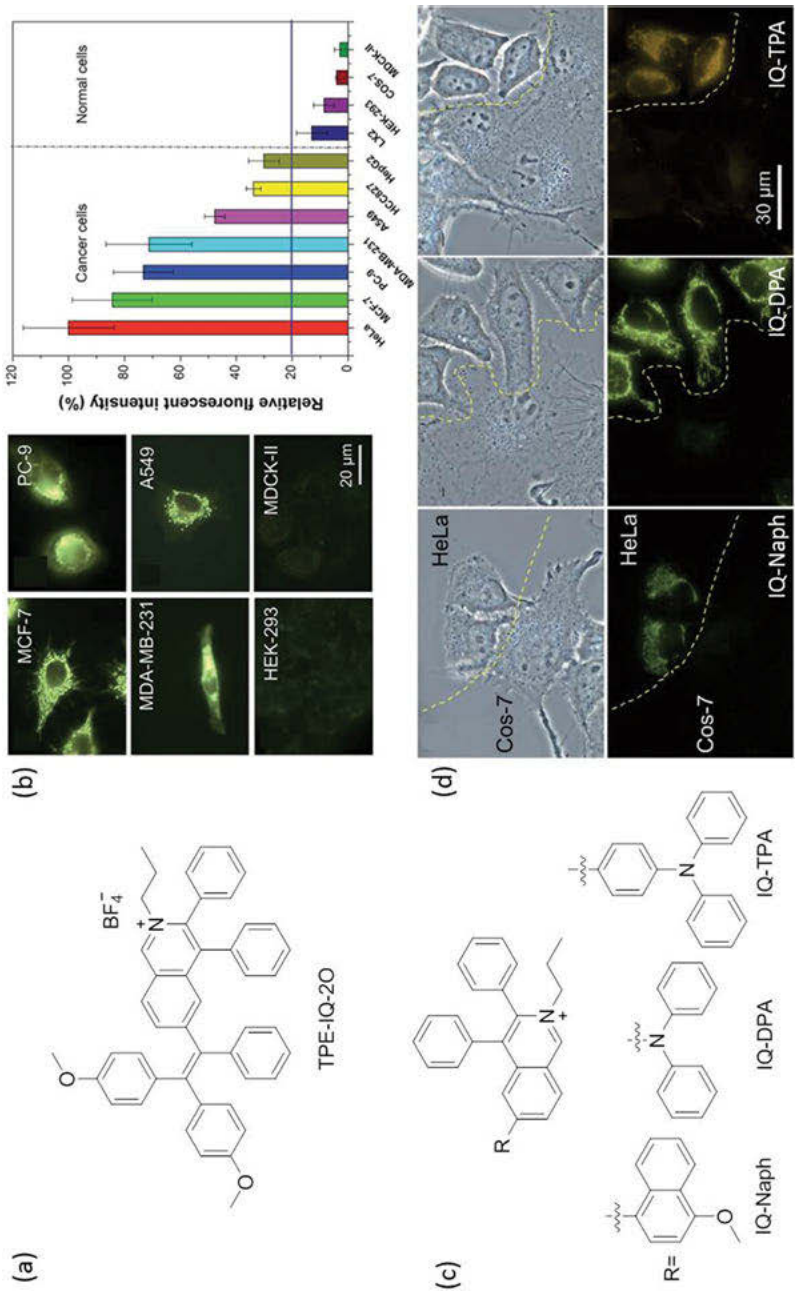


**Figure 6.13:** Chemical structures of (a) TPE-IQ-2O and (c) IQ-Naph, IQ-DPA and IQ-TPA. (b) Fluorescent images and fluorescent intensity of different cancer cells and normal cells stained with TPE-IQ-2O. Copyright 2017, Royal Society of Chemistry. (d) Fluorescent images of HeLa cells and Cos-7 cells in same dish stained with IQ-Naph, IQ-DPA and IQ-TPA. Copyright 2018, Wiley-VCH.

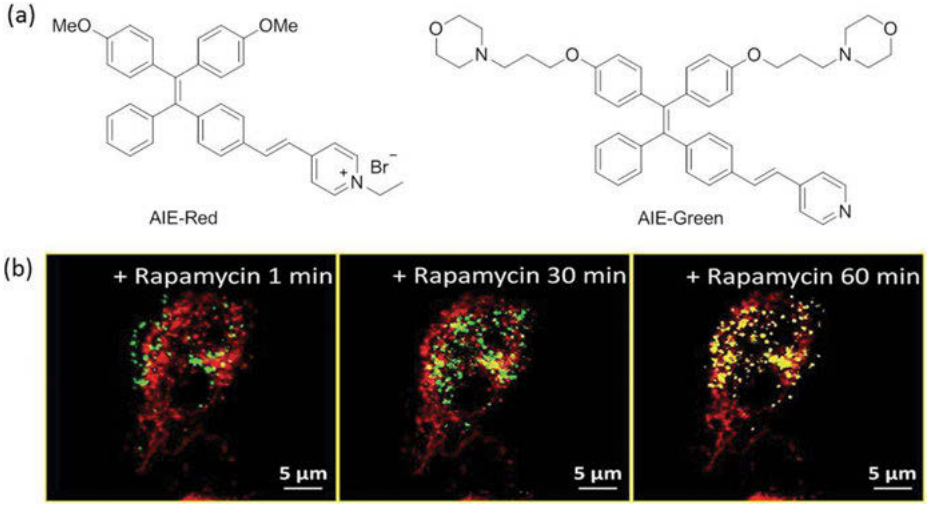


**Figure 6.14:** (a) Chemical structures of AIE-Red and AIE-Green. (b) Overlay images of AIE-Red- and AIE-Green-stained HeLa cells after treating with rapamycin. Copyright 2018, Royal Society of Chemistry.

## 6.4 Lipid droplet

Lipid droplet (LD) is a dynamic organelle in cells, which is the storage site for neutral lipids. LDs play crucial roles in many biological processes, including lipid metabolism, membrane transport, protein degradation, and signal transduction. Abnormal lipid storage in LDs was reported to be related to several metabolic diseases, such as fatty liver and cardiovascular diseases. In view of the hydrophobic lipid environment, the fluorophores with high hydrophobicity, such as commercial BODIPY 493/503 and Nile Red prefer to aggregate in the LDs [65, 66].

The first AIE probe for LDs is TPE-AmAl, which is a TPE derivative (Figure 6.15a) [67]. TPE-AmAl exhibited excellent biocompatibility, which was verified by the MTT assay. After incubating the HeLa cells with TPE-AmAl, the spherical LDs in cells were selectively stained. Different from the orange emission in the aggregated state, greenish-blue emission in LDs was observed, which was attributed to the strong twisted intramolecular charge transfer (TICT) effect of TPE-AmAl as well as the low polarity of LDs interior (Figure 6.15b). Compared to the commercial Nile Red, TPE-AmAl possesses the advantages of low background, high specificity, fast staining time, and superior photostability, which enable it to serve as an excellent probe to track the dynamic motions of LDs. Upon treatment of the LO2 cells with TPE-AmAl and oleic acid, the increment of LDs in cells was clearly visualized.

To avoid the interference of autofluorescence from cells, it is necessary to extend the emission wavelength of AIEgens. A novel AIEgen of TPE-AC with near-infrared

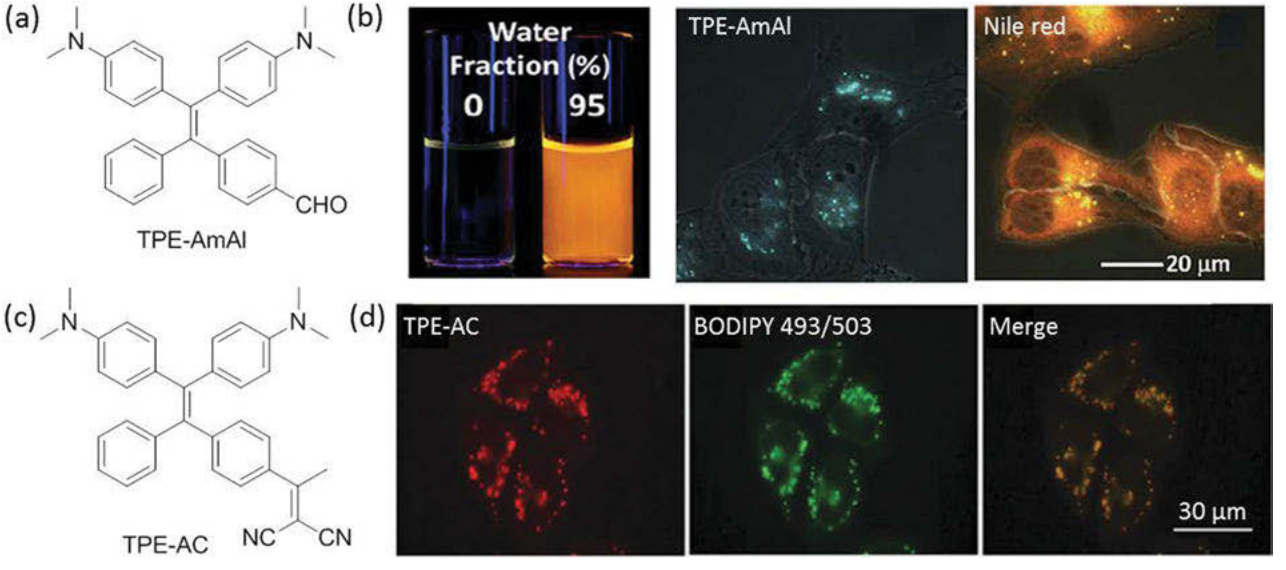


**Figure 6.15:** Chemical structures of (a) TPE-AmAl and (c) TPE-AC. (b) Photographs of TPE-AmAl in THF-water mixtures with 0 and 95 vol. % water fractions under UV illumination and the fluorescence images of LO2 cells stained with TPE-AmAl and Nile Red, respectively. Copyright 2014, Royal Society of Chemistry. (d) Fluorescence images of HeLa cells co-stained with TPE-AC and BODIPY493/503. Copyright 2016, Royal Society of Chemistry.

emission (705 nm) was developed by conjugating the strong electron-withdrawing group of malononitrile into the aforementioned TPE-AmAl derivative (Figure 6.15c) [68]. Almost no significant change in cell viability was observed even when the concentration of TPE-AC reached 100 μM, revealing its excellent biocompatibility. Similar to TPE-AmAl, TPE-AC could also penetrate the cell membrane and accumulate in LDs. The high Pearson's correlation coefficient of 0.92 was obtained for TPE-AC by using a BODIPY 493/503 as reference, demonstrating TPE-AC was highly specific to LDs (Figure 6.15d). When the HeLa cells were pre-treated with oleic acid and stained with TPE-AC, increased fluorescent intensity and a large amount of LDs in cells were detected with increasing incubation time, which suggested TPE-AC could be utilized to monitor the LDs accumulation in cells. Taking advantage of the long absorption and emission wavelength, TPE-AC could be an ideal agent for imaging of LDs in vivo.

Excited-state intramolecular proton transfer (ESIPT), a four-level photochemical process, involves the transfer of an intramolecular proton from a proton donor to a proton acceptor, in the excited state [69, 70]. ESIPT process leads to dual emission from keto and tautomer enol groups and offers a large Stokes shift, which is favorable for bioimaging application. Some AIEgens with ESIPT property were reported to target LDs in living cells. For example, two AIEgens (DPAS and FAS), with ESIPT effect, based on the salicylaldehyde Schiff group were fabricated by Tang and co-workers (Figure 6.16a) [71]. Thanks to the unique ESIPT process, DPAS and FAS showed large Stokes shifts (200 nm) in the aggregated state. As shown in Figure 6.16b, after incubating with the A549 cells, DPAS and FAS were able to stain the LDs with good resolution and high contrast, while the overlap coefficients with the BODIPY 493/503 was 97.70% and 98.30%, respectively. Moreover, no remarkable change in fluorescence was observed for two probes when the pH varied from 1.0 to 11.0, indicating their high tolerance to pH.

Zhao and co-workers developed a facile approach to construct a series of AIEgens, with the ESIPT process, termed, TS derivatives, through molecular hybridization of triphenylamine and salicylaldehyde units, in which, triphenylamine serves as the intramolecular rotor and salicylaldehyde unit serves as the ESIPT generator (Figure 6.17a) [72]. Given the AIE and ESIPT features, TS derivatives exhibited strong emissions and large Stokes shifts (>140 nm) in the aggregated state. Owing to their good biocompatibilites and suitable lipophilicites, TS derivatives could enrich in the LDs with high specificity. However, in the absence of the washing step, an excellent specificity to LDs with negligible background was also observed for TS derivatives. Conversely, BODIPY493/503 and Nile Red gave poor imaging performance for LDs, while fluorescence from the cytoplasm and other organelles, apart from LDs, could be visualized (Figure 6.17b). Furthermore, the bright fluorescence from the LDs was presented when the cells were incubated with TS derivatives for 48 h, confirming their good ability for long-term tracking of LDs.

Boranil is a kind of boron complex that adopts anil (also called salicylaldimine) as the ligand [73, 74]. Traditional boranil complex (DEFB) is a typical ACQ fluorophore

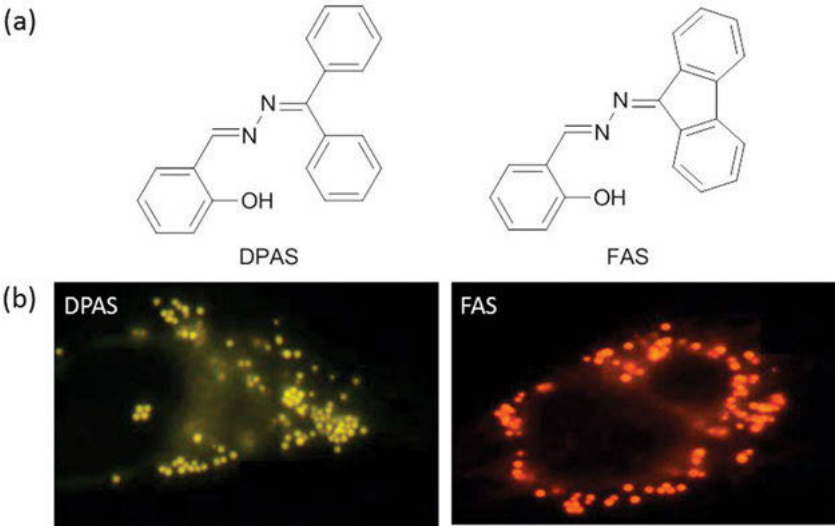


**Figure 6.16:** (a) Chemical structures of DPAS and FAS. (b) CLSM images of A549 cells incubated with DPAS and FAS. Copyright 2016, Royal Society of Chemistry.

due to its coplanar configuration. By installing a benzene ring as the intramolecular rotor into the anil ligand, Zhao and co-workers developed a facile strategy for preparing an AIE-active boranil complex, named DPFB (Figure 6.18a) [75]. By introducing suitable substituents, the solid-state emission of the DPFB derivatives was red-shifted from 550 nm to 610 nm. By virtue of good biocompatibility and suitable lipophilicity, DPFB derivatives could selectively and fast stain LDs in living cells, which was further confirmed by the co-localization imaging with the commercial HCS LipidTOX Deep Red Neutral Lipid Stain (Figure 6.18b). The strong fluorescence signals from LDs, with negligible background, were obtained for DPFB derivatives without washing, revealing their excellent washing-free staining performance. Moreover, after incubating the living zebrafish with DPFB derivatives, an intense orange fluorescence emerged from the lipid-rich yolk sac, demonstrating that DPFB derivatives could image the lipid-rich tissue in vivo (Figure 6.18c).

Most of the reported LDs, specific to AIEgens, focus on the performance of imaging; the multifunctional AIEgen for tracking the dynamics, metabolism, and functionalities of LDs is still rare. Recently, Zhao and co-workers developed a series of multifunctional AIEgens (Pyr-1 to Pyr-5) by integrating various functionalized units with the pyrazoline core (Figure 6.19) [76]. All Pyr probes have large ClogP values (6.516–7.820), which is much higher than those of BODIPY 493/503 (5.028) and Nile Red (4.618). Therefore, they can specifically accumulate in the LDs. Pyr probes displayed excellent biocompatibility and photostability, which endowed them with the capability for high-resolution 3D imaging of LDs. Meanwhile, the long-term tracking of lipid metabolism in live zebrafish was achieved by using Pyr probes.

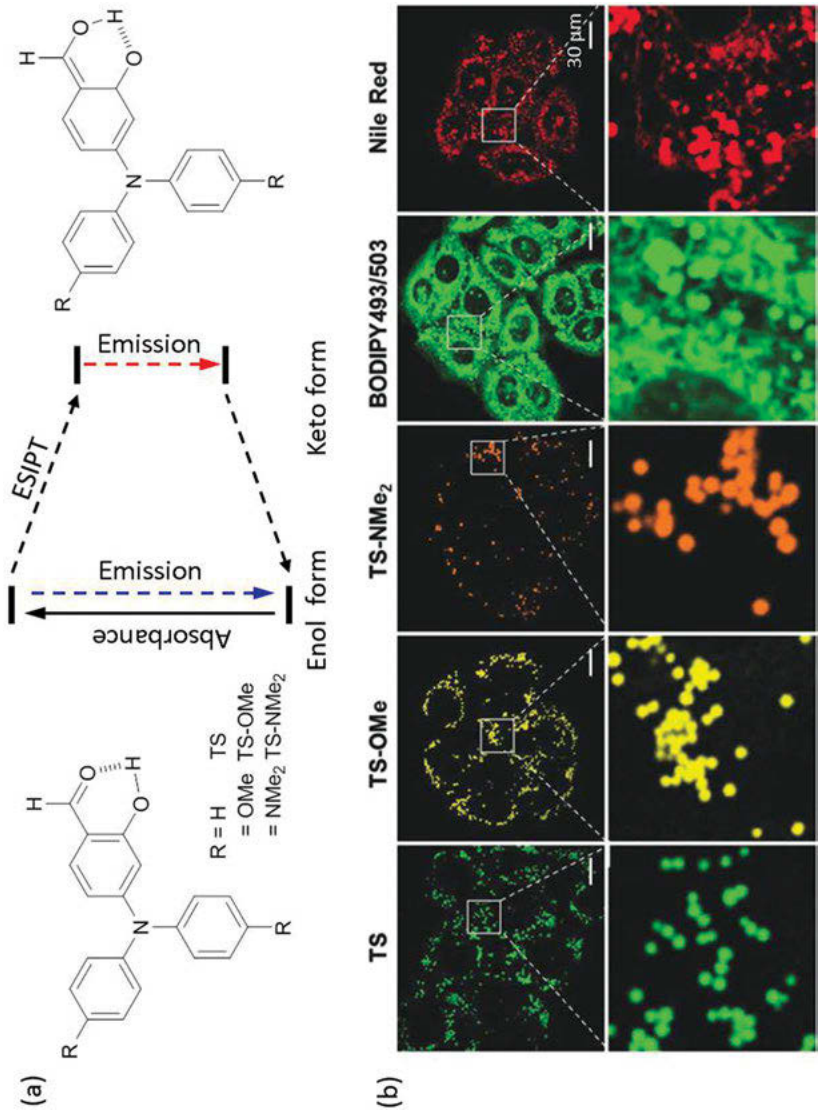


**Figure 6.17:** (a) Chemical structures of TS derivatives. (b) CLSM images of HeLa cells stained with TS derivatives, BODIPY493/503 and Nile Red in the absence of washing step. Copyright 2020, Wiley-VCH.

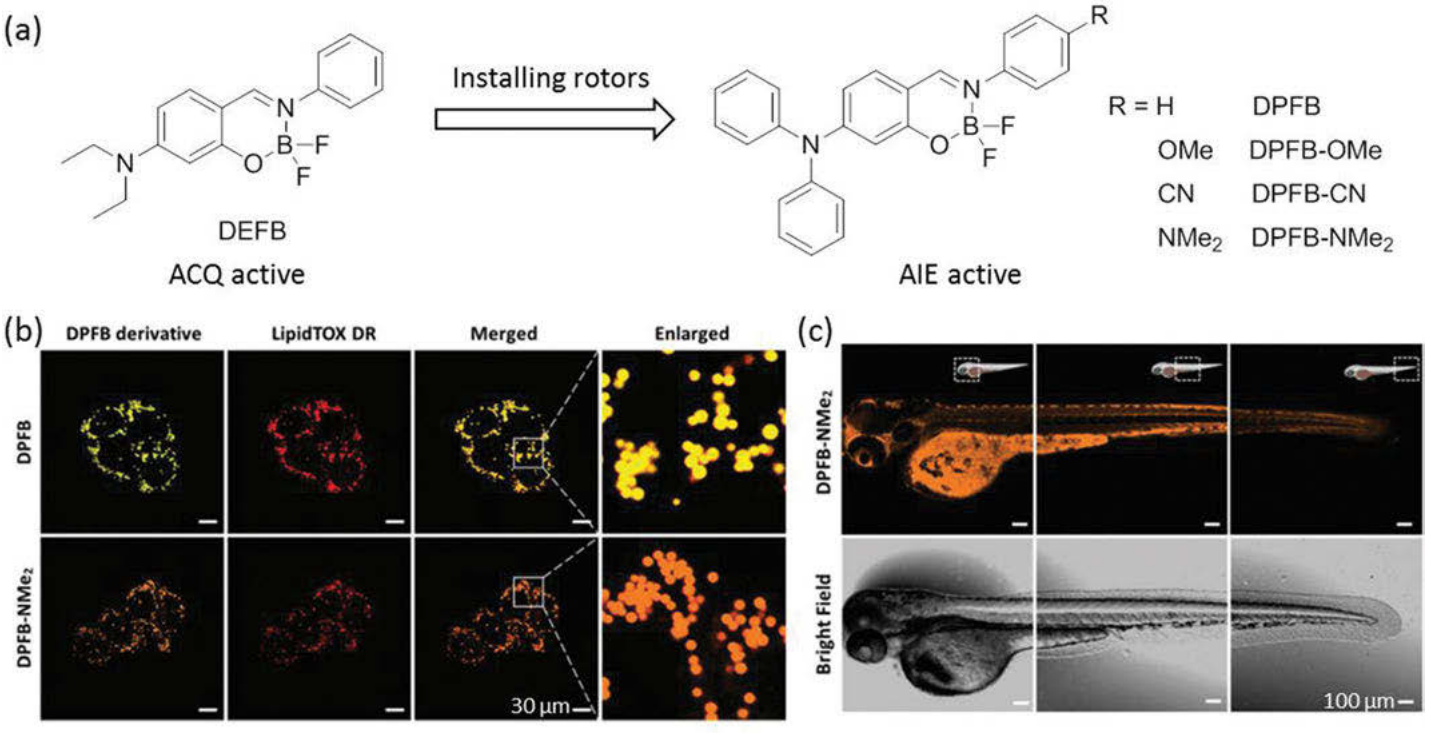


**Figure 6.18:** (a) Chemical structures of DEFB and DPFB derivatives. (b) Co-localization images of HeLa cells stained with DPFB derivatives and HCS LipidTOXt Deep Red Neutral Lipid Stain. (c) CLSM images of living zebrafish stained with DPFB-$NMe_2$. Copyright 2019, Royal Society of Chemistry.

Interestingly, Pyr-5 contains a diethylamino group that can be protonated in the acidic environment, accompanied by the emission color change from orange to blue. The protonation of Pyr-5 was able to migrate from LDs to mitochondria, and this intracellular migration was reversible when the intracellular pH changed between 5 and 7. In view of the nucleophile-based reactivity of the pentafluorophenyl units with the thiol group, Pyr probes were further explored to label the proteins associated with LDs.

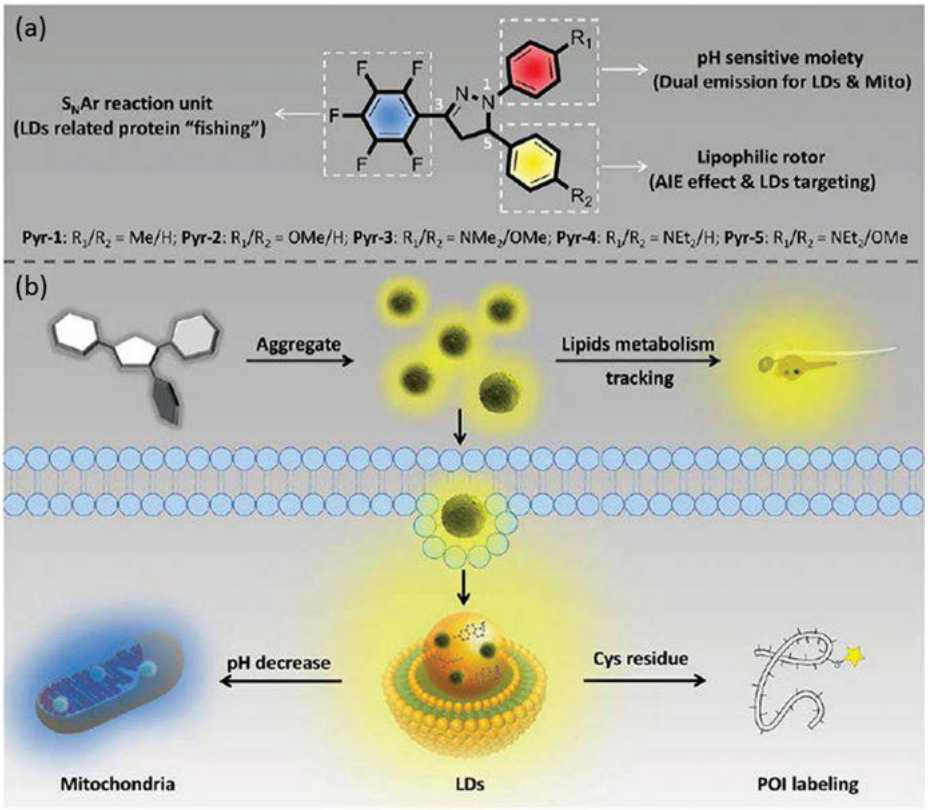


**Figure 6.19:** (a) Chemical structures of Pyr probes. (b) Illustration of bio-applications of Pyr probes. Copyright 2019, Royal Society of Chemistry.

Lipophagy is an important pathway to degrade excess and damaged LDs, which is mediated by the lysosome. An AIEgen TPA-LD was constructed to visualize the lipophagy process (Figure 6.20a) [77]. Thanks to the AIE effect, TPA-LD gave intense red emission in oil/water emulsion. Meanwhile, TPA-LD possesses high stability even in the presence of different interfering species. When the HepG2 cells were incubated with TPA-LD, the LDs could be selectively stained with a high Pearson's

co-localization coefficient of 0.91 between TPA-LD and commercial HCS LipidTOX Deep Red. TPA-LD exhibited better biocompatibility and photostability than BODIPY493/503. The process of LDs production and enlargement in cells was successfully monitored by employing TPA-LD. Meanwhile, the lipophagy process was visualized when the cells were co-stained with TPA-LD and LysoTracker. As shown in Figure 6.20b, the LDs and lysosomes presented distinct morphology initially. Prolonging the starvation time from 0 to 4 h, the size and number of LDs were gradually decreased, and the Pearson's co-localization coefficient between TPA-LD and LysoTracker increased from −0.03 to 0.46, indicating the presence of lipophagy process.

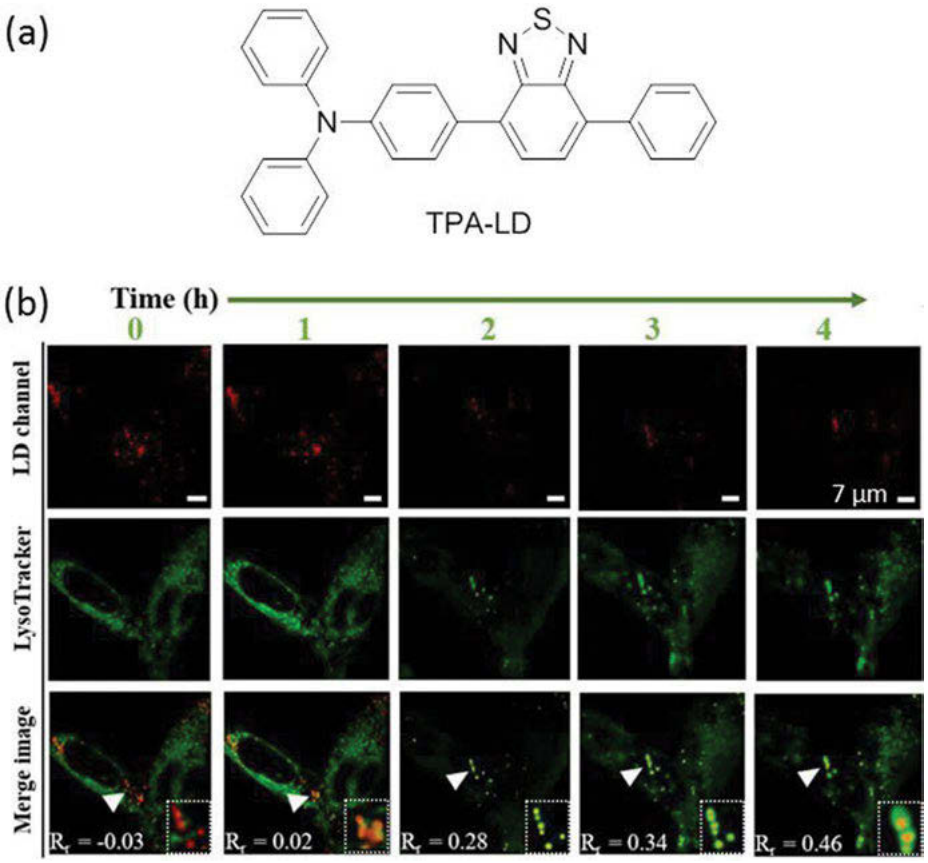


**Figure 6.20:** (a) Chemical structure of TPA-LD. (b) Fluorescence images of HepG2 cells stained with TPA-LD and LysoTracker in serum-free medium at different times. Copyright 2020, American Chemical Society.

## 6.5 Lysosome

Lysosome is a crucial organelle that decomposes the biological macromolecules, including proteins, nucleic acids, and polysaccharides. Lysosome-mediated autophagy is a vital process that eliminates the disabled organelles in cells. The lysosomal dysfunction would result in many serious diseases. Considering the acidic environment (pH of 4.5–5.0) in the lysosome, weak basic groups, including N,N-dimethylamino and morpholine as the targeting group, are selected to fabricate the fluorescent probes for lysosome [78].

An AIE probe with ESIPT process (AIE-LysoY) for lysosome imaging and autophagy process tracking was prepared by combining the morpholine unit with an AIEgen (Figure 6.21a) [79]. The cell viability was higher than 80% when the concentration was 15 μM, indicating that AIE-LysoY has low cytotoxicity. When the MCF-7 cells were treated with AIE-LysoY and LysoTracker Red (LTR), the yellow fluorescence from AIE-LysoY overlapped perfectly with the red fluorescence from LTR (overlapping coefficient is 0.90), confirming that AIE-LysoY was able to stain the lysosomes in living cells. Moreover, AIE-LysoY exhibited better contrast and affinity to lysosome than LTR. The higher working concentration of AIE-LysoY led to excellent photostability, and helped AIE-LysoY to be used to monitor the autophagy process. HeLa cells were incubated with AIE-LysoY and then treated with rapamycin for different times to trigger the autophagy process. As shown in Figure 6.21b, along with the autophagy proceeding, the yellow spots increased and the new lysosomes were also lit up. Excessive amount of AIE-LysoY was also removed by the washing step. But, for LTR, the emission from lysosomes significantly reduced under the same conditions.

Based on the AIE-active building block of tricyano-methylene-pyridine (TCM), an AIEgen TCM-PI was developed to specifically stain the lysosome (Figure 6.22a) [80]. TCM-PI exhibited NIR emission (677 nm), with a large Stokes shift (162 nm), in an aqueous solution. TCM-PI could aggregate and give strong emission in the high viscosity environment due to the unique AIE effect. Upon illuminating with a Hg/Xe lamp, the half-life of 6.0 min was detected for TCM-PI, which was 1.6 and 17.1-fold than that of LTR and ICG, respectively, revealing better photostability of TCM-PI. A high Pearson's correlation coefficient (0.89) between TCM-PI and LTR was observed in the co-localization experiment, suggesting excellent lysosomal targeting of TCM-PI. Considering the excellent lysosome imaging property, TCM-PI was utilized to track the movement of lysosomes. When the HeLa cells were stained with TCM-PI and then treated with chloroquine to induce lysosome migration, an irregular movement of lysosomes was clearly visualized (Figure 6.22b). The high-fidelity and long-term tracking of the escaping process about the fluorescent drugs from lysosomes to nucleus was also successfully achieved by using TCM-PI.

Recently, organic thermally-activated delayed fluorescence (TADF) materials have received considerable attention in the field of time-resolved biological imaging due to their long-lived fluorescence [81]. A TADF material, PXZ-NI, was obtained by

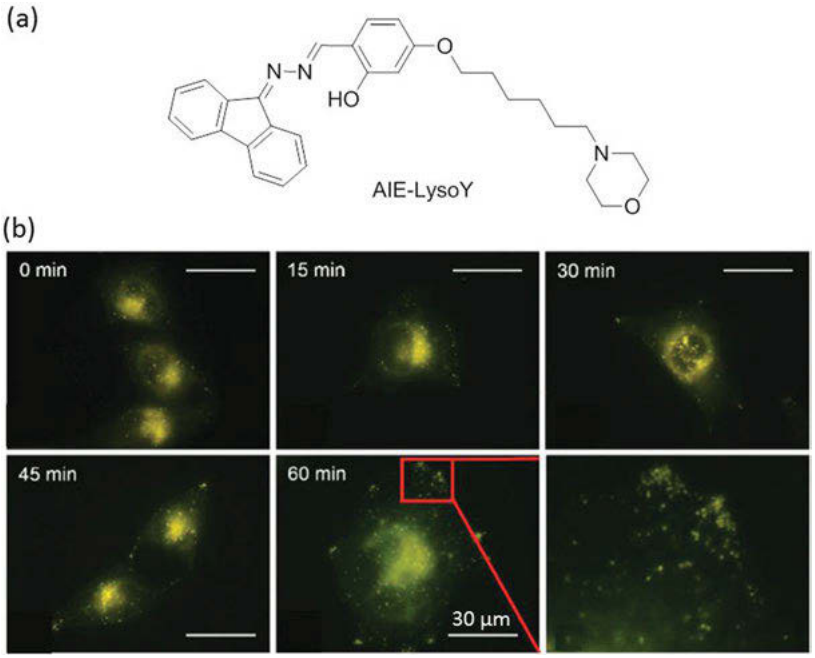


**Figure 6.21:** (a) Chemical structure of AIE-LysoY. (b) Fluorescence images of AIE-LysoY stained HeLa cells after treatment with rapamycin for different times. Copyright 2016, Wiley-VCH.

conjugating the electron-donor group of phenoxazine (PXZ) into the electron-acceptor group of 1,8-naphthalimide (NI). 2-Morpholine group, as the lysosome-targeting moiety was then introduced into PXZ-NI to give lysosome-targeting TADF material Lyso-PXZ-NI (Figure 6.23a) [82]. With the increasing water content in THF solution, the emission of Lyso-PXZ-NI was enhanced gradually, suggesting its typical AIE effect. Lyso-PXZ-NI showed very low cytotoxicity to cells even at a high concentration of 50 μM. When the HeLa cells were stained with both Lyso-PXZ-NI and LysoTracker green (LTG), it was clear that the signals of Lyso-PXZ-NI overlapped very well with that of LTG (Pearson's correlation coefficient is 0.92), demonstrating that Lyso-PXZ-NI specifically stained the lysosomes (Figure 6.23b). Furthermore, fluorescence lifetime imaging of Lyso-PXZ-NI was carried out by using the time-resolved fluorescence microscopy. After incubating HeLa cells with Lyso-PXZ-NI for 2 h, the long fluorescence lifetime signals (>180 ns) were detected. Compared to the fluorescence images, fluorescence lifetime images exhibited higher signal-to-noise ratios (Figure 6.23c).

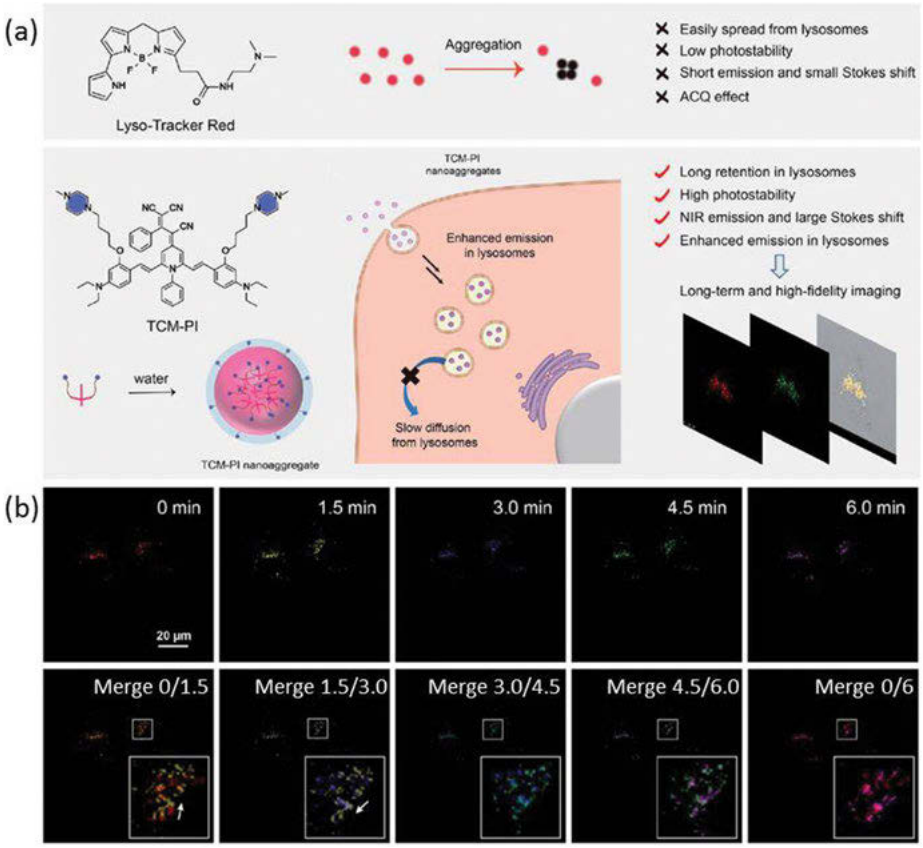


**Figure 6.22:** (a) Schematic illustration of lysosome stained by TCM-PI. (b) CLSM images of HeLa cells incubated with TCM-PI, followed by treating with chloroquine for different times. Copyright 2020, Royal Society of Chemistry.

## 6.6 Endoplasmic reticulum

Endoplasmic reticulum (ER) is the site for the synthesis of important biological macromolecules, including proteins, lipids, and sugars. The ER plays a vital role in biological processes such as cellular metabolism and the transport of signaling molecules [83, 84]. Additionally, the smooth ER has the function of detoxification. For example, the smooth ER in liver cells contains enzymes that can remove the fat-soluble waste and harmful substances from metabolism.

Liu and co-workers developed an ER-targeting AIE probe TPECA-ER by conjugating a TPE-based AIEgen with ER-specific peptide sequence of CFFKDEL (Figure 6.24a) [85]. The hydrophilic peptide of CFFKDEL endows the TPECA-ER with good solubility and weak emission in an aqueous solution. Once the TPECA-ER entered the cells and

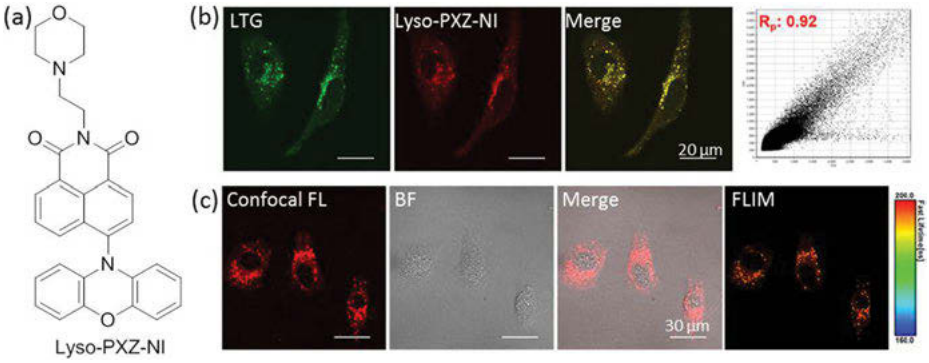


**Figure 6.23:** (a) Chemical structure of Lyso-PXZ-NI. (b) Co-localization images of Lyso-PXZ-NI and LTG. (c) Confocal and FLIM images of HeLa cells stained with Lyso-PXZ-NI. Copyright 2020, American Chemical Society.

targeted the ER, bright red emission was triggered due to the restriction of free intramolecular rotation. The high Pearson's correlation coefficient (0.95) with commercial ER tracker revealed that TPECA-ER is an excellent probe for ER (Figure 6.24b). In addition, almost no inhibition of cell growth was observed when the concentration of TPECA-ER was 6 μM whether under dark or with light irradiation, revealing its good biocompatibility. Meanwhile, it was observed that TPECA-ER possesses higher photostability than commercial ER tracker.

Tang and co-workers reported an AIE zwitterionic pyridinium salt CDPP-3$SO_3$ (Figure 6.25a) [86]. CDPP-3$SO_3$ could form spherical nanoaggregates with high emission at water fraction of 90%. When the cells were co-stained by CDPP-3$SO_3$ and commercial ER-Tracker Red, the merged image demonstrated that fluorescence from CDPP-3$SO_3$ overlapped well with that from ER-Tracker Red (Pearson's correlation factor = 0.85) (Figure 6.25b). An analogue of CDPP-BzBr, with one positive charge, accumulated in the mitochondria rather than in ER, suggesting that the zwitterionic property of CDPP-3$SO_3$ is indispensable for ER targeting. It is reported that abundant phosphocholine cytidylyltransferase (CCT) exists on the ER membrane, which is an enzyme for regulating the synthesis of membrane phospholipid. The positive nature of the domain M region makes CCT bind to the negatively charged membrane of ER, which might provide an appropriate site to catch the CDPP-3$SO_3$ through efficient electrostatic interactions. CDPP-3$SO_3$ displayed minimal toxicity at its working concentration, suggesting that it could be used for long-term tracking of ER.

Zhu and co-workers developed an amphiphilic AIEgen QM-$SO_3$-ER through grafting the ER-targeting moiety of *p*-toluenesulfonamide into an amphiphilic AIE compound (Figure 6.26a) [87]. Taking advantage of its unique amphiphilic behavior, QM-$SO_3$-ER exhibited good solubility and dispersion in both hydrophilic and lipophilic systems with faint emission. After accumulating in ER, the AIE nature of the QM-$SO_3$-ER was activated and intense emission was observed. The special molecular structure

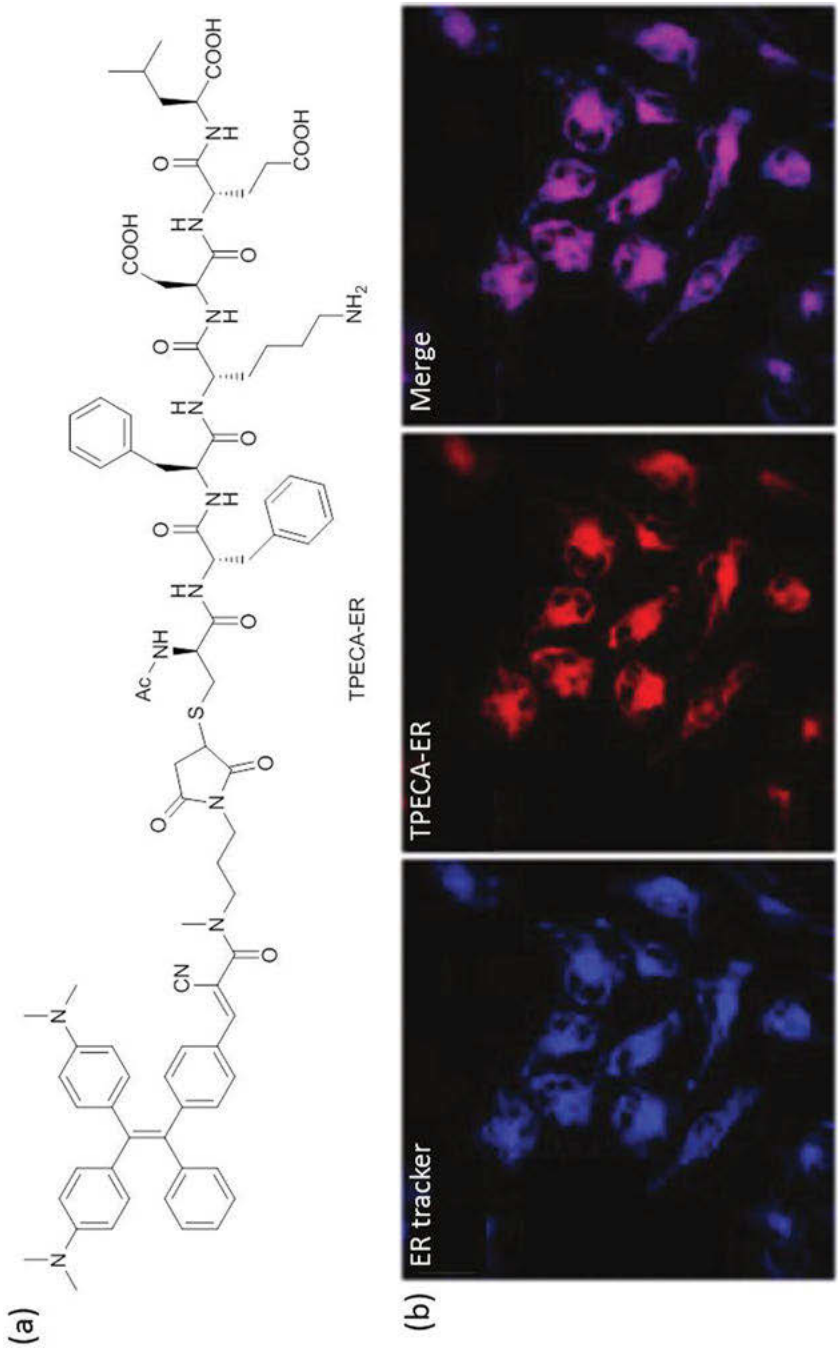


**Figure 6.24:** (a) Chemical structure of TPECA-ER. (b) Co-localization images of TPECA-ER and commercial ER tracker (ER Tracker Blue-White DPX). Copyright 2017, Royal Society of Chemistry.

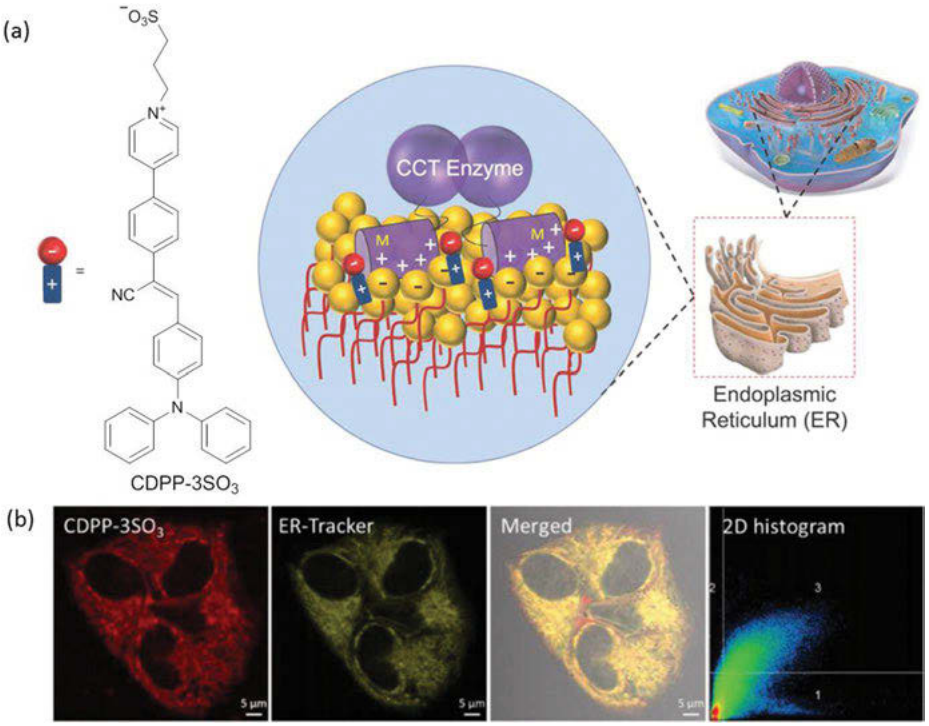


**Figure 6.25:** (a) Chemical structure of CDPP-3SO$_3$ and schematic representation of ER targeting by CDPP-3SO$_3$. (b) Co-localization images of CDPP-3SO$_3$ and ER-Tracker Red. Copyright 2020, Wiley-VCH.

endows QM-SO$_3$-ER with several advantages, such as washing-free behavior, super specificity, and high fidelity for ER imaging. As shown in Figure 6.26b, after the cells were incubated with QM-SO$_3$-ER and commercial ER-tracker Red for varying times, almost no fluorescence appeared for QM-SO$_3$-ER at 10 min. With increasing incubation time, QM-SO$_3$-ER gradually aggregated in ER and gave distinct fluorescence with low background at 60 min. However, the ER-tracker Red stained the ER at 10 min and gave a significant background fluorescence around the cells. The signal-to-noise ratio of QM-SO$_3$-ER enhanced from 18.32 to 15436.33, while the value for ER-tracker Red did not change (from 5.36 to 7.28) when the incubation time was prolonged from 10 to 60 min.

## 6.7 Golgi apparatus

Golgi apparatus is one of the components of the intimal system in eukaryotic cells, which takes part in the process of cell secretion and intracellular substances transportation [88]. The morphological change of Golgi apparatus is closely related to

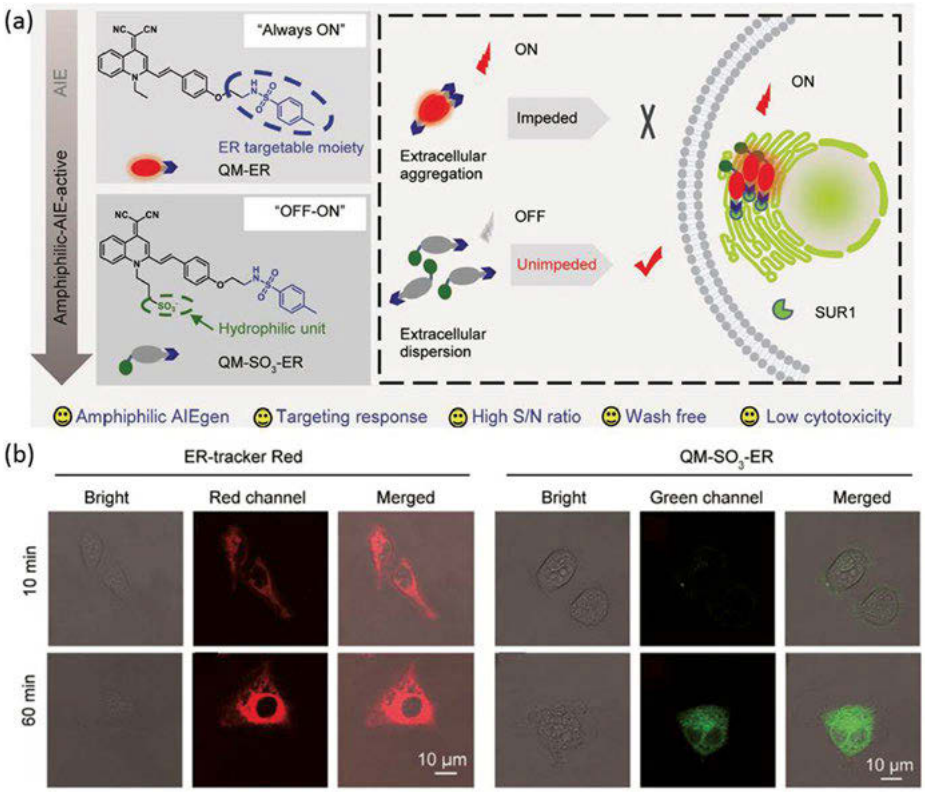


**Figure 6.26:** (a) Illustration of the structures and bio-applications of QM-$SO_3$-ER. (b) HeLa cells incubated with ER-tracker Red and QM-$SO_3$-ER for different time. Copyright 2020, Oxford University Press.

external stimulation, which provides key information for disease diagnosis. However, due to the lack of targeting moiety, the fluorescent probe for specific Golgi apparatus staining is still rare.

By introducing the 2′,3′-O-isopropylideneadenosine (Ade) group, an AIE probe (TPE-Ade), based on the TPE group was developed by Zhao and co-workers (Figure 6.27a) [89]. TPE-Ade exhibited low cytotoxicity when the concentration was less than 10 μM. When the HL-7402 cells were incubated with TPE-Ade and Golgi-Tracker Red (a commercially available probe for Golgi apparatus), a perfect overlap between the fluorescence of TPE-Ade and that of Golgi-Tracker Red was obtained while the Pearson's correlation coefficient reached up to 0.86 (Figure 6.27b). The appropriate hydrophobicity and lipophilicity of TPE-Ade enabled it to aggregate in the Golgi apparatus and thus exhibited intense emission. Clearly, TPE-Ade can serve as an ideal probe for Golgi apparatus imaging.

Li and co-workers reported NIR emissive probes based on a supramolecular co-assembly, in which, dodecyl-modified sulfonatocalix-[4]arene (SC4AD) was the

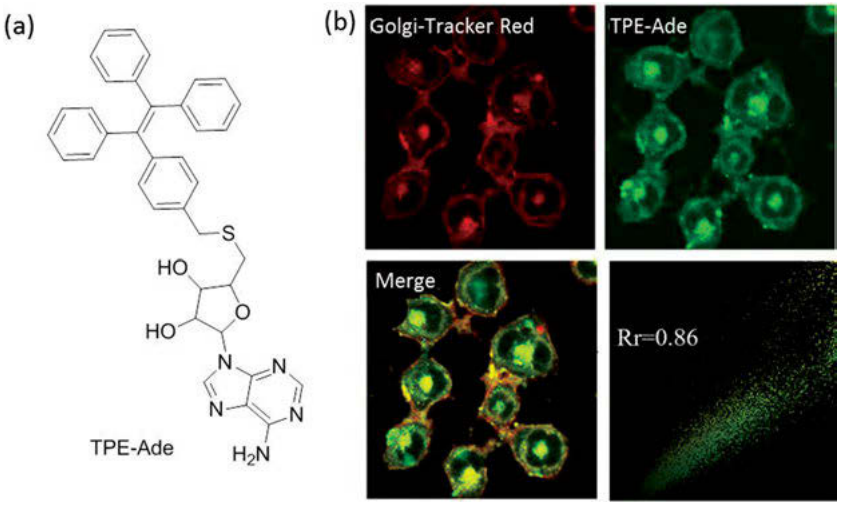


**Figure 6.27:** (a) Chemical structure of TPE-Ade. (b) Co-localization images of TPE-Ade with Golgi-Tracker Red in HL-7402 cells. Copyright 2021, Elsevier.

lower-rim and naphthyl-1,8-diphenyl pyridinium derivative (NPS) was employed for light-harvesting (Figure 6.28a,b) [90]. NPS exhibited weak emission at 593 nm, but gave strong emission at 550 nm, after forming supramolecular nanoparticles with SC4AD. Nile blue (NiB) was then loaded into the above nanoparticles, resulting in a NIR emissive light-harvesting system (675 nm). The high antenna effect of 33.1 at a donor/acceptor ratio of 250:1 was achieved in the NPS-SC4AD-NiB system. Interestingly, this efficient light-harvesting system was further applied for cell imaging. When the PC-3 cells were incubated with NPS-SC4AD-NiB for 4 h, the red emission appeared from the Golgi apparatus under the excitation of 405 nm. The co-staining experiments with NBD $C_6$-ceramide (a commercial probe for Golgi apparatus) confirmed that the NPS-SC4AD-NiB could specifically target the Golgi apparatus (Pearson's correlation coefficient of 0.90) (Figure 6.28c). After treating PC-3 cells with the cyclooxygenase-2 (COX-2), a biomarker in the Golgi apparatus of cancer cells, the emission of NiB increased, suggesting that NPS-SC4AD-NiB accumulated in the Golgi apparatus through interacting with COX-2.

## 6.8 Nucleus

The nucleus is the biggest organelle in the cell, which is the control center for cell inheritance and metabolism. The nucleic acids, including DNA and RNA, are primarily located in the nucleus [91]. The nucleus-targeting probes generally possess the capability to target the nucleoproteins or nucleic acids. DNA-targeted fluorescent

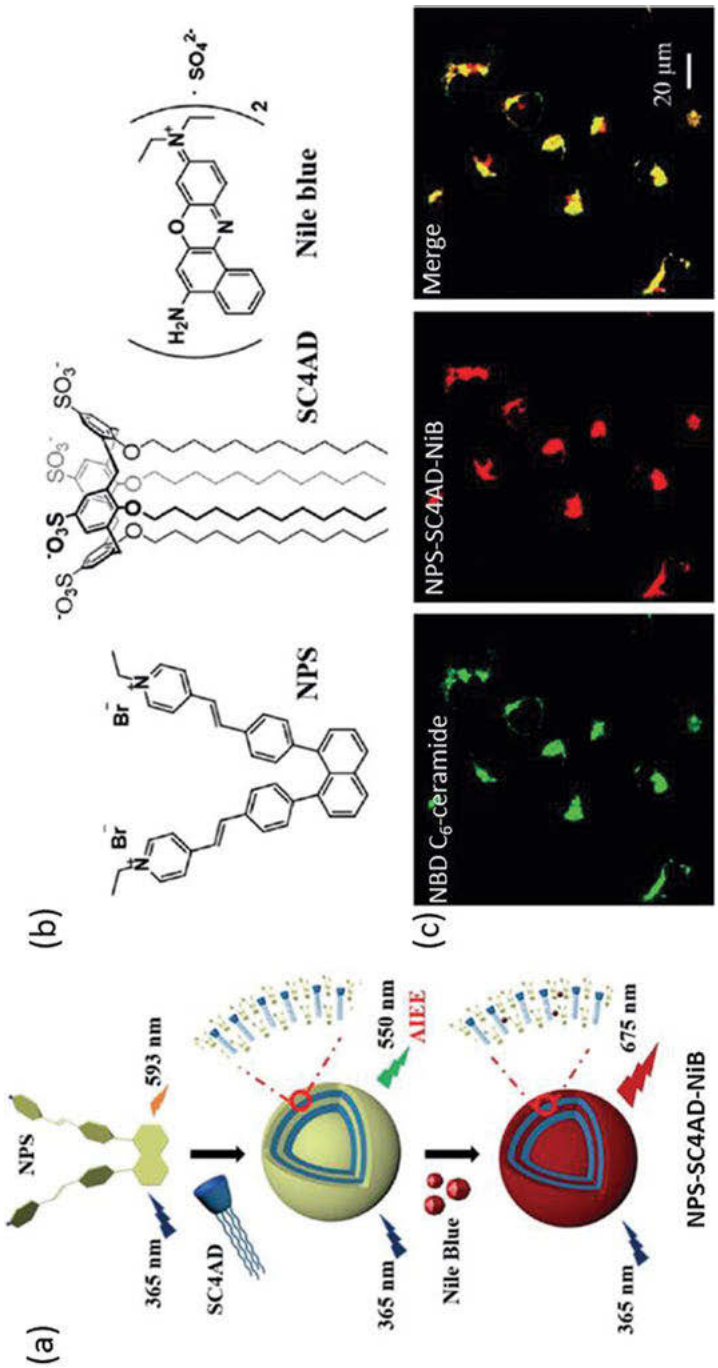


**Figure 6.28:** (a) Schematic illustration of the assembly process of the NPS-SC4AD-NiB. (b) The chemical structure of NPS, SC4AD and Nile blue. (c) CLSM images of PC-3 cells co-stained with NPS-SC4AD-NiB and NBD $C_6$-Ceramide. Copyright 2020, Wiley-VCH.

probes are divided into three categories: intercalating dyes (ethidium bromide, propidium iodide), minor-groove binders (DAPI, Hoechst dyes), and nucleic acid stains (acridine orange) [91, 92]. Due to the negatively-charged nature of RNA, the corresponding RNA-targeted fluorescent probes are positively charged [93].

Adapting the TPE-based imidazolium salts as a cationic unit and alkyl carboxylate as counteranion, a fluorescent probe (TPEI-C8) with AIE feature was fabricated (Figure 6.29a) [94]. TPEI-C8 could form fluorescent vesicles in an aqueous solution, with a mean diameter of 220 nm (Figure 6.29b). When the Hela cells were incubated with TPEI-C8 for 4 h, TPEI-C8 crossed the cell membrane and entered the nucleus with bright blue emission, which was further confirmed by the co-staining experiment with the red nucleus tracker of Reddot1 (Pearson's correlation coefficient = 0.83) (Figure 6.29c). The multiple imidazolium cations and octanoate anions of TPEI-C8 provide the appropriate electrophoretic force and lipophilicity, which might be the main reason for its precise imaging of the nucleus. Additionally, the high survival rate of HeLa cells (>85%) was observed for TPEI-C8 even when the concentration was as high as 80 μM, indicative of its great biocompatibility.

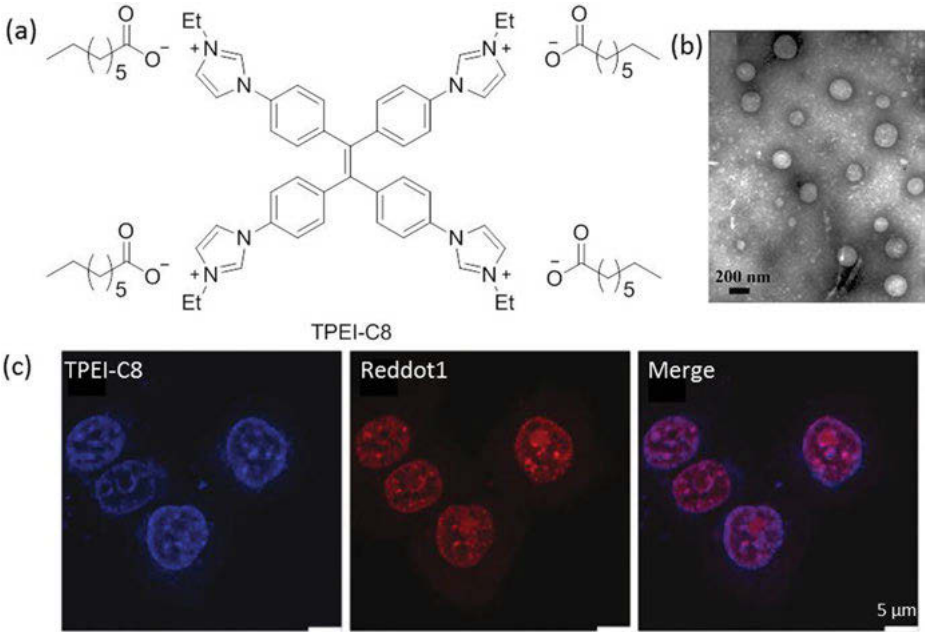


**Figure 6.29:** (a) Chemical structure of TPEI-C8. (b) TEM micrograph of TPEI-C8 in aqueous solution. (c) CLSM images of HeLa cells stained with TPEI-C8 and Reddot1. Copyright 2018, Royal Society of Chemistry.

Zeng and co-workers designed and synthesized a water-soluble cationic molecule (DPMPB), based on the imidazole unit (Figure 6.30a) [95]. DPMPB was weakly emissive in an aqueous solution, owing to its hydrophilic nature. With the increase of

the THF fraction, emission of DPMPB was enhanced, revealing its AIE effect. Meanwhile, the SEM image demonstrated that DPMPB formed the nanoparticles (DPMPB-FONs) in an aqueous solution, with an average diameter of 219 nm (Figure 6.30b). The presence of cationic pyridinium makes DPMPB-FONs positively charged. When different cancer cells (C666-1, CNE2, AGS) and normal GES-1 cells were incubated with DPMPB-FONs, respectively, the intense fluorescent signals mainly came from C666-1, CNE2, and AGS cells, while faint emission stemmed from the GES-1 cells. Furthermore, the fluorescence of DPMPB-FONs in cancer cells overlapped perfectly with that of DAPI, manifesting that DPMPB-FONs could selectively target the nucleus of cancer cells (Figure 6.30c). Even upon the indication time for 112 h, the morphology change of nucleus was negligible, indicating low cytotoxicity and long-term tracing capability of DPMPB-FONs. In addition, DPMPB-FONs could differentiate the clinic breast cancer tissues over the para-carcinoma tissues and image the breast cancer tissues, with a penetration depth of 100 μm under the two-photon excitation.

ASCP is an AIE-active pyridinium salt, which could simultaneously stain the mitochondria and nucleus with different emissions (Figure 6.31a) [96]. Owing to the typical TICT effect, the emission of ASCP was red-shifted with increasing solvent polarity. Low toxicity was observed for ASCP at the concentration of 10 μM, suggestive of its good biocompatibility. After incubating HeLa cells with ASCP, it is interesting that the orange emission came from the mitochondria while the red emission was located in the nucleolus of cells. The red-shifted emission in nucleolus could be caused by the more co-planar conformation of ASCP as well as the polar environment of nucleolus. In order to investigate the mechanism of nucleus targeting, the ASCP pre-stained cells were fixed and treated with deoxyribonuclease (DNase) and ribonuclease (RNase). The red fluorescence remained in cells treated with DNase, but disappeared in the cells treated with RNase, indicating that the nucleolus imaging of ASCP was attributed to the efficient interactions with RNAs. After optimizing the collecting conditions, mitochondria and nucleolus could be visualized individually in different channels under 405 and 560 nm light excitation, respectively (Figure 6.31b). Additionally, only a 5% signal loss was observed after 50 scans under the 560 nm light irradiation. Conversely, the fluorescent signal almost completely disappeared for the commercial SYTO RNAselect after 15 scans under the 488 nm laser irradiation (Figure 6.31c). The above results implied that ASCP possesses higher photostability than SYTO RNAselect.

## 6.9 Conclusions and perspectives

In this chapter, recent applications of AIEgens for subcellular organelles imaging and related biological process monitoring have been summarized and discussed. Compared to the conventional fluorescent probes, AIEgens exhibit distinct advantages

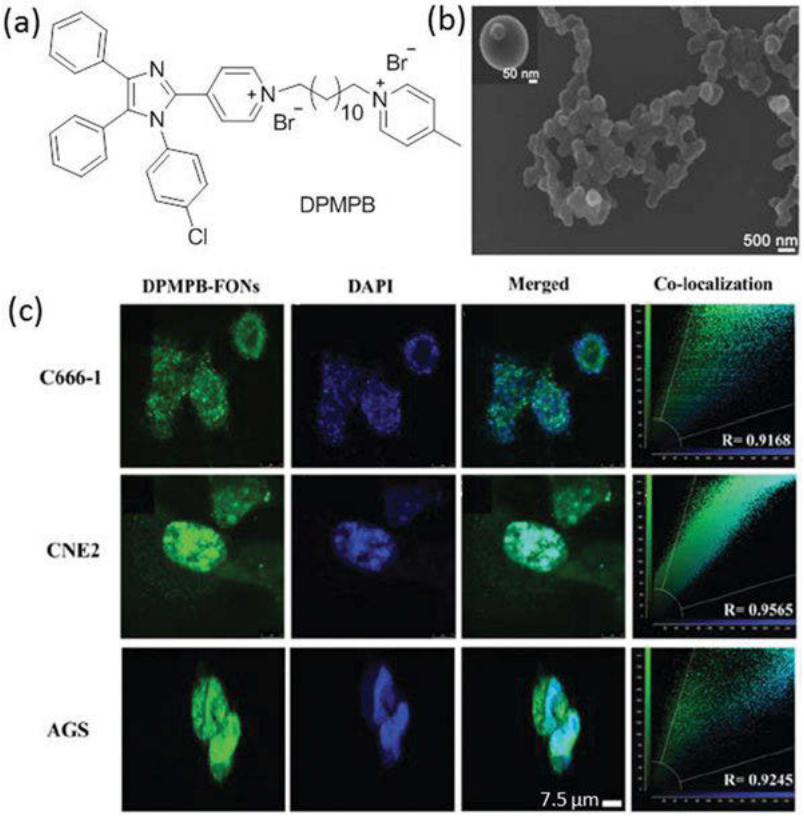


**Figure 6.30:** (a) Chemical structure of DPMPB. (b) SEM image of DPMPB-FONs. (c) CLSM images of different cancer cells co-stained with DPMPB-FONs and DAPI. Copyright 2018, Royal Society of Chemistry.

such as bright emission, high specificity, strong resistance to photobleaching, and long-term retention ability. The high photostability and biocompatibility enable AIE probes to track the morphology and movements of organelles, as well as the related biological processes. Future work about AIEgens for organelle imaging will focus on the development of multifunctional AIE probes. For example, some excellent organelle-targeted AIEgens not only stain the cancer cells over the normal cells, but also generate reactive oxygen species under light illumination. These multifunctional AIE probes can act as the theranostic reagent for precisely imaging-guided photodynamic cancer therapy [97–100]. In addition, two probes with separated emissions are usually employed to stain two different organelles to investigate their interactions. It is highly desirable to develop smart AIE probes to target dual organelles simultaneously with different emission colors and track organelle interactions. We strongly believe AIEgens will offer new insights in the areas of organelle imaging and related biological interaction tracking.

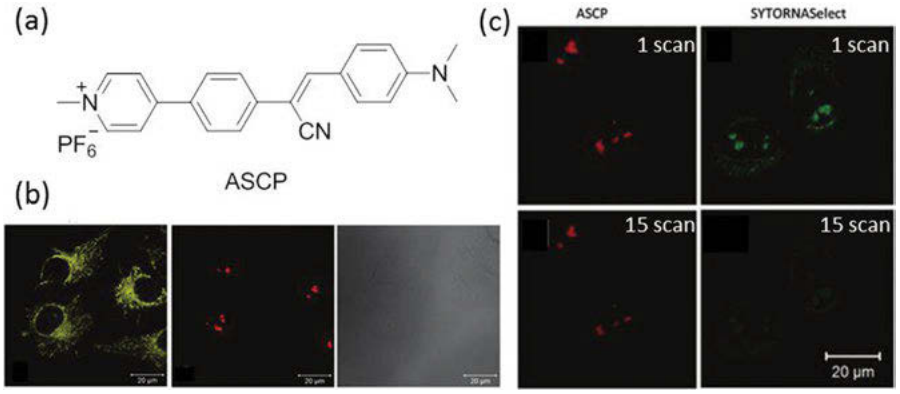


**Figure 6.31:** (a) Chemical structure of ASCP. (b) CLSM images of HeLa cells stained with ASCP and collected in different channels. (c) CLSM images of HeLa cells stained with ASCP and SYTO RNASelect acquired under continuous excitation. Copyright 2016, Royal Society of Chemistry.

# References

[1] Green DR, Reed JC, Mitochondria and apoptosis, Science, 1998, 281, 1309–1312.
[2] Settembre C, Fraldi A, Medina DL, Ballabio A, Signals from the lysosome: A control centre for cellular clearance and energy metabolism, Nat Rev Mol Cell Biol, 2013, 14, 283–296.
[3] Martin S, Parton RG, Lipid droplets: A unified view of a dynamic organelle, Nat Rev Mol Cell Biol, 2006, 7, 373–378.
[4] Mizushima N, Komatsu M, Autophagy: Renovation of cells and tissues, Cell, 2011, 147, 728–741.
[5] Chan DC, Mitochondria: Dynamic organelles in disease, aging, and development, Cell, 2006, 125, 1241–1252.
[6] Walther TC, Farese RV, Lipid droplets and cellular lipid metabolism, Annu Rev Biochem, 2012, 81, 687–714.
[7] Ohta S, A multi-functional organelle mitochondrion is involved in cell death, proliferation and disease, Curr Med Chem, 2003, 10, 2485–2494.
[8] Mizushima N, Levine B, Cuervo AM, Klionsky DJ, Autophagy fights disease through cellular self-digestion, Nature, 2008, 451, 1069–1074.
[9] Camoes F, Bonekamp NA, Delille HK, Schrader M, Organelle dynamics and dysfunction: A closer link between peroxisomes and mitochondria, J Inherit Metab Dis, 2009, 32, 163–180.
[10] Kowada T, Maeda H, Kikuchi K, BODIPY-based probes for the fluorescence imaging of biomolecules in living cells, Chem Soc Rev, 2015, 44, 4953–4972.
[11] Liu J, Bu W, Shi J, Chemical design and synthesis of functionalized probes for imaging and treating tumor hypoxia, Chem Rev, 2017, 117, 6160–6224.
[12] Zhu H, Fan J, Du J, Peng X, Fluorescent probes for sensing and imaging within specific cellular organelles, Acc Chem Res, 2016, 49, 2115–2126.
[13] Ma X, Gong N, Zhong L, Sun J, Liang XJ, Future of nanotherapeutics: Targeting the cellular sub-organelles, Biomaterials, 2016, 97, 10–21.

[14] Xu W, Zeng Z, Jiang JH, Chang YT, Yuan L, Discerning the chemistry in individual organelles with small-molecule fluorescent probes, Angew Chem Int Ed, 2016, 55, 13658–13699.
[15] Kobayashi H, Ogawa M, Alford R, Choyke PL, Urano Y, New strategies for fluorescent probe design in medical diagnostic imaging, Chem Rev, 2010, 110, 2620–2640.
[16] Chan J, Dodani SC, Chang CJ, Reaction-based small-molecule fluorescent probes for chemoselective bioimaging, Nat Chem, 2012, 4, 973–984.
[17] Guo Z, Park S, Yoon J, Shin I, Recent progress in the development of near-infrared fluorescent Probes for bioimaging applications, Chem Soc Rev, 2014, 43, 16–29.
[18] Mei J, Hong Y, Lam JWY, Qin A, Tang Y, Tang BZ, Aggregation-induced emission: The whole is more brilliant than the parts, Adv Mater, 2014, 26, 5429–5479.
[19] Luo J, Xie Z, Lam JWY, Cheng L, Chen H, Qiu C, Kwok HS, Zhan X, Liu Y, Zhu D, Tang BZ, Aggregation-induced emission of 1-methyl-1,2,3,4,5-pentaphenylsilole, Chem Commun, 2001, 1740–1741.
[20] Mei J, Leung NLC, Kwok RTK, Lam JWY, Tang BZ, Aggregation-induced emission: Together we shine, united we soar!, Chem Rev, 2015, 115, 11718–11940.
[21] Hong Y, Lam JWY, Tang BZ, Aggregation-induced emission: Phenomenon, mechanism and applications, Chem Commun, 2009, 4332–4353.
[22] Hong Y, Lam JWY, Tang BZ, Aggregation-induced emission, Chem Soc Rev, 2011, 40, 5361–5388.
[23] Wang D, Tang BZ, Aggregation-induced emission luminogens for activity-based sensing, Acc Chem Res, 2019, 52, 2559–2570.
[24] Ding D, Li K, Liu B, Tang BZ, Bioprobes based on AIE fluorogens, Acc Chem Res, 2013, 46, 2441–2453.
[25] Liang J, Tang BZ, Liu B, Specific light-up bioprobes based on AIEgen conjugates, Chem Soc Rev, 2015, 44, 2798–2811.
[26] Hu F, Liu B, Organelle-specific bioprobes based on fluorogens with aggregation-induced emission (AIE) characteristics, Org Biomol Chem, 2016, 14, 9931–9944.
[27] Chen S, Wang H, Hong Y, Tang BZ, Fabrication of fluorescent nanoparticles based on AIE luminogens (AIE dots) and their applications in bioimaging, Mater Horiz, 2016, 3, 283–293.
[28] Zhang X, Wang K, Liu M, Zhang X, Tao L, Chen Y, Wei Y, Polymeric AIE-based nanoprobes for biomedical applications: Recent advances and perspectives, Nanoscale, 2015, 7, 11486–11508.
[29] Qian J, Tang BZ, AIE luminogens for bioimaging and theranostics: From organelles to animals, Chem, 2017, 3, 56–91.
[30] Mei J, Huang Y, Tian H, Progress and trends in AIE-based bioprobes: A brief overview, ACS Appl Mater Interfaces, 2018, 10, 12217–12261.
[31] Gu X, Kwok RTK, Lam JWY, Tang BZ, AIEgens for biological process monitoring and disease theranostics, Biomaterials, 2017, 115, 115–135.
[32] Cai X, Liu B, Aggregation-induced emission: Recent advances in materials and biomedical applications, Angew Chem Int Ed, 2020, 59, 9868–9886.
[33] Song N, Xiao P, Ma K, Kang M, Zhu W, Huang J, Wang D, Tang BZ, Recent advances of AIEgens for targeted imaging of subcellular organelles, Chem Res Chinese Universities, 2021, 37, 52–65.
[34] Huang X, Zhang R, Chen C, Kwok RTK, Tang BZ, Wash-free detection and bioimaging by AIEgens, Mater Chem Front, 2021, 5, 723–743.
[35] Yan L, Zhang Y, Xu B, Tian W, Fluorescent nanoparticles based on AIE fluorogens for bioimaging, Nanoscale, 2016, 8, 2471–2487.
[36] Mueller P, Rudin DO, Tien H, Wescott WC, Reconstitution of cell membrane structure in vitro and its transformation into an excitable system, Nature, 1962, 194, 979–980.

[37] Sezgin E, Levental I, Mayor S, Eggeling C, The mystery of membrane organization: Composition, regulation and roles of lipid rafts, Nat Rev Mol Cell Biol, 2017, 18, 361–374.
[38] Zhao N, Li Y, Yin W, Zhuang J, Jia Q, Wang Z, Li N, Controllable coumarin-based NIR fluorophores: Selective subcellular imaging, cell membrane potential indication, and enhanced photodynamic therapy, ACS Appl Mater Interfaces, 2020, 12, 2076–2086.
[39] Zhang W, Huang Y, Chen Y, Zhao E, Hong Y, Chen S, Lam JWY, Chen Y, Hou J, Tang BZ, Amphiphilic tetraphenylethene-based pyridinium salt for selective cell-membrane imaging and room-light-induced special reactive oxygen species generation, ACS Appl Mater Interfaces, 2019, 11, 10567–10577.
[40] Jiang QY, Lai LH, Shen J, Wang QQ, Xu FJ, Tang GP, Gene delivery to tumor cells by cationic polymeric nanovectors coupled to folic acid and the cell-penetrating peptide octaarginine, Biomaterials, 2011, 32, 7253–7262.
[41] Liu M, Li ZH, Xu FJ, Lai LH, Wang QQ, Tang GP, Yang WT, An oligopeptide ligand-mediated therapeutic gene nanocomplex for liver cancer-targeted therapy, Biomaterials, 2012, 33, 2240–2250.
[42] Li Y, Wu Y, Chang J, Chen M, Liu R, Li F, A bioprobe based on aggregation induced emission (AIE) for cell membrane tracking, Chem Commun, 2013, 49, 11335–11337.
[43] Zhang C, Jin S, Yang K, Xue X, Li Z, Jiang Y, Chen WQ, Dai L, Zou G, Liang XJ, Cell membrane tracker based on restriction of intramolecular rotation, ACS Appl Mater Interfaces, 2014, 6, 8971–8975.
[44] Shi L, Liu YH, Li K, Sharma A, Yu KK, Ji MS, Li LL, Zhou Q, Zhang H, Kim JS, Yu XQ, An AIE-based probe for rapid and ultrasensitive imaging of plasma membranes in biosystems, Angew Chem Int Ed, 2020, 59, 9962–9966.
[45] Zheng Y, Ding Y, Ren J, Xiang Y, Shuai Z, Tong A, Simultaneously and selectively imaging a cytoplasm membrane and mitochondria using a dual-colored aggregation-induced emission probe, Anal Chem, 2020, 92, 14494–14500.
[46] Zhang W, Yu CYY, Kwok RTK, Lam JWY, Tang BZ, A photostable AIE luminogen with near infrared emission for monitoring morphological change of plasma membrane, J Mater Chem B, 2018, 6, 1501–1507.
[47] Zhang Y, Yan Y, Xia S, Wan S, Steenwinkel TE, Medford J, Durocher E, Luck RL, Werner T, Liu H, Cell membrane-specific fluorescent probe featuring dual and aggregation-induced emissions, ACS Appl Mater Interfaces, 2020, 12, 20172–20179.
[48] Perry SW, Norman JP, Barbieri J, Brown EB, Gelbard HA, Mitochondrial membrane potential probes and the proton gradient: A practical usage guide, BioTechniques, 2011, 50, 98–115.
[49] Luo S, Zhang E, Su Y, Cheng T, Shi C, A review of NIR dyes in cancer targeting and imaging, Biomaterials, 2011, 32, 7127–7138.
[50] Zhao Z, Chan PS, Li H, Wong KL, Wong RNS, Mak NK, Zhang J, Tam HL, Kwong DWJ, Wong WK, Highly selective mitochondria-targeting amphiphilic silicon(IV) phthalocyanines with axially ligated rhodamine B for photodynamic therapy, Inorg Chem, 2011, 51, 812–821.
[51] Leung CWT, Hong Y, Chen S, Zhao E, Lam JWY, Tang BZ, A photostable AIE luminogen for specific mitochondrial imaging and tracking, J Am Chem Soc, 2013, 135, 62–65.
[52] Zhao N, Li M, Yan Y, Lam JWY, Zhang YL, Zhao YS, Wong KS, Tang BZ, A tetraphenylethene-substituted pyridinium salt with multiple functionalities: Synthesis, stimuli-responsive emission, optical waveguide and specific mitochondrion imaging, J Mater Chem C, 2013, 1, 4640–4646.
[53] Li N, Liu YY, Li Y, Zhuang JB, Cui RR, Gong Q, Zhao N, Tang BZ, Fine tuning of emission behavior, self-assembly, anion sensing, and mitochondria targeting of pyridinium-functionalized tetraphenylethene by alkyl chain engineering, ACS Appl Mater Interfaces, 2018, 10, 24249–24257.

[54] Situ B, Chen S, Zhao E, Leung CWT, Chen Y, Hong Y, Lam JWY, Wen Z, Liu W, Zhang W, Zheng L, Tang BZ, Real-time imaging of cell behaviors in living organisms by a mitochondria-targeting AIE fluorogen, Adv Funct Mater, 2016, 26, 7132–7138.
[55] Zhang W, Kwok RTK, Chen Y, Chen S, Zhao E, Yu CYY, Lam JWY, Zheng Q, Tang BZ, Real-time monitoring of the mitophagy process by a photostable fluorescent mitochondrion specific bioprobe with AIE characteristics, Chem Commun, 2015, 51, 9022–9025.
[56] Song Z, Zhang W, Jiang M, Sung HHY, Kwok RTK, Nie H, Williams ID, Liu B, Tang BZ, Synthesis of imidazole-based aiegens with wide color tunability and exploration of their biological applications, Adv Funct Mater, 2016, 26, 824–832.
[57] Perry SW, Norman JP, Barbieri J, Brown EB, Gelbard HA, Mitochondrial membrane potential probes and the proton gradient: A practical usage guide, BioTechniques, 2011, 50, 98–115.
[58] Zhao N, Chen S, Hong Y, Tang BZ, A red emitting mitochondria-targeted AIE probe as an indicator for membrane potential and mouse sperm activity, Chem Commun, 2015, 51, 13599–13602.
[59] Li J, Kwon N, Jeong Y, Lee S, Kim G, Yoon J, Aggregation-induced fluorescence probe for monitoring membrane potential changes in mitochondria, ACS Appl Mater Interfaces, 2018, 10, 12150–12154.
[60] Gandre-Babbe S, Bliek AM, The novel tail-anchored membrane protein Mff controls mitochondrial and peroxisomal fission in mammalian cells, Mol Biol Cell, 2008, 19, 2402–2412.
[61] Gui C, Zhao E, Kwok RTK, Leung ACS, Lam JWY, Jiang M, Deng H, Cai Y, Zhang W, Su H, Tang BZ, AIE-active theranostic system: Selective staining and killing of cancer cells, Chem Sci, 2017, 8, 1822–1830.
[62] Jiang M, Gu X, Kwok RTK, Li Y, Sung HHY, Zheng X, Zhang Y, Lam JWY, Williams ID, Huang X, Wong KS, Tang BZ, Multifunctional AIEgens: Ready synthesis, tunable emission, mechanochromism, mitochondrial, and bacterial imaging, Adv Funct Mater, 2018, 28, 1704589.
[63] Chen LB, Mitochondrial membrane potential in living cells, Annu Rev Cell Biol, 1988, 4, 155–181.
[64] Hu F, Cai X, Manghnani PN, Kenry WW, Liu B, Multicolor monitoring of cellular organelles by single wavelength excitation to visualize the mitophagy process, Chem Sci, 2018, 9, 2756–2761.
[65] Jr HT, Sedgwick AC, Han HH, Sen S, Chen GR, Zang Y, Sessler JL, James TD, Li J, He XP, Fluorescent probes for the imaging of lipid droplets in live cells, Coord Chem Rev, 2021, 427, 213577.
[66] Fam TK, Klymchenko AS, Collot M, Recent advances in fluorescent probes for lipid droplets, Materials, 2018, 11, 1768.
[67] Wang E, Zhao E, Hong Y, Lam JWY, Tang BZ, A highly selective AIE fluorogen for lipid droplet imaging in live cells and green algae, J Mater Chem B, 2014, 2, 2013–2019.
[68] Kang M, Gu X, Kwok RTK, Leung CWT, Lam JWY, Li F, Tang BZ, A near-infrared AIEgen for specific imaging of lipid droplets, Chem Commun, 2016, 52, 5957–5960.
[69] Demchenko AP, Tang KC, Chou PT, Excited-state proton coupled charge transfer modulated by molecular structure and media polarization, Chem Soc Rev, 2013, 42, 1379–1408.
[70] Padalkar VS, Seki S, Excited-state intramolecular proton-transfer (ESIPT)-inspired solid state emitters, Chem Soc Rev, 2016, 45, 169–202.
[71] Wang Z, Gui C, Zhao E, Wang J, Li X, Qin A, Zhao Z, Yu Z, Tang BZ, Specific fluorescence probes for lipid droplets based on simple AIEgens, ACS Appl Mater Interfaces, 2016, 8, 10193–10200.

[72] Yin W, Li Y, Li N, Yang W, An H, Gao J, Bi Y, Zhao N, Hybridization of triphenylamine and salicylaldehyde: A facile strategy to construct aggregation-induced emission luminogens with excited-state intramolecular proton transfer for specific lipid droplets and gram-positive bacteria imaging, Adv Opt Mater, 2020, 8, 1902027.
[73] Frath D, Azizi S, Ulrich G, Retailleau P, Ziessel R, Facile synthesis of highly fluorescent boranil complexes, Org Lett, 2011, 13, 3414–3417.
[74] Frath D, Azizi S, Ulrich G, Ziessel R. Chemistry on boranils: An entry to functionalized fluorescent dyes, Org Lett, 2012, 14, 4774–4777.
[75] Zhao N, Ma C, Yang W, Yin W, Wei J, Li N, Facile construction of boranil complexes with aggregation-induced emission characteristics and their specific lipid droplet imaging applications, Chem Commun, 2019, 55, 8494–8497.
[76] Zhao N, Li Y, Yang W, Zhuang J, Li Y, Li N, Multifunctional pyrazoline based AIEgens: Real-time tracking and specific protein "fishing" of lipid droplets, Chem Sci, 2019, 10, 9009–9016.
[77] Zhang X, Yuan L, Jiang J, Hu J, Rietz A, Cao H, Zhang R, Tian X, Zhang F, Ma Y, Zhang Z, Uvdal K, Hu Z, Light-up lipid droplets dynamic behaviors using a red-emitting fluorogenic probe, Anal Chem, 2020, 92, 3613–3619.
[78] Yuan L, Wang L, Agrawalla BK, Park SJ, Zhu H, Sivaraman B, Peng J, Xu QH, Chang YT, Development of targetable two-photon fluorescent probes to image hypochlorous acid in mitochondria and lysosome in live cell and inflamed mouse model, J Am Chem Soc, 2015, 137, 5930–5938.
[79] Leung CWT, Wang Z, Zhao E, Hong Y, Chen S, Kwok RTK, Leung ACS, Wen R, Li B, Lam JWY, Tang BZ, A lysosome-targeting AIEgen for autophagy visualization, Adv Healthc Mater, 2016, 5, 427–431.
[80] Liu Z, Wang Q, Zhu Z, Liu M, Zhao X, Zhu WH, AIE-based nanoaggregate tracker: High-fidelity visualization of lysosomal movement and drug escaping processes, Chem Sci, 2020, 11, 12755–12763.
[81] Xiong X, Song F, Wang J, Zhang Y, Xue Y, Sun L, Jiang N, Gao P, Tian L, Peng X, Thermally activated delayed fluorescence of fluorescein derivative for time-resolved and confocal fluorescence imaging, J Am Chem Soc, 2014, 136, 9590–9597.
[82] Qi S, Kim S, Nguyen VN, Kim Y, Niu G, Kim G, Kim SJ, Park S, Yoon J, Highly efficient aggregation-induced red-emissive organic thermally activated delayed fluorescence materials with prolonged fluorescence lifetime for time-resolved luminescence bioimaging, ACS Appl Mater Interfaces, 2020, 12, 51293–51301.
[83] Wang M, Kaufman RJ, The impact of the endoplasmic reticulum protein-folding environment on cancer development, Nat Rev Cancer, 2014, 14, 581–597.
[84] Lin W, Popko B, Endoplasmic reticulum stress in disorders of myelinating cells, Nat Neurosci, 2009, 12, 379–385.
[85] Zhang CJ, Cai X, Xu S, Zhan R, Jien W, Liu B, A light-up endoplasmic reticulum probe based on a rational design of red-emissive fluorogens with aggregation-induced emission, Chem Commun, 2017, 53, 10792–10795.
[86] Alam P, He W, Leung NLC, Ma C, Kwok RTK, Lam JWY, Sung HHY, Williams ID, Wong KS, Tang BZ, Red AIE-active fluorescent probes with tunable organelle specific targeting, Adv Funct Mater, 2020, 30, 1909268.
[87] Zhu Z, Wang Q, Liao H, Liu M, Liu Z, Zhang Y, Zhu W, Trapping endoplasmic reticulum with amphiphilic AIE-active sensor via specific interaction of ATP-sensitive potassium ($K_{ATP}$), Natl Sci Rev, 2020, nwaa198.
[88] Jackson CL, Mechanisms of transport through the Golgi complex, J Cell Sci, 2009, 122, 443–452.

[89] Xing X, Jia Y, Zhang J, Wu Z, Qin M, Li P, Feng X, Sun Y, Zhao G, A novel aggregation induced emission (AIE) fluorescence probe by combining tetraphenylethylene and 2′,3′-O-isopropylideneadenosine for localizing Golgi apparatus, Sensor Actuat B-Chem, 2021, 329, 129245.
[90] Chen XM, Cao Q, Bisoyi HK, Wang M, Yang H, Li Q, An efficient near-Infrared emissive artificial supramolecular light-harvesting system for imaging in the Golgi apparatus, Angew Chem Int Ed, 2020, 59, 10493–10497.
[91] Collas P, Aleström P, Rapid targeting of plasmid DNA to zebrafish embryo nuclei by the nuclear localization signal of SV40 T antigen, Mol Mar Biol Biotechnol, 1997, 6, 48–58.
[92] Darzynkiewicz Z, Traganos F, Kapuscinski J, Staiano-Coico L, Melamed MR, Accessibility of DNA in situ to various fluorochromes: Relationship to chromatin changes during erythroid differentiation of friend leukemia cells, Cytometry, 1984, 5, 355–363.
[93] Tan W, Wang K, Drake TJ, Molecular beacons, Curr Opin Chem Biol, 2004, 8, 547–553.
[94] Kong Q, Zhuang W, Li G, Jiang Q, Wang Y, Cation-anion interaction-directed formation of functional vesicles and their biological application for nucleus-specific imaging, New J Chem, 2018, 42, 9187–9192.
[95] Gao T, Wang S, Lv W, Liu M, Zeng H, Chen Z, Dong J, Wu Z, Feng X, Zeng W, A self-assembled nanoprobe for long-term cancer cell nucleus-specific staining and two-photon breast cancer imaging, Chem Commun, 2018, 54, 3578–3581.
[96] Yu CYY, Zhang W, Kwok RTK, Leung CWT, Lam JWY, Tang BZ, A photostable AIEgen for nucleolus and mitochondria imaging with organelle-specific emission, J Mater Chem B, 2016, 4, 2614–2619.
[97] Yang H, Zhuang J, Li N, Li Y, Zhu S, Hao J, Xin J, Zhao N, Efficient near-infrared photosensitizer with aggregation-induced emission characteristics for mitochondria-targeted and image-guided photodynamic cancer therapy, Mater Chem Front, 2020, 4, 2064–2071.
[98] Zhao N, Li P, Zhaung J, Liu Y, Xiao Y, Qin R, Li N, Aggregation-induced emission luminogens with the capability of wide color tuning, mitochondrial and bacterial imaging, and photodynamic anticancer and antibacterial therapy, ACS Appl Mater Interfaces, 2019, 11, 11227–11237.
[99] Zhuang J, Yang H, Li Y, Wang B, Li N, Zhao N, Efficient photosensitizers with aggregation-induced emission characteristics for lysosome-and Gram-positive bacteria-targeted photodynamic therapy, Chem Commun, 2020, 56, 2630–2633.
[100] Wang D, Lee MMS, Shan G, Kwok RTK, Lam JWY, Su H, Cai Y, Tang BZ, Highly efficient photosensitizers with far-red/near-infrared aggregation-induced emission for in vitro and in vivo cancer theranostics, Adv Mater, 2018, 30, 1802105.

Yahui Zhang, Zhengxu Cai, Yuping Dong

# Chapter 7
# AIE-active 1,3-butadiene-based biosensors and bioimagings

## 7.1 Introduction

Multiphenyl-substituted 1,3-butadiene (MPB) and its derivatives are of immense importance not only due to their presence as key structural units in several natural products and important pharmaceuticals [1, 2], but also due to their considerable potential in liquid crystals, illuminants, and nonlinear optical materials [3–8]. The majority of the interest in MPB and its derivatives originates from their role as models in the investigation of conformational properties and photoisomerization reactions involving a polyene double bond in compounds of biological interest (such as proteins, vitamin-D, visual pigments, etc.) as well as in terms of their nonlinear optical response and charge transport in conducting polymers.

Similar to the role of MPBs as a companion structure to the "star molecular" and "iconic fluorogen" tetraphenylethene (TPE) [9–13], MPBs also exhibit an advantage in their simple synthesis. Double bonds are added to MPBs to extend the conjugated system on the basis of the tetraphenylethene (TPE) structure via a one-pot reaction. Therefore, the emission wavelength of MPB is considerable red-shifted compared with that of TPE, and its fluorescence quantum yield is slightly inferior to that of TPE. On the other hand, compared to TPE, MPBs have a higher number of isomers due to one more double bond. Meanwhile, tetraphenyl-1,3-butadiene (TPB, Figure 7.1) exhibits three isomers because of the different positions of benzene ring, including 1,1,4,4-tetraphenyl-1,3-butadiene (1,1,4,4-TPB), 1,1,2,4-tetraphenyl-1,3-butadiene (1,1,2,4-TPB), and 1,2,3,4–tetraphenyl-1,3-butadiene (1,2,3,4-TPB), respectively. Similarly, owing to the different positions of the substituents, TPB and 1,1,2,3,4,4-hexaphenyl-1,3-butadiene (HPB) exhibit cis-trans (E/Z) isomerism. MPBs are a new type of compounds based

**Yahui Zhang,** Beijing Key Laboratory of Construction Tailorable Advanced Functional Materials and Green Applications, School of Materials Science and Engineering, Beijing Institute of Technology, Beijing 100081, China and Department of Chemistry, School of Science, Xihua University, Chengdu, 610039, China, e-mail: yahuizhang@mail.xhu.edu.cn
**Zhengxu Cai,** Beijing Key Laboratory of Construction Tailorable Advanced Functional Materials and Green Applications, School of Materials Science and Engineering, Beijing Institute of Technology, Beijing 100081, China, e-mail: caizx@bit.edu.cn
**Yuping Dong,** Beijing Key Laboratory of Construction Tailorable Advanced Functional Materials and Green Applications, School of Materials Science and Engineering, Beijing Institute of Technology, Beijing 100081, China, e-mail: chdongyp@bit.edu.cn

https://doi.org/10.1515/9783110672220-007

on TPE. While retaining some of the advantages of TPE, MPB derivatives exhibit their own unique performance with respect to optical properties.

MPBs exhibit typical aggregation-induced emission (AIE), a process in which the inhibition of the intramolecular motion by dye aggregation leads to a considerable increase in the fluorescence emission efficiency [14–17]. MPBs adopt a helical structure similar to polyacetylene, which undergoes low-frequency torsional motions as isolated molecules. MPBs satisfy conditions of multiple rotors and the restriction of intramolecular motion (RIM) [18], as well as exhibit typical AIE behavior.

In addition, MPBs exhibit immense potential in biosensor and bioimaging. Due to their attractive three-dimensional helical shape and physicochemical properties, MPBs can occupy distinct pockets in proteins for the detection and imaging of proteins, viruses, cells, and tissues. Such detections or imaging exhibit the advantages of strong specificity, high sensitivity, and short response time, which permit the direct visualization of biological analytes at the molecular level, and offer beneficial insights into complex biological structures and processes.

In this chapter, the application of MPB and its derivatives in biology is explained according to the following aspects: Structure and synthesis, Photophysical properties, and Biological applications.

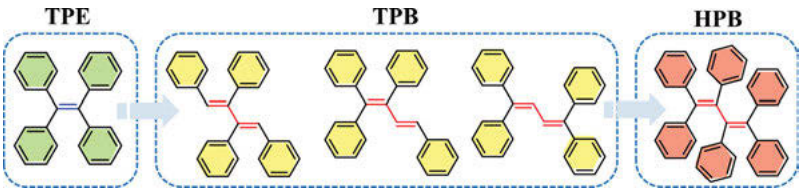


**Figure 7.1:** Structures of TPE, TPBs, and HPB.

## 7.2 Systematic synthesis of MPBs

MPBs can be constructed by various synthetic strategies. A majority of MPBs are synthesized by one-pot reaction under mild conditions and easily purified in high yields by silica-gel column chromatography.

Scheme 7.1 shows the synthetic routes for 1,2,3,4-TPB, 1,1,2,4-TPB, 1,1,4,4-TPB, and their derivatives [19–22]. Derivatives of diphenylacetylene, iodobenzene, and styrene-based derivatives were used to synthesize 1,1,2,4-TPB, with $NaHCO_3$, LiCl, $Pd(OAc)_2$, and $PPh_3$. Scheme 7.1 shows the synthetic route for 1,1,4,4-TPB. Moreover, a series of ester-containing 1,1,4,4-TPB compounds were easily prepared by the Suzuki coupling reaction between phenylboronic acid or its derivatives and bromo-substituted 1,4-diphenyl-1,3-butadienes in the subsequent synthesis and

application [23]. The ester groups can be transformed easily to carboxyl groups by hydrolysis using NaOH and acidification using HCl (Scheme 7.2). Pyridine can be easily converted into pyridinium under mild experimental conditions with different counterions (TPB-5 and HPB-2). Carboxyl and pyridinium are excellent candidates for biological probes and/or chemical sensors. Phenylboronic acid derivatives with different functional groups at the para-position react with 1,2-diphenylacetylene under Pd- and Ag-based catalysis to afford HPBs decorated with different functional groups (Scheme 7.1).

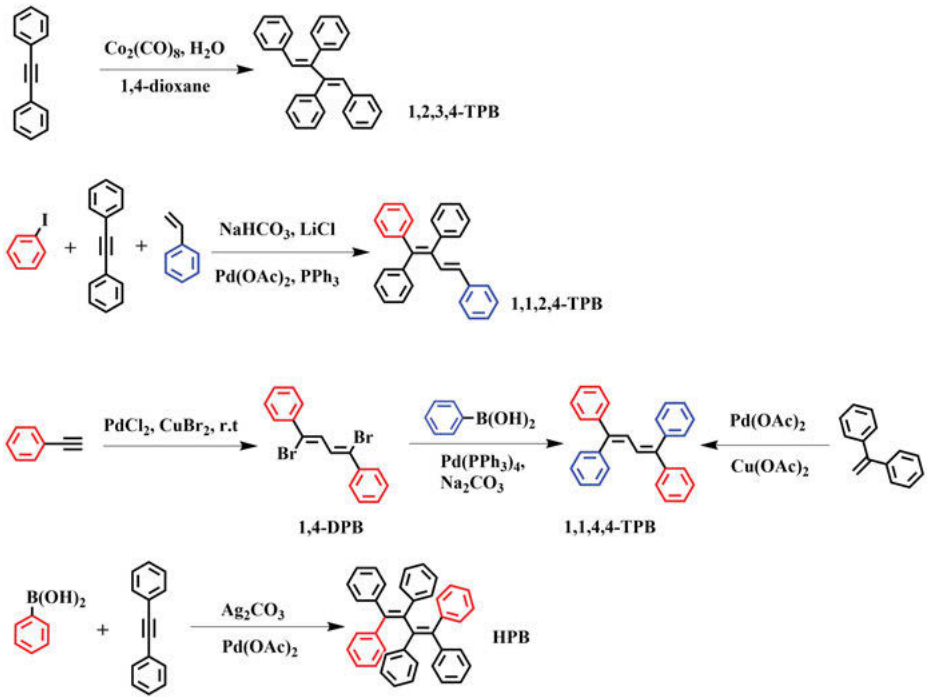


**Scheme 7.1:** Synthetic routes for TPB, HPB, and their derivatives.

## 7.3 Structures and photophysical properties

### 7.3.1 Structures

Considering that their different properties are related to the different numbers and positions of aromatic groups, 1,1,2,4-TPB, 1,1,4,4-TPB, and HPB exhibit different structures, thermal stability, dipole moments, AIE performance, and applications [24]. Figure 7.2 shows the single crystals of 1,1,2,4-TPB, 1,1,4,4-TPB, and HPB. Large torsion

angles (θ) between the phenyl groups and ethylenic moieties were observed, with C–C bond angles greater than 120° in the 1,3-butadiene building block (Table 7.1). The 1,3-butadiene building block in TPBs was almost in a plane, while that in HPBs adopted an extremely twisted conformation, which can maintain $\alpha_1$–$\alpha_4$ for all ~120°. Large torsion angles indicated that all phenyl groups can freely rotate in solution and thus consume excitation energy, leading to no or weak emissions in their solutions. Upon aggregation, these intramolecular rotations are highly restricted, thereby enhancing emission efficiency. The synthesis of MPBs, belonging to a large family of aggregation-enhancement emission (AEE) probes, provided further insights into the RIM mechanism as well as additional potential platforms for the design and application of these AEEgens.

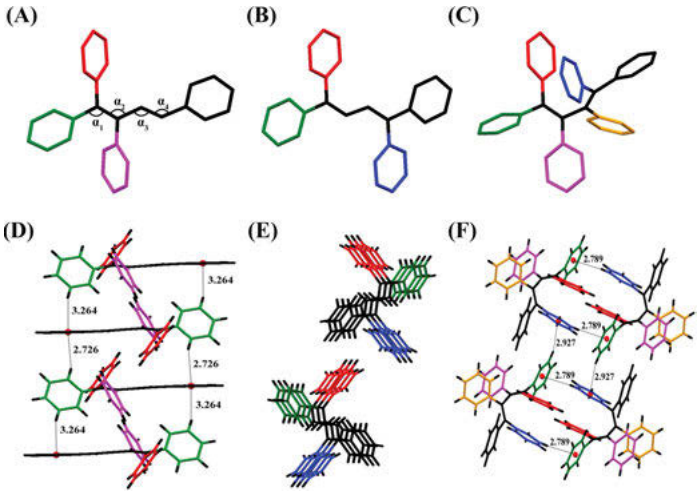


**Figure 7.2:** Single-crystal structure, packing structure, and intermolecular forces of (A), (D) 1,1,2,4-TPB, (B), (E) 1,1,4,4-TPB, and (C), (F) HPB.

**Table 7.1:** Torsion angles and angles among C-C bonds.

| Compounds | Torsion Angle (θ) / ° | | | | | Angle / ° | | | |
|---|---|---|---|---|---|---|---|---|---|
| | Red Ph | Green Ph | Purple Ph | Blue Ph | Black Ph | $\alpha_1$ | $\alpha_2$ | $\alpha_3$ | $\alpha_4$ |
| 1,1,2,4-TPB | 63.44 | 33 | — | 63.1 | 34.4 | 121.4 | 125.5 | 125.6 | 120.5 |
| 1,1,4,4-TPB | 51.33 | 62 | 64.29 | — | 8.55 | 121.5 | 122.3 | 125.5 | 127.1 |
| HPB | 39.21 | 61.85 | 62.60 | 47.60 | 83.04 | 121.5 | 121.7 | 121.6 | 124.0 |

### 7.3.2 AIE performance

MPBs have provided a number of excellent candidates for AIE/AEE-active materials. The fluorescent intensities of their solutions are extremely low when MPBs are molecularly dissolved in a good solvent. However, when the ratio of poor solvent reaches a key point in solvent mixtures, their emissions are drastically intensified. The formation of aggregates by the addition of poor solvents into their solutions is supported by dynamic light scattering (DLS) analysis and scanning electron microscopy (SEM). Results of size distribution by intensity analysis indicated that the content of large nanoparticles in mixtures is significantly increased in the case of gradual aggregation under a high-poor solvent content. Rotor-containing MPBs undergo high-frequency motions in dilute solutions, leading to the rapid nonradiative decay of the excited states that renders MPBs nonemissive. In the aggregated states, these motions are blocked by intermolecular tight packing, subsequently leading to the radiative pathway. Figure 7.3 shows the AIE-active of TPB-1, TPB-2, and TPB-3 by taking 1,1,2,4-TPB as an example [25]. The net change in the photoluminescence (PL) intensity $[(I - I_0)/I_0]$ and their maximum emission wavelengths are summarized. The fluorescence intensity of TPBs in water fraction ($f_w$), less than 70%, was negligibly small due to the nonradiative decay caused by the free intramolecular rotation of the single bonds between the phenyl and alkenyl groups. At $f_w = 99\%$, the fluorescence intensity of TPB-1 increased ~29-fold, while that of TPB-2 and TPB-3 increased ~5- and 0.5-fold at $f_w = 99\%$, respectively. Moreover, DLS results revealed that the aggregate sizes of TPB-1, TPB-2, and TPB-3 at $f_w = 99\%$ are 208.4, 156.6, and 135.0 nm, respectively (Figure 7.4). In addition, fluorescence quantum yield (Φ) is also a performance indicator for AIE. TPB-1 was weakly emissive in a THF solution with Φ of 0.84%, but was highly emissive in a mixture of THF/water ($f_w = 99\%$) with Φ of 17.35%, indicating that it is a typical AIE compound. The quantum yields of TPB-2 and TPB-3 in THF were 2.43% and 2.11%, respectively, while those in a mixture of THF/water ($f_w = 99\%$) were 13.22% and 15.50%, respectively. These results indicated that TPBs exhibit good AIE properties and can be another new series of AIE compounds.

### 7.3.3 E/Z isomers

In biomedicine, cis-trans isomers play a vital role in the efficacy and therapeutic effects of drugs. Therefore, it is of significance to examine cis–trans isomers. Owing to the presence of different substituent groups, MPBs exhibit different stereoisomers, e.g., (Z,Z), (Z,E), and (E,E)-isomers. Structural properties can be significantly affected by their E/Z isomerization. TPB-4 and HPB-1 are considered as examples to explain the effect of E/Z isomerism on their properties, including, photophysical properties, and mechanochromic performance.

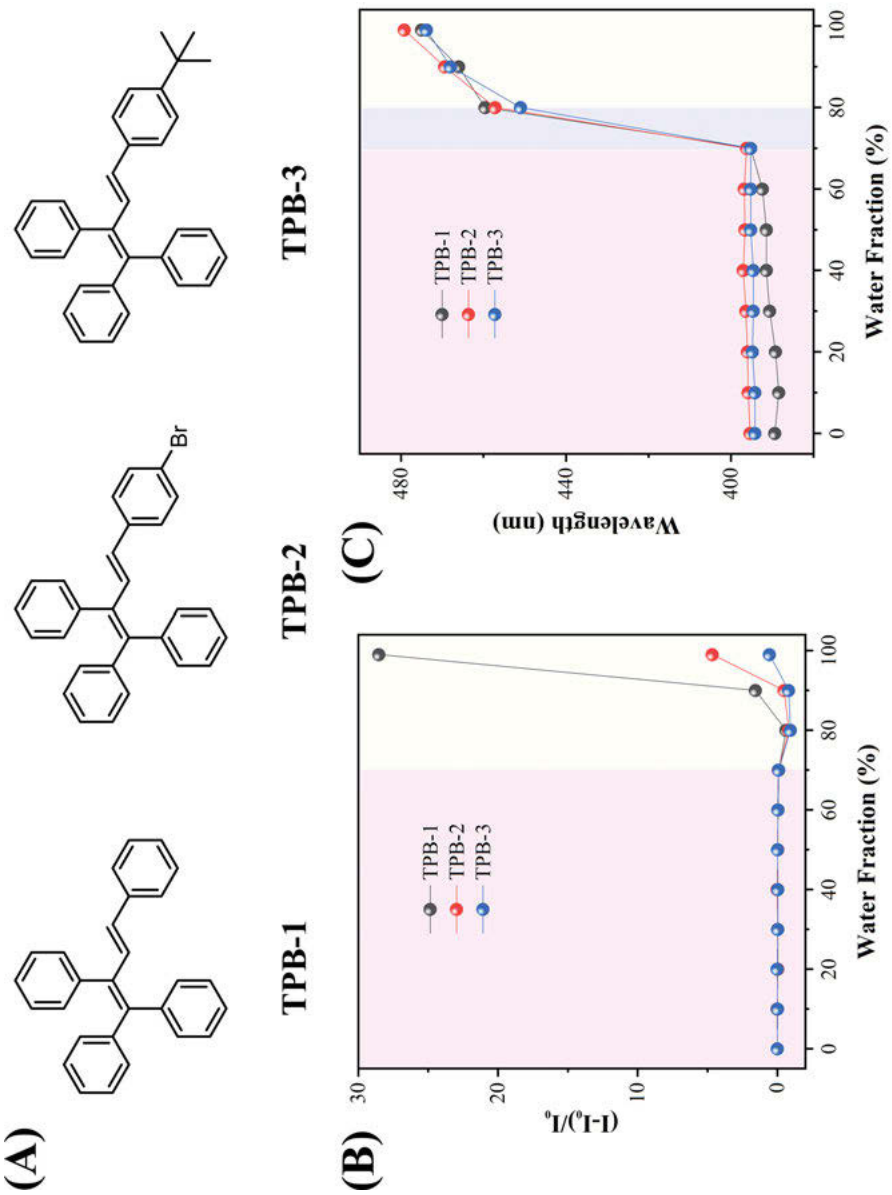


**Figure 7.3:** (A) Correlation between the net change in the PL intensity $[(I - I_0)/I_0]$ and (B) the maximum emission wavelengths ($\lambda_{max}$) of TPBs with different water fractions in THF/water mixtures. $I_0$: The maximum PL intensity in THF; I: the maximum PL intensity in a mixture of THF/water; [TPB-1] = [TPB-2] = [TPB-3] = $1 \times 10^{-5}$ mol/L; excitation wavelength: 330 nm.

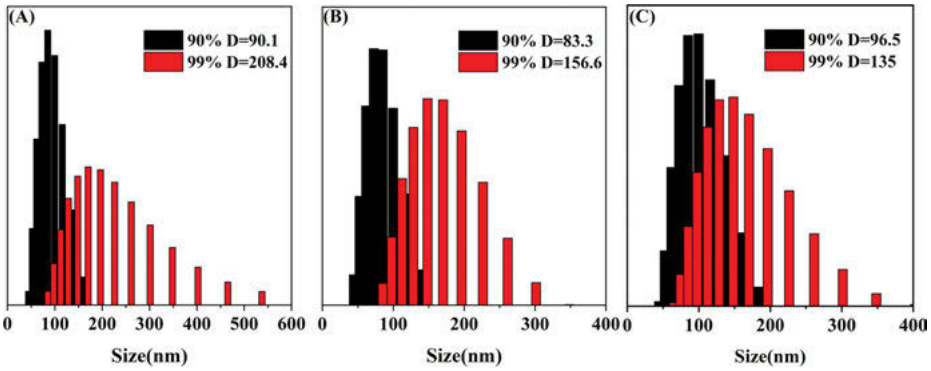


**Figure 7.4:** Dynamic light scattering results of (A) TPB-1, (B) TPB-2, and (C) TPB-3 at $f_w$ = 90% and 99% in THF/water mixtures. [TPBs] = $1 \times 10^{-5}$ mol/L.

E/Z isomers of HPB-1 containing dialdehyde groups, 4,4′-((1E,3E)-1,2,3,4-tetraphenylbuta-1,3-diene-1,4-diyl)dibenzaldehyde (EE-HPB-1), 4,4′-((1Z,3E)-1,2,3,4-tetraphenylbuta-1,3-diene-1,4-diyl)-dibenzaldehyde (EZ-HPB-1) and 4,4′-((1Z,3Z)-1,2,3,4-tetra-phenylbuta-1,3-diene-1,4-diyl)dibenzaldehyde (ZZ-HPB-1), were synthesized in one-pot and readily separated by silica gel column chromatography [26]. The three E/Z isomers containing conjugated diene exhibited remarkable differences in terms of their AIE or AEE behavior, thermostability, and mechanochromic performance, as shown in Figure 7.5. Among them, with a dense molecular packing and strong intermolecular interactions, EE-HPB-1 was a better AIEgen, while EZ- and ZZ-isomers exhibited AEE behavior. Experimental results revealed that RIR is the primary reason for the AIE/AEE behavior of HPB-1 luminogens. Moreover, EZ-HPB-1 irreversibly exhibited a blue-shift of 23 nm by grinding treatment, which could not be restored by fuming with organic solvents or heating. EE-HPB-1 did not exhibit the mechanochromic performance due to its blue shift from 553 to 551 nm. In contrast, owing to its twisting conformation and relative loose packing, ZZ-HPB-1 reversibly exhibited a red-shift of 20 nm during multiple repeat cycles of grinding and fuming treatments, exhibiting superior mechanochromic performance.

Owing to the presence of CN and CHO, TPB-4 also exhibits cis-trans isomerism (Figure 7.6). Similarly, EZ- and ZZ-TPB-4 were synthesized in one-pot and readily separated by silica-gel column chromatography.

## 7.4 Application of MPB-based materials

The simple synthesis and fluorescence turn-on features of MPB bioprobes offer the direct visualization of specific analyses and biological processes in aqueous media with higher sensitivity and better accuracy than traditional fluorescence turn-off probes in biosensing and bioimaging.

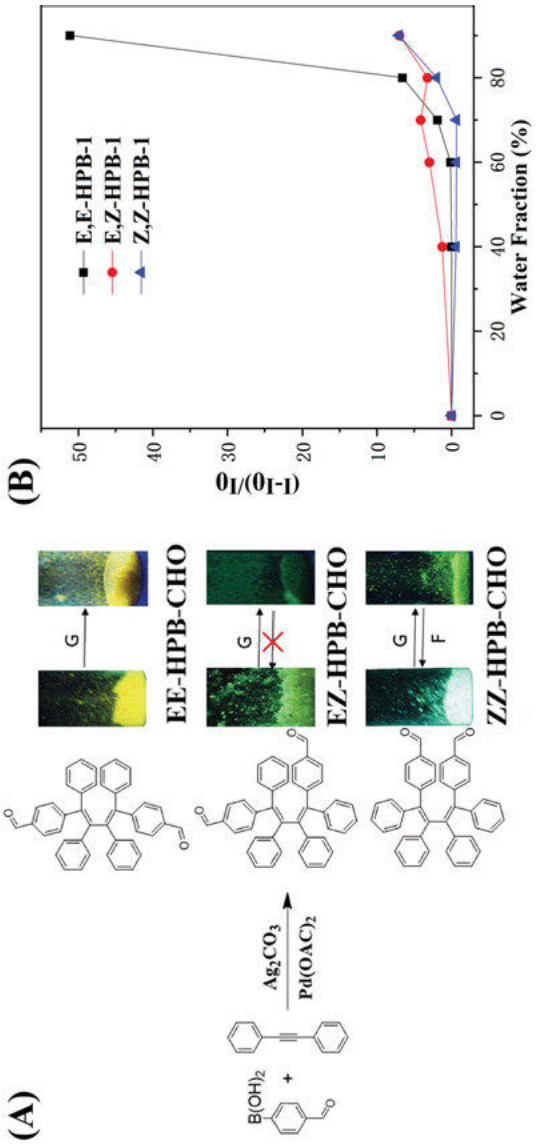


**Figure 7.5:** (A) Synthetic routes and mechanochromic performance of EE-, EZ-, and ZZ-HPB-1; (B) Correlation between the net change in PL intensity $[(I - I_0)/I_0]$. [HPB-1] = $1 \times 10^{-5}$ mol/L.

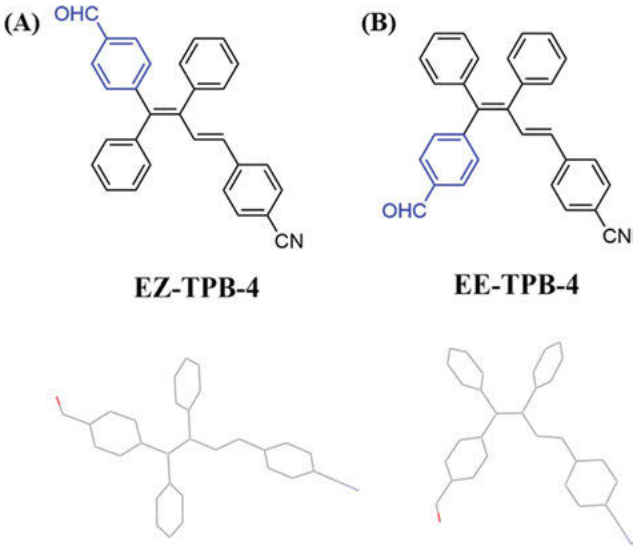


**Figure 7.6:** Structures and single crystals of (A)EZ-TPB-4 and (B) EE-TPB-4.

## 7.4.1 Biosensors

Ionic AIE fluorogens are able to respond to different DNA structures, protein, and virus with good sensitivity via both electrostatic and hydrophobic interactions [27]. Owing to their unique three-dimensional structures, MPBs can be combined with protein cavities. If they are modified with positive ions, they can become a good candidate for protein detection. By a combination of the above viewpoints, Dong et al. developed two charged MPB derivatives, TPB-5 and HPB-2, for the specific detection of γ-globulin and avian influenza virus.

γ-Globulins play a vital role in disease recognition and control [28]. High and low levels of γ-globulins induce diseases. High γ-globulin levels can cause rheumatoid arthritis, liver diseases, and infectious diseases. Low γ-globulin levels can cause humoral immunodeficiency and metabolic diseases. Therefore, the development of ultrasensitive and reliable analytical methods for detecting and quantifying γ-globulins in the human blood serum is of great significance in diagnostics [29].

Dong et al. designed and synthesized 4-((1Z,3Z)-1,4-bis(4-(methoxycarbonyl)-phenyl)-4-(pyridin-4-yl)buta-1,3-dien-1-yl)-1-methylpyridin-1-ium hexafluoro-phosphate (TPB-5), as shown in Scheme 7.2. This anionic fluorogen in different ratios of THF/$H_2O$ systems exhibited typical AIE performance. As a novel "turn-on" fluorescent probe, TPB-5 was synthesized for the in situ quantification of γ-globulins in the blood serum [30].

TPB-5 probe exhibited high selectivity for γ-globulins over other components in the blood serum, including serum albumins, fibrinogen, glucose, urea, and cholesterol (Figure 7.7). In fact, these species can barely interfere with the molecular interactions between TPB-5 and γ-globulins. The high specificity of TPB-5 probe enabled the in situ quantitative detection of γ-globulins without isolating γ-globulins from the blood serum. The fluorescence intensity of TPB-5 was linearly correlated with γ-globulins concentration, in the range of 7.89 to 300 μg/mL, and the detection limit of γ-globulins was determined to be 7.89 μg/mL. The fluorescence response time of TPB-5 for detecting γ-globulins was extremely short (as low as 5 s), thereby enabling the real-time detection of γ-globulins in complicated blood serum samples. Additional studies suggested that TPB-5 interacts with γ-globulins, possibly through electrostatic interactions via its methylpyridinium group. The highly specific binding between TPB-5 and γ-globulins restricted intra-molecular rotation, thereby inducing the fluorescent turn-on behavior of TPB-5. TPB-5 is a promising fluorescent biosensor specific for γ-globulins, with immense potential in clinical applications.

A biological virus constitutes multiple types of noncellular organisms with a small size and simple structure. The viruses only contain one type of nucleic acid (i.e., DNA or RNA). The high pathogenicity, infectivity, and harmfulness of the avian influenza virus are caused by H5N1 strains [31–33]. The hemagglutinin proteins (H) and neuraminidase proteins (N) located in the flu surface are the main specificities that determine the pathogenicity of the virus and change the course of the disease. Therefore, it is imperative to determine a rapid, quantitative, low-cost, and reliable detection and staining method for H proteins, for the diagnosis of infectious diseases [34, 35].

Four salts of hexaphenylbutadiene methyl pyridine, with AIE characteristics, were designed and synthesized (Scheme 7.3). AIE features of HPB-2 were investigated in DMSO-water mixtures. Experimental results indicated that HPB-2 can be a "turn-on" by H5 with high selectivity [36].

With the addition of 0–5.00 μg/mL of H5, a "turn-on" response was observed using a hand-hold UV lamp, indicating that HPB-2 also can be used for the colorimetric detection of H5 by the naked eye. The fluorescence intensity of HPB-2 rapidly reached the maximum and was maintained constant, once H5 was added to the solution of HPB-I within 10 s. This response was extremely rapid, which can be regarded as real-time detection and exhibits an immense advantage compared to the traditional detection methods for H5.

To confirm the detection selectivity of H5, throat swaps, including secretions and residues, in the oral cavity of chickens were added to detection systems to investigate whether the secretions and residues can interfere with the response of HPB-2 to H5. Experimental results of the simulation detection of the actual situation indicated that the response of HPB-2 is only determined by the H5 content (Figure 7.8A). The fluorescence intensity also exhibited an excellent linear relationship with the H5 concentration ($R^2 = 0.98$). The limit of detection (LOD) was estimated to be 179.5 ng/mL (6.08 nM), according to the IUPAC-based approach. Notably, HPB-2 still

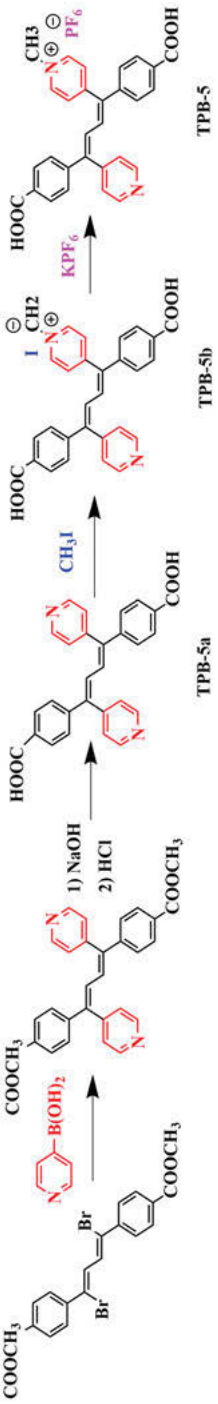


**Scheme 7.2:** Synthetic routes for TPB-5.

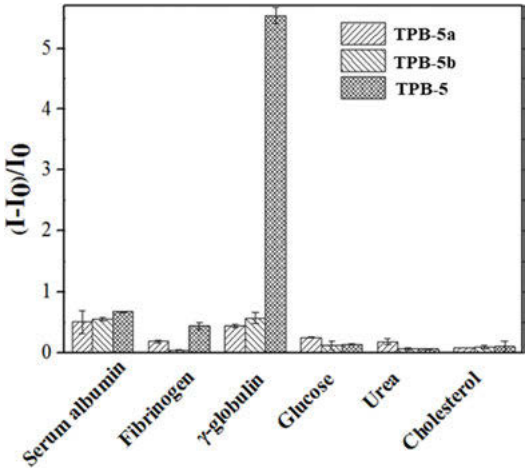


**Figure 7.7:** Effect of different components in the blood serum on the PL intensity of TPB-5a (performed in the PBS buffer with 10% DMSO), TPB-5b, and TPB-5 (performed in PBS buffer). [TPB-5] = $10^{-5}$ M; the concentration of each component was 300 μg/mL; $\lambda_{ex}$ = 370 nm. The results are presented as means ± standard deviations (n = 3).

distinguished the presence of H5 by the naked eye under a UV lamp, despite the presence of interfering substances.

Experimental results revealed that H5 provides a special microenvironment to restrict the intramolecular motion of HPB-2, thereby increasing the fluorescence intensity of HPB-I molecules. Zeta potential (ζ), DLS, and simulation calculation were performed to further elucidate the mechanism. AutoDock vina software for molecular docking was employed to simulate the optimal complex structures of HPB-I and H5 (Figure 7.8B, C). The binding site of the small molecule with protein was in the cavity of the top of the H trimer, and the docking score of the protein with the small molecule was −6.38, indicative of its stable combination.

As a biosensor, it not only refers to the detection of biological components such as proteins and viruses, but also to the surrounding biomedical industries. For example, MPB and its derivatives can detect the oxidant cerium ion during the preparation of modified starch, which is the main raw material of surgical implants, as well as polyazole compounds as medicines.

Cerium (Ce) demonstrates immense potential applications in biocatalysis, drug release, and biomedical science [37]. For example, $Ce^{4+}$ is the mainly used oxidant for natural starch modification [38]. These modified starches are nontoxic and biodegradable and are promising biomedical materials for surgical implants [39]. As a result of its enormous usage, there is an increasing demand to investigate environmental, medical, and biological effects of cerium. A recent study also reported that $Ce^{4+}$ exhibits a destructive effect on several biological processes, such as the metabolism of RNA and

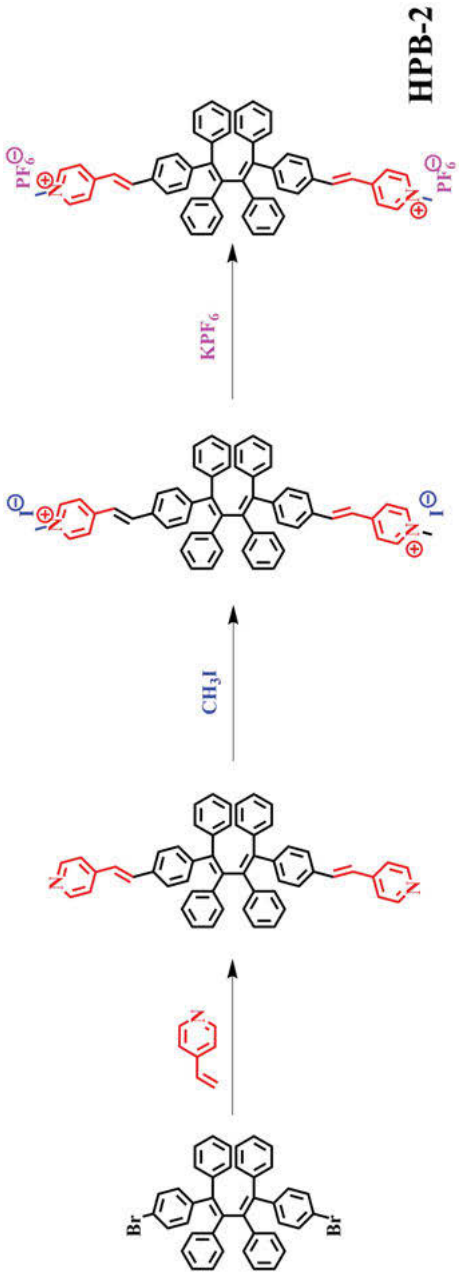


**Scheme 7.3:** Synthetic routes for HPB-2.

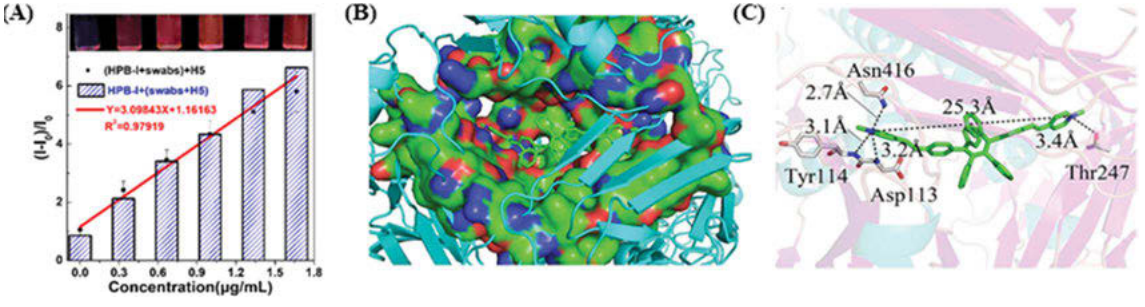


**Figure 7.8:** (A) Plots of the relative PL intensity $(I–I_0)/I_0$ of HPB-2 in throat swabs at ~ 600 nm against H5. $I_0$ represents the PL intensity in the absence of H5. Column chart of the relative PL intensity $(I–I_0)/I_0$ of HPB-2 at ~ 600 nm against the H5 in throat swabs. Inset: Photographs of HPB-2 by the addition of 0 (left) to 2.5 (right) μg/mL of H5 upon UV-lamp excitation ($\lambda_{ex}$ = 365 nm). [HPB-2] = 1.0 × $10^{-6}$ mol/L; $\lambda_{ex}$ = 423 nm. Results are presented as means ± standard deviation (n = 3). (B) Binding sites of HPB-2 and H5. (C) Docking results and interaction between HPB-2 and hemagglutinin protein.

DNA, gene expression, as well as signal transduction in several diseases, due to the generation of reactive oxygen species by $Ce^{4+}$. Therefore, it is of significance to develop highly selective, sensitive methods for the detection of trace cerium produced in biomedicine fields.

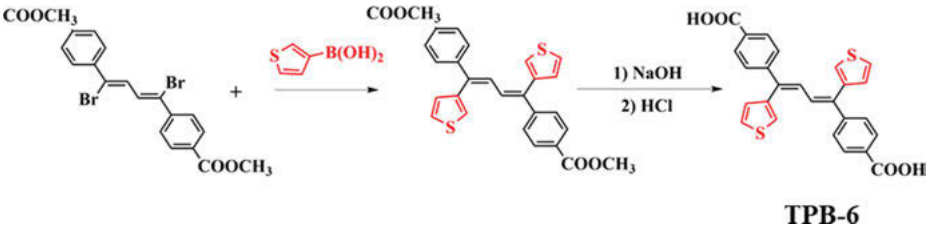


**Scheme 7.4:** Synthetic route to TPB-6.

As a novel fluorescent probe, TPB-6 (shown in Scheme 7.4) was designed for the detection of $Ce^{3+}$. This "turn-on" chemosensor with a high selectivity, short response time, and wide linear response range can be further exploited for several applications such as monitoring of $Ce^{3+}$-based photocatalysts and optical film sensors [40].

The specific interaction between TPB-6 and $Ce^{3+}$ was investigated by fluorescence spectroscopy. By the titration of TPB-6 with $Ce^{3+}$ in a water/THF mixture, fluorescence was switched on with a 5-fold-enhanced fluorescence intensity (Figure 7.9A). The fluorescence intensity of TPB-6 aggregates linearly increased with the $Ce(NO_3)_3$ concentration, from 0 to 18 μmol/L ($R^2 = 0.9952$), as shown in Figure 7.9B. According to the curve fitting equation, the detection limit ($3\sigma/k$, $\sigma = 0.213$) of TPB-6 to $Ce^{3+}$ was calculated to be 2.27 μmol/L, thereby satisfying the testing requirements for practical applications. To investigate the selectivity of the probe, 13 metal cations, with different valences, were examined. Figure 7.9C summarizes the variations in their fluorescence intensity. The probe rapidly responded to the titration of $Ce^{3+}$ due to the extremely rapid aggregation process, and the fluorescence intensity remained constant at 2 min, providing a "highly stable" and "zero-wait" detection method for $Ce^{3+}$ (Figure 7.9D).

Polyazole derivatives exhibit biological and/or pharmaceutical activities and serve as vital units in antibiotics [41]. For example, triazoles can be used as antifungal, antibacterial, antiviral, analgesic, and antituberculosis agents [42], while tetrazoles may serve as lipophilic spacers and carboxylic acid surrogates in biologically active molecules [43]. Therefore, triazoles and tetrazoles are widely observed in some well-known antibiotics and are key precursors in synthesis.

A novel fluorescent probe for the detection of polyazoles was developed [44]. With typical AIE features, HPB-3 (Scheme 7.5) exhibited visible emissions and a high quantum yield (QY) in the solid state (ΦF = 27.90%).

As a proof-of-concept experiment, 5-nitro-2,4-dihydro-3 H-1,2,4-triazole-3-one (NTO) was selected as the target triazole material (Figure 7.10). HPB-3 ($1 \times 10^{-4}$ mol/L)

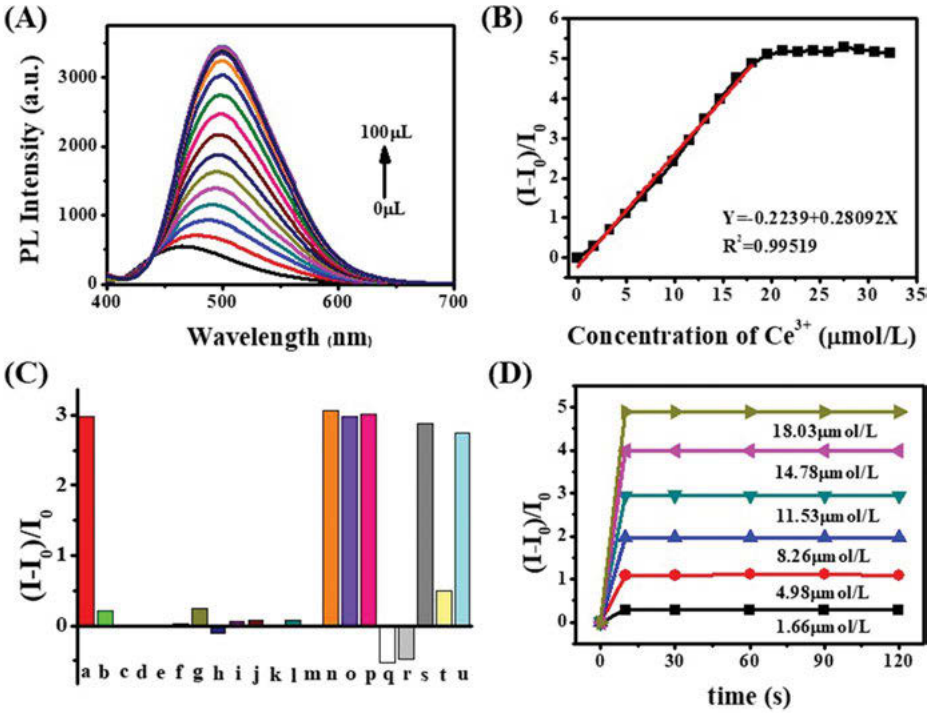


**Figure 7.9:** (A) Emission spectra of TPB-6 (10 μmol/L, THF:$H_2O$ = 1:9) containing different amounts of $Ce^{3+}$; (B) the linear relationship between emission and concentration of $Ce^{3+}$ ranging from 2.27 μmol/L to 20 μmol/L. Curve-fit equation: $(I–I_0)/I_0 = – 0.2239 + 0.2809\ [Ce^{3+}]$, $R^2 = 0.9952$; (C) Fluorescence response of TPB-6 (10 μmol/L, THF:H2O = 1:9) upon the addition of different metal ions (14.8 μmol/L) (a:$Ce^{3+}$, b:$Al^{3+}$, c:$Ba^{2+}$, d:$Ca^{2+}$, e:$Cd^{2+}$, f:$Ag^{+}$, g:$Cr3^{+}$, h:$Hg^{2+}$, i:$K^{+}$, j:$Mg^{2+}$, k:Na +, l:$Pb^{2+}$, m:$Zn^{2+}$, n:$Ce^{3+}$ + $Cr^{3+}$ + $Al^{3+}$, o:$Ce^{3+}$ + $Ca^{2+}$ + $Zn^{2+}$, p:$Ce^{3+}$ + $K^{+}$ + $Na^{+}$, q:$Fe^{3+}$, r:$Ce^{3+}$ + $Fe^{3+}$, s:$Ce^{3+}$ + $Fe^{3+}$ + $SCN^{-}$, t:$Ce^{4+}$, u:$Ce^{4+}$ + 1,2-propanediol). (D) Time-dependent changes in the fluorescence intensity of TPB-6 (10 μmol/L) at 470 nm after adding different concentrations of $Ce^{3+}$.

was preassembled to nanoscale particles, with a size of 172 nm in a 90% water fraction solution, without stirring rotation. This aggregate was stable and did not coagulate for at least one night (Figure 7.10B insets). By the titration of freshly prepared nanoparticles with NTO, up to 3-fold enhancement in the PL intensity of HPB-3 particles was noted (black line in Figure 7.10B). The dissociated HPB-3 nanoparticles further aggregated to larger particles (~2,100 nm determined by DLS), and the emission was boosted as a result of RIM. The maximum emission wavelengths exhibited a gradual blue-shift (20 nm) as well, most likely because of the further twisting of the molecular conformations by the condensed packing. The LOD of HPB-3, with a size of 99.5 nm toward NTO, was calculated to be 0.9 μg/mL ($7 \times 10^{-6}$ mol/L).

To explore the sensitivity of HPB-3 to other polyazoles, fluorescence titration was performed by the incremental addition of several triazoles and tetrazoles to water, in

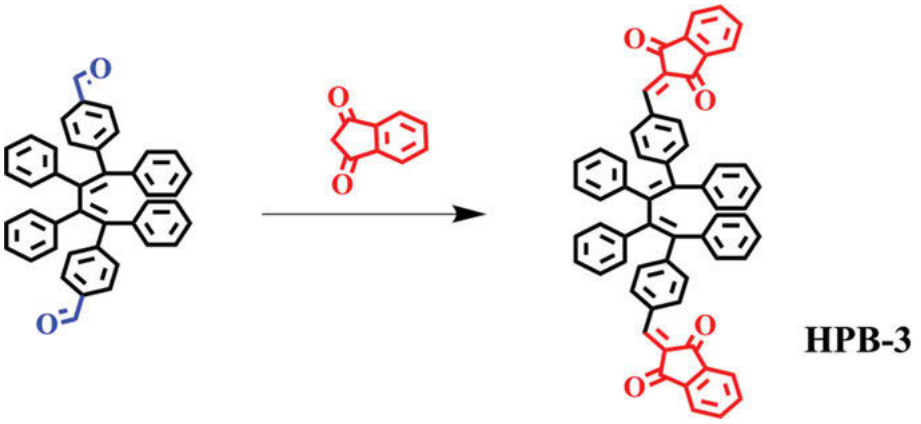


**Scheme 7.5:** Synthetic route to HPB-3.

which, HPB-3 was dispersed. Compared to common explosives (such as PA, TNT, HMX, CL-20 and RDX) and imidazole derivatives (N-IM, 2N-IM and IM), triazole, and tetrazole derivatives exhibited an outstanding "turn-on" response (Figure 7.10C), suggesting that most of the explosives do not interfere with the detection of polyazoles in water. The method exhibited advantages of universality, high sensitivity, and facile visualization, and can be practically employed for the detection of polyazoles in water.

Here is other example detected polyazoles showed in Scheme 7.6 – three metal – organic frameworks (MOFs), TPB-7-MOF-1, TPB-7-MOF-2, and TPB-7-MOF-3, constructed from $Mg^{2+}$, $Ni^{2+}$, and $Co^{2+}$ with deprotonated TPB-7, respectively [45].

These MOFs enable highly sensitive and selective detection of polyazoles in a few seconds, with low detection limits, through emission shift and/or "turn-on" signal. Remarkably, the cobalt-based MOF, TPB-7-MOF-3, can selectively sense the powerful explosive NTO with high sensitivity, discernible by the naked eye (detection limit = 6.5 ng on a 1 $cm^2$ testing strip), and parts per billion-scale sensitivity by spectroscopy via pronounced fluorescence emission. To confirm the mechanism of NTO detection by TPB-7-MOFs, NTO explosive was added in their solutions. Experimental results and analysis demonstrated that the TPB-7-MOFs barely retain their structural integrity, upon addition of NTO, because of the competitive coordination substitution, and thus free TPB-7 molecules were released into the solutions. Upon evaporation of THF solvent during the paper strip tests or addition of hexane in the solution tests, the dissociated TPB-7 molecules begin to aggregate, and the emission was boosted as a result of the restriction of intramolecular rotations.

In addition to detecting polyazoles, TPB-based MOFs can also specifically detect aluminum ions [46]. Zhao et al. have designed a hydroxyl-functionalized ligand (TPB-8) for MOF with AIE feature. Their study shows that the occurrence of exciton migration between the AIE linker and conjugated auxiliary ligand TPB-8 causes fluorescence quenching.

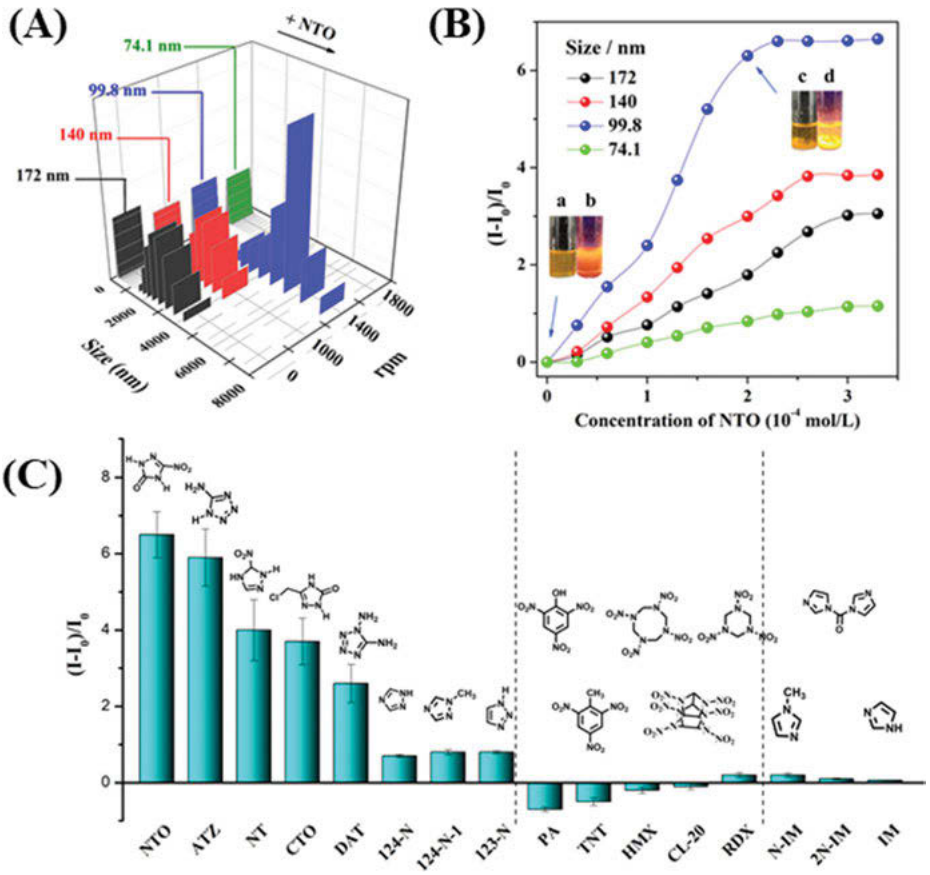


**Figure 7.10:** (A) DLS results of HPB-3 versus different stirring rotational speeds in 90% water fraction before and after the addition of NTO (2 eq); (B) Stern-Volmer plots of different sizes of HPB-4 aggregates in 90% water fraction upon incremental addition of NTO. Inset picture, a,b: 90% water fraction without NTO under sunlight and UV light; c,d: 90% water fraction with NTO (2 eq) under sunlight and UV light at a size of 99.8 nm Stern-Volmer equation: $(I_0/I) = 1 + K_{sv}[Q]$, where $K_{sv}$ is the quenching constant (M-1), [Q] is the molar concentration of the analyte, I0 and I are the luminescence intensities before and after the addition of the analyte, respectively; (C) Fluorescence enhancement $((I - I_0)/I_0)$ of E,E-HPB-ID by different analytes ($M_{HPB-4}$: $M_{analytes}$ = 1:2) in the 90% water fraction in THF/water mixtures. [HPB-3] = $1 \times 10^{-4}$ mol/L; Excitation wavelength: 410 nm.

Using this strategy, the prepared MOF material can perform as a fluorescence "off – on" probe for highly sensitive detection of $Al^{3+}$ in aqueous media. The hydroxyl group plays a crucial role in sensing, as it can selectively chelate $Al^{3+}$, which is directly related to the dissociation of nonfluorescent MOF and the consequent activation of the AIE process. As is well known, excessive intake of aluminum has severe toxicity to human health and can induce many serious diseases, including Alzheimer's disease,

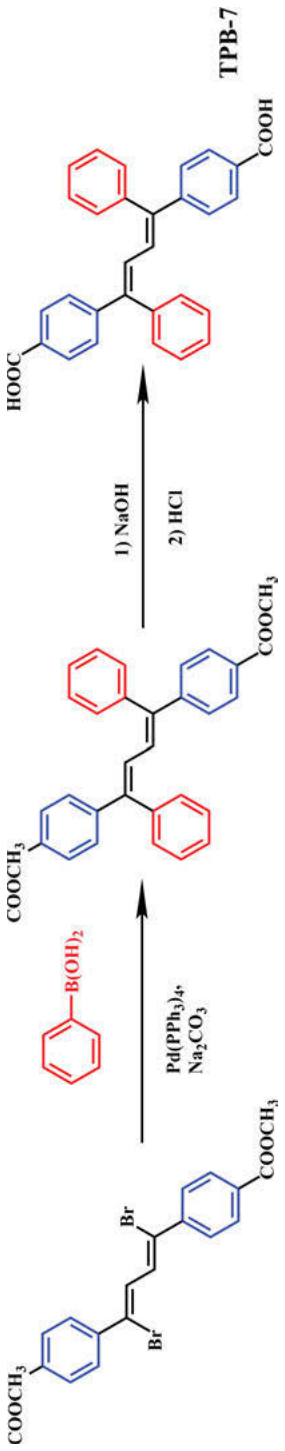


**Scheme 7.6:** Synthetic route to TPB-7.

osteoporosis, rickets, anemia, softening of the bones, etc. [47, 48]. Especially, TPB-8-MOF exhibits superior sensitivity for $Al^{3+}$, with detection limit as low as 3.73 ppb, which is significantly lower than the higher limit of the U.S. Environmental Protection Agency (EPA) recommendation of $Al^{3+}$ ion for drinking water (200 ppb). At the same time, it also demonstrated excellent specific selectivity.

## 7.4.2 Bioimaging

Organic dyes and proteins (e.g., green fluorescent protein) are the commonly used fluorescence imaging reagents; however, their molar absorptivity and photobleaching resistance are low. In addition, inorganic QDs have been used, but suffer from high cytotoxicity in an oxidative environment. The development of organic dots has been considerably hampered by the aggregation-caused quenching (ACQ) effect, observed in conventional fluorophore systems. The high brightness of AIE fluorogens in the solid state and the distinct feature that AIE fluorogens become strong emitters at high concentrations, make them promising candidate materials for fluorescence imaging applications. Owing to their typical AIE properties, higher fluorescence quantum yields, and an increased number of modification sites, MPB and its derivatives have become powerful candidates for bioimaging applications. Moreover, the bioimaging of MPBs demonstrate immense potential for practical applications, such as real-time imaging in cryosurgery and intraoperative pathological diagnosis of hepatocellular carcinoma.

Therapeutic use of freezing to treat infected wounds can be traced back to ancient Egyptian times (around 3,000 BC) [49]. Only with the recent achievement of key technological advances, modern cryosurgery – using freezing to kill cancer cells – can be applied to combat several of cancers, such as cancers of skin, bone, kidney, lung, and liver [50–52]. Cryosurgery exhibits incomparable advantages for cancer treatment in terms of low pain, low bleeding, low morbidity, short recovery time, as well as lower costs [53, 54]. However, key challenges such as maximizing the therapeutic efficacy of cryosurgery still remain, and one of them involves the incapability of real-time and selective imaging of cancer cells, leading to the cryoinjury of surrounding normal cells as well as the incomplete killing of cancer cells.

As an AIEgen, TPB-9 (Figure 7.11A, B) can specifically interact with ice crystal and form aggregates at the ice/water interface [55]. TPB-9 molecules can be reasonably proposed to accumulate and aggregate at the ice/water interface when ice grows, as can be schematically illustrated in Figure 7.11D. This special interaction endows TPB-9 with a unique feature of freezing-induced emission. This was further verified experimentally – TPB-9 molecules exhibited unique freezing-induced turn-on feature inside the cancer cell. At room temperature, living HeLa cells, stained with TPB-9, exhibited blue color under a light illumination of 405 nm, while the cells stained with neutral red exhibited a red color, as observed by confocal laser scanning microscopy (CLSM) images, as shown in Figure 7.12A–D. Upon freezing,

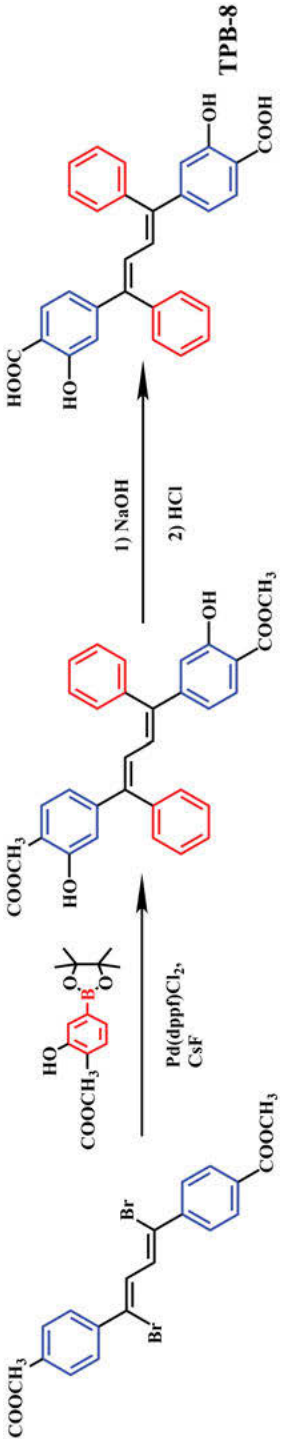


**Scheme 7.7:** Synthetic route to TPB-8.

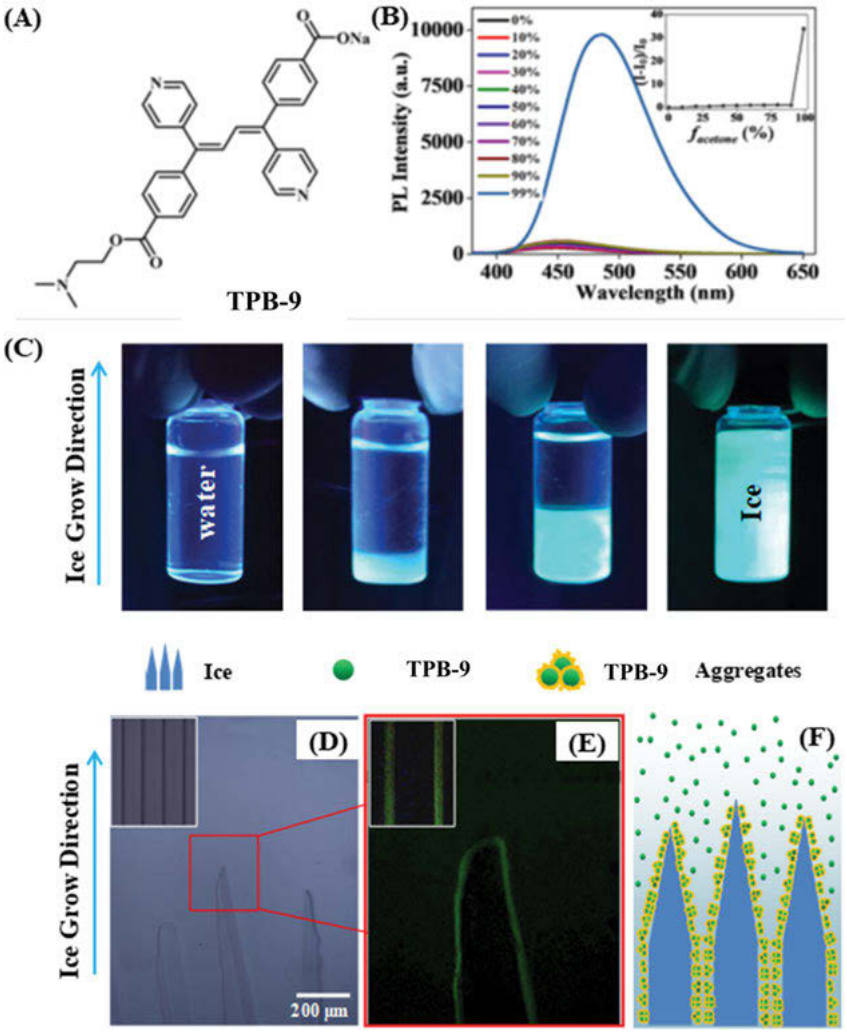


**Figure 7.11:** (A) Molecular structure of TPB-9, and (B) Emission spectra of TPB-9 molecule in acetone/water mixtures with various volume fractions of acetone ($f_{acetone}$). Inset: Plot of the emission peak intensity vs $f_{acetone}$. (C) Fluorescence pictures of a vial containing TPB-9 solution ($10^{-3}$ mol/L) under UV-light irradiation of 365 nm as ice crystals form via controlled directional freezing. (D) Optical microscope images, (E) enlarged view of fluorescence microscope images, and (F) schematic representation of the ice growth front as well as frozen zones (insets) with the TPB-9 molecules being accumulated and aggregated at the ice/water interface. The growing ice front velocity is 8 μm/s.

the PL intensity of TPB-9-stained HeLa cells considerably increased, whereas that of the cancer cells, stained with neutral red, decreased substantially (Figure 7.12E–H).

Another requirement for real-time imaging during cryosurgery involves the differentiation of the surrounding normal tissues from tumor tissues. NIH 3T3 cells stained with TPB-9 exhibited dim fluorescence at room temperature (Figure 7.13A, B); in strong contrast, HeLa cells exhibited clear blue fluorescence after the staining of TPB-9 under the same condition. These results unambiguously suggested that TPB-9 exhibits the desired selectivity to cancer cells. To evaluate the feasibility of TPB-9 for the selective imaging of cancer cells upon freezing, Dong et al. have further examined the fluorescence images of NIH 3T3 and HeLa cells in the frozen state. The NIH 3T3 cells exhibited an extremely weak PL intensity in the frozen state (Figure 7.13C), while the frozen HeLa cells were highly emissive (Figure 7.13D). This unique turn-on imaging method is of practical importance to assist surgeons in real-time to kill cancer cells via freezing, while simultaneously preventing injury to normal cells.

Another aspect of the application of MPBs in biological imaging is mainly reflected in the intraoperative pathological diagnosis of hepatocellular carcinoma. Hepatocellular carcinoma (HCC) is one of most common cancers and a leading cause of overall cancer-related mortality worldwide due to the high incidence and mortality. However, it is difficult to distinguish small HCC lesions in cirrhotic patients from benign-appearing regenerative and dysplastic nodules during hepatectomy [56]. Thus, surgeons are troubled by this clinical difficulty, because the site and pathological nature of suspicious nodules must be identified in order to further resect tumor lesions completely. In clinical practice, intraoperative frozen-section consultation is commonly carried out when the surgeon cannot judge the pathological nature of nodule [57]. However, it comprises multiple steps and is time-consuming. Furthermore, intraoperative frozen-section diagnosis needs to be performed by a senior pathologist with abundant clinical experience, who is expected to prepare an accurate report in a short duration under immense pressure that will influence the intra-operational decision of the surgeon. Thus, the development of a novel intraoperative rapid diagnosis technique is imperative to identify the nature of tumor nodules.

In the last few decades, fluorescence imaging has been developed to distinguish cancer cells from normal cells. Herein, Dong et al. developed a one-step synthetic protocol to prepare novel HPB-4 with typical AIE characteristics, which emits strong green fluorescence in the aggregated state or at high concentration [58]. Unexpectedly, HPB-4 can distinguish HCC cells from normal liver cells with high specificity and only by a simple staining procedure. Notably, after staining intraoperative specimen slides with HPB-4, the HCC folic slides are lit up with green fluorescence, and not paratumor cirrhosis, benign liver focal nodular hyperplasia and healthy liver tissues, which barely emit fluorescence, which is consistent with the conventional intraoperative frozen-section diagnosis. This result demonstrated that intraoperative fluorescence pathological diagnosis technique (FPDT), using HPB-4 staining, is a promising alternative for the intraoperative diagnosis of HCC. Compared to conventional intraoperative frozen-section

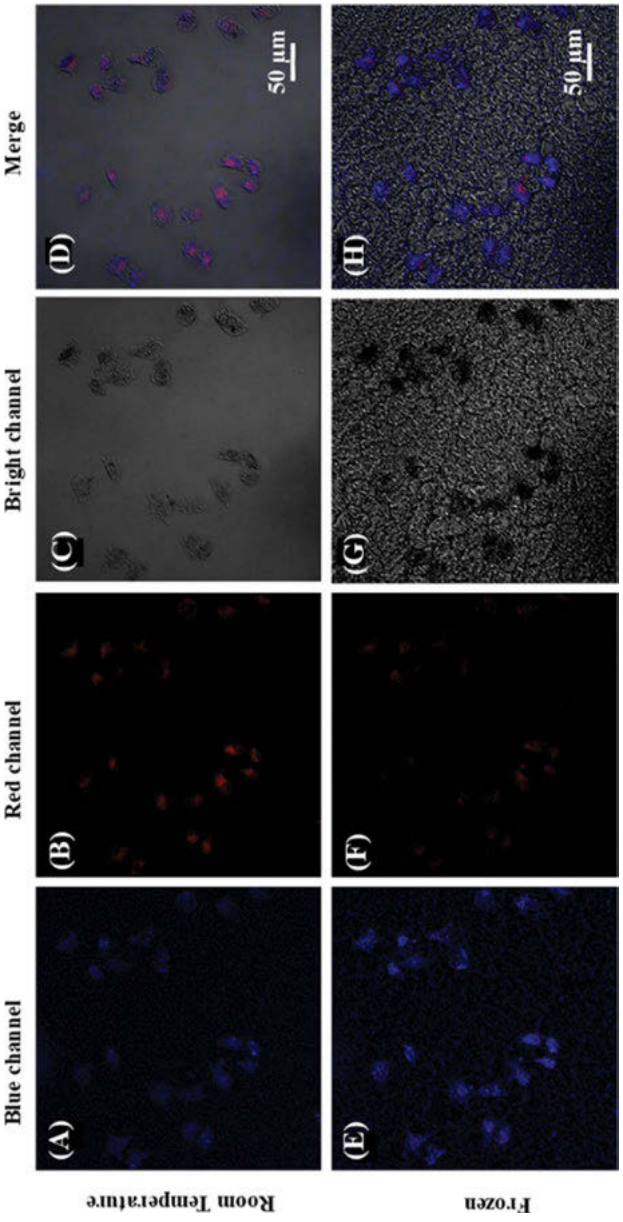


**Figure 7.12:** CLSM images of HeLa cells incubated with TPB-9 and neutral red with (A)-(D) taken at room temperature and (E)-(H) taken in the frozen state. (A), (E) TPB-9; (B), (F) neutral red; (C), (G) bright field; (D) is the merged image of (A), (B) and (C), and (H) is the merged image of (E), (F) and (G).

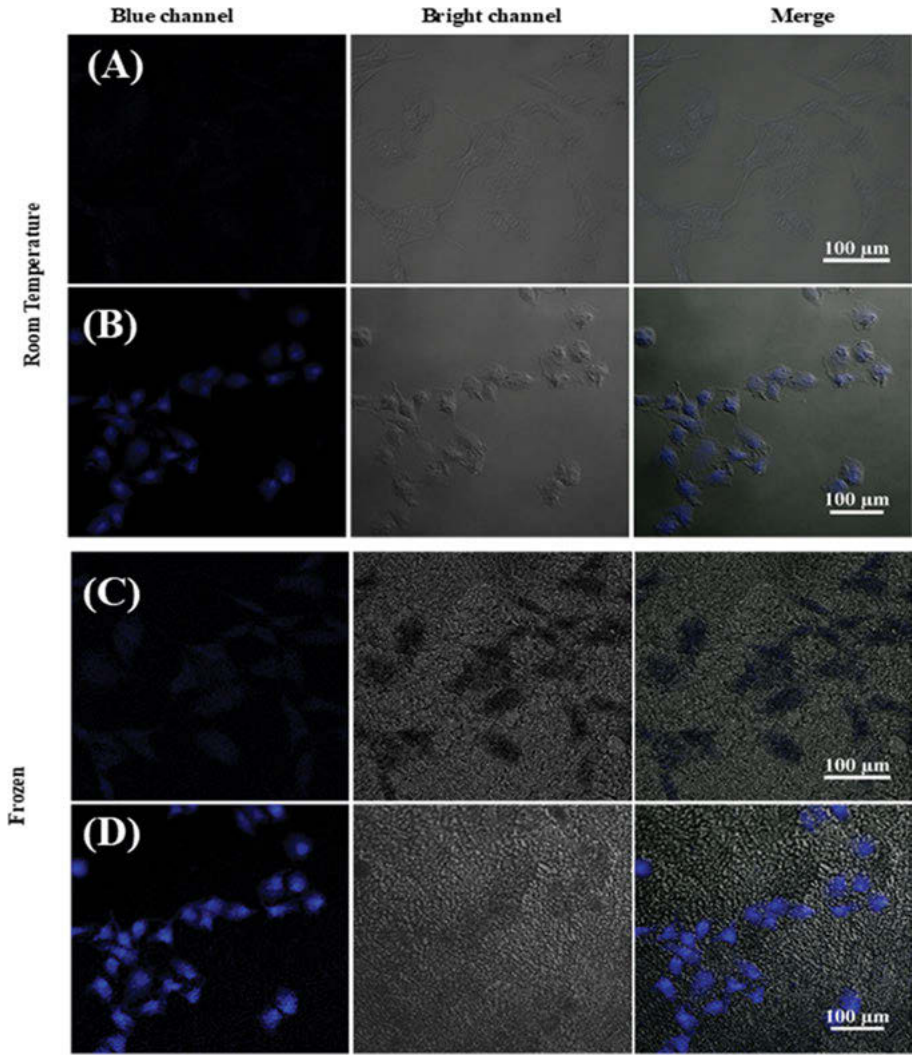


**Figure 7.13:** CLSM images of (A) NIH 3T3 cells and (B) HeLa cells at room temperature. CLSM images of (C) NIH 3T3 cells and (D) HeLa cells in the frozen state. Both NIH 3T3 and HeLa cells were incubated with TPB-9. The ice domains can be observed in bright field in the frozen state.

diagnosis with ten steps, this novel technique can provide a pathological report after a three-step treatment: staining, rinsing, and diagnosis. Moreover, it can overcome the drawbacks of H&E staining, such as poor-quality section, ungraded cell morphology and poorly stained section, as well as judgment by senior pathologist. Although the mechanism via which only HCC tissues exhibit "turn-on" fluorescence by HPB-4 is not clear and requires to be further investigated, the FPDT using HPB-4

staining is a simple, rapid technique with a high efficiency and meets the objectives of intraoperative HCC diagnosis, with potential clinical applications.

Figure 7.14 shows the synthetic route, AIE performance and photophysical properties of HPB-4. Experimental results revealed that the fluorescence intensity of HPB-4 with 90% water content is 16-fold greater than that in a pure THF solution (Figure 7.14C).

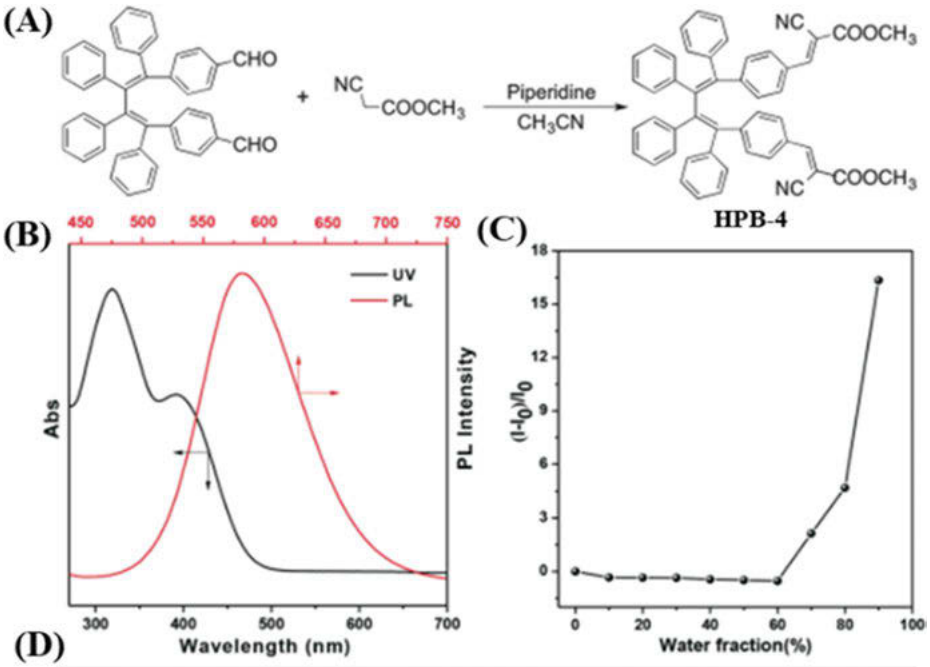


(D)

| DMSO ratio (%) | Abs (nm) | Emission (nm) | Quantum yield (%) | Lifetime (ns) |
|---|---|---|---|---|
| 100 | 318.0, 397.5 | 604.0 | 0.9 | 1.05 |
| 1 | 321.5, 409.5 | 595.0 | 7.04 | 1.71 |
| 0.1 | 323.0, 413.0 | 594.8 | 8.56 | 1.69 |
| 0 (solid powder) | 322.5, 412.0 | 556.8 | 23.58 | 2.4 |

**Figure 7.14:** (A) Synthesis route for HPB-4; (B) UV absorption and fluorescence spectra of HPB-4; (C) PL intensity change of HPB-4 with different water fractions in THF/$H_2O$ mixture, $\lambda_{ex}$ = 400 nm; (D) In a DMSO/PBS mixed system, the photophysical properties of HPB-4 with different DMSO ratios. [HPB-4] = 10 μM.

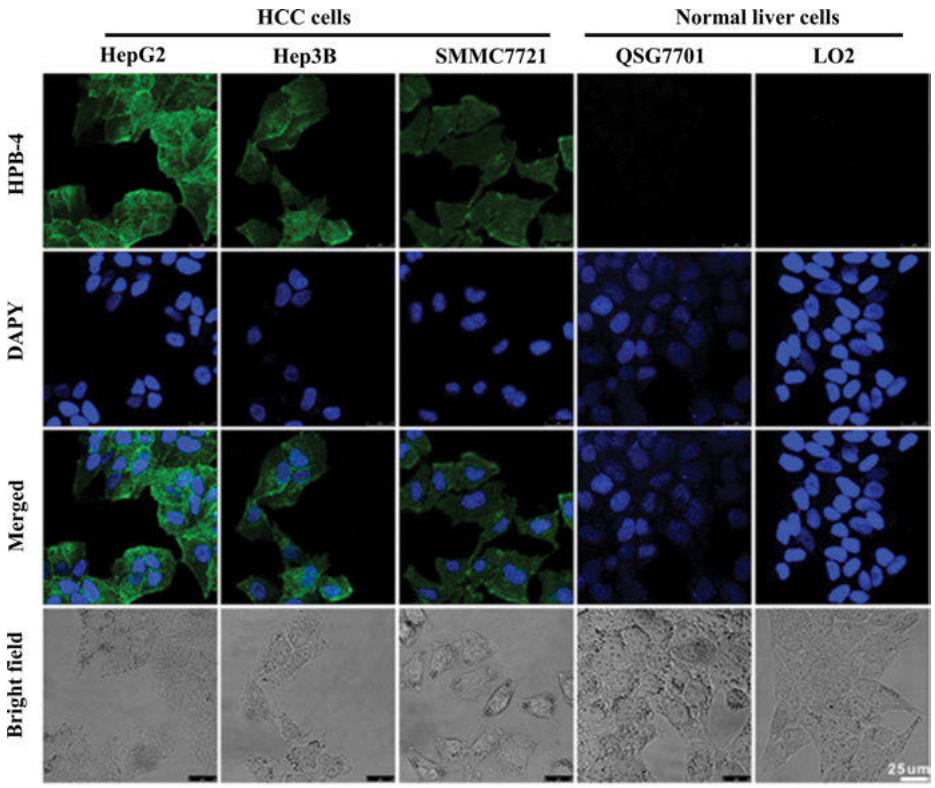


**Figure 7.15:** Fluorescence images of HCC cell lines and normal liver cell lines with HPB-4 and DAPI, [HPB-4] = 10 μM, [DAPI] = 0.1 μM; the concentration-dependent fluorescence images of in the HepG2 cell, [HPB-4] = 100 μM, 10 μM, 5 μM, 1 μM, 0.5 μM.

HCC cells could be lit up, while normal hepatocytes did not emit fluorescence after staining with HPB-4. As shown in Figure 7.15, HCC cells such as HepG2, Hep3B, and SMMC7721 cells showed strong green fluorescence in the cytoplasm, but no fluorescence signal was detected except blue fluorescence from commercial nucleus probe DAPI in normal hepatocytes QSC7701 and LO2, demonstrating that the HPB-4 can effectively distinguish HCC cells from normal hepatocytes.

FPDT, using HPB-4 staining, demonstrated that "turned-on" bright-green fluorescence in all HCC foci slides, while the other slides, including paratumor cirrhosis, FNH and adjacent tissue, as well as healthy liver tissue, still remained dark. To further understand the specificity of HCC staining, the slice of the border area between the tumor foci and paratumor cirrhosis was stained with 10-μM HPB-4 for 5 min (Figure 7.16B). Clearly, stronger fluorescence was observed at the tumor foci location, but no fluorescence was observed at the paratumor cirrhosis. These results indicated that HPB-4 can illuminate HCC cells in tissues with high specificity and no

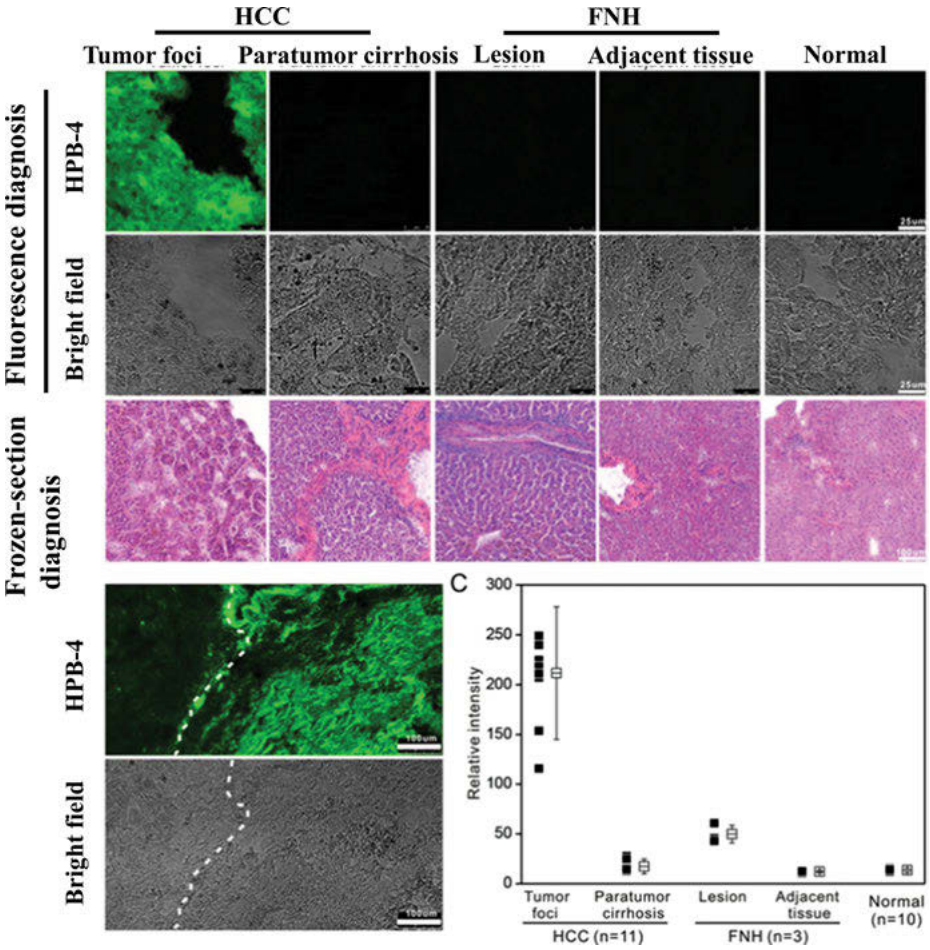


**Figure 7.16:** (A) Fluorescent images of HPB-4 in HCC, FNH and normal liver specimen compared to frozen-section diagnosis; (B) Fluorescent images of HPB-4 in tumor foci and neighboring paratumor cirrhosis at the same section; (C) Discrete transformation analysis of HPB-4 fluorescence strategy. [HPB-4] = 10 μM.

signal interference by a complex microenvironment, which was also consistent with conventional frozen-section diagnosis. Quantitative analysis of the fluorescence signal recorded under the same parameters of CLSM was further performed to investigate the sensitivity of this FPDT for HCC using HPB-4. The mean fluorescence intensity of malignant HCC foci was significantly greater than that of paratumor cirrhosis (Figure 7.16C), with a high ratio of 12.2. In addition, the intensity of benign FNH was slightly greater than that of adjacent tissues, but the intensity of HCC foci was 4.3-fold greater than that of FNH. Furthermore, the fluorescence intensities of paratumor cirrhosis and normal liver tissues were almost similar, including three cases of adjacent tissues from

FNH patients. Hence, HCC can be easily diagnosed due to the high sensitivity, compared to the other tissues, especially nontumoral liver tissues, as a negative control recommended by clinical guidelines.

In summary, MPB and its derivatives can perform biological imaging, not only at the cellular level, but also in organs and tissues, and these derivatives play a key role for clinical surgical navigation.

## 7.5 Conclusion and outlook

In summary, MPBs exhibit typical AIE/AEE characteristics and are potential candidates for biosensing and bioimaging due to their rich structures and conformations. In this chapter, most of the outstanding developments in this field are summarized, mainly outlining the syntheses, structures, and properties of MPBs as well as the related applications of these AIE/AEEgens. According to the general mechanism of AIE/AEE, both multiple rotors and twisted conformation are crucial for achieving good performance in biosensing and bioimaging.

1. MPBs have enriched the AIE molecular library and expanded the AIE family. Furthermore, the mechanism of AIE is clarified, and the relationship between structure and performance is investigated. In addition, ideas and theoretical guidance for the future design of new AIE molecules have been provided.
2. A deeper understanding of the cis-trans isomerism of AIE molecules is achieved, and a new platform for the future design and synthesis of cis-trans isomerism is provided.
3. MPSs can detect viruses and proteins, and it can be used for navigation in clinical operations. It has potential application prospects in biomedicine.

As a “star” class of molecules in the AIE field, TPEs have been applied in several fields, but the development of MPBs is only in its infancy. To the best of our knowledge, there is a small number of macromolecular studies probably due to its “freshman” role in the AIE/AEE field. Occasionally, new developments can come along with new possibilities and discoveries. Indeed, a considerable number of studies on MPBs should be conducted to further deepen the understanding of the AIE/AEE mechanism, improve AIE/AEE efficiency, and broaden AIE/AEE applications, which include but are not limited to designing totipotent molecules, with full-color emission in different external environments, near-infrared fluorophores with high emission in aqueous surroundings, and pure organic materials with strong and long-lived phosphorescence at room temperature. In short, MPB will also become a “star” structure suitable for the fast-developing AIE/AEE fields.

# References

[1] Amans D, Bellosta V, Cossy J, Synthesis of two bioactive natural products: FR252921 and pseudotrienic acid B, Chem Eur J, 2009, 15, 3457–3473.
[2] Ramamoorthy G, Acevedo CM, Alvira E, Lipton MA, Synthesis and spectroscopic correlation of the diastereoisomers of 2,3-dihydroxy-2,6,8-trimethyldeca-(4Z,6E)-dienoic acid: Implications for the structures of papuamides A–D and mirabamides A–D, Tetrahedron Asymmetry, 2008, 19, 2546–2554.
[3] Bartkowiak W, Zaleśny R, Niewodniczański W, Leszczynski J, Quantum chemical calculations of the first- and second-order hyperpolarizabilities of molecules in solutions, J Phys Chem A, 2001, 105, 10702–10710.
[4] Davis R, Mallia VA, Das S, Reversible photochemical phase transition behavior of alkoxy-cyano-substituted diphenylbutadiene liquid crystals, Chem Mater, 2003, 15, 1057–1063.
[5] Davis R, Mallia VA, Das S, Tamaoki N, Butadienes as novel photochromes for color tuning of cholesteric glasses: Influence of microscopic molecular reorganization within the helical superstructure, Adv Funct Mater, 2004, 14, 743–748.
[6] Denmark SE, Tymonko SA, Sequential cross-coupling of 1,4-bissilylbutadienes: Synthesis of unsymmetrical 1,4-disubstituted 1,3-butadienes, J Am Chem Soc, 2005, 127, 8004–8005.
[7] Abraham S, Mallia VA, Ratheesh KV, Tamaoki N, Das S, Reversible thermal and photochemical switching of liquid crystalline phases and luminescence in diphenylbutadiene-based mesogenic dimers, J Am Chem Soc, 2006, 128, 7692–7698.
[8] Davis R, Saleesh Kumar NS, Abraham S, Suresh CH, Rath NP, Tamaoki N, Das S, Molecular packing and solid-state fluorescence of alkoxy-cyano substituted diphenylbutadienes: Structure of the luminescent aggregates, J Phys Chem C, 2008, 112, 2137–2146.
[9] Huang W, Bender M, Seehafer K, Wacker I, Schröder RR, Bunz UHF, A tetraphenylethene-based polymer array discriminates nitroarenes, Macromolecules, 2018, 51, 1345–1350.
[10] Zheng X, Zhu W, Zhang C, Zhang Y, Zhong C, Li H, Xie G, Wang X, Yang C, Self-assembly of a highly emissive pure organic imine-based stack for electroluminescence and cell imaging, J Am Chem Soc, 2019, 141, 4704–4710.
[11] Feng H-T, Zou S, Chen M, Xiong F, Lee M-H, Fang L, Tang BZ, Tuning push–pull electronic effects of aiegens to boost the theranostic efficacy for colon cancer, J Am Chem Soc, 2020, 142, 11442–11450.
[12] Feng H-T, Li Y, Duan X, Wang X, Qi C, Lam JWY, Ding D, Tang BZ, Substitution Activated precise phototheranostics through supramolecular assembly of AIEgen and calixarene, J Am Chem Soc, 2020, 142, 15966–15974.
[13] Chen C, Ni X, Jia SR, Liang Y, Wu XL, Kong DL, Ding D, Massively evoking immunogenic cell death by focused mitochondrial oxidative stress using an AIE luminogen with a twisted molecular structure, Adv Mater, 2019, 31.
[14] Luo J, Xie Z, Lam JWY, Cheng L, Chen H, Qiu C, Kwok HS, Zhan X, Liu Y, Zhu D, Tang BZ, Aggregation-induced emission of 1-methyl-1,2,3,4,5-pentaphenylsilole,Chem Commun, 2001, 1740–1741.
[15] Zhu L, Zhu B, Luo J, Liu B, Design and property modulation of metal–organic frameworks with aggregation-induced emission, ACS Mater Lett, 2021, 3, 77–89.
[16] Würthner F, Aggregation-Induced Emission (AIE): A HISTORICAL PERSpective, Angew Chem Int Ed, 2020, 59, 14192–14196.
[17] Wu WB, Li Z, Nanoprobes with aggregation-induced emission for theranostics, Mater Chem Front, 2021, 5, 603–626.
[18] Mei J, Leung NLC, Kwok RTK, Lam JWY, Tang BZ, Aggregation-Induced emission: Together we shine, united we soar!, Chem Rev, 2015, 115, 11718–11940.

[19] Wen Y, Xie J, Deng C, Wu Y, ChemInform abstract: Synthesis of buta-1,3-dienes through palladium-catalyzed homocoupling of aromatic alkenes, ChemInform, 2015, 46.
[20] Bacchi A, Brillante A, Crocco D, Chierotti MR, Della Valle RG, Girlando A, Masino M, Pelagatti P, Venuti E, Exploration of the polymorph landscape for 1,1,4,4-tetraphenyl-1,3-butadiene, CrystEngComm, 2014, 16, 8205–8213.
[21] Mora S, Tavazzi S, Spearman P, Melt-growth of 1,1,4,4-tetraphenyl-1,3-butadiene crystals on different substrates, Synth Met, 2012, 162, 1737–1740.
[22] Zhang Y, Kong L, Shi J, Tong B, Zhi J, Feng X, Dong Y, Aggregation-induced emission of hexaphenyl-1,3-butadiene, Chin J Chem, 2015, 33, 701–704.
[23] Zhang Y, Han T, Gu S, Zhou T, Zhao C, Guo Y, Feng X, Tong B, Bing J, Shi J, Zhi J, Dong Y, Mechanochromic Behavior of aryl-substituted buta-1,3-diene derivatives with aggregation enhanced emission, Chem EurJ, 2014, 20, 8856–8861.
[24] Zhang Y, Mao H, Xu W, Shi J, Cai Z, Tong B, Dong Y, Aggregation-induced emission of multiphenyl-substituted 1,3-butadiene derivatives: synthesis, properties and application, Chem EurJ, 2018, 24, 15965–15977.
[25] Zhang Y, Xu H, Xu W, Zhang C, Shi J, Tong B, Cai Z, Dong Y, Conformational sensitivity of tetraphenyl-1,3-butadiene derivatives with aggregation-induced emission characteristics, Sci China Chem, 2019, 62, 1393–1397.
[26] Zhang Y, Mao H, Kong L, Tian Y, Tian Z, Zeng X, Zhi J, Shi J, Tong B, Dong Y, Effect of E/Z isomerization on the aggregation-induced emission features and mechanochromic performance of dialdehyde-substituted hexaphenyl-1,3-butadiene, Dyes Pigm, 2016, 133, 354–362.
[27] Ding D, Li K, Liu B, Tang BZ, Bioprobes based on AIE fluorogens, Acc Chem Res, 2013, 46, 2441–2453.
[28] Ahn J, Shin Y-B, Lee J, Kim M-G, Human alpha-fetal protein immunoassay using fluorescence suppression with fluorescent-bead/antibody conjugate and enzymatic reaction, Biosens Bioelectron, 2015, 71, 115–120.
[29] Alonso MC, Trapiella-Alfonso L, Fernández JMC, Pereiro R, Sanz-Medel A, Functionalized gold nanoclusters as fluorescent labels for immunoassays: Application to human serum immunoglobulin E determination, Biosens Bioelectron, 2016, 77, 1055–1061.
[30] Liu P, Chen D, Wang Y, Tang X, Li H, Shi J, Tong B, Dong Y, A highly sensitive “turn-on” fluorescent probe with an aggregation-induced emission characteristic for quantitative detection of γ-globulin, Biosens Bioelectron, 2017, 92, 536–541.
[31] Rowe T, Abernathy Robert A, Hu-Primmer J, Thompson William W, Lu X, Lim W, Fukuda K, Cox Nancy J, Katz Jacqueline M, Detection of Antibody to Avian Influenza A (H5N1) Virus in Human Serum by Using a Combination of Serologic Assays, J Clin Microbiol, 1999, 37, 937–943.
[32] Covalciuc Kristi A, Webb Kenneth H, Carlson Curtis A, Comparison of four clinical specimen types for detection of influenza A and B viruses by optical immunoassay (FLU OIA Test) and cell culture methods, J Clin Microbiol, 1999, 37, 3971–3974.
[33] Von Itzstein M, The war against influenza: Discovery and development of sialidase inhibitors, Nat Rev Drug Discov, 2007, 6, 967–974.
[34] Caliendo AM, Gilbert DN, Ginocchio CC, Hanson KE, May L, Quinn TC, Tenover FC, Alland D, Blaschke AJ, Bonomo RA, Carroll KC, Ferraro MJ, Hirschhorn LR, Joseph WP, Karchmer T, MacIntyre AT, Reller LB, Jackson AF, Better tests, better care: Improved diagnostics for infectious diseases, Clin Infect Dis, 2013, 57, NP–NP.
[35] Stöhr K, The global agenda on influenza surveillance and control, Vaccine, 2003, 21, 1744–1748.

[36] Pan X, Liu P, Wu X, Zhang Y, Cai Z, Shi J, Zhi J, Li Z, Wang D, Tong B, Dong Y, A "Turn-on" fluorescent bioprobe with aggregation-induced emission characteristics for detection of influenza virus-specific hemagglutinin protein, Sens Actuators B Chem, 2021, 345, 130392.
[37] Bouzigues C, Gacoin T, Alexandrou A, Biological applications of rare-earth based nanoparticles, ACS Nano, 2011, 5, 8488–8505.
[38] Lutfor MR, Sidik S, Wan Yunus WMZ, Ab Rahman MZ, Mansoor A, Jelas H, Preparation and swelling of polymeric absorbent containing hydroxamic acid group from polymer grafted sago starch, Carbohydr Polym, 2001, 45, 95–100.
[39] Gupta KC, Sahoo S, Graft copolymerization of acrylonitrile and ethyl methacrylate comonomers on cellulose using ceric ions, Biomacromolecules, 2001, 2, 239–247.
[40] Wang Y, Pan X, Peng Z, Zhang Y, Liu P, Cai Z, Tong B, Shi J, Dong YA, "Turn-On" fluorescent chemosensor with the aggregation-induced emission characteristic for high-sensitive detection of Ce ion, Sens Actuators B Chem, 2018, 267, 351–356.
[41] Cheng K, Lee J-S, Hao P, Yao SQ, Ding K, Tetrazole-Based LZ, Probes for integrated phenotypic screening, affinity-based proteome profiling, and sensitive detection of a cancer biomarker, Angew Chem Int Ed, 2017, 56, 15044–15048.
[42] Rosenthal J, Lippard SJ, Direct Detection of Nitroxyl in Aqueous Solution Using a Tripodal Copper(II) BODIPY Complex, J Am Chem Soc, 2010, 132, 5536–5537.
[43] Nishino M, Hirano K, Satoh T, Miura M, Copper-Mediated C-H/C-H biaryl coupling of benzoic acid derivatives and 1,3-azoles, Angew Chem Int Ed, 2013, 52, 4457–4461.
[44] Zhang Y, Xu W, Kong L, Han B, Cai Z, Shi J, Tong B, Dong Y, Tang B, Turn-on fluorescent probe with aggregation-induced emission characteristics for polyazoles, Mater Chem Front, 2018, 2, 1779–1783.
[45] Guo Y, Feng X, Han T, Wang S, Lin Z, Dong Y, Wang B, Tuning the luminescence of metal–organic frameworks for detection of energetic heterocyclic compounds, J Am Chem Soc, 2014, 136, 15485–15488.
[46] Li Q, Wu X, Huang X, Deng Y, Chen N, Jiang D, Zhao L, Lin Z, Zhao Y, Tailoring the fluorescence of AIE-active metal–organic frameworks for aqueous sensing of metal ions, ACS Appl Mater Interfaces, 2018, 10, 3801–3809.
[47] Altschuler E, Aluminum-containing antacids as a cause of idiopathic Parkinson's disease, Med Hypotheses, 1999, 53, 22–23.
[48] Wang B, Xing W, Zhao Y, Deng X, Effects of chronic aluminum exposure on memory through multiple signal transduction pathways, Environ Toxicol Pharmacol, 2010, 29, 308–313.
[49] Hamburger WW, The earliest known reference to the heart and circulation: The Edwin Smith surgical papyrus, circa 3,000, B C Am Heart J, 1939, 17, 259–274.
[50] Korpan NN, A history of cryosurgery: its development and future, J Am Coll Surg, 2007, 204, 314–324.
[51] Gage AA, Baust JM, Baust JG, Experimental cryosurgery investigations in vivo, Cryobiology, 2009, 59, 229–243.
[52] Sabel MS, Cryo-immunology: A review of the literature and proposed mechanisms for stimulatory versus suppressive immune responses, Cryobiology, 2009, 58, 1–11.
[53] Benoit RM, Cohen JK, Miller RJ, Cryosurgery for prostate cancer: New technology and indications, Curr Urol Rep, 2000, 1, 41–47.
[54] Chu KF, Dupuy DE, Thermal ablation of tumours: Biological mechanisms and advances in therapy, Nat Rev Cancer, 2014, 14, 199–208.
[55] He Z, Liu P, Zhang S, Yan J, Wang M, Cai Z, Wang J, Dong Y, A freezing-induced turn-on imaging modality for real-time monitoring of cancer cells in cryosurgery, Angew Chem Int Ed, 2019, 58, 3834–3837.

[56] Yang JD, Hainaut P, Gores GJ, Amadou A, Plymoth A, Roberts LR, A global view of hepatocellular carcinoma: Trends, risk, prevention and management, Nat Rev Gastroenterol Hepatol, 2019, 16, 589–604.
[57] Kaufman Z, Lew S, Griffel B, Dinbar A, Frozen-section diagnosis in surgical pathology. A prospective analysis of 526 frozen sections, Cancer, 1986, 57, 377–379.
[58] Chen D, Mao H, Hong Y, Tang Y, Zhang Y, Li M, Dong Y, Hexaphenyl-1,3-butadiene derivative: A novel “turn-on” rapid fluorescent probe for intraoperative pathological diagnosis of hepatocellular carcinoma, Mater Chem Front, 2020, 4, 2716–2722.

Minglun Liu, Yuncong Chen, Zijian Guo

# Chapter 8
# AIEgens for intracellular microenvironment analysis

## 8.1 Introduction

Intracellular microenvironment plays a pivotal role in maintaining normal physiological homeostasis of cells. Different subcellular organelles show different pH values. Lysosomes possess a medium acidic microenvironment to sustain the highest activities of the hydrolases, while mitochondria need slightly basic environment to maintain a steady proton gradient for ATP synthesis [1]. Intracellular microviscosity has a significant impact on the transportation of mass and energy and the diffusion of reactive metabolites [2]. Micropolarity in biological systems reflects the permeability of membrane of subcellular compartments and affects the activity of a variety of proteins and enzymes [3]. Oxygen concentration determines the intracellular metabolic pathway. Low supply of oxygen or hypoxia condition is one of the major characteristics of tumors and their metastasis lesion [4]. The disturbance of intracellular microenvironment homeostasis is closely associated with many diseases such as cancer, diabetes, and Alzheimer's disease. Therefore, real-time monitoring of dynamic changes of intracellular microenvironment is of great significance. Fluorescence technique shows advantages such as noninvasiveness and high sensitivity, making it an ideal method for providing spatial–temporal information of analytes. However, traditional fluorescent dyes have to face challenges such as aggregation-caused quenching (ACQ) and poor photostability for long-term biological imaging. Aggregation-induced emission luminogens (AIEgens) have emerged as a novel type

**Acknowledgements:** The work was under financial support from the National Natural Science Foundation of China (22122701, 21977044, 21907050, 21731004, 91953201), the Natural Science Foundation of Jiangsu Province (BK20202004, BK20190282), and the Excellent Research Program of Nanjing University (ZYJH004).

**Minglun Liu,** State Key Laboratory of Coordination Chemistry, School of Chemistry and Chemical Engineering, Chemistry and Biomedicine Innovation Center (ChemBIC), Nanjing University, Nanjing, 210023, China
**Yuncong Chen,** State Key Laboratory of Coordination Chemistry, School of Chemistry and Chemical Engineering, Chemistry and Biomedicine Innovation Center (ChemBIC), Nanjing University, Nanjing, 210023, China, e-mail: chenyc@nju.edu.cn
**Zijian Guo,** State Key Laboratory of Coordination Chemistry, School of Chemistry and Chemical Engineering, Chemistry and Biomedicine Innovation Center (ChemBIC), Nanjing University, Nanjing, 210023, China, e-mail: zguo@nju.edu.cn

https://doi.org/10.1515/9783110672220-008

of advanced materials with unique advantages, such as high photostability, high quantum yield in solid states, etc. AIEgens have attracted continuously increasing attention and have been widely used in various fields including light emitting diodes, chemosensing, bioimaging and theranostics. The excellent photobleaching resistance of AIEgens makes them ideal imaging agents for long-term tracking of physiological processes. In this chapter, we will focus on the topic of AIEgen-based sensors for intracellular microenvironment analysis (Figure 8.1).

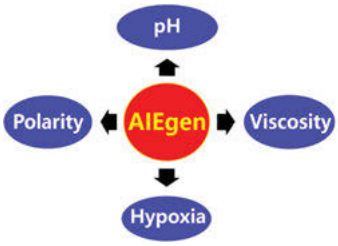


**Figure 8.1:** AIEgen-based sensors for intracellular microenvironment analysis.

## 8.2 AIEgen-based sensors for pH

Protons play an important role in physiological processes such as ion transport, receptor-mediated signal transduction, endocytosis, homeostasis, and cell proliferation [1]. The urgent demand for pH measurement and imaging in biological systems promotes the development of pH fluorescent probes. Under normal physiological conditions, cytoplasmic pH ($pH_c$) and extracellular pH ($pH_e$) are between 7.2 and 7.4. However, the pH of different subcellular organelles is different; for example, the pH of lysosomes is in the range of 4.5–5.5, while the pH of mitochondria is about 8.0 [5]. Studies have shown that an abnormal pH value in the cell will lead to the destruction of the pH homeostasis of the whole cell, resulting in the production of free radicals and even cell apoptosis. Intracellular pH mutation can lead to organelle dysfunction, and abnormal pH can lead to neurodegenerative diseases (such as Alzheimer's disease) [6]. Therefore, the accurate monitoring of physiological pH is crucial to understand the information about various cell functions and pathological processes, so as to design better drugs and realize individualized treatment in precision medicine.

Fluorescence imaging is a necessary and effective tool for monitoring pH fluctuation in life systems [7]. Compared to nuclear magnetic resonance (NMR) and microelectrode methods, fluorescence method has the advantages of noninvasiveness, real-time imaging of pH distribution, and high spatial and temporal resolution, which can help in better understanding of the internalization pathway and pathogenic process of cells. There are two main design concepts for pH detection: (1) the acid base neutralization reaction of phenol, amine, and N-Heterocycle (2) nucleophilic addition

of hydroxyl ions to cyanine dyes [8, 9]. However, due to the small Stokes shift (a few to 20 nm) and concentration quenching effect (i.e., ACQ), traditional dyes such as cyanine limit the realization of the full potential in bioimaging.

Tong and his colleagues designed a pH-sensitive fluorescent probe, which has a Schiff base structure of carboxyl and hydroxyl groups and exhibits AIE properties. This pH-sensitive AIE probe has been shown to monitor the pH value of living cells [10]. In the pH range of 5.0 to 7.0, probe **1** showed the characteristic of proportional fluorescence response by switching its aggregated and dissolved states fluorescence, with the color changed from orange to green (Figure 8.2). It has good stability, membrane permeability, and selectivity for metal ions, and has been successfully applied in the determination of intracellular pH of HepG2 cells.

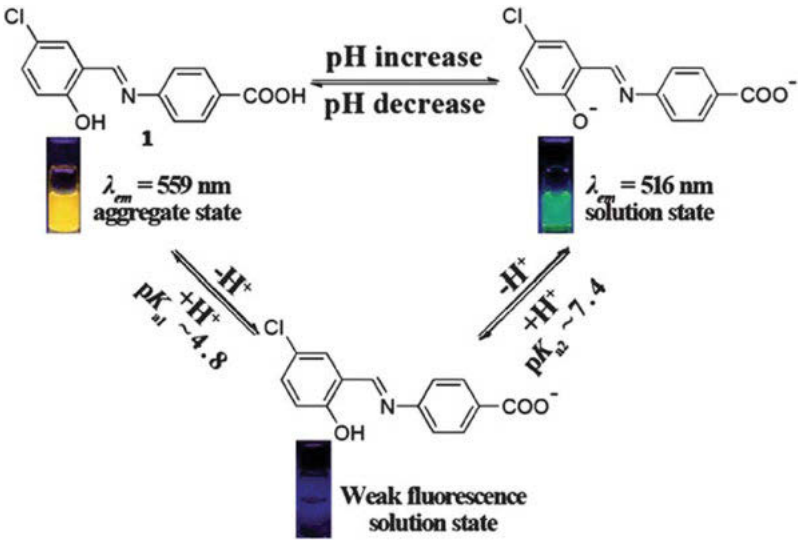


**Figure 8.2:** Proposed deprotonation processes of probe **1**.

The fluorescence response of probe **1** at different pH was studied. As shown in Figure 8.2, probe **1** tends to aggregate at neutral pH and exhibits aggregation-induced emission enhancement (AIEE) with a maximum fluorescence emission of 559 nm. With the increase of pH from 3.43 to 5.63, the carboxyl group gradually deprotonated, resulting in the weakening of AIEE effect. Then, with the increase of pH from 5.63 to 9.56, the hydroxyl group of probe **1** was deprotonated in higher pH solution, resulting in a new emission peak for the dianion form of **1** appearing at 516 nm in a higher pH solution. The fluorescence color of **1** changed from orange to green in the above process, and the ratio of two channels ($I_{516}$ nm / $I_{559}$ nm) gradually increased in the range of pH 5.0 to 7.0. The results showed that probe **1** had good performance in neutral pH measurement.

Next, fluorescence imaging of pH fluctuation of HepG2 cells was performed with probe **1**. As shown in Figure 8.3, the dye-loaded cells showed weak fluorescence in both channel I (490–535 nm) and channel II (540–585 nm), with pH of 5 in PBS. With the increase of pH, the fluorescence brightness of channel I increased significantly. The ratio fluorescence image is shown in Figure 8.3(g–i), which indicates that probe **1** can easily reveal the near-neutral pH change in HepG2 cells by a ratiometric response.

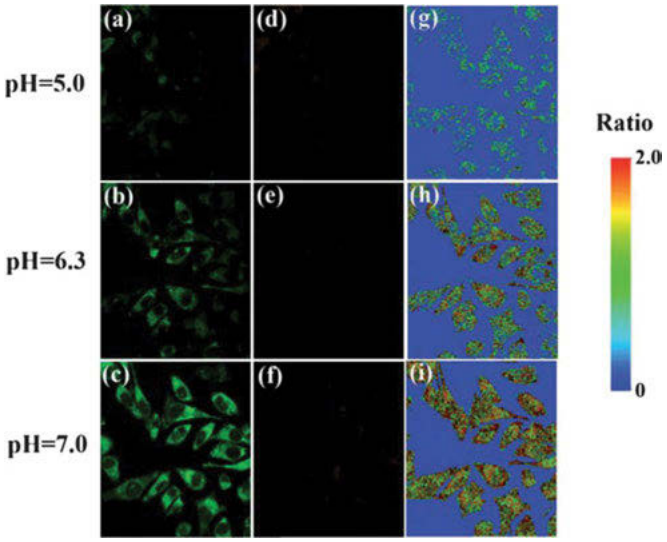


**Figure 8.3:** Confocal fluorescence images of pH in HepG2 cells after incubation with 1 (60 μM) and nigericin at 37° C ($\lambda_{ex}$ 405 nm). Left: collected at channel I (490–535 nm) at pH 5.00 (a), 6.30 (b), and 7.00 (c); middle: collected at channel II (540–585 nm) at pH 5.00 (d), 6.30 (e), and 7.00 (f); and right (g–i): ratiometric fluorescence images generated from channel I and channel II.

In 2013, Tang's group reported an AIE fluorescent probe based on nucleophilic addition reaction, which was used to detect the whole range of intracellular pH [8]. Tetraphenylvinyl cyanine derivatives modified by sulfonate showed two fluorescence responses with change of pH value (Figure 8.4). The probe TPE-Cy showed strong to moderate red emissions at pH 5–7 ($\lambda_{ex}$ = 380 nm, $\lambda_{em}$ = 615 nm), weak-to-nil red emissions at pH 7 – 10, and nil-to-strong blue emissions at pH 10 – 14 ($\lambda_{ex}$ = 380 nm, $\lambda_{em}$ = 489 nm). In the acidic range, with the increase of pH value, the sulfonic acid and sulfonate in TPE-Cy are in equilibrium, which leads to the change of fluorescence emission.

At the same time, in the alkaline range, when the pH value is more than 10, the C=N in the indolinium unit will react with hydroxyl group through nucleophilic addition reaction. The process breaks the conjugation system of TPE-Cy and further induces fluorescence responses. Considering that TPE-Cy also has good biocompatibility, the

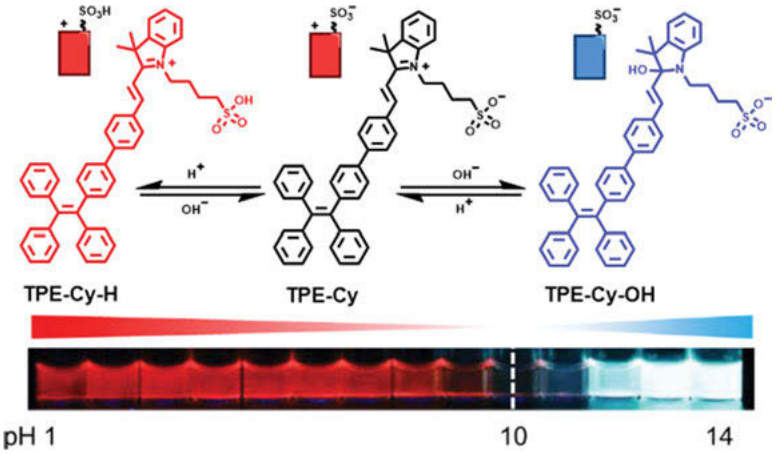


**Figure 8.4:** Working principle: fluorescence response mechanism of TPE-Cy to different pH.

specific fluorescence signals ($I_{489}/I_{615}$, the lower the ratio, the more acidic) of blue and red channels are further used as the indicator of pH imaging. As shown in Figure 8.5, TPE-Cy has significant AIE properties in the n-hexane and ethanol system.

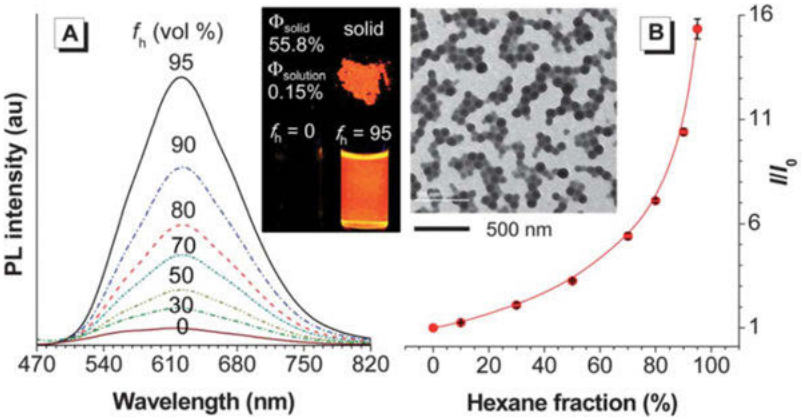


**Figure 8.5:** (A) PL spectra of TPE cy in ethanol / n-hexane mixtures with different n-hexane volume fractions. (B) The change of $I/I_0$ ratio with the increase of n-hexane volume fraction.

The living cells stained with TPE-Cy were incubated with acetic acid, a weak acid that can penetrate cells, and observed with confocal microscope (Figure 8.6). After treatment, the acid region of pseudo red in the cell (low I489/I615 ratio) was significantly expanded, indicating that the acidification effect was obvious. In contrast, when DMEM (pH 8.5) was used to treat cells, the false blue region (high $I_{489}/I_{615}$ ratio) was

the main area. The results of flow cytometry also show that TPE-Cy has great potential in high resolution and high-throughput analysis of the intracellular environment.

Mitochondria play an important role in the process of oxidative metabolism and apoptosis. Their morphology is closely related to the occurrence and development of some diseases [11]. The changes of cell microenvironment are one of the most important indicators related to these diseases, especially the pH value in cells. The function of mitochondria is also highly dependent on the intracellular pH value. Therefore, it is necessary to distinguish the mitochondria at different pH values and to study the relationship between mitochondrial morphology and pH change among cells.

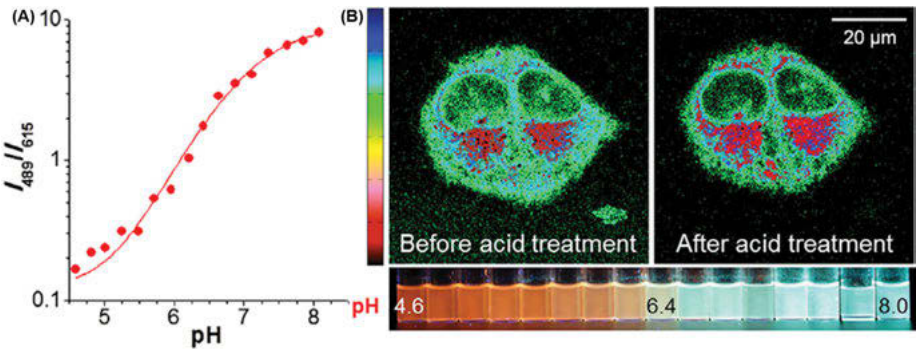


**Figure 8.6:** (A) Changes of $I_{489}/I_{615}$ ratio with different pH values. I489 and I615 represent the emission intensity of the solution at 489 and 615 nm, respectively. (B) Pseudo color ratio fluorescence images of cells before and after treatment with acetic acid.

In 2017, Meng's group reported TPE-Xan-In, which exhibits AIE characteristics at neutral pH and can illuminate mitochondria specifically and with good biocompatibility, superior photostability, and tolerance to mitochondrial membrane potential changes [12]. From Figure 8.7a, the probe shows strong fluorescence emission at 705 and 750 nm ($\lambda_{Ex}$ = 660 nm) at acid pH of 4.0. When the water content increases from 0 to 70%, the fluorescence intensity of both peaks decreased, indicating that the probe shows the traditional ACQ characteristics when pH = 4.0. On the other hand, TPE-Xan-In has weak fluorescence emission at 705 nm at neutral pH of 7.0 (Figure 8.7b), while when the water content increases to 70%, it has obvious fluorescence emission at 740–750 nm.

The author then assumes that TPE-Xan-In has pH-dependent AIE properties that may be due to the change of phenolate to the phenolic form at different pH values (Figure 8.8).

Then, HeLa cells were incubated with TPE-Xan-In, MTG, and then, the pH of HeLa cells was adjusted to 4.0–7.0 by nigericin. The confocal fluorescence image (Figure 8.9) shows that the fluorescence emission of TPE-Xan-In is very weak when

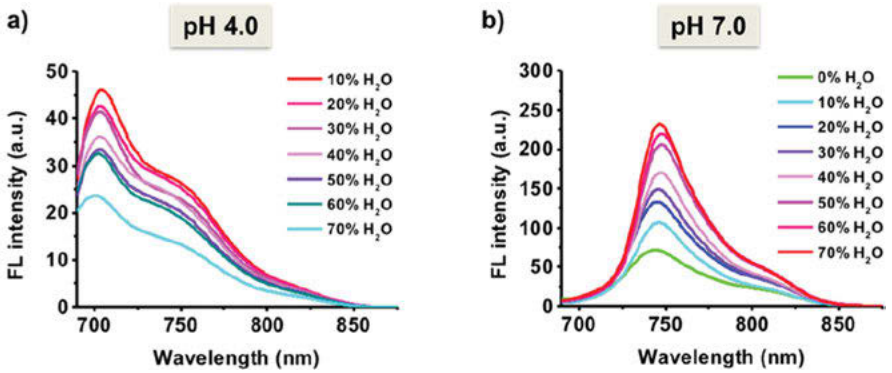


**Figure 8.7:** (a) Fluorescence emission spectra of TPE – Xan – In with different $H_2O$/THF ratios at pH 4.0 and (b) 7.0, respectively.

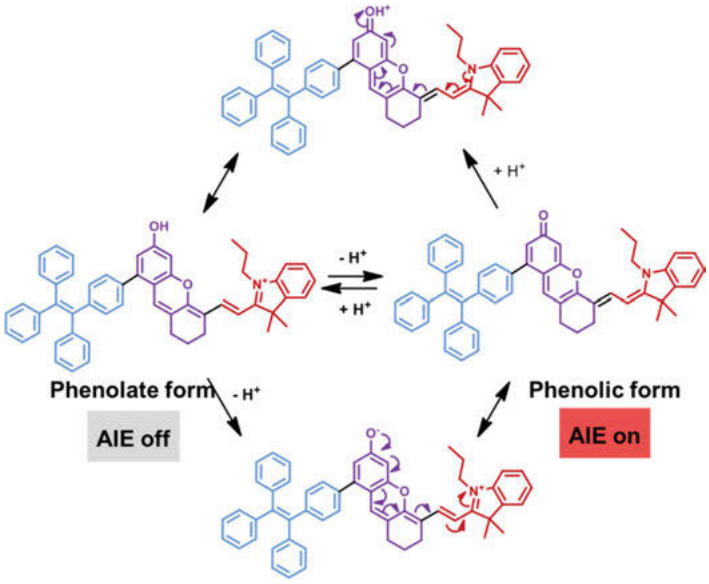


**Figure 8.8:** Proposed mechanisms for pH-dependent AIE properties of TPE-Xan-In.

pH is 4.0. With increase in pH, the fluorescence intensity in TPE-Xan-In channel increased obviously, while the change of fluorescence intensity of MTG channel was inconspicuous. These results confirmed that TPE-Xan-In had pH dependence on mitochondrial imaging and that the probe could be used to study the relationship between mitochondrial morphology and pH change between cells.

Studies have shown that 2-benzimidazole is a classical reversible pH-sensing group [13]. In 2018, Guo's group designed and synthesized a series of ratiometric pH probes through modified BODIPY fluorophore, with a pH-sensitive group benzimidazole on its

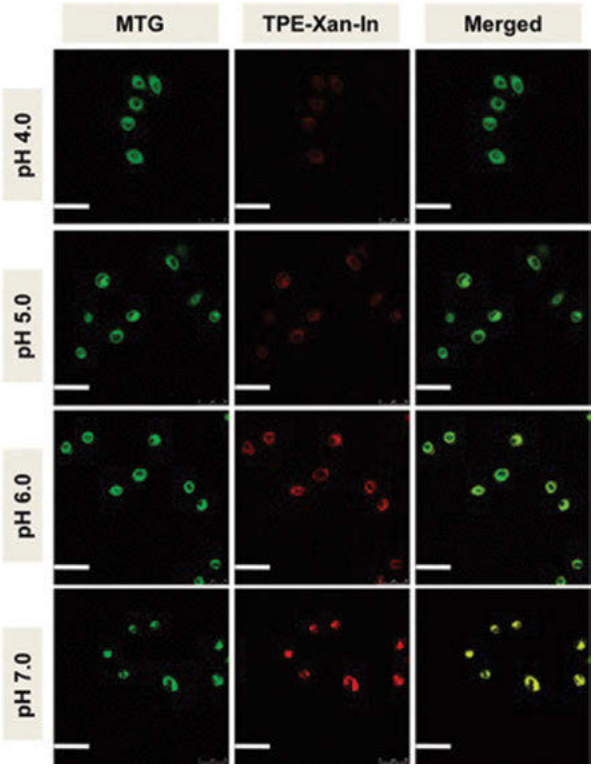


**Figure 8.9:** Fluorescence images of HeLa cells incubated with 2.5 μM TPE – Xan – In and 0.05 μM MTG solutions with different pH values containing 5 μg $mL^{-1}$ nigericin.

*β*-position to form three 2-(benzoimidazol-2-)yl-1,3,5,7-tetramethyl-BODIPY derivatives, named **BBI-1/2/3** (Figure 8.10) [14]. The BODIPY intrinsic emission and AIE emission of these probes are regulated by different pH values, and the pH-sensitive range is adjusted by modifying benzimidazole with different substituents.

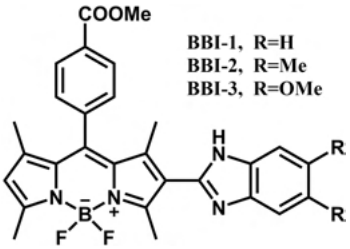


**Figure 8.10:** Chemical structures of **BBI-1/2/3.**

For the BBI-1 probe, the ratiometric pH-sensing behavior was retained when the BODIPY and AIE emission were excited at 488 nm and 543 nm, respectively. When the pH

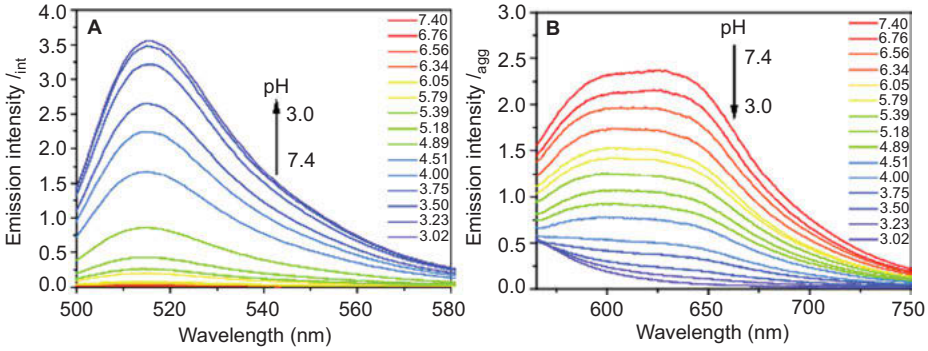


**Figure 8.11:** (A) Intrinsic emission ($I_{int}$, λex:488 nm) and (B) AIE ($I_{agg}$, λex: 543 nm) spectra of **BBI-1.**

value decreased from 7.4 to 3.0, rise in intrinsic emission ($I_{int}$, Figure 8.11A) and fall in AIE emission ($I_{agg}$, Figure 8.11B) were observed. Therefore, the $I_{int}/I_{agg}$ ratio is significantly enhanced, showing the pH ratio-sensing ability through dual excitation / dual emission mode. Next, the pH calibration curve of BBI in A549 cells was measured by dual excitation and dual emission. As shown in the Figure 8.12, when pH is from 6.5 to 3.8, the $I_{int}$ of green fluorescent channel is significantly enhanced, while the $I_{agg}$ of red channel is significantly decreased. In addition, with the decrease of pH value from 6.0 to 3.8, the ratio of green to red channels ($I_{int}/I_{agg}$) increased linearly, which indicated that BBI-1 could be applied to the ratiometric pH imaging of A549 cells.

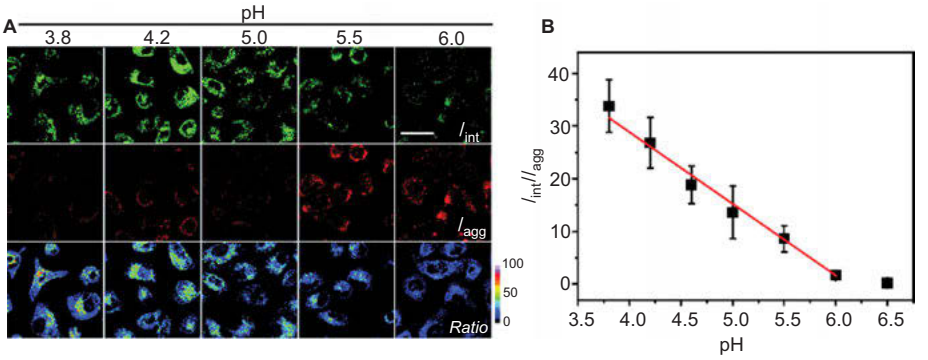


**Figure 8.12:** (A) Ratiometric imaging ($I_{int}/I_{agg}$) of A549 cells stained by BBI-1. (B) Mean $I_{int}/I_{agg}$ ratios in the ratiometric images at different pH and the linear fitting line of $I_{int}/I_{agg}$ ratio from pH 3.8 to 6.0.

## 8.3 AIEgen-based sensors for hypoxia

As a state of hypoxic tension in a certain area of the body, hypoxia is closely related to a variety of pathological conditions. In many diseases, the occurrence of local hypoxia will further increase the severity of the disease [15]. Therefore, the degree of hypoxia can reflect the related pathological conditions and diseases, and the detection of hypoxia is of great significance. In addition, hypoxia is an important feature of cancer, and the construction of fluorescent probes for early diagnosis of cancer has become an extremely important direction for researchers. Compared with traditional fluorophores, AIE fluorophores have many advantages, such as linear increase of brightness with concentration, long-term tracking and imaging of cells, etc. In this section, we introduce the recently reported AIE-based hypoxic fluorescent probes, which may be instructive for the construction of AIE probes for tumor hypoxic imaging, in the future [16].

The basic principle of designing hypoxia-responsive fluorescent probe is to attach a hypoxia-reactive group on the fluorescent molecule as a marker, such as nitro group and azo group. Azobenzene has been used as a quencher, and together with a variety of fluorophores, it has been used to construct hypoxic reaction fluorescent probes for tumor imaging. Because the absorption spectrum of azobenzene part overlaps with the emission spectrum of tetraphenylethylene (TPE), azobenzene part can be used as an effective quencher of TPE. Azo reductase overexpressed in hypoxic tumor site can effectively reduce the -N = N- via a two-electron transfer process [17]. For example, NADPH reduction of rat liver microsomes containing various metabolic enzymes is also an effective method to reduce -N = N- bond [18]. In addition, hydrazine and sodium dithionite ($Na_2S_2O_4$) can be used as chemical agents of -N = N- bond [19].

He and his colleagues successfully prepared a hypoxia-responsive polymer containing TPE and azobenzene by azo coupling reaction (Figure 8.13). Homogeneous nanoparticles with TPE azo core and PEG shell were synthesized by azo coupling reaction of macromolecular diazonium salt ($PEG_{43}$-b-$PSN_2^+{}_{10}$), N, N-dimethylaniline (DMA), and N-ethyl-N-(2-(4-(1,2,2-triphenylvinyl) phenoxy) ethyl) aniline in aqueous solution.

From the UV visible spectrum of Figure 8.14a, it can be seen that after the treatment of azo reductase, the absorption peak is the maximum in the visible region ($\lambda_{max}$ = 415 nm), which means that all azobenzene chromophores are completely cleaved. After the reduction reaction, the color of the solution changes from yellow to colorless, and can also be observed by naked eyes.

On the contrary, due to the FRET process, no fluorescence peak was found before the reduction reaction (blue line in Figure 8.14b). After the reduction reaction by azo reductase treatment under hypoxic condition, when excited by 365 nm light, an obvious emission peak of TPE was found at 475 nm (red line in Figure 8.14b). This study not only provides a new method for the preparation of polymer aggregates containing

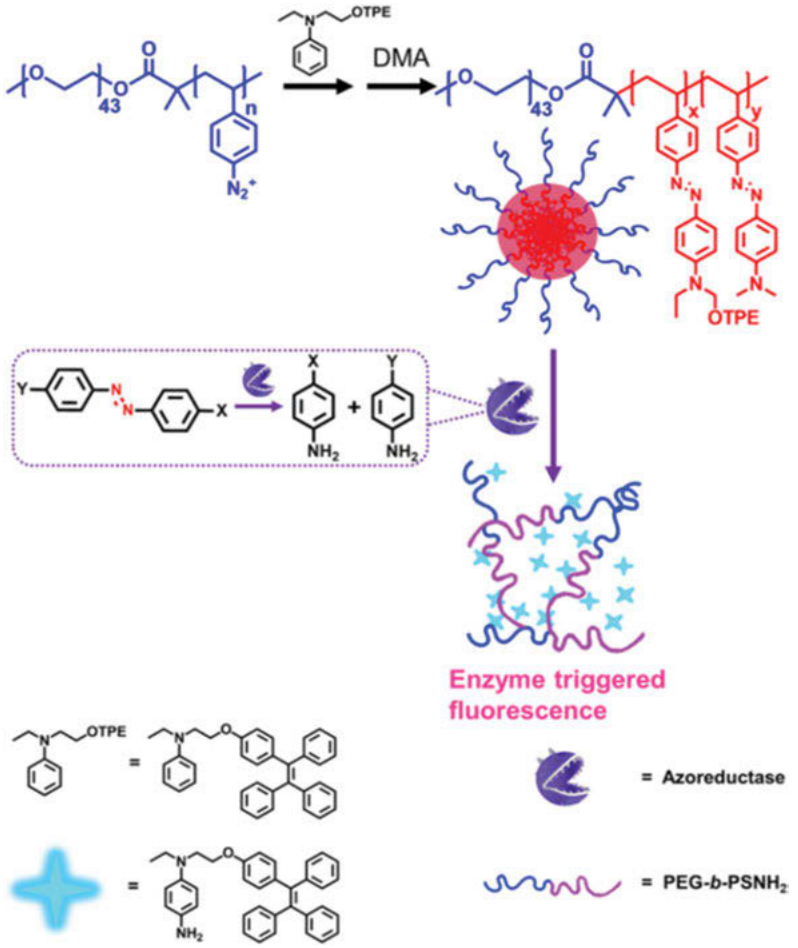


**Figure 8.13:** Preparation of enzymatic fluorescent polymer aggregates by self-assembly of macromolecules, induced by azo coupling reaction in aqueous solution.

azobenzene, but also provides inspiration for researchers to easily construct azobenzene cage-type hypoxia-responsive nanoaggregates based on TPE.

Based on the above research, He and his colleagues have recently constructed a fluorescent probe TPE with amphiphilic PEGylated azobenzene (PEG-Azo-TPE) (Figure 8.15a) by using the macromolecular azo coupling reaction between PEG diazonium salt and TPE-modified aniline [20]. Due to the amphiphilic structure, the probe can form micelles in aqueous medium and produce stable azobenzene cage activator AIE quantum dots. Similarly, the fluorescence of TPE was restored under 365 nm light excitation after enzyme treatment. Azo reductase therapy and in vitro imaging were used to verify the properties of the probe and detect tumor hypoxia. According to the microscopic images of A549 cells incubated with PEG azo TPE

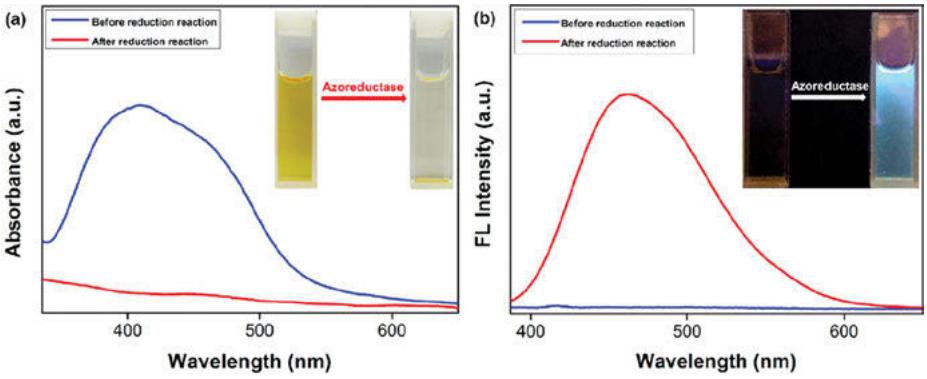


**Figure 8.14:** UV-Vis (a) and fluorescence (b) spectra of the self-assembled aggregates induced by azo coupling reaction, before and after the reduction reaction under hypoxic condition.

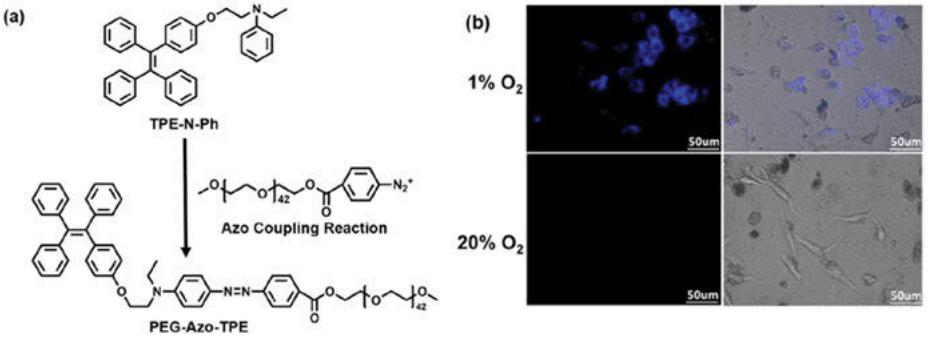


**Figure 8.15:** (a) Fabrication and chemical structure of PEG-Azo-TPE. (b) Microscopy images of A549 cells treated with PEG-Azo-TPE probes under normoxic (20% $O_2$) and hypoxic (1% $O_2$) condition.

under normoxia (20% $O_2$) and hypoxia (1% $O_2$), it was proved that the probe had the ability to detect hypoxic tumor (Figure 8.15b).

Nitroreductase overexpressed in hypoxic tissue and tumor microenvironment acts as a cofactor to provide electrons through NAD(P)H, and reduces nitroaromatic compounds, nitrobenzyl alcohol derivatives, nitroimidazole, nitrofuranone, and other oxidants in vivo through electron transfer process [21]. The reduction of electron-withdrawing nitro group by nitroreductase results in structural changes, which may lead to fluorescence changes. Therefore, nitroreductase-sensitive fluorescent probe can be used for tumor hypoxia imaging.

Using nitro and TPE, Zhang, and colleagues developed a nitro-containing fluorescent probe for NTR (nitroreductase) detection and tumor hypoxia imaging (Figure 8.16). Compared to TPE-PY, TPE-$NO_2$ shows good molecular dispersion and weak fluorescence in aqueous medium. When treated with nitroreductase

and NADH, the reduction of nitro group led to 2,5-rearrangement and elimination, yielding pyridine-substituted TPE (TPE-PY). The change from hydrophilic state to hydrophobic state made reduction product TPE-PY aggregate in aqueous medium, resulting in strong fluorescence emission at 525 nm. As shown in Figure 8.17A, in the presence of NADH, there was almost no fluorescence in PBS solution; however, with the addition of NTR, the fluorescence at 525 nm was significantly enhanced. Next, HeLa cells were used to detect whether TPE-$NO_2$ has ability to detect tumor hypoxia (Figure 8.17B). It could be that the cell-induced red shift limits the rotation of TPE-$NO_2$, and the orange–red fluorescence of TPE-$NO_2$ can be observed under normoxic condition. The blue-green fluorescence was observed under hypoxic condition, which indicated that the reduction process induced by NTR occurred. Therefore, TPE-$NO_2$ can also be used to detect different levels of NTR in tumor under hypoxic condition. At the same time, it provides a new method for the design of nitro-containing AIE fluorescent probe for tumor hypoxia.

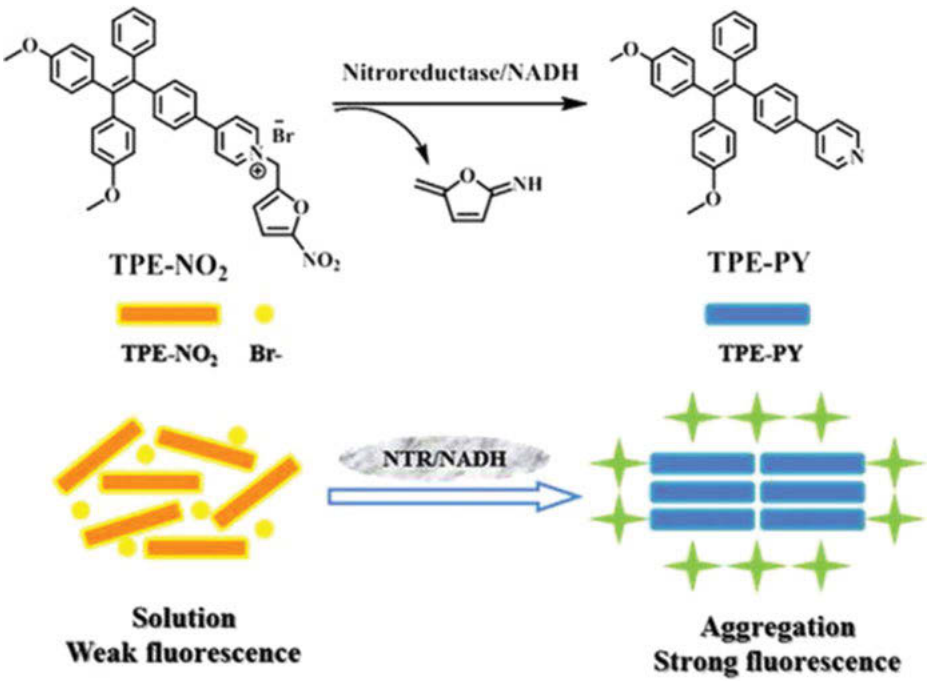


**Figure 8.16:** Structures of TPE-$NO_2$, TPE-PY and detection mechanism of tumor hypoxia.

N-oxides are synthesized by adding oxygen to the lone pair electrons of nitrogen atoms. Due to the semi-polar nature of nitrogen oxygen covalent-bond, it can be described as $N^+$-$O^-$. Cytochrome P450 and other blood proteins in tumor hypoxic microenvironment can lead to double electron reduction of N-oxides [22]. In the

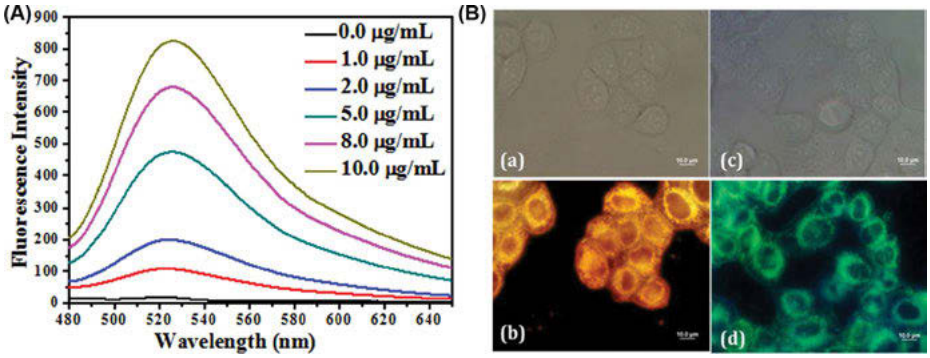


**Figure 8.17:** (A) Fluorescence response of TPE-$NO_2$ in the presence of NADH, upon the addition of different amounts of NTR. (B) Bright-field (a, c) and fluorescence microphotographs (b, d) of HeLa cells that had been incubated with TPE-$NO_2$ for 30 min.

presence of $Fe^{2+}$, deoxygenation of nitrogen oxides also occurs. In recent years, several conventional fluorescent probes have been based on $N^+$-$O^-$ [23].

Tang and his colleagues synthesized the first $N^+$-$O^-$-based hypoxia-responsive AIE probe in 2019 (Figure 8.18) [24]. They are all derivatives based on TPE group, including TPE-2M N-oxide, TPE-2E N-oxide, and TPE-2M2F N-oxide. As shown in Figure 8.19, the PL intensity of TPE-2M N-oxide and TPE-2M2F N-oxide at 520 nm was significantly increased by prolonging the incubation time with $Fe^{2+}$ to 30 min at room temperature. The enhanced emission at 520 nm indicates that the N-oxide is reduced to TPE-2M and TEM-2M2F. TPE-2M and TPE-2M2F are insoluble in water and form emission aggregates.

As shown in Figure 8.20, HeLa cells showed the strongest fluorescence intensity in the three experimental groups under extremely low oxygen environment (0% $O_2$). However, only HeLa cells treated with TPE-2E-N-oxide did not emit fluorescence under normoxic condition. It is suggested that the low sensitivity of TPE-2MN-oxide and TPE-2M2F Noxide to hypoxia may be attributed to the perfect match between their molecular structures and enzymes. In addition, TPE-2MN-oxide can selectively kill cancer cells under hypoxic conditions, which indicates the potential application of TPE-2MN-oxide probe in the diagnosis and treatment of AIE activation. This work provides a new method for the design of tumor hypoxia probe, based on AIE.

## 8.4 AIEgen-based sensors for viscosity

Viscosity is the key factor in controlling the diffusion process. It plays an important role in biology, chemistry, and other fields, and determines the transfer rate of fluid system. Diffusion events usually occur at the interface of heterogeneous fluid systems.

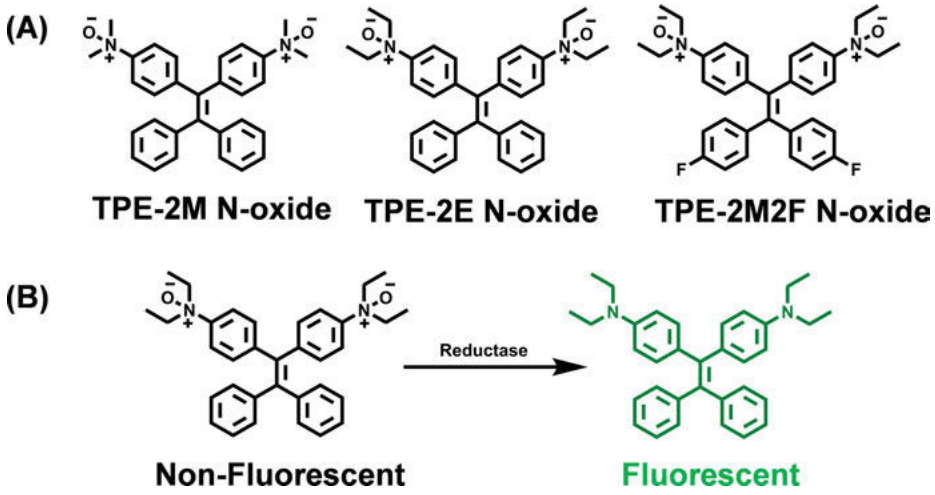


**Figure 8.18:** (A) Chemical structures of TPE-2M N-oxide, TPE-2E N-oxide, and TPE-2M2F N-oxide fluorescent probes for tumor hypoxia imaging. (B) Tumor hypoxia detection mechanism of TPE-2E N-oxide.

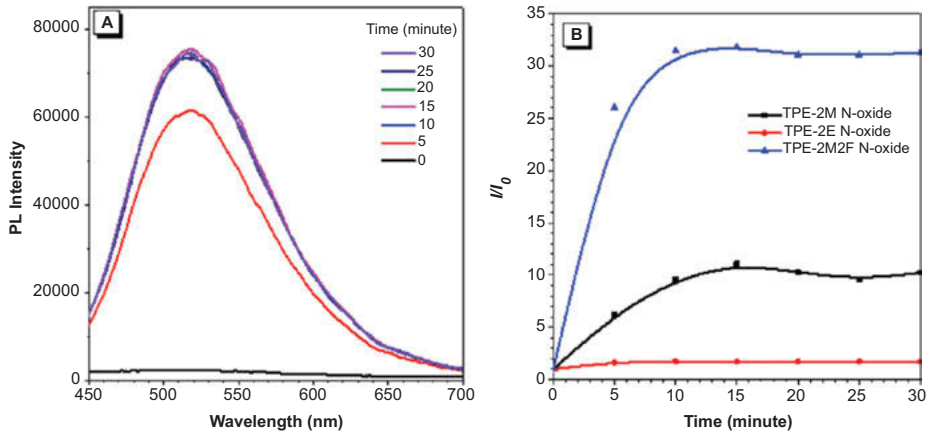


**Figure 8.19:** (A) PL of TPE-2M2F N-oxide with time, upon addition of $100 \times 10^{-6}$ M of $(NH_4)_2Fe(SO_4)_2$. (B) The kinetics of fluorescence change of TPE-2M N-oxide, TPE-2E N-oxide, and TPE-2M2F N-oxide.

In biological systems, intracellular viscosity plays an important role in controlling the transport of nutrients and metabolic wastes, intracellular/intercellular signal transduction, and interactions between biomacromolecules [25].

Moreover, at the subcellular level, the micro-viscosity of mitochondria has a great influence on the respiratory state and the tricarboxylic cycle, which indicates that the changes of mitochondrial matrix viscosity may interfere with the metabolism

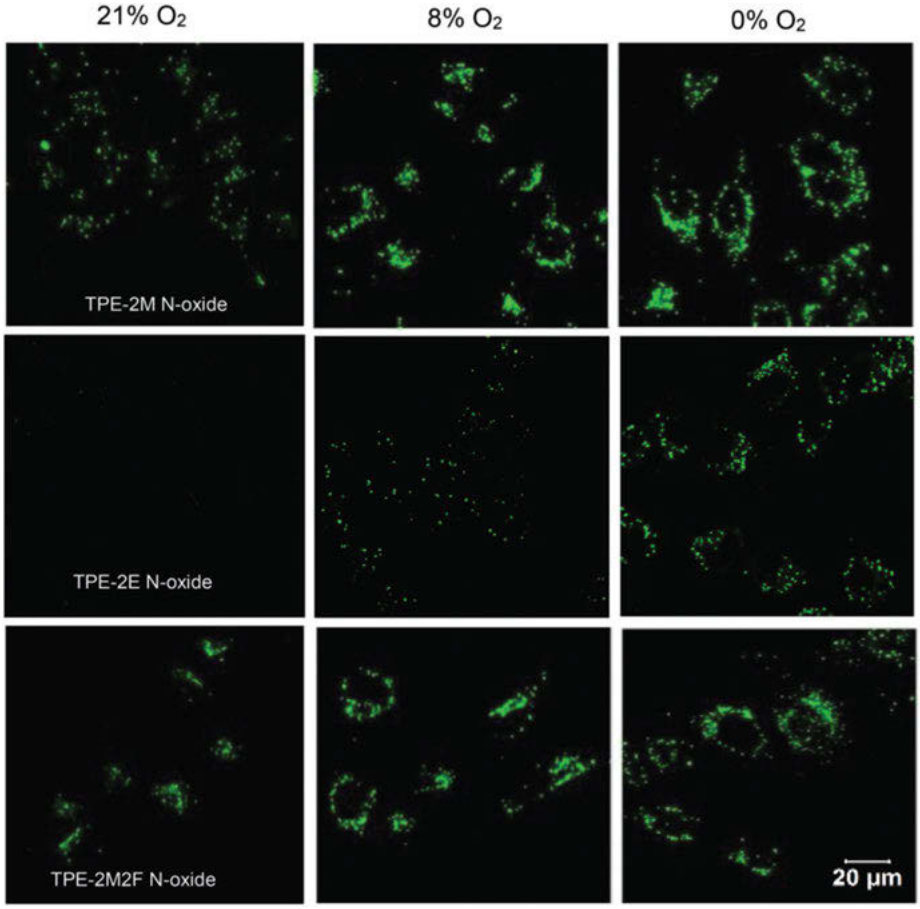


**Figure 8.20:** Fluorescent images of HeLa cells cultured with TPE-2M N-oxide, TPE-2E N-oxide, and TPE-2M2F N-oxide.

of mitochondria, to a great extent. Abnormal changes in viscosity are considered to be important factors or indicators leading to a variety of serious diseases, such as atherosclerosis, diabetes, Alzheimer's disease, and even cellular malignancies [26].

With the application of fluorescence technology, the fluorescence sensor with microviscosity as the target (called "molecular rotor") has gradually attracted attention. It has the characteristics of fast response, high sensitivity, and easy detection. In terms of chemical structure, they are composed of fluorophores that can rotate freely, relative to the whole molecule, and participate in conjugation in the nonviscous environment; the rapid rotation of molecules releases energy, leading to significant quenching of fluorescence or shortening of fluorescence lifetime [27, 28]. In the viscous medium, the rotation is gradually inhibited, which reduces the possibility of nonradiative pathway and improves the fluorescence intensity or significantly

prolongs the fluorescence lifetime. This is mainly the mechanism of AIE effect and is widely accepted. So far, great progress has been made in the research of AIE molecular design, and various AIE probes based on different structures have been successfully developed.

In recent years, BODIPY and its derivatives have been widely studied because of their excellent photophysical and chemical properties. BODIPY dye has strong solid-state emission ability, which provides a new choice for the synthesis of new, unconventional, and efficient viscosity probes.

In 2019, Jiao's group first reported the meso-2-pyrrolidone viscosity probe based on BODIPY (Figure 8.21A) [29]. The Stokes shift of the probe is much larger than that of the traditional BODIPY probe (653–986 $cm^{-1}$). It shows strong red fluorescence in viscous solvent and powder state, and has significant AIE characteristics. In the viscosity experiment, it is found that the increasing viscosity limits the rotation of meso-2-ketopyrrole groups, reduces their nonradiative energy loss rate, and enhances their fluorescence, when the viscosity increases from 0.6 to 360 CP (Figure 8.21B). Confocal laser imaging showed that the two compounds could show obvious green fluorescence after 10 min incubation. In addition, the survival rate of MCF-7 cells incubated with 0–10 for 24 h was still above 85%, indicating that the two compounds have low cytotoxicity and can be used in cell imaging. The experimental results show that this kind of probe has good applicability in real-time tracking the viscosity change in the process of apoptosis, monitoring normal and abnormal cell viscosity, and further quantifying the local viscosity of living cells (Figure 8.22).

Mitochondrial autophagy removes dysfunctional mitochondria and circulates their components through lysosomal degradation pathway, leading to changes in the mitochondrial microenvironment, which plays a key role in maintaining cell homeostasis. Therefore, it is necessary to develop a low-cost and efficient method to monitor the dynamic changes of mitochondrial phagocytosis in real time.

In 2021, Dong and his colleagues reported a mitochondria-specific AIE probe, CS-Py-BC, which can switch the fluorescence response of viscosity to monitor the change of viscosity during mitochondrial autophagy in real time (Figure 8.23) [30]. The system consists of a cyano-styrene skeleton as the active core and viscosity sensitive unit of AIE, pyridine cation as the mitochondrial targeting group, and benzyl chloride-induced mitochondrial immobilization.

The fluorescence emission spectra of CS-Py-BC at different viscosities are depicted in Figure 8.24. When the excitation wavelength is fixed at 470 nm, only weak fluorescence can be observed in anhydrous solution. and the viscosity increases (η) from 0.903cp (0% glycerol) to 965cp (99% glycerol); the fluorescence intensity increases gradually at 650 nm, indicating that CS-Py-BC can be potentially used as a near-infrared emission viscometer for biological imaging.

As shown in Figure 8.25, the probe CS-Py-BC was colocalized with mitochondria and lysosome dye, respectively. The colocalization experiment showed that CS-Py-BC could be significantly distributed in mitochondria, but less in lysosome. Then, they

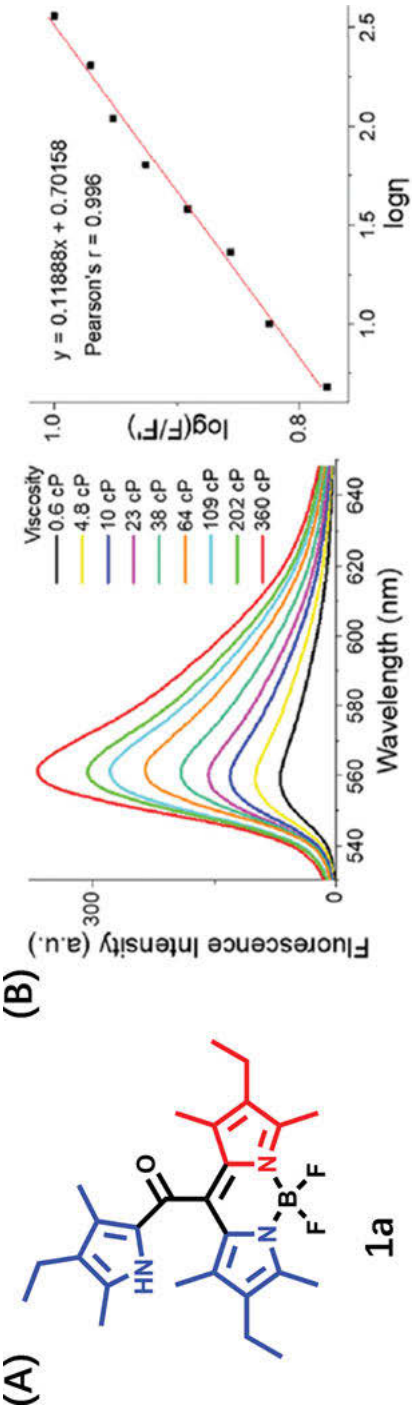


**Figure 8.21:** (A) The chemical structures of 1a. (B) Fluorescence intensity of 1a with the variation of the viscosity of the system in the methanol–glycerol system and linear working curve between log(*F*/*F*) and logη of 1a.

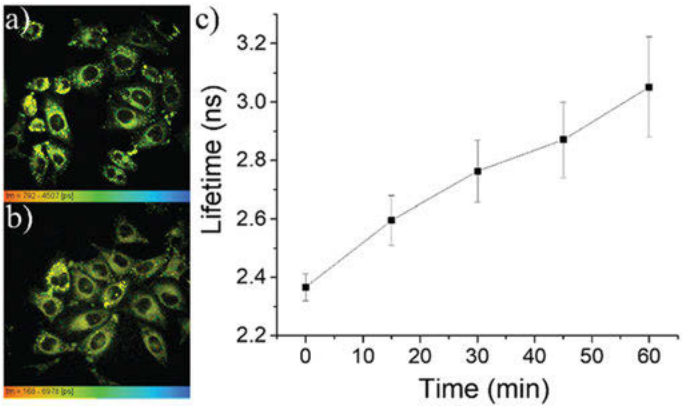


**Figure 8.22:** (a and b) FLIM images of MCF-7 cells incubated with etoposide for 0 and 45 min, respectively. (c) Variation of the fluorescence lifetimes of 1a with the extension of the cell apoptosis time.

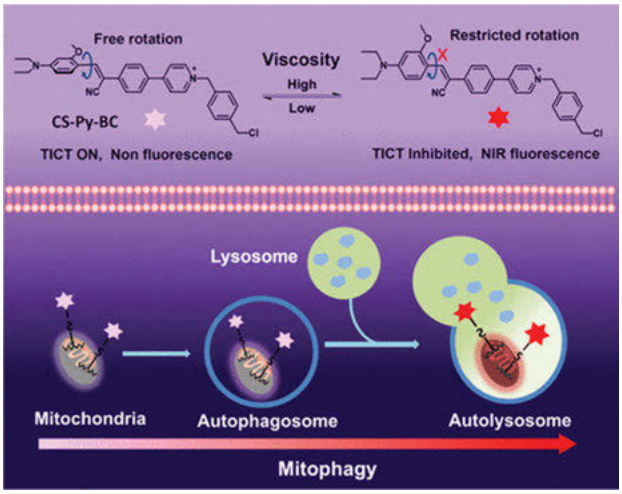


**Figure 8.23:** Schematic illustration of real-time monitoring of mitophagy, using the mitochondria-immobilized NIR emissive AIE probe CS-Py-BC in Cells.

co-incubated HeLa cells with CS-py-BC and MTDR, and the Pearson correlation coefficient remained above 0.90 in starvation-induced mitochondrial autophagy, which further proved that CS-Py-BC was reliably retained in mitochondria during the process of mitochondrial phagocytosis. In addition, colocalization imaging experiments between CS-Py-BC and LB NIR were also performed in serum-free medium for 0, 1, 2, and 3 h, respectively (Figure 8.26). With the prolongation of autophagy time, the overlapping regions of CS-Py-BC and LB-NIR (lysosomal probe) increased significantly, and PC

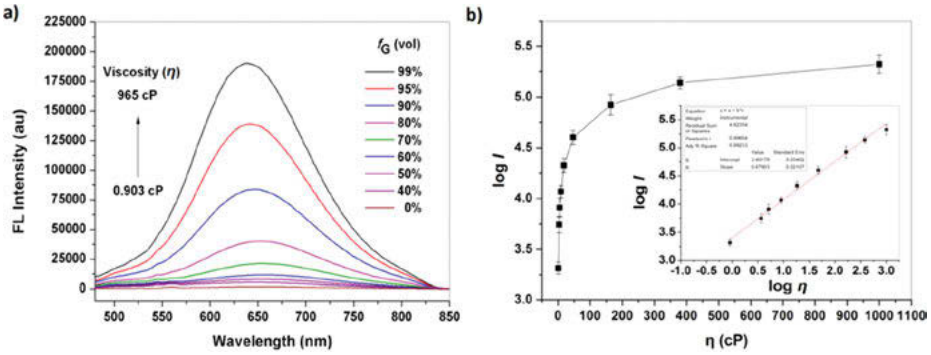


**Figure 8.24:** (a) Fluorescence spectral changes of CS-Py-BC (5 μM) in different water/glycerol mixtures (glycerol from 0 to 99%), excited at 470 nm. (b) Fluorescence intensity (log *I*) *vs* viscosity (η) curves for CS-Py-BC.

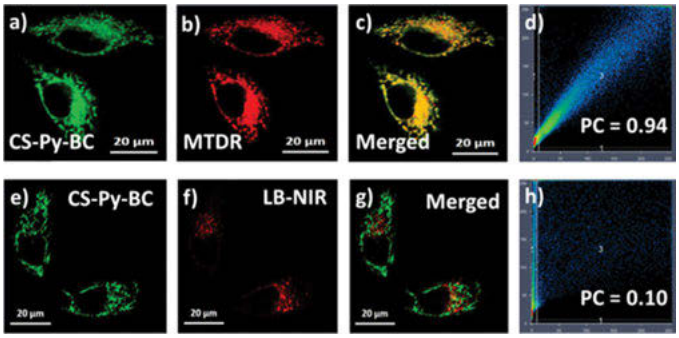


**Figure 8.25:** Fluorescence images of HeLa cells co-incubated with (a,e) CS-Py-BC (5 μM, 30 min) and (b) MTDR (0.3 μM, 30 min) or (f) LB-NIR (0.3 μM, 30 min). (c,g) Merged images.

increased from 0.17 to 0.72, indicating that more and more mitochondria with autophagy were gradually fused by lysosomes, and CS-Py-BC can be used to track this process. Therefore, CS-Py-BC has a good ability to target and immobilize mitochondria and can monitor the changes of viscosity during starvation-induced mitochondrial autophagy in real time.

## 8.5 Probe based on AIE for detection the polarity

Polarity (hydrophilicity/hydrophobicity) is another important factor in cell microenvironment. As hydrophobic interaction plays a dominant role in biological processes, it charges cell functional proteins and starts signal transduction and membrane system.

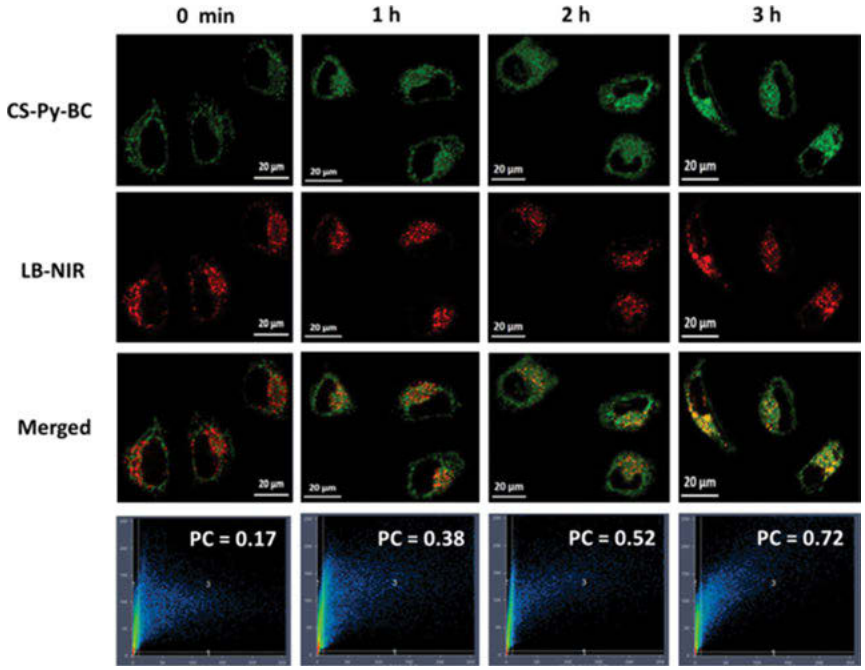


**Figure 8.26:** Fluorescence images of HeLa cells co-stained with CS-Py-BC (5 μM) and LB-NIR (0.3 μM) in serum-free medium for 0 min, 1 h, 2 h, and 3 h, respectively.

Intracellular polarity is one of the key microenvironment factors that change the diffusion, interaction, and function of biomolecules (proteins, nucleic acids, etc.) and cell membrane transport [31]. Polarity determines the interaction activity of a large number of proteins or reflects the permeability of membrane chambers. The specific recognition and interaction between proteins (such as enzymes) mainly depend on their hydrophobic interactions. These studies show that the polarity of specific organelles or subcellular structures is related to cell state, endoplasmic reticulum stress, autophagy, and so on [32].

Recent studies have shown that fluorescence imaging can provide local polarity information of cells. The polarity-sensitive fluorescent probe is considered to be an ideal choice for detecting polarity or its change. These probes mainly consist of environmentally sensitive chromophores composed of intramolecular electron donors (such as amino groups), conjugated spacer groups, and electron acceptors, forming a typical intramolecular charge transfer (ICT) system. When the surrounding polarity changes, their maximum emission peak appears as obvious blue/red shift or the fluorescence quantum yield changes greatly, sometimes showing dual emission bands (local excitation (LE) band and ICT band).

Folding polypeptide chain into correct natural structure is a necessary condition for protein function [33]. The relationship between misfolded proteins and the

formation of membrane-free compartments such as pressure granules, P-bodies, and nucleosomes indicates that these compartments play a crucial role in buffering protease deposition stress [34]. Phase separation process mediates the formation of these bodies, in which the internal polarity is different from the general environment of cytoplasm and nucleus. Therefore, quantifying the change of environmental polarity can make us better understand the mechanism of intracellular stress response and the pathogenicity of protein folding-related diseases.

Based on the above problems, Hong and his colleagues developed a general strategy in 2019 to determine the dielectric constant $\varepsilon$ [35], to quantify the polarity of the local environment around the unfolded protein in a cell. This method is based on a unique environment-sensitive fluorescent dye: fluorescence is activated when it reacts with unfolded protein, and the emission curve can be decoded to obtain quantitative information of cell dielectric constant. The design principle of this paper is to use cysteine (Cys)-reactive AIE fluorophore to target unfolded proteins in cells. There are two criteria for the fluorescence activation of probe NTPAN-MI (Figure 8.27A): removing the photoinduced electron transfer (PET) quenching effect of maleimide (MI) and limiting the intramolecular movement of TPE. The MI fraction can specifically target Cys residues in the form of free sulfhydryls, which are usually embedded in folded proteins but exposed during protein unfolding. After reacting with Cys, the effect of PET can be inhibited. At the same time, the hydrophobic side chain on the unfolded protein can provide an environment conducive to the fluorescence of TPE, thus turning on the fluorescence. In order to maintain the similar molecular structure and construct donor–acceptor type AIE fluorophore, one benzene ring of TPE was changed to electron-withdrawing cyano group, and dimethylamino substituent was used as electron donor, which also improved the water compatibility of NTPAN-MI.

With increase in solvent polarity, the emission spectrum (excitation wavelength 405 nm) of NTPAN-MI shows a large red shift. The emission peak shifts from 463 nm in nonpolar toluene to 586 nm in PBS solution (Figure 8.27B). The relationship between the maximum emission and the dielectric constant of the solvent is linear (Figure 8.27C). The absorption and emission properties of thiol-bound NTPAN-MI enable it to estimate and report the local environment of bound unfolded proteins in cells. In cell experiments, puromycin, tunicamycin, brefeldin A, and MG132 were selected to interfere with protein synthesis, folding, transport, and degradation. Disruption of any of these pathways may lead to accumulation of unfolded proteins in cells, which is confirmed by a significant increase in NTPAN-MI fluorescence of pre-labeled cell protein lysates.

After adding puromycin, tunicamycin, brefeldin A, and MG132, the whole intracellular environment became more discrete (Figure 8.28). Although each stressor leads to a different distribution pattern, the common feature is that the unfolded protein environment in the nucleus becomes more hydrophilic (dielectric constant from 45 to 54). In conclusion, they developed an AIE-based probe, NTPAN-MI, to quantify the intracellular polarity changes associated with protein misfolding.

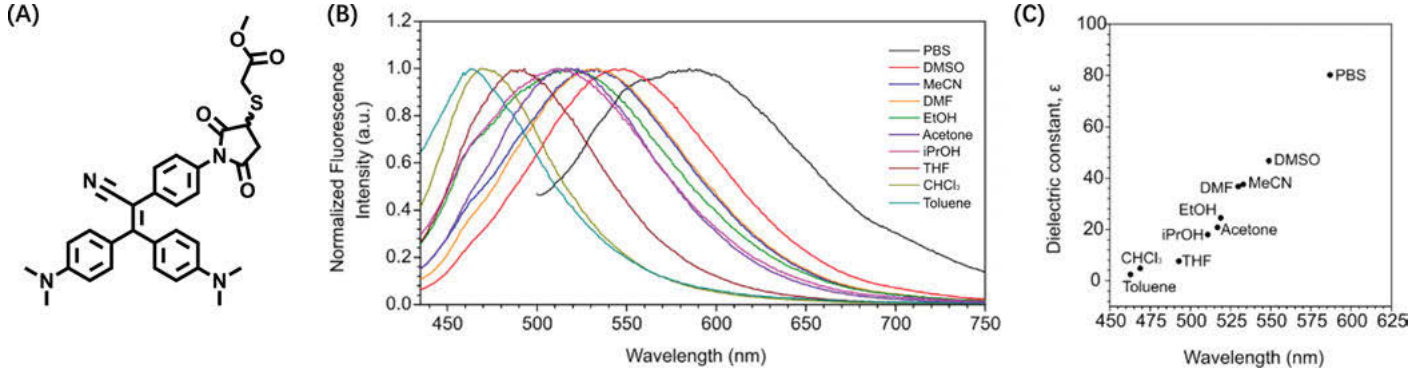


**Figure 8.27:** (A) Molecular structure of probe NTPAN-MI. (B) The normalized fluorescence spectra of NTPAN-MI in different polar solvents were studied. (C) The relationship between the position of the maximum emission peak of NTPAN-MI and the dielectric constant of the solvent was studied.

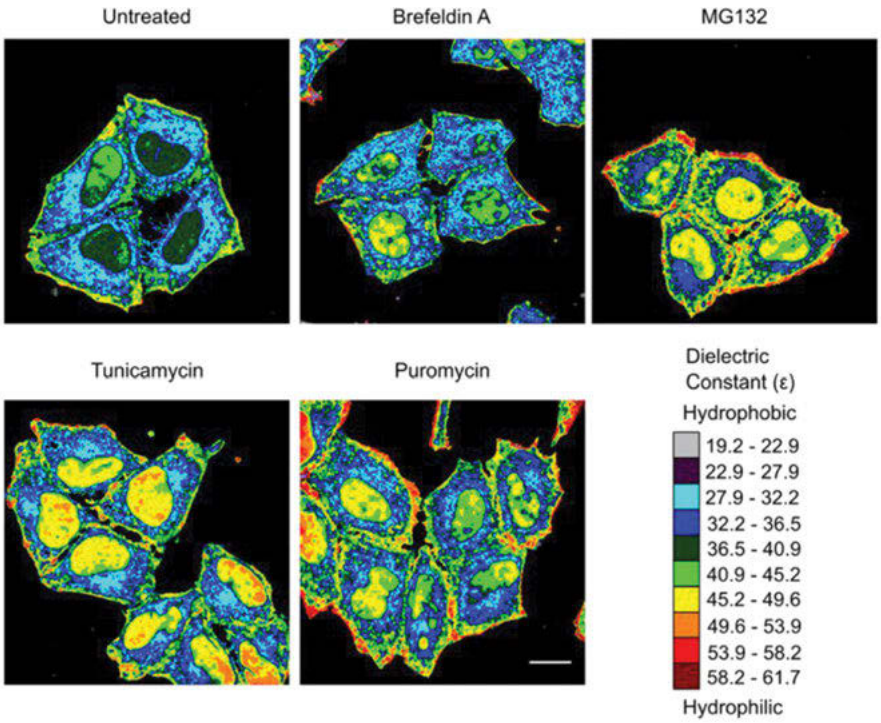


**Figure 8.28:** Mapping and quantifying intracellular polarity of unfolded protein environment. Representative images of intracellular dielectric constant distribution in untreated and stressed cells stained by NTPAN-MI resolved from spectral phasor analysis.

## 8.6 Conclusions and future remarks

Due to the general accepted working mechanism of restriction of intramolecular motion (RIM), the spectroscopic properties of AIEgens are easily affected by environmental factors such as viscosity, polarity, rigidity, and temperature. These features of AIEgens offered a promising strategy for developing fluorescent sensors for intracellular microenvironment analysis. Benefiting from the high photostability of AIEgen-based sensors, longer-term monitoring intracellular processes can easily be achieved. In this chapter, we have mainly introduced the imaging applications of AIEgens for intracellular viscosity, polarity, pH, and hypoxia. The reports of AIEgen-based sensors for other microenvironment such as temperature, osmotic pressure, and ionic strength are not enough and needs further exploration. The spectroscopic change of AIEgens in response to viscosity and polarity originated from their intrinsic chemical structure, resulting in a reversible sensing behavior. However, pH and hypoxia sensing mechanism are mainly based on chemical reactions, which might result in irreversible response, especially for

hypoxia sensing. For real-time monitoring of intracellular microenvironment, which are usually changing dynamically, AIEgen-based sensors with reversible response are in highly demand [36]. Moreover, under various internal or external stresses, the change of microenvironment in different subcellular organelles might be different, yet closely associated with each other. Therefore, it would be highly desirable to develop AIEgen-based sensors that are able to monitor certain microenvironment in two or more organelles simultaneously [37]. On the other hand, monitoring two or more microenvironment changes under different stimuli inside one organelle should also be of great importance for the study of the physiology and pathology of microenvironment. In addition, the resolution of tradition optical imaging techniques is 200–300 nm, which is not enough for tracking microenvironment changes inside organelles, because the sizes of some subcellular compartments are very small (down to 100 nm). In this regard, developing AIEgen-based sensors suitable for super-resolution fluorescence imaging should be an attractive approach [38]. To sum up, there is still plenty of room to explore in the field of AIEgen-based sensors for the study of intracellular microenvironment.

# References

[1] Webb BA, Chimenti M, Jacobson MP, Barber DL, Dysregulated pH: A perfect storm for cancer progression, Nat Rev Cancer, 2011, 11(9), 671–677.
[2] Peng X, Yang Z, Wang J, Fan J, He Y, Song F, Wang B, Sun S, Qu J, Qi J, Yan M, Fluorescence ratiometry and fluorescence lifetime imaging: Using a single molecular sensor for dual mode imaging of cellular viscosity, J Am Chem Soc, 2011, 133(17), 6626–6635.
[3] Jiang N, Fan J, Xu F, Peng X, Mu H, Wang J, Xiong X, Ratiometric fluorescence imaging of cellular polarity: Decrease in mitochondrial polarity in cancer cells, Angew Chem Int Ed, 2015, 54(8), 2510–2514.
[4] Wilson WR, Hay MP, Targeting hypoxia in cancer therapy, Nat Rev Cancer, 2011, 11(6), 393–410.
[5] Casey JR, Grinstein S, Orlowski J, Sensors and regulators of intracellular pH, Nat Rev Mol Cell Biol, 2010, 11(1), 50–61.
[6] Hou JT, Ren WX, Li K, Seo J, Sharma A, Yu XQ, Kim JS, Fluorescent bioimaging of pH: From design to applications, Chem Soc Rev, 2017, 46(8), 2076–2090.
[7] Wang R, Yu C, Yu F, Chen L, Yu C, Molecular fluorescent probes for monitoring pH changes in living cells, Trac-Trend Anal Chem, 2010, 29(9), 1004–1013.
[8] Chen S, Hong Y, Liu Y, Liu J, Leung CW, Li M, Kwok RT, Zhao E, Lam JW, Yu Y, Tang BZ, Full-range intracellular pH sensing by an aggregation-induced emission-active two-channel ratiometric fluorogen, J Am Chem Soc, 2013, 135(13), 4926–4929.
[9] Fan L, Liu Q, Lu D, Shi H, Yang Y, Li Y, Dong C, Shuang S, A novel far-visible and near-infrared pH probe for monitoring near-neutral physiological pH changes: Imaging in live cells, J Mater Chem B, 2013, 1(34), 4281–4288.
[10] Song P, Chen X, Xiang Y, Huang L, Zhou Z, Wei R, Tong A, A ratiometric fluorescent pH probe based on aggregation-induced emission enhancement and its application in live-cell imaging, J Mater Chem C, 2011, 21(35), 13470–13475.

[11] Marshall WF, How cells measure length on subcellular scales, Trends Cell Biol, 2015, 25(12), 760–768.
[12] Zhao X, Chen Y, Niu G, Gu D, Wang J, Cao Y, Yin Y, Li X, Ding D, Xi R, Meng M, Photostable pH-sensitive near-infrared aggregation-induced emission luminogen for long-term mitochondrial tracking, ACS Appl Mater Interfaces, 2019, 11(14), 13134–13139.
[13] Kim HJ, Heo CH, Kim HM, Benzimidazole-based ratiometric two-photon fluorescent probes for acidic pH in live cells and tissues, J Am Chem Soc, 2013, 135(47), 17969–17977.
[14] Bai Y, Liu D, Han Z, Chen Y, Chen Z, Jiao Y, He W, Guo Z, BODIPY-derived ratiometric fluorescent sensors: PH-regulated aggregation-induced emission and imaging application in cellular acidification triggered by crystalline silica exposure, Sci China Chem, 2018, 61(11), 1413–1422.
[15] Xu L, Sun L, Zeng F, Wu S, Activatable fluorescent probe based on aggregation-induced emission for detecting hypoxia-related pathological conditions, Anal Chim Acta, 2020, 1125, 152–161.
[16] Xue T, Shen J, Shao K, Wang W, Wu B, He Y, Strategies for tumor hypoxia imaging based on aggregation-induced emission fluorogens, Chemistry, 2020, 26(12), 2521–2528.
[17] Medina SH, Chevliakov MV, Tiruchinapally G, Durmaz YY, Kuruvilla SP, Elsayed ME, Enzyme-activated nanoconjugates for tunable release of doxorubicin in hepatic cancer cells, Biomaterials, 2013, 34(19), 4655–4666.
[18] Kiyose K, Hanaoka K, Oushiki D, Nakamura T, Kajimura M, Suematsu M, Nishimatsu H, Yamane T, Terai T, Hirata Y, Nagano T, Hypoxia-sensitive fluorescent probes for in vivo real-time fluorescence imaging of acute ischemia, J Am Chem Soc, 2010, 132(45), 15846–15848.
[19] Eom T, Yoo W, Kim S, Khan A, Biologically activatable azobenzene polymers targeted at drug delivery and imaging applications, Biomaterials, 2018, 185, 333–347.
[20] Xue T, Jia X, Wang J, Xiang J, Wang W, Du J, He Y, "Turn-On" Activatable AIE Dots for Tumor Hypoxia Imaging, Chemistry, 2019, 25(41), 9634–9638.
[21] Thambi T, Park JH, Lee DS, Hypoxia-responsive nanocarriers for cancer imaging and therapy: Recent approaches and future perspectives, Chem Commun, 2016, 52(55), 8492–8500.
[22] Patterson L, Rationale for the use of aliphatic N-oxides of cytotoxic anthraquinones as prodrug DNA binding agents: A new class of bioreductive agent, Cancer Metast Rev, 1993, 12(2), 119–134.
[23] Hirayama T, Tsuboi H, Niwa M, Miki A, Kadota S, Ikeshita Y, Okuda K, Nagasawa H, A universal fluorogenic switch for Fe(ii) ion based on N-oxide chemistry permits the visualization of intracellular redox equilibrium shift towards labile iron in hypoxic tumor cells, Chem Sci, 2017, 8(7), 4858–4866.
[24] Xu C, Zou H, Zhao Z, Zhang P, Kwok RTK, Lam JWY, Sung HHY, Williams ID, Tang BZ, New A, Strategy toward "Simple" water-soluble AIE probes for hypoxia detection, Adv Funct Mater, 2019, 29(34), 1903278–1903289.
[25] Ning P, Dong P, Geng Q, Bai L, Ding Y, Tian X, Shao R, Li L, Meng X, A two-photon fluorescent probe for viscosity imaging in vivo, J Mater Chem B, 2017, 5(15), 2743–2749.
[26] Tan HY, Qiu YT, Sun H, Yan JW, Zhang L, A lysosome-targeting dual-functional fluorescent probe for imaging intracellular viscosity and beta-amyloid, Chem Commun, 2019, 55(18), 2688–2691.
[27] Hou L, Ning P, Feng Y, Ding Y, Bai L, Li L, Yu H, Meng X, Two-photon fluorescent probe for monitoring autophagy via fluorescence lifetime imaging, Anal Chem, 2018, 90(12), 7122–7126.
[28] Chen W, Gao C, Liu X, Liu F, Wang F, Tang LJ, Jiang JH, Engineering organelle-specific molecular viscosimeters using aggregation-induced emission luminogens for live cell imaging, Anal Chem, 2018, 90(15), 8736–8741.

[29] Yu C, Huang Z, Gu W, Wu Q, Hao E, Xiao Y, Jiao L, Wong W-Y, A novel family of AIE-active meso-2-ketopyrrolyl BODIPYs: Bright solid-state red fluorescence, morphological properties and application as viscosimeters in live cells, Mater Chem Front, 2019, 3(9), 1823–1832.
[30] Wang X, Fan L, Wang S, Zhang Y, Li F, Zan Q, Lu W, Shuang S, Dong C, Real-time monitoring mitochondrial viscosity during mitophagy using a mitochondria-immobilized near-infrared aggregation-induced emission probe, Anal Chem, 2021, 93(6), 3241–3249.
[31] Yang Z, Cao J, He Y, Yang JH, Kim T, Peng X, Kim JS, Macro-/micro-environment-sensitive chemosensing and biological imaging, Chem Soc Rev, 2014, 43(13), 4563–4601.
[32] Yang Z, He Y, Lee JH, Chae WS, Ren WX, Lee JH, Kang C, Kim JS, A Nile Red/BODIPY-based bimodal probe sensitive to changes in the micropolarity and microviscosity of the endoplasmic reticulum, Chem Commun, 2014, 50(79), 11672–11675.
[33] Dobson CM, Principles of protein folding, misfolding and aggregation, Semin Cell Dev Biol, 2004, 15(1), 3–16.
[34] Banani SF, Lee HO, Hyman AA, Rosen MK, Biomolecular condensates: Organizers of cellular biochemistry, Nat Rev Mol Cell Biol, 2017, 18(5), 285–298.
[35] Owyong TC, Subedi P, Deng J, Hinde E, Paxman JJ, White JM, Chen W, Heras B, Wong WWH, Hong Y, A molecular chameleon for mapping subcellular polarity in an unfolded proteome environment, Angew Chem Int Ed, 2020, 59(25), 10129–10135.
[36] Zhang Y, Zhao W, Chen Y, Yuan H, Fang H, Yao S, Zhang C, Xu H, Li N, Liu Z, Guo Z, Zhao Q, Liang Y, He W, Rational construction of a reversible arylazo-based NIR probe for cycling hypoxia imaging in vivo, Nat Commun, 2021, 12, 2772.
[37] Guo L, Tian M, Zhang Z, Lu Q, Liu Z, Niu G, Yu X, Simultaneous two-color visualization of lipid droplets and endoplasmic reticulum and their interplay by single fluorescent probes in lambda mode, J Am Chem Soc, 2021, 143((8)), 3169–3179.
[38] Fang H, Geng S, Hao M, Chen Q, Liu M, Liu C, Tian Z, Wang C, Takebe T, Guan J-L, Chen Y, Guo Z, He W, Diao J, Simultaneous $Zn^{2+}$ tracking in multiple organelles using super-resolution morphology-correlated organelle identification in living cells, Nat Commun, 2021, 12, 109.

Jiaxin Wang, Chunlei Zhu

# Chapter 9
# Engineering the bioprobes with AIE properties to study tumor hypoxia

## 9.1 Introduction

Hypoxia refers to low oxygen conditions, which is a common characteristic of most solid tumors due to the insufficient supply of oxygen by the abnormal vasculature to the rapidly proliferating tumor cells. Hypoxic response is primarily associated with the hypoxia-inducible factor 1 (HIF-1), which is a basic helix–loop–helix transcription factor, composed of two subunits, that is, HIF-1α and HIF-1β. In principle, the HIF-1α subunit is regulated by oxygen tension, whereas HIF-1β is constitutively expressed [1]. Recent studies suggest that hypoxic tumors are less susceptible to traditional radiotherapy and chemotherapy, giving rise to decreased survival rates [2, 3]. Specifically, radiotherapy relies on the sensitization of ground-state oxygen to reactive singlet oxygen for the killing of tumor cells, which is greatly impeded by the limited amount of oxygen in the tumor microenvironment. Chemotherapeutic drugs are also impotent in the treatment of hypoxic tumors due to the deficient blood supply to favor their efficient diffusion into the tumor sites; moreover, some oxygen-dependent drugs even become deactivated in the hypoxic microenvironment. In terms of photodynamic therapy (PDT), two types of photochemical reactions have been established, which are electron transfer-based type-I PDT and energy transfer-based type-II PDT [4, 5]. Since type-II PDT is highly dependent on oxygen content, it exhibits limited efficacy in combating hypoxic tumors. On the contrary, Type-I PDT involves a relatively oxygen-independent process to produce reactive radicals for the ablation of tumor cells, holding great potential in the treatment of hypoxic tumors. However, precise control on the molecular structure of the photosensitizers to perform type-I PDT remains a challenge.

To realize efficient ablation of hypoxic tumors, the prerequisite is to characterize the degree of hypoxia in the tumor microenvironment. To this end, a plethora of approaches have been developed to monitor tumor hypoxia. Clinically, the golden standard for hypoxia characterization is to insert electrodes into tumors to directly

**Jiaxin Wang,** Key Laboratory of Functional Polymer Materials of Ministry of Education, State Key Laboratory of Medicinal Chemical Biology, Institute of Polymer Chemistry, College of Chemistry, Nankai University, Tianjin, 300071, China
**Chunlei Zhu,** Key Laboratory of Functional Polymer Materials of Ministry of Education, State Key Laboratory of Medicinal Chemical Biology, Institute of Polymer Chemistry, College of Chemistry, Nankai University, Tianjin, 300071, China, e-mail: chunlei.zhu@nankai.edu.cn

https://doi.org/10.1515/9783110672220-009

measure the contents of oxygen. Such invasive method, however, brings in high risks of infection and potentially promotes tumor metastasis; moreover, it is unable to portray the entire hypoxic map within solid tumors. In this respect, noninvasive characterization methods, such as fluorescence imaging [6, 7], magnetic resonance imaging [8], and positron emission tomography [9], have attracted extensive attention. Among the various approaches, fluorescence imaging is particularly advantageous for hypoxia-related studies, as the hypoxic conditions within tumors can be visualized at the cellular and/or subcellular level. Despite hypoxia describing only the oxygen-deficient nature of solid tumors, the tumor microenvironment also has other unique attributes that are closely related to hypoxia [10, 11], including low pH, and high contents of reactive oxygen species (ROS) and reductive substances. In hypoxic tumors, reductive substances, such as nicotinamide adenine dinucleotide (NADH) and flavin adenine dinucleotide ($FADH_2$), are largely accumulated due to oxygen deficiency, which can further consume the residual oxygen to elevate the ROS level. Meanwhile, anaerobic respiration is concurrently turned on in hypoxic cells, and the produced lactic acid contributes to decreased pH in the tumor microenvironment. In addition, the hypoxic condition of tumor also promotes the expression of a variety of reductases [12–14], such as DT-diaphorase (DTD), cytochrome P450 reductase, cytochrome B5 reductase, xanthine dehydrogenase, carbonyl reductase, azoreductase, and nitro reductase (NTR). The presence of these reductases and reductive substances contribute to the reductive nature of hypoxic tumors, which can be delicately employed for the design of hypoxia-responsive probes.

## 9.2 Design principles for hypoxia-responsive probes

In terms of the design of hypoxia-responsive probes, the regulation of a quenching process or solubility changes are the most widely used strategies. For the quenching strategy, the classical design is to shut down the probe fluorescence in normoxia and selectively turn it on when in hypoxia [7]. In general, the quenching process is primarily fulfilled by directly attaching a responsive quenching group to the fluorophore or connecting a quenching group to the fluorophore *via* a responsive linker. In normoxic conditions, the excitation energy of an appropriate incident light is primarily dissipated through nonradiative pathways due to the presence of the quenching group, leading to significant fluorescence quenching. In hypoxic conditions, the responsive group is selectively reduced by the reductive substances, making the quenching group either deactivated (Figure 9.1A) or disassociated from the fluorophore (Figure 9.1B) and thus the remarkably recovered fluorescence. Typically, the involved quenching mechanisms include fluorescence resonance energy transfer (FRET) [15, 16] and photoinduced electron transfer (PET) [17]. FRET refers to

the energy transfer between adjacent excited fluorophores and quenchers, which requires significant spectral overlap between the emission of the fluorophores (donor) and the absorption of the quenchers (acceptor). In the presence of certain factors that are able to disrupt the energy resonance, the fluorescence of the donor molecule will recover. PET refers to the electron transfer process between or within molecules, upon light excitation. In this case, the fluorophores are nonemissive or weakly emissive as a result of the electron transfer from the donor to the acceptor, giving rise to nonradiative relaxation from the excited fluorophores. In particular, PET requires energy level matching of the molecular orbitals between the donor and acceptor molecules, which can be easily disrupted by structural alteration. Modern quantum chemistry software can supply adequate estimation of the energies of the frontier orbitals, greatly boosting the development of PET-based hypoxia-responsive probes. Overall, if any of these quenching processes is impeded in hypoxic conditions, the fluorophores will become emissive upon excitation.

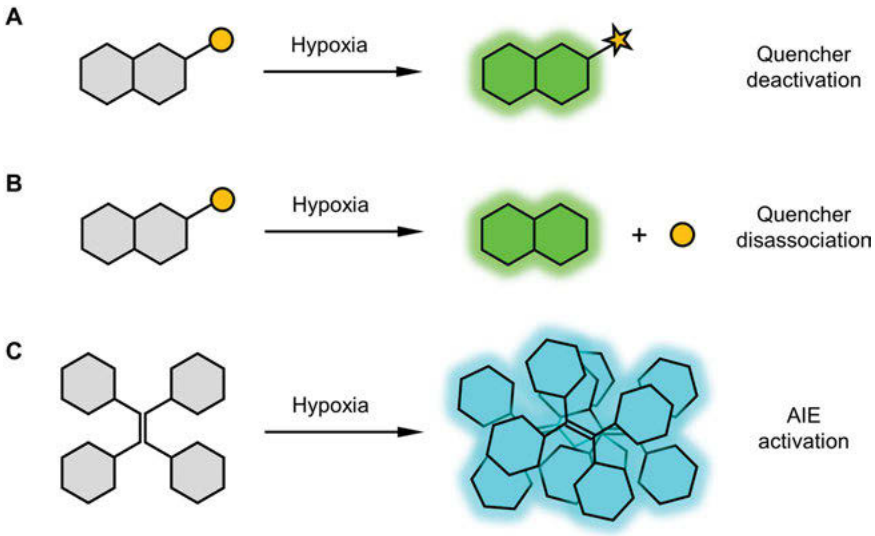


**Figure 9.1:** "Turn-on" mechanisms for hypoxia-responsive probes. (A) Fluorescence "turn-on" *via* quencher deactivation. (B) Fluorescence "turn-on" *via* quencher disassociation (C) Fluorescence "turn-on" *via* AIE activation.

In addition to the quenching mechanism, the manipulation of molecular aggregation states has emerged as another promising strategy for the investigation of tumor hypoxia [13], in which, molecularly dispersed fluorophores with weak or no fluorescence become highly emissive when subjected to hypoxia-induced molecular aggregation (Figure 9.1C). Such concept is also known as aggregation-induced emission (AIE), which was coined by Tang and coworkers in 2001 to describe the "unusual"

photophysical phenomenon of fluorescence enhancement caused by molecular aggregation [18]. Different from traditional organic dyes with aggregation-caused quenching (ACQ) effect (due to intermolecular π–π stacking), AIE luminogens (AIEgens) exhibit completely opposite photophysical properties, that is, the more aggregated the molecules are, stronger is the luminescence. Currently, the restriction of intramolecular motions (RIM), including the restriction of intramolecular rotations (RIR) and the restriction of intramolecular vibrations (RIV), is regarded as the primary mechanism to interpret the AIE phenomenon [19–21]. Specifically, the occurrence of RIM significantly alters the energy consumption pathways of the excited AIEgens from nonradiative relaxation (in dispersed state) to radiative decay (in solid or aggregated state); in addition, the undesired π–π stacking in ACQ luminogens is also hindered due to the nonplanar conformations of AIEgens. Taking advantage of the high fluorescence brightness and excellent photostability, AIEgens are widely considered as a promising class of prominent luminescent materials for long-term and stable fluorescence imaging [22, 23]. In recent years, by virtue of hypoxia-responsive functional groups, three types of AIE-based probes have been developed for the specific monitoring of tumor hypoxia. In particular, all these groups contain nitrogen atoms, and the involved reactions are related to the reduction of nitrogen atoms by the reductive substances in the hypoxic environment. To facilitate easy comparison, the responsive mechanisms and the advantages and disadvantages of these functional groups are summarized in Figure 9.2.

### 9.2.1 Nitro-containing AIE probes for hypoxic response

As a strong electron-withdrawing functional group, the nitro group significantly shuts down the fluorescence of the fluorophore that it attaches to *via* a process called intramolecular charge transfer (ICT). In mitochondria, the nitro group can be reduced to amino group by NTR, in the presence of reducing coenzymes (e.g., NADH) [24–30]. The detailed mechanism is shown in Figure 9.2 (upper box), which involves two routes, that is, the one-electron pathway and the two-electron pathway [30, 31]. The two-electron pathway is relatively slow and hypoxia-independent, in which, the nitro group can be directly reduced to the nitroso group. In contrast, the one-electron pathway is relatively fast, in which, the nitro group is first reduced to a nitro radical by an electron, followed by further reduction to the nitroso group *via* another single-electron process. Notably, the formed nitro radical can be reversibly oxidized to the nitro group by oxygen molecules, which is accompanied by the production of a superoxide radical. As such, the one-electron pathway is highly dependent on hypoxia. For both pathways, the nitroso group is eventually reduced to the amino group *via* a two-electron process.

By means of the quenching effect of the nitro group, a series of hypoxia-triggered fluorescence "turn-on" systems have been established for the ultrasensitive detection

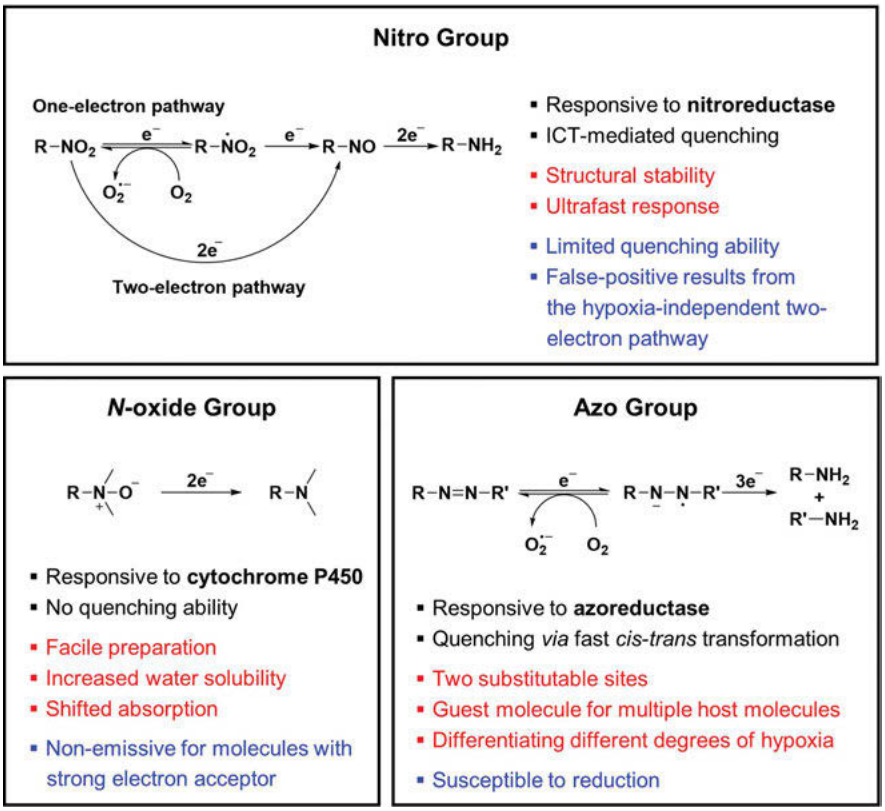


**Figure 9.2:** Nitrogen-containing responsive groups for the development of hypoxia-specific AIEgens and the corresponding reaction mechanism (black), advantages (red), and disadvantages (blue).

of tumor hypoxia *via* the single-electron pathway [30, 31]. Besides, the nitro group can also serve as a leaving group (e.g., 4-nitrobenzyl and 2-submethyl-5 nitromethyl furan), in response to hypoxia, *via* the reduction-mediated rearrangement and/or elimination, which provides the possibility to design AIE-type hypoxia-responsive probes that utilize the hydrophilic-to-hydrophobic transition. In this respect, You et al. modified **TPE-PY** with 2-bromomethyl 5-nitrofuran and obtained **TPE-$NO_2$**, which was characterized by a pyridinium group (Figure 9.3A) [32]. Since the pyridinium salt partially improved the water solubility of **TPE-$NO_2$**, the probe was weakly emissive in aqueous solution. In the presence of NADH, the nitro group in **TPE-$NO_2$** was reduced to the amino group, followed by 2,5-rearrangement elimination to release **TPE-PY**. In contrast to **TPE-$NO_2$**, the released **TPE-PY** was more hydrophobic and thus prone to form self-aggregates, leading to the remarkable fluorescence enhancement, as a result of the activation of the AIE process (Figure 9.3B). As shown in Figure 9.3C, the fluorescence signal linearly increased when different concentrations of NTR were added into the aqueous solution of **TPE-$NO_2$**; furthermore, the

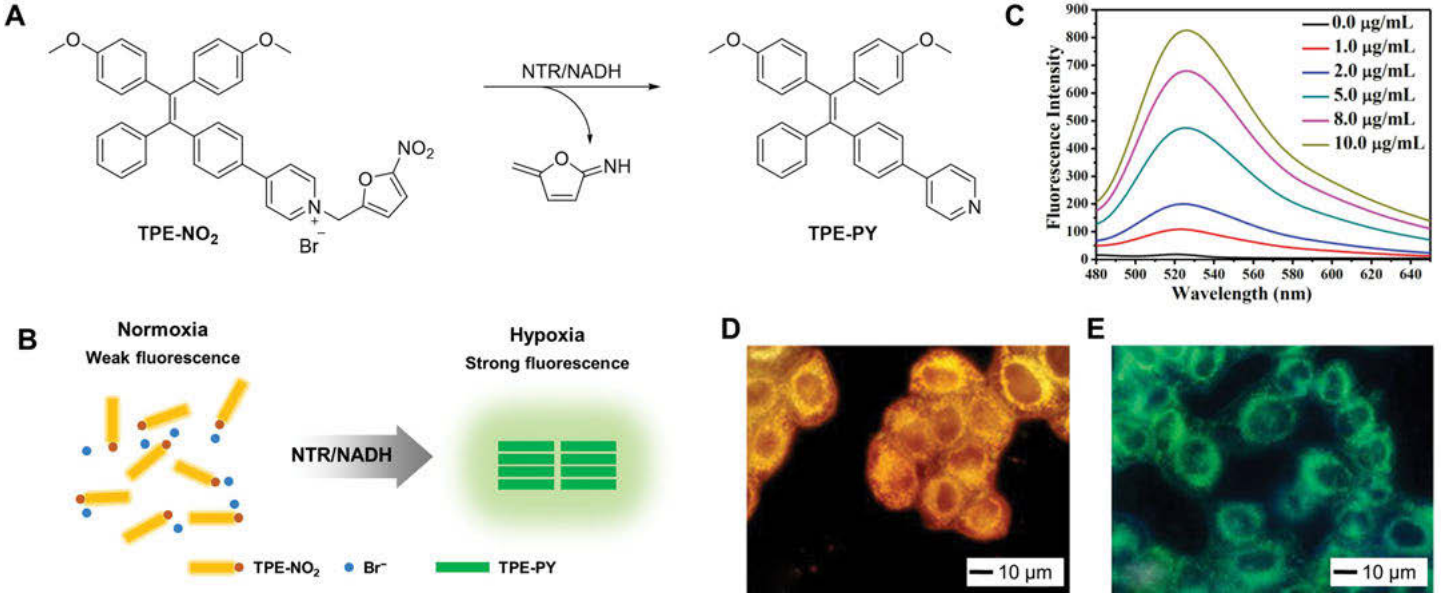


**Figure 9.3:** A nitro-based AIEgen for NTR detection and hypoxic imaging in tumor cells. (A) Chemical structure of **TPE–$NO_2$** and **TPE–PY** as well as the NTR-catalyzed mechanism. (B) Schematic illustration showing the principle of fluorescence "turn-on" detection of NTR. (C) Fluorescence spectra of **TPE–$NO_2$** (10 μM) in the presence of NADH (50 μm) upon the addition of different amounts of NTR (0, 1.0, 2.0, 5.0, 8.0, and 10.0 μg/mL, Ex = 450 nm). (D, E) Fluorescence images of HeLa cells incubated with **TPE–$NO_2$** (10 μM) at 37 °C for 30 min under (D) normoxic (20% $O_2$) and (E) hypoxic (1% $O_2$) conditions (Ex = 330–380 nm). Scale bar: 10 μm. Adapted with permission from ref. [32]. Copyright 2016 Wiley-VCH.

detection limit for NTR was determined to be 5 ng/mL. It should be noted that although a nitro group was attached to the AIEgen, the fluorescence of **TPE-$NO_2$** was not completely quenched; therefore, **TPE-$NO_2$** still exhibited strong fluorescence upon aggregation and/or electrostatic association with negatively charged species to trigger AIE, regardless of hypoxia. Nevertheless, **TPE-$NO_2$** and **TPE-PY** showed completely different fluorescence spectra because of the distinct electronic effect. Specifically, the presence of the electron-withdrawing pyridinium salt greatly red-shifted the emission color of **TPE-$NO_2$** to orange, whereas **TPE-PY** was a green-emissive AIEgen. When HeLa tumor cells were incubated with **TPE-$NO_2$** in normoxic and hypoxic conditions, fluorescence signals could be detected for both situations (Figure 9.3D,E). However, the emission color significantly changed from orange to green when the hypoxic conditions were exerted, indicating the specific response of **TPE-$NO_2$** toward hypoxia-upregulated NTR in tumor cells.

Although the nitro-containing probes are readily synthesized, their specificity for hypoxia is relatively poor, primarily due to the presence of the hypoxia-independent two-electron pathway. Moreover, the quenching effect of the nitro group does not take effect on all fluorophores. For example, some nitro-containing molecules remain highly emissive (e.g., nitrobenzoxadiazole); in certain cases, the fluorophores still keep quenched even after the reduction of the nitro group [33], primarily due to the activated charge- or electron-transfer processes (e.g., ICT and PET). Accordingly, when designing nitro-based AIE-type hypoxic probes, these factors need to be considered.

## 9.2.2 *N*-oxide-containing AIE probes for hypoxic response

*N*-oxide group is another type of functional group that can be reduced under hypoxic conditions. Specifically, the *N*-oxide group is irreversibly reduced to the amino group *via* a two-electron process by hypoxia-upregulated enzymes (e.g., DTD and cytochrome P450 in the presence of reductive coenzymes) (Figure 9.2, lower left box) [34]. In particular, this biochemical reaction remarkably enhances the hydrophobicity of the resultant compounds by consuming the hydrophilic *N*-oxide group, leading to the formation of irregular self-aggregates in aqueous solution. Such feature can be exquisitely borrowed for the design of AIE-based hypoxia-responsive probes. Similar to the aforementioned nitro-based leaving groups, there is also a significant change in the electronic effect after the reduction of the *N*-oxide group [35]. The resultant product (*i.e.*, amine) can act as a strong electron donor, which typically gives rise to the red-shifted absorption and emission spectra. Taking advantage of these merits, Tang and coworkers synthesized a water-soluble AIE probe, **TPE-2E *N*-oxide**, simply by oxidizing **TPE-2E** with *meta*-chloroperoxybenzoic acid (*m*-CPBA) [36]. Since **TPE-2E *N*-oxide** and **TPE-2E** exhibited distinct water-solubility, the reduction of **TPE-2E *N*-oxide** in hypoxic conditions resulted in the formation of **TPE-2E** self-aggregates

and thus the activation of the AIE process (Figure 9.4A). To testify this argument, **TPE-2E *N*-oxide** was incubated with $(NH_4)_2Fe(SO_4)_2$ to initiate the reduction reaction, as the heme-iron center was proven to be the active site of cytochrome P450. It was found that the remarkable fluorescence enhancement was observed when the concentration of $(NH_4)_2Fe(SO_4)_2$ increased from 100 μM to 1 mM. To verify that the *N*-oxide group was indeed reduced to the amino group by Fe(II), the size-distribution change of the incubation system was monitored by dynamic light scattering. As shown in Figure 9.4B, incubation of **TPE-2E *N*-oxide** with $(NH_4)_2Fe(SO_4)_2$ resulted in a marked increase in the particle size; moreover, in contrast to the aqueous dispersion of **TPE-2E *N*-oxide**, the resulting dispersion exhibited particularly strong green fluorescence, suggesting the successful transformation of **TPE-2E *N*-oxide** to **TPE-2E**, as well as the formation of large aggregates (Figure 9.4C). Furthermore, **TPE-2E *N*-oxide** was incubated with HeLa tumor cells at different contents of oxygen. The results shown in Figure 9.4D demonstrated that the fluorescence intensity was negatively correlated with the contents of oxygen, with almost no signal detected under normoxia, which agreed well with different levels of hypoxia. To prove that such a process was specifically medicated by hypoxia-upregulated reductases, diphenyliodonium chloride (DPI), an inhibitor of intracellular reductases, was used to mitigate the reduction process. When the concentration of DPI reached 500 μM, fluorescence recovery was completely shut down (Figure 9.4E). Flow cytometry analysis further confirmed this result (Figure 9.4F). By adopting a similar design principle, Zhang et al. developed a four-diethylamino *N*-oxide decorated tetraphenylethene (TPE) and further achieved deep penetration of the tumor tissue for hypoxia detection and imaging-guided surgery *in vivo* [37].

Since the *N*-oxide-based strategy is highly dependent on the hydrophilic-to-hydrophobic transition, the water-solubility of *N*-oxide-containing AIEgens and the hydrophobicity of the reduced AIEgens need to be precisely balanced; otherwise, no evident responses will be triggered under hypoxia conditions. In addition, the *N,N'*-dialkylamine groups are able to impose a strong electron-donating effect, which possibly compromises the fluorescence recovery *via* the enhanced ICT when a strong electron acceptor is present [38].

### 9.2.3 Azo-containing AIE probes for hypoxic response

Similar to the nitro group, the azo group can be reduced to an anion radical by azoreductase (mostly in lysosomes) *via* a single-electron reduction process; moreover, this process can be reversibly switched back to the azo group by oxygen, together with the generation of a superoxide radical. The formed reactive anion radical can be further reduced by receiving another electron to produce hydrazine, which is subsequently split into two amino compounds by a two-electron reduction process (Figure 9.2, lower right box) [39]. Unlike the nitro group, the azo group has two substitutable

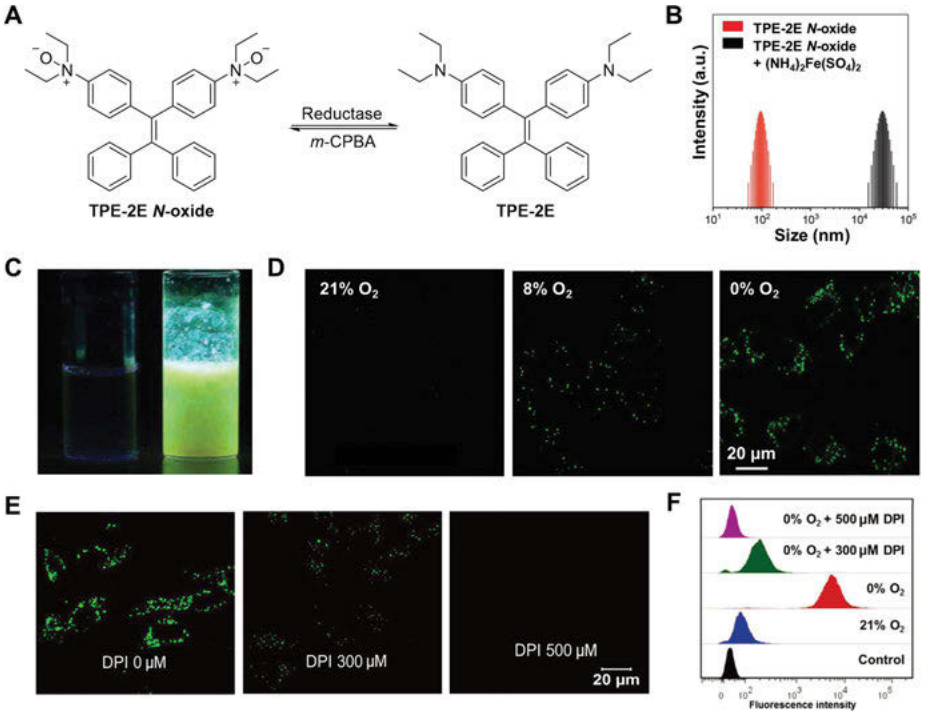


**Figure 9.4:** A *N*-oxide-based water-soluble AIEgen for hypoxia detection. (A) Schematic illustration of hypoxia detection based on the hydrophilic-to-hydrophobic transition of **TPE-2E *N*-oxide** to **TPE-2E** catalyzed by intracellular reductases. (B) The size distribution of **TPE-2E *N*-oxide** (2 mM) dispersed in water with or without the addition of $(NH_4)_2Fe(SO_4)_2$ (20 mM). (C) A photograph of the aqueous solution of 2 mM **TPE-2E *N*-oxide** before (left) and after (right) treated with $(NH_4)_2Fe(SO_4)_2$ (20 mM) taken under UV light. (D) Fluorescence images of HeLa cells incubated with **TPE-2E *N*-oxide** (200 μM). The HeLa cells were exposed to various oxygen concentrations for 3 h. (E) Fluorescence images of HeLa cells incubated with **TPE-2E *N*-oxide** (200 μM) and different DPI concentrations for 3 h under hypoxic conditions. (F) Flow cytometry analysis of HeLa cells incubated with **TPE-2E *N*-oxide** (200 μM). Adapted with permission from Ref. [36]. Copyright 2019 Wiley-VCH.

sites and is commonly used in host–guest recognition, enabling their potentials in a spectrum of applications. In particular, the *N*–*N* double bond in the azo group can efficiently dissipate the excitation energy *via* fast *cis*–*trans* isomerization to quench the fluorescence of the covalently bounded fluorophores [40, 41]. In addition, as demonstrated in a study, the azo-containing probe was able to differentiate different levels of hypoxia [42]. In terms of the molecular design, the azo group can be directly used as a quencher and/or employed as a linker to bridge hydrophobic AIEgens with hydrophilic moieties to enhance its water solubility. In one study, Tang and coworkers reported an azo-based pro-AIEgen for "turn-on" sensing of hypoxia. Specifically, the probe **TPE-Azo** was synthesized *via* diazonium coupling of

**TPE-Am** and *N*,*N*'-dimethylailine (Figure 9.5A) [43], in which, **TPE-Am** possessed typical AIE character (Figure 9.5B). As shown in Figure 9.5C, the THF solution and the powder of **TPE-Azo** showed no fluorescence, which was attributed to the active photoisomerization of the azo group. Further analysis on the crystal structure of **TPE-Azo** suggested the weak C–H···N intermolecular interactions, which caused deficient confinement on the azo group and thus accounted for the nonemission of **TPE-Azo** powder at room temperature (Figure 9.5D). However, when the temperature of the powder was cooled down to 77 K, the restricted intramolecular motions switched the energy dissipation pathways from nonradiative transition to radiative decay, suggesting that the azo group played a pivotal role in fluorescence quenching. To testify that the cleavage of the azo group could facilitate fluorescence recovery, sodium dithionite ($Na_2S_2O_4$), a potent reducing agent, was added into the suspension of **TPE-Azo**. As shown in Figure 9.5E, the fluorescence intensity gradually enhanced when the incubation time was prolonged, with the plateau phase occurring at 15 min (Figure 9.5E). Furthermore, **TPE-Azo** was applied to the detection of hypoxia in HeLa cells. The "turn-on" fluorescence was observed for the group with low contents of oxygen, which could be selectively shut down by the addition of DPI (Figure 9.5F). In another study, Xue et al. attached the hydrophilic polyethylene glycol moiety to a conventional AIEgen *via* the azo group so as to correlate the florescence intensity with hypoxia by means of hydrophobicity changes [44]. Specifically, the probe **PEG-AZO-TPE** was prepared by linking PEG diazonium salt and a TPE-modified aniline through an azo coupling reaction (Figure 9.6A). The resulting probe was water-soluble under normoxic conditions and showed no fluorescence. On the contrary, under hypoxic conditions, the azo group was reduced by azoreductase, leading to the separation of the AIEgen and the PEG chain. In this case, the hydrophobic AIEgens started to form self-aggregates, leading to decreased absorption (due to the cleavage of azobenzene) and increased fluorescence (due to the AIE property). These arguments could be reflected from the absorption and emission spectra of **PEG-AZO-TPE**, before and after incubation with azoreductase (Figure 9.6B,C). Further incubation of A549 tumor cells with **PEG-Azo-TPE**, under normoxic (20% $O_2$) and hypoxic (1% $O_2$) conditions, evidenced the specific response of the probe toward hypoxia, which was reflected by the remarkably enhanced fluorescence (Figure 9.6D). Given that the multicellular tumor spheroid was a well-established model to recapitulate tumor growth and hypoxia *in vivo*, **PEG-Azo-TPE** was also applied to hypoxia detection in HeLa multicellular tumor spheroids (Figure 9.6E). In contrast to the group treated with PBS, the probe-treated one exhibited significantly enhanced fluorescence at 72 h post incubation, indicating its potential in labeling hypoxic areas in solid tumors for precise surgical removal.

Since the two sides of the azo group can be pendent with different substituents, the introduction of intramolecular FRET switches is also a feasible approach for the

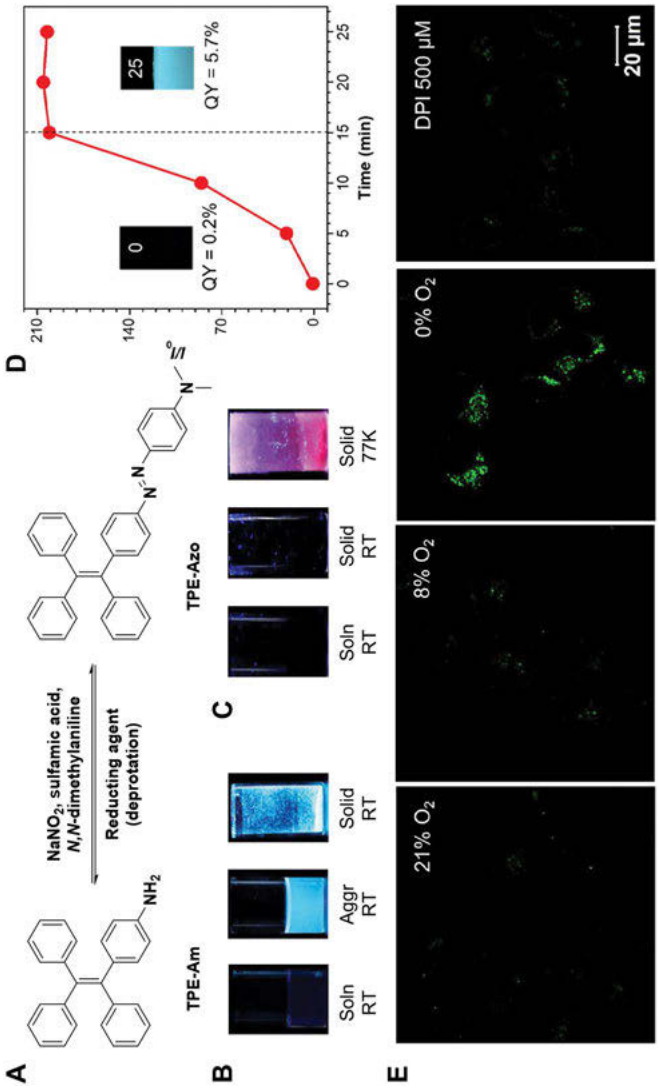


**Figure 9.5:** An azo-based pro-AIEgen for "turn-on" sensing of hypoxia *via* reductase-modulated derotation. (A) Interconversion between **TPE-Azo** and **TPE-Am** by azo coupling (left to right) and reduction-mediated derotation (right to left). (B) Photographs of **TPE-Am** in THF solution (Soln), THF/water mixture (water fraction = 99%), and solid state taken at room temperature (RT) under UV light. (C) Photographs of **TPE-Azo** in THF solution (Soln) at RT as well as **TPE-Azo** powders at 77 K and RT taken under UV light. (D) Crystal packing of **TPE-Azo**. (E) Changes in emission intensity (*I*) as a function of reaction time between **TPE-Azo** (50 μM) and $Na_2S_2O_4$ (5 mM). Insets: photographs of **TPE-Azo** suspensions before (0 min) and after reaction with $Na_2S_2O_4$ for 25 min taken under UV light. (F) Fluorescence images of HeLa cells incubated with 200 μM **TPE-Azo** at various oxygen concentrations for 3 h in the absence or presence of DPI. Adapted with permission from ref. [43]. Copyright 2021 Wiley-VCH.

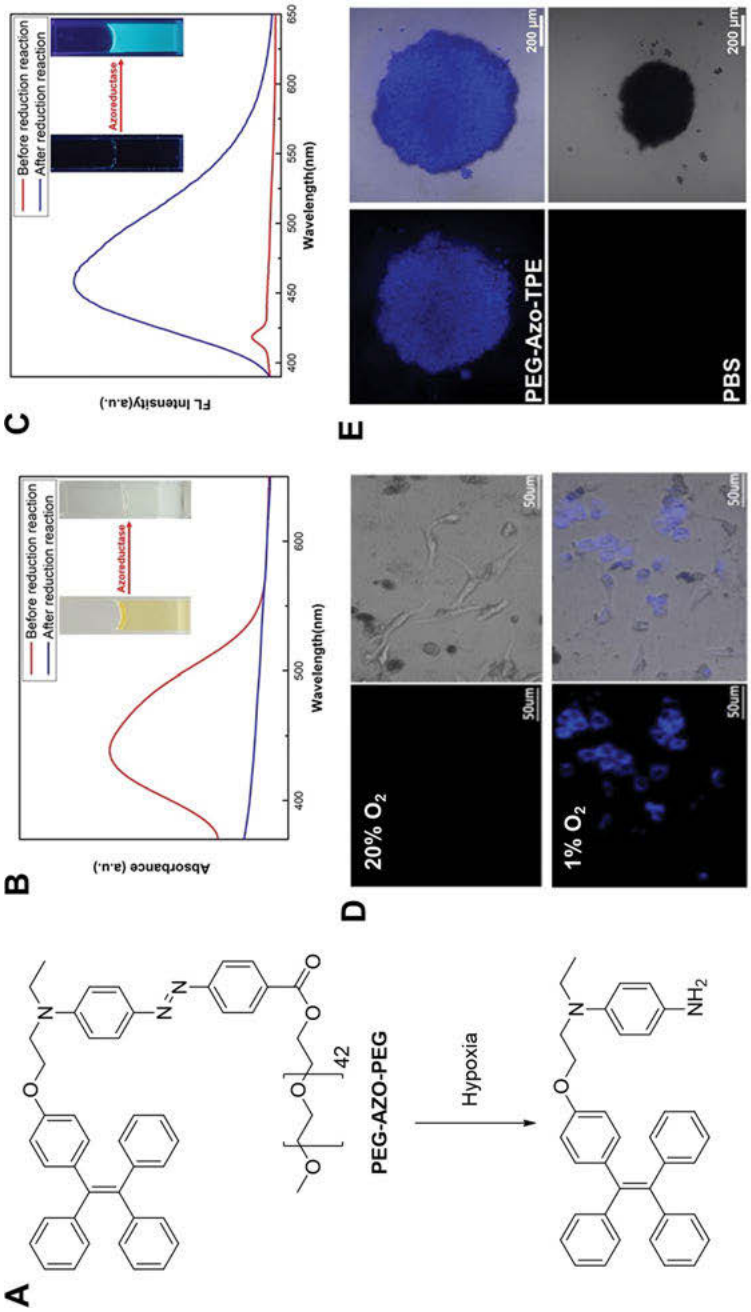


**Figure 9.6:** A water-soluble azo-based AIEgen for hypoxia imaging of multicellular tumor spheroids. (A) Chemical structure of **PEG-AZO-TPE** and its reduction reaction under hypoxic conditions. (B) UV/Vis absorption spectra of the self-assembled nanoaggregates in aqueous

design of hypoxia-responsive probes [39]. In addition, for the strategy of making use of the hydrophilic-to-hydrophobic transition, the hydrophilic group can also be replaced by various water-soluble prodrugs, which provides multiple functionalities to achieve simultaneous imaging and therapy. It should be noted that the azo group is susceptible to a variety of reducing agents (e.g., intracellular glutathione) and its specificity toward hypoxia detection is relatively limited.

## 9.3 Summary

In view of the advantages of high brightness and sensitivity, noninvasiveness attribute, and excellent photostability, several AIE-based hypoxia-responsive probes have been developed to enable sensitive and stable fluorescence imaging, holding great potential for tumor diagnosis and therapy. To date, three types of functional groups have been designed to respond to the overexpressed reductases in the hypoxic environment, including the nitro, *N*-oxide, and azo groups. By means of the reductase-mediated reduction reaction, a series of signal changes (primarily refer to fluorescence) are triggered to reflect the hypoxic situations. In terms of hypoxia responsiveness, different functional groups have different unique advantages. For example, the nitro group is able to facilitate ultrasensitive response; the *N*-oxide group can bring in shifted absorption and emission spectra for improved specificity; and the azo group can linearly reflect different levels of hypoxia in solid tumors. In spite of these achievements, the development of AIE-based hypoxia probes is still in its infant stage, and several issues need to be addressed in the future. On the one hand, currently reported AIE probes are primarily based on the classical building block, that is, TPE. However, its absorption spectrum is mainly located in the ultraviolet region, which is not suitable for biological studies due to its photo-toxicity toward healthy tissues and inability to penetrate deep tissues. In this respect, the development of AIE-based probes, with near-infrared absorption and/or emission, are greatly preferred [45, 46]. On the other hand, the functionality of the aforementioned AIE-based probes is only limited to hypoxia detection. The design of multifunctional probes can desirably boost the establishment of "all-in-one" theranostic systems for multi-modal treatment of hypoxic tumors [47, 48]. Looking ahead, the

**Figure 9.6** (continued)
solution before and after cleavage by azoreductase. (C) The corresponding fluorescence spectra of the systems as described in (B). Insets: photographs of the aggregates before and after the enzymatic reaction. (D) Fluorescence images of A549 cells treated with **PEG-AZO-TPE** under normoxic (20% $O_2$) and hypoxic (1% $O_2$) conditions. (E) Fluorescence images of HeLa multicellular tumor spheroids treated with **PEG-AZO-TPE** and PBS. Ex = 760 nm (two-photon fluorescence imaging). Adapted with permission from ref. [44]. Copyright 2019 Wiley-VCH.

design and synthesis of high-performance AIE-based hypoxia probes will surely provide in-depth understanding of the pathological status of hypoxic solid tumors, and, hopefully, accelerate the capability of human beings to overcome tumors.

## References

[1] Zhang L, Huang G, Li X, et al., Hypoxia induces epithelial-mesenchymal transition via activation of SNAI1 by hypoxia-inducible factor-1α in hepatocellular carcinoma, BMC Cancer, 2013, 13, 108.
[2] Harrison L, Blackwell K, Hypoxia and anemia: Factors in decreased sensitivity to radiation therapy and chemotherapy? Oncologist, 2004, 9, 31–40.
[3] Shannon AM, Bouchier-Hayes DJ, Condron CM, Toomey D, Tumour hypoxia, chemotherapeutic resistance and hypoxia-related therapies, Cancer Treat Rev, 2003, 29, 297–307.
[4] Jung HS, Han J, Shi H, et al., Overcoming the limits of hypoxia in photodynamic therapy: A carbonic anhydrase IX-targeted approach, J Am Chem Soc, 2017, 139, 7595–7602.
[5] Pucelik B, Sulek A, Barzowska A, Dabrowski JM, Recent advances in strategies for overcoming hypoxia in photodynamic therapy of cancer, Cancer Lett, 2020, 492, 116–135.
[6] Liu HW, Chen L, Xu C, et al., Recent progresses in small-molecule enzymatic fluorescent probes for cancer imaging, Chem Soc Rev, 2018, 47, 7140–7180.
[7] Elmes RB, Bioreductive fluorescent imaging agents: Applications to tumour hypoxia, Chem Commun, 2016, 52, 8935–8956.
[8] O'Connor JP, Boult JK, Jamin Y, et al., Oxygen-enhanced MRI accurately identifies, quantifies, and maps tumor hypoxia in preclinical cancer models, Cancer Res, 2016, 76, 787–795.
[9] Carlin S, Humm JL, PET of hypoxia: Current and future perspectives, J Nucl Med, 2012, 53, 1171–1174.
[10] Challapalli A, Carroll L, Aboagye EO, Molecular mechanisms of hypoxia in cancer, Clin Transl Imaging, 2017, 5, 225–253.
[11] Eales KL, Hollinshead KE, Tennant DA, Hypoxia and metabolic adaptation of cancer cells, Oncogenesis, 2016, 5, e190.
[12] Yan J, Lee S, Zhang A, Yoon J, Self-immolative colorimetric, fluorescent and chemiluminescent chemosensors, Chem Soc Rev, 2018, 47, 6900–6916.
[13] Xu G, McLeod HL, Strategies for enzyme/prodrug cancer therapy, Clin Cancer Res, 2001, 7, 3314–3324.
[14] Xue T, Shen J, Shao K, Wang W, Wu B, He Y, Strategies for tumor hypoxia imaging based on aggregation-induced emission fluorogens, Chem Eur J, 2020, 26, 2521–2528.
[15] Algar WR, Hildebrandt N, Vogel SS, Medintz IL, FRET as a biomolecular research tool – Understanding its potential while avoiding pitfalls, Nat Methods, 2019, 16, 815–829.
[16] Takahashi S, Piao W, Matsumura Y, et al., Reversible off-on fluorescence probe for hypoxia and imaging of hypoxia-normoxia cycles in live cells, J Am Chem Soc, 2012, 134, 19588–19591.
[17] Daly B, Ling J, de Silva AP, Current developments in fluorescent PET (photoinduced electron transfer) sensors and switches, Chem Soc Rev, 2015, 44, 4203–4211.
[18] Luo J, Xie Z, Lam JWY, et al., Aggregation-induced emission of 1-methyl-1,2,3,4,5-pentaphenylsilole, Chem Commun, 2001, 1740–1741.
[19] Zhao Z, Zhang H, Lam JWY, Tang BZ, Aggregation-induced emission: New vistas at the aggregate level, Angew Chem Int Ed, 2020, 59, 9888–9907.

[20] Mei J, Leung NLC, Kwok RTK, Lam JWY, Tang BZ, Aggregation-induced emission: Together we shine, united we soar! Chem Rev, 2015, 115, 11718–11940.
[21] Yan L, Zhang Y, Xu B, Tian W fluorescent nanoparticles based on AIE fluorogens for bioimaging, Nanoscale, 2016, 8, 2471–2487.
[22] Mei J, Hong Y, Lam JWY, et al, Aggregation-induced emission: The whole is more brilliant than the parts, Adv Mater, 2014, 26, 5429–5479.
[23] Liu S, Feng G, Tang BZ, Liu B, Recent advances of AIE light-up probes for photodynamic therapy, Chem Sci, 2021, 12, 6488–6506.
[24] Ji Y, Wang Y, Zhang N, et al., Cell-permeable fluorogenic probes for identification and imaging nitroreductases in live bacterial cells, J Org Chem, 2019, 84, 1299–1309.
[25] Fang Y, Shi W, Hu Y, Li X, Ma H, A dual-function fluorescent probe for monitoring the degrees of hypoxia in living cells via the imaging of nitroreductase and adenosine triphosphate, Chem Commun, 2018, 54, 5454–5457.
[26] Tian X, Li Z, Sun Y, Wang P, Ma H, Near-infrared fluorescent probes for hypoxia detection via joint regulated enzymes: Design, synthesis, and application in living cells and mice, Anal Chem, 2018, 90, 13759–13766.
[27] Zheng J, Shen Y, Xu Z, et al., Near-infrared off-on fluorescence probe activated by NTR for in vivo hypoxia imaging, Biosens Bioelectron, 2018, 119, 141–148.
[28] Liu Z, Song F, Shi W, et al., Nitroreductase-activatable theranostic molecules with high PDT efficiency under mild hypoxia based on a TADF fluorescein derivative, ACS Appl Mater Interfaces, 2019, 11, 15426–15435.
[29] Luo S, Zou R, Wu J, Landry MP, A Probe for the Detection of Hypoxic Cancer Cells, ACS Sens, 2017, 2, 1139–1145.
[30] Zheng X, Wang X, Mao H, Wu W, Liu B, Jiang X, Hypoxia-specific ultrasensitive detection of tumours and cancer cells in vivo, Nat Commun, 2015, 6, 5834.
[31] Li Y, Sun Y, Li J, et al., Ultrasensitive near-infrared fluorescence-enhanced probe for in vivo nitroreductase imaging, J Am Chem Soc, 2015, 137, 6407–6416.
[32] You X, Li L, Li X, Ma H, Zhang G, Zhang D, A new tetraphenylethylene-derived fluorescent probe for nitroreductase detection and hypoxic-tumor-cell imaging, Chem Asian J, 2016, 11, 2918–2923.
[33] Zhao X, Long S, Li M, et al., Oxygen-dependent regulation of excited-state deactivation process of rational photosensitizer for smart phototherapy, J Am Chem Soc, 2020, 142, 1510–1517.
[34] Tredan O, Garbens AB, Lalani AS, Tannock IF, The hypoxia-activated ProDrug AQ4N penetrates deeply in tumor tissues and complements the limited distribution of mitoxantrone, Cancer Res, 2009, 69, 940–947.
[35] Knox HJ, Hedhli J, Kim TW, Khalili K, Dobrucki LW, Chan J, A bioreducible *N*-oxide-based probe for photoacoustic imaging of hypoxia, Nat Commun, 2017, 8, 1794.
[36] Xu C, Zou H, Zhao Z, et al., A new strategy toward “simple” water-soluble AIE probes for hypoxia detection, Adv Funct Mater, 2019, 29, 1903278.
[37] Zhang Z, Wang R, Huang X, et al., A simple aggregation-induced emission nanoprobe with deep tumor penetration for hypoxia detection and imaging-guided surgery in vivo, Anal Chem, 2021, 93, 1627–1635.
[38] Xu S, Wu W, Cai X, et al., Highly efficient photosensitizers with aggregation-induced emission characteristics obtained through precise molecular design, Chem Commun, 2017, 53, 8727–8730.
[39] Kiyose K, Hanaoka K, Oushiki D, et al., Hypoxia-sensitive fluorescent probes for in vivo real-time fluorescence imaging of acute ischemia, J Am Chem Soc, 2010, 132, 15846–15848.

[40] Bandara HM, Burdette SC, Photoisomerization in different classes of azobenzene, Chem Soc Rev, 2012, 41, 1809–1825.
[41] Li S, Wang J, Shen J, Wu B, He Y, Azo coupling reaction induced macromolecular self-assembly in aqueous solution, ACS Macro Lett, 2018, 7, 437–441.
[42] Piao W, Tsuda S, Tanaka Y, et al., Development of azo-based fluorescent probes to detect different levels of hypoxia, Angew Chem Int Ed, 2013, 52, 13028–13032.
[43] Xu C, Zou H, Zhao Z, et al., Turning on light emission of a dark pro-aggregation-induced emission luminogen in aqueous media through reductase-modulated derotation, Adv NanoBiomed Res, 2021, 1, 2000080.
[44] Xue T, Jia X, Wang J, et al., "Turn-on" activatable AIE dots for tumor hypoxia imaging, Chem Eur J, 2019, 25, 9634–9638.
[45] Fu W, Yan C, Guo Z, et al., Rational design of near-infrared aggregation-induced-emission-active probes: In situ mapping of amyloid-beta plaques with ultrasensitivity and high-fidelity, J Am Chem Soc, 2019, 141, 3171–3177.
[46] Zhang R, Duan Y, Liu B, Recent advances of AIE dots in NIR imaging and phototherapy, Nanoscale, 2019, 11, 19241–19250.
[47] Wu W, Li Z, Nanoprobes with aggregation-induced emission for theranostics, Mater Chem Front, 2021, 5, 603–626.
[48] Zhang Z, Xu W, Kang M, et al., An all-round athlete on the track of phototheranostics: Subtly regulating the balance between radiative and nonradiative decays for multimodal imaging-guided synergistic therapy, Adv Mater, 2020, 32, 2003210.

Miaomiao Kang, Panpan Sun, Dong Wang, Ben Zhong Tang

# Chapter 10
# AIE probes for bacterial detection and antibacterial applications

## 10.1 Introduction

Bacteria represent an important category of microorganisms and exist in every conceivable area [1]. The widely distributed bacteria have a significant impact on the daily life of humans, in various ways [2]. Most of the bacteria inhabit on the human body in a mutualistic symbiotic way, where both bacteria and human body can benefit from each other [3]. For example, intestinal bacteria can be useful for the normal physiological functions of the human body by virtue of their active metabolism [4, 5]. However, many specific bacterial species are hostile or even fatal to mankind because they can lead to serious diseases, such as foodborne illness, tuberculosis, sepsis, meningitis, skin and soft tissue infection, and urinary tract infections, some of which could even be life-threatening, especially for the patients with low immune function [6, 7]. This challenging dilemma was temporarily solved, since highly effective antibiotics such as sulfa drug [8] and penicillin [9] were discovered in the 1930s, with many of the originally fatal bacterial infections now becoming only minor inconveniences. However, this satisfactory scene was shattered shortly after, with the emergence of antibiotics-resistant bacteria [11–13], which can be ascribed to the abuse and overprescription of antibiotics, in the past decades. At present, the fast-increasing antibiotic resistance has been causing millions of deaths per year, worldwide [14]. Worse still, in contrast with the alarming incidence rate of antibiotic resistance, the development of new robust antibiotic candidates is stalling. In view of this growing serious crisis in the global healthcare landscape, more

**Acknowledgements:** Miaomiao Kang and Panpan Sun contributed equally to this chapter. This work was partially supported by the National Natural Science Foundation of China (22105130, 51903163, 21801169), the Natural Science Foundation for Distinguished Young Scholars of Guangdong Province (2020B1515020011), and the Science and Technology Plan of Shenzhen (JCYJ20190808153415062).

**Miaomiao Kang, Panpan Sun,** Center for AIE Research, College of Materials Science and Engineering, Shenzhen University, Shenzhen, 518060, China
**Dong Wang,** Center for AIE Research, College of Materials Science and Engineering, Shenzhen University, Shenzhen, 518060, China, e-mail: wangd@szu.edu.cn
**Ben Zhong Tang,** Shenzhen Institute of Aggregate Science and Technology, School of Science and Engineering, The Chinese University of Hong Kong (Shenzhen), Shenzhen, 518172, China, e-mail: tangbenz@cuhk.edu.cn

https://doi.org/10.1515/9783110672220-010

pertinent strategies to combat pathogenic bacteria are urgently desired for human beings to survive in the "post-antibiotic era."

Accurate diagnosis is always the cornerstone in efficient management of antibiosis. Therefore, prior to antibacterial therapy, rapid detection and reliable identification of bacteria play crucial roles in clinical practice, because determining of bacteria type is significant for the medical staff to choose appropriate antibacterial agents and develop pertinent therapeutic schedule, efficiently and rapidly. In the clinical setting, culture-based diagnosis is the gold standard for bacterial identification, but this time-consuming method requires tedious labor from specialized technicians and lacks the in situ detection capability of living bacteria [15]. In addition, there are other techniques reported in the literature these years, like polymerase chain reaction (PCR) [16], gene-related techniques [17, 18], immunological techniques [19], fluorescence in situ hybridization (FISH) [20], mass spectrometry [21], and surface-enhanced Raman spectroscopy (SERS) [22]. Although these techniques could bring about relative high sensitivity and selectivity, the high expense, complex procedures, and sophisticated instrumentation dependence inevitably limit their practical applications, as well. Consequently, more advanced technologies are urgently required for the accurate and visualized detection and discrimination of diverse bacteria.

Under this circumstance, fluorescence technology, as a rapid and powerful tool, has lately emerged as an ideal alternative for bacterial detection and discrimination by virtue of its low cost, easy operation, noninvasiveness, in situ detection, and real-time response, as well as high sensitivity and specificity [23, 24]. Nevertheless, due to the aggregation-caused quenching (ACQ) effect, the fluorescence signals of the conventional fluorescent materials are always diminished or even quenched at high concentrations or in the aggregated state as a result of intermolecular π–π stacking [25, 26]. Moreover, since most of the bioapplication scenarios are usually water-filled, these structurally hydrophobic traditional fluorescent probes are prone to form irregular aggregates in this aqueous condition, resulting in severe self-quenched fluorescence, thus greatly restricting their bioapplication. By contrast, profiting from the aggregation-induced emission (AIE) characteristic, the fluorescent probes with AIE feature display stronger fluorescence emission upon aggregates formation than that in dilute solutions or single molecular state, due to the restriction of intramolecular motion (RIM) and prohibition of energy dissipation [27, 28]. The timely appearance and subsequent mechanism elucidation of AIE luminogens (AIEgens) successfully solved the dilemma of ACQ and largely expanded the application scope of fluorescent technology in practical biological systems [29–32]. Up to now, a lot of successes in various biomedical imaging fields based on AIE probes have been witnessed [33–35], proving their favorable superiorities of good biocompatibility, high fluorescence quantum efficiency in aggregates, large Stokes shift, outstanding photostability, as well as facile processability. Furthermore, combining the structural features of different bacterial membranes and the foundation of varying mechanisms that trigger aggregate formation, different

detection systems have been designed and synergistically integrated to realize the light-up detection and specific classification of various bacteria [36–39].

On the other hand, effective regulation of antibiosis on the basis of accurate bacterial detection and discrimination is the final goal in the battle against pathogenic bacteria. Accompanying the termination of the satisfactory "antibiotic era" indicated by the appearance of antibiotic resistance, huge research efforts have been continuously devoted to seek alternative antibacterial therapeutics which can potentially avoid the bacterial resistance. Among the developed alternative therapeutics, photodynamic therapy (PDT) that has the merits of minimal invasion, precise controllability, and high spatiotemporal accuracy, as well as unique antibiosis mechanism has attracted great attention [40, 41]. Generally, PDT exerts antibacterial effect mainly relying on the highly toxic reactive oxygen species (ROS) generated by photosensitizers (PSs) upon light irradiation [40]; and ROS could provide an aggressive and random attack on bacteria, even though the PSs could not completely enter the bacteria, preventing the generation of specific resistant strains [42, 43]. In this respect, the photosensitizing property of PSs presents as the most critical factor in photodynamic bacteria killing. Contrary to the conventional PSs that suffer from fluorescence quenching and reduced ROS generation caused by ACQ [44, 45], AIE-active PSs exhibit favorable aggregation-induced enhancement of ROS generation capacity in addition to the AIE features, which guarantees sufficient ROS generation of the aggregated PSs in the physiological environment [25, 29, 46–48]. On the basis of these collective unique characteristics, AIE probes exhibited great advantages in imaging-guided PDT of pathogenic bacteria [49–53]. In addition to the photodynamic therapy, AIE probes also exhibited outstanding performances in imaging-guided chemotherapy, biotherapy, and combination therapy of pathogenic bacteria, which constitute indispensable approaches on the bumpy road of antibacterial therapy [54–58].

This chapter will provide a systematic overview about the wide applications of AIE probes in bacterial detection and antibacterial therapy. For the bacterial detection part, bacterial imaging including selective imaging over mammalian cells, discrimination of gram-positive and gram-negative bacteria, as well as selective detection and identification of specific bacteria will be enumerated, in sequence. For the antibacterial application part, the AIEgen-based theranostic systems including imaging-guided photodynamic therapy, chemotherapy, biotherapy, and combination therapy will be described, with an emphatic discussion on photodynamic therapy. Finally, a short conclusion and future perspectives in this field will be also presented briefly.

## 10.2 Bacterial detection and identification

Compared with the constant fluorescence signal of traditional fluorescence probes, the aggregation-induced emission feature endows AIE probes an advantageous fluorescence turn-on capacity upon binding to the bacteria, due to the restriction of intramolecular motion, which favors the light-up detection of various bacteria [36, 37]. Furthermore, bacterial identification and classification could be concomitantly achieved based on corresponding fluorescent signals. Using the RIM mechanism, a number of AIE-based diagnostic systems for bacterial detection and identification have been constructed, relying on the various interactions between the diagnostic systems and bacteria, including nonspecific electrostatic or hydrophobic interactions [59, 60], specific recognition of receptor-ligand [61, 62], biological affinity [63, 64], and metabolic engineering [65–67], etc.

### 10.2.1 Bacterial imaging

In view of the negatively charged envelopes of bacteria [37, 68], several positively charged AIE probes have been developed to realize bacterial imaging on the basis of electrostatic interactions between cationic AIE probes and negatively charged bacterial surface. Lu et al. [69] substantiated the role of electrostatic interactions in bacterial imaging through cocultivating *E. coli* with the cationic AIE-active surfactant, tetraphenylethene-dodecyltrimethylammonium bromide (TPE-DTAB) and the anionic AIE-active surfactant, tetraphenylethene-sodium dodecyl sulfonate (TPE-SDS), respectively. After mixing with *E. coli*, turn-on fluorescence signal of cationic TPE-DTAB was observed that could be ascribed to the RIM mechanism of TPE moiety after binding with the bacteria surface driven by electrostatic interactions (Figure 10.1A, B). However, the anionic TPE-SDS hardly interacted with bacteria due to electrostatic repulsion, showing almost no change in fluorescence signal being found in the anionic TPE-SDS group (Figure 10.1C). The distinct fluorescence imaging results further supported this statement (Figure 10.1D). Moreover, they demonstrated that the hydrophobic chains of cationic TPE-DTAB could subsequently insert into the bacterial membrane upon contact with the bacteria surface via hydrophobic-hydrophobic interaction, resulting in membrane damage and death of *E. coli*. On this basis, Tang et al. [59] designed and synthesized three positively charged AIE probes with different emission colors, namely IQ-Naph, IQ-DPA, and IQ-TPA (Figure 10.1E). Profiting from the positive charge, all these three probes could bind onto the negatively charged bacterial surface. Bright fluorescence could be observed from both live and dead *E. coli* after staining for 10 min, respectively, attributing to the RIM of the probes, upon being trapped in the bacterial walls or membranes (Figure 10.1F). Additionally, no extra washing step was needed after staining, due to the good solubility of these AIE probes in PBS buffer at the staining concentration.

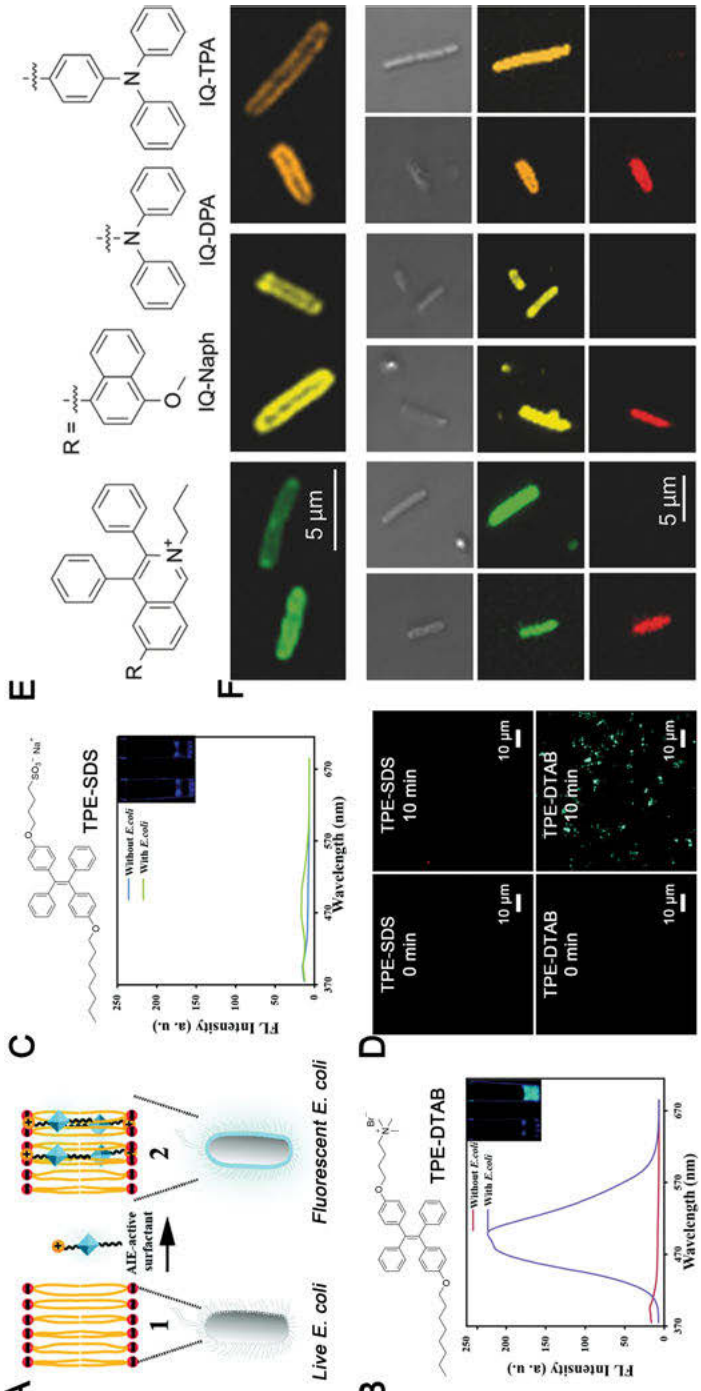


**Figure 10.1:** Bacterial imaging. (A) Schematic illustration of the interactions between the AIE-active surfactant and gram-negative *E. coli*. (B) Chemical structure of TPE-DTAB and the fluorescence spectra as well as photographs of TPE-DTAB in the presence and absence of *E. coli*. (C) Chemical structure of TPE-SDS and the fluorescence spectra as well as photographs of TPE-SDS in the presence and absence of *E. coli*. (D) Fluorescence images of mixtures of *E. coli* and TPE-SDS or TPE-DTAB after different incubation time. Reproduced with permission: Copyright 2017, Royal Society of Chemistry [69]. (E) Molecular structures of IQ-Naph, IQ-DPA and IQ-TPA. (F) CLSM images of *E. coli* stained by IQ-Naph, IQ-DPA and IQ-TPA. Reproduced with permission: Copyright 2018, John Wiley and Sons [59].

Since most of bacterial detection scenarios involve mammalian cells in the clinical setting, it is fundamentally important to selectively stain the pathogenic bacteria over cells for the purpose of accurate diagnosis. For the theranostic agents, the targeting ability to the pathogenic bacteria also contributes good biosafety to the healthy cells. Tang et al. [70] reported an AIE-active conjugated polymer (PTB-APFB) based on benzothiadiazole and TPE moieties, which exhibited ultra-strong ROS generation ability owing to its AIE characteristics and donor-π-acceptor structure. By virtue of the quaternary ammonium group, PTB-APFB could readily stain both gram-positive and gram-negative bacteria efficiently, through electrostatic interaction. Meanwhile, instead of being located in the terminal of the linker, this middle-seated cation endowed the polymer balanced hydrophilicity and hydrophobicity, which accounted for the selective binding toward bacteria over mammalian cells as well as good biosafety for the cells. Additionally, by employing positively charged Zinc (II)-dipicolylamine (ZnDPA) as a ligand, Liu et al. [71] developed a theranostic probe (AIE-ZnDPA) to realize the selective targeting and photodynamic killing of negatively charged bacteria over mammalian cells, due to its stronger binding affinity with bacteria. Generally, it is the ligand-ion complex that served as the recognition group in the probe; a mass of probes will be required to achieve good detection signal if the binding affinity between the ligand and ion is weak, and thus, they will leave more unbound free probes in the detection system, leading to higher background signals. Therefore, in order to reduce the background signals of the probes, Liu's group further designed and synthesized a light-up AIE probe (TPETH-2Zn) on the basis of a red-emissive AIE PS with better zinc(II)-binding affinity (Figure 10.2A) [72]. Thanks to the larger amount of net negative charges on the bacterial membrane surface, positively charged TPETH-2Zn could selectively light up the gram-negative *E. coli* and gram-positive *B. subtilis* upon binding to the bacterial membranes with no additional washing steps needed, whereas the mammalian HeLa cells could not be lighted up as the membranes of mammalian cells were nearly neutral, with only a small quantity of negative charge in the physiological conditions (Figure 10.2B).

Owing to its high sensitivity and specificity, direct bio-orthogonal labeling has been emerging as a promising approach for selective bacterial detection, based on the particular component of the bacterial peptidoglycan [73, 74]. Inspired by this strategy, Liu et al. [66] developed a bacterial metabolic AIE probe TPACN-$_D$-Ala, consisting of an AIE PS and $_D$-alanine ($_D$-Ala). Compared to the traditional bio-orthogonal labeling that required two steps, TPACN-$_D$-Ala, inherently bearing AIE fluorophores (TPACN), made the one-step bio-orthogonal labeling possible (Figure 10.2C). Since $_D$-amino acids are typically not needed in the biosynthesis of mammalian cells, whereas they are highly required for the peptidoglycan of bacteria, the introduced $_D$-amino acids ($_D$-Ala) in TPACN-$_D$-Ala significantly favored the selective imaging of intracellular bacteria, instead of their host cells. As Figure 10.2D shows, bright red fluorescence signal of methicillin-resistant *S. aureus* (MRSA) was observed after 10 min incubation with

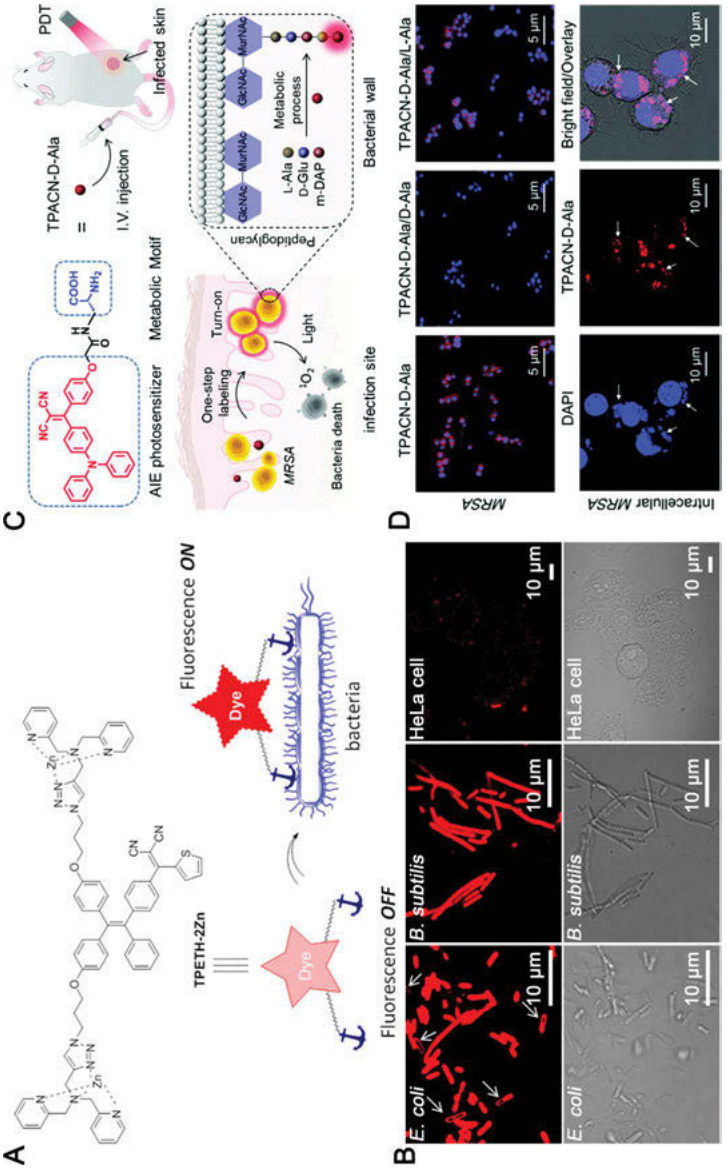


**Figure 10.2:** Selective bacterial imaging over mammalian cells. (A) Molecular structure of TPETH-2Zn and schematic illustration of the light-up imaging of bacteria. (B) CLSM images of *E. coli*, *B. subtilis* and HeLa cells after incubation with the TPEPH-2Zn probe. Reproduced with permission: Copyright 2017, American Chemical Society [72]. (C) Schematic illustration of the developed bacterial metabolic probe TPACN-$_D$-Ala for bacterial tracking and photodynamic therapy. (D) CLSM images showing the specific labeling of TPACN-$_D$-Ala on *MRSA* over normal cells. Reproduced with permission: Copyright 2020, Royal Society of Chemistry [66].

TPACN-$_D$-Ala, which, however, vanished when the competitive agent (Az-$_D$-Ala) was additionally added in the labeling process, evidently suggesting the efficient labelling of bacteria via the metabolic integration of $_D$-Ala into the peptidoglycan of the bacterial wall. Expectedly, the red fluorescence signal exhibited no visual change after the addition of noncompetitive agent, (Az-$_L$-Ala). It was also illustrated that TPACN-$_D$-Ala could precisely and specifically label the invasive bacteria hiding inside the host cells through metabolic labeling of $_D$-Ala-modified AIE probe (Figure 10.2D).

### 10.2.2 Discrimination of gram-positive and gram-negative bacteria

The efficient discrimination of gram-positive and gram-negative bacteria could provide valuable information for the prescription of antibacterial agents in clinical application. The outer envelope of the gram-positive bacteria is a thick and porous layer of peptidoglycan decorated with lipoteichoic acid (LTA), while that of gram-negative bacteria is much more complicated, consisting of a relative thin peptidoglycan layer as well as an outer membrane covered outside with lipopolysaccharide (LPS) mounted on it [75–77]. Based on the conspicuous structural differences, Tang and coworkers synthesized a DPAS-based AIE probe containing morpholine and naphthyl units, namely 2-{[(diphenylmethylene)hydrazono]methyl} naphthalene (M1-DPAN) to discriminate gram-positive bacteria from gram-negative ones (Figure 10.3A) [78]. Profiting from the negative charge of M1-DPAN as well as the much higher binding affinity of M1-DPAN toward gram-positive-bacteria-specific LTA than gram-negative-bacteria -specific LPS driven by the electrostatic interaction, M1-DPAN could selectively stain gram-positive bacteria (*S. aureus*, *B. subtilis,* and *E. faecalis*) even in the presence of gram-negative bacteria (*P. aeruginosa* and *E. coli*) and fungi (*S. cerecisiae* and *C. albicans*) (Figure 10.3B). Further, the morpholine moieties in M1-DPAN were demonstrated to play a crucial role in selective recognition of gram-positive bacteria. In addition, compared with the gram-negative bacteria with outer membrane, the DPAN moieties could easily insert into the thick and loose outer layers of gram-positive bacteria, resulting in the light-up response due to the AIE feature of M1-DPAN; whereas, the inserted parts into the layer structure of fungus were easily removed, leaving no fluorescence response of the fungus (Figure 10.3C).

Rapid discrimination of bacteria is persistently being pursued in the diagnosis of bacterial infectious diseases, as it can reserve precious treatment time for patients. Recently, the ultrafast discrimination of gram-positive bacteria was actualized by a water-soluble near-infrared (NIR) emissive AIE probe (TTVP) reported by Tang and coworkers [79]. Thanks to its excellent monodispersity in the culture media, strong electrostatic interaction with negatively charged gram-positive bacteria, as well as typical AIE characteristics, TTVP could rapidly and selectively light

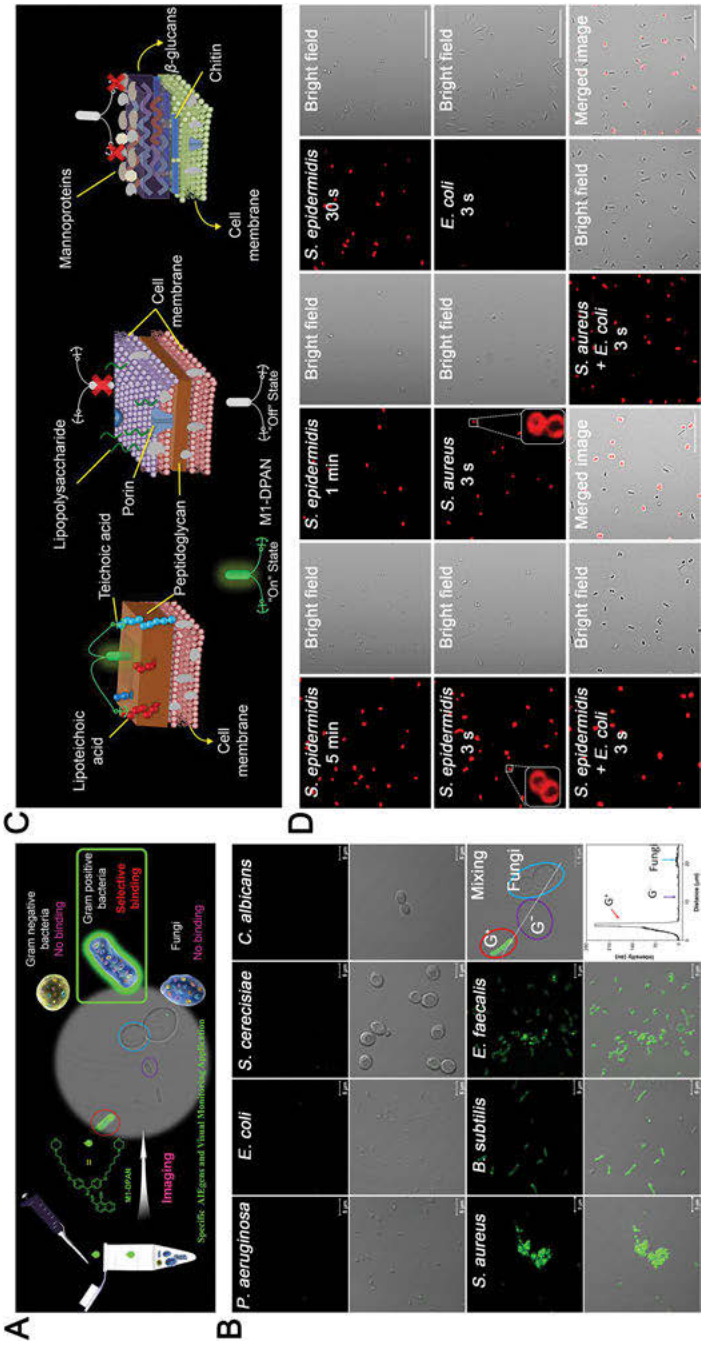


**Figure 10.3:** Discrimination of gram-positive and gram-negative bacteria via electrostatic interaction. (A) Illustration of applying AIEgen M1-DPAN for gram-positive bacteria specific

up the gram-positive bacteria (*S. epidermidis* and *S. aureus*) after incubation for only 3 s without further washing steps, which was 100-fold shorter than the already published protocols, implying its ultrafast bacterial discrimination features. However, gram-negative bacteria (*E. coli*) could not be stained after the same incubation time of 3 s even in the cocultivation systems (Figure 10.3D), and the fluorescence signal from *E. coli* could only be seen when the incubation time extended to 5 min, due to their more complicated outer envelopes that serve as efficient barriers in preventing the insertion of probes.

In addition to positively charged AIE probes, antibiotic-conjugated AIE probes have been developed for the discrimination of gram-positive and gram-negative bacteria by employing antibiotics as targeting moieties. Liu et al. [80] reported a red emissive AIE light-up probe, AIE-2Van, via conjugating a kind of glycopeptide antibiotic, vancomycin (Van), to the AIEgen. Taking advantage of the specific binding affinity of Van to peptidoglycan sequence N-acyl-D-Ala-D-Ala presented on gram-positive bacterial cell walls, the selective recognition as well as naked-eye detection of gram-positive bacteria including vancomycin-resistant *Enterococcus* (VRE) strains over gram-negative bacteria was successfully realized. Similarly, Ding and coworkers actualized the selective visualization of gram-negative bacteria by taking advantage of the conjugation of a far-red/near-infrared emissive AIEgen and two gram-negative bacteria-targeting peptides (polymyxin B) which intrinsically exhibited strong binding affinity to the LPS in the cell wall of gram-negative bacteria [81].

Recently, motivated by the distinctive structures of bacteria, Liu et al. [65] reported a bio-orthogonal fluorescence turn-on probe TPEPA with AIE feature for the specific staining of both gram-positive and gram-negative bacteria. After metabolic labeling by the metabolic precursors based on $_{D}$-alanine ($_{D}$-Ala) and 3-deoxy-$_{D}$-manno-octulosonic acid (Kdo), which could be specifically incorporated into peptidoglycan and LPS on bacteria, respectively, the bacteria would be firstly modified with azide group. Since Kdo is an essential component of LPS that exists only on the surface of gram-negative bacteria, gram-negative bacteria could thus be selectively detected via the click reaction of the azide group with the alkyne groups in TPEPA. For the gram-positive bacteria detection, although $_{D}$-Ala-$N_3$ could be metabolized to the peptidoglycan on the cell wall of both gram-negative and gram-positive bacteria,

**Figure 10.3** (continued)
discrimination. (B) CLSM images indicating the binding behaviors of M1-DPAN towards different microbes including gram-positive bacteria, gram-negative bacteria and fungus. (C) Illustration of interaction model between M1-DPAN and the outer cell walls of gram-positive bacteria, gram-negative bacteria and fungus, respectively. Reproduced with permission: Copyright 2018, Elsevier [78]. (D) CLSM images of *S. epidermidis*, *S. aureus*, *E. coli* and the corresponding mixtures after incubation with AIEgen TTVP for different time periods. Reproduced with permission: Copyright 2020, Elsevier [79].

azide group decorated on the gram-negative bacteria was passively prevented from clicking with TPEPA (1,235 Da) due to the poor permeability of the bacterial outer membrane to probes with a weight larger than 650 Da. Thus, only the gram-positive ones of the $_{D}$-Ala-$N_3$ metabolic labeled bacteria could be selectively lit up by TPEPA through clicking with the azide group, contributing to the specific identification of gram-positive bacteria (Figure 10.4A). The excellent discrimination performance was validated even in the cocultivation system of gram-positive and gram-negative bacteria (Figure 10.4B). Additionally, the good water solubility and AIE feature of TPEPA benefitted the turn-on detection of both gram-positive and gram-negative bacteria pretreated with $_{D}$-Ala-$N_3$ or Kdo-$N_3$, respectively.

## 10.2.3 Selective detection and identification of specific bacteria

Other than for visual imaging and discrimination of gram-positive and gram-negative bacteria, AIEgens can also be designed to selectively identify specific bacteria. In recent years, sensor arrays based on probes with fluorescence characteristics for bacteria identification with the assistance of statistical methods have been extensively explored by virtue of their good sensitivity, versatile signal output, as well as easy-to-read features. Moreover, analytical strategy based on sensor arrays is conducive to high-throughput screening and can be applied to identify multiple analytes, simultaneously. Owing to high quantum yield, good photostability, and satisfactory biocompatibility, AIEgens-based fluorescence arrays have recently been reported to be a powerful tool for bacteria identification. For example, Zhou et al. [82] designed a series of AIE-active probes bearing different positive, negative, or zero charges and used them to develop a six-channel sensor array for the pattern recognition of bacteria. Due to the various charges of AIEgens as well as the different surface structures of diverse bacteria, the interactions between AIE probes and bacteria were disparate, accompanied by differential fluorescent responses. Through the recognition of the fluorescence pattern of pathogens assisted by linear discriminant analysis (LDA), these AIE probes could serve as an “artificial tongue” to rapidly and efficiently distinguish eight kinds of representative bacterial species including three gram-positive bacteria and five gram-negative bacteria.

Tang et al. [83] reported a series of competent sensor arrays based on seven types of TPE derivatives to detect and discriminate pathogens. As shown in Figure 10.5A, these TPE-based AIEgens (TPE-ARs) had a common cationic ammonium group but bore different hydrophobic substitutions, which endowed them with tunable ClogP (*n*-octanol/water partition coefficient) values ranging from 3.426 to 6.071, to guarantee the different multivalent interactions with pathogens. With the ClogP value increasing, the affinity of TPE-ARs toward gram-positive bacteria and fungi gradually weakened, while that toward gram-negative bacteria increased (Figure 10.5B). Relying on the diverse affinity of TPE-ARs with the pathogens, each sensor array could afford a

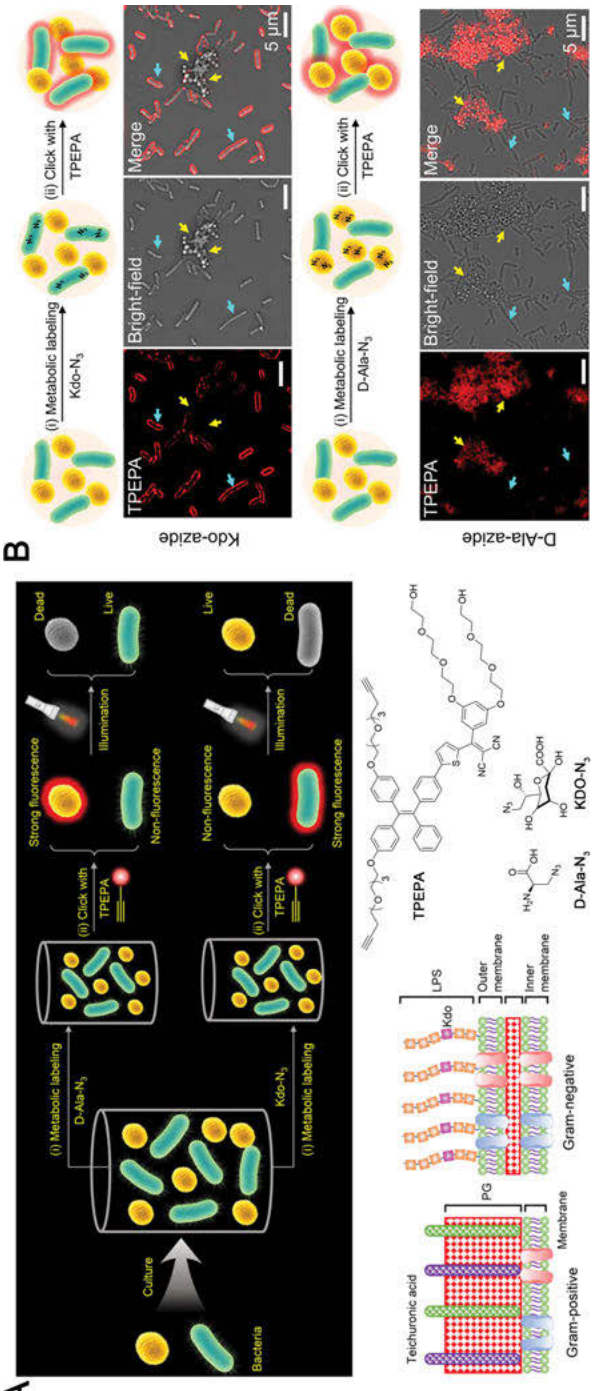


**Figure 10.4:** Discrimination of gram-positive and gram-negative bacteria via metabolic engineering. (A) Schematic illustration of metabolic labeling process for precise discrimination of bacterial pathogens. (B) TPEPA-selective metabolic labeling of gram-negative *E. coli* and gram-positive *S. aureus* after incubation with Kdo-$N_3$ or D-Ala-$N_3$. The blue and yellow arrows represent *E. coli* and *S. aureus*, respectively. Reproduced with permission: Copyright 2020, American Chemical Society [65].

unique fluorescence response pattern for different pathogens (Figure 10.5C). With the aid of special statistical analysis, these sensor arrays could effectively determine seven different pathogens, including gram-positive and gram-negative bacteria as well as their drug-resistant counterparts with nearly 100% accuracy (Figure 10.5D). Moreover, the advantages of simple operation, high throughput screening, and rapid identification procedure offered an opportunity for timely and reliable pathogen detection that could potentially be used for clinical decision-making and trend monitoring of infectious disease. In addition, Tang et al. [84] also built a graphene oxide (GO)-assisted fluorescence sensor array using a range of AIEgens, with various charges for microbial lysate determination. Microbial lysates, instead of living microbes, used as analytical target could eliminate potential health threats to the analyst and offered information about the inside composition of microbes, which was useful in distinguishing different strains of bacteria from the same family.

In an attempt to further improve the specificity of AIE probes to specific bacteria, Tang and coworkers presented a type of AIE-bacteriophage (PAP) bioconjugate (TVP-PAP) by integrating an AIE PS (TVP-S) with PAP through a simple amino-carboxyl reaction (Figure 10.6A) [63]. By virtue of the inherent targeting ability and the preserved infection activity of the bacteriophage as well as the unique AIE feature of TVP-S, TVP-PAP could specifically recognize the specific host bacteria (*P. aeruginosa*) from the bacteria mixture including *A. baumannii* and *P. aeruginosa* through light-up fluorescence response. As shown in Figure 10.6B, all *P. aeruginosa* could be successfully stained with red fluorescence of TVP-S, while no fluorescence was observed from *A. baumannii* after 30 min incubation. The results demonstrated that the introduction of bacteriophage could contribute to the selective detection and identification of specific bacteria by guiding AIEgen to realize discriminative light-up imaging of the host bacteria.

Another novel strategy was put forward, based on bacterial metabolic pathways by Liu et al. [64]. In their contribution, they reported a material platform that exploited bacteria as a template to synthesize polymers with AIE characteristic by copper-catalyzed atom transfer radical polymerization for self-selective theranostics of bacteria. Since the bacteria were able to select the binding monomers and synthesize the polymers on their surface, the obtained templated polymers (TP) with the sequence of monomers that mirrored the components of the bacterial surface exhibited a better capability to recognize the matched bacterial cells. As depicted in Figure 10.6C and D, strong red fluorescence could be clearly seen from the surfaces of all the four types of representative bacteria including *E. coli*, *P. aeruginosa*, BAK085 (a multidrug-resistant *K. pneumoniae* strain), and SGH10 (a hypervirulent *K. pneumoniae* strain with a hypermucoviscous capsule) after incubation with the *E. coli*-TP, *P. aeruginosa*-TP, BAK085-TP, and SGH10-TP, respectively, while very faint fluorescence was observed from only a few number of tested bacteria after incubation with mismatched polymers at the same concentration. The above results

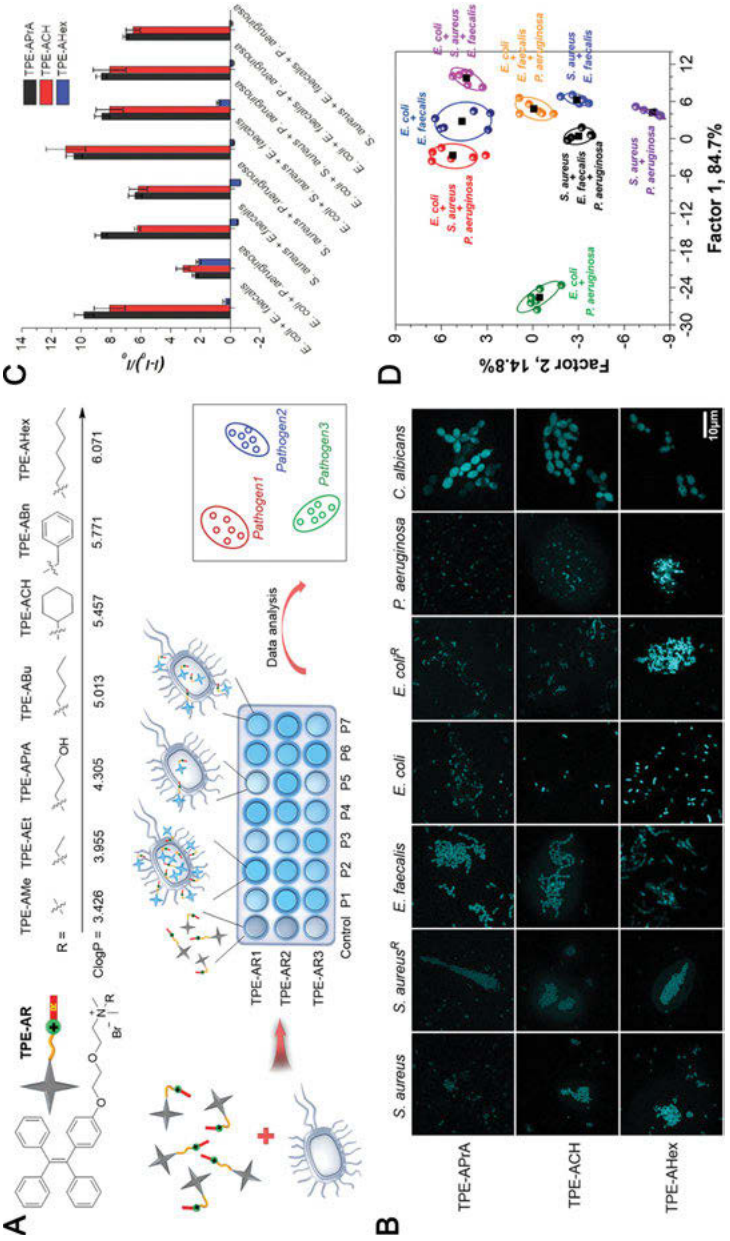


**Figure 10.5:** Bacterial identification via engineering sensor arrays. (A) Structures of TPE-ARs with various ClogP values and schematic illustration of a sensor array composed of three TPE-ARs to achieve bacteria identification. (B) CLSM images of seven pathogens after incubation with three TPE-ARs. (C) Fluorescence response patterns of eight microbe mixtures stained by three TPE-ARs. (D) Canonical score plot for the fluorescence response patterns determined by LDA. Reproduced with permission: Copyright 2018, John Wiley and Sons [83].

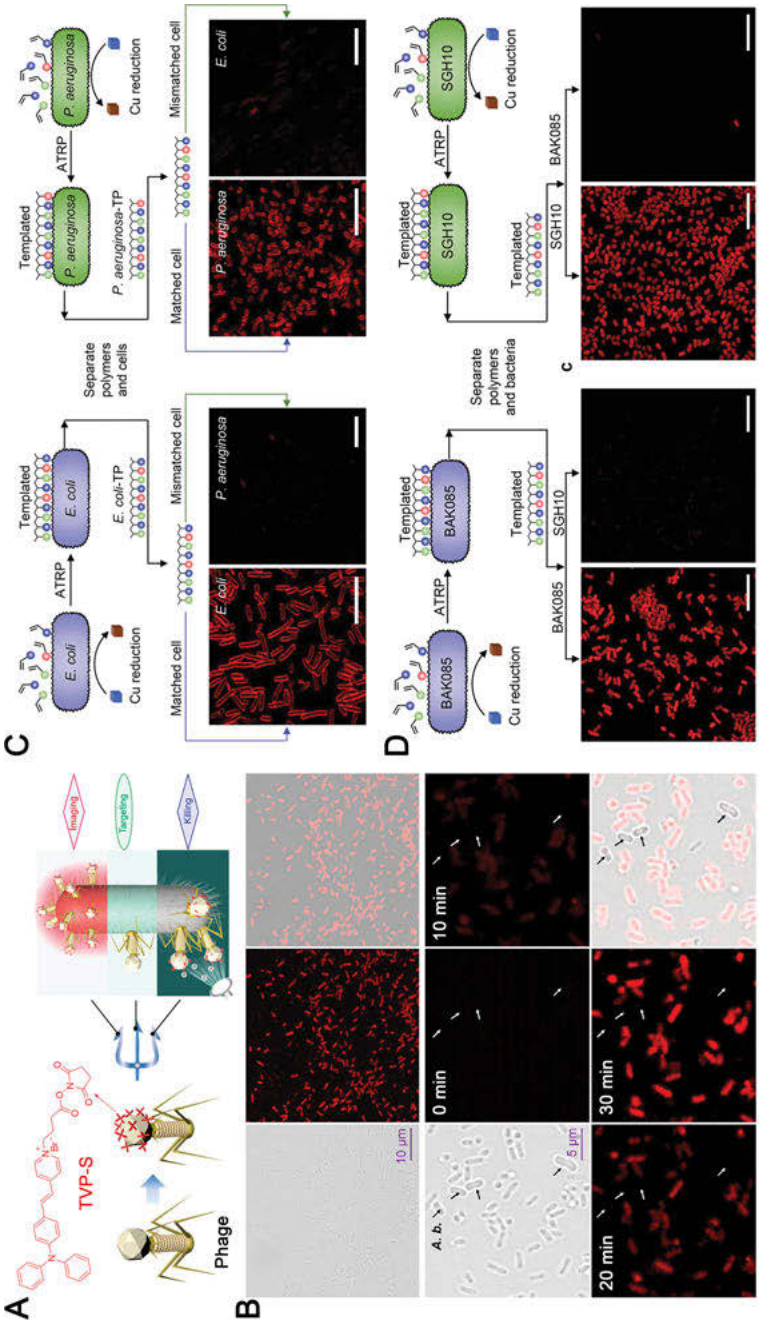


**Figure 10.6:** Specific bacterial detection via biological affinity. (A) Cartoon illumination of TPV-S modified phage (TVP-PAP) for specific bacterial infection, real-time fluorescent tracking, and photodynamic bacterial killing. (B) CLSM images showing targeted recognition of TVP-PAP on

suggested that the bacterium-templated polymers could bind to their target bacteria with high selectivity. This work provided a new platform for the development of adaptive materials for the selective detection and identification of specific bacteria.

## 10.3 AIE probes for antibacterial therapy

Facing the grave challenge that the pathogenic bacteria-related infection posed to human beings in the "post-antibiotic era" as well as the serious situation of rapidly increasing difficulty and cost in producing new antibiotics, researchers had been putting in a lot of efforts to develop new antibacterial strategies based on novel materials, among which AIE materials have been proven to be promising candidates for the construction of antibacterial agents. Integrating the outstanding fluorescence emission with the excellent antibacterial properties, many AIEgen-based imaging-guided antibacterial therapeutic approaches have been explored, and considerable successes in this field have been accordingly achieved, in these years. In this section, important achievements about AIEgen-based bacterial theranostic systems, including imaging-guided photodynamic therapy, imaging-guided chemotherapy, imaging-guided biotherapy, and imaging-guided combination therapy, will be discussed.

### 10.3.1 Imaging-guided photodynamic therapy

Thanks to its noninvasiveness and spatiotemporal controllable properties, light has been widely used for bacterial therapeutics. PDT represents a kind of typical light-excited treatment paradigm for bacterial killing by using ROS produced upon light irradiation [37, 38]. Holding the advantage of aggregation-induced enhancement of ROS generation capacity, AIE probes have achieved great breakthroughs in the imaging-guided photodynamic therapy of pathogenic bacteria.

**Figure 10.6** (continued)
*P. aeruginosa*. Arrow indicated *A. baumannii* without staining by TVP-PAP. Reproduced with permission: Copyright 2020, American Chemical Society [63]. (C) Schematic illustration of the bacteria-mediated polymer synthesis process and CLSM images of *E. coli* and *P. aeruginosa* after incubation with their templated polymers and mismatched polymers. (D) Schematic illustration of the templated polymer grown in the presence of clinical bacterial strain of *K. pneumoniae* (BAK085 and SGH10) and CLSM images of subsequent self-selective binding experiments. Reproduced with permission: Copyright 2020, John Wiley and Sons [64].

#### 10.3.1.1 Imaging-guided PDT against planktonic bacteria

The first example of AIEgen-based imaging-guided PDT against bacteria was reported by Tang et al. in 2015 [85]. Enthused by the efficient photosensitizing property of AIEgens, they designed a new AIE PS (TPE-Bac) for bacterial imaging as well as light-enhanced killing of bacteria. Thanks to the two positively charged ammonium and hydrophobic alkyl chains, the amphiphilic TPE-Bac were able to selectively intercalate into the negatively charged bacterial membrane, resulting in turn-on fluorescence imaging of both gram-positive and gram-negative bacteria quickly as well as changes in bacterial membrane permeability, which is responsible for the dark toxicity of TPE-Bac. Further, TPE-Bac could exert extra phototoxicity to the bacteria upon light irradiation due to the ROS generation. After room-light irradiation for 1 h, the viability of both gram-positive and gram-negative bacteria dropped to less than 1%.

Subsequently, aiming to elevate the photosensitizing property of PSs for higher antibacterial efficiency, various strategies were developed. Typically, dwindling the energy gap ($\Delta E_{S\text{-}T}$) between singlet state ($S_1$) and triplet state ($T_1$) could promote the intersystem crossing (ISC) rate from $S_1$ to $T_1$ and increase the yield of triplet state, representing one of the most widely used tactics [86, 87]. For example, Zhang et al. [88] reported two positively charged AIE PSs, namely TPE-A-Py$^+$ and TPE-Py$^+$. Owing to its lower calculated $\Delta E_{S\text{-}T}$, TPE-A-Py$^+$ with an alkyne group exhibited higher photosensitizing efficiency compared to TPE-Py$^+$ (without alkyne group) when employing $I^-$ as a counter anion. The outstanding ROS generation ability of TPE-A-Py$^+I^-$ endowed it with excellent antibacterial performance against both gram-positive and gram-negative bacteria, under white light irradiation. Similarly, Li et al. [89] reported a sequence of cyanopyridinium (CP)-based cationic AIEgens (CP1-CP5) for multiple bacterial imaging and photodynamic killing of bacteria. By virtue of the benign biocompatibility and cationic nature, these AIEgens could specifically image both gram-positive and gram-negative bacteria via a wash-free procedure. Moreover, under white light irradiation, CP1-CP5 showed obvious structure-dependent singlet oxygen ($^1O_2$) generation ability, with CP4 exhibiting the best ROS generation efficiency, contributed by its extremely low $\Delta E_{S\text{-}T}$ value. Particularly, with a quantum yield of $^1O_2$ determined to be 52% upon light irradiation, CP4 could serve as an ideal PS for photodynamic elimination of bacteria.

PSs featured with typical electron donor (D) and electron acceptor (A) structure have been proved to have reduced $\Delta E_{S\text{-}T}$ value resulting from the complete separation between the occupied molecular orbital (HOMO) and the lowest unoccupied molecular orbital (LUMO) [86, 87]. Tang and coworkers synthesized a series of AIEgens with orderly enhanced D-A interaction (Figure 10.7A) [90]. Due to their inherent positive charge and moderate ClogP value, four of these AIEgens were capable of selectively staining gram-positive bacteria with high specificity. Moreover, the strong D-A effect and the introduction of heteroatoms resulted in smaller $\Delta E_{S\text{-}T}$ and

efficient ISC, supporting the high ROS generation efficiency of TTPy and MeOTTPy. As the best candidate, TTPy with balanced NIR emission, suitable ClogP value, and high ROS production efficacy could stain gram-positive bacteria and eliminate *S. aureus* via PDT strategy, with high specificity. This AIEgen-based PDT system successfully suppressed the *S. aureus*-caused wound infection of rats. Additionally, Tang's group designed another D-A structured AIE-active PS, 4TPA-BQ, exhibiting extremely high $^1O_2$ generation efficiency of 97.8%, which was much higher than that of the commonly used Chlorin E6 (Ce6) and Rose Bengal (RB) in aggregate state, thanks to its sufficiently small $\Delta E_{S\text{-}T}$ (0.03 eV) and the aggregation-induced ROS generation effect (Figure 10.7B) [91]. Particularly, 4TPA-BQ could realize time-dependent imaging and PDT for bacteria over mammalian cells through collaboration of the electrostatic interactions and hydrophobic effect between 4TPA-BQ and targets. As depicted in Figure 10.7C, bright orange fluorescence was observed on both gram-positive *S. epidermidis* and gram-negative *E. coli* within 15 min staining. Only by extending the incubation time to 12 h, 4TPA-BQ could effectively accumulate into cancer cells, leaving normal cells unstained. This time-dependent property realized selective targeting of bacteria with low toxicity to normal cells. By virtue of its high $^1O_2$ generation efficiency, 4TPA-BQ exhibited prominent bacteria-eliminating capability toward both *S. epidermidis* and *E. coli*, and even toward ampicillin-resistant *E. coli*, with excellent biocompatibility in a short timescale.

Good selectivity to the infection site and activatable photosensitization of high-performance PSs could significantly facilitate the efficient photodynamic bacterial ablation as well as benign biosafety of an ideal theranostic system. Tang and coworkers reported a bacterial infection-activatable nanotheranostic system (33%IRTP NPs) relying on the self-assembly of amphiphilic polymer (TBD-PEG) derived from an efficient AIE PS (TBD) as well as $ONOO^-$ and $ClO^-$-responsive NIR dye (IR786S) for in vivo imaging-guided photodynamic bacterial ablation (Figure 10.7D) [92]. Because of the Förster resonance energy transfer (FRET) process between TBD and IR786S inside the nanoparticles (NPs), the fluorescence emission as well as the $^1O_2$ generation of TBD-PEG were significantly quenched, and 33%IRTP NPs exhibited bright NIR emission of IR786S in normal tissues. Once the NPs arrived at the bacteria infection sites, IR786S could be decomposed by the overexpressed $ONOO^-$ or $ClO^-$, accompanied by the inhibition of FRET process. By this time, the red emission and $^1O_2$ generation ability of TBD-PEG were recovered, facilitating the detection of bacterial infection and photodynamic bacterial ablation. Considering the negligible in vivo dark toxicity, the activatable 33%IRTP NPs exhibited great potential in imaging-guided photodynamic antibacterial applications.

Except for the organic synthetic molecules, AIE-active natural agents can also be engineered as theranostic agents for image-guided photodynamic antibacterial therapy. In 2019, Tang et al. [93] investigated the application of a naturally occurring AIEgen, Berberine Chloride (BBR), as a fluorescence imaging and PDT agent against both cancer cells and bacteria (Figure 10.7E). Compared to many organic

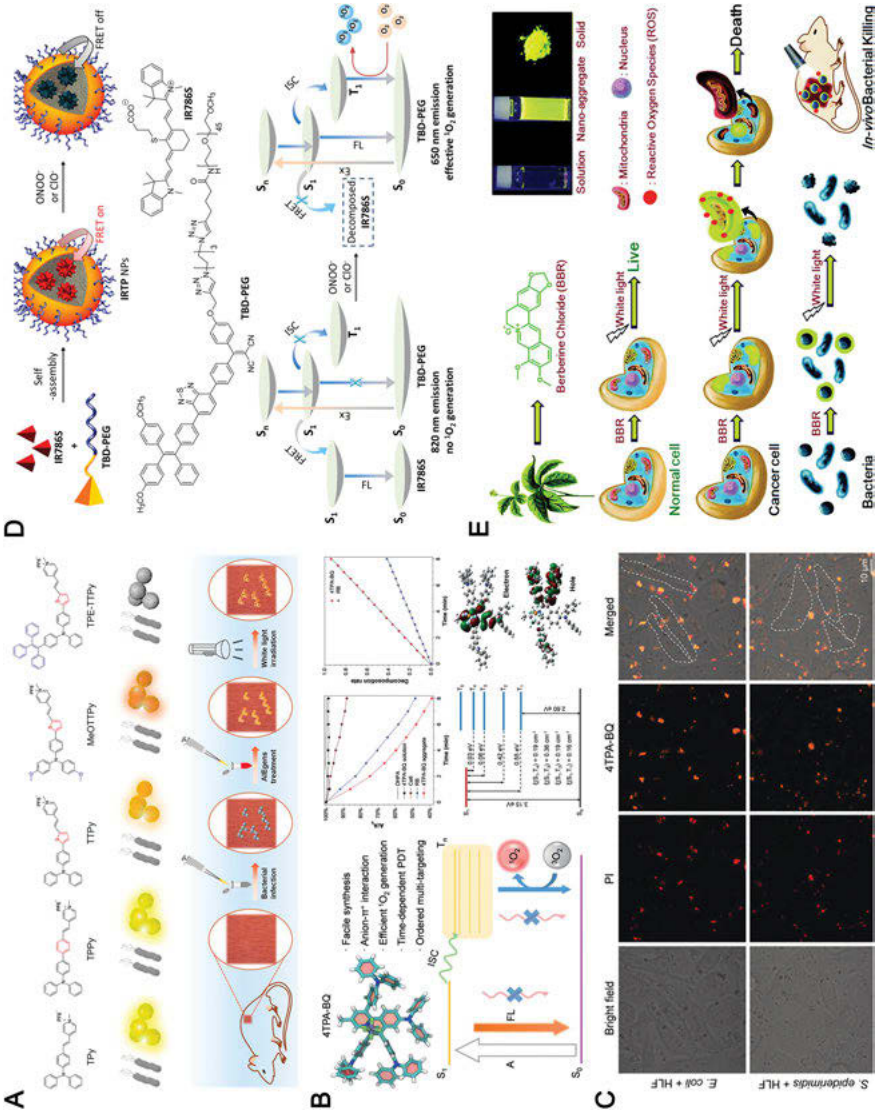


**Figure 10.7:** Imaging-guided photodynamic ablation of planktonic bacteria. (A) Molecular structures of AIE photosensitizers and cartoon illustration of their imaging-guided antibacterial applications. Reproduced with permission: Copyright 2019, American Chemical Society [90]. (B) Schematic illustration, experimental evaluation and theoretical calculation elucidations of the high ROS generation ability of 4TPA-BQ. (C) Selective bacterial imaging and killing of 4TPA-BQ over normal cells. Reproduced with permission: Copyright 2019, John Wiley and Sons [91]. (D) Preparation procedure and working mechanism of 33% IRTP NPs. Reproduced with permission: Copyright 2018, American Chemical Society [92]. (E) The chemical structure of natural AIEgen BBR and schematic illustration of their theranostic applications. Reproduced with permission: Copyright 2019, Royal Society of Chemistry [93].

AIE PSs, BBR was water-soluble, biocompatible and green to environment, which enabled it to be a remarkable candidate for cell and bacterial imaging and treatment. This positively charged BBR was able to successfully discriminate and efficiently ablate gram-positive bacteria over gram-negative ones via fluorescence imaging and PDT pathway. Both in vitro and in vivo studies demonstrated that BBR exhibited excellent photo-inactivation efficiency against *S. aureus*-related infection.

#### 10.3.1.2 Imaging-guided PDT against multidrug resistant (MDR) bacteria

In recent days, along with the continuing emergence of antibiotic-resistant pathogenic bacteria, some bacteria have evolved into MDR strains that show resistance to more than one of the most conventional antibiotics, resulting in a rapidly escalating threat to human health worldwide. PDT, with the unique antibiosis mechanism of ROS-mediated bacterial killing represents a promising approach to combat MDR bacteria. Thus, AIE PSs with highly efficient ROS generation ability could serve as a powerful weapon in this battle.

By introducing a fluorine substituent, Li's group developed a planar AIEgen (DMA-AB-F) with evident AIE effect and enhanced ROS generation for combating MDR bacterial infection [94]. The $\Delta E_{S\text{-}T}$ of DMA-AB-F trimer was small enough to trigger the ISC process, resulting in efficient ROS generation. DMA-AB-F could stain both MDR *E. coli* and MRSA with intense fluorescence driven by electrostatic and hydrophobic interactions. As shown in Figure 10.8A, DMA-AB-F showed profound inhibition effect against both MDR strains, under light exposure. The cell wall of both MDR bacteria were obviously destroyed only in the group of PS plus light, while nearly intact morphology and bacteria cell walls were observed in other test groups. As an effective AIE PS for PDT, DMA-AB-F successfully eliminated the MDR *E. coli*-caused infection, in vivo. Another efficient AIE PS (TBD-anchor) exhibiting high inhibition capacity on MDR bacteria was designed and synthesized by Liu et al. (Figure 10.8B) [95]. The $^1O_2$ quantum yield of TBD-anchor was demonstrated to be 48%. Bearing three quaternary ammonium salt tails, TBD-anchor could anchor on the surface of bacterial membranes through both hydrophobic and electrostatic interactions, which contributed to the photodynamic elimination of both gram-positive and gram-negative bacteria, under light irradiation. Particularly, TBD-anchor displayed great potential in eliminating drug-resistant bacteria. More than 99.8% of MRSA could be killed by only 0.8 μM TBD-anchor, under a low dose of light irradiation (25 mW $cm^{-2}$, 10 min).

In an attempt to actualize the systemic delivery of AIE PSs into the infection site and realize high specific elimination of MDR bacterial infection in vivo, Liu et al. [67] developed a novel two-step strategy for specific in vivo imaging of MDR bacteria, based on the metabolic labeling technique for in situ imaging-guided antibacterial therapy. By utilizing the $H_2O_2$-responsive MIL-100 (Fe) NPs as the nanocarrier, the

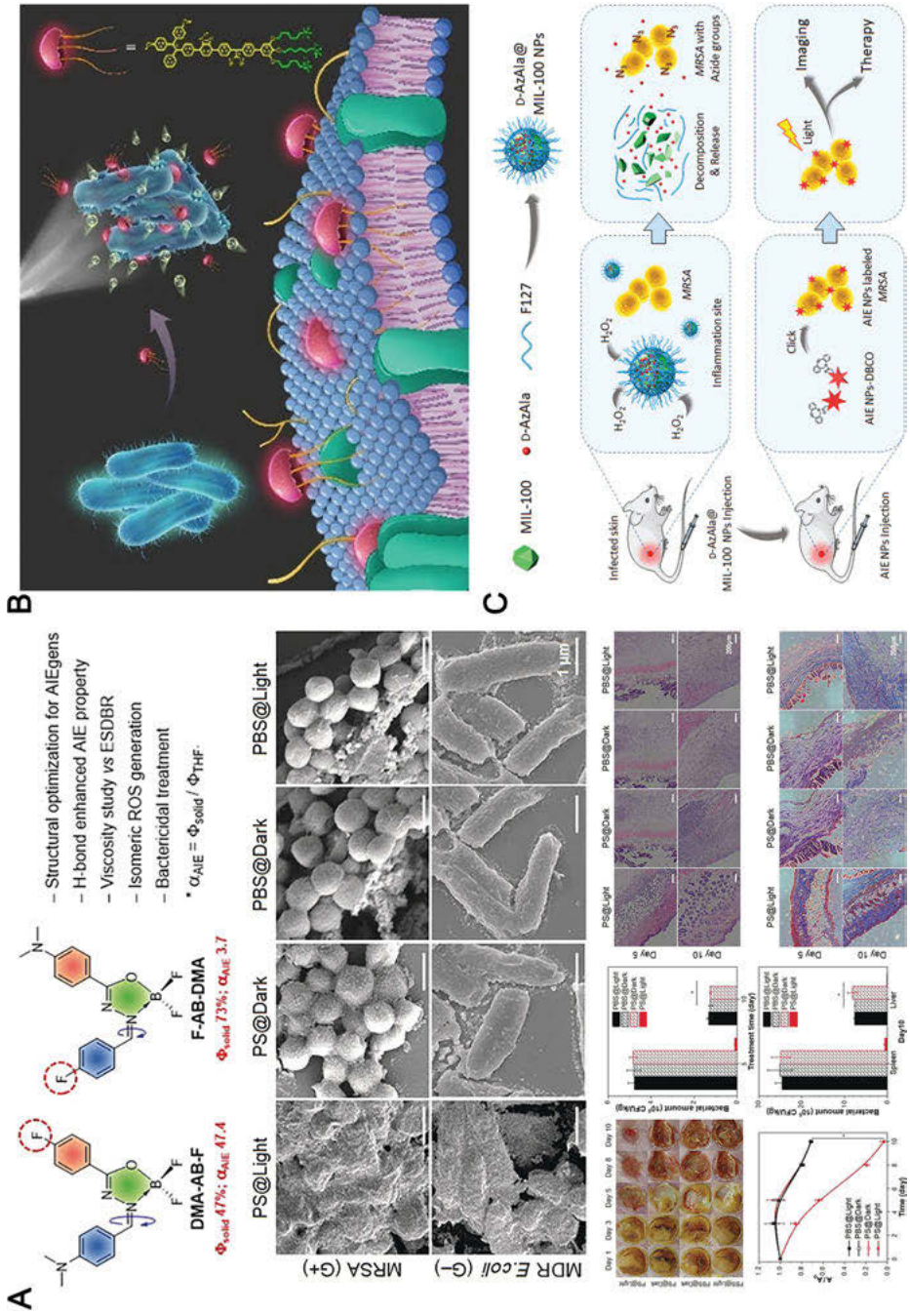


**Figure 10.8:** Imaging-guided photodynamic ablation of MDR bacteria. (A) Design strategy of fluoro-substituted planar AIEgens and the *in vitro* and *in vivo* bactericidal performance. Reproduced with

metabolic precursor 3-azido-D-alanine ($_D$-AzAla) encapsulated inside the MIL-100 (Fe) NPs could be selectively delivered to the high $H_2O_2$ inflammatory environment, released from the nanoparticles due to the degradation of MIL-100 (Fe) NPs, and then specifically integrated into the cell walls of bacteria, leaving the bacterial cell wall modified with unnatural azide groups. Subsequently, the dibenzocyclooctyne (DBCO)-modified ultra small nanoparticles based on AIE PS (US-TPETM) could gradually accumulate onto the azide group-labeled bacteria through in vivo click chemistry (Figure 10.8C). The intense fluorescence and $^1O_2$ generation ability of the AIE NPs under light irradiation guaranteed the good performance of this system in imaging-guided photodynamic antibacterial therapy. After successive treatments of d-AzAla@MIL-100 (Fe) NPs and US-TPETM NPs followed by white light irradiation, the number of MRSA in the infected tissue decreased significantly, and the inflammation was successfully cured.

#### 10.3.1.3 Imaging-guided PDT against intracellular bacteria

Serving as the front line of defense against pathogen-associated infection, phagocytes can attack the invading bacterial pathogens through the process of recognition, ingurgitation, and digestion [96]. However, some bacteria are capable of surviving inside the cells, which makes the infected cells "Trojan Horses," hampers the detection of bacteria, and protects them from antibiotic treatment and immune elimination [97, 98]. What's worse, the infected cells could increase the dissemination of pathogens from the initial infection sites. Thus, it is of great importance to exploit new approaches for the detection and elimination of intracellular bacteria.

On the basis of its good selectivity to gram-positive bacteria over gram-negative ones, Tang et al. [99] further utilized TTVP as an effective imaging and PDT agent for simultaneous detection and photo-inactivation of intracellular gram-positive bacteria (Figure 10.9A). TTVP could act as not only the fluorescence probe to monitor the phagocytosis process of *S. aureus* toward macrophages, but also as a profound PS to effectively eliminate cell-entrapped *S. aureus* by PDT pathway, under light irradiation. Liu et al. [100] constructed an AIE bioprobe (PyTPE-CRP) through the conjunction of an AIE molecule (PyTPE) and a caspase-1(casp-1)-responsive peptide linker (NEAYVHDAP) for fluorescence detection and photodynamic elimination

**Figure 10.8** (continued)
permission: Copyright 2020, John Wiley and Sons [94]. (B) Molecular structure and cartoon illustration of TBD-anchor for bacteria ablation. Reproduced with permission: Copyright 2020, John Wiley and Sons [95]. (C) Schematic illustration of the proposed strategy of bacterial diagnosis and elimination by the $H_2O_2$-responsive $_D$-AzAla@MIL-100 NPs assisted *in vivo* metabolic labeling of bacteria. Reproduced with permission: Copyright 2018, John Wiley and Sons [67].

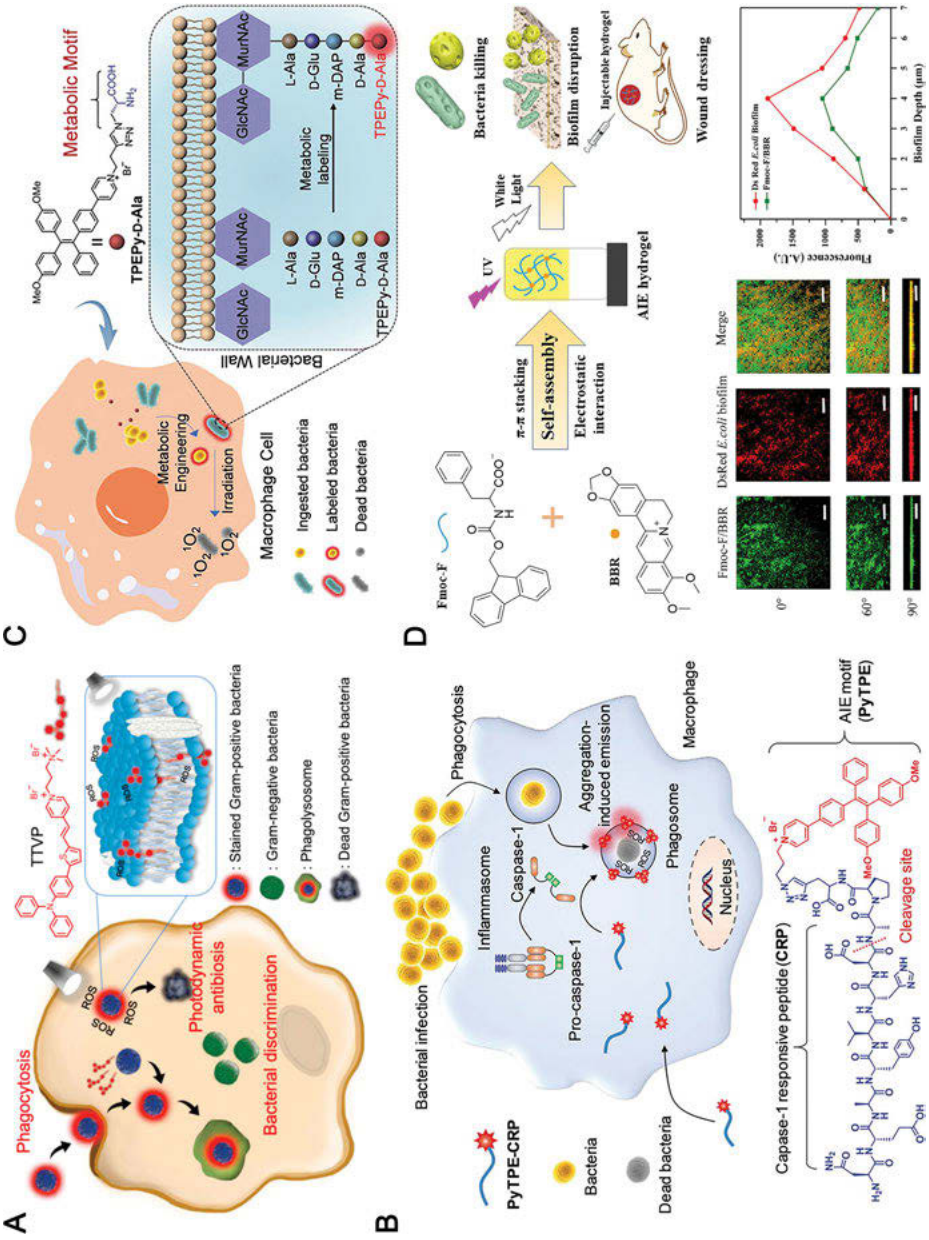


**Figure 10.9:** Imaging-guided photodynamic ablation of intracellular bacteria and bacterial biofilms. (A) Chemical structure of TTVP and schematic illustration of TTVP for phagocytosis monitoring and macrophage-engulfed gram-positive bacteria ablating. Reproduced with permission: Copyright 2020, Elsevier [99]. (B) Schematic illustration of macrophage-mediated intracellular bacteria detection and elimination using PyTPE-CRP. Reproduced with permission: Copyright 2019, John

of intracellular bacteria (Figure 10.9B). Owing to its good water solubility, the PyTPE-CRP was almost nonfluorescent in aqueous staining buffer. Upon entering the bacteria-infected macrophages, the peptide linker of PyTPE-CRP could be specifically cleaved by the casp-1 activated by proteolytic cleavage due to the bacterial infection, leading to self-assembly of the resultant residues and accumulation on the bacteria-contained phagosomes. Thanks to the typical AIE feature and aggregation-induced ROS generation effect, the fluorescence of PyTPE and ROS generation capacity could be accordingly lighted up, upon the aggregates formation inside the bacteria-infected macrophages, which endowed PyTPE-CRP with great potential for selective and sensitive detection of bacterial infection via fluorescence turn-on feature and efficient intracellular bacteria eradication through PDT.

One of the important issues in the elimination of intracellular bacteria is the minimization of the cytotoxicity of antibacterial agents toward macrophages. Generally, this goal can be achieved by employing ingenious tactics with high specificity to bacteria over the host cells. Motivated by the metabolic labeling technology, Liu et al. [96] developed a metabolic probe (TPEPy-$_D$-Ala) by integrating an AIE PS (TPEPy) with $_D$-alanine for fluorescence detection and in situ photodynamic killing of intracellular bacteria (Figure 10.9C). The existence of hydrophilic $_D$-Ala and pyridinium resulted in the weak emission of TPEPy-D-Ala in aqueous media. Boosted fluorescence was observed, once TPEPy-D-Ala metabolically incorporated into peptidoglycan, allowing real-time imaging of bacteria in live macrophages. Subsequent light irradiation realized efficient ablation of the labeled intracellular bacteria via in-situ $^1O_2$ generation. Since host mammalian cells do not require $_D$-amino acids for biosynthesis, TPEPy-$_D$-Ala could only specifically incorporate into peptidoglycan, but not the organelles in the macrophage. Hence, TPEPy-$_D$-Ala could effectively ablate the intracellular MRSA through photodynamic killing and affect macrophage cells only negligibly.

#### 10.3.1.4 Imaging-guided PDT against bacterial biofilms

Generally, bacteria tend to adhere on the surface of substrates and organize themselves into multicellular communities known as biofilms. Shielded by the self-synthesized extracellular matrix (EPS), bacteria can significantly withstand the attack of the immune response and undermine the efficiency of antibiotics [101, 102]. The inability to

**Figure 10.9** (continued)
Wiley and Sons [100]. (C) The schematic illustration of intracellular bacteria labeling and inactivation by TPEPy-$_D$-Ala. Reproduced with permission: Copyright 2020, John Wiley and Sons [96]. (D) Schematic illustration of the preparation and application of amino acid/berberine hydrogels with enhanced photodynamic antibacterial and anti-biofilm activity. Reproduced with permission: Copyright 2020, Elsevier [106].

completely ablate bacterial biofilms often results in intractable and chronic infections [103]. It has been reported that two-thirds of the chronic infections in humans are associated with bacterial biofilms, posing serious threat to public health [104]. Thus, there is pressing need to develop new antibacterial strategies to counter the threat of bacterial biofilms to human beings.

In 2020, Zhong et al. [106] designed a novel and biocompatible hybrid hydrogel with AIE behavior by virtue of the supramolecular self-assembly of *N*-(9-fluorenylmethoxycarbonyl)-$_L$-phenylalanine (Fmoc-F) and the natural PS (BBR) (Figure 10.9D). Driven by the intermolecular electrostatic attraction and π–π stacking, BBR could self-assemble into small-sized nanoparticles, which could be further dispersed throughout the hydrogel matrix. Owing to its typical AIE behavior and good $^1O_2$ generation upon white light illumination, this hydrogel could efficiently eliminate both *E. coli* and *S. aureus* via PDT mechanism. Moreover, the Fmoc-F/BBR hydrogel was demonstrated to be able to penetrate into the bacterial biofilms, and effective elimination was observed with about 59.3% of *E. coli* biofilms and 85.8% of *S. aureus* biofilms being eradicated, respectively, after light irradiation for 1 h. Ding et al. [107] employed a positively charged AIE PS, DPA-SCP, with strong $^1O_2$ generation ability as an antibacterial agent to explore the antibacterial application in infected root canal (RC). DPA-SCP could selectively bind to *E. faecalis* and exhibited photodynamic antibacterial effect against planktonic *E. faecalis* under light irradiation. Furthermore, DPA-SCP was proved to exhibit powerful germicidal potency toward *E. faecalis* biofilms. An equivalent antibiofilm potency to that resulted by 1% NaOCl was achieved via DPA-SCP-mediated PDT, leaving no significant change and chemical corrosion in the dentin surface.

## 10.3.2 Imaging-guided chemotherapy

Aside from PDT-based antibacterial therapy, AIE probes have been intensively studied as direct antimicrobial agents for imaging-guided chemotherapy of bacterial infection. The positive charges of AIE probes were generally designed not only for bacteria detection relying on the contact with the negatively charged bacterial surface driven by electrostatic interaction, but could also endow AIE probes with antibacterial capacity, because the cationic units of AIE probes could insert into the bacterial cell wall and may cause cell wall lysis and leakage of intracellular substances, thus leading to the bacterial death [108]. Yan et al. [109] designed and synthesized a sequence of AIE-based imidazolium-type ionic liquids (ILs). Bearing the cation-anion structure, these AIE-based ILs showed antibacterial activities against both *E. coli* and *S. aureus*. Besides, thanks to the AIE feature, the ILs could stain the dead bacteria after killing, with the fluorescence intensity varying along with the bacteria concentration. Yan's group also reported a kind of imidazolium-type poly(ionic liquids) (PIL)s, namely PIL-TPExBr$_{1-x}$ ($x$ = 0.9, 0.3, 0.1), through anion exchange of

bromide ($Br^-$) in poly(3-butyl-1-vinylimidazolium bromide) (PIL-Br) with a 3-(4-(1,2,2-triphenylvinyl)phenoxy)propane-1-sulfonate ($TPESO_3^-$) for bacterial killing and dead bacterial imaging (Figure 10.10A) [110]. The introduction of $TPESO_3^-$ endowed the PILs with the AIE characteristic. Through regulating the ratio of $Br^-/TPESO_3^-$, diverse fluorescence intensities and antibacterial property could be obtained. Moreover, the PILs were demonstrated to be able to effectively inhibit biofilm growth. Aiming to realize the real-time detection of bacterial infection as well as concomitant bacteria killing, Ren et al. [108] designed thermo- and pH-responsive poly(vinyl alcohol) derivatives (PVA-TPE) consisting of the iconic AIE-active core TPE and quaternary ammonium moieties (Figure 10.10B). At pH 7.4, PVA-TPE could selectively image and kill gram-positive bacteria as the positively charged quaternary ammonium could guide the PVA-TPE to interact and insert into the negatively charged cell wall of gram-positive bacteria, rather than that of gram-negative bacteria due to the different bacterial wall structures, leading to the death of bacteria. Nevertheless, an enhanced broad-spectrum antimicrobial activity against both gram-negative and gram-positive bacteria was observed at acidic environment (pH 5.5), attributable to the higher protonation degree, a condition in which the number of positive charges on PVA-TPE increases significantly, facilitating the interactions towards cell walls of gram-negative bacteria and, thereby, enhancing the antibacterial property. This work represented the first example of pH-switchable integrated system for "monitoring and killing of bacteria."

Studies have shown that branched antibacterial polymers could provide rich cations causing greater disturbance of the bacterial membrane via electrostatic interactions [111]; meanwhile the formation of cationic nanostructures is able to increase the local cation density of the antibacterial polymers and improve their antibacterial properties [112]. Inspired by this fact, Wang et al. [113] constructed a type of novel nanoengineered peptide-grafted hyperbranched polymers (NPGHPs) by ring-opening polymerization of α-amino acid *N*-carboxyanhydrides on the periphery of the H-PAMAM (Figure 10.10C). Without additional introduction of fluorophore, these NPGHPs could intrinsically exhibit favorable AIE property, which fundamentally contributed to the concentration monitoring of *E. coli*, the exploration of interaction between NPGHPs and bacteria, as well as the visualization of antibacterial process via lighting up bacteria. As expected, the NPGHPs could penetrate the bacteria membrane as well as cause cell rupture and apoptosis, due to the significantly enhanced ionic interactions between the bacterial membranes and the charge-concentrated NPGHPs resulting from its nanoengineered hyperbranched architecture. Additionally, NPGHPs showed outstanding selectivity toxicity toward bacteria over mammalian cells, providing promising potential in the field of in vivo theranostics of infectious bacterial diseases.

One major issue for traditional chemotherapy is the nonspecific and premature release of antibacterial agents. The exploitation of a bacteria-targeted and image-guided chemotherapy platform can realize boosted antibacterial effect. Gao et al. [114] designed

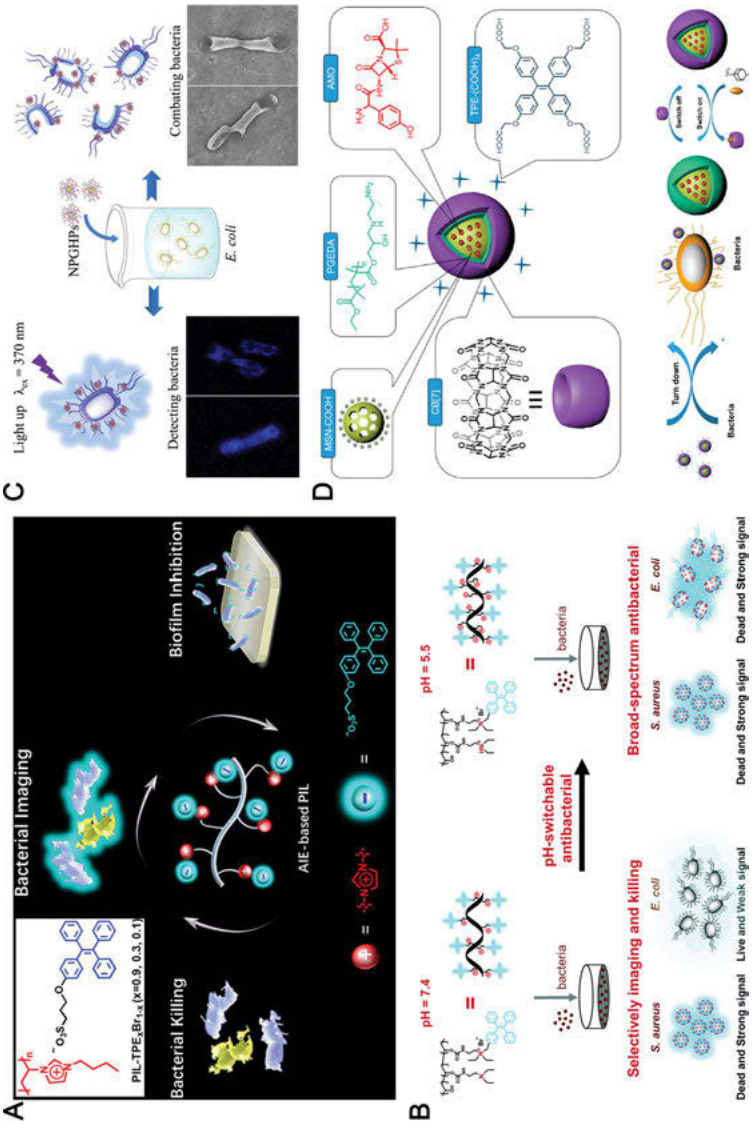


**Figure 10.10:** Imaging-guided chemotherapy. (A) Molecular structure of PIL-TPExBr$_{1-x}$ ($x$ = 0.9, 0.3, 0.1) and schematic illustration of the selective bacterial killing and imaging as well as biofilm inhibition. Reproduced with permission: Copyright 2019, American Chemical Society [110]. (B) Schematic illustration of pH-switchable bacterial imaging and killing of PVA-TPE. Reproduced with permission: Copyright 2020, Royal Society of Chemistry [108]. (C) Schematic illustration of theranostics integrated detecting bacteria and combating bacteria based on NPGHPs. Reproduced with permission: Copyright 2018, American Chemical Society [113]. (D) Schematic illustration of MSN-PEGDA-CB[7]-TPE and its possible bacterial detection and inhibition mechanism. Reproduced with permission: Copyright 2017, American Chemical Society [114].

a multifunctional nanoparticle (MSN-PGEDA-CB [7]-TPE) by the layer-by-layer (LbL) self-assembly technique for bacterial detection and controllable antibacterial therapy, which was composed of mesoporous silica nanoparticles (MSNs), amoxicillin (AMO), EDA-modified polyglycerol methacrylate (PGEDA), cucurbit [7] uril (CB [7]), and TPE-$(COOH)_4$ (Figure 10.10D). The fluorescent emission of TPE-$(COOH)_4$ was significantly weakened in the presence of bacteria, because the competitive binding between the anionic bacterial cell wall and cationic PGEDA layer could reduce or break the interactions between the PGEDA layer and the TPE-$(COOH)_4$ layer, leading to the dissolution of TPE aggregates. The detection limit of the nanoparticles was calculated as $2.5 \times 10^6$ and $5 \times 10^6$ CFU/mL for *E. coli* and *S. aureus*, respectively. What's more, the addition of adamantaneamine (AD) would result in the formation of more stable AD⊂CB [7] complex and liberation of PGEDA due to the competitive replacement, consequently leading to the release of AMO and much higher antibacterial ability. This study successfully provided a way to control the activity of antimicrobial through the realization of its on-demand release and opened up an alternative new avenue for bacterial detection and eradication.

### 10.3.3 Imaging-guided biotherapy

As one of the major components of mammalian innate immune system, antimicrobial peptides (AMPs) possess intrinsic defense capability against bacterial infections [115, 116]. Due to their broad-spectrum antibacterial properties and low possibility to induce bacterial resistance, AMPs have attracted much attention as alternatives to conventional antibiotics [117]. By virtue of the excellent fluorescence property of AIE probes, several imaging-guided AMP-based systems consisting of AIEgens were constructed to realize the visualization of AMP-based bacterial killing as well as the exploration of antibacterial mechanism. For example, Xu et al. [118] developed a TPE-containing AMP (TPE-AMP) by decorating the synthetic AMP (CysHHC10) with TPE derivatives to study the bacterial membrane interactions as well as the antibacterial actions of AMPs. TPE-AMP exhibited a better antibacterial performance against gram-positive *S. aureus* and *S. epidermidis* than gram-negative *E. coli* and *P. aeruginosa*, which can be ascribed to its higher affinity with the gram-positive bacterial membranes. Since the introduction of hydrophobic TPE derivatives could probably change the insertion of CysHHC10 into bacterial membranes, the minimum inhibitory concentration (MIC) values of TPE-AMP against these bacteria were enhanced compared to that of CysHHC10. TPE-AMP exhibited very weak fluorescence emission in the staining buffer, while enhanced blue fluorescence was observed at microscopic level once the bacteria was added. The light-up characteristics of TPE-AMP could be utilized to visualize the interactions between TPE-AMP and bacteria via confocal microscopy. Furthermore, TPE-AMP showed negligible in vivo toxicity, providing it the potential for visualizing the location of AMPs in the infection sites of the animal model. Tang et al. [119] constructed an AIE-active probe, AMP-2HBT, by

conjugation of the AMP (HHC36) and AIEgen (HBT) for the real-time monitoring of the AMPs' bactericidal process (Figure 10.11A). AMP-2HBT showed excellent bactericidal activities against both gram-positive *S. aureus* and gram-negative *E. coli*. Importantly, the similar antibacterial performance of AMP-2HBT with HHC36 peptide suggested that the decoration of AIEgens did not compromise the bactericidal activity of HHC36 peptide (Figure 10.11B). The fluorescence light-up characteristic of AMP-2HBT in the presence of bacteria could be utilized to visualize the antibacterial process of AMPs. As revealed by the super-resolution fluorescence microscopy (STORM), transmission electron microscope (TEM), and scanning electron microscope (SEM) images in Figure 10.11C, the membrane structure of bacteria was obviously destroyed by

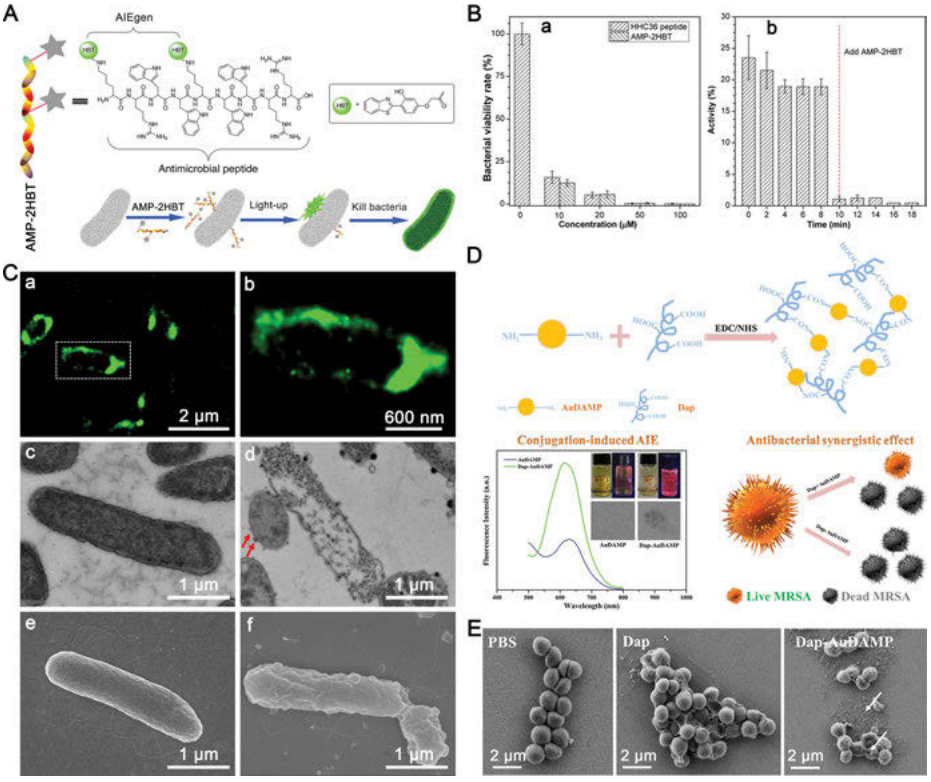


**Figure 10.11:** Imaging-guided biotherapy. (A) Schematic illustration of AIE-active antimicrobial peptide AMP-2HBT for light-up fluorescence imaging and effective killing on bacteria. (B) (a) Antimicrobial ability of HHC36 peptide and AMP-2HBT as well as (b) time-dependent motility of *E. coli* before and after the adding of AMP-2HBT. (C) (a,b) Super-resolution fluorescence images of *E. coli* after treatment with AMP-2HBT; TEM and SEM images of *E. coli* before (c,e) and after (d,f) treatment with AMP-2HBT. Reproduced with permission: Copyright 2018, American Chemical Society [119]. (D) Schematic illustration of the formation of Dap-AuDAMP NCs, conjugation-enhanced AIE effect, and synergistic bactericidal efficacy. (E) SEM images of bacteria treated with PBS, Dap, and Dap-AuDAMP. Reproduced with permission: Copyright 2019, Elsevier [120].

the high-density aggregation of HHC36 peptide on bacteria membrane, resulting in the flowing out of inner components and subsequent bacterial death.

To improve the bactericidal efficiency of AMPs, Wang et al. [120] reported a novel antibacterial strategy that combined daptomycin (Dap, an acyclic lipopeptide AMP) with 4,6-diamino-2-mercaptopyrimidine (DAMP)-anchored gold nanoclusters (Au NCs) (Figure 11D and E). Owing to the AIE effect of Au NCs, the conjugated Dap-AuDAMP exhibited significantly enhanced fluorescence. The conjugated structure was capable of effectively killing 100% of the MRSA cells after a co-incubation of 1 h, while the relative viability of MRSA in the Dap-treated and AuDAMP-treated group was 37.5% and 41.7%, respectively, indicating the enhanced synergistic antibacterial effect of the Dap-AuDAMP. It was reasonable to speculate that the damaged bacteria membrane disrupted by Dap motivated the antibacterial hybrid to enter into the bacteria and resulted in more serious oxidative damage at the subcellular level caused by the aggregated Au NCs.

### 10.3.4 Imaging-guided combination therapy

In contrast to the single therapy modality, the combination therapy consisting of multiple antibacterial modalities is effective in achieving strikingly enhanced therapeutic potency with reduced bactericide dose and fewer side effects. Thanks to the structural diversity of AIEgens as well as the features of easy modification, multifunctional AIE probes have been developed for the combination therapy of bacterial infection. In 2018, Tang et al. [121] synthesized a multifunctional antibacterial agent, TriPE-NT, by conjugation of an AIE unit, triphenylethylene (TriPE) with naphthalimide triazole (NT). The TriPE unit rendered TriPE-NT as a fluorescence agent to monitor the interactions with bacteria, owing to its AIE feature. Meanwhile, since azoles-substituted naphthalimide has been proven to be an important class of antimicrobial agents [122], the NT unit was designed to serve as an antibacterial group favoring the dark toxicity of TriPE-NT to the bacteria. Moreover, TriPE-NT was demonstrated to show effective ROS generation capability under white light irradiation. The in vitro and in vivo experiments suggested that this multifunctional AIE probe exhibited excellent performances in the imaging-guided chemo-photodynamic combined therapy of bacterial infection (Figure 10.12A and 10.12B). For example, TriPE-NT could effectively kill both gram-positive bacteria (*S. aureus, S. epidermidis*) and gram-negative bacteria (*E. coli, K. pneumoniae*), and even their MDR strains. The outstanding bactericidal efficiency of TriPE-NT could be ascribed to the combination of the antibacterial ability of NT as well as ROS generated by TriPE-NT.

Aside from the multifunctional AIE probes, some novel strategies involving the combination of AIE PSs with antibiotics or photothermal agents have emerged recently. As a proper example, Huang et al. [123] developed an imaging-guided chemo-

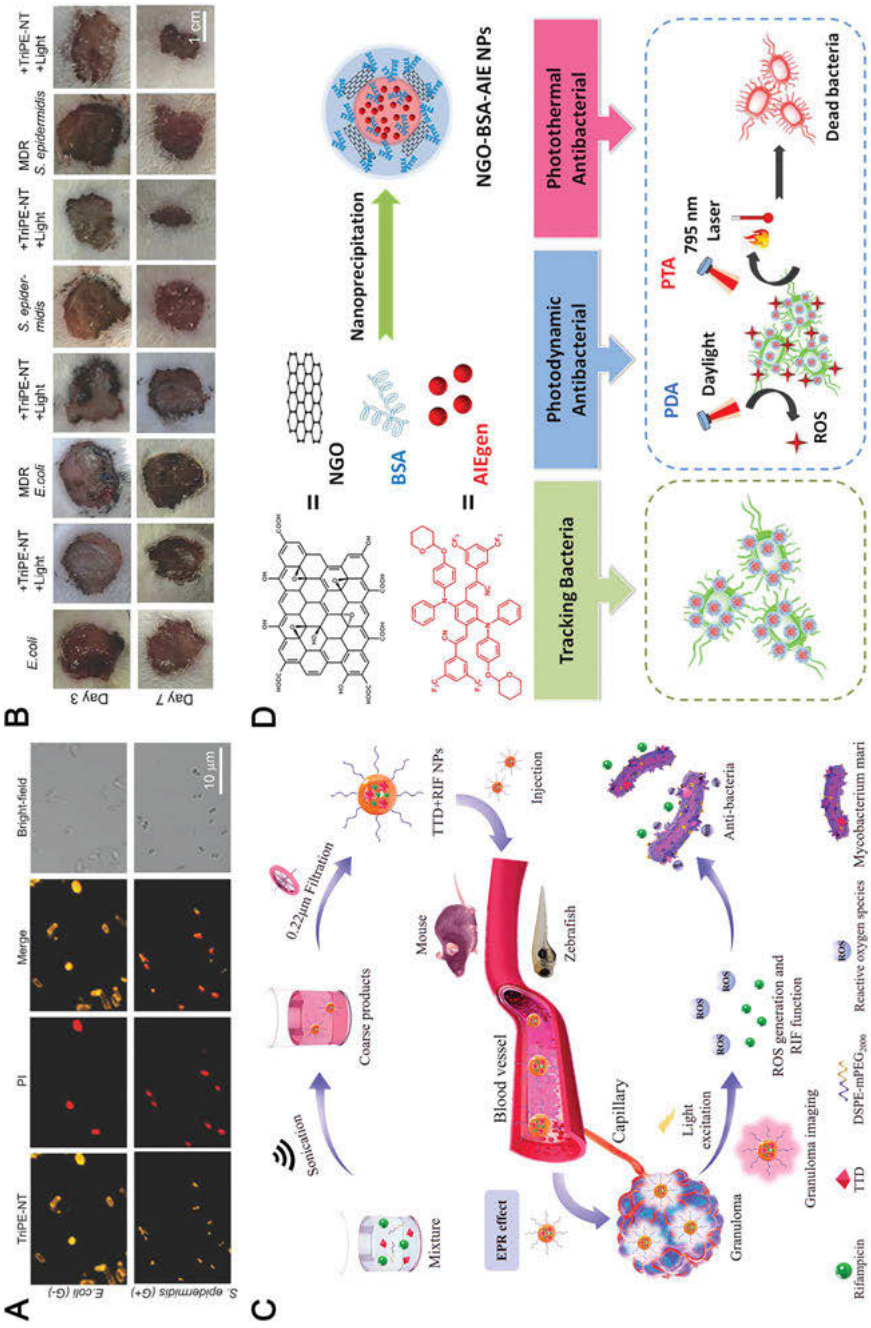


**Figure 10.12:** Imaging-guided combination therapy. (A) Fluorescent and bright-field images of *E. coli* and *S. epidermidis* incubated with TriPE-NT (orange) and propidium iodide (PI) (red) for 10 min. (B) Photographs of wounds treated by TriPE-NT plus white-light irradiation after bacterial

photodynamic combined therapeutic system by employing a kind of broad-spectrum antibiotic, rifampicin (RIF), and a type of AIE PS, 2-(2,6-bis((*E*)-4-(phenyl(4′-(1,2,2-triphenylvinyl)-[1,1′-biphenyl]-4-yl)amino)styryl)-4H-pyran-4-ylidene) malononitrile (TTD), for the targeted therapy of tuberculosis (TB) caused by Mycobacterium tuberculosis (*M.tb*) (Figure 10.12C). RIF and TTD were firstly fabricated into TTD+RIF NPs through a modified bottom-up approach, using DSPE-$mPEG_{2000}$ as encapsulation matrix. Thanks to the EPR effect, the TTD+RIF NPs could accumulate in the granulomas and emit fluorescent signals even at the early stage of infection, favoring the diagnosis and imaging-guided therapy of TB. Additionally, TTD could generate ROS efficiently, and the loaded RIF could be released, which jointly benefits the eradication of infection, endowing the TTD+RIF NPs with high bactericidal efficacy against both *M.tb* and its MDR strains, under white light illumination. Furthermore, targeted therapy of TB could also be achieved relying on this synergistic effect of light-controlled production of ROS and accurate delivery of RIF.

Photothermal therapy (PTT) excited by NIR radiation has attracted great attention for pathogen elimination recently [124]. This method utilizes photothermal agents to convert light energy to heat, inducing rise in local temperature to inactivate the bacteria. Thus, the synergistic antibacterial system combined with photodynamic and photothermal effects, was a promising approach. Gao's group [125] developed a ternary nanoparticle (NGO-BSA-AIE NPs) based on nanographene oxide (NGO) and a type of AIE PS, combining both functions together (Figure 10.12D). Taking advantage of the moderate photothermal property of NGO under NIR laser irradiation and the efficient ROS generation of AIE PS under daylight irradiation, NGO-BSA-AIE NPs exhibited superiorly antibacterial effect (more than 99%) against both amoxicillin (AMO)-resistant *E. coli* and *S. aureus*, when compared to single photothermal or photodynamic therapy. More importantly, the AIE feature of AIEgen made NGO-BSA-AIE NPs an ideal fluorescent tracer for better antibacterial therapy. Therefore, this system provided a new platform for imaging-guided collaborative dual-mode phototherapy of bacterial infection. Additionally, another synergistic antibacterial strategy involving photodynamic and photothermal therapy was reported by Yuan et al. [126] They developed hybrid nanoparticle DDNPs by employing the conjugated polymer, DPPT as photothermal agent and AIEgen DPATP-CN as photosensitizer. On the basis of both the efficient photothermal conversion ability and outstanding ROS production capability of DDNPs, efficient killing performances on both gram-negative and gram-positive bacteria were

**Figure 10.12** (continued)
infection for different time periods. Reproduced with permission: Copyright 2018, John Wiley and Sons [121]. (C) Schematic illustration of preparation process and targeted theranostic applications of TTD+RIF NPs on tuberculosis. Reproduced with permission: Copyright 2020, American Chemical Society [123]. (D) Schematic illustration of the preparation process of NGO-BSA-AIE NPs and the applications in bacterial tracking and dual-mode antibacterial phototherapies. Reproduced with permission: Copyright 2019, BioMed Central [125].

successfully achieved, demonstrating that this combination antibacterial strategy held greater potential than any one of the single therapy modalities.

## 10.4 Conclusion and perspective

As enumerated here, intensive studies have been performed on AIE probes for bacterial detection and antibacterial applications. Owing to the unique AIE feature and outstanding optical properties, such as intensive fluorescence in aggregated state, real-time and in-situ responsive emission, excellent photostability, etc., AIE probes could selectively light up bacteria in a fluorescence turn-on manner, with no additional washing steps. On the basis of the structural features of different bacterial membranes and the characterized RIM mechanism of AIE probes, smart strategies based on AIE probes have been designed and synergistically integrated for the specific identification and classification of various bacteria. On the other hand, thanks to the structure diversity and the flexibility in molecular designing, AIE probes could be easily endowed with desired dark toxicity or/and phototoxicity in addition to the AIE feature, facilitating the imaging-guided chemotherapy or/and phototherapy of bacterial infection. Besides, by integrating other therapeutic materials, such as AMPs and photothermal agents, imaging-guided biotherapy as well as imaging-guided combination therapy based on AIE probes could be successfully achieved.

Although remarkable progress of AIE probes in bacterial detection and antibacterial applications has been made, there are still some challenging but exciting research directions that could be considered. Firstly, PTT based on AIE-active photothermal agents has rarely been applied for antibacterial application up to now. In view of the outstanding performance of AIE-active photothermal agents in tumor eradication, it is reasonable to anticipate the future perspectives of AIE probes on photothermal antibacterial therapy. Moreover, most of the present combination therapeutic systems are a combination of various components with individual functions. Although effective to some extent, the further application of these systems is usually hindered by their reduced reproducibility and uncertain pharmacokinetics as a result of the complicated composition. Thus, antibacterial system with one-for-all features based on single multifunctional AIE probe bearing high reproducibility and uniformity is highly desirable for the purpose of practical/clinical application. Additionally, in order to slow down the development of antibiotic resistance, upgrade the targeting ability of antibacterial therapy, and reduce the systemic toxicity, more efforts should be devoted to constructing stimuli-responsive AIE theranostics. We hope that this chapter can provide a comprehensive overview of AIE probes in bacterial detection and antibacterial applications as well as meaningful inspiration for the further development of AIEgen-based systems for bacterial theranostics in clinical practice.

# References

[1] Microbiology by numbers, Nat Rev Microbiol, 2011, 9, 628–628. https://doi.org/10.1038/nrmicro2644
[2] Ivnitski D, Abdel-Hamid I, Atanasov P, Wilkins E, Biosensors for detection of pathogenic bacteria, Biosens Bioelectron, 1999, 14, 599–624.
[3] Blaser M, Antibiotic overuse: Stop the killing of beneficial bacteria, Nature, 2011, 476, 393–394.
[4] Nicholson JK, Holmes E, Kinross J, et al., Host-gut microbiota metabolic interactions, Science, 2012, 336, 1262–1267.
[5] Tremaroli V, Bäckhed F, Functional interactions between the gut microbiota and host metabolism, Nature, 2012, 489, 242–249.
[6] Wolfe ND, Dunavan CP, Diamond J, Origins of major human infectious diseases, Nature, 2007, 447, 279–283.
[7] Singh SR, Krishnamurthy NB, Mathew BB, A review on recent diseases caused by microbes, J Appl Environ Microbiol, 2014, 2, 106–115.
[8] Domagk G, Ein beitrag zur chemotherapie der bakteriellen infektionen, Dtsch Med Wochenschr, 1935, 61, 250–253.
[9] Fleming A, On the antibacterial action of cultures of a penicillium, with special reference to their use in the isolation of B. influenzae, B World Health Organ, 2001, 79, 780–790.
[10] Levy SB, The challenge of antibiotic resistance, Sci Am, 1998, 278, 46–53.
[11] Levy SB, Marshall B, Antibacterial resistance worldwide: Causes, challenges and responses, Nat Med, 2004, 10, S122–9.
[12] WHO Scientific Working Group. Antimicrobial resistance. B World Health Organ 1983;61: 383–394.
[13] Watanabe T, Infective heredity of multiple drug resistance in bacteria, Bacteriol Rev, 1963, 27, 87–115.
[14] Garland M, Loscher S, Bogyo M, Chemical strategies to target bacterial virulence, Chem Rev, 2017, 117, 4422–4461.
[15] Reisner BS, Woods GL, Times to detection of bacteria and yeasts in BACTEC 9240 blood culture bottles, J Clin Microbiol, 1999, 37, 2024–2026.
[16] Wang J, Wang X, Li Y, et al., A novel, universal and sensitive lateral-flow based method for the detection of multiple bacterial contamination in platelet concentrations, Anal Sci, 2012, 28, 237–241.
[17] Hu Y, Liu J, Xia D, Chen S, Simultaneous analysis of foodborne pathogenic bacteria by an oligonucleotide microarray assay, J Basic Microbiol, 2012, 52, 27–34.
[18] Martinez-Garcia M, Swan BK, Poulton NJ, et al., High-throughput single-cell sequencing identifies photoheterotrophs and chemoautotrophs in freshwater bacterioplankton, ISME J, 2012, 6, 113–123.
[19] Hossain SM, Ozimok C, Sicard C, et al., Multiplexed paper test strip for quantitative bacterial detection, Anal Bioanal Chem, 2012, 403, 1567–1576.
[20] Lantz AW, Bisha B, Tong MY, Nelson RE, Brehm-Stecher BF, Armstrong DW, Rapid identification of Candida albicans in blood by combined capillary electrophoresis and fluorescence in situ hybridization, Electrophoresis, 2010, 31, 2849–2853.
[21] Krader P, Emerson D, Identification of archaea and some extremophilic bacteria using matrix-assisted laser desorption/ionization time-of-flight (MALDI-TOF) mass spectrometry, Extremophiles, 2004, 8, 259–268.

[22] Mello C, Ribeiro D, Novaes F, Poppi RJ, Rapid differentiation among bacteria that cause gastroenteritis by use of low-resolution Raman spectroscopy and PLS discriminant analysis, Anal Bioanal Chem, 2005, 383, 701–706.
[23] Kobayashi H, Ogawa M, Alford R, Choyke PL, Urano Y, New strategies for fluorescent probe design in medical diagnostic imaging, Chem Rev, 2010, 110, 2620–2640.
[24] Baker M, Whole-animal imaging: The whole picture, Nature, 2010, 463, 977–980.
[25] Zhao Z, Zhang H, Lam JWY, Tang BZ, Aggregation-induced emission: New vistas at the aggregate level, Angew Chem Int Ed, 2020, 59, 9888–9907.
[26] Zhang H, Zhao Z, McGonigal PR, et al., Clusterization-triggered emission: Uncommon luminescence from common materials, Mater Today, 2020, 32, 275–292.
[27] Luo J, Xie Z, Lam JWY, et al., Aggregation-induced emission of 1-methyl-1,2,3,4,5-pentaphenylsilole, Chem Commun (Camb), 2001, 1740–1741.
[28] Hong Y, Lam JWY, Tang BZ, Aggregation-induced emission, Chem Soc Rev, 2011, 40, 5361–5388.
[29] Kang M, Zhang Z, Song N, et al., Aggregation-enhanced theranostics: AIE sparkles in biomedical field, Aggregate, 2020, 1, 80–106.
[30] Qi J, Ou H, Liu Q, Ding D, Gathering brings strength: How organic aggregates boost disease phototheranostics, Aggregate, 2021, 2, 95–113.
[31] Mao D, Liu B, Perspective biology-oriented design strategies of AIE theranostic orobes, Matter, 2021, 4, 350–376.
[32] Wang D, Tang BZ, Aggregation-induced emission luminogens for activity-based sensing, Acc Chem Res, 2019, 52, 2559–2570.
[33] Kang M, Gu X, Kwok RTK, et al., A near-infrared AIEgen for specific imaging of lipid droplets, Chem Commun (Camb), 2016, 52, 5957–5960.
[34] Zhang Z, Xu W, Kang M, et al., An all-round athlete on the track of phototheranostics: Subtly regulating the balance between radiative and nonradiative decays for multimodal imaging-guided synergistic therapy, Adv Mater, 2020, 32, e2003210.
[35] Li Y, Cai Z, Liu S, et al., Design of AIEgens for near-infrared IIb imaging through structural modulation at molecular and morphological levels, Nat Commun, 2020, 11, 1255–1264.
[36] He X, Xiong LH, Zhao Z, et al., AIE-based theranostic systems for detection and killing of pathogens, Theranostics, 2019, 9, 3223–3248.
[37] Bai H, He W, Chau J, et al., AIEgens for microbial detection and antimicrobial therapy, Biomaterials, 2021, 268, 120598.
[38] He W, Zheng Z, Bai H, et al., A biocompatible dual-AIEgen system without spectral overlap for quantitation of microbial viability and monitoring of biofilm formation, Mater Horiz, 2021, 8, 1816–1824.
[39] Zhou C, Jiang M, Du J, et al., One stone, three birds: One AIEgen with three colors for fast differentiation of three pathogens, Chem Sci, 2020, 11, 4730–4740.
[40] Soncin M, Fabris C, Fantetti L, Dei D, Roncucci G, Jori G, Photodynamic therapy with a cationic phthalocyanine: A new antimicrobial approach to infectious diseases, Int J Antimicrob Ag, 2004, 242, S205–6.
[41] Wainwright M, Maisch T, Nonell S, et al., Photoantimicrobials-are we afraid of the light? Lancet Infect Dis, 2017, 17, e49–55.
[42] Almeida A, Faustino MA, Tomé JP, Photodynamic inactivation of bacteria: Finding the effective targets, Future Med Chem, 2015, 7, 1221–1224.
[43] Maisch T, A new strategy to destroy antibiotic resistant microorganisms: Antimicrobial photodynamic treatment, Mini Rev Med Chem, 2009, 9, 974–983.
[44] Park SY, Baik HJ, Oh YT, Oh KT, Youn YS, Lee ES, A smart polysaccharide/drug conjugate for photodynamic therapy, Angew Chem Int Ed, 2011, 50, 1644–1647.

[45] Feng G, Liu B, Aggregation-induced emission (AIE) dots: Emerging theranostic nanolights, Acc Chem Res, 2018, 51, 1404–1414.
[46] Ni J, Wang Y, Zhang H, Sun JZ, Tang BZ, Aggregation-induced generation of reactive oxygen species: Mechanism and photosensitizer construction, Molecules, 2021, 26, 268–289.
[47] Kim S, Zhou Y, Tohnai N, et al., Aggregation-induced singlet oxygen generation: Functional fluorophore and anthrylphenylene dyad self-assemblies, Chem-Eur J, 2018, 24, 636–645.
[48] Liu S, Zhang H, Li Y, et al., Strategies to enhance the photosensitization: Polymerization and the donor-acceptor even-odd Effect, Angew Chem Int Ed, 2018, 57, 15189–15193.
[49] Hu R, Deng Q, Tang Q, et al., More is less: Creation of pathogenic microbe-related theranostic oriented AIEgens, Biomaterials, 2021, 271, 120725.
[50] Shi X, Sung SHP, Chau JHC, et al., Killing G(+) or G(–) bacteria? The important role of molecular charge in AIE-active photosensitizers, Small Methods, 2020, 4, 2000046.
[51] Kang M, Kwok RTK, Wang J, et al., A multifunctional luminogen with aggregation-induced emission characteristics for selective imaging and photodynamic killing of both cancer cells and Gram-positive bacteria, J Mater Chem B, 2018, 6, 3894–3903.
[52] Liu X, Li M, Han T, et al., In situ generation of azonia-containing polyelectrolytes for luminescent photopatterning and superbug killing, J Am Chem Soc, 2019, 141, 11259–11268.
[53] Li Y, Liu F, Zhang J, et al., Efficient killing of multidrug-resistant internalized bacteria by AIEgens in vivo, Adv Sci, 2021, 8, 2001750.
[54] Xie S, Manuguri S, Proietti G, et al., Design and synthesis of theranostic antibiotic nanodrugs that display enhanced antibacterial activity and luminescence, Proc Natl Acad Sci U S A, 2017, 114, 8464–8469.
[55] Chen S, Chen Q, Li Q, et al., Biodegradable synthetic antimicrobial with aggregation-induced emissive luminogens for temporal antibacterial activity and facile bacteria detection, Chem Mater, 2018, 30, 1782–1790.
[56] Chen M, He J, Xie S, et al., Intracellular bacteria destruction via traceable enzymes-responsive release and deferoxamine-mediated ingestion of antibiotics, J Control Release, 2020, 322, 326–336.
[57] Chen J, Shi X, Zhu Y, et al., On-demand storage and release of antimicrobial peptides using Pandora's box-like nanotubes gated with a bacterial infection-responsive polymer, Theranostics, 2020, 10, 109–122.
[58] Panigrahi A, Are VN, Jain S, Nayak D, Giri S, Sarma TK, Cationic organic nanoaggregates as AIE luminogens for wash-free imaging of bacteria and broad-spectrum antimicrobial application, ACS Appl Mater Interfaces, 2020, 12, 5389–5402.
[59] Jiang M, Gu X, Kwok RTK, et al., Multifunctional AIEgens: Ready synthesis, tunable emission, mechanochromism, mitochondrial, and bacterial imaging, Adv Funct Mater, 2018, 28, 1704589.
[60] Sayed SM, Xu KF, Jia HR, et al., Naphthalimide-based multifunctional AIEgens: Selective, fast, and wash-free fluorescence tracking and identification of Gram-positive bacteria, Anal Chim Acta, 2021, 1146, 41–52.
[61] Schmidt B, Sankaran S, Stegemann L, Strassert CA, Jonkheijm P, Voskuhl J, Agglutination of bacteria using polyvalent nanoparticles of aggregation-induced emissive thiophthalonitrile dyes, J Mater Chem B, 2016, 4, 4732–4738.
[62] Guo Y, Zhao C, Liu Y, et al., A novel fluorescence method for the rapid and effective detection of Listeria monocytogenes using aptamer-conjugated magnetic nanoparticles and aggregation-induced emission dots, Analyst, 2020, 145, 3857–3863.
[63] He X, Yang Y, Guo Y, et al., Phage-guided targeting, discriminative imaging, and synergistic killing of bacteria by AIE bioconjugates, J Am Chem Soc, 2020, 142, 3959–3969.

[64] Qi G, Hu F, Kenry, et al, Bacterium-templated polymer for self-selective ablation of multidrug-resistant bacteria, Adv Funct Mater, 2020, 30, 2001338.
[65] Wu M, Qi G, Liu X, Duan Y, Liu J, Liu B, Bio-orthogonal AIEgen for specific discrimination and elimination of bacterial pathogens via metabolic engineering, Chem Mater, 2020, 32, 858–865.
[66] Mao D, Hu F, Kenry, et al, One-step in vivo metabolic labeling as a theranostic approach for overcoming drug-resistant bacterial infections, Mater Horiz, 2020, 7, 1138–1143.
[67] Mao D, Hu F, Kenry, et al, Metal-organic-framework-assisted in vivo bacterial metabolic labeling and precise antibacterial therapy, Adv Mater, 2018, 30, e1706831.
[68] Wang Y, Corbitt TS, Jett SD, et al., Direct visualization of bactericidal action of cationic conjugated polyelectrolytes and oligomers, Langmuir, 2012, 28, 65–70.
[69] Zhang L, Jiao L, Zhong J, Guan W, Lu C, Lighting up the interactions between bacteria and surfactants with aggregation-induced emission characteristics, Mater Chem Front, 2017, 1, 1829–1835.
[70] Zhou T, Hu R, Wang L, et al., An AIE-active conjugated polymer with high ROS-generation ability and biocompatibility for efficient photodynamic therapy of bacterial infections, Angew Chem Int Ed, 2020, 59, 9952–9956.
[71] Gao M, Hu Q, Feng G, et al., A multifunctional probe with aggregation-induced emission characteristics for selective fluorescence imaging and photodynamic killing of bacteria over mammalian cells, Adv Healthc Mater, 2015, 4, 659–663.
[72] Feng G, Zhang CJ, Lu X, Liu B, Zinc(II)-tetradentate-coordinated probe with aggregation-induced emission characteristics for selective imaging and photoinactivation of bacteria, ACS Omega, 2017, 2, 546–553.
[73] Lang K, Chin JW, Cellular incorporation of unnatural amino acids and bioorthogonal labeling of proteins, Chem Rev, 2014, 114, 4764–4806.
[74] Kenry, Liu B, Bio-orthogonal click chemistry for in vivo bioimaging, Trends Chem, 2019, 1, 763–778.
[75] Navarre WW, Schneewind O, Surface proteins of gram-positive bacteria and mechanisms of their targeting to the cell wall envelope, Microbiol Mol Biol Rev, 1999, 63, 174–229.
[76] Beveridge TJ, Structures of Gram-negative cell walls and their derived membrane vesicles, J Bacteriol, 1999, 181, 4725–4733.
[77] Simpson BW, Trent MS, Pushing the envelope: LPS modifications and their consequences, Nat Rev Microbiol, 2019, 17, 403–416.
[78] Hu R, Zhou F, Zhou T, et al., Specific discrimination of gram-positive bacteria and direct visualization of its infection towards mammalian cells by a DPAN-based AIEgen, Biomaterials, 2018, 187, 47–54.
[79] Lee MMS, Xu W, Zheng L, et al., Ultrafast discrimination of Gram-positive bacteria and highly efficient photodynamic antibacterial therapy using near-infrared photosensitizer with aggregation-induced emission characteristics, Biomaterials, 2020, 230, 119582.
[80] Feng G, Yuan Y, Fang H, et al., A light-up probe with aggregation-induced emission characteristics (AIE) for selective imaging, naked-eye detection and photodynamic killing of Gram-positive bacteria, Chem Commun (Camb), 2015, 51, 12490–12493.
[81] Bao P, Li C, Ou H, et al., A peptide-based aggregation-induced emission bioprobe for selective detection and photodynamic killing of Gram-negative bacteria, Biomater Sci, 2021, 9, 437–442.
[82] Liu GJ, Tian SN, Li CY, Xing GW, Zhou L, Aggregation-induced emission materials with different electric charges as an artificial tongue: Design, construction, and assembly with various pathogenic bacteria for effective bacterial imaging and discrimination, ACS Appl Mater Interfaces, 2017, 9, 28331–28338.

[83] Zhou C, Xu W, Zhang P, et al., Engineering sensor arrays using aggregation-induced emission luminogens for pathogen identification, Adv Funct Mater, 2018, 29, 1805986.
[84] Shen J, Hu R, Zhou T, et al., Fluorescent sensor array for highly efficient microbial lysate identification through competitive interactions, ACS Sens, 2018, 3, 2218–2222.
[85] Zhao E, Chen Y, Wang H, et al., Light-enhanced bacterial killing and wash-free imaging based on AIE fluorogen, ACS Appl Mater Interfaces, 2015, 7, 7180–7188.
[86] Hu F, Xu S, Liu B, Photosensitizers with aggregation-induced emission: Materials and biomedical applications, Adv Mater, 2018, 30, 1801350.
[87] Zhao J, Wu W, Sun J, Guo S, Triplet photosensitizers: From molecular design to applications, Chem Soc Rev, 2013, 42, 5323–5351.
[88] You X, Ma H, Wang Y, et al., Pyridinium-substituted tetraphenylethyleneentailing alkyne moiety: Enhancement of photosensitizing efficiency and antimicrobial activity, Chem Asian J, 2017, 12, 1013–1019.
[89] Zhao N, Li P, Zhuang J, et al., Aggregation-induced emission luminogens with the capability of wide color tuning, mitochondrial and bacterial imaging, and photodynamic anticancer and antibacterial therapy, ACS Appl Mater Interfaces, 2019, 11, 11227–11237.
[90] Kang M, Zhou C, Wu S, et al., Evaluation of structure-function relationships of aggregation-induced emission luminogens for simultaneous dual applications of specific discrimination and efficient photodynamic killing of Gram-positive bacteria, J Am Chem Soc, 2019, 141, 16781–16789.
[91] Li Q, Li Y, Min T, et al., Time-dependent photodynamic therapy for multiple targets: A highly efficient AIE-active photosensitizer for selective bacterial elimination and cancer cell ablation, Angew Chem Int Ed, 2020, 59, 9470–9477.
[92] Wu W, Mao D, Cai X, et al., $ONOO^-$ and $ClO^-$ responsive organic nanoparticles for specific in vivo image-guided photodynamic bacterial ablation, Chem Mater, 2018, 30, 3867–3873.
[93] Lee MMS, Zheng L, Yu B, et al., A highly efficient and AIE-active theranostic agent from natural herbs, Mater Chem Front, 2019, 3, 1454–1461.
[94] Ni JS, Min T, Li Y, et al., Planar AIEgens with enhanced solid-state luminescence and ROS generation for multidrug-resistant bacteria treatment, Angew Chem Int Ed, 2020, 59, 10179–10185.
[95] Chen H, Li S, Wu M, et al., Membrane-anchoring photosensitizer with aggregation-induced emission characteristics for combating multidrug-resistant bacteria, Angew Chem Int Ed, 2020, 59, 632–636.
[96] Hu F, Qi G, Kenry, et al, Visualization and in situ ablation of intracellular bacterial pathogens through metabolic labeling, Angew Chem Int Ed, 2020, 59, 9288–9292.
[97] Guo H, Callaway JB, Ting JP, Inflammasomes: Mechanism of action, role in disease, and therapeutics, Nat Med, 2015, 21, 677–687.
[98] Mahamed D, Boulle M, Ganga Y, et al., Intracellular growth of Mycobacterium tuberculosis after macrophage cell death leads to serial killing of host cells, Elife, 2017, 6, e22028.
[99] Lee MMS, Yan D, Chau J, et al., Highly efficient phototheranostics of macrophage-engulfed Gram-positive bacteria using a NIR luminogen with aggregation-induced emission characteristics, Biomaterials, 2020, 261, 120340.
[100] Qi G, Hu F, Kenry SL, Wu M, An LB, AIEgen-peptide conjugate as a phototheranostic agent for phagosome-entrapped bacteria, Angew Chem Int Ed, 2019, 58, 16229–16235.
[101] Olson ME, Ceri H, Morck DW, Buret AG, Read RR, Biofilm bacteria: Formation and comparative susceptibility to antibiotics, Can J Vet Res, 2002, 66, 86–92.
[102] Flemming H, Wingender J, The biofilm matrix, Nat Rev Microbiol, 2010, 8, 623–633.
[103] Bjarnsholt T, The role of bacterial biofilms in chronic infections, APMIS Suppl, 2013, 121, 1–51.

[104] Guo S, Huang Q, Chen Y, et al., Synthesis and bioactivity of guanidinium-functionalized Pillar [5]arene as a biofilm disruptor, Angew Chem Int Ed, 2021, 60, 618–623.
[105] Wolfmeier H, Pletzer D, Mansour SC, Hancock R, New perspectives in biofilm eradication, ACS Infect Dis, 2018, 4, 93–106.
[106] Xie Y, Zhang Y, Liu X, et al., Aggregation-induced emission-active amino acid/berberine hydrogels with enhanced photodynamic antibacterial and anti-biofilm activity, Chem Eng J, 2021, 413, 127542.
[107] Zhang X, Chen Y, Li C, et al., Root canal disinfection using highly effective aggregation-induced emission photosensitizer, ACS Appl Bio Mater, 2021, 4, 3796–3804.
[108] Wang J, Gao M, Cui Z, et al., One-pot quaternization of dual-responsive poly(vinyl alcohol) with AIEgens for pH-switchable imaging and killing of bacteria, Mater Chem Front, 2020, 4, 2635–2645.
[109] Shi J, Wang M, Sun Z, et al., Aggregation-induced emission-based ionic liquids for bacterial killing, imaging, cell labeling, and bacterial detection in blood cells, Acta Biomater, 2019, 97, 257–259.
[110] Wang M, Shi J, Mao H, et al., Fluorescent imidazolium-type poly(ionic liquid)s for bacterial imaging and biofilm inhibition, Biomacromolecules, 2019, 20, 3161–3170.
[111] Gao J, Wang M, Wang F, Du J, Synthesis and mechanism insight of a peptide-grafted hyperbranched polymer nanosheet with weak positive charges but excellent intrinsically antibacterial efficacy, Biomacromolecules, 2016, 17, 2080–2086.
[112] Liu L, Xu K, Wang H, et al., Self-assembled cationic peptide nanoparticles as an efficient antimicrobial agent, Nat Nanotechnol, 2009, 4, 457–463.
[113] Zhao J, Dong Z, Cui H, Jin H, Wang C, Nanoengineered peptide-grafted hyperbranched polymers for killing of bacteria monitored in real time via intrinsic aggregation-induced emission, ACS Appl Mater Interfaces, 2018, 10, 42058–42067.
[114] Li Q, Wu Y, Lu H, et al., Construction of supramolecular nanoassembly for responsive bacterial elimination and effective bacterial detection, ACS Appl Mater Interfaces, 2017, 9, 10180–10189.
[115] Zasloff M, Antimicrobial peptides of multicellular organisms, Nature, 2002, 415, 389–395.
[116] Stach M, Siriwardena TN, Köhler T, van Delden C, Darbre T, Reymond JL, Combining topology and sequence design for the discovery of potent antimicrobial peptide dendrimers against multidrug-resistant Pseudomonas aeruginosa, Angew Chem Int Ed, 2014, 53, 12827–12831.
[117] Seo MD, Won HS, Kim JH, Mishig-Ochir T, Lee BJ, Antimicrobial peptides for therapeutic applications: A review, Molecules, 2012, 17, 12276–12286.
[118] Li NN, Li JZ, Liu P, et al., An antimicrobial peptide with an aggregation-induced emission (AIE) luminogen for studying bacterial membrane interactions and antibacterial actions, Chem Commun (Camb), 2017, 53, 3315–3318.
[119] Chen J, Gao M, Wang L, et al., Aggregation-induced emission probe for study of the bactericidal mechanism of antimicrobial peptides, ACS Appl Mater Interfaces, 2018, 10, 11436–11442.
[120] Zheng Y, Liu W, Chen Y, Li C, Jiang H, Wang X, Conjugating gold nanoclusters and antimicrobial peptides: From aggregation-induced emission to antibacterial synergy, J Colloid Interface Sci, 2019, 546, 1–10.
[121] Li Y, Zhao Z, Zhang J, et al., A bifunctional aggregation-induced emission luminogen for monitoring and killing of multidrug-resistant bacteria, Adv Funct Mater, 2018, 28, 1804632.
[122] Zhang YY, Zhou CH, Synthesis and activities of naphthalimide azoles as a new type of antibacterial and antifungal agents, Bioorg Med Chem Lett, 2011, 21, 4349–4352.

[123] Liao Y, Li B, Zhao Z, et al., Targeted theranostics for tuberculosis: A rifampicin-loaded aggregation-induced emission carrier for granulomas tracking and anti-infection, ACS Nano, 2020, 14, 8046–8058.
[124] Tian S, Bai H, Li S, et al., Water-soluble organic nanoparticles with programmable intermolecular charge transfer for NIR-II photothermal anti-bacterial therapy, Angew Chem Int Ed, 2021, 60, 11758–11762.
[125] Zhang Y, Fu H, Liu DE, An J, Gao H, Construction of biocompatible bovine serum albumin nanoparticles composed of nano graphene oxide and AIEgen for dual-mode phototherapy bacteriostatic and bacterial tracking, J Nanobiotechnol, 2019, 17, 104–125.
[126] Han Q, Lau JW, Do TC, Zhang Z, Xing B, Near-infrared light brightens bacterial disinfection: Recent progress and perspectives, ACS Appl Bio Mater, 2021, 4, 3937–3961.

Jiangman Sun, Hui Li, Xinggui Gu, Ben Zhong Tang

# Chapter 11
# AIE-based systems for photoactivatable imaging, delivery, and therapy

## 11.1 Introduction

Photoactivatable materials have aroused wide attention over a long period of time; they can undergo photochemical reactions or photophysical processes [1–4]. Due to their unique features such as excellent sensitivity, high contrast ratio, and quick responsiveness, photoactivatable materials have been developed for various advanced high-tech applications, such as super-resolution imaging [5], information storage [6], and light stimuli-responsive drug delivery [7].

Thanks to their excellent features, such as high sensitivity and accuracy, convenient adjustability and noninvasiveness, photoactivatable materials are great for biomedical applications, such as cell lineage [8], living cell tracing [9], and super-resolved fluorescence imaging, including photoactivated localization microscopy (PALM), stochastic optical reconstruction microscopy (STORM) [10, 11]. In the recent decades, some photoactivatable organic molecules, based on their own photochemical reactions, including photodimerization, photocyclization, photo-isomerization, and photo-removal, have been readily developed to meet different requirements due to their excellent emissive properties, good biocompatibility, and rapid transforming process [12]. However, some drawbacks, such as poor photostability, small Stokes shift, and aggregation-caused quenching effect (ACQ), are also present [13, 14], which limit their applications in some fields.

Aggregation-induced emission (AIE) is a fluorescence phenomenon first reported by Ben Zhong Tang in 2001 [15, 16], which has been developed rapidly due to its unique features, such as bright fluorescence in the solid state with a large Stocks shift and good photostability, which overcome the phenomenon of aggregation-caused

**Jiangman Sun, Hui Li,** Beijing Advanced Innovation Center for Soft Matter Science and Engineering, College of Materials Science and Engineering, Beijing University of Chemical Technology, Beijing, 100029, China
**Xinggui Gu,** Beijing Advanced Innovation Center for Soft Matter Science and Engineering, College of Materials Science and Engineering, Beijing University of Chemical Technology, Beijing, 100029, China. e-mail: guxinggui@mail.buct.edu.cn
**Ben Zhong Tang,** Shenzhen Institute of Aggregate Science and Technology, School of Science and Engineering, The Chinese University of Hong Kong (Shenzhen), Shenzhen, 518172, China, e-mail: tangbenz@cuhk.edu.cn

https://doi.org/10.1515/9783110672220-011

quenching effect (ACQ) suffered by most traditionally fluorescent dyes. Moreover, the AIEgens can be synthesized and modified with different functional groups to realize various functions easily, which makes them to be widely applied in the fields of fluorescence imaging, near infrared II fluorescence imaging [17], photoacoustic (PA) imaging [18], chemical therapy [19], photodynamic therapy (PDT) [20], photothermal therapy (PTT) [21], bioprocess monitoring [22], organic light-emitting diodes (OLEDs) [23], and so on.

Thus, photoactivatable materials with AIE features have emerged in biomedical imaging and clinical treatment. These materials not only display light-controlled advantages but also show strong emissive feature in aggregated states. Owing to their excellent features, such as touching off, noninvasive control, high spatiotemporal resolution, convenient adjustable properties, and bright fluorescence in aggregates, AIE-based photoactivatable materials can be suitably used for biological fields. In this chapter, we will discuss the applications of photoactivatable AIE-based materials for biomedical applications, including various bioimaging, drug/gen delivery, and light-controlled cancer therapy.

## 11.2 Bioimaging based on photoactivatable AIEgens

To realize the fluorescent visualization of biological process, it is necessary to develop ideal fluorescent probes with high specificity to organelle, high photostability, high brightness, and high resolution ratio, which can visualize the physiological process of organelles, enzymes, and so on, in situ and over long-term, with high resolution. AIE-based fluorescent probes have been widely used to visualize and analyze organism species and bioprocess in the recent decades [22, 24], While most of them lack high spatiotemporal resolution, the development of photoactivatable fluorophores provides an effective way to solve the problem due to the unique “turn on” property of converting from weak or no emissive state to a fluorescent state, upon light irradiation. Though many fluorescence protein-based photoactivatable materials have been developed for imaging, they are far from ideal because of the tedious synthesis, photobleaching, and low photoactivation efficiency [25]. Recently, due to the efforts of researchers, photoactivable AIEgens possessing both photoactivatable and AIE features upon light irradiation, have been investigated and have become the most promising tool for research of biological process, for example, photoactivatable imaging [26], dual-color fluorescence imaging [27], spatiotemporal imaging [28], super-resolved fluorescence imaging, including PALM [11], STORM [29], etc.

### 11.2.1 Cell imaging

It is known that lots of diseases including angiocardiopathy, genopathy and metabolic diseases, cancers are closely related to the morphology and dynamics of mitochondrion [30]. Thus, monitoring the morphology and dynamics of mitochondrion using suitable probes are important to study the biological process *in situ* and over long-term, which are essential in modern diagnosis and treatment. To realize this, probes with high photostability, excellent fluorescence, and high resolution ratio are desired. Of late, inherent positive-charged AIEgens, with specific targeting ability to mitochondrion, have been developed rapidly and applied in monitoring the mitochondrial events [31, 32].

Tang and Wang et al. reported a rare N-containing fused five-membered heterocycle photoactivable AIE probe **1′**, with positive charge, transforming from **1** under UV irradiation (Figure 11.1a) [33]. Owing to its positive charge and enhanced emission intensity upon light irradiation, a light-driven amplification of fluorescence was proposed and applied in recognizing the selective mitochondria-targeted cancer cells. As a study, both **1** and **1′** showed acceptable biocompatibility, providing the precondition in a biosystem, and the specificity of **1** towards mitochondria was also demonstrated when costaining with the commercial bioprobe for mitochondria, Mito Tracker Red (MTR), whose fluorescence signal well merged with that of probe **1**. Surprisingly, the visualization of mitochondria was clear even at low concentration of probe **1**, 50 nM, employed for staining the cell; however, the emission signal from MTR was indistinct at the same concentration (Figure 11.1b). So far, probe **1** has held the lowest working concentration in contrast to other mitochondria-targeted AIEgens. Further, an enhanced emission in cell was observed after laser irradiation due to the formation of excellent photostable **1′** via photocyclization reaction (Figure 11.1c). On the contrary, the fluorescent signal of MTR was obviously quenched after 230 s irradiation under the same circumstances. It is indicated that the photoactivatable probe **1**, with accessible photoreaction to the exceptional fluorescence-featured cyclized product **1′**, can be applied in cell tracking and improve the photostability of fluorescence imaging. What is more, probe **1** is also a promising candidate to distinguish the cancer cells and normal cells. As shown in Figure 11.1d, fluorescence signal from probe **1** for normal cell (including HLF and CCOS-7 cells) is barely observed even at an enhanced concentration of 1 mM, while a bright fluorescence is observed for cancer cell (HepG2 cells).

The excited state intramolecular proton transfer (ESIPT) process often occurs across a hydrogen bond when excited by light, which plays an important role in constructing hydroxyl-containing photochromic compounds due to its new excited tautomer with an electronic structure, distinct from the original excited state. Salicylaldehyde hydrazone derivatives, as a kind of hydroxyl-containing Schiff-base derivatives, are considered to be potential photoactivatable compounds via a rational molecular design, which always possess the ESIPT process [34]. However, this kind

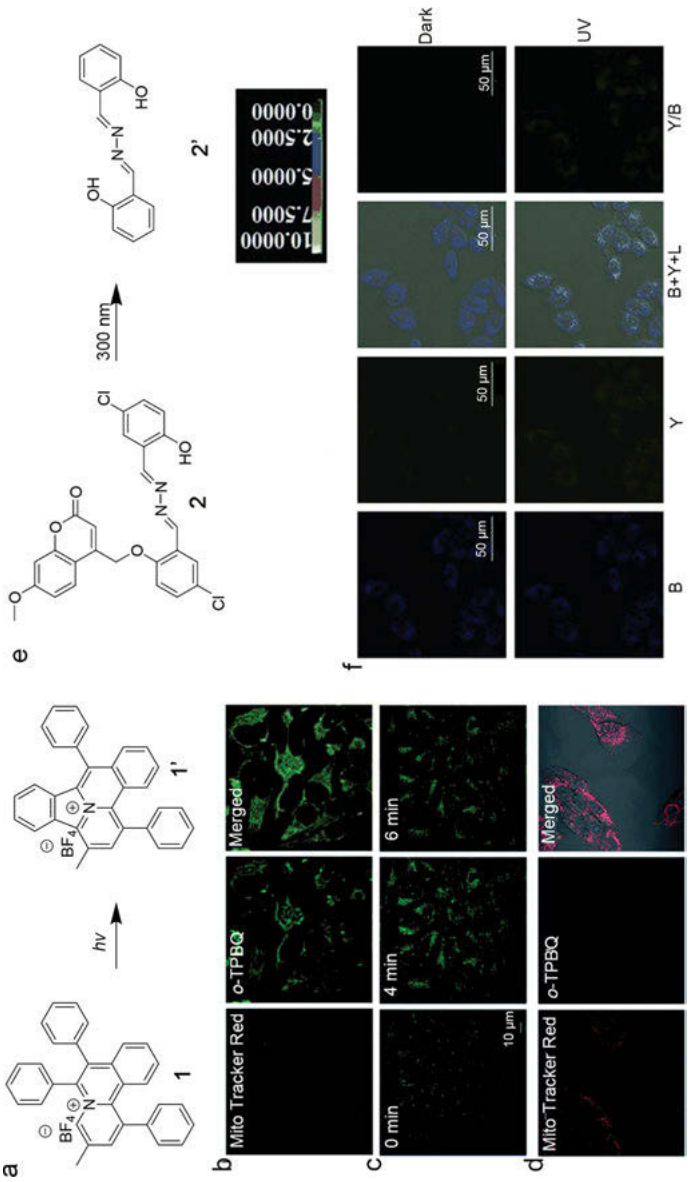


**Figure 11.1:** a) The switching of **1** to **1′** under UV irradiation. b) Images for HeLa cells constrained with MTR and **1** at a Concentration of 50 nM. c) Images of HeLa cells stained with **1** at different photoactive times. d) Images of normal cells stained with MTR and **1** at a concentration if 1 mM. e) The transformation of **2** to **2′** under UV light irradiation selectively. f) Ratiometric fluorescent images of MCF-7 cells treated with **2** in dark and under UV irradiation, respectively. Reprinted with permission from Ref. [33]. Copyright © 2021 The Royal Society of Chemistry. Reprinted with permission from Ref. [35]. Copyright © 2015 Wiley-VCH Verlag GmbH & Co. KGaA, Weinheim.

of photoactivatable solid-state fluorophores for biological application, such as photoactivatable cell imaging, is still rare. Xiang et al. developed a series of caged solid-state salicylaldehyde hydrazone derivatives, in which, the ESIPT process and strong fluorescence could recover by leaving the caging group on the hydroxyl moiety under suitable light irradiation in the aggregation state [35]. Moreover, the caging group, including 2-nitrobenzyl, phenacyl, or 7-methoxylcoumarin-4-yl, together with the substitutions on the salicylaldehyde hydrazine contributed to the multicolor fluorescence of these photoactivatable compounds, upon selective wavelength activation.

More interestingly, compound **2**, with a caging group of 7-methoxylcoumarin-4-yl, showed a ratiometric (photochromic) fluorescence switch after UV irradiation (Figure 11.1e), which presents blue emission in its solid states due to the presence of a caging group of coumarin and exhibits a doublet emission character, contributed by 7-methoxylcoumarin (blue) and salicylaldehyde hydrazones **2′** (yellow), after the coumarin caging group was removed from **2** upon UV light irradiation at 300 nm. The application of caged compounds **2** in its colloid solution (aggregate states) for photoactivatable cell imaging was subsequently investigated. After incubating MCF-7 cells with the colloid solutions of the caged probes **2**, the cells were later washed exhaustively in dark or under light irradiation at 300 nm for 40 min before imaging. It was found that cells containing **2** exhibited ratiometric fluorescence switches (Figure 11.1f) after illumination at 300 nm, where "B," "G," "Y," "R" and "L" are blue, green, yellow, red, bright channels, respectively, and "Y/B" is the intensity ratio of yellow channel divided by the blue channel. Thus, the images based on color scales of intensity ration, such as yellow channel divided by blue channel (Y/B), are almost not interfered by photobleaching or concentration distributions of probes inside cells, in contrast to the images with fluorescence enhancement alone. Due to the negative charges generated by some of the uncaged fluorophores on the surface of the particles, it was found that probes mostly localized in the cytoplasm, rather than in the nucleus of the cells.

## 11.2.2 Dual-color fluorescence imaging

Photoswitchable fluorescent materials, with dual-color emissive properties, in high contrast ratio have attracted enhanced attention for use in fluorescence imaging, due to their unique advantages over conventional single-color fluorophores, such as differentiating the emission signals, eliminating the background noise, and providing images with high signal-to-noise ratio [36–38]. Generally, photoswitchable fluorescent materials, with fluorescence resonance energy transfer (FRET) characteristics, always reveal excellent dual-color emissive materials [39]. It is well-known that the closed spiropyran (SP) can switch to the open merocyanine (MC) form

under UV light irradiation, which is a favorable candidate for constructing photo-responsive AIE molecules by the strategy of connecting AIEgens into SP.

As is known, lysosomes, as a kind of cytoplasmic organelles, are closely correlated to many biological processes, including intracellular transport, cellular metabolism, and apoptosis [40]. Hydrogen sulfide ($H_2S$) played a tremendous role in lysosomes, such as disturbing the lysosomal membrane and inducing cell apoptosis via the activation of calpain proteases [41, 42]. Therefore, it is necessary to develop methods for monitoring the $H_2S$ levels of lysosome selectively with high signal-to-noise ratio.

Chen et al. combined photochromic spiropyran moiety with $H_2S$-recognizing AIE group and obtained a novel photoswitchable AIE nanoprobe **3** for detecting lysosomal $H_2S$, with excellent spatiotemporal resolution (Figure 11.2a) [43]. The BNBS moiety would leave from **3** due to the band cleavage induced by $H_2S$ and resulting in **3′**, which triggered fluorescence at about 592 nm, with a good sensitivity and high specificity for monitoring $H_2S$ over other thiols. Moreover, the fluorescence of AIE nanoprobe **3′** can be transformed through selective FRET from the AIE fluorophore to ring-opened state of spiropyran (MC), rather than ring-closed SP via alternating UV/visible light irradiation. As shown in Figure 11.2b, the orange emission of **3′** at 592 nm vanished and a new strong red emission of **3″** at 650 nm emerged at the same time, upon irradiation by 365 nm UV light. Subsequently, an opposite process is observed after the visible light irradiation. Further cycled "switch-on" and "switch-off" studies in different pH conditions demonstrated that the probe showed a potential to realize light-controlled switchable dual-color imaging with high spatiotemporal resolution even in the acidic environment of lysosomes. Later, the nanoprobe **3** was used for performing living cells dual-color imaging. As shown in Figure 11.2c, the reversible transformation between green and red emission color under the irradiation of remote UV or visible light is observed in the living cells with the $H_2S$-activated probe. The intelligent features of this probe not only displayed several excellent advantages, including high signal-to-noise ratio and spatiotemporal resolution, but also provided an intelligent platform of optical address for living cells dual-color imaging. The fluorescence was from nanoparticles in cell and not from the interference, which was further confirmed by the overlay images.

Zhang et al. also reported a spiropyran (SP) grafted polymer **4** and AIEgen **5**, and then fabricated a novel nanoparticle via a simple coprecipitation of **4** and **5**, which exhibited superior long-term photostability, sensitive photo-responsiveness, high fluorescence contrast, and excellent photoreversibility due to the FRET from AIEgen **5** to the MC group of the polymer **4** [27]. As shown in Figure 11.2e, the fluorescence of nanoparticles, containing **4** and **5**, at 520 nm, dramatically decreased after UV irradiation and emerged at the same time around 650 nm, which could be due to the FRET process, from **5** to the MC (**4′**). Upon treatment with visible light, an opposite process was observed because the FRET process from **5** to the SP (**4**) was inhibited. Owing to the prominent cell-membrane permeability, fast light responsibility of the above

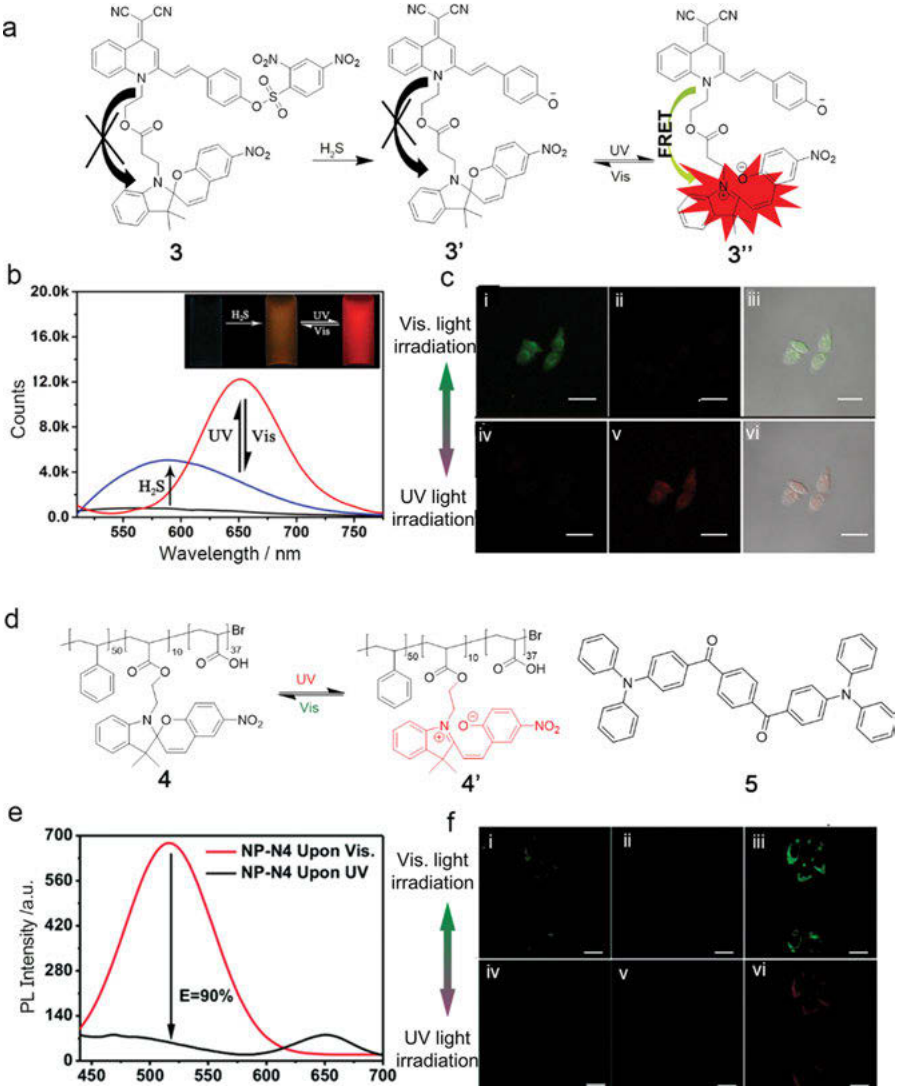


**Figure 11.2:** a) The schematic diagram of **3** for sensing $H_2S$ and reversible dual-color imaging. b) Fluorescence spectra of **3** in the absence (black), presence (blue) of $H_2S$, and switched between UV (365 nm) and visible light (525 nm) irradiation after $H_2S$ activation. c) Images of HeLa cells incubated with $H_2S$ after treated with **3** under visible light (i, ii and iii) or UV irradiation (iv, v and vi). $\lambda_{ex}$ = 468 nm, $\lambda_{em1}$ = 550–600 nm (Channel 1), $\lambda_{em2}$ = 650–700 nm (Channel 2) scale bar = 20 μm. d) The Schematic of the photoswitchable behavior of **4** under UV and visible light illumination and the molecular structure of **5**. e) Fluorescence spectra of nanoparticle sample manipulated by UV or visible light illumination. $\lambda_{ex}$ = 410 nm, 25 °C. f) Fluorescence images of HeLa cells treated with a nanoparticle dispersion at 37 °C for 2 h under visible light (i–iii) or UV irradiation (iv–vi). Scale bar: 20 μm. Reprinted with permission from Ref. [43]. Copyright © 2018 Elsevier B.V. Reprinted with permission from Ref. [27]. Copyright © 2017 The Royal Society of Chemistry.

mentioned nanoparticle, it was promising in intracellular dual-color imaging. As shown in Figure 11.2f, HeLa cells displayed green emissive color in high brightness under visible light (Figure 11.2f, i) and iii), because of the unquenched fluorescence of **5** by the nonfluorescent ring-closed SP. After UV irradiation, the green fluorescence quenched (Figure 11.2f, iv), and red fluorescence emerged (Figure 11.2f, v and vi), due to the presence of the FRET process from **5** to ring-opened MC. It was indicated that the dual-color nanoparticle was a promising probe for selectively marking intricate systems, including cell imaging, cell marking, and photo-tracking with fluorescence in a high contrast ratio.

### 11.2.3 Spatiotemporal fluorescence imaging

The physiological and biochemical processes in cells almost occurred in a strictly spatiotemporal modulated manner. It would be helpful to better understand the functions of biological targets by studying the dynamic level of the biological targets with high spatiotemporal resolution. Thus, a fluorescence probe with a high spatiotemporal resolution in complex biological system was desirable. Photoactivatable dyes with a light triggered turn-on manner that could be controlled by light irradiation with high spatiotemporal precision have been a promising tool, permitting spatial and temporal manipulation during imaging studies [44, 45].

Cancer cells require a lot of fatty acids and phospholipids during their quick growth; thus, the increased expression level of lipid droplets (LDs) is considered as a biomarker of cancer [46–48]. Probes with photoactivability and LDs specificity are powerful tools for living cell imaging to study their biological functions through accurate spatial and temporal manipulation. Therefore, to develop LDs-specific photoactivatable probes for spatiotemporal fluorescence imaging were highly desirable. Tang et al. developed probes **6** with photoactivation property and LDs specificity (Figure 11.3a) [26]. As shown in Figure 11.3b, a gradually enhanced emission was observed for **6a**, upon UV light irradiation at 365 nm, indicating the formation of AIE-featured **6′a**, transformed from **6a**, through a photooxidative reaction. When **6a** was used as a photoactivatable probe for lung cancer HCC827 cells imaging, a rapid fluorescence turn-on process (less than 2 min) was detected under 405 nm light irradiation (Figure 11.3c). Further, the excitation of **6a** in selected HCC827 cells could be realized in the complex multicellular environment by using an external light trigger in a high spatiotemporal precision.

Lysosome, as a key subcellular organelle, is important in the autophagy process [40]. Thus, it is necessary to visualize and track lysosomal activities for deep study of the autophagy, which depends on the development of various lysosome-specific probes [49–51]. For example, the emerging photoactivatable probes are promising candidates that could be used for studying the dynamics of lysosome, with both high spatial and temporal resolution. Chenoweth et al. reported lysosome-specific

photoactivated fluorescence probes, **7** and **7′**, with good water solubility and biocompatibility (Figure 11.3e) [52]. Moreover, the observed emission at 525 nm was assigned for the pre-activated, **7** and **7′**, when excited by laser at 405 nm. The observed emission at 675 nm was for the post-activated species **7″**, using a 488 nm excitation wavelength. Due to the photoactivation property of **7** and **7′**, a temporally manipulated sequential photoactivation of individual cells in dense cellular environment was demonstrated. Importantly, it was also confirmed that the monomethylated derivative could be photoactivated in cells, permitting spatiotemporal manipulation during the imaging process.

Tang et al. developed a new mitochondria-specific fluorescence turn-on photoactivatable probe **8** for spatiotemporal imaging of mitochondria [53]. Under light irradiation, the weakly emissive **8** transformed to the strongly emissive **8′** by photocyclodehydrogenation. Thus, through controlling the power of laser at 405 nm, the generation of **8** from **8′** were spatiotemporally controlled in living Hela cells in situ. They found that the fluorescence intensity from mitochondria in the selectively activated cells was 17-fold higher than that in the unactivated cells, indicating that probe **8** was an efficient photoactivatable probe for imaging of selected cells spatiotemporally.

Tang et al. further found that the generation compounds **9′** from **9** *in situ*, which could be photoactivated and afford the AIE-featured compound **9″** through photooxidative dehydrogenation reaction under both one- and two-photon irradiation [28]. Under both UV irradiations, at 365 nm and two-photon excitation at 780 nm, the PL intensity of **9′** increased to the maximum emission peak of 576 nm. Compounds **9′** with a methoxy or morpholinomethyl substituent showed specificity for lipid droplets (LDs) and lysosomes, respectively, and also displayed excellent photoactivation efficiency. Consequently, the selected cells could be sequentially photoactivated with superior spatiotemporal resolution in a multi-cellular environment under both one and two-photon illumination, indicating that the probes **9** were promising for organelle study in a complex physiological environment.

### 11.2.4 Super-resolution imaging

Owing to the advantages of optical fluorescence microscopy, such as high sensitivity, in situ workability and noninvasiveness, it has been widely used in studying cellular dynamics over the years. However, according to the Abbe's diffraction limit, it was hard to distinguish two objects that are closer than half the wavelength in a target objective. Thus, a spatial resolution of about 200 nm for visible light microscopy was limiting, which seriously limited their applications [54–56]. For example, due to the small size of mitochondria, the optical microscopy could not present several pivotal issues relative to mitochondrial structures at the nanoscale level, which was under the limit of diffraction of fluorescence microscopy. In the recent

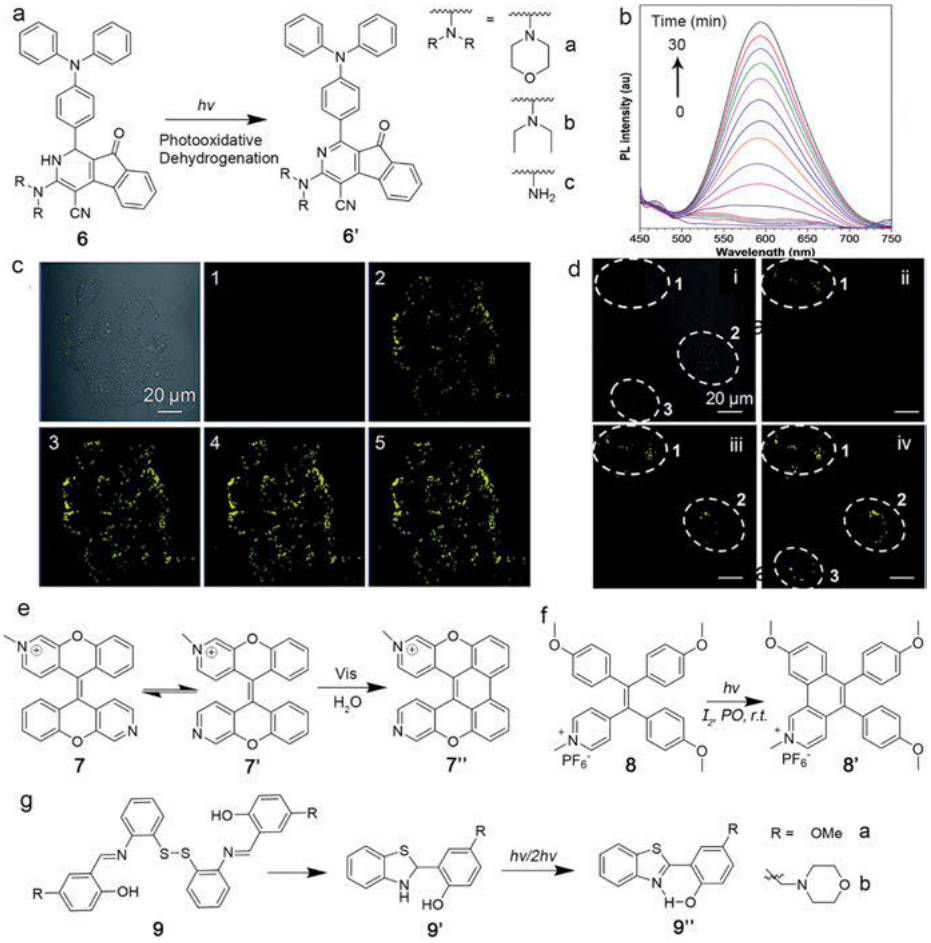


**Figure 11.3:** a) Photo-oxidative dehydrogenation of **6** to **6′**. b) The PL spectra of **6a** under different UV light irradiation times in DMSO/water mixture with 99% water fraction. c) Images of live HCC827 cells under white light irradiation and increasing scans at 405 nm with 1% laser power (the upper left corner showed the number of scans with a scanning rate of 22.4 s per-frame). d) Sequentially photo-activated HCC827 cells (cells 1, 2, and 3) under illumination at 405 nm. Dashed lines indicated the periphery of cells. Scale bar = 20 μm. e), f) and g) Transformation of **7′, 8, 9′** to **7″, 8′, 9″** under light illumination, respectively. Reprinted with permission from Ref. [26]. Copyright © 2017 The Royal Society of Chemistry. Reprinted with permission from Ref. [52]. Copyright © 2015 The Royal Society of Chemistry. Reprinted with permission from Ref. [53]. Copyright © 2015 Wiley-VCH Verlag GmbH & Co. KGaA, Weinheim. Reprinted with permission from Ref. [28]. Copyright © 2018 The Royal Society of Chemistry.

decades, the development of super-resolution microscopy (SRM) techniques made it possible to achieve the fluorescence image of the subcellular organelles below the diffraction limit (200 nm). However, SRM techniques were highly dependent on

the validity of ideal fluorescent probes, especially the organelle-targeted markers and probes with specificity to organelle, because of the complete exposure of the objects to an intense laser beam in the SRM optical system. Therefore, the development of probes exhibiting certain specialized features for SRM was key to investigate subcellular organelles with high accuracy.

Tang and coworkers developed a novel mitochondrion-specified photoactivatable AIE bioprobe **10**, which was successfully used for SRM imaging [29]. As shown in Figure 11.4a, based on the photocyclodehydrogenation, **10′**, with a closed-ring, structure generated from **10**, upon visible light irradiation (>500 nm) and displayed pH- and environment-insensitive emission. Initially, **10** was nearly nonemissive in aqueous solution due to the twisted intramolecular charge-transfer (TICT) and rotation, while, the ring-closed **10′** with AIE feature showed strong yellow emission in the aggregated state. Due to its high cell permeability, biocompatibility, and spontaneously blinking, probe **10** was successfully applied in the mitochondria imaging of HeLa cells. As shown in Figure 11.4b and c, with increased irradiation time (20%, 405 nm), a gradually enhanced fluorescence of the activated state in HeLa cells was observed due to the light-triggered transformation from **10** to **10′**. Sequentially, the fluorescence photobleaching process occurred under a strong power laser at 514 nm because of the switch from **10′** to **10.** After continuous scanning for 920 s, a serious fluorescent decline of more than 90% occurred. It indicated that probe **10** was potential for use in SRM imaging due to its feature of switching between the fluorescence in the on and off states.

The feasibility of applying **10** in SRM imaging was confirmed by performing STORM imaging in HeLa cells treated with **10** to mark the mitochondrial structure (Figure 11.4d–i). After preparing the sample and locating the desired area, they acquired data under the excitation of a laser at 561 nm and a weak activation laser at 405 nm. As shown in Figure 11.4d–f, a blurred structure of mitochondria with low resolution was shown in the epifluorescent image, with a large full-width at half-maximum of 697.1 nm, while a clear structure of mitochondria with more structural details was presented by the STORM image of the same area, with a smaller full-width at half-maximum of 104.5 nm. It was confirmed that probe **10** was suitable for SRM imaging with a higher resolution than traditional fluorescence-based methods because of its unique photoactivation feature. Moreover, probe **10** also monitors the fission (green arrowheads) and fusion (red arrowheads) behaviors of mitochondria successfully through STORM imaging (Figure 11.4g–i). Tang and coworkers provided us a new general strategy to develop more organelle-specific fluorescent probes for SRM imaging in both fixed and live cells.

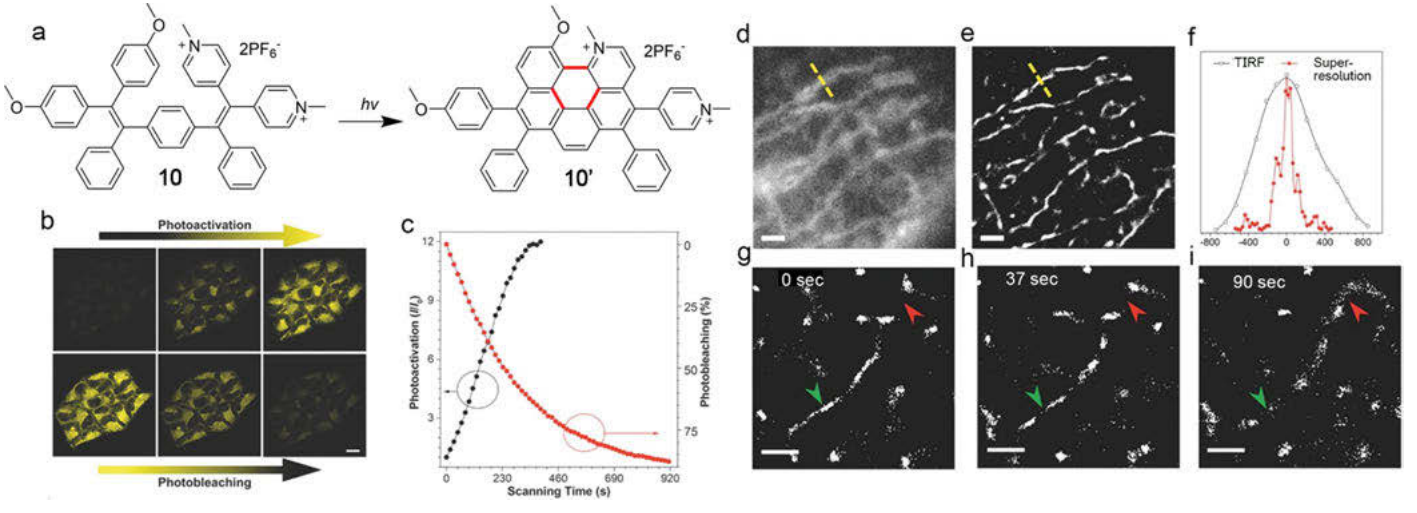


**Figure 11.4:** a) Photocyclodehydrogenation process of **10**. b) Fluorescent images of photoactivation and photobleaching behaviors for **10** in fixed HeLa cells. c) Plots of the relative fluorescence intensity ($I/I_0$) against scanning time. Scale bar: 20 μm. SRM imaging of mitochondria in a fixed HeLa cell: d) Diffraction-limited TIRF image with totally fuzzy structure. e) Super-resolution image. f) Transverse profiles of the single mitochondrion along the yellow dotted line marked in the images (d) and (e). Scale bar: 2 μm. Images of fission and fusion events captured at (g) 0, (h) 37, and (i) 90 s by a STORM. Scale bars: 500 nm. Reprinted with permission from Ref. [29]. Copyright © 2016 Wiley-VCH Verlag GmbH & Co. KGaA, Weinheim.

### 11.2.5 Dual-mode fluorescence and PA imaging

As mentioned above, fluorescence imaging showed many advantages, such as excellent sensitivity, real-time, and long-term tracking, but lacked spatial resolution [57]. While, as a promising imaging technology, the PA technique emerged with unique advantages, such as real-time three-dimensional (3D) images, 5–7 cm deep imaging, and relatively high spatial resolution, but suffered from low sensitivity [58]. Thus, realizing high sensitivity and imaging depth beyond the optical diffusion limit by combining the advantages of both the fluorescence and PA imaging modes was significant but challenging. According to Jablonski diagram, energy usually decays in three key pathways, including radiative transition, intersystem crossing (ISC) to a triplet excited state, and nonradiative transition, which probably happens after light excitation. Thus, PA imaging, which originated from the absorbed energy for nonradiation decay pathway, was competitive with fluorescence imaging, relative to the radiation decay pathway. It was difficult to develop probes with both, PA effects and fluorescence, but really valuable [59, 60].

Tang and coworkers developed a photoactivatable probe **11**, whose photophysical properties were easily tunable [61]. The absorbed energy of the probe could be manipulated to mostly focus on either fluorescence or PA channel, according to the requirement, by adjusting the molecular structure from opening (**11′**) to closing states (**11**), reversibly, through controlling the external UV or visible light illumination (Figure 11.5a). In the ring-closing form **11**, the nonradiation decay (NR) pathway dominated due to its relatively planar geometric structure, which was a benefit for intramolecular energy transfer and as a result, the absorbed energy (A) concentrated on PA imaging (Figure 11.5b). On the contrary, for the ring-opening form **11′**, the radiative and ISC with ROS production pathway dominated (Figure 11.5c). To investigate the performance of the photoactivatable probes in fluorescence and PA imaging in biological application, nanoparticles with **11** or **11′**, doped with amphiphilic maleimide-bearing lipid-PEG2000, were prepared, respectively, and yielded **11**-doped or **11′**-doped lipid-PEG2000 NPs, namely, RClosed NPs or ROpen NPs, respectively. Then, the NPs were used for cancer surgery. Before surgery, PA imaging was used for visualizing the deeper message of the tumors, which was carried out after injecting nanoparticles. As shown in Figure 11.5d, for the mice in both the NPs with YSA (a targeting ligand for activing tumor-targeting ability), modification (RClosed-YSA NPs) and without YSA modification (RClosed NPs) groups, the PA signals reached the maximum at 4 h and then decreased with increasing time scale (Figure 11.5d). Surgery was then carried out to cut off the tumors in vivo by the guidance of the preoperative PA imaging, with RClosed-YSA NPs as the probe. What was more, after tumor resection, the operative incision site was illuminated under light at 610 nm for 5 min. Consequently, no emissive signal was observed at/around the incision site, indicating the total removal of tumors by the surgeon, which was also demonstrated by hematoxylin and eosin (H&E) histological analyses (Figure 11.5e and f).

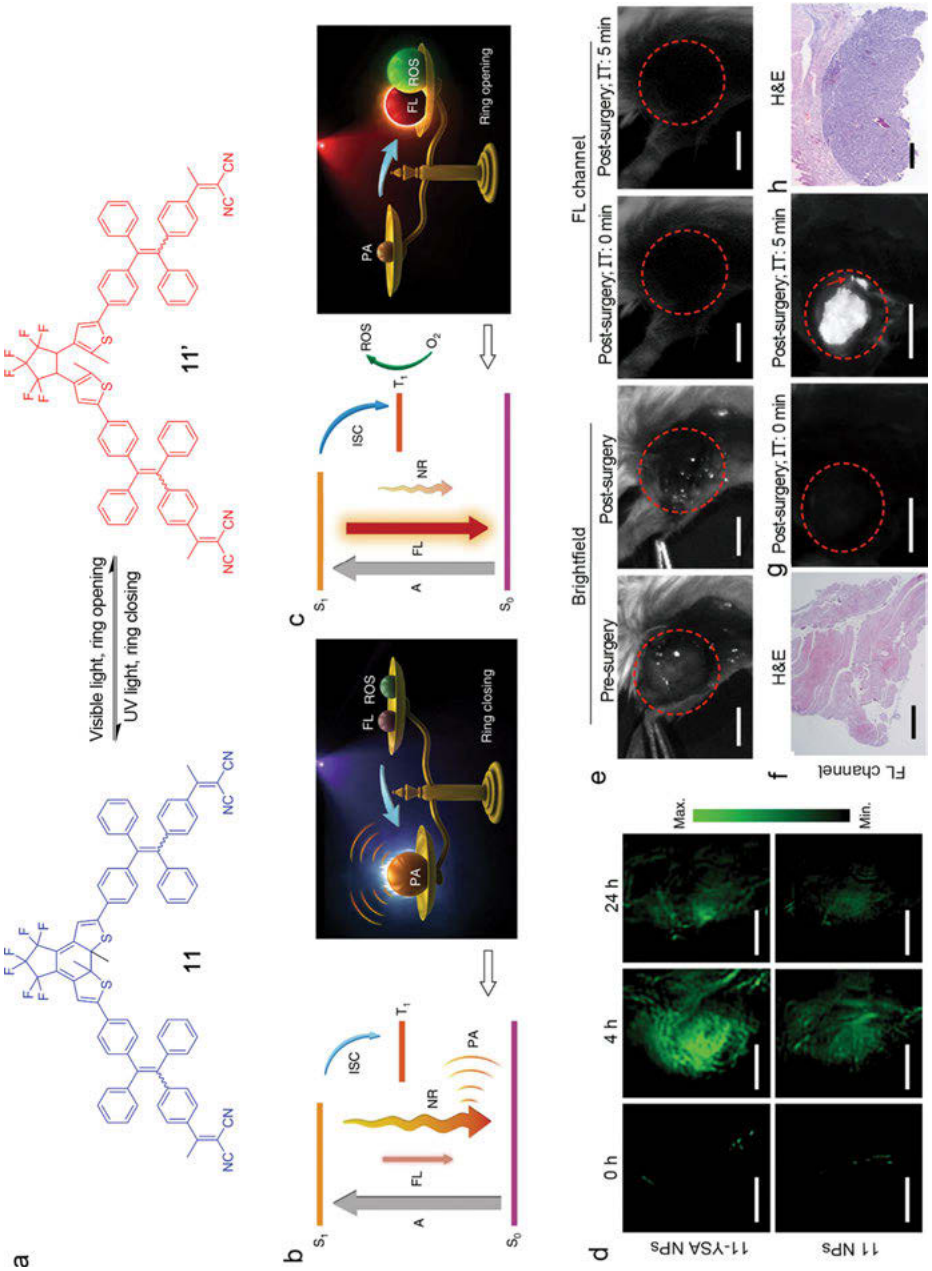


**Figure 11.5:** a) Photo-controlled reversibility structures of **11** (ring closing) and **11′** (ring opening). b) and c) Photophysical processes of **11** and **11′**, respectively with photo-controlled tilts. d) PA images of subcutaneous tumors from mice at different time after intravenously injected with RClosed-YSA and RClosed NPs, respectively. Scale bars, 2 mm. e) Typical bright field and fluorescence images of mice with tumor treated by RClosed-YSA NP. Scale bars, 3 mm. FL,

However, an emissive signal gradually turned on at/around the incision site within 5 min of irradiation due to the transformation of RClosed-YSA NPs to the fluorescent ROpen-YSA NPs, indicating residual tumors after surgery (Figure 11.5g). The existence of residual tumors was also confirmed by H&E staining (Figure 11.5h). Therefore, this experiment demonstrated the advantage of the transition of the nanoparticles' PA and fluorescence imaging properties, which could improve the results of cancer surgery by combining PA imaging, fluorescent imaging of residual tumors, and PDT, to eliminate them completely.

### 11.2.6 Others

According to the above, the behavior of most photoactivatable materials was relative to their intrinsic photochemical processes, including photo-removal, photocyclization, and photoisomerization, which require energy consumption and probably impose additional inconvenience [12, 62]. However, the photophysical process could be conveniently manipulated. For example, the AIE effect, reported by Professor Tang, was an important photophysical behavior that developed rapidly since 2001 [16], while the photophysical-dominant behavior was rarely reported, relative to the general photochemical mechanism. But, it was significant to develop new photoactivatable materials, based on photophysical processes, for photoactivation application, such as imaging and biosensing the areas relative to light-controlled switch.

Tang and coworkers reported a luminogen with AIE characteristics, named **12**, which exhibited a photo-induced crystallization with emission enhancement (PICEE) (Figure 11.6a, b) [63]. Under UV light irradiation, an interesting fluorescence "turn on" phenomenon was observed in the aqueous solution of **12**, whose yellow bright fluorescence enhanced with prolonged illumination time. As previously reported, the occurrence of the photoactivation phenomenon was a photophysics-dominant behavior from the aggregation process, which was confirmed by visualizing the nanostructure formation and transformation processes through the scanning electron microscopy (SEM) [15]. As shown in Figure 11.6c, the irregular nanoparticles of **12** were observed before light illumination. However, after illumination under UV light for 30 min, tighter nanoparticles and nano-block crystals appeared (Figure 11.6d).

**Figure 11.5** (continued)
fluorescence. IT, 610 nm red light (0.3 W $cm^{-2}$) irradiation at the operative incision site for 5 min after completely surgical resection of tumors. f) H & E stained tissues at the operative incision site in e). Scale bar, 1 mm. g) Typical fluorescence images of mice treated by RClosed-YSA NP with residual tumors after surgery. FL, fluorescence, IT, 610 nm red light (0.3 W $cm^{-2}$) irradiation at the operative incision site for 5 min after surgery. h) H & E stained tissues at the operative incision site in g) indicating the existence of residual tumors. Scale bar, 0.5 mm. Reprinted with permission from Ref. [61]. Copyright © 2018 Springer Nature.

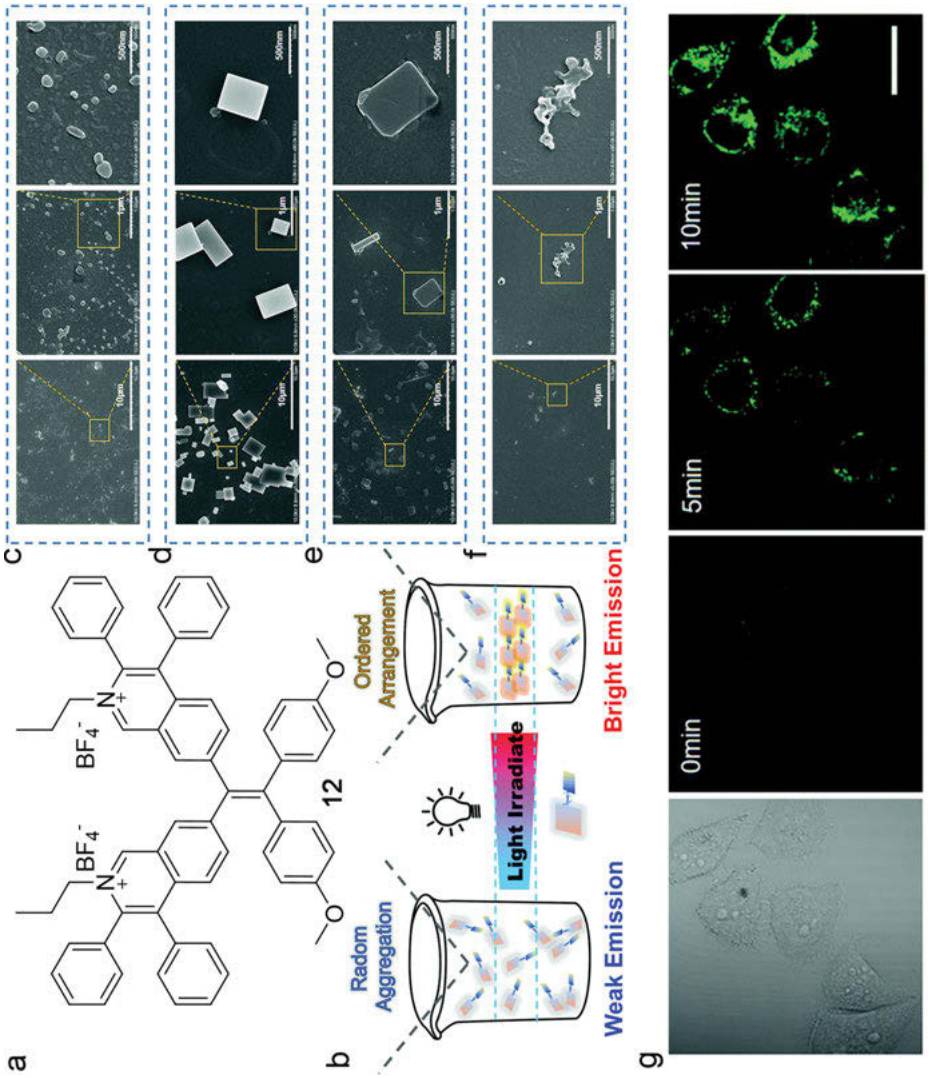


**Figure 11.6:** a) Molecular structures and b) illustration of the photoexcitation process of **12**. SEM images for visualizing the aggregation processes of the **12** aqueous solution at different time c) before irradiation; e) after irradiation for 30 min; e) after irradiation for 60 min; f) the controlled group of **12** aqueous allowed to stand for 60 min. Concentration: 10 mM. g) Fluorescence imaging of Hela cells after incubation with **12** for 15 min. Scale bar: 20 μm. Reprinted with permission from Ref. [63]. Copyright © 2020 The Royal Society of Chemistry.

Then, nano-block crystals with larger sizes developed to a large scale with a prolonged irradiation time of 60 min, as shown in Figure 11.6e, whose fluorescence intensity also increased quickly. However, irregular shapes were observed for the **12** aqueous solution, when permitted to stand for 60 min as control (Figure 11.6f), confirming that light was a key factor to form the nanocrystals. Moreover, they explored the performance of **12** in cell imaging. As shown in Figure 11.6g, a temporal light-up fluorescence was observed in cells due to the retentive photoactive behavior of **12**, which indicated a promising practical applications of **12**, owing to its simpler manipulation. The mitochondria-targeted ability and cancer cell killing performance of **12** were also demonstrated. This work provided a novel photoactivatable mechanism for the formation of nanocrystals *in situ*, which would boost the development of diverse photoactivatable materials.

## 11.3 Photoactivatable delivery

Sending therapeutic agents into the focal zone was one of the most important challenges for drug/gene delivery systems [64–66]. In order to realize precision delivery, a stimuli-responsive delivery system was required, which should not only be responsive to a specific stimulus, but also allow controlled drug release to enhance the therapeutic index and reduce nonspecific toxicity [67, 68]. Nowadays, tremendous efforts are involved in developing and investigating the stimuli-responsive systems, and significant achievements have been realized [69, 70]. For example, the stimuli-responsive delivery system explored typical endogenous stimuli, such as the reactive oxygen species (ROS) [71], redox [72], pH [73], thermal [74] and enzyme [75], and by exogenous stimuli such as light, temperature, magnetic field, and ultrasound. Among them, light as an exogenous stimulus, possessed unique advantages including high spatiotemporal accuracy, relative safety, and high background contrast [76–78]. Thus, photoresponsive drug/gene delivery systems have aroused increasing attention due to their advantages of enabling precision release and activation by manipulating the light illumination site, dosage, and duration time, precisely. As was known, photosensitisers (PSs) are the key factors in the photoresponsive delivery systems. In the recent few decades, luminogens with AIE characteristics (AIEgens) have been developed rapidly and used for biomedical applications [79]. Due to the unique features of AIEgens as PSs, such as high signal-to-noise ratios and reactive oxygen species (ROS) generation efficiency, it was promising for photo-controlled ROS generation and image-guided PDT. Thus, to develop the light stimuli-responsive delivery system by taking advantage of light-controlled release performance and AIE characteristics would be useful and valuable.

### 11.3.1 AIE-featured polymer for photo-controlled gene delivery

The development of highly efficient and low cytotoxic vectors for gene therapy are challenging. When the vectors accessed cells through endocytosis and were entrapped in endo/lysosomes, resulting in the destruction of nucleic acids due to the abundance of enzymes, they would reduce or even prohibit the release of nucleic acids in cytosol [80]. Thus, methods for an efficient gene delivery that could facilitate the escape of nucleic acids from the endo/lysosomes and undergo unpacking was required [69, 70]. Recently, light-triggered endo/lysosomal escape, based on the generation of ROS by PSs under visible light irradiation, has attracted much attention.

Liu and coworkers controlled the release of gene with light through the use of AIE-featured PS nanoparticles as transporters for gene/ drug delivery with the introduction of singlet oxygen responsive linker [71]. As shown in Figure 11.7a–c, an amphiphilic polymer of **13** was generated by linking the TPECM and hydrophilic oligoethylenimine (OEI) with a singlet oxygen-cleavable linker, aminoacrylate (AA). Further, the PEG side chains were introduced to fine-tune the water solubility of the polymer. As a result, nanoparticles with hydrodynamic sizes of (134 ± 12) nm were obtained uniformly, which could serve as a gene vector to trap gene via electrostatic interaction, due to the ability of OEI, and release DNA upon light irradiation due to the single oxygen-cleavable linker. Through self-assembly, the mixture of polymer **13** and DNA formed into nanoparticles, with efficiency as high as (92 ± 6)%. The amphiphilic polymer **13** was then damaged and the nanoparticles were disassembled under light irradiation due to the generation of singlet oxygen by PS TPECM, and as a result, the captured genes were released due to the disassembled nanoparticles.

Recently, Liu et al. additionally designed carrier-free hybrid DNAzyme NPs to realize light-triggered self-delivery of DNAzymes, which presented excellent lysosome escape capacity by efficiently suppressing the expression of EGR-1 mRNA [81]. As shown in Figure 7d, a self-assembled spherical nucleic acids (SNA)-like micellar nanoparticles were generated by the amphiphilic DNAzyme-TBD conjugate and the hybrid DNAzyme NPs **14** formed with $Zn^{2+}$, coordinating with the surface phosphoric acid group. As shown in Figure 11.7e, MCF-7 cells internalized the hybrid DNAzyme NPs successfully, which could be demonstrated by the time-dependent red fluorescence enhancement of TBD in cells. Then, the intracellular situation of hybrid DNAzyme NPs was studied by confocal imaging, after incubating MCF-7 cells with lyso-trackers. As shown in Figure 11.7f, well overlaid images between the signals of lyso-tracker and TBD under dark conditions indicated that the lysosomes entrapped a huge amount of hybrid DNAzyme NPs. Subsequently, when under light irradiation (Figure 11.7g), the intracellular red signals of TBD escaped from lysosomes, indicating that the majority of hybrid DNAzyme NPs separated from lysosomes because of the destruction of the lysosome membrane by the generated $^1O_2$

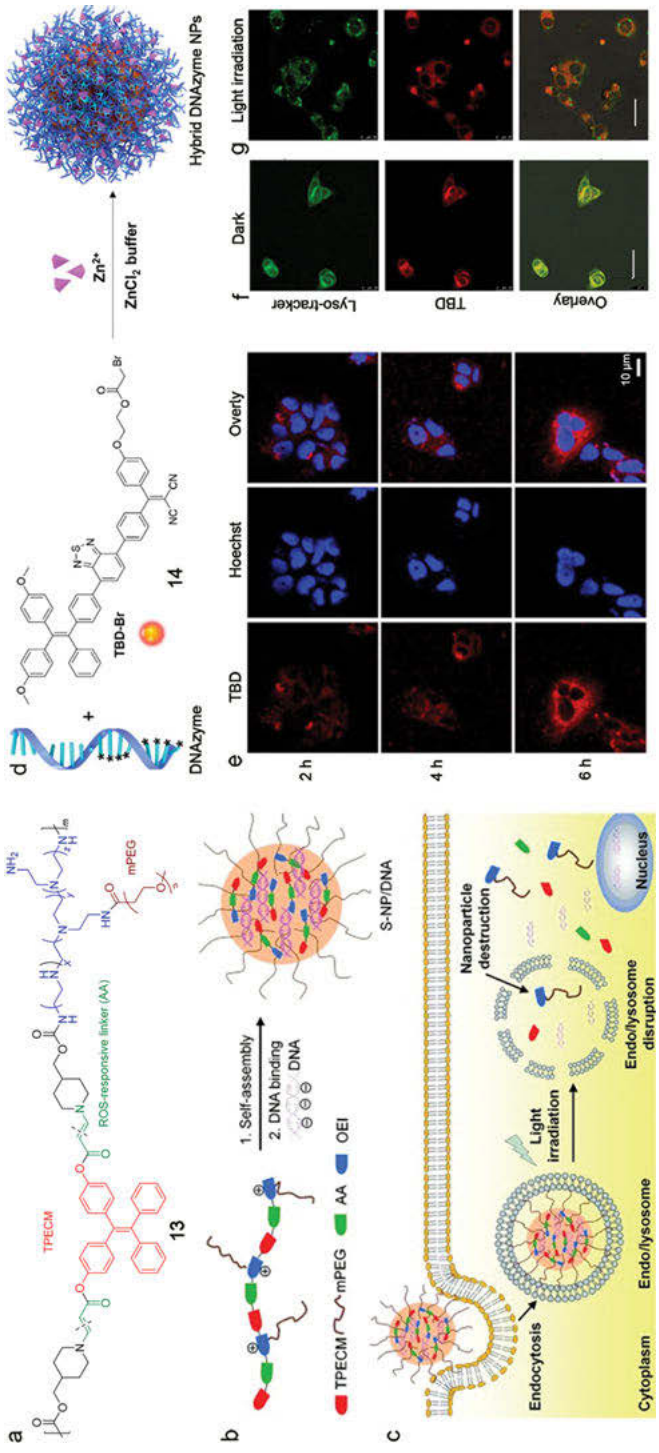


**Figure 11.7:** Illustrations of the chemical structure of photoactivatable polymer **13** a), b) the preparation of nanoparticles (S-NPs/DNA) self-assembled from the mixture of **13** and DNA, and c) the process of S-NPs/DNA to the transgene expression. d) Schematic illustration of preparation of hybrid DNAzyme NPs. e) Images of live MCF-7 cells treated with hybrid DNAzyme NPs for 2, 4, and 6 h. f) and g) Images of MCF-7 cells costaining with lysotracker (green) and hybrid DNAzyme NPs (red) under dark conditions and light irradiation, respectively. Reprinted with permission from Ref. [71]. Copyright © 2015 Wiley-VCH Verlag GmbH & Co. KGaA, Weinheim. Reprinted with permission from Ref. [81]. Copyright © 2021 American Chemical Society.

of TBD-Br under light irradiation. DNAzyme NPs could also be used for killing tumor cells due to the $^1O_2$ generated by the NP core (TBD-Br) under light irradiation, which could inhibit tumor cell growth by precisely suppressing the early growth response factor-1 protein (EGR-1) mRNA.

### 11.3.2 AIEgens for light-controlled drug delivery

Compared to drug release systems that are based on external stimuli, including PH and enzymes or reduction, light-triggered drug delivery system has been regarded as an attractively controlled release mode due to its spatiotemporal precision [76–78]. However, most traditional carriers with photo-responsive linkers in the UV-region limited the development of photo-controlled drug delivery. Thanks to the development of photosensitizer for PDT, an avenue for the development light-controlled drug delivery system was opened [82, 83]. Especially, the delivery system with photo-release performance and the characteristics could not only realize the light-controlled drug release but could also monitor the release process by the fluorescence phenomena.

Liu and coworkers developed a drug delivery system **15** for image-guided PDT and chemotherapy with accurately controlled targeted drug delivery (Figure 11.8a) [84]. In this work, they prepared the amphiphilic polymer **15** by conjugating polyethylene glycol (PEG) and the AIEgen with a ROS cleavable thioketal (TK) linker, which could form nanoparticles (NPs) and load drugs efficiently by self-assembly in aqueous media. Upon white light illumination, the NPs escaped to the cytosol easily due to the ROS-induced enhancement of permeability of the endo-/lysosomal membrane. Meanwhile, drugs accumulation in cancer cells increased, which resulted from the ROS-inducing TK linker cleavage and the broken polymer, triggering drug release in the cytosol. The ROS-generation ability of the NPs in the MDA-MB-231/DOX cells was demonstrated by the indicator, 2′,7′-dichlorofluorescein diacetate (DCF-DA), whose fluorescence was very weak but could yield strong emissive 2′,7′-dichlorofluorescein (DCF), if oxidized by ROS. As shown in Figure 11.8b, after white light irradiation, strong green emission of DCF could be detected in MDA-MB-231/DOX cells incubated with AIE-NPs, indicating ROS generation in the cells (A1-A4). Further, damage of the endo-/lysosomal membrane was also evaluated by the indicator, acridine orange (AO), which presented green emission in the cytoplasm or nuclei, but showed red emission in endo-/lysosomes with low pH. As shown in Figure 11.8b, the MDA-MB-231/DOX cells displayed red and green fluorescence without ROS generated from AIE-NPs, indicating the damage-free of the endo-/lysosomes membrane (B1–B4). However, under light irradiation, the red emission weakened obviously, indicating the damage of the endo-/lysosomal membrane due to the ROS generation of AIE-NPs.

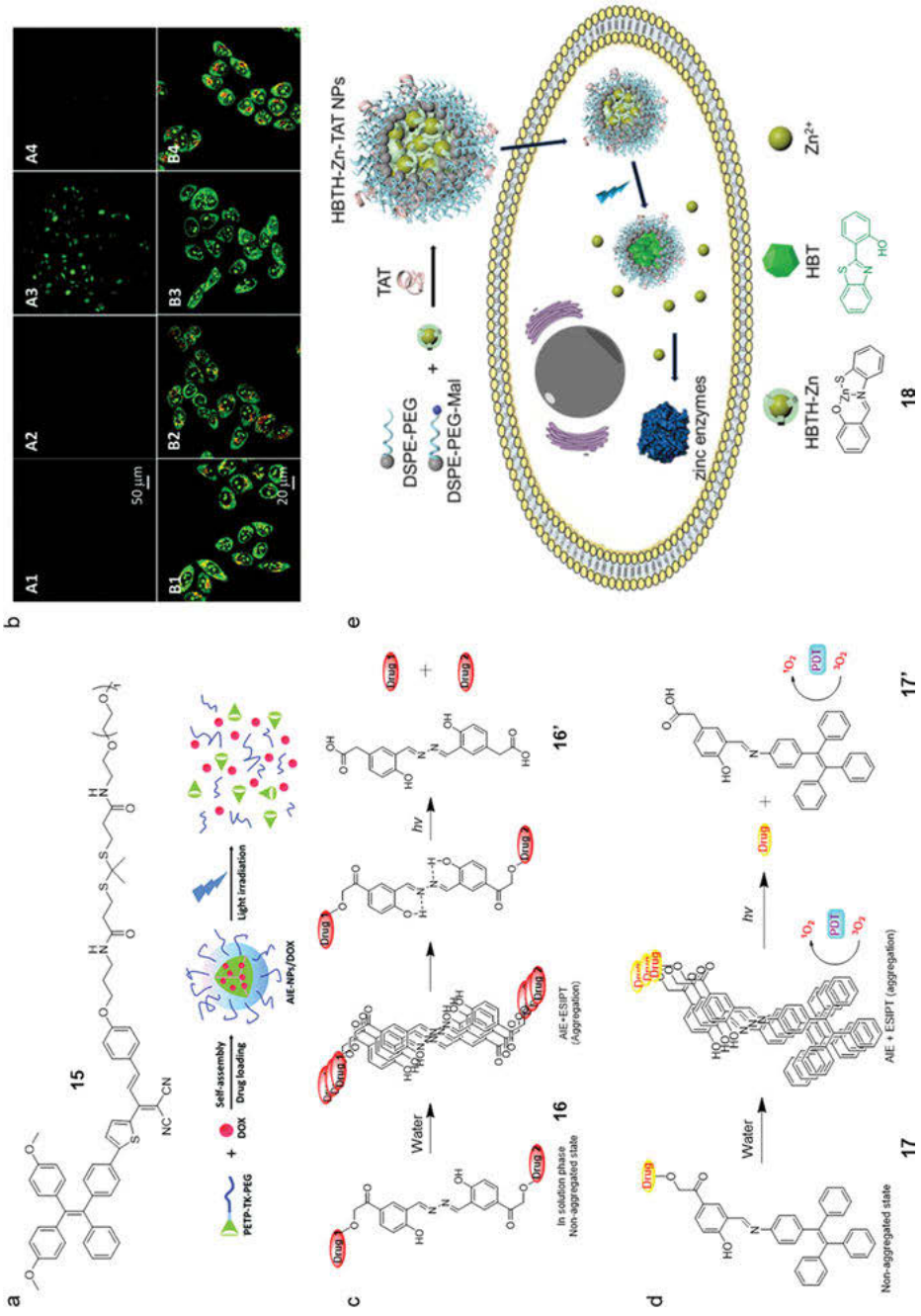


**Figure 11.8:** a) Molecular structure of a thioketal (TK)-bridged polymer **15** and illustration of the preparation of nanoparticles self-assembled from the mixture of **15** and anticancer drug doxorubicin (DOX) in aqueous media and the visible light-controlled drug release. b) Evaluation of

The photophysical properties of ESIPT, coupled with AIE, always presented excellent photophysical characteristics, including large Stokes shift, low inner-filter effect, and self-quenching. Singh et al. designed an intriguing photoactivatable drugs delivery system **16** with AIE and ESIPT properties via the easy introduction of a salicylaldazine unit into the *p*-hydroxyphenacyl (*p*HP) photo-trigger [85]. As shown in Figure 11.8c, the drugs were successfully released from system **16** upon visible light illumination, which were started with aggregation, and occurred from triplet excited states through rearrangement. Due to the properties of AIE and ESIPT, an obvious emission change from yellow to blue was observed, which was accompanied with the process of drug release, thus offering large opportunities to timely detect the drug release. What was more, the ability to release two different drugs sequentially of **16** indicated an effectively application in combined chemotherapy. Further, Singh and coworkers developed a synergistic therapy system **17**, combining the AIE and ESIPT effects, which was based on the light-triggered drug release of chemotherapy and PDT (Figure 11.8d) [86]. Thus, photoactivatable drug release has great potential for application in the field of biomedicine, due to its unique advantages, including green and tunable stimulation mode, high sensitivity, excellent spatiotemporal accuracy, and high signal-to-noise ratio. Tang et al. designed and synthesized **18** to realize precise photo-triggered $Zn^{2+}$ release, which is promising for the regulation of zinc enzymes (Figure 11.8e) [87]. The mixture of **18** as the $Zn^{2+}$ ligand, DSPE-PEG/DSPE-PEG-Mal polymer as matrix, and TAT peptide as the cell penetrating ligand formed into nanoparticles, could quickly release $Zn^{2+}$ under white light irradiation with a high spatiotemporal resolution. Thus, the extra- and intracellular zinc enzyme bioactivities are regulated successfully.

**Figure 11.8** (continued)
the ROS generation with indicator DCF-DA in in MDA-MB-231/DOX cells after incubation with AIE-NPs (A1), DCF-DA (A2), DCF-DA and AIE-NPs with light irradiation (A3), DCF-DA and AIE-NPs in the presence of ROS scavenger $A_{sc}$ with light irradiation (A4). Evaluation of membrane damage of endo-/lysosomes with indicator AO in MDA-MB-231/DOX cells treated with AO with light irradiation (B1), AIE-NPs and AO in the dark (B2), AIE-NPs and AO with white light irradiation (B3), AIE-NPs and AO in the presence of Asc with white light irradiation (B4). c) and d) Schematic illustration 'AIE + ESIPT' assisted photorelease from **16** and **17**, respectively. e) The design principle of the photo-triggered $Zn^{2+}$ release of **18** for the regulation of zinc enzyme activities. Reprinted with permission from Ref. [84]. Copyright © 2016 The Royal Society of Chemistry. Reprinted with permission from Ref. [85]. Copyright © 2018 The Royal Society of Chemistry. Reprinted with permission from Ref. [86]. Copyright © 2018 American Chemical Society. Reprint with permission from Ref. [87]. Copyright © 2021 The Royal Society of Chemistry and the Chinese Chemical Society.

## 11.4 Photoactivation assistant therapy

Over the past few decades, among the diseases, cancer has been the biggest challenge to human health[88, 89]. The diagnostics and therapeutics for cancer has been widely studied by many researchers. However, many therapeutic methods have lots of weaknesses, such as drug resistance, nontargeted therapy, and invisible treatment effect. In order to solve these problems, many researchers have utilized AIE materials as powerful tools for efficient therapy, including photo-controlled treatment reagent delivery, PDT, PTT, and so on [90, 91].

### 11.4.1 Photo-controlled chemotherapy

Compared to conventional chemotherapy for cancer with its drawbacks such as low therapeutic effect and toxicity of invalid targeting, photo-controlled chemotherapeutics is a more promising strategy that could achieve image-guided accurate manipulation of therapeutic dosage and site [92, 93]. However, so far, the development and application of conventional photoactivatable chemotherapeutics in clinic are still limited due to the tedious synthetic procedures and toxic byproducts. Thus, there is urgency to develop novel photoactivatable chemotherapeutics with simple synthetic methods and enhanced safety.

Fortunately, Tang and co-workers found that, based on a photooxidative dehydrogenation reaction, **19a** and **19b** could efficiently generate **19′a** and **19′b**, with a high in situ concentration *in situ*, which would kill selectively cancer cells (Figure 11.9a–c) [19]. Moreover, under the irradiation at 365 nm, both **19a** and **19b** could transform to **19′a** and **19′b** in aqueous solution by photooxidative dehydrogenation, which was confirmed by the decreased fluorescence intensity of **19a** and **19b** at 438 nm and 436 nm, respectively, and increased PL intensity of **19′a** and **19′b** at 584 nm and 602 nm, respectively. Notably, the in situ generated **19′a** from **19a** featured AIE characteristics, which could also be applied in image-guided cancer therapy with a high local concentration of chemotherapeutics. Then, the photoactivatable cytotoxicities of **19a** and **19b** were examined using the MTT assay. As shown in Figure 11.9d, e, under dark conditions, the cell viabilities were stable for cancer cells, including HeLa and A549, when treated with **19a** and **19b**. However, the corresponding cell viabilities decreased significantly after light irradiation for 5 min, which was due to the rapid generation of **19′a** and **19′b**, with the ability of killing cancer cells. Then, the obvious changes of fluorescence signal and cell morphology were also *in situ* monitored by imaging experiments after light irradiation. As shown in Figure 11.9f, g, after exposure under light for 3 min and further incubation under dark conditions for 10 min, a significantly decreased signal in nucleus was observed, indicating that karyolysis featured with the damage nuclei and dissolution of the chromatin. Simultaneously, cell swelling and membrane blistering were monitored because of cell apoptosis, induced by the

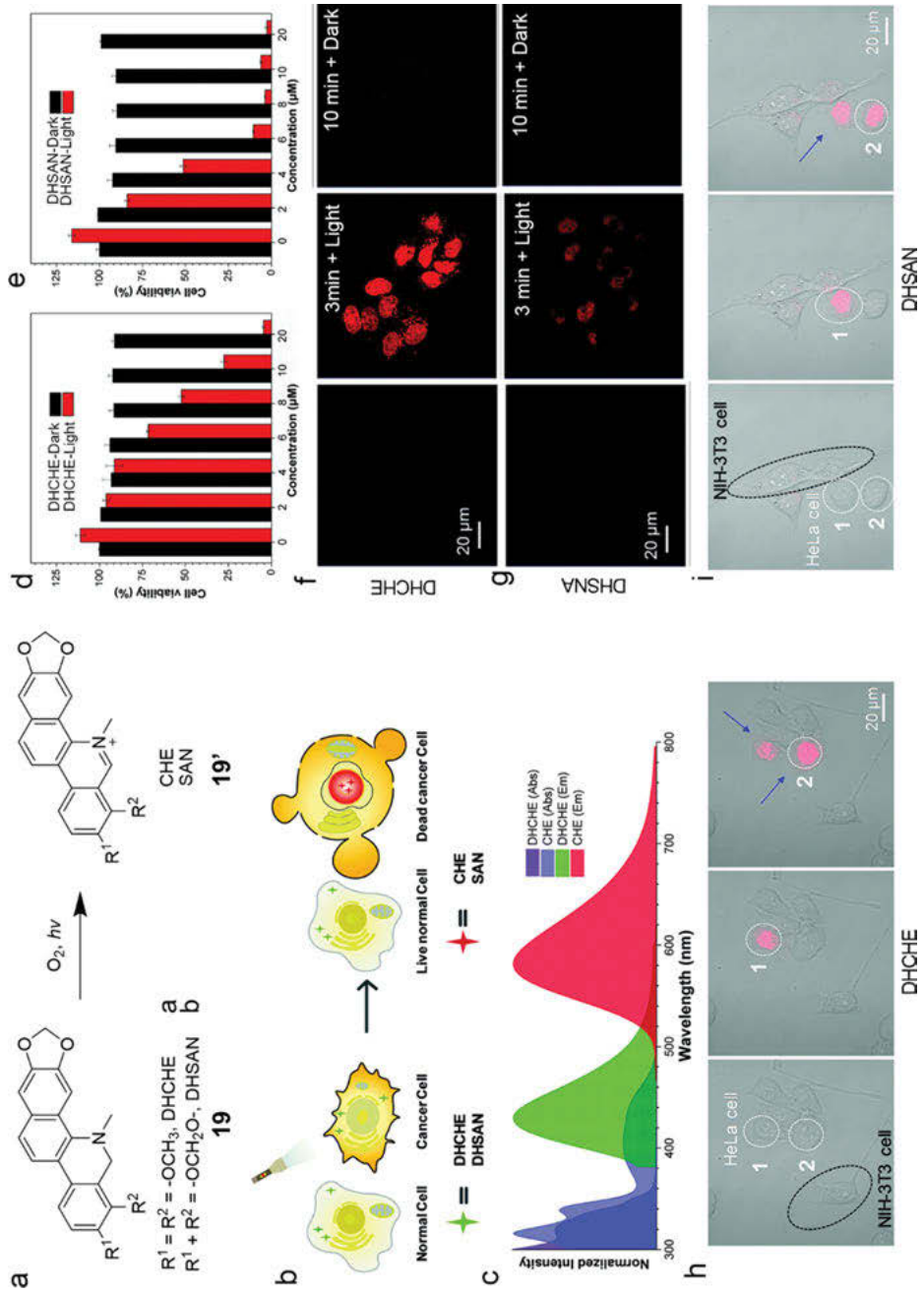


**Figure 11.9:** a) The reaction schematic for the transformation of **19** to **19′**. b) Illustration of the selectively killing cancer cells guided by the nucleus-targeted imaging. c) The normalized absorption and emission spectra of **19a** and **19′a**. Concentration-depended cell viabilities of HeLa

generated **19′a** and **19′b**. The ability of photoactivatable **19a** and **19b** for selectively killing cancer cells was also confirmed by co-culturing the Hela cancer cells and NIH-3T3 normal cells in a multi-cellular environment, which could be distinguished by their different morphological characteristics. After incubation with **19a** and **19b**, the HeLa cells could be selectively killed gradually under photoillumination, which was demonstrated by images of cancer cells with red fluorescence turn on in the nucleus and obvious membrane blisters (Figure 11.9h, i). It was indicated that the photoactivatable **19a** and **19b** could selectively kill cancer cells at the desired site with high accuracy, without harm to the normal cells.

## 11.4.2 Photo-controlled PDT

PDT, which employs PSs, light, and endogenous molecular oxygen to destroy the cell and tissue, is a kind of noninvasive clinical treatment [82, 83]. Especially in cancer therapy, PDT displayed a lot of advantages such as selectivity, microtrauma, high efficiency, and negligible drug resistance [94, 95]. For PDT, the key components are the PSs that can generate ROS, which are responsible for cytotoxicity and cell death under light irradiation. However, undesired long-lasting of photosensitivity and nonspecificity of PSs are unfavorable for disease treatment. Thus, to develop novel PSs, whose activity could be controlled, is attractive nowadays.

Feng et al. introduced spiropyrans into the cationic polymers (**20** and **20′**) to assemble plasmid DNA into the functional nanoparticles (NPs) [96]. As shown in Figure 11.10a, the spiropyran pendent groups could isomerize between a zwitterionic ring opened form (MC) and a hydrophobic ring closed form (SP). Under UV light irradiation, **20** with SP pendent switched to **20′** with MC pendent that had red fluorescence and ROS-generation ability, whose process was the opposite of excitation by visible light or thermal relaxation under the dark state. Thus, the emission and ROS-generation ability of NPs could be controlled reversibly, using light, to realize the dual functions of cell imaging and cell killing. The cell uptake of NPs was investigated by fluorescence imaging of HeLa cells, incubated with NPs, for 4 h. As shown in Figure 11.10b, bright red fluorescence was observed under simple UV light irradiation (Figure 11.10b: 1, 3, 5), which was contributed by the **20′** (MC); however, the red fluorescence disappeared after visible light irradiation due to the generation

**Figure 11.9** (continued)
cells incubated with d) **19a**, e) **19b** in dark and under light illumination. f) and g) Images of live HeLa cells incubated with **19a** and **19b** before or after light illumination at 405 nm for 3 min, and further incubation under dark conditions for 10 min. h) and i) Images of HeLa cancer cells and NIH-3T3 normal cells treated with **19a** and **19b**, respectively, and selectively killing of HeLa cancer cells with spatiotemporal red fluorescence turn on. The plasma membrane blebs are indicated by blue arrows. Reprinted with permission from Ref. [19]. Copyright © 2020 The Royal Society of Chemistry.

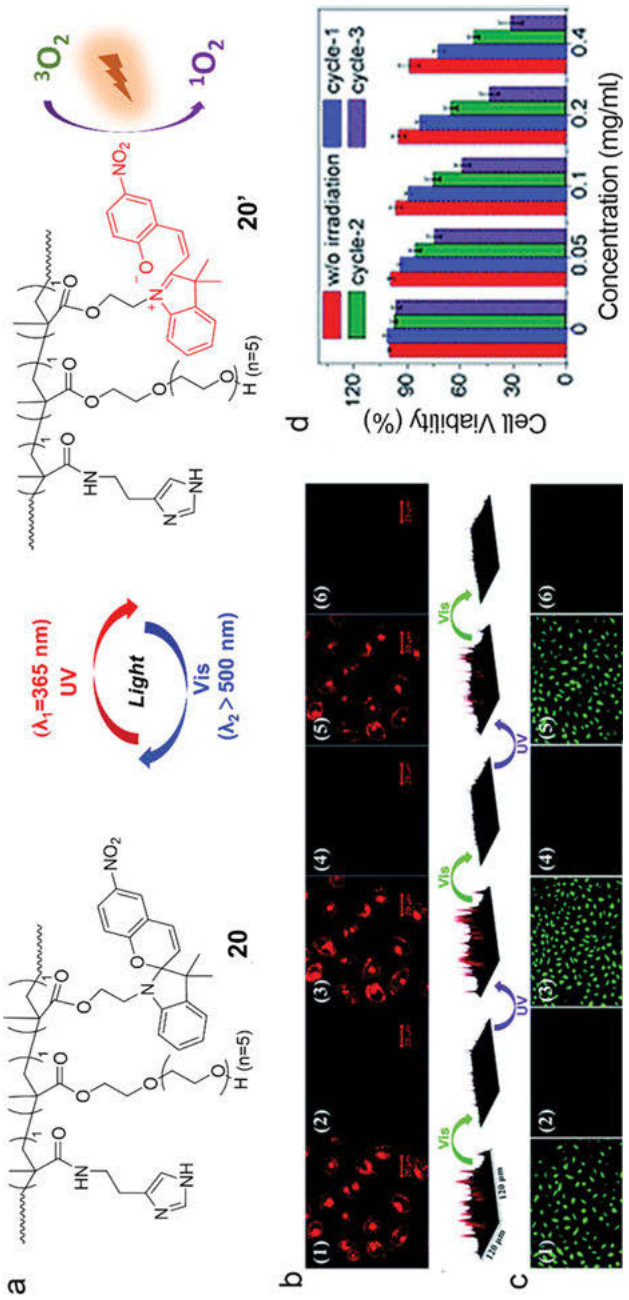


**Figure 11.10:** a) Schematic presentations of the transformation of **20** (SP) and **20'** (MC), and light-triggered ROS generation. b) Images and intensity profiles of HeLa cells incubated with **20** NPs under switchable UV and visible light treatments. c) Oxidized DCF fluorescence images after visible light irradiation on the **20** NPs-treated HeLa cells which were pre-treated by the switchable UV and visible light. d) Irradiation cycles-dependent MTT analysis of the **20** NPs-incubated HeLa cells under switchable UV and visible light treatments. Reprinted with permission from Ref. [96]. Copyright © 2018 The Royal Society of Chemistry.

of **20** (SP). Moreover, owing to the endolysosome barrier for the internalized nanoparticles, no fluorescence was observed in the nuclei, which was consistent with the previously studied polymer-based nucleic acid delivery systems.

The light-controlled reversible ROS-generation ability of the NPs in Hela cells was demonstrated by using DCF-DA as the indicator, whose fluorescence was very weak but can yield strong green emissive DCF, if oxidized by ROS. As shown in Figure 11.10c, the **20′**-abundant cells, which were exposed to UV light before going into the ROS detection procedure, presented bright green fluorescence from the ROS-induced DCF. However, negligible green emission was monitored in the thermally stable **20**-abundant cells, indicating no generation of ROS and hence, no DCF. Thus, the ROS level in cells could be manipulated by the selected light with desirable wavelengths at appropriate times, which is necessary for light-controlled PDT. However, the oxygen photosensitization capability of NPs would gradually lose due to the simultaneous transformation from **20′** to **20**, during the process of ROS generation under visible light irradiation, unless they were re-activated. Then, the treatment of the HeLa cells was carried out with successive alternating irradiation cycles, which included sequential UV light for re-activing the NPs to **20′** state and visible light for the generation of ROS. As shown in Figure 11.10d, an irradiation cycle-dependent cytotoxicity was observed, which correlated with the ROS accumulation level. After three irradiation cycles, about 70% of the HeLa cells were killed. Thus, the cytotoxic effect of NPs could be manipulated conveniently by controlling the number of irradiation cycles.

### 11.4.3 Photoactivatable immunotherapy

In the past few years, cancer immunotherapy has quickly become one of the most important methods of cancer therapy, owing to its ability to orchestrate the body's own immune system to target and eliminate tumor cells [97–99]. Compared to traditional treatments, immunotherapy may achieve permanent antitumor responses and inhibit metastasis and recurrence. Evidence has also been accumulated that the tumor microenvironment can be altered by ROS generation during PDT, and the inflammatory and immune mediators could also be recruited, which are favorable to prime the immune response [100, 101]. Thus, among the diverse immune-stimulating methods, photodynamic therapy (PDT), induced by ROS generated from PSs under light irradiation, has attracted wide attention, with an initial success.

Gu and coworkers developed a kind of polymeric fluorescent particles (PFPs) with uniform and adjustable sizes by precipitation polymerization of vinyl-modified AIEgen (**21**, TPE-VBC), maleic anhydride (MAH), and styrene (St) (Figure 11.11a) [102]. Owing to the AIE features of TPE-VBC, the as-prepared PFPs presented unique photophysical functionalities. What was more, due to the distribution of the anhydride groups on the surface of PFPs, it was convenient to realize the functionalization of

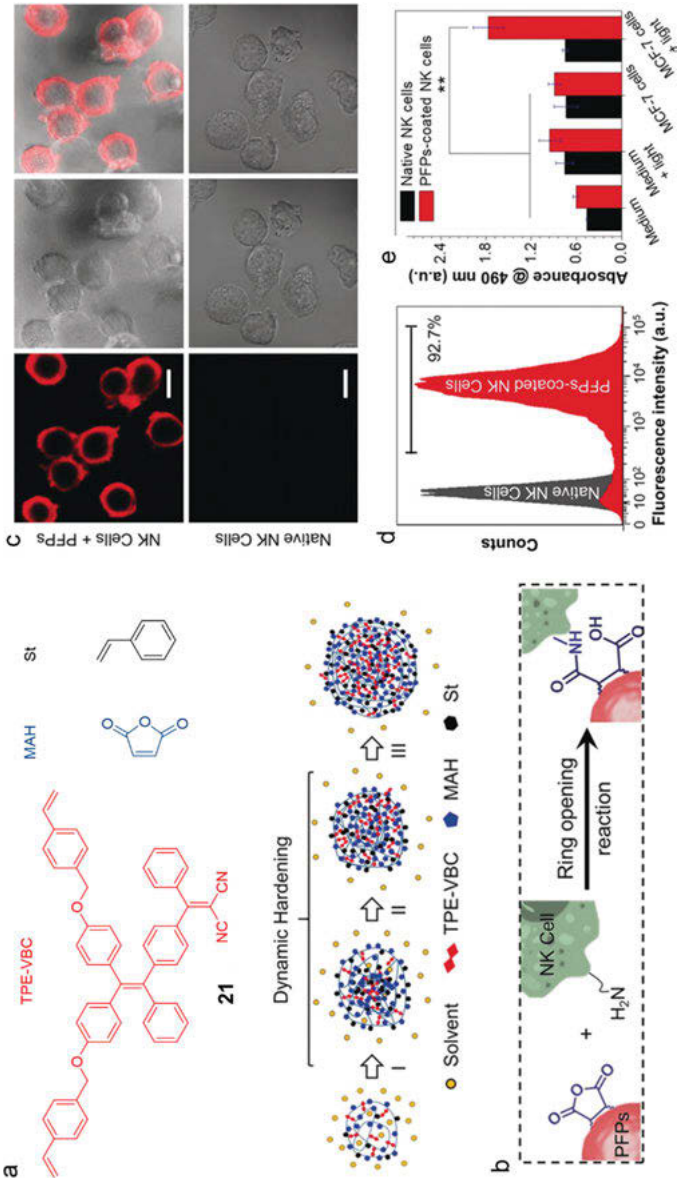


**Figure 11.11:** a) Chemical structures of the monomers used for the precipitation polymerization and illustration of the growth process in isopentyl acetate (IAAC) solution containing three stages (I, II, and III). b) Illustration of the biolabeling mechanism of PFPs and NK cells. c) Images of PFPs-coated NK cells and Native NK cells, respectively. d) Flow cytometer analysis of NK cells during the biolabeling of PFPs. e) Lytic activity of PFPs-coated NK cells under light irradiation. Reprinted with permission from Ref. [102]. Copyright © 2019 Wiley-VCH Verlag GmbH & Co. KGaA, Weinheim.

PFPs (Figure 11.11b). Thus, based on the biolabeling and photosensitizing abilities of PFPs, they were used for modulating the activity of Natural Killer (NK) cells to realize the light-controlled cancer immunotherapy.

As shown in Figure 11.11c, the strong red emission of **21** was monitored around the NK cells with PFPs labeling; however, no fluorescent emission could be observed in the native NK cells without PFPs marking. The membrane of the NK cells targeted by PFPs were also verified by the circular-shaped red fluorescence covering, which is the superficial part of the NK cells. Based on this strategy, a high labeling efficiency of about 97.2% was achieved within 1 h, when NK cells were coated with PFPs (Figure 11.11d), and a good biocompatibility was also confirmed by PFPs without any dark toxicity. The ROS-generation ability of PFPs, under light irradiation, was also confirmed by using DCFH-DA as indicator. Based on the ROS-sensitizing ability of PFPs, the immunotherapy efficiency of PFP-coated NK cells was regulated in the light-controlled way. By monitoring the levels of lactate dehydrogenase (LDH) release, the immunogenic phenotypes in cancer cells, induced by PFPs-coated NK cells under light irradiation, was evaluated. As shown in Figure 11.11e, the same LDH release level for PFPs-coated NK cells and native NK cells was demonstrated upon treatment of MCF-7 cancerous cells in the dark. However, PFPs-coated NK cells displayed distinct LDH release, from MCF-7 cancerous cells, after light irradiation, compared to that of the control group. The results demonstrated that NK cells coated with low-concentration PFPs kept its initial immunocompetence and such immunocompetence could be further promoted by PFPs under light irradiation in the PFPs-coated NK cells. It was due to the promoted generation of ROS of the TPE-VBC under light irradiation that it could activate the immunocompetence by ROS signal transduction of the NK cells.

### 11.4.4 Others

Besides, it is also necessary to develop fast and efficient methods for antimicrobial applications with high spatiotemporal accuracy due to urgency of increased drug-resistant bacteria. Based on the ROS-generation ability, many AIEgens as PSs were reported for antimicrobial application. Similar to photo-controlled PDT, based on ROS mentioned above, photo-controlled antimicrobial treatments are desirable for realizing accurate therapy, while photoacid generator, as one of the interesting photoresponsive materials, is also an important antimicrobial agent with infrequent bacterial resistance.

Recently, Tang and coworkers reported a kind of photoresponsive polysulfonates **22** by an in situ catalyst-free spontaneous polymerization of disulfonic acids and dihaloalkynes (Figure 11.12a), which could generate photoacid efficiently by undergoing photodegradation, accompanied by an obvious emission change [103]. After UV irradiation, the PH of bacteria resuspension containing **22** decreased from

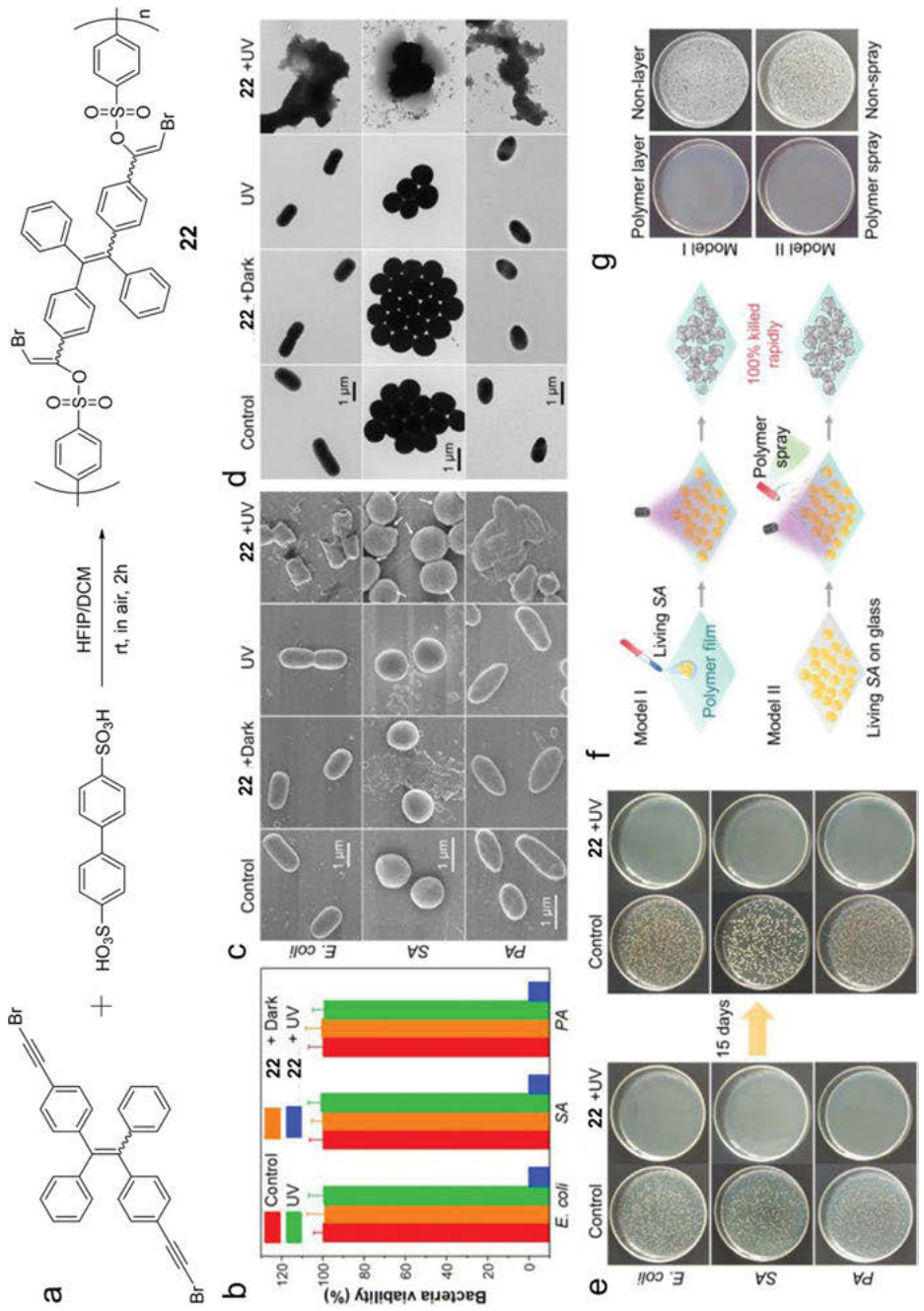


**Figure 11.12:** a) Catalyst-free polymerization of disulfonic acids and dihaloalkynes to **22**. b) Survival rates of *E. coli*, S. aureus (SA), and P. aeruginosa (PA) with/without treatment of **22** in the presence or absence of UV light irradiation. c) and d) Morphology change of bacteria upon diverse

6.7 to 2.3 due to the generation of photoacid, which was promising for bacterial killing. As shown in Figure 11.12b, three representative bacteria, such as Staphylococcus aureus, Escherichia coli and Pseudomonas aeruginosa, were used to evaluate the bacteria-killing ability of **22** by the traditional plate counting method. In the presence of **22**, all three bacteria were killed effectively without colony formation, under UV irradiation, indicating the excellent antibacterial effect of **22**, which was also verified by the obvious cell deformation, broken cells with the leakage of intracellular contents, and cell fragments of bacterial cells treated with **22** and UV light, by employing the measurement of SEM and TEM (Figure 11.12c and 11.12d). Moreover, after incubation, the bacteria treated with **22** and UV light at 37 °C for 15 days, no bacteria was observed on the agar plate, demonstrating the irreversible bacteria-killing effect of **22** (Figure 11.12e). The potential of polysulfonates as flexible antibacterial materials for different situations, including the surface sterilization of commodities, resistance to corrosion caused by microorganisms on ships, and customized bacterial scaffolds, was also demonstrated. The bacteria, S. aureus on the **22** coated glass (model I) or the bacteria treated with 22 spray (model II), was 100% killed after UV irradiation for 30 min (Figure 11.12f, g).

## 11.5 Conclusions and perspectives

In summary, the AIE-based photoactivatable materials not only have advantages, such as high sensitivity and accuracy, easy adjustability and noninvasiveness, but also showed bright fluorescence and excellent photostability in the aggregated state. Based on the advantages of the AIE-featured photoactivatable materials, various biomedical applications have been developed, such as organelle imaging, cell imaging, drug/gen delivery, and cancer therapy. Nevertheless, some challenges and problems also come into notice, which urgently need to be solved in the development of AIE-featured photoactivatable materials. First, the structures of AIE-featured small molecules with intrinsic photo-responsive properties or photo-responsive nanosystems with AIE characteristics applied in biology are still far from a variety of classifications. Therefore, there is urgency to develop new photo-responsive molecules or nanosystems *via* elaborate molecule engineering. Second, most photoactivatable AIE-featured photoactivatable materials work in the biological system, depending on the UV light irradiation, which not only limits penetration depth and spatial resolution,

**Figure 11.12** (continued)
treatments observed by SEM and TEM, respectively. e) Photographs of agar plates of *E. coli*, SA, and PA after 1 day and 15 days. f) Two antimicrobial methods for practical applications. g) Photographs of the agar plates from two antimicrobial methods. Reprinted with permission from Ref. [103]. Copyright © 2021 American Chemical Society.

but also photo-damage to the living organisms. Therefore, it is necessary to develop AIE-featured photoactivatable molecules that respond to visible or even near-infrared light, which could be more suitable for biomedical application.

## References

[1] Li W, Zheng G, Photoactivatable fluorophores and techniques for biological imaging applications, Photochem Photobiol Sci, 2012, 11, 460–471.
[2] Guo J, Fan J, Liu X, Zhao Z, Tang BZ, Photomechanical luminescence from through-space conjugated AIEgens, Angew Chem Int Ed, 2020, 59, 8828–8832.
[3] Huang G, Xia Q, Huang W, Tian J, He Z, Li SB, Tang BZ, Multiple anti-counterfeiting guarantees from a simple tetraphenylethylene derivative – High-contrasted and multi-state mechanochromism and photochromism, Angew Chem Int Ed, 2019, 58, 17814–17819.
[4] Qi Q, Li C, Liu X, Jiang S, Xu Z, Lee R, Zhu M, Xu B, Tian W, Solid-state photoinduced luminescence switch for advanced anticounterfeiting and super-resolution imaging applications, J Am Chem Soc, 2017, 139, 16036–16039.
[5] Lee HD, Lord SJ, Iwanaga S, Zhan K, Xie H, Williams JC, Wang H, Bowman GR, Goley ED, Shapiro L, Twieg RJ, Rao J, Moerner WE, Superresolution imaging of targeted proteins in fixed and living cells using photoactivatable organic fluorophores, J Am Chem Soc, 2010, 132, 15099–15101.
[6] Zheng Y, Zheng X, Xiang Y, Tong A, Photoactivatable aggregation-induced emission of triphenylmethanol, Chem Commun, 2017, 53, 11130–11133.
[7] Jang Y, Kim T, Kim H, Choi Y, Kim Y, A photoactivatable BODIPY platform: Light-triggered anticancer drug release and fluorescence monitoring, ACS Appl Bio Mater, 2019, 2(6), 2567–2572.
[8] Patterson GH, Lippincott-Schwartz J, A photoactivatable GFP for selective photolabeling of proteins and cells, Science, 2002, 297, 1873–1877.
[9] Politz JC, Use of caged fluorochromes to track macromolecular movement in living cells, Trends Cell Biol, 1999, 9, 284–287.
[10] Dempsey GT, Joshua CV, Chen KH, Bates M, Zhuang X, Evaluation of fluorophores for optimal performance in localization-based superresolution imaging, Nat Methods, 2011, 8, 1027–1040.
[11] Raymo FM, Photoactivatable synthetic dyes for fluorescence imaging at the nanoscale, J Phys Chem Lett, 2012, 3, 2379–2385.
[12] Luo W, Wang G, Photo-responsive fluorescent materials with aggregation-induced emission characteristics, Adv Opt Mater, 2020, 8, 2001362–2001380.
[13] Reisch A, Klymchenko AS, Fluorescent polymer nanoparticles based on dyes: Seeking brighter tools for bioimaging, Small, 2016, 12, 1968–1992.
[14] Swiecicki J-M, Thiebaut F, Pisa MD, Bertin SG, Tailhades J, Mausuy C, Burlina F, Chwetzoff S, Trugnan G, Chassaing G, Lavielle S, How to unveil self-quenched fluorophores and subsequently map the subcellular distribution of exogenous peptides, Sci Rep, 2016, 6, 20237–20234.
[15] Hong Y, Lam JWY, Tang BZ, Aggregation-induced emission, Chem Soc Rev, 2011, 40, 5361–5388.

[16] Luo J, Xie Z, Lam JWY, Cheng L, Chen H, Qiu C, Kwok HS, Zhan X, Liu Y, Zhu D, Tang BZ, Aggregation-induced emission of 1-methyl-1,2,3,4,5-pentaphenylsilole, Chem Commun, 2001, 18, 1740–1741.
[17] Xu W, Wang D, Tang BZ, NIR-II AIEgens: A win-win integration towards bioapplications, Angew Chem Int Ed, 2021, 60, 7476–7487.
[18] Cheng H-B, Li Y, Tang BZ, Yoon J, Assembly strategies of organic-based imaging agents for fluorescence and photoacoustic bioimaging applications, Chem Soc Rev, 2020, 49, 21–31.
[19] Ling X, Huang L, Li Y, Wan Q, Wang Z, Qin A, Gao M, Tang BZ, Photoactivatable dihydroalkaloids for cancer cell imaging and chemotherapy with high spatiotemporal resolution, Mater Horiz, 2020, 7, 2696–7701.
[20] Gao M, Tang BZ, AIE-based cancer theranostics, Coord Chem Rev, 2020, 402, 213076–213116.
[21] Wang J, Li J, Wang L, Han T, Wang D, Tang BZ, AIEgen-based polymer nanocomposites for imaging-guided photothermal therapy, ACS Appl Polym Mater, 2020, 2, 4306–4318.
[22] Gu X, Kwok RTK, Lam JWY, Tang BZ, AIEgens for biological process monitoring and disease theranostics, Biomaterials, 2017, 146, 115–135.
[23] Qin W, Yang Z, Jiang Y, Lam JWK, Liang G, Kwok HS, Tang BZ, Construction of efficient deep blue aggregation-induced emission luminogen from triphenylethene for nondoped organic light-emitting diodes, Chem Mater, 2015, 27(11), 3892–3901.
[24] Li Y, Zhong H, Huang Y, Zhao R, Recent advances in AIEgens for metal ion biosensing and bioimaging, Molecules, 2019, 24, 4593–4611.
[25] Day RN, Davidson MW, The fluorescent protein palette: Tools for cellular imaging, Chem Soc Rev, 2009, 38, 2887–2921.
[26] Gao M, Su H, Lin Y, Ling X, Li S, Qin A, Tang BZ, Photoactivatable aggregation-induced emission probes for lipid droplets-specific live cell imaging, Chem Sci, 2017, 8, 1763–1768.
[27] Zhong W, Zeng X, Chen J, Hong Y, Xiao L, Zhang P, Photoswitchable fluorescent polymeric nanoparticles for rewritable fluorescence patterning and intracellular dual-color imaging with AIE-based fluorogens as FRET donors, Polym Chem, 2017, 8, 4849–4855.
[28] Li S, Ling X, Lin Y, Qin A, Gao M, Tang BZ, In situ generation of photoactivatable aggregation-induced emission probes for organelle-specific imaging, Chem Sci, 2018, 9, 5730–5735.
[29] Gu X, Zhao E, Zhao T, Kang M, Gui C, Lam JWY, Du S, Loy MMT, Tang BZ, A mitochondrion-specific photoactivatable fluorescence turn-on AIE-based bioprobe for localization super-resolution microscope, Adv Mater, 2016, 28, 5064–5071.
[30] Cao Y-L, Meng S, Chen Y, Feng J-X, Gu -D-D, Yu B, Li J-Y, Liao S, Chan DC, Gao S, MFN1 structures reveal nucleotide-triggered dimerization critical for mitochondrial fusion, Nature, 542, 2017, 372–376.
[31] Chen WD, Zhang DW, Gong WT, et al., Aggregation-induced emission of a novel conjugated phosphonium salt and its application in mitochondrial imaging, Spectrochim Acta A Mol Biomol Spectrosc, 2013, 110, 471–473.
[32] Leung CWT, Hong Y, Chen S, Zhao E, Lam JWY, Tang BZ, A photostable AIE luminogen for specific mitochondrial imaging and tracking, J Am Chem Soc, 2013, 135, 62–65.
[33] Li Q, Gong J, Li Y, Zhang R, Wang H, Zhang J, Yan H, Lam JWY, Sung HHY, Williams ID, Kwok RTK, Li M-H, Wang J, Tang BZ, Unusual light-driven amplification through unexpected regioselective photogeneration of five-membered azaheterocyclic AIEgen, Chem Sci, 2021, 12, 709.
[34] Gao M, Hu Q, Feng G, Tang BZ, Liu B, A fluorescent light-up probe with “AIE + ESIPT” characteristics for specific detection of lysosomal esterase, J Mater Chem B, 2014, 2, 3438–3442.

[35] Lu P, Zheng Y, Wang X, Tong A, Xiang Y, Photoactivatable aggregation-induced emission fluorophores with multiple-color fluorescence and wavelength-selective activation, Chem Eur J, 2015, 21, 4326–4332.
[36] Chen J, Zhong W, Tang Y, Wu Z, Li Y, Yi P, Jiang J, Amphiphilic BODIPY-based photoswitchable fluorescent polymeric nanoparticles for rewritable patterning and dual-color cell imaging, Macromolecules, 2015, 48, 3500–3508.
[37] Klajn R, Spiropyran-based dynamic materials, Chem Soc Rev, 2014, 43, 148–184.
[38] Zhang Y, Zhang K, Wang J, Tian Z, Li ADQ, Photoswitchable fluorescent nanoparticles and their emerging applications, Nanoscale, 2015, 7, 19342–19357.
[39] Rad JK, Mahdavian AR, Salehi-Mobarakeh H, Abdollahi A, FRET phenomenon in photoreversible dual-color fluorescent polymeric nanoparticles based on azocarbazole/spiropyran derivatives, Macromolecules, 2016, 49, 141–152.
[40] Surendran K, Vitiello SP, Pearce DA, Lysosome dysfunction in the pathogenesis of kidney diseases, Pediatr Nephrol, 2014, 29, 2253–2261.
[41] Cheung NS, Peng ZF, Chen MJ, Moore PK, Whiteman M, Hydrogen sulfide induced neuronal death occurs via glutamate receptor and is associated with calpain activation and lysosomal rupture in mouse primary cortical neurons, Neuropharmacology, 2007, 53, 505–514.
[42] Kimura H, Hydrogen sulfide: Its production and functions, Exp Physiol, 2011, 96, 833–835.
[43] Hong Y, Zhang P, Wang H, Yu M, Gao Y, Chen J, Photoswitchable AIE nanoprobe for lysosomal hydrogen sulfide detection and reversible dual-color imaging, Sens Actuat B-Chem, 2018, 272, 340–347.
[44] Raymo FM, Photoactivatable synthetic fluorophores, Phys Chem Chem Phys, 2013, 15, 14840–14850.
[45] Shao Q, Xing B, Photoactive molecules for applications in molecular imaging and cell biology, Chem Soc Rev, 2010, 39, 2835–2846.
[46] Abramczyk H, Surmacki J, Kopec M, Olejnik AK, Lubecka-Pietruszewska K, Fabianowska-Majewska K, The role of lipid droplets and adipocytes in cancer. Raman imaging of cell cultures: MCF10A, MCF7, and MDA-MB-231 compared to adipocytes in cancerous human breast tissue, Analyst, 2015, 140, 2224–2235.
[47] Santos CR, Schulze A, Lipid metabolism in cancer, FEBS J, 2012, 279, 2610–2623.
[48] Tirinato L, Liberale C, Franco SD, Candeloro P, Benfante A, Rocca RL, Potze L, Marotta R, Ruffilli R, Rajamanickam VP, Malerba M, Angells FD, Falqui A, Carbone E, Todaro M, Medema JP, Stassi G, Fabrizio ED, Lipid droplets: A new player in colorectal cancer stem cells unveiled by spectroscopic imaging, Stem Cells, 2015, 33, 35–44.
[49] Cai S, Liu C, Gong J, Song H, Zhao L, Zeng X, A lysosome-targeted fluorescent probe for the specific detection and imaging of formaldehyde in living cells, Spectrochim Acta Part A, 2021, 245, 118949–11856.
[50] Liu Z, Wang Q, Zhu Z, Liu M, Zhao X, Wh Z, AIE-based nanoaggregate tracker: High-fidelity visualization of lysosomal movement and drug-escaping processes, Chem Sci, 2020, 11, 12755–12763.
[51] Wang H, Zhang P, Zhang C, Chen S, Zeng R, Cui J, Chen J, Rational A, Design of a cancer-specific and lysosome-targeted fluorescence nanoprobe for glutathione imaging in living cells, Mater Adv, 2020, 1, 1739–1744.
[52] Tran MN, Rarig RAF, Chenoweth DM, Synthesis and properties of lysosome-specific photoactivatable probes for live-cell imaging, Chem Sci, 2015, 6, 4508–4512.
[53] Gu X, Zhao E, Lam JWY, Peng Q, Xie Y, Zhang Y, Wong KS, Sung HHY, Williams ID, Tang BZ, Mitochondrion-specific live-cell bioprobe operated in a fluorescence turn-on manner and a well-designed photoactivatable mechanism, Adv Mater, 2015, 27, 7093–7100.

[54] Betzig E, Single molecules, cells, and super-resolution optics (Nobel Lecture), Angew Chem Int Ed, 2015, 54, 8034–8053.
[55] Liu Z, Liu J, Wang X, Mi F, Wang D, Wu C, Fluorescent bioconjugates for super-resolution optical nanoscopy, Bioconjug Chem, 2020, 31, 1857–1872.
[56] Xu Y, Xu R, Wang Z, Zhou Y, Shen Q, Ji W, Dang D, Meng L, Tang BZ, Recent advances in luminescent materials for super-resolution imaging via stimulated emission depletion nanoscopy, Chem Soc Rev, 2021, 50, 667–690.
[57] Antaris AL, Chen H, Cheng K, Sun Y, Hong G, Qu C, Diao S, Deng Z, Hu X, Zhang B, Zhang X, Yaghi OK, Alamparambil ZR, Hong X, Cheng Z, Dai H, A small-molecule dye for NIR-II imaging, Nat Mater, 2016, 15, 235–242.
[58] Ho I-T, Sessler JL, Gambhir SS, Jokerst JV, Parts per billion detection of uranium with a porphyrinoid-containing nanoparticle and in vivo photoacoustic imaging, Analyst, 2015, 140, 3731–3737.
[59] Lovell JF, Jin CS, Huynh E, Jin H, Kim C, Rubinstein JL, Chan WCW, Cao W, Wang LV, Zheng G, Porphysome nanovesicles generated by porphyrin bilayers for use as multimodal biophotonic contrast agents, Nat Mater, 2011, 10, 324–332.
[60] Pu K, Mei J, Jokerst JV, Hong G, Antaris AL, Chattopadhyay N, Shuhendler AJ, Kurosawa T, Zhou Y, Gambhir SS, Bao Z, Rao J, Diketopyrrolopyrrole-based semiconducting polymer nanoparticles for in vivo photoacoustic imaging, Adv Mater, 2015, 27, 5184–5190.
[61] Qi J, Chen C, Zhang X, Hu X, Ji S, Kwok RTK, Lam JWY, Ding D, Tang BZ, Light-driven transformable optical agent with adaptive functions for boosting cancer surgery outcomes, Nat Commun, 2018, 9, 1848–1860.
[62] Petermayer C, Dube H, Indigoid photoswitches: Visible light responsive molecular tools, Acc Chem Res, 2018, 51, 1153–1163.
[63] Chen K, Zhang R, Li G, Li B, Ma Y, Sun M, Wang Z, Tang BZ, Photo-induced crystallization with emission enhancement (PICEE), Mater Horiz, 2020, 7, 3005–3010.
[64] Gu Z, Wang Q, Shi Y, Huang Y, Zhang J, Zhang X, Lin G, Nanotechnology-mediated immunochemotherapy combined with docetaxel and PD-L1 antibody increase therapeutic effects and decrease systemic toxicity, J Control Release, 2018, 286, 369–380.
[65] Mao B, Liu C, Zheng W, Li X, Ge R, Shen H, Guo X, Lian Q, Shen X, Li C, Cyclic cRGDfk peptide and chlorin e6 functionalized silk fibroin nanoparticles for targeted drug delivery and photodynamic therapy, Biomaterials, 2018, 161, 306–320.
[66] Cho K, Wang X, Nie S, Chen Z, Shin DM, Therapeutic nanoparticles for drug delivery in cancer, Clin Cancer Res, 2008, 14, 1310–1316.
[67] Hoare T, Timko BP, Santamaria J, Goya GF, Irusta S, Lau S, Stefanescu CF, Lin D, Langer R, Kohane DS, Magnetically triggered nanocomposite membranes: A versatile platform for triggered drug release, Nano Lett, 2011, 11, 1395–1400.
[68] Mura S, Nicolas J, Couvreur P, Stimuli-responsive nanocarriers for drug delivery, Nat Mater, 2013, 12, 991–1003.
[69] Kuchelmeister HY, Gutschmidt A, Tillmann S, Knauer S, Schmuck C, Efficient gene delivery into cells by a surprisingly small three-armed peptide ligand, Chem Sci, 2012, 3, 996–1002.
[70] Luo K, He B, Wu Y, Shen Y, Gu Z, Functional and biodegradable dendritic macromolecules with controlled architectures as nontoxic and efficient nanoscale gene vectors, Biotechnol Adv, 2014, 32, 818–830.
[71] Yuan Y, Zhang CJ, Liu B, A photoactivatable AIE polymer for light-controlled gene delivery: Concurrent endo/lysosomal escape and DNA unpacking, Angew Chem Int Ed, 2015, 54, 1141–11423.
[72] Tu Y, Peng F, White PB, Wilson DA, Redox-sensitive stomatocyte nanomotors: Destruction and drug release in the presence of glutathione, Angew Chem, 2017, 129, 7728–7732.

[73] Xue X, Jin S, Zhang C, Yang K, Huo S, Chen F, Zou G, Liang X-J, Probe-inspired nano-prodrug with dual-color fluorogenic property reveals spatiotemporal drug release in living cells, ACS Nano, 2015, 9, 2729–2739.
[74] Yatvin MB, Weinsteion JN, Dennis WH, Blumenthal R, Design of liposomes for enhanced local release of drugs by hyperthermia, Science, 1978, 202, 1290–1293.
[75] Shim MS, Kwon YJ, Stimuli-responsive polymers and nanomaterials for gene delivery and imaging applications, Adv Drug Deliver Rev, 2012, 64, 1046–1059.
[76] Wang Y, Deng Y, Luo H, Zhu A, Ke H, Yang H, Chen H, Light-responsive nanoparticles for highly efficient cytoplasmic delivery of anticancer agents, ACS Nano, 2017, 11, 12134–12144.
[77] Yao C, Wang P, Li X, Hu X, Hou J, Wang L, Zhang F, Near-infrared-triggered azobenzene-liposome/upconversion nanoparticle hybrid vesicles for remotely controlled drug delivery to overcome cancer multidrug resistance, Adv Mater, 2016, 28, 9341–9348.
[78] Goodman AM, Neumann O, Norregaard K, Henderson L, Choi M-R, Clare SE, Halas NJ, Near-infrared remotely triggered drug-release strategies for cancer treatment, PNAS, 2017, 114, 12419–12424.
[79] Liu M, Li C, Recent advances in activatable organic photosensitizers for specific photodynamic therapy, Chempluschem, 2020, 85, 948–957.
[80] Nguyen J, Szoke FC, Nucleic acid delivery: The missing pieces of the puzzle? Acc Chem Res, 2012, 45, 1153–1162.
[81] Shi L, Wu W, Duan Y, Xu L, Li S, Gao X, Liu B, Carrier-free hybrid DNA nanoparticles for light-induced self-delivery of functional nucleic acid enzymes, ACS Nano, 2021, 15, 1841–1849.
[82] Dai J, Wu X, Ding S, Lou X, Fan X, Wang S, Hong Y, Aggregation-induced emission photosensitizers: From molecular design to photodynamic therapy, J Med Chem, 2020, 63, 1996–2012.
[83] Yi G, Hong SH, Son J, Yoo J, Park C, Choi Y, Koo H, Recent advances in nanoparticle carriers for photodynamic therapy, Quant Imaging Med Surg, 2018, 8, 433–443.
[84] Yuan Y, Xu S, Zhang C-J, Liu B, Light-responsive AIE nanoparticles with cytosolic drug release to overcome drug resistance in cancer cells, Polym Chem, 2016, 7, 3530–3539.
[85] Biswas S, Mengji R, Barman S, Venugopal V, Jana A, Singh NDP, 'AIE + ESIPT' assisted photorelease: Fluorescent organic nanoparticles for dual anticancer drug delivery with real-time monitoring ability, Chem Commun, 2018, 54, 168–171.
[86] Parthiban C, Pavithra M, Vinod Kumar Reddy L, Dwaipayan S, Melvin Samuel S, Ndp S, Visible-light -triggered fluorescent organic nanoparticles for chemo-photodynamic therapy with real-time cellular imaging, ACS Appl Nano Mater, 2018, 1, 6281–6288.
[87] Zhang M, Jia Y, Gao M, Ren L, Tang BZ, Photo-triggered $Zn^{2+}$ release for the regulation of zinc enzymes, Mater Chem Front, 2021, 5, 1824–1829.
[88] Bray F, Ferlay J, Soerjomataram I, Siegel RL, Torre LA, Jemal A, Global cancer statistics 2018: GLOBOCAN estimates of incidence and mortality worldwide for 36 cancers in 185 countries, CA Cancer J Clin, 2018, 68, 394–424.
[89] Smith RA, Andrews KS, Brooks D, Fedewa SA, Manassaram-Baptiste D, Saslow D, Brawley OW, Wender RC, Cancer screening in the United States, 2017: A review of current American Cancer Society guidelines and current issues in cancer screening, CA Cancer J Clin, 2017, 67, 100–121.
[90] Wang D, Lee MMS, Xu W, Kwok RTK, Lam JWY, Tang BZ, Theranostics based on AIEgens, Theranostics, 2018, 8, 4925–4956.
[91] Yi X, Li J, Zhu Z, Liu Q, Xue Q, Ding D, In vivo cancer research using aggregation-induced emission organic nanoparticles, Drug Discov Today, 2017, 22, 1412–1420.
[92] Galmarini D, Galmarini CM, Galmarini FC, Cancer chemotherapy: A critical analysis of its 60 years of history, Crit Rev Oncol Hemat, 2012, 84, 181–199.

[93] Hansen MJ, Feringa FM, Kobauri P, Szymanski W, Medema RH, Feringa BL, Photoactivation of MDM2 inhibitors: Controlling protein-protein interaction with light, J Am Chem Soc, 2018, 140, 13136–13141.
[94] Castano AP, Mroz P, Hamblin MR, Photodynamic therapy and anti-tumour immunity, Nat Rev Cancer, 2006, 6, 535–545.
[95] Fan H, Yan G, Zhao Z, Hu X, Zhang W, Liu H, Fu X, Fu T, Zhang X-B, Tan W, A smart photosensitizer-manganese dioxide nanosystem for enhanced photodynamic therapy by reducing glutathione levels in cancer cells, Angew Chem Int Ed, 2016, 55, 5477–5482.
[96] Ji J, Li X, Wu T, Feng F, Spiropyran in nanoassemblies as a photosensitizer for photoswitchable ROS generation in living cells, Chem Sci, 2018, 9, 5816–5821.
[97] Kheir GB, Aoun F, Roumeguere T, CD47 targeted near-infrared photo-immunotherapy: A promising tool combining monoclonal antibodies and photodynamics for treating human bladder cancer, Transl Androl Urol, 2019, 8, 779–780.
[98] Hanci D, Sahin E, Muluk NB, Cingi C, Immunotherapy in all aspects, Eur Arch Otorhinolaryngol, 2016, 273, 1347–1355.
[99] Zhang X, Tang J, Li C, Lu Y, Cheng L, Liu J, A targeting black phosphorus nanoparticle based immune cells nano-regulator for photodynamic/photothermal and photo-immunotherapy, Bioact Mater, 2021, 6, 472–489.
[100] Banerjee S, Ghosh S, Mandal A, Ghosh N, Sil PC, ROS-associated immune response and metabolism: A mechanistic approach with implication of various diseases, Arch Toxicol, 2020, 94, 2293–2317.
[101] Myers AL, Harris CM, Choe KM, Brennan CA, Inflammatory production of reactive oxygen species by Drosophila hemocytes activates cellular immune defenses, Biochem Biophys Res Commun, 2018, 505, 726–732.
[102] Wang G, Zhou L, Zhang P, Zhao E, Zhou L, Chen D, Sun J, Gu X, Yang W, Tang BZ, Fluorescence self-reporting precipitation polymerization based on aggregation-induced emission for constructing optical nanoagents, Angew Chem Int Ed, 2020, 59, 10122–10128.
[103] Liu X, Liang X, Hu Y, Han L, Qu Q, Liu D, Guo J, Zeng Z, Bai H, Kwok RTK, Qin A, Lam JWY, Tang BZ, Catalyst-free spontaneous polymerization with 100% atom economy: Facile synthesis of photoresponsive polysulfonates with multifunctionalities, JACS Au, 2021, 1, 344–353.

# Index



https://doi.org/10.1515/9783110672220-012